TESIS DOCTORAL

NUEVOS CATALIZADORES PARA LA DEGRADACIÓN FOTOCATALÍTICA DE CONTAMINANTES EN AGUA

Ana María Chávez Águedo

MODELIZACIÓN Y EXPERIMENTACIÓN EN CIENCIA Y TECNOLOGÍA

2020

UNIVERSIDAD DE EXTREMADURA

TESIS DOCTORAL

TÍTULO:

NUEVOS CATALIZADORES PARA LA DEGRADACIÓN FOTOCATALÍTICA DE CONTAMINANTES EN AGUA

NEW CATALYSTS FOR PHOTOCATALYTIC DEGRADATION OF POLLUTANTS IN WATER

AUTORA:

ANA MARÍA CHÁVEZ ÁGUEDO

PROGRAMA DE DOCTORADO EN:

MODELIZACIÓN Y EXPERIMENTACIÓN EN CIENCIA Y TECNOLOGÍA

CONFORMIDAD DE LOS DIRECTORES:

Fdo:	Fdo:	Fdo:
Fernando J. Beltrán Novillo	Pedro M. Álvarez Peña	Ana Rey Barroso

2020

A mis padres, hermano
y Carlos

Este trabajo ha sido posible gracias al soporte económico recibido a través del Ministerio de Economía y Competitividad (MINECO), Junta de Extremadura, co-financiados a su vez por los Fondos Europeos de Desarrollo Regional (FEDER).

Llegados a este punto, no puedo dar por finalizado mi trabajo sin antes agradecer a todas las personas que me han acompañado y apoyado en esta ardua etapa.
Parte de este trabajo ha sido gracias a todos vosotros.
A todos, muchas gracias.

Failure is not an option.
Gene Kranz, NASA

INDEX

Relevance of the Thesis

Preface

The Doctoral Thesis hereby has been developed within the PhD program "Modelización y Experimentación en Ciencia y Tecnología" following a research line of the "Trataguas" research group, from the Departamento de Ingeniería Química y Química Física and Instituto Universitario de Investigación del Agua, Cambio climático y Sostenibilidad (IACYS) at the University of Extremadura. The research activity has focused on water treatment methods, particularly on advanced oxidation processes (AOPs) based on ozone and radiation for the removal of contaminants of emerging concern (CECs). More specifically, a number of new photocatalysts have been synthesized and their activity in combination with ozone and/or different low-cost radiation sources have been investigated. The research has been economically supported with funds from several projects: "CTQ2012-35789-C02-01: *Preparación de catalizadores y su aplicación en la eliminación de contaminantes refractarios de aguas residuales mediante ozonación fotocatalítica*" and "CTQ2015-64944-R: *LED y fotocatalizadores polifuncionales basados en grafeno y estructuras metal-orgánicas para el tratamiento de aguas por ozonación fotocatalítica"* financed by the Ministerio de Economía y Competitividad (Spain); and group research grants GR 18014 and GR15033, financed by the Junta de Extremadura. Moreover, a fellowship for a predoctoral contract (ref: BES-2013-064186, call 2013) and a predoctoral research short stay (ref: EEBB-I-2016-11456, call 2016) were granted by the aforementioned Ministery. As a result of the latter, a part of this study was carried out at the Laboratory of Separation and Reaction Engineering - Laboratory of Catalysis and Materials (LSRE-LCM) at the University of Porto (Portugal).

THESIS ORGANIZATION

The Thesis hereby has been written meeting the requirements of the doctoral program "Modelización y Experimentación en Ciencia y Tecnología" from the Universidad de Extremadura" and according to the current academic rules for the International Mention in the PhD Degree. Hence, the Thesis is written in English, but additionally, the "Summary" and "Conclusions" chapters are also written in Spanish.

This work is presented as a collection of research articles, which either have been already published or submitted for publication to international scientific journals. For a better comprehension, this book has been organized into ten chapters as follows:

CHAPTER I contains a summary of the whole content of this work.

CHAPTER II provides the state of the art and background information about the issue of this study, highlighting the presence of contaminants in water bodies and the different alternative methods for their removal. Fundamentals of the processes, catalysts and contaminants used in this work are also considered in this chapter.

CHAPTER III details the description of the materials, methodology and the analytical methods employed in this work.

The most relevant results and discussion are given in chapters IV to IX, which are organized as research papers. Each of them contains the following sections: Abstract, Introduction, Materials and Methods, Results and Discussion, Conclusions and References.

CHAPTER IV is already published as a regular research paper entitled "*Solar photo-ozonation: A novel treatment method for the degradation of water pollutants*" in Journal of Hazardous Materials. It focuses on the influence of solar radiation on the decomposition of aqueous ozone for further application in the removal of contaminants.

CHAPTER V has been recently submitted as a regular research paper to Chemical Engineering Journal with the title "*Solar photocatalytic ozonation of contaminants of emerging concern and effluent organic matter in secondary effluents by a reusable magnetic catalyst*". It deals with the synthesis of a magnetic TiO_2/Fe_3O_4/activated carbon composite and its use as

a photocatalyst for the removal of four CECs and effluent organic matter of real and simulated effluents from municipal wastewater treatment plants.

CHAPTER VI examines the treatment of an industrial wastewater aimed to incineration by means of a feasible activated sludge process in a sequential batch reactor coupled with advanced oxidation processes based on ozone. This work, entitled "*Treatment of highly polluted industrial wastewater by means of sequential aerobic biological oxidation-ozone based AOP*", is already published in Chemical Engineering Journal.

CHAPTER VII deals with the optimization of the synthesis of a new magnetic carbon composite based on graphene and TiO_2. This composite was further used as catalyst in the photocatalytic ozonation of a real wastewater matrix doped with a mixture of ten CECs. This research has been published in the journal Applied Catalysis B: Environmental, under the title "*Magnetic graphene TiO_2-based photocatalyst for the removal of pollutants of emerging concern in water by simulated sunlight aided photocatalytic ozonation*".

CHAPTER VIII is a trending research which studies the photocatalytic ozonation in a more realistic scenario, leading to detect and quantify the contaminants in real urban wastewater with the goal of applying UVA-LED technology for their removal in continuous operation mode. This work was partially carried out in Porto (Portugal) during a short research stay, mandatory to obtain the International Mention in the PhD. It is available in the open access journal Catalysts, as "*Removal of organic micropollutants from a municipal wastewater secondary effluent by UVA-LED photocatalytic ozonation*".

CHAPTER IX is a preliminary investigation on the suitability of the metal organic framework designated as MIL-100(Fe) as a porous photocatalytic material. The stability of the material in water and under typical conditions of advanced oxidation processes is addressed. This work has been very recently submitted to Applied Catalysis B: Environmental with the title "*Insights into the stability and catalytic activity of MIL-100 (Fe) for different advanced oxidation processes*".

CHAPTER X summarizes the final conclusions of this research.

Finally, the APPENDIX section provides the accepted journal publications in addition to congress communications, showing their corresponding abstract and/or poster.

OBJECTIVES

Being granted with a pre-doctoral contract gave the opportunity to participate in national projects "CTQ2012-35789-C02-01" and "CTQ2015-64944-R". Thus, the objectives of this work have also been linked to the development of the aims of these projects.

The main objective of this Thesis is focused on the suitability of different novel materials for the removal of different contaminants in water by means of advanced oxidation processes, i.e. photocatalysis or ozone-based processes, using different radiation sources. For this purpose, other objectives and more specific goals were developed.

OBJECTIVE 1: Influence of solar radiation in the water photo-ozonation process.

Ozonation is a very complex process to understand, where different variables concerning the ozone decomposition such as pH, ions or radiation among others might play an important role. However, the influence of solar radiation had not been studied, so far.

1.1. Evaluation of the different wavelength ranges from the solar spectrum in the decomposition of aqueous ozone at different pHs.
1.2. Determination of the role of hydrogen peroxide as by-product during the photo-ozonation process.
1.3. Finding a kinetic model of aqueous ozone decomposition under illumination at pH 4.
1.4. Evaluation of the hydroxyl radical concentration in the solar photolytic ozonation using oxalic acid as a model compound.
1.5. Validation of the results obtained through the degradation of four contaminants of emerging concern in a synthetic secondary effluent by photo-ozonation.

OBJECTIVE 2: Application of the solar photocatalytic ozonation using a magnetic recoverable activated carbon-titania composite for the degradation of organic matter in urban or industrial wastewater.

TiO_2 onto magnetic activated carbon was previously optimized by the research group, succeeding in the degradation of metoprolol in ultrapure water. Going further, the photocatalyst has been proposed in order to assess its efficiency in the treatment of different wastewater matrixes. Depending on the water matrix, two sets of goals are considered.

Treatment of municipal secondary wastewater

2.1. Comparison of the photo-activity of the material in a real and synthetic effluent.
2.2. Assessing the influence of the organic and typical inorganic matter employing the solar photocatalytic ozonation.
2.3. Evaluation of the stability of the photocatalyst facing consecutive solar photocatalytic ozonation runs.

Treatment of highly polluted wastewater

2.4. Characterization of the industrial wastewater, including organic and inorganic chemicals.
2.5. Planning a feasible and sustainable process to treat the industrial wastewater, dealing with biological oxidation and ozone-based processes as cost-effective treatments.
2.6. Acclimation of the activated sludge bacteria to a diluted industrial wastewater in a short period.
2.7. Evaluation of the effectiveness of different ozonation processes after biological oxidation of the industrial wastewater in terms of global parameters and toxicity.
2.8. Fulfill the legal requirements for the discharge of treated wastewater into the aquatic environment.

OBJECTIVE 3: Preparation of a magnetic recoverable graphene and TiO_2 composite to be used in water treatment.

After studying the efficiency of TiO_2-magnetic activated carbon, a new carbonaceous composite based on graphene has been prepared and tested as photocatalyst in water treatment.

3.1. Preparation of a magnetic recoverable photoactive catalyst with titania onto graphene.

3.2. Characterization of the catalyst properties and evaluation of its activity in the degradation of contaminants of emerging concern, refractory to ozone, in ultrapure water using simulated solar light.
3.3. Optimization of the synthesized material varying the graphene:magnetite ratio and the TiO_2 load.
3.4. Evaluation of the reusability of the catalyst in the most effective treatment applied.
3.5. Determination of the applicability in a real wastewater effluent spiked with a mixture of ten contaminants.

OBJECTIVE 4: Application of commercial titania for the removal of contaminants of a real wastewater effluent using UVA-LEDs.

Different radiation sources may be employed for the generation of hydroxyl radicals. With the aim to reduce some costs and make a treatment more feasible at larger scale, titania coated glass rings in combination with UVA-LEDs were proposed for the photocatalytic ozonation.

4.1. Detection and quantification of organic micropollutants in a real secondary effluent.
4.2. Evaluation of the efficiency of photocatalytic processes using UVA-LEDs as a new radiation source.
4.3. Performing the photocatalytic processes in continuous operation using supporting glass materials with commercial titania (TiO_2 P25).
4.4. Characterization of the continuous reactor.
4.5. Evaluation of the reaction pathways of hydroxyl radicals or molecular ozone in the ozonation processes.

OBJECTIVE 5: Preparation of a metal organic framework material to be used as catalyst in different advanced oxidation processes.

Metal organic frameworks (MOFs) are very versatile materials used in several applications. Some MOFs like MIL-100(Fe) having a large surface area as well as a great photocatalytic activity under illumination, even using visible radiation, have been reported. In this sense, MOFs may be an alternative to titania. However, this field is still developing and quite uncertainty exists about the actual catalytic activity and stability.

5.1. Synthesizing a Fe-based MOF in water, specifically the MIL-100(Fe), using an eco-friendly method.

5.2. Characterization of the synthetized MIL-100(Fe) materials.

5.3. Assessing the stability of MIL-100(Fe) in water at different pHs and also in oxidizing environments similar to advanced oxidation processes based on simulated solar radiation, ozone and hydrogen peroxide.

5.4. Purification of the MIL-100(Fe) material using advanced oxidation treatments prior to its use for contaminants removal.

5.5. Evaluation of its catalytic activity and stability during the treatment of a mixture of contaminants of emerging concern in water applying the processes of heterogeneous Fenton-like and photo-Fenton-like, catalytic ozonation and photocatalytic ozonation.

SUMMARY
RESUMEN

CHAPTER 1

SUMMARY

Human activity is causing damaging effects on the environment. The disruption of ecosystems due to pollution and poor management of water resources are issues of great concern nowadays. This fact has warned public organisms, to increasingly impose more restrictive water quality policies. In Europe, Directive 2013/39/EU and Decision 2018/840/EU establish the regulation of 45 priority substances and a watch list for monitoring with other 8 groups, respectively. In this sense, contaminants of emerging concern (CECs) are of special relevance. In spite of the relatively low concentration of CECs in different water bodies, their extensive use, difficulty to be removed by conventional methods in wastewater treatment plants (WWTPs) and the lack of knowledge about their toxicity at long term, make necessary the design of new alternative processes for water treatment.

One of the strategies under consideration for the destruction of the undesirable pollutants in water considers the use of strong oxidizing processes with the generation of free radical species as secondary oxidants, the so called Advanced Oxidation Processes (AOPs). For that purpose, the action of powerful oxidants such as ozone or hydrogen peroxide is usually needed. Besides, the efficiency of AOPs can be further enhanced if radiation and/or a catalysts are combined.

Unfortunately, expensive costs are typically associated to these AOPs. Cost cuts in energy demand, operation, maintenance and acquisition of equipment is a challenge for the real applicability of AOPs at large scale. In this sense the use of cheap, renewable radiation sources (i.e. solar radiation) or energy-saving light (i.e. LEDs) are being examined.

For radiation assisted treatments, there are some semiconductor materials capable to be photo-excited under illumination (i.e. photocatalyts), yielding great amount of radical species in water, for instance the commonly used titanium dioxide (TiO_2). However, despite the high water stability, low toxicity and excellent photocatalytic activity of TiO_2, there are some disadvantages to point out: i) hard separability from the aqueous medium due to its particle size that difficults its settling behavior and ii) limited photocatalytic activity in the UV range. To overcome these drawbacks, other possibilities such as combining this material with others to improve the separability and/or using different photo-active materials with higher activity at broader wavelengths in the visible range of the solar spectrum are considered.

In this line, the hereby work deals with the applicability of photo-chemical advanced oxidation processes in combination with ozone and different photocatalytic materials.

Firstly, as an introduction to photo-ozonation processes, a study on the role of radiation on the aqueous ozone decomposition has been carried out. The essays were performed into a solar box provided with wavelength cut-off filters (below 320 nm and 390 nm). Firstly, the influence of the UV-visible radiation and pH was discussed after the determination of the first order apparent rate constants of aqueous ozone decomposition (k_{obs}). Given the fact that greater effects of radiation were observed at pH 4, a series of semi-batch experiments were designed with the purpose of quantifying hydrogen peroxide as an intermediate of ozone decomposition. Taking that into account an ozone decomposition model was proposed and two kinetic constants due to the influence of solar radiation were estimated ($k_{O_3\text{-rad}}$ y $k_{H_2O_2\text{-rad}}$). Subsequently, this effect was further examined by the removal of oxalic acid (refractory to ozone), which allowed the determination of the R_{et} parameter. Finally, the photo-ozonation process was tested for the degradation of a mixture of recalcitrant CECs (metoprolol, ibuprofen, DEET and clofibric acid) in both, ultrapure water and a synthetic secondary effluent of a WWTP. The mineralization degree (conversion of the organic matter into CO_2 and H_2O) and the accumulation of short-chain organic acids (SCOAs) in the solar photo-ozonation process was measured to evaluate the process performance

The following sections of the Thesis are focused on the use of different photocatalysts for the enhancement of the degradation of the organic matter in water. This part is divided into three sections depending on the catalyst employed: i) supported TiO_2 onto magnetic carbonaceous materials, ii) supported TiO_2 onto glass rings and iii) Fe-based metal-organic framework.

A magnetic activated carbon loaded with TiO_2 (TiFeC) had been promisingly used as photocatalyst in the degradation of metoprolol in ultrapure water by solar photocatalyic ozonation in a previous study. As part of this continuing work, the performance of the photocatalyst to degrade a mixture of CECs in real and synthetic secondary effluents was examined. Experiments were performed in semi-batch mode, using a solar simulator as radiation source and an optimum photocatalyst load (0.4 $g \cdot L^{-1}$). The efficiencies of different ozone-based processes to treat real and synthetic effluents were compared. As no significant differences were found between effluents, a more in deep study was further carried out with the synthetic effluent (SSE). Thus, the effects of the effluent organic matter (EfOM), carbonate alkalinity and phosphate concentration on the solar photocatalytic ozonation process efficiency were ascertain.

Despite the success in the degradation of pollutants and EfOM with the TiFeC catalyst, the increase of inorganic and organic carbon negatively affected the yield of the solar photocatalytic process. In addition, an increase of the SCOAs analyzed in the presence of inorganic matter was found. Finally, the evaluation of the separability, stability and reusability of the TiFeC photocatalyst was assessed after consecutive solar photocatalytic ozonation cycles by means of exhaustive characterization studies of fresh and reused catalyst as well as the analysis of final aqueous sample. In summary, the TiFeC catalyst might be suitable for the tertiary treatment of a domestic wastewater in order to safely degrade CECs, though additional studies for the economic feasibility at larger scale would be required before the scale-up of the process.

Going further with the TiFeC catalyst, its efficiency in solar photocatalytic ozonation of a highly polluted industrial wastewater was also investigated. The main purpose of this research was addressed to find a treatment leading to an effluent able to fulfil the quality requirements for its discharge into the aquatic environment. First, the wastewater was fully characterized analyzing potential organic substances, metal species, global pollution indicators (e.g., BOD_5, COD, TOC, etc.) and toxicity. Later, in spite of its low biodegradability index (i.e. BOD_5/COD ~0.2), after a period of bacteria acclimation, an activated sludge treatment could be applied to degrade the industrial wastewater (in a 1:5 by volume mixture with synthetic wastewater). Thus, about 50% TOC could be removed by batch activated sludge runs with c.a. 1.5 $mg \cdot L^{-1}$MLVSS and a hydraulic retention time of 8 h. After the biological treatment, ozone-based processes (i.e. ozonation, solar photolytic ozonation and solar photocatalytic ozonation) were applied to polish the quality of the biologically treated effluent. The combination of ozone, solar radiation and the TiFeC catalyst was the most effective treatment that fulfil the required effluent discharge limits (i.e., COD < 125 $mg \cdot L^{-1}$, BOD_5 < 25 $mg \cdot L^{-1}$). Aiming to improve the efficiency of the treatment, the impact of alkalinity, catalyst load, ozone dosage and pH were studied. While the concentration of inorganic carbon was not a decisive parameter, the pH of the media was crucial in these AOPs.

Given the promising results achieved with the TiFeC catalyst, magnetic graphene-based materials were synthesized, which were furtherly tested for their photocatalytic activity under solar simulated radiation in order to degrade an aqueous solution of cotinine (10 $mg \cdot L^{-1}$). First, graphene composites were fully characterized by XRD, chemical composition, textural, optical and magnetic properties. Materials with five different percentages of titanium dioxide or magnetite:graphene ratio (M:G) were synthesized, being the so-called 10-MG1-Ti (90% TiO_2 and 10%M:G, theorically) which leads to the best catalytic performance. In addition, the hydroxyl radical

concentration ($C_{HO^{\cdot}}$), R_{ct} parameter, hydroxyl radical exposure per consumed ozone molecule ($R_{OH,O3}$) and the importance of the indirect reaction route (η) were quantified to determine de effectiveness of each oxidation process (photocatalysis, ozonation, catalytic, photolytic and photocatalytic ozonation), finding that the photocatalytic ozonation is the most effective treatment for the removal and mineralization of cotinine. Besides, the stability and reusability of 10-MG1-Ti were tested in a 5-cycle O_3/radiation/catalyst runs, without noticing significant iron leaching. In contrast, a substantial loss of carbon at the end of the experiments was observed. The titania-magnetite-graphene composite was also evaluated for the removal of a wastewater spiked with 10 micropollutants (cotinine, caffeine, ciprofloxacin, metoprolol, sulfamethoxazole, DEET, clofibric acid, bezafibrate, tritosulfuron and ibuprofen) which present different reactivity towards direct ozone reactions observing that pH and carbonates played a key role in the process.

Another part of the Thesis focused into the study of a tertiary treatment of a real domestic wastewater effluent (i.e., secondary effluent) by a continuous photocatalytic treatment. In this case, commercial nanosized TiO_2 (P25) was used as catalyst and UV-A LED lamps as radiation sources. A number of CECs were detected and quantified in the WWTP effluent by means of solid phase extraction coupled with high performance liquid chromatography with tandem mass spectrometry (SPE-HPLC-MS/MS). Subsequently, a series of batch experiments were performed in order to assess the efficiency of the photocatalytic ozonation process. Thereafter, a photoreactor containing coated P25 glass rings was used for continuous experiments. A residence time distribution (RTD) analysis was carried out to determine the flow pattern in the reactor and also the supported photocatalyst was characterized. Moreover, a kinetic modelling through Hatta number (Ha), apparent rate constants of aqueous ozone decomposition (k_d) and the prevalence of the radical over direct route (r_{HO}/r_{O3}) was conducted, so that verifying the better decomposition of ozone in the photocatalytic ozonation and also the better elimination of the most refractory pollutants.

Finally, an iron-based metal-organic framework (MOF), MIL-100(Fe), was used as catalyst. There is a growing interest in the application of this kind of materials as photocatalysts in water treatment and also a wide variety of synthesized MOFs. However, prior to studying their applicability in realistic scenarios, it is compulsory to investigate their stability. For that reason, the behavior of sustainable synthesized MIL-100(Fe) in ultrapure water at different pH (unbuffered and buffered solution) was studied in long-term experiments (15 days), showing that the organic linker (trimesic acid, TMA) was partially released into the aqueous medium, especially in the presence

of phosphates (0.01M). Also, the stability of the MOF under typical AOPs oxidizing conditions (i.e., ozone, hydrogen peroxide and radiation presence) was studied. Some of the treatments completely removed the residual TMA improving some properties of the MOF (e.g. C/Fe ratio, BET surface area or TMA released during MOF-water contact, etc.); however, a partial degradation of the MOF resulted in mass loss in the reused material, surface oxidation, etc. Moreover, activity of MIL-100(Fe) for the degradation of the CECs (metoprolol, ibuprofeno, DEET and clofibric acid) by solar photocatalytic ozonation was investigated. Clearly, MIL-100(Fe) was found to be a photocatalytic material under simulated solar irradiation, improving its efficiency in the presence of ozone or hydrogen peroxide. Nevertheless, its stability is rather questionable when used in AOPs in water treatment.

RESUMEN

El impacto de la actividad humana se ve cada vez más reflejado en el medio ambiente. La alteración de los ecosistemas debida a la contaminación y a la mala gestión de los recursos hídricos son actualmente temas de gran preocupación. Este hecho ha alertado a organismos públicos, los cuales imponen normas cada vez más estrictas para mantener una adecuada calidad del agua. Así, a nivel europeo han surgido la Directiva 2013/39/EU, que establece un seguimiento de 45 sustancias prioritarias, y la Decisión 2018/840/EU, ampliando la lista con 8 nuevos grupos de sustancias que deben ser vigiladas. Entre ellas se encuentran los denominados contaminantes de preocupación emergente, que a pesar de que son detectados en muy baja concentración en diversos ecosistemas acuáticos, su uso extensivo, su dificultad de eliminación por los sistemas convencionales de tratamiento en las estaciones depuradoras de aguas residuales (EDAR) y el desconocimiento de su toxicidad a largo plazo, hace que sean necesarios procesos alternativos para el tratamiento de aguas.

A raíz de ello, una de las estrategias planteadas es la destrucción de la materia orgánica indeseable del agua mediante procesos fuertemente oxidantes que implican la generación de radicales, los denominados procesos avanzados de oxidación (PAO). Para ello, es necesaria la acción de un oxidante como el oxígeno, ozono o peróxido de hidrógeno, pudiendo mejorar su eficacia si se combina con una fuente de radiación y/o un catalizador.

Desafortunadamente estos PAO consumen gran cantidad de energía, que además de los costes de operación, mantenimiento y adquisición de equipos, dificultan su aplicación a escala industrial. Así, para disminuir ciertos costes y favorecer la viabilidad económica de estos procesos se estudia la posibilidad de utilizar fuentes de radiación renovables (ej.: radiación solar) o de bajo coste y larga duración (ej.: LED, del inglés *light-emitting diode*).

Por otro lado, existen catalizadores capaces de aprovechar la radiación y generar aún mayor cantidad de especies oxidantes secundarias (ej.: radicales libres) en agua cuando son foto-excitados (fotocatalizadores), como el dióxido de titanio (TiO_2). Sin embargo, a pesar de su elevada estabilidad, baja toxicidad y excelente actividad fotocatalítica, el dióxido de titanio presenta también ciertas desventajas, entre las que se incluyen las siguientes: i) dificultad de separación del medio acuoso dado su tamaño de partículas y ii) actividad fotocatalítica limitada prácticamente al rango de radiación UV. Para hacer frente a estos inconvenientes se plantea la posibilidad de combinar este material con

otros para mejorar la separabilidad del catalizador y/o emplear otros tipos de materiales que absorben en la zona visible del espectro electromagnético.

El presente trabajo se centra en la aplicación de procesos fotoquímicos de oxidación avanzada empleando ozono y distintos fotocatalizadores.

En primer lugar, como aspecto preliminar al uso de ozono en procesos fotoquímicos de oxidación avanzada, se llevó a cabo un estudio del papel de la radiación en la descomposición de ozono en agua. Los ensayos se realizaron en un simulador solar provisto con filtros de corte de radiación (paso de longitudes de onda mayores a 320 nm y 390 nm). Por un lado, se evaluó la influencia de la radiación UV-visible y pH mediante la determinación de las constantes cinéticas aparentes de primer orden de la descomposición de ozono (k_{obs}). Puesto que el efecto de la radiación fue más significativo a pH 4, se efectuaron ensayos adicionales a este pH para identificar peróxido de hidrógeno como intermedio en la descomposición de ozono. Así, a partir de los resultados obtenidos se propuso un mecanismo de descomposición de ozono en presencia de radiación y se determinaron las constantes cinéticas debidas al efecto de la radiación solar ($k_{O_3\text{-rad}}$ y $k_{H_2O_2\text{-rad}}$). Posteriormente, se evaluó el efecto de la radiación en la eliminación de ácido oxálico (refractario al ozono) mediante el cálculo de R_{ct}. Finalmente, dicho sistema se probó para la degradación de una mezcla de contaminantes emergentes persistentes (metroprolol, ibuprofeno, DEET y ácido clofíbrico) en agua ultrapura y residual sintética que simulaba un efluente secundario de EDAR, determinando el grado de mineralización (conversión de la materia orgánica a CO_2 y H_2O) y los productos ácidos orgánicos de cadena corta (AOCC) del proceso de foto-ozonización solar.

Los siguientes apartados de esta Tesis se centran en el empleo de diferentes fotocatalizadores para la degradación de materia orgánica en agua. Básicamente, se dividen en tres secciones atendiendo al tipo de catalizador empleado: i) TiO_2 soportado en materiales carbonosos magnetizados, ii) TiO_2 soportado en anillos de vidrio y iii) compuesto metal-orgánico de hierro.

Para comenzar, tras haberse sintetizado, optimizado y probado previamente un catalizador de carbón activado magnético con TiO_2 (TiFeC) en la degradación de metoprolol en agua ultrapura mediante ozonización fotocatalítica solar, se continuó la investigación para estudiar la efectividad de dicho material en agua residual real y sintética con la mezcla de contaminantes del bloque anterior (2 $mg \cdot L^{-1}$ de cada uno). Los experimentos se realizaron en régimen semi-continuo de operación empleando un

simulador solar. Tras haber realizado una optimización de la dosis de fotocatalizador (0.3 $g \cdot L^{-1}$) se comparó el efecto del mismo al aplicar diferentes PAO en agua residual doméstica real y sintética. Puesto que se obtuvieron resultados similares con ambos efluentes, se profundizó en el estudio determinando la influencia de la carga de materia orgánica, la presencia de fosfatos y carbonatos en los rangos de concentración habituales empleando solo uno de los efluentes (agua residual sintética). A pesar de que la ozonización fotocatalítica con TiFeC mejoraba en cualquier caso la degradación de los contaminantes y de la materia orgánica del agua residual, la presencia de carbonatos y la matriz orgánica del agua afectaron negativamente al rendimiento del proceso de ozonización fotocatalítica. Adicionalmente, se analizó la concentración de los ácidos orgánicos de cadena corta, observándose una gran relación entre estos y la presencia de materia inorgánica. Finalmente, se evaluó la separabilidad, estabilidad y capacidad de reutilización del fotocatalizador tras varios ciclos de ozonización solar fotocatalítica mediante una exhaustiva caracterización del catalizador fresco y reutilizado, así como de un análisis del producto final acuoso. De esta manera se pudo considerar que el fotocatalizador TiFeC era apto para el tratamiento terciario en agua residual doméstica. No obstante, se requerirían estudios adicionales para establecer la viabilidad económica del proceso a escala real.

Yendo más allá con este catalizador, se probó su eficacia en la ozonización fotocatalítica solar para la degradación de un efluente de agua residual industrial, cuyo tratamiento actual es la incineración debido a la presencia de una mezcla compleja de contaminantes. El objetivo principal de esta parte de la investigación se planteó de manera que el agua tratada final cumpliera la normativa autonómica para su descarga al medio ambiente. Por ese motivo, dicho efluente se caracterizó meticulosamente evaluando así los posibles productos orgánicos del agua, el índice de biodegradabilidad (DBO_5/DQO o relación entre las demandas biológica y química de oxígeno) y su toxicidad. De este modo, a pesar de su baja biodegradabilidad (DBO_5/DQO~0.2) se decidió realizar un tratamiento secuencial biológico (lodos activos) y de oxidación química. Previamente a los tratamientos se realizó una rápida y exitosa aclimatación de microorganismos aerobios en 15 días al agua contaminada, compuesta por una mezcla de agua sintética de un efluente residual del tratamiento primario de una EDAR y el agua industrial (dilución 1:5). Una vez que se disponía de biomasa aclimatada, esta se empleó para efectuar ensayos de biodegradación con un tiempo de retención hidráulico de 8 horas con el objetivo de eliminar toda la posible materia orgánica biodegradable (un 50% del carbono orgánico aproximadamente). El efluente del tratamiento biológico se sometió a varios tratamientos basados en ozono (ozonización, ozonización fotolítica

solar y ozonización fotocatalítica solar), siendo el proceso combinado de ozono, radiación solar y fotocatalizador de TiFeC el que lograba un efluente que satisfacía los límites establecidos por la directiva de aguas vigente (DQO < 125 $mg \cdot L^{-1}$, DBO_5 < 25 $mg \cdot L^{-1}$). Con la intención de mejorar aún más la eficacia del tratamiento se estudió el efecto de algunas variables: alcalinidad, dosis de catalizador, dosis de ozono y pH. Se observó que, en este caso, el efecto de la concentración de carbonatos no era decisivo a diferencia del pH del medio.

Dados los buenos resultados del catalizador TiFeC, se sintetizaron catalizadores similares basados en grafeno, evaluándose posteriormente su actividad en la degradación de cotinina (10 $mg \cdot L^{-1}$) con radiación solar simulada. En primer lugar, se caracterizaron los materiales, determinándose el patrón de difracción de rayos X, su composición, propiedades texturales, ópticas y magnéticas. De entre los 5 catalizadores sintetizados con distinta proporción de dióxido de titanio y diferente relación magnetita:grafeno (M:G), fue el catalizador 10-MG1-Ti (90% TiO_2 y 10% M:G 1:1 teórico) el que condujo a mejores resultados. Para determinar la efectividad de cada proceso de oxidación empleado (fotocatálisis, ozonización, ozonización catalítica, fotolítica y fotocatalítica) se cuantificó la concentración de radicales hidroxilo ($C_{HO\cdot}$), y se determinaron los valores de R_{ct}, la exposición de radicales hidroxilo por molécula de ozono consumida ($R_{OH,O3}$) y la importancia de la vía indirecta de ozonización (η), verificándose que la ozonización fotocatalítica era el tratamiento más eficaz en la eliminación de cotinina y su mineralización. Además, se probó la estabilidad y reutilización del 10-MG1-Ti después de 5 ciclos de O_3/radiación/catalizador, sin llegarse a apreciar una gran cantidad de hierro disuelto pero sí una pérdida notoria de carbono al finalizar los tratamientos. Aun así, también se quiso evaluar este proceso terciario para el tratamiento de un agua real dopada con 10 contaminantes con diferente reactividad frente al ozono (cotinina, cafeína, ciprofloxacina, metroprolol, sulfametoxazol, DEET, ácido clofíbrico, bezafibrato, tritosulfurón e ibuprofeno), corroborándose que el pH y los carbonatos son dos factores clave en el proceso.

El segundo sub-bloque tuvo como fin el estudio para un proceso de tratamiento terciario aplicado a un efluente real en continuo. En este caso, se detectaron y cuantificaron diversos compuestos orgánicos de preocupación emergente en un agua residual de salida de una EDAR usando un método de extracción en fase sólida junto con análisis por cromatografía líquida acoplada a detección de masas (SPE-HPLC-MS/MS) previamente validado para este tipo de compuestos. Posteriormente se diseñaron una serie de experimentos en discontinuo usando como fuente de radiación lámparas LED de UV-A y TiO_2 comercial (P25) para evaluar el sistema de ozonización

fotocatalítica. A partir de ese estudio se desarrolló un sistema en flujo continuo soportando P25 sobre anillos de vidrio. Además, en este sistema se analizó la curva de la distribución de tiempos de residencia del agua y se caracterizaron los anillos de vidrio. Finalmente se realizó un modelado cinético, calculando el número de Hatta (Ha), las constantes aparentes de descomposición de ozono (k_d) y la importancia de la vía radical sobre la directa (r_{HO}/r_{O3}), corroborándose que la ozonización fotocatalítica lograría una mejor descomposición de ozono en radicales libres y, por tanto, una mejor destrucción de los contaminantes más refractarios.

Para concluir el trabajo, se utilizó un material novedoso de estructura metal-orgánica (MOF, del inglés *metal-organic framework*) basado en hierro, denominado MIL-100(Fe). Dado el creciente interés en estos materiales como fotocatalizadores en el tratamiento de aguas en los últimos años y la multitud de MOF sintetizados, es necesario estudiar en profundidad la estabilidad de este tipo de materiales en agua, entre otros aspectos, previo a su aplicación en condiciones reales. Por ese motivo, tras la síntesis del material, se estudió su estabilidad en agua ultrapura a diferentes pH (en un medio sin tamponar y tamponado), dando como resultado una liberación parcial del ligando orgánico (ácido trimésico, ATM), empeorando dicho efecto en presencia de fosfatos. Además, se evaluó el efecto de varios PAO empleando MIL-100(Fe), concretamente procesos basados en radiación, ozono y peróxido de hidrógeno. Algunos tratamientos consiguieron eliminar el ATM residual, mejorando incluso algunas propiedades del MOF (relación teórica de C/Fe, superficie específica, ATM liberado, etc.), sin embargo, se observó la degradación parcial del material (pérdida de masa del catalizador reutilizado, oxidación de su superficie, etc.). Finalmente se profundizó en la actividad fotocatalítica solar del MOF en la degradación de una mezcla de los contaminantes anteriormente estudiados (metroprolol, ibuprofeno, DEET y ácido clofíbrico). Claramente, el material resultó ser fotocatalítico cuando era irradiado con luz solar, aumentando su rendimiento en presencia de ozono y peróxido de hidrógeno, si bien deben tenerse ciertas precauciones en cuanto a su estabilidad si se quiere emplear para el tratamiento de agua mediante PAO.

INTRODUCTION

CHAPTER II

2.1. BACKGROUND: THE IMPORTANCE OF WATER TREATMENT

There is nothing more essential to life than water. However, only 0.4% is directly available and suitable for human consumption. Water resources depend on the water or hydrological cycle, which deals with the continuous circulation of water in the Earth's hydrosphere. Thus, water moves on, over, and under the Earth's surface, being transformed into various phases (ice, water and vapor), remaining the total mass of water fairly constant.

Notwithstanding, the overpopulation, the badly-distribution of water worldwide and/or the climate change increased by human activity, make the available water scarce in quantity and quality.

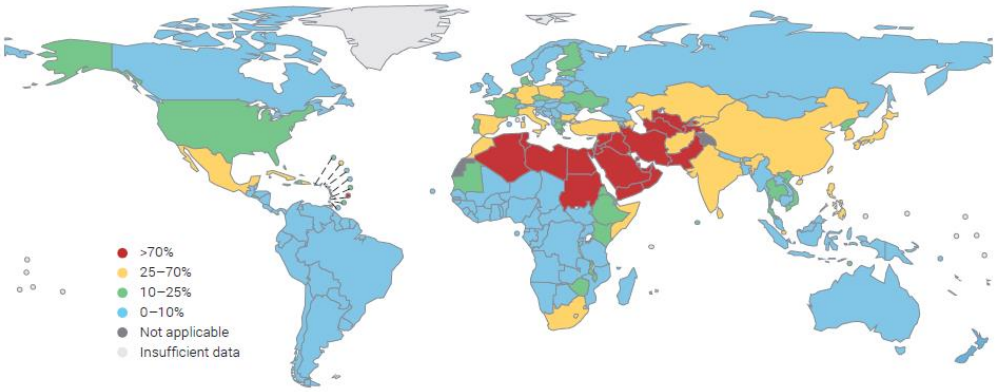

Figure 2.1. Physical water stress percentage all over the world. Adopted from [1].

The United Nation Educational, Scientific and Cultural Organization (UNESCO) reports that the world's population is facing a water crisis. Over 31 countries (2 billion people) are experiencing high physical water stress as shown in **Figure 2.1**. Stress occurs when the available water does not meet the demand in a certain period or it is restricted due to its low quality, driving to a deterioration of fresh water resources in terms of quantity (e.g. water over-exploitation or dryness) and quality (e.g. eutrophication or pollution).

Spain is one of the countries facing a high rate of water stress. The fact is that water use has been increasing not only in Spain but also worldwide primarily due to surging demand in developing countries and emerging economies. According to the UNESCO 2019 report, agriculture is so far the largest water consumer sector, accounting for 69%

of annual water withdrawals globally, while industry and households account for 19% and 12%, respectively.

Apart from that, UNESCO warns about the fact that water quality problems cause changes in hydromorphology, the rise of pollutants of emerging concern and the spread of invasive species [1]. In terms of pollution, water can be naturally or undesirably contaminated from industrial, domestic/municipal, or agricultural sources. In this sense, the extensive use of fertilizers and pesticides in the agricultural sector induces to the eutrophication of surface water and the contamination of groundwater by soil filtration. Conversely, the industrial sector produces a serious impact into the environment, delivering a wide variety of organic substances or heavy metals. Likewise, municipal waste contains a source of nitrogen, phosphorous, microbial and organic matter from pharmaceuticals, cleaning and daily products to large extent.

Summarizing, the human activity has seriously damaged the natural water resources. As a result, regulatory measures must be taken to ensure the sustainability of the planet. For that reason, the European Union Water Framework Directive (WFD) already set out different strategies against pollution of water, including the establishment of the first list of priority substances in the Directive 2000/60/EC, which was later modified by Directive 2008/105/EC. Afterwards, both directives were amended with the current Directive 2013/39/EU, extending the list to 45 priority substances and other pollutants. In addition, Decision 2018/840/EU included 8 new groups of substances that not only might pose a significant risk but also were rarely monitored.

As shown in **Table 2.1**, the substances or group of substances in the field of water policy included in Directive 2013/39/EU and Decision 2018/840/EU include a broad range of compounds such as pesticides, pharmaceuticals, metals, polyaromatic hydrocarbons, perflurocarbons or dioxins among others.

Table 2.1. List of substances or group of substances in the field of water policy included in Directive 2013/39/EU and Decision 2018/840/EU [2,3].

Label	Substance	CAS number	EU number
	Individual substances		
	Aclonifen	74070-46-5	277-704-1
	Alachlor	15972-60-8	240-110-8
W	Amoxicillin	26787-78-0	248-003-8
P	Anthracene	120-12-7	204-371-1
	Atrazine	1912-24-9	217-617-8
	Benzene	71-43-2	200-753-7
	Bifenox	42576-02-3	255-894-7
P	Cadmium and its compounds	7440-43-9	231-152-8
P	Chloroalkanes, C_{10-13}	85535-84-8	287-476-5
	Chlorfenvinphos	470-90-6	207-432-0
	Chlorpyrifos (Chlorpyrifos-ethyl)	2921-88-2	220-864-4
W	Ciprofloxacin	85721-33-1	617-751-0
	Cybutryne	28159-98-0	248-872-3
	1,2-dichloroethane	107-06-2	203-458-1
	Dichloromethane	75-09-2	200-838-9
	Dichlorvos	62-73-7	200-547-7
	Dicofol	115-32-2	204-082-0
P	Di(2-ethylhexyl)phthalate (DEHP)	117-81-7	204-211-0
	Diuron	330-54-1	206-354-4
P	Endosulfan	115-29-7	204-079-4
W	17-α-ethinylestradiol (EE2)	57-63-6	200-342-2
	Fluoranthene	206-44-0	205-912-4
P	Hexachlorobenzene	118-74-1	204-273-9
P	Hexachlorobutadiene	87-68-3	201-765-5
P	Hexachlorocyclohexane	608-73-1	210-168-9
	Isoproturon	34123-59-6	251-835-4
W	Metaflumizone	139968-49-3	604-167-6
W	Methiocarb	2032-65-7	217-991-2
	Naphthalene	91-20-3	202-049-5
P	Pentachlorobenzene	608-93-5	210-172-0
	Pentachlorophenol	87-86-5	201-778-6
	Quinoxyfen	124495-18-7	not applicable
	Simazine	122-34-9	204-535-2
	Trichlorobenzenes	12002-48-1	234-413-4
	Trichloromethane (chloroform)	67-66-3	200-663-8
	Trifluralin	1582-09-8	216-428-8

Table 2.1. (continued) List of substances or group of substances in the field of water policy included in Directive 2013/39/EU and Decision 2018/840/EU [2,3].

Label	Substance	CAS number	EU number
	Group of substances		
P	Brominated diphenylethers:		not applicable
	Tetrabromodiphenylether	40088-47-9	
	Pentabromodiphenylether	32534-81-9	
	Hexabromodiphenylether	36483-60-0	
	Heptabromodiphenylether	68928-80-3	
	Cypermethrin (mixture of isomers):	52315-07-8	257-842-9
	α-Cypermethrin	67375-30-8	
	β-Cypermethrin	65731-84-2	
	θ-Cypermethrin	71697-59-1	
	ζ-Cypermethrin	52315-07-8	
	Dioxins and dioxin-like compounds:		not applicable
	2,3,7,8-T4CDD	1746-01-6	
	1,2,3,7,8-P5CDD	40321-76-4	
	1,2,3,4,7,8- H6CDD	39227-28-6	
	1,2,3,6,7,8-H6CDD	57653-85-7	
	1,2,3,7,8,9-H6CDD	19408-74-3	
	1,2,3,4,6,7,8-H7CDD	35822-46-9	
	1,2,3,4,6,7,8,9-O8CDD	3268-87-9	
	2,3,7,8-T4CDF	51207-31-9	
	1,2,3,7,8-P5CDF	57117-41-6	
	2,3,4,7,8,-P5CDF	5711731-4	
	1,2,3,4,7,8-H6CDF	70648-26-9	
	1,2,3,6,7,8-H6CDF	57117-44-9	
	1,2,3,7,8,9-H6CDF	72918-21-9	
	2,3,4,6,7,8-H6CDF	60851-34-5	
	1,2,3,4,6,7,8-H7CDF	67562-39-4	
	1,2,3,4,7,8,9-H7CDF	55673-89-7	
	1,2,3,4,6,7,8,9-O8CDF	39001-02-0	
	PCB 77	32598-13-3	
	PCB 81	70362-50-4	
	PCB 105	32598-14-4	
	PCB 114	74472-37-0	
	PCB 118	31508-00-6	
	PCB 123	65510-44-3	
	PCB 126	57465-28-8	
	PCB 156	38380-08-4	
	PCB 157	69782-90-7	
	PCB 167	52663-72-6	
	PCB 169	32774-16-6	
	PCB 189	39635-31-9	
W	17-β-estradiol (E2)	50-28-2	200-023-8
	Estrone (E1)	53-16-7	

Table 2.1. (continued) List of substances or group of substances in the field of water policy included in Directive 2013/39/EU and Decision 2018/840/EU [2,3].

Label	Substance	CAS number	EU number
	Heptachlor	76-44-8	200-962-3
	Heptachlor epoxide	1024-57-3	213-831-0
	Hexabromocyclododecanes (HBCDD):	not applicable	not applicable
	1,3,5,7,9,11-Hexabromocyclododecane	25637-99-4	
	1,2,5,6,9,10- Hexabromocyclododecane	3194-55-6	
	α-Hexabromocyclododecane	134237-50-6	
	β-Hexabromocyclododecane	134237-51-7	
	γ- Hexabromocyclododecane	134237-52-8	
	Lead and its compounds	7439-92-1	231-100-4
	Macrolide antibiotics:		
W	Erythromycin	114-07-8	204-040-1
	Clarithromycin	81103-11-9	not applicable
	Azithromycin	83905-01-5	617-500-5
P	Mercury and its compounds	7439-97-6	231-106-7
	Neonicotinoids:		
	Imidacloprid	105827-78-9	428-040-8
		138261-41-3	not applicable
W	Thiacloprid	111988-49-9	428-650-4
	Thiamethoxam	153719-23-4	433-460-1
	Clothianidin	210880-92-5	not applicable
	Acetamiprid	135410-20-7	not applicable
		160430-64-8	
	Nickel and its compounds	7440-02-0	231-111-4
	Nonylphenols:		
P	Nonylphenol	25154-52-3	246-672-0
	4-nonylphenol	104-40-5	203-199-4
	4-nonylphenol (branched)	84852-15-3	284-325-5
	Octylphenols:		
	Octylphenol	1806-26-4	217-302-5
	4-(1,1',3,3'-tetramethylbutyl)-phenol	140-66-9	205-426-2
	Polyaromatic hydrocarbons (PAH):		
	Benzo(a)pyrene	50-32-8	200-028-5
P	Benzo(b)fluoranthene	205-99-2	205-911-9
	Benzo(g,h,i)perylene	191-24-2	205-883-8
	Benzo(k)fluoranthene	207-08-9	205-916-6
	Indeno(1,2,3-cd)pyrene	193-39-5	205-893-2
P	Tributyltin compounds	not applicable	not applicable
	Tributyltin-cation	36643-28-4	not applicable
	Perfluorooctane sulfonic acid and its derivatives (PFOS)	1763-23-1	217-179-8

CAS: Chemical Abstract Service
EU number: European inventory
P: priority substance in Directive 2013/39/EC
W: substance in Decision 2018/840/EU

The improvement of analytical techniques has allowed the detection of some of these groups of compounds in natural water effluents. So far, they have been detected in $\mu g \cdot L^{-1}$-$ng \cdot L^{-1}$ range at the outlet effluent of wastewater treatment plants (WWTPs). This demonstrates the fact that many substances are continuously discharged in the environment and inefficiently removed during wastewater treatments. These substances, also known as contaminants of emerging concern (CECs), may have potential ecological and human health effects [4,5]. Though they might not exhibit significant acute toxicity at low concentrations, their long-term effects are still unknown. Therefore a synergistic toxicity phenomena cannot be disregarded [6]. **Table 2.1** includes some of those CECs, for instance, amoxicillin (pharmaceutical), diuron (pesticide) or estrone (hormone).

Although some CECs may be inorganic compounds (e.g. nanomaterials), in most of the cases are organic substances [7,8]. The latter comprise a wide variety of compounds distributed into the following categories: pharmaceuticals, endocrine disruptors, personal care products, drugs, stimulants, pesticides, additives, surfactants, plasticizers, flame retardants or disinfection by-products [9]. **Table 2.2** gives some examples of micropollutants typically detected in natural water bodies.

Table 2.2. Categories and examples of CECs [9–11].

Category	Examples
Pharmaceuticals (PhCs)	
Analgesics and anti-inflammatory	Ibuprofen, Diclofenac, Ketoprofen
Antidepressants/Psychiatric drugs	Diazepam, Fluoxetine, Venlafaxine
Antibiotics	Amoxicillin, Ciprofloxacin, Lincomycin
Lipid regulators	Bezafibrate, Gemfibrozil
β-blockers	Metoprolol, Propanolol, Atenolol
X-Ray contrast media	Iopamidol, Iopromide
Veterinary medicine	Sulfamethazine
Endocrine disruptors (EDCs)	Estrone, 17-β-estradiol, estriol
Personal care products (PPCPs)	Galoxalide, Crotamiton, Oxybenzone
Drugs/Stimulants	Nicotine, Caffeine, Cocaine
Pesticides/Insecticide/Herbicide	Atrazine, Endosulfan, Diclorvos, Isoproturon
Additives	Methyl-*tert*-butyl eter
Surfactants	Nonylphenol
Plasticizers	Bisphenol A
Flame retardants	Polybrominated Diphenyl Ethers (PBDE), tris(2-chloroethyl)phosphate (TCEP)
Disinfection by-products	Trihalomethanes (THMs), Bromate

To face these problems of scarcity, pollution and demand, water must be regenerated and reused, being disposed into the ecosystem in good quality conditions. Moreover, this new directive suggests the implementation of innovative water treatment technologies in the most economically and environmentally way to face the threat of chemical pollution in aquatic environments.

Water treatment deals with the importance of having safe water, free of bacterial contamination, heavy metals, odor and possessing little to no turbidity. Thus, WWTPs must be designed to comprise physical, chemical and/or biological treatments in order to safely control the pollution load.

Typically, the pre-treatment at WWTPs is based on the removal of solids as well as greases and oils to prevent problems in further stages. Afterwards, primary treatment takes place so as to remove suspended solids and colloids by means of coagulation-flocculation and settling processes. Then, the secondary treatment deals with the abatement of biodegradable organic load using microorganisms under aerobic or anaerobic conditions.

Though bioremediation has been practiced for years as an energy-efficient treatment to degrade toxic chemicals in soils, groundwater, surface water and even atmosphere, the process is often long, unsafe and requires a post-treatment of the biological matter (i.e., sludge). Thus, the development of innovative, high-performance and low-cost remediation techniques could be evaluated. Several technologies, such as advanced oxidation processes (AOPs), have been developed for recalcitrant and toxic pollutants removal from aqueous effluents [12].

2.2. ADVANCED OXIDATION PROCESSES

There are two methods for the removal of pollutants in water: physical and chemical processes. The physical processes deals with the removal of substances without modifying the chemical structure and putting aside the media. The chemical processes are based on the reactions of certain substances (i.e., oxidants) with the pollutants leading to the degradation of the latter into simpler compounds.

Focusing on the chemical processes, the classical treatments are based on the addition of an oxidizing agent to water. Oxidants may be employed to remove both inorganic and

organic contaminants. For instance chlorine, ozone, hydrogen peroxide or permanganate have been widely used to degrade several toxic compounds in water [13].

However, other technologies involving free radicals are gaining the interest of researchers. AOPs were defined by Glaze et al. (1987) as those processes involving the generation of hydroxyl radicals ($HO^{\bullet}$) in sufficient quantity in order to degrade the organic compounds in water [14]. Other free radical oxygen species (ROS), such as superoxide radical ($O_2^{\bullet-}$) or singlet oxygen ($^1O_2$), could be produced during certain AOPs and contribute to the degradation of contaminants. Nevertheless, it is the hydroxyl radical which plays the main role during oxidation [15]. Hence, this technology allows the degradation of a number of water pollutants that are recalcitrant to conventional treatments.

The hydroxyl radical is a powerful and reactive species with a redox potential of 2.80 V, highly superior to other conventional oxidizing agents such as ozone, hydrogen peroxide or permanganate (see **Table 2.3**). This non-selective chemical is effective to destroy almost any organic compound by hydrogen abstraction or electron transfer ($k_{OH} \approx 10^8$-10^{10} $M^{-1} \cdot s^{-1}$) [16], leading frequently to the complete mineralization of organic and inorganic matter in water.

Table 2.3. Standard redox potential of some oxidant species [17].

Oxidant		Redox potential (V)
Fluorine	F^-	3.06
Hydroxyl radical	$HO^{\bullet}$	2.80
Ozone	O_3	2.07
Hydrogen peroxide	H_2O_2	1.77
Permanganate	MnO_4^-	1.67
Chlorine	Cl^-	1.36
Bromine	Br^-	1.09

Because of its high reactivity, $HO^{\bullet}$ is a short-lived species that must be generated in situ for AOPs purposes. Thus, AOPs have been classified taking into account the way of hydroxyl radical production. Typically depending on whether or not radiation is used, different photochemical or non-photochemical processes are found. These processes involve the combination of one or more oxidants, catalyst and/or radiation to generate radicals [18].

Unfortunately, AOPs are not suitable to directly degrade complex matrices or effluents with high organic load because of the high cost associated with reagents or energy sources to reach the required production of $HO^{\bullet}$. In this sense, AOPs are

considered as cost-efficient technologies to deal with natural water and low-polluted wastewaters (i.e., chemical oxygen demand (COD) < 5 $g \cdot L^{-1}$) [12,19]. However, provided that biological treatments cannot always successfully remove organic pollutants from wastewaters, AOPs can also be recommended to be used in a combined process to improve results of biodegradation [20–22].

In this work, AOPs constituted by photochemical processes using both simulated solar radiation and light-emitting diodes (LEDs) have been studied for the photocatalytic degradation of contaminants in water.

2.2.1. PHOTOCATALYTIC OXIDATION

The photocatalytic oxidation process generates hydroxyl radicals by means of the absorption of light incident by a catalyst, i.e. photocatalyst. Depending on the state of the photocatalyst with regard the media, two types of photocatalytic processes are distinguished: heterogeneous and homogeneous photocatalysis. In this sense, semiconductors (e.g. TiO_2, ZnO, WO_3) are typically used in heterogeneous photocatalysis while dissolved species (e.g. Fe(II), Fe (III), H_2O_2) are employed in homogeneous photocatalysis [23].

A. <u>Heterogeneous photocatalysis</u>

In heterogeneous photocatalysis, the catalytic reaction is based on the photo-excitation of a solid semiconductor with a sufficient energy to promote electrons from the valence band (VB) to the conduction band (CB), generating simultaneously an electron-hole pair [24]. **Figure 2.2(A)** depicts a scheme of the heterogeneous photocatalytic process in a semiconductor for the removal of organic matter (P) in presence of oxygen.

Although inorganic species such as TiO_2, ZnO, WO_3 are the semiconductors typically used in heterogeneous photocatalysis, some organic species (i.e. metal organic frameworks (MOFs) or graphene) might as well act as photocatalysts when after light absorption, electrons migrate from the highest occupied molecular orbital (HOMO or valence band) to the lowest unoccupied molecular orbital (LUMO or conduction band). Additionally, the linker-to-metal-cluster charge-transfer (LCCT) mechanism has been proposed in heterogeneous photocatalysis using MOFs. LCCT considers the organic linkers as antennas that absorb light and transfer the photo-excited charge carriers to the central metal clusters, that might react with an oxidant (X) [25] (**Figure 2.2(B)**).

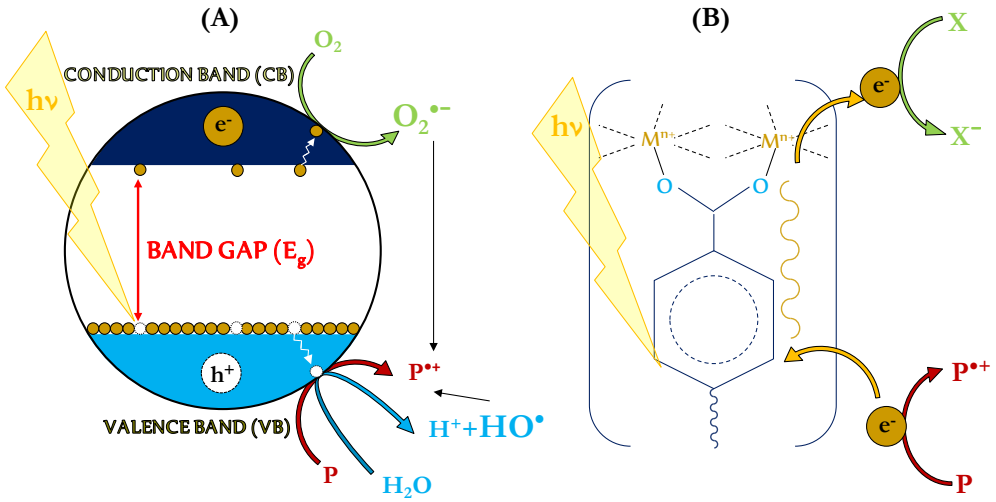

Figure 2.2. Scheme of the photocatalytic process for the degradation of organic matter in a semiconductor (A); and the proposed linker-to-metal-cluster charge-transfer (LCCT) mechanism in MOFs (B).

Therefore, in a typical photocatalytic process, the radiation is absorbed by the photocatalysts causing the excitation of electrons from VB or HOMO to CB or LUMO, respectively (reaction (2.1)). As a consequence, a deficit of electronic charge (hole) with a high oxidation potential is produced in the VB or HOMO. If electron and hole do not react fast to initiate the degradation process, the energy is undesirably dissipated by the electron/hole recombination (reaction (2.2)):

$$\text{Photocatalyst} \xrightarrow{h\nu} e^- + h^+ \qquad (2.1)$$

$$e^- + h^+ \xrightarrow{\text{heat } (\Delta)} \text{Photocatalyst} \qquad (2.2)$$

As a rule of thumb, the heterogeneous photocatalytic process also involves several reactions, which give place to oxidizing species: superoxide/hydroperoxyl radical ($O_2^{\bullet-}/HO_2^{\bullet}$), hydroxyl radical ($HO^{\bullet}$) and hydrogen peroxide (H_2O_2). The overall degradation reaction can be described as:

$$\text{Pollutant} + O_2 \xrightarrow{h\nu/\text{Phtocataltyst}} CO_2 + H_2O \qquad (2.3)$$

It is important to highlight that the efficiency and rate of a photocatalytic process depends on the mass of catalyst, radiation source, pH, temperature, oxygen concentration and initial reactant concentration [26]. **Table 2.4** summarizes the effect of each parameter in a photocatalytic process for the removal of contaminants in water.

Table 2.4. Summary of the parameters and their effects in a photocatalytic process.

Parameter	Main effect
Catalyst load	The photocatalyst is effective up to a certain quantity. Higher loads led to photon scavenging due to the increase of the turbidity of the media.
Radiation source	Reaction rates typically depend on the radiant flux and wavelength because of the photo-induced nature of the catalytic process. Thus, the efficiency of a photocatalytic process is directly related to the formation of e^-/h^+ and the reaction of reactants with them.
pH	pH of an aqueous solution affects the charge, size of aggregates and the position of VB/CB of the catalysts as well as the chemical speciation of the contaminants.
Temperature	Temperatures below 0 ºC increases the activation energy, being the desorption of the final products a limiting factor. Temperatures above 80 ºC are near to the boiling point of water, being the adsorption of the products a limiting step.
O_2 concentration	Oxygen (or other oxidant) is necessary to generate ROS. However, slightly enhancement using pure O_2 than air is observed.
Pollutant concentration	Adsorption of pollutants onto the catalyst and reaction with oxidizing species are influenced by the concentration of target pollutants and scavengers in solution.

B. Homogeneous photocatalysis

The typical homogeneous catalytic processes are those combining iron salts and hydrogen peroxide in acidic conditions, labeled as Fenton (Fe (II)/H_2O_2) or Fenton-like (Fe (III)/H_2O_2) processes [27]. The performance of these systems can be considerably enhanced by the presence of UV or solar radiation, then called photo-Fenton or photo-Fenton-like processes, respectively [28–30]. Particularly, the photo-Fenton-like system is based on the hydroxyl radical generation by different pathways including the following: (i) chemical reaction of Fe (II) with H_2O_2, (ii) photolysis of H_2O_2 and (iii) the photo-reduction of the ferric to ferrous ion under illumination (**Figure 2.3**). In addition, the superoxide ion radical, $O_2^{\bullet-}$, may be generated during the Fenton processes, leading to a higher amount of H_2O_2.

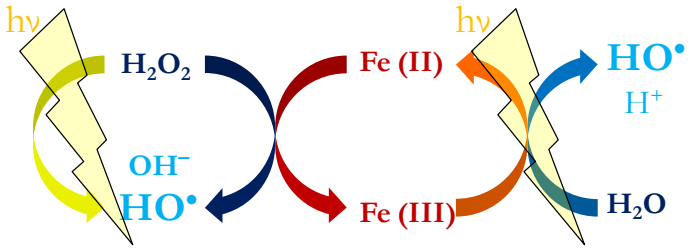

Figure 2.3. Scheme of the reaction cycle for the photo-Fenton process. Adapted from [27].

However, the process is limited to low pH, otherwise precipitation of iron hydroxides take place. Furthermore, iron, which must be recovered at the end of the treatment, does not have to exceed the concentration limits of the environmental regulation. To overcome these drawbacks, other forms of iron have been proposed [31,32].

2.2.2. OZONE-BASED PROCESSES

Ozone, discovered by Schönbein in 1840, is a well-known oxidizing agent in both water and air. In water and wastewater treatment, ozone is used as disinfectant to eliminate pathogenic bacteria and viruses and as oxidant to remove ions, algae, odor, flavor, color and organic pollutants. It can also be used as pre-treatment in order to enhance further operation units (e.g. coagulation, flocculation, sedimentation, biological oxidation) [33].

Ozone is highly unstable, and for that reason, it cannot be neither stored nor distributed and it must be generated in situ. Regardless of the purpose, in water treatment plants using ozone, there are four points or operations involving this oxidant: (i) ozone generation, (ii) ozone gas-liquid transfer, (iii) ozone chemical reaction and (iv)residual ozone removal.

The most commonly used method for ozone generation is through electrical shock in an oxygen containing gas (e.g., oxygen or air). Hence, oxygen molecule is split up into two atomic oxygen radicals, which rapidly react with molecular oxygen to yield ozone molecules. Electrolytic and photochemical methods may also be used [34,35].

In practice, reactions of ozone take place in a heterogeneous process where the mass transfer stage or ozone dissolution has to be improved so that the highest amount of ozone could reach the water. The ozone absorption phenomenon is typically explained by the film theory (gas and liquid phases are separated by a thin film of gas and liquid respectively) and is influenced by multiple factors, such as pH, ionic species, temperature and chemical reactions that ozone undergoes in water [36,37]. The characteristic

parameters of mass transfer are the individual and volumetric mass transfer coefficients, k_L and k_La, respectively, and the equilibrium Henry's law. Additionally, the kinetics of ozonation could be studied determining the kinetic regime of ozone reactions, that could be predicted by calculating the Hatta number (Ha) and the instantaneous factor (Ei). **Table 2.5** shows the kinetic regime of gas-liquid reactions depending on the values of Ha and Ei numbers.

Table 2.5. Kinetic regimes of gas-liquid reactions according to Hatta number criteria.

Ha number	Reaction place	Kinetic Regime
≤0.002	Liquid bulk	Very slow
≈0.3	Liquid bulk	Slow
0.3<Ha<3	Liquid film and bulk	Moderate
3≤Ha≤Ei/2	Liquid film	Fast (1st order)
Ha≤10·Ei	Plane in liquid film or at interface	Instantaneous

Once dissolved in water, if regimes are fast, ozone is consumed through direct reactions in the liquid film while, in case of slow regimes, an ozone chain reaction mechanism is triggered as well. This involves ozone decomposition into other ROS according to the Stahelin, Bühler and Hoigné (SBH) or Tomiyasu, Fukutomi and Gordon (TFG) mechanisms, that hold in acidic or alkaline conditions, respectively [38–40]. This ROS species are: superoxide ion/hydroperoxyl radical ($O_2^{\bullet-}/HO_2^{\bullet}$), hydroxyl radical ($HO^{\bullet}$) and ozonide ion/trioxidanyl radical ($O_3^{\bullet-}/HO_3^{\bullet}$).

As shown in **Figure 2.4.**, the decomposition rate of ozone at basic pH may be highlighted as a catalytic process itself. Likewise, these and other species can be involved into the ozone aqueous decomposition mechanism, acting as initiators, promoters or inhibitors depending on their role. Initiators are those species responsible for the ROS generation (mainly $O_2^{\bullet-}$, $O_3^{\bullet-}$ and $HO^{\bullet}$) through direct ozone reaction (e.g. OH^-). Both, promoters and inhibitors consume hydroxyl radicals. Species involved with the hydroxyl radical reaction to promote hydroperoxide/supeoxide ion radicals are labelled as promoters, such as H_2O_2 or some humic substances. Special attention should be paid to the $O_2^{\bullet-}$ promoter, owing to the fact that it rapidly reacts with ozone to yield free radicals ($k=1.6 \times 10^9\ M^{-1}\cdot s^{-1}$). In contrast, inhibitors or scavengers react ineffectively with $HO^{\bullet}$ decreasing the available concentration of the latter. Carbonate/bicarbonate ions ($k_{OH}=3.9 \times 10^8/8.5 \times 10^6\ M^{-1}\cdot s^{-1}$), tert-buthanol ($k_{OH}=6 \times 10^8\ M^{-1}\cdot s^{-1}$) or p-chlorobenzoic acid ($k_{OH}=5.2 \times 10^9\ M^{-1}\cdot s^{-1}$) are well-known inhibitors, scavenging $HO^{\bullet}$ during ozonation and other advanced oxidation processes [41–43]. **Figure 2.4** summarizes the ozone decomposition mechanisms considering the main species involved.

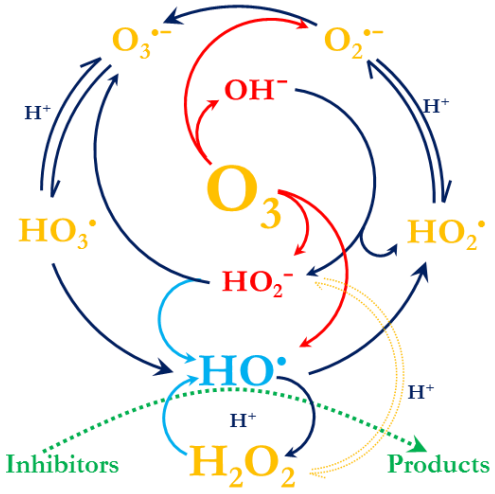

Figure 2.4. Reaction chain mechanisms and species involved in aqueous ozone decomposition. Initiation steps in red, promotion steps in light blue and termination steps in green.

Decomposition of ozone in water can also be improved in the presence of other reagents or agents such as hydrogen peroxide, light (UV radiation) and/or catalysts as shown in the following sections. HO• radicals, generated from ozone decomposition, that react with the matter present in water are involved in the indirect ozone reactions.

As far as direct ozone reactions are concerned, the electronic configuration of ozone makes it as a double-edge sword, acting as nucleophilic or electrophilic agent. In fact, it can react with most species containing double bonds (C=C, C=N, N=N, etc.), some functional groups (–NH_2) or even ions (NO_2^-, S^{2-} y SO_3^{2-}) [44]. The rate constant of ozone reactions with organic contaminants usually fluctuates between 10^2 to 10^7 $M^{-1}\cdot s^{-1}$, if such compound contains unsaturations or aromatic rings [45]. However, ozone fails to completely degrade the organic matter since it is a very selective reagent. The presence of specific substituting groups (i.e. –COOH, –CHO, C≡N) and ions (F^-, Cl^-, Br^-) in aromatic rings strongly affect the reactivity of the molecule, being able to deaccelerate the direct ozone attack ($k_{O_3} < 10^2\ M^{-1}\cdot s^{-1}$) [46,47].

The relative contribution of direct or indirect ozonation routes, strongly depends on pH, temperature, nature of the contaminants, ozone dose applied and the presence of agents of diverse nature (e.g., radiation, oxidants and/or catalysts).

A. CATALYTIC OZONATION

As previously mentioned, when the pH is increased, ozonation processes are triggered since hydroxide ion acts as an initiator of ozone decomposition as summarized in reaction

(2.4) and also because of the higher reactivity with molecular ozone of dissociating species present in water. Indeed, at basic pH, ozone is decomposed within seconds if does not react directly with dissociating species with specific functional groups in their molecules. Both processes (direct and indirect reactions) take place simultaneously when kinetic regimes are slow, which is typical of wastewater ozonation. In single ozonation the main reactions at high pH can be summarized as:

$$O_3 + OH^- \rightarrow \left[O_2^{\bullet -}, HO_2^{\bullet}, O_3^{\bullet -}\right] \rightarrow HO^{\bullet} \quad (2.4)$$

Nonetheless, addition of other species could improve the ozonation process. For instance, the combination of H_2O_2 or activated carbon with ozone is being proved to considerably increase the efficiency removal of organics in water, such as pharmaceuticals [48].

Addition of hydrogen peroxide (the so-called peroxone process) can activate the system yielding hydroxyl radicals according to reaction (2.5).

$$O_3 + H_2O_2 \longrightarrow HO^{\bullet} + O_2 + HO_2^{\bullet} \quad (2.5)$$

Although, in practice ozone processes are heterogeneous reactions since ozone has to be solved in water to further react, the ozone process at high pH or in the presence of hydrogen peroxide or some metal ions (Fe (II), Mn (II), etc.) are considered as homogeneous catalytic ozonation. On the other hand, when catalysts are solid materials, the ozone processes are named heterogeneous catalytic ozonation. Regarding these latter processes different catalysts have so far been used such as activated carbon (AC), metal oxides, etc. [49–51].

For instance, in the presence of AC, ozone decomposition is mainly influenced by AC dose, pH and AC chemical surface [52]. According to previous studies, AC can be an initiator of the ozone and H_2O_2 decomposition into $HO^{\bullet}$ in solution (reactions 2.6-2.8). In addition ozone is chemisorbed and reacts on the AC surface, yielding surface free radicals (reaction 2.9) [53].

$$O_3 + AC \rightarrow \left[HO^{\bullet} + HO_2^{\bullet} + H_2O_2\right] \quad (2.6)$$

$$H_2O_2 + AC \longrightarrow \left[HO^{\bullet}\right] \quad (2.7)$$

$$HO^{\bullet} + AC \longrightarrow \left[H_2O_2\right] \quad (2.8)$$

$$O_3 + AC \longrightarrow AC\text{-}O^{\bullet} \quad (2.9)$$

Given the higher concentration of free radical species in the O_3/AC combination, some studies report the use of this heterogeneous system to remove ozone-refractory compounds from water [54].

However, not all the catalytic ozonation processes go through free radical mechanisms. For example, removal of oxalic acid, an important ozonation end product very refractory to ozone direct reaction, in an Fe_2O_3/O_3 or Co_2O_3 process develops through formation of iron or cobalt oxalate complexes that further react with ozone [55,56].

B. PHOTOLYTIC OZONATION

The combination of ozone with radiation has also been investigated. First studies in photolytic ozonation (O_3/light) in aquatic systems were performed using UV-C radiation, demonstrating that additional oxygen species may be produced with a powerful radiation source [18,42]. More environmental sustainable is the use of solar radiation as radiation source. However, studies in solar photo-ozonation are scarce [57]. Briefly, ozone may be photo-excited under illumination to give place to excited oxygen $O(^1D)$, $O(^1\Delta_g)$, possibly $O(^3P)$ and as consequence, hydrogen peroxide and hydroxyl radicals according to reactions (2.10)-(2.12) and also reactions (4.1)-(4.3), furtherly given in the Chapter IV [58]. Focusing on $O(^1D)$, the atomic oxygen is a powerful species with the ability to react with other substances (10^9-10^{10} $M^{-1}\cdot s^{-1}$) and even water ($k=1.8 \times 10^{10} M^{-1}\cdot s^{-1}$) (reaction 2.11) [59].

$$O_3 \xrightarrow{h\nu(\lambda<320nm)} O_2 + O(^1D) \quad (2.10)$$

$$O(^1D) + H_2O \longrightarrow H_2O_2 \quad (2.11)$$

$$H_2O_2 \xrightarrow{h\nu(\lambda=200\text{-}400nm)} 2HO^{\bullet} \quad (2.12)$$

Moreover, hydrogen peroxide can be photo-excited under radiation below 400 nm to yield $HO^{\bullet}$ in spite of its molar extinction decay in the range 300-400 nm ($< 2\ M^{-1}\cdot cm^{-1}$) [60,61].

Therefore, as shown in reactions (2.10) to (2.12) and (4.1) to (4.3), the efficiency of photolytic ozonation strongly depends on the wavelength employed.

C. PHOTOCATALYTIC OZONATION

Photocatalytic ozonation (O_3/light/cat) is the combination of ozone, a radiation source and a semiconductor with a band gap equal or lower than the energy of the incident

radiation. In the event that ozone was used in a photocatalytic process, additional mechanisms of radical generation by the interaction between both systems have to be considered. In this sense, it is important to highlight the role of the photo-induced electrons in the photocatalytic ozonation, which leads to the ozonide ion radical (2.13). Consequently, the presence of ozone would reduce the electron-hole recombination and increase of HO• production in the adsorption layer [62], according to the following reaction:

$$O_3 + e^-_{CB} \longrightarrow O_3^{\bullet -} \quad (2.13)$$

In conventional photocatalytic processes, oxygen is used instead of ozone. Nevertheless, the disadvantage of using oxygen as electron trap is the slow electron transfer rate from the photocatalyst to oxidant. The rate constant of e^- trapped by ozone is superior to the one when only oxygen is used ($k_{O_3\text{-}e^-}=3.6 \times 10^{10}$ $M^{-1}\cdot s^{-1}$ vs. $k_{O_2\text{-}e^-}=1.76 \times 10^{10}$ $M^{-1}\cdot s^{-1}$) [63].

Summarizing, when the photocatalyst is irradiated in the presence of O_3, a synergistic effect may be developed causing a greater amount of HO• formation which leads to higher mineralization rates [64,65].

2.3. RADIATION SOURCES

Radiation, especially energetic radiation (e.g. UV light), may play a role in the degradation of water pollutants. The degradation rate varies depending on the type of radiation source employed. First studies were performed using monochromatic mercury based UV lamps (maximum intensity at 254 nm) or polychromatic UV lamp (up to 400 nm) [66–70]. Nonetheless, solar radiation can be highlighted for being a renewable, inexhaustible and free natural resource, or LED lamps, with a long life and energy-saving technology, are gaining popularity in photochemical processes for the degradation of water contaminants [62,70–72].

2.4.1. SOLAR RADIATION

The Sun is an extremely powerful energetic source, though most of its intensity is dissipated due to Earth's atmosphere and clouds, which absorb or scatter as much as 54% of the incoming sunlight. The spectral distribution of sunlight comprises ultraviolet-A (%5), visible (50%) and infrared (45%) radiation, being the UV-A range the most

energetic, followed by visible and IR. This radiation can reach the earth's surface as direct, diffuse and reflected radiation, which can be taken advantage as free energy source.

Different solar photo-reactors have been widely used in several AOPs for water treatment. Parabolic trough reactor (PTR), compound parabolic reactor (CPR), inclined plate collector (IPC), double skin sheet reactor (DSS) or compound parabolic collector (CPC) are included [73]. The latter has demonstrated to be suited in pilot-scale plants with a high water flow rates and solar concentration, distributing uniformly the light all around the tubular receiver [26].

Unfortunately, the radiation intensity varies geographically as well as hourly and monthly. Concretely in Spain, the maximum irradiance values are reached in June and July, while January and December get the lowest values [74].

In order to not be influenced by climate variability, solar boxes or solar simulators have been designed at lab scale. They simulate quite well the solar spectrum and the irradiance distribution of the natural sunlight (see **Figure 3.1**). For that reason, some researchers prefer these devices in order to test the efficiency of their photo-chemical processes [75–79].

2.4.2. LIGHT EMITTING DIODES (LEDs)

A light-emitting diode has an anode and a cathode separated by a crystal of semiconductor material, which emits light when electrical current flows from the anode (P side) to the cathode (N side). This light is emitted when the electrical-excited electrons of the semiconductor are recombined with electron holes, and then energy is released in the form of photons. Single-color LEDs that emit light in a narrow band of wavelengths from near-IR through the visible spectrum and into the UV range can be performed by selection of different semiconductor materials.

LEDs have many advantages, including lower energy consumption, longer lifetime, improved physical robustness, smaller size, and faster switching. These upsides make the LEDs as a light source alternative to other radiation lamps. Numerous studies have begun to use this innovative technology in wate treatement[71,80,81].

2.4. CATALYSTS

2.4.1. TITANIA

Among photocatalysts, titanium dioxide, also known as titania, has been of great research interest due to its thermal and chemical stability, low toxicity, high oxidizing ability and low cost [82,83]. Titania has been used for decades for the degradation of water pollutants [84–87].

Titania could be synthesized into different crystalline phases, being anatase, rutile and brookite the main ones [82,88]. The band gap for anatase is 3.2 eV, whereas for rutile and brookite are 3.02 eV and 2.96 eV, respectively [89,90]. Despite of the lower band gap energy in rutile and brookite phases, it is anatase which has demonstrated to possess higher photocatalytic activity [88,91]. However, the combination of two phases of TiO_2 (anatase and brookite or anatase and rutile) can improve the photocatalytic activity of titania, due to the increase of electron-hole transitions [82].

A low cost-effective titanium dioxide material is the commercial TiO_2 P25 (Evonik). It is a white powder characterized by having an anatase:rutile ratio between 70:30 and 80:20 [92], nanocrystal sizes ranging around 30 to 90 nm and BET surface area of 55 ± 15 $m^2 \cdot g^{-1}$ [26].

Nevertheless, there are some drawbacks of using TiO_2 (P25) as photocatalyst in water processes: the difficulty of separating the catalyst from the treated water and its inefficiency of using radiation higher than 390 nm caused by its large band gap. These disadvantages have led to develop different strategies so as to enhance the physical-chemical properties of titania [82].

Focusing on synthesizing TiO_2-based materials by band gap modification to diminish the electron-hole recombination, doping TiO_2 with metal or non-metal elements (e.g. carbon, nitrogen, iron, manganese) modifies the structure as well as extend its activity to visible range, improving the photocatalytic process at the same time [93–95].

In the same way, coupling titania to other semiconductors is another possible method to raise the photocatalytic efficiency. In this sense, the energy of a photon may be adsorbed by one of the semiconductors and be further transferred to the second one. For that purpose, an appropriate semiconductor choice is crucial for an efficient charge transfer. Materials such as TiO_2-CdS, TiO_2-WO_3, or TiO_2-Fe_2O_3 among others have been reported [26,96–98].

Another promising research field on TiO_2-based photocatalysts deals with the fabrication of titania with a desired morphology and structural properties [83]. For instance, an increase on the BET surface area allows the enhancement of surface chemical reaction on the active catalyst centers. Thus, improved TiO_2 nanosctructures (e.g. nanotubes, nanospheres, nanowires, mesocrystals) have been attracted the attention of researches [99].

In this way, Trataguas' group has already investigated the use of been improved titania-based materials in photoctatalytic removal of water pollutants as shown in **Table 2.6.**

2.4.2. SUPPORTED CATALYSTS

Catalytic reactions are sensitive to the structure of the catalyst, surface atomic arrangement and coordination. Bearing in mind the idea of modifying the mechanical and morphological properties of a catalyst as well as cutting down operational costs in water treatment, photocatalysts immobilized onto different supports have also been studied.

The immobilization can be carried out on either transparent or opaque substrates provided that there is a strong cohesion between support and catalyst. Among supports glass, silica, alumina, carbon or even organic materials are included [71,100–102]. To overcome the problems with powdered titania, numerous techniques have been developed for preparing supported TiO_2. For instance sol–gel, thermal treatment, chemical vapor deposition, electrodeposition, sol-spray, and hydrothermal [103–105].

This work comprises the use of the activated carbon, glass rings and graphene as support materials of titanium dioxide.

Table 2.6. Some literature studies using modified titania-based materials in photocatalytic process for the removal of water contaminants by Trataguas' research group. Photocatalysts, their properties, experimental conditions and main findings.

Photocatalyst/ Properties	Experimental	Main findings	Ref.
B-doped TiO_2 xB-TiO_2-w (Sol-gel method) S_{BET} =120-126, (TiO_2=68.3) $m^2 \cdot g^{-1}$ E_g=3.01-3.12 (TiO_2=3.07) eV	Pesticides (diuron, o-phenylphenol, MCPA, terbuthylazine) $C_{i,0}$=5 $mg \cdot L^{-1}$ Simulated sunlight (Xe lamp) C_{CAT}=0.33 $g \cdot L^{-1}$, Gas: O_2	Washed catalyst led to the removal of unstable boron without further leaching. Degradation rates of pesticides and TOC removal were enhanced by the presence of B. (TiO_2 25%, 6B-TiO_2-w 37%, 12B-TiO_2-w 45% TOC removal in 2h).	[93]
N-doped TiO_2 (Sol-gel method) S_{BET} =11-35 $m^2 \cdot g^{-1}$ E_g=2.99-3.13 eV	Herbicides (clopyralid, triclopyr and picloram) $C_{,0}$=5 $mg \cdot L^{-1}$ (each) UV-A lamps C_{CAT}=0.5 $g \cdot L^{-1}$, Gas: O_3,O_2	TiO_2 crystal only in anatase phase. Mineralization percentages were about 50% and 95% in O_2/UVA/cat and O_3/UVA/cat after 180-min treatment using a Ti:N ratio of 1:1.6. Stable after 5-cycle run of O_3/UVA/cat.	[106]
4%WO_3-TiO_2 (Precipitation, thermal treatment) S_{BET}= 195 $m^2 \cdot g^{-1}$; E_g=2.98 eV	Contaminants (caffeine, metoprolol and ibuprofen) $C_{,0}$=2 $mg \cdot L^{-1}$ (each) Simulated sunlight (Xe lamp) C_{CAT}=0.5 $g \cdot L^{-1}$, Gas: O_3,O_2	NT is a good precursor of composite catalysts due to its textural and surface properties. NT–WO_3 was more active under visible and solar radiation. 64% TOC of the mixture in municipal wastewater was removed in 2 hour by means of O_3/rad/cat.	[96]
TiO_2 nanotubes (NT) (hydrothermal) S_{BET}=320 $m^2 \cdot g^{-1}$; E_g=3.18 eV			
(SiO_2)-Fe_3O_4-TiO_2 (Sol-gel and thermal treatment) S_{BET}=195 $m^2 \cdot g^{-1}$ E_g=2.98 eV	Acetaminophen and/or antipyrine, caffeine, metoprolol and bisphenol A $C_{i,0}$=30 $mg \cdot L^{-1}$ UV lamp C_{CAT}=0.5-1.34 $g \cdot L^{-1}$, Gas: air	Easily recoverable magnetic photocatalysts. Better stability of SiO_2-Fe_3O_4-TiO_2 in solution under UV illumination than Fe_3O_4-TiO_2. Photoactivity was almost comparable to that of commercial TiO_2.	[97]

x=percentage of doped material

A. Carbonaceous materials

In general, carbon materials have been considered as catalyst supports due to their large surface area, promising thermal stability, recovery and recyclability [107].

In nature, carbon presents allotropic structures, exhibiting distinctive physical properties. The different allotropic types of carbon can be divided into amorphous and crystalline forms, such as activated carbon and graphene respectively. **Figure 2.5** schemes different carbon allotropes.

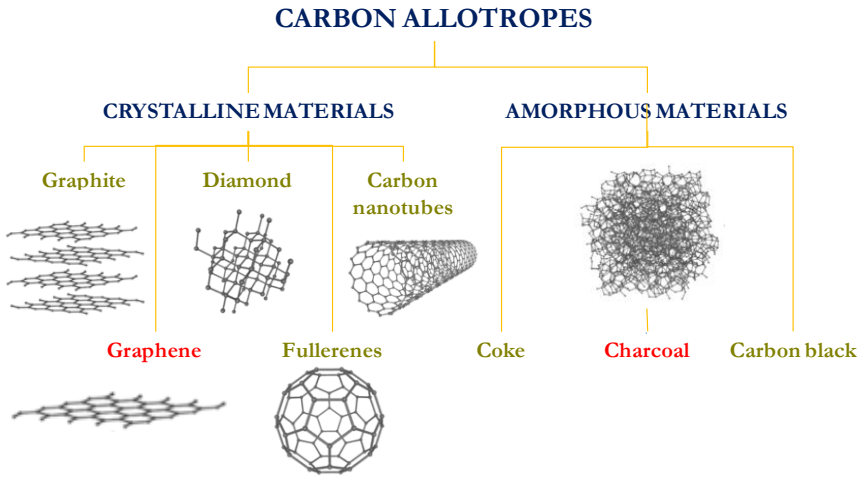

Figure 2.5. Scheme of some examples of carbon allotropes and their internal structures. Adapted from [108].

Activated carbon (AC), also known as activated charcoal, is an extremely porous material with a large surface area (>1000 $m^2 \cdot g^{-1}$), greater than other carbon materials (e.g. carbon nanotubes) [109]. It is commonly used in environmental applications due to its adsorption properties both in liquid and gas phases. For that reason, activated carbon has attracted much attention to support titania for being used in photocatalytic processes. In this sense, the photoactive material could be uniformly distributed on the surface, increasing the contact between the photocatalyst (i.e. TiO_2) and the compounds adsorbed [105]. However, the use of activated carbon implicates using it in granular o powder form.

The two-dimensional honeycomb structure of sp^2 carbon atoms from **graphene (G)** confers it unique properties, outlining among them its flexible structure and high electrical conductivity. These properties make graphene a promising material in the optical, electronic, biological and catalytic fields. In the latter, graphene has been found to be as conductive support, adsorbent, photosensitizer, photostabilizer, photocatalyst, and co-catalyst in the nanocomposites [110]. In spite of not having porosity, metal and

semiconductor nanoparticles deposition onto graphene have been reported [111–114]. In fact, nanoparticles may extend the distance between sheets, leading to increase the surface area of the composite and improving the catalytic activity of graphene-semiconductor based photocatalysts [114].

Table 2.7 compares some properties of activated carbon and graphene while **Figure 2.6** shows structures and electronic microscope images of both carbonaceous materials.

Table 2.7. Mechanical and chemical properties of activated carbon and graphene materials.

Properties	Activated Carbon[a]	Graphene[b]
Surface area ($m^2 \cdot g^{-1}$)	<2500	<2600
Pore volume ($cm^3 \cdot g^{-1}$)	0.7	not available (low)
Thermal conductivity ($W \cdot m^{-1} \cdot K^{-1}$)	0.1	3000-5000
Mobility carriers ($cm^2 \cdot V^{-1} \cdot s^{-1}$)[c]	not available (low)	~10^5
Conductivity ($S \cdot cm^{-1}$)	<20	~10^6
Capacitance ($F \cdot g^{-1}$)	~150	~550

[a:] [115,116] [b:][117,118]; [c:]: at room temperature

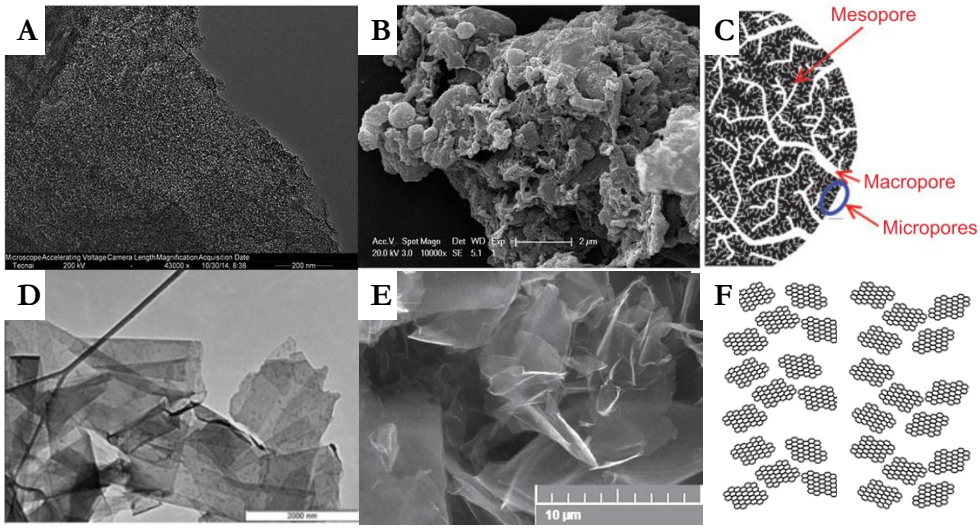

Figure 2.6. Activated carbon and graphene images: TEM and SEM images of AC from rice-straw (A and B), scheme of porous structure of an AC (C), TEM and SEM images of nanoplatelets of commercial graphenes (D and E) and scheme of graphene nanoplatelets (F). Adopted from [119–123].

In general, carbon-TiO_2 hybrid materials are a new class of photocatalysts. However, their uses in photocatalytic ozonation processes for wastewater treatment are still to develop. **Table 2.8** shows some recent works where activated carbon or graphene derivatives have been used as photocatalyst supports in O_3/light/cat processes for the removal of water pollutants.

Table 2.8. Collection of studies using activated carbon and graphene in O_3/light/cat. Photocatalysts, their properties, experimental conditions and main conclusions.

Photocatalyst /Properties	Experimental	Main results	Ref.
TiO_2 +AC	Plasticizers (Bisphenol A, BPA) UV-C (264 nm)	Activated carbon added to O_3/UV-C/TiO_2 system improves the TOC depletion rate (100% of mineralization in 20 min).	[124]
Fe^{3+}-TiO_2 nanotubes/AC %Fe^{3+}-TiO_2= 1 (%Fe= 1)	Toluene UV light	In ultrapure water a 91% of removal was achieved while 70% and 58% of toluene and TOC removal efficiencies were reached in a petrochemical wastewater respectively.	[125]
TiO_2/Fe_3O_4/AC %Ti= 61, %Fe= 4.7 S_{BET} =331 $m^2 \cdot g^{-1}$ M_S=1.56 $emu \cdot g^{-1}$	Pharmaceutical (Metoprolol, MTP) $C_{i,0}$=10 $mg \cdot L^{-1}$ Simulated sunlight (Xe lamp) C_{CAT}=0.33 $g \cdot L^{-1}$	Synthesized material containing TiO_2 in the form of anatase has moderate surface area and pore volume to allow adsorption of organic matter. High photocatalytic activity with a complete MTP removal, 60% of TOC conversion and minor metals leaching.	[126]
N-TiO_2/GO/Titan grid S_{BET} =10.5 $m^2 \cdot g^{-1}$ E_g=1.8 eV	Pharmaceutical (Cefixime) $C_{i,0}$=5 $mg \cdot L^{-1}$ Visible LED light	N-TiO_2/GO-coated titan grid sheets by the electrophoretic deposition (EPD). Maximum degradation efficiency (ca. 80%) was achieved employing 6 grid sheets of N-TiO_2/GO.	[127]
TiO_2/GO %GO= 0.3-4, S_{BET} =203-265 $m^2 \cdot g^{-1}$ E_g=2.54 eV	Pharmaceutical (primidone, PM) $C_{i,0}$=20 $mg \cdot L^{-1}$ Visible LED light C_{CAT}=0.25 $g \cdot L^{-1}$	Lower band gap and a more developed surface area in TiO_2/GO composites. Optimum TiO_2/GO with 0.75%GO loading giving place to 80% of PM mineralization in 2 hours higher than bare TiO_2.	[80]
TiO_2/rGO %GO= 2-4	Plasticizers (Bisphenol A, BPA) $C_{i,0}$=10 $mg \cdot L^{-1}$ UV (365 nm; high pressure Hg lamp) C_{CAT}=0.5 $g \cdot L^{-1}$	Efficient mineralization level (i.e. 98.4%) by TiO_2/rGO and stable catalyst after five consecutive photocatalytic ozonation runs. GO sheets enhanced the photo-induced carriers and the O_3 decomposition.	[128]
TiO_2/N-rGO; TiO_2/S-rGO S_{BET} =26-272 $m^2 \cdot g^{-1}$ E_g=3.10 eV	Pharmaceutical (dyphenhydramine, DP) $C_{i,0}$=100 $mg \cdot L^{-1}$ UV-vis (medium pressure Hg lamp) C_{CAT}=1.0 $g \cdot L^{-1}$	Doped rGOs synthetized by Brodie's method led to higher S_{BET} though better degradation rate (k_{app}= 52.5 $\times 10^{-3}$ min^{-1}) of DP is achieved with N-doped rGO by Hummers' method.	[129]

% element expressed as weight percentage; M_S: Saturation moment; GO: graphene oxide; rGO: reduced graphene oxide; k_{app}: apparent rate constant

B. Glass materials

Commonly, borosilicate glass is a particular glass consisted of silica (c.a. 70%), boron oxide (10%), sodium oxide (8%), potassium oxide (8%) and other impurities such as calcium oxide and alumina. It is a rigid material, transparent to radiation over 300 nm which makes it appropriate for UV-A and solar photochemical processes. Besides, working at high temperatures (T_g=550 ºC), a plastic-viscous material is formed, and as consequence, it is being widely used as to be coated material. Several types and shapes of glass materials are being employed in the photo-degradation of water pollutants, including glass beads, glass plates, glass tubes or glass rings (e.g. Raschig rings) [71,100,130].

2.4.3. METAL ORGANIC FRAMEWORKS (MOFs)

Metal-organic frameworks are organic-inorganic hybrid materials based on a coordination of metal ions (nodes) and an organic linker [131]. The most common ligands are polycarboxylates, especially benzene carboxylic acids, such as terepthalic acid (i.e. MIL-53) or trimesic acid (ie. MOF-177). Regarding nodes, zinc, cooper, cobalt, iron or titanium are the most widely used metals [81,132–134]. **Figure 2.2 (B)** depicts a scheme of a carboxylate-based MOF chemical structure.

A wide range of metal-organic compounds may be synthesized for several applications (e.g. drug delivery, electronic and electrical applications, catalysis) [135]. In the heterogeneous catalysis field, in comparison to traditional materials, MOFs are known to enhance the mass transfer and substrate-active site reaction rate. In addition, MOFs can raise the ability to perfom selective reactions with specific compounds since large size molecules could not react into the catalytic active sites [136]. Futhermore, the combination of some organic compounds and metal ions confers to some materials several features such as large surface area, flexible structure and/or UV-visible response [25,135,137]. Thus, MOFs could absorb photons and transfer an electron from the ligand to the positive metal ions bounded (i.e. LCCT mechanism), improving at the same time its photocatalytic activity [25].

All things considered, MOFs might work as support for other nanoparticles, as catalyst itself or being a sacrifical template for heteroatoms-doped carbon-based nanocatalysts [136]. For that reason, the metal-organic structures has gained attention in the field of water treatment for the removal of water pollutants. Specifically the employment of MIL-100(Fe) such as candidate for photocatalysis has been recently studied.

Table 2.9. Some reports on MIL-100 (Fe) material as catalyst for the degradation of water contaminants by different AOPs.

Synthesis	Treatment	Experimental conditions	Main results	Ref.
Hydrothermal 150 ºC in acid water S_{BET}= 1714 $m^2 \cdot g^{-1}$	Photocatalysis	1000W UV-C lamp Methylente blue (64 $mg \cdot L^{-1}$) MOF: 0.05 $g \cdot L^{-1}$	A 20% of dye is degraded in 3h, being previously adsorbed a 10% of methylene blue in 1 h. **Stability study**: n.r	[138]
TMA, Fe in water (room T, atm P) S_{BET}= 1934 $m^2 \cdot g^{-1}$	Photocatalysis	150W UV lamp/Natural sun light Methyl orange (5 $mg \cdot L^{-1}$) MOF: 0.35 $g \cdot L^{-1}$	Higher removal degree using UV-lamp resource (65% in 7h) in contrast to the natural sun light (40% in 6h). **Stability study**: n.r	[139]
Hydrothermal 150 ºC S_{BET}= n.r.	Photocatalysis	500W Xe lamp (Visible light) Rhodamine B (10 $mg \cdot L^{-1}$) MOF: 1 $g \cdot L^{-1}$	A high catalyst dose with a minor enhancement of the degradation after 1.5 h of photocatalysis (i.e. 50%). A 44% is adsorbed in 30 min prior reaction. **Stability study**: n.r	[140]
Hydrothermal 150 ºC in acid water S_{BET}= 1556 $m^2 \cdot g^{-1}$	Photocatalysis	300W Xe lamp (Visible light) Methylente blue (16 $mg \cdot L^{-1}$) Rhodamine B (24 $mg \cdot L^{-1}$) MOF: 1 $g \cdot L^{-1}$	Slight improvement during photocatalysis in comparison with the adsorption period (ca. 90% of methylene blue and 80% of Rhodamine B in both cases). **Stability study**: n.r	[141]
Hydrothermal (Fe salts + TMA) 200 ºC S_{BET}= n.r.	Photocatalysis	9W UV-C lamp Basic blue 41 dye (BB41) (20 $mg \cdot L^{-1}$) MOF: 0.01-0.04 $g \cdot L^{-1}$	The removal efficiencies were about 90-100% of BB41 in 3 hour for photocatalysis. The adsorption step can be neglected (i.e. <5% in any case in 3h). **Stability study**: Recoverability of catalysts after 3 cycle runs (98, 94 and 86 wt.% depending on the material).	[142]
Hydrothermal 160 ºC in acid water S_{BET}= 1203 $m^2 \cdot g^{-1}$	Photocatalysis	300W Xe lamp (Visible light) Tetracycline (50 $mg \cdot L^{-1}$) MOF: 0.5 $g \cdot L^{-1}$	Over a 50% of Tetracycline was removed under 3-hour illumination, though a 44% was already adsorbed in 1h. **Stability study**: n.r	[133]
Fe+TMA 95 ºC in water S_{BET}= n.r.	Photocatalysis	150W Xe lamp (Visible light) Tetracycline (10 $mg \cdot L^{-1}$) MOF: 0.2 $g \cdot L^{-1}$	Degradation degree below 10% in just 1 hour. **Stability study**: n.r	[143]

n.r.: not reported

~ 50 ~

Table 2.9. (continued) Some reports on MIL-100 (Fe) material as catalyst for the degradation of water contaminants by different AOPs.

Synthesis	Treatment	Experimental conditions	Efficiency results	Ref.
Hydrothermal 150 ºC in acid water SBET= n.r.	Photocatalysis	300W Xe lamp (White light) Tetracycline (10 mg·L^{-1}) MOF: 0.25 g·L^{-1}	The removal by adsorption reached a 10% (1h), increasing this value up to 38% in 2.3h of photocatalysis. **Stability study**: n.r.	[144]
Hydrothermal 150 ºC in acid water S_{BET}= 1646 m^2/g	Fenton-like	H_2O_2 (40 mM) Methylente blue (500 mg·L^{-1}) MOF: 1 g·L^{-1}	Almost 95% of MB was removed in 4h, being a 30% of MB previously adsorbed (50 min). TOC efficiency increased from 40% in 4-hour reaction up to 80% in 25h. **Stability**: Fe leaching about 2 mg·L^{-1} (4h)	[32]
Hydrothermal 160 ºC in acid water S_{BET}= 2000 m^2·g^{-1}	Photo-Fenton-like	H_2O_2 (8.3 mM) 300W Xe lamp (Visible light) Theophylline (TPH) (20 mg·L^{-1}) Ibuprofen (IBP) (20 mg·L^{-1}) Bisphenol A (BphA) (20 mg·L^{-1}) MOF: 0.125 g·L^{-1}	High efficiency removals (i.e. 80% TPH, 65% IBP and 35%BphA). The mineralization degree were 29%, 46% and 16%, respectively for 2 hour of treatment. **Stability study**: n.r.	[145]
Hydrothermal 130 ºC S_{BET}= 1670 m^2·g^{-1}	Photo-Fenton-like	H_2O_2 (17 mM) 500W Xe lamp (Visible light) Methylente blue (50 mg·L^{-1}) MOF: 0.20 g·L^{-1}	An additional improvement of dye removal up to 85% in 1h after the adsorption period (55% in 1hour). **Stability study**: n.r.	[102]
Hydrothermal 160 ºC S_{BET}= 1203 m^2·g^{-1}	Photo-Fenton-like	H_2O_2 (55 mM) 55W Xe lamp (Visible light) Formaldehyde (700 mg·L^{-1}) MOF: 1.13 g·L^{-1}	Though formaldehyde is highly adsorbed onto the MOF (75%, 1h), a 95% of removal in 2.6h after the treatment. The effectivity gradually decreased to 65.9% in the 5th cycle. **Stability study**: Fe leaching <4 mg·L^{-1} after 5 cycle runs	[146]
Hydrothermal 130 ºC S_{BET}= 982 m^2·g^{-1}	Ozonation	O_3 (12 g·h^{-1}) Rhodamine B (40 mg·L^{-1}) MOF: 0.2 g·L^{-1}	A 48% of dye was adsorbed in 30 min. However, Rhodamine B was totally removed in less than 10 min of catalytic ozonation. **Stability study**: n.r.	[147]

n.r.: not reported

Despite of that fact, their applicability and stability in water under oxidizing conditions is still uncertain [148]. **Table 2.9** gathers a collection of articles where MIL-100(Fe) has been employed as catalyst for water remediation.

2.5. PROBE COMPOUNDS

In this research, some organic compounds have been selected as model compounds to study their degradation in water and the efficiency of the treatments applied. The use, importance of study, background and some of their physicochemical properties are detailed in this section.

2.5.1. CARBOXYLIC ACIDS

O**xalic acid** is a dicarboxylic acid, a typical organic by-product by biological oxidation and ozonation. It has a role as a human metabolite, produced in the body during the metabolism of some organic acids [149]. This strong dicarboxylic acid is also present in many plants and vegetables in form of oxalate, primarily as potassium oxalate. These plants include leafy greens, vegetables, fruits or seed that frequently take part into the human diet such as pepper or spinach among others [150]. Oxalic acid or oxalate anion is not metabolized by humans; consequently, it is then expelled in the urine. High-oxalate diets lead to a risk of kidney stones and other health problems.

Also, low molecular weight carboxylic acids are well-known by-products in ozonation processes [17,151–153] and generally refractory to ozone (e.g. $k_{O3\text{-}oxalic} < 0.04\ M^{-1}\cdot s^{-1}$, except formic acid) [47]. Moreover, the removal of oxalic acid leads to a complete mineralization into CO_2 and H_2O, without generating other intermediates, which makes it a perfect candidate as probe compound.

T**rimesic acid** is a benzene derivative with three carboxylic acid groups, highly soluble in water. It is widely used in different applications, from water soluble resin syntheses to pharmaceutical, such as drugs and gene carriers intermediate [154]. Recently, it is being applied as organic precursor of different MOF structures. Despite of that, its reactivity toward ozone and hydroxyl radical is unknown, so far.

The physicochemical properties and spectra of both carboxylic acids are summarized in **Table 2.10**.

Table 2.10. Physicochemical properties and absorption spectra of oxalic and trimesic acids.

OXALIC ACID	
IUPAC name	Ethanedioic acid
CAS number	144-62-7
Molecular formula	$C_2H_2O_4$
Molecular weight	90.03 g·mol^{-1}
Water solubility	2.2 x 10^5 mg·L^{-1} at 25 ºC
pKa	1.46, 4.40
Category	Metabolite
TRIMESIC ACID	
IUPAC name	benzene-1,3,5-tricarboxylic acid
CAS number	554-95-0
Molecular formula	$C_9H_6O_6$
Molecular weight	210.14 g·mol^{-1}
Water solubility	2.7 x 10^4 mg·L^{-1} at 25 ºC
pKa	3.12, 3.89, 4.70
Category	Material for synthesis

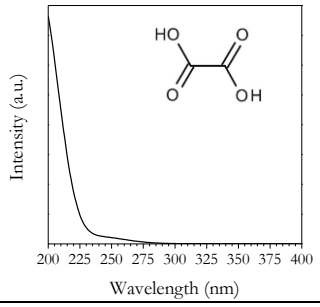

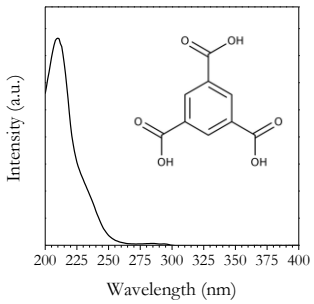

2.5.2. CONTAMINANTS OF EMERGING CONCERN

Contaminants of emerging concern are those mainly organics found at extremely low concentrations in water bodies and wastewaters (especially urban wastewater) (μg·L^{-1} or ng·L^{-1}). A representative mixture of contaminants of emerging concern have been chosen as model compounds due to their recalcitrance to biological wastewater treatment [4,11,155–157] and/or its reactivity toward molecular ozone (see **Table 7.S1**). Examples of these compounds are:

Bezafibrate, a fibric acid derivative, is extensively used to reduce blood triglyceride and cholesterol levels in patients with hyperlipidaemia [79]. Bezafibrate produces an increase of the high density lipoprotein (HDL) cholesterol levels, and decreases the total and low density lipoprotein (LDL) cholesterol levels [158]. Moreover, only 50% of this chemical is metabolized by the human organism. This fact linked to its high polar and acid-base character, make bezafibrate to be discharged into the sewage system and dispersed in the aquatic environments unchanged [159].

Caffeine, a well-known psychoactive drug, legally recognized as safe and highly consumed all over the world. Despite of this, stimulant properties of caffeine are weak

in comparison with other drugs [160]. It is naturally found in seeds, nuts, or leaves of many plants since it helps them to protect against insects. Moreover, the coffee bean is the most used source for caffeine-containing drinks. Toxic doses are given over 10 g·day^{-1}, highly superior to the typical daily consumption of a cup of coffee, which contains around 80 to 175 mg of caffeine.

Ciprofloxacin, a synthetic broad spectrum antibiotic, categorized as a second-generation fluoroquinolone. It is available in both intravenous and oral formulations to treat several infections, such as urinary tract infections, gastrointestinal infections, lower respiratory tract or otitis among others [161]. However, it is a persistent compound through conventional water treatments, becoming a risk even at the predicted environmental concentrations [162].

Clofibric acid, a primary metabolite of clofibrate which, as other fibrates, is widely used as active principle of blood lipid regulator. It is also considered as herbicide due to its function as plant growth regulator against the hormone auxin. Its polar character makes clofibric acid does not significantly adsorb in soil and easily spread in surface and groundwater, remaining in the environment for a long time [163,164]. Its biological long-term effects are not completely known, nonetheless it may be considered as a potential endocrine disruptor [165], being able to affect at hematological, biochemical, ion regulatory, hormonal and enzymological levels [166,167].

Cotinine, the major metabolite of nicotine, is found in tobacco leaves. It even remains in the blood of tobacco smokers after giving up smoking. Besides, it has a role as a biomarker and therapeutic agent as antidepressant since it may be pharmacologically active, having effects in the nervous system [168].

DEET, a chemical (*N*,*N*-diethyl-meta-toluamide) is used as active compound in many insect repellent for protection against mosquitos [78]. This personal care product (PPCP) is available in liquids, lotions, sprays or impregnated materials (i.e. wristbands) at concentration of 4-100%. It was developed by the U.S. Army and nowadays it is extensively used worldwide. Although toxicity studies indicates that DEET is slightly toxic to aquatic invertebrates and fresh-water fishes [169,170], it may have potential carcinogenic properties in human nasal mucosal cells [171], or even worst, it may result in coma and seizures if children ingest a low dose of DEET [172].

Ibuprofen, one of the most consumed over-the-counter drug together with the commercial paracetamol (i.e. acetaminophen) and aspirin (i.e. acetylsalicylic acid) [173].

It is enclosed into the nonsteroidal anti-inflammatory drug (NSAID) class and is commonly used to release pain, fever and inflammation, including migraines or rheumatoid arthritis. Some studies with *Daphnia magna* reported that minor consequences may occur at environmentally realistic concentrations [173]. In contrast, other studies with different species (e.g. *Lemna minor*) outlined that low concentration of ibuprofen may have potential implications associated with the presence of pharmaceuticals in aquatic ecosystems [4,174].

Metoprolol, a cardioselective β_1-adrenergic blocking agent used to prevent problems related to heart such as myocardial infarction or hypertension [175]. It is commonly employed as succinate and tartrate form. Besides, metoprolol is one of the preferred β-blockers being widely prescribed worldwide. The widespread use of b-blockers has resulted in their appearance in the aquatic environment [176–178]. This compound have endocrine-disrupting effects, causing problems of reproduction and growth of some species [179].

Sulfamethoxazole, an antibiotic, categorized as a sulfonamide. It is used for fighting against bacterial infections (e.g. urinary tract infections or bronchitis). It is now mostly used in combination with the trimethoprim (TMP) antibiotic owing to the synergistic effect in the SMX:TMP ratio 5:1. Sulfamethoxazole is primarily metabolized in the liver, with approximately 30% excreted unchanged in the urine [180].

Tritosulfuron, a xenobiotic sulfonylurea herbicide, is used as broad-spectrum post-emergence control mainly to take action in cereals, rice, maize and turf. It was developed by BASF Company and is commercialized worldwide. Tritosulfuron acts through leaves instead of soil [181].

Some physicohemical properties of each CEC mentioned above that have been considered important for the studies of this Thesis are given in **Table 2.11.**

Table 2.11. Physicochemical properties and absorption spectra of CECs studied.

BEZAFIBRATE

IUPAC name	2-[4-[2-[(4-chlorobenzoyl)amino] ethyl]phenoxy]-2-methylpropanoic acid
CAS number	41859-67-0
Molecular formula	$C_{19}H_{20}ClNO_4$
Molecular weight	361.8 g·mol^{-1}
Water solubility	1.55 mg·L^{-1} at 25 ºC
pKa	3.8
Category	Pharmaceutical: lipid regulator.

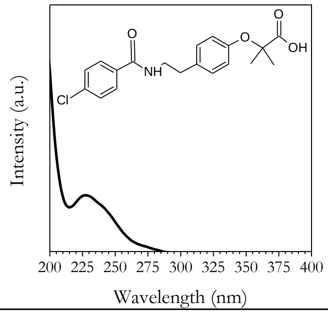

CAFFEINE

IUPAC name	1,3,7-trimethylpurine-2,6-dione
CAS number	58-08-2
Molecular formula	$C_8H_{10}N_4O_2$
Molecular weight	194.2 g·mol^{-1}
Water solubility	2.16 x 10^4 mg·L^{-1} at 25 ºC
pKa	10.4
Category	Drug: stimulant

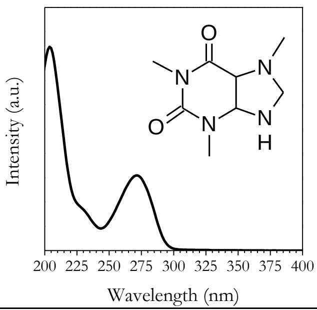

CIPROFLOXACIN

IUPAC name	1-cyclopropyl-6-fluoro-4-oxo-7-piperazin-1-ylquinoline-3-carboxylic acid
CAS number	85721-33-1
Molecular formula	$C_{17}H_{18}FN_3O_3$
Molecular weight	331.34 g·mol^{-1}
Water solubility	3 x 10^4 mg·L^{-1} at 20 ºC
pKa	6.1, 8.8
Category	Pharmaceutical: antibiotic

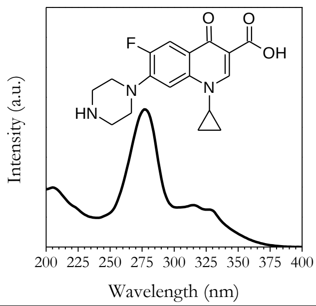

CLOFIBRIC ACID

IUPAC name	2-(4-Chlorophenoxy)-2-methylpropanoic acid
CAS number	882-09-7
Molecular formula	$C_{10}H_{11}ClO_3$
Molecular weight	214.64 g·mol^{-1}
Water solubility	583 mg·L^{-1} at 25 ºC
pKa	3.2
Category	Pharmaceutical: lipid regulator. Herbicide: growth regulator

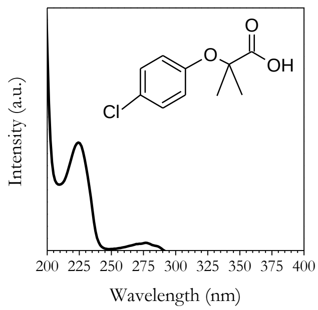

Table 2.11. (continued) Physicochemical properties and absorption spectra of CECs studied.

COTININE	
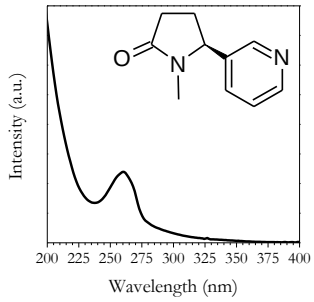	(5*S*)-1-methyl-5-pyridin-3-ylpyrrolidin-2-one — IUPAC name
	486-56-6 — CAS number
	$C_{10}H_{12}N_2O$ — Molecular formula
	176.21 g·mol^{-1} — Molecular weight
	10^6 mg·L^{-1} at 25 ºC — Water solubility
	- — pKa
	Drug (metabolite) — Category
DEET	
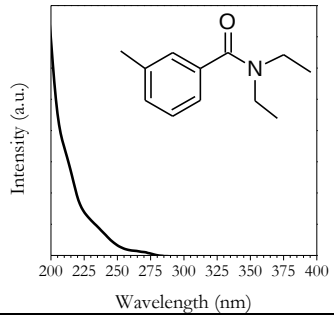	*N*,*N*-diethyl-3-methylbenzamide — IUPAC name
	134-62-3 — CAS number
	$C_{12}H_{17}NO$ — Molecular formula
	191.27 g·mol^{-1} — Molecular weight
	1680 mg·L^{-1} at 25 ºC — Water solubility
	- — pKa
	PCP: insect repellent — Category
IBUPROFEN	
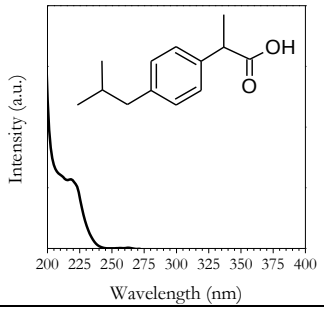	2-(4-Isobutylphenyl)propanoic acid — IUPAC name
	15687-27-1 — CAS number
	$C_{13}H_{18}O_2$ — Molecular formula
	206.28 g·mol^{-1} — Molecular weight
	21 mg·L^{-1} at 25 ºC — Water solubility
	5.3 — pKa
	Pharmaceutical: anti-inflamatory — Category
METOPROLOL	
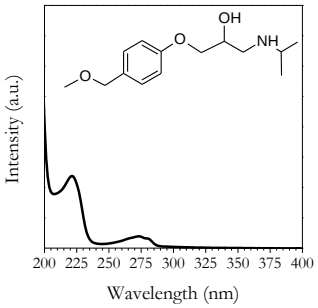	1-[4-(2-methoxyethyl)phenoxy]-3-(propan-2-ylamino)propan-2-ol — IUPAC name
	51384-51-1 — CAS number
	$C_{15}H_{25}NO_3$ — Molecular formula
	206.28 g·mol^{-1} — Molecular weight
	402 mg·L^{-1} at 25 ºC — Water solubility
	9.7, 14.1 — pKa
	Pharmaceutical: β-blocker — Category

Table 2.11.(continued) Physicochemical properties and absorption spectra of CECs studied.

SULFAMETHOXAZOLE	
IUPAC name	4-amino-N-(5-methyl-1,2-oxazol-3-yl) benzenesulfonamide
CAS number	723-46-6
Molecular formula	$C_{10}H_{11}N_3O_3S$
Molecular weight	253.28 g·mol^{-1}
Water solubility	459 mg·L^{-1} at 25 ºC
pKa	1.7, 5.6
Category	Pharmaceutical: antibiotic

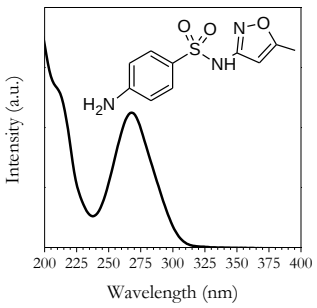

TRITOSULFURON	
IUPAC name	1-[4-methoxy-6-(trifluoromethyl)-1,3,5-triazin-2-yl]-3-[2-(trifluoro-methyl) phenyl] sulfonylurea
CAS number	142469-14-5
Molecular formula	$C_{13}H_9F_6N_5O_4S$
Molecular weight	445.3 g·mol^{-1}
Water solubility	78.3 mg·L^{-1} at 25 ºC
pKa	4.7
Category	Herbicide

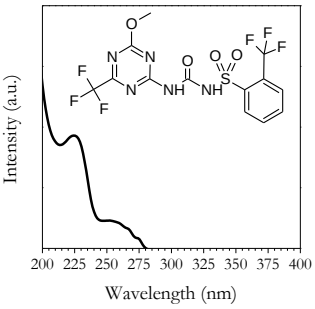

REFERENCES

[1] UNESCO-United Nations Educational Scientific and Cultural Organization, "The United Nations World Water Development Report. Leaving no one behind" (**2019**).

[2] Directive 2013/39/EU, "Directive 2013/39/EU of the European Parliament and of the Council of 12 August 2013 amending Directives 2000/60/EC and 2008/105/EC as regards priority substances in the field of water policy" (**2013**).

[3] Decision 2018/840/EU, "Commission implementing decision (EU) 2018/840 of 5 June 2018 establishing a watch list of substances for Union-wide monitoring in the field of water policy pursuant to Directive 2008/105/EC of the European Parliament and of the Council and repealing Comm" (**2018**).

[4] A. Pal, K.Y.H. Gin, A.Y.C. Lin, M. Reinhard, "Impacts of emerging organic contaminants on freshwater resources: review of recent occurrences, sources, fate and effects" *Sci. Total Environ.* 408 (**2010**) 6062–6069.

[5] M. Gavrilescu, K. Demnerová, J. Aamand, S. Agathos, F. Fava, "Emerging pollutants in the environment: present and future challenges in biomonitoring, ecological risks and bioremediation" *N. Biotechnol.* 32 (**2015**) 147–156.

[6] P.E. Rosenfeld, L.G.H. Feng, P.E. Rosenfeld, L.G.H. Feng, "Emerging Contaminants" in: "*Risks of Hazardous Wastes*" 1st edition. *William Andrew (Applied Science Publishers)*, Oxford (**2011**).

[7] M.A. Marcoux, M. Matias, F. Olivier, G. Keck, "Review and prospect of emerging contaminants in waste - Key issues and challenges linked to their presence in waste treatment schemes: General aspects and focus on nanoparticles" *Waste Manag.* 33 (**2013**) 2147–2156.

[8] S.D. Richardson, T.A. Ternes, "Water analysis: emerging contaminants and current issues" *Anal. Chem.* 86 (**2014**) 2813–2848.

[9] M.J. Gil, A.M. Soto, J.I. Usma, O.D. Gutiérrez, "Contaminantes emergentes en aguas, efectos y posibles tratamientos" *Prod. + Limpia.* 7 (**2012**) 52–73.

[10] D.J. Lapworth, N. Baran, M.E. Stuart, R.S. Ward, "Emerging organic

contaminants in groundwater: a review of sources, fate and occurrence" *Environ. Pollut.* 163 (**2012**) 287–303.

[11] N.H. Tran, M. Reinhard, K.Y.-H. Gin, "Occurrence and fate of emerging contaminants in municipal wastewater treatment plants from different geographical regions-a review" *Water Res.* 133 (**2018**) 182–207.

[12] F.E. Hancock, "Catalytic strategies for industrial water re-use" *Catal. Today*. 53 (**1999**) 3–9.

[13] P.C. Singer, D.A. Reckhow, "Chemical Oxidation" in: "*Water Quality & Treatment: A Handbook of Community Water Supplies.*" 5th edition. *American Water Works Association (AWWA), McGraw-Hill*, New York (**1999**).

[14] W.H. Glaze, J.-W. Kang, D.H. Chapin, "The chemistry of water treatment processes involving ozone, hydrogen peroxide and ultraviolet radiation" *Ozone Sci. Eng.* 9 (**1987**) 335–352.

[15] C. Tai, X. Gu, H. Zou, Q. Guo, "A new simple and sensitive fluorometric method for the determination of hydroxyl radical and its application" *Talanta*. (**2002**).

[16] R. Munter, "Advanced oxidation processes - Current status and processes" *Proc. Est. Acad. Sci. Chem*. 50 (**2001**) 59–80.

[17] F.J. Beltrán, "Ozone reaction kinetics for water and wastewater systems" *Lewis Publishers*, Florida (**2004**).

[18] O. Legrini, E. Oliveros, A.M. Braun, "Photochemical processes for water treatment" *Chem. Rev.* 93 (**1993**) 671–698.

[19] R. Andreozzi, V. Caprio, A. Insola, R. Marotta, "Advanced oxidation processes (AOP) for water purification and recovery" *Catal. Today*. 53 (**1999**) 51–59.

[20] J. Rivas, F. Beltrán, B. Acedo, O. Gimeno, "Two-step wastewater treatment: sequential ozonation - aerobic biodegradation" *Ozone Sci. Eng. J. Int. Ozone Assoc.* 22 (**2000**) 617–636.

[21] A. Espejo, A. Aguinaco, J.F. García-Araya, F.J. Beltrán, "Sequential ozone advanced oxidation and biological oxidation processes to remove selected pharmaceutical contaminants from an urban wastewater" *J. Environ. Sci. Heal. -*

Part A Toxic/Hazardous Subst. Environ. Eng. 49 (**2014**) 1015–1022.

[22] B. Guieysse, Z.N. Norvill, "Sequential chemical–biological processes for the treatment of industrial wastewaters: Review of recent progresses and critical assessment" *J. Hazard. Mater.* 267 (**2014**) 142–152.

[23] M. Klavarioti, D. Mantzavinos, D. Kassinos, "Removal of residual pharmaceuticals from aqueous systems by advanced oxidation processes" *Environ. Int.* 35 (**2009**) 402–417.

[24] B. Ohtani, "Photocatalysis A to Z-What we know and what we do not know in a scientific sense" *J. Photochem. Photobiol. C Photochem. Rev.* 11 (**2010**) 157–178.

[25] Y. Li, H. Xu, S. Ouyang, J. Ye, "Metal-organic frameworks for photocatalysis" *Phys. Chem. Chem. Phys.* 18 (**2016**) 7563–7572.

[26] S. Malato, P. Fernández-Ibáñez, M.I. Maldonado, J. Blanco, W. Gernjak, "Decontamination and disinfection of water by solar photocatalysis: Recent overview and trends" *Catal. Today*. 147 (**2009**) 1–59.

[27] M. Zhang, H. Dong, L. Zhao, D. Wang, D. Meng, "A review on Fenton process for organic wastewater treatment based on optimization perspective" *Sci. Total Environ.* (**2019**).

[28] W. Gernjak, M. Fuerhacker, P. Fernández-Ibañez, J. Blanco, S. Malato, "Solar photo-Fenton treatment — Process parameters and process control" *Appl. Catal. B Environ.* 64 (**2006**) 121–130.

[29] L. Prieto-Rodríguez, I. Oller, N. Klamerth, A. Agüera, E.M. Rodríguez, S. Malato, "Application of solar AOPs and ozonation for elimination of micropollutants in municipal wastewater treatment plant effluents" *Water Res.* 47 (**2013**) 1521–1528.

[30] A. Durán, J.M. Monteagudo, I. Sanmartín, A. Carrasco, "Solar photo-Fenton mineralization of antipyrine in aqueous solution" *J. Environ. Manage.* 130 (**2013**) 64–71.

[31] M. Hartmann, S. Kullmann, H. Keller, "Wastewater treatment with heterogeneous Fenton-type catalysts based on porous materials" *J. Mater. Chem.* 20 (**2010**) 9002–9017.

[32] H. Lv, H. Zhao, T. Cao, L. Qian, Y. Wang, G. Zhao, "Efficient degradation of high concentration azo-dye wastewater by heterogeneous Fenton process with iron-based metal-organic framework" *J. Mol. Catal. A Chem.* 400 (**2015**) 81–89.

[33] J. Hoigné, "Chemistry of aqueous ozone and transformation of pollutants by ozonation and advanced oxidation processes" in: J. Hrubec (Ed.), "*Quality and Treatment of Drinking Water II*" *Springer Berlin Heidelberg*, Berlin, Heidelberg (**1998**).

[34] O.J. Murphy, G.D. Hitchens, "Method and apparatus for electrochemical production of ozone" no. 5,460,705 (**1995**).

[35] A.J. Pincon, "Method and apparatus for producing ozone" no. 4,124,467 (**1978**).

[36] J.L. Sotelo, F.J. Beltrán, F.J. Benítez, J. Beltrán-Heredia, "Ozone decomposition in water: kinetic study" *Ind. Eng. Chem. Res.* 26 (**1987**) 39–43.

[37] Y. Ku, W.J. Su, Y.S. Shen, "Decomposition kinetics of ozone in aqueous solution" *Ind. Eng. Chem. Res.* 35 (**1996**) 3369–3374.

[38] R.E. Bühler, J. Staehelin, J. Hoigné, "Ozone decomposition in water studied by pulse radiolysis. 1. HO2/O2- and HO3/O- as intermediates" *J. Phys. Chem.* 88 (**1984**) 2560–2564.

[39] J. Staehelin, R.E. Bühler, J. Hoigné, "Ozone decomposition in water studied by pulse radiolysis. 2. Hydroxyl and hydrogen tetroxide (HO_4·) as chain intermediates" *J. Phys. Chem.* 88 (**1984**) 5999–6004.

[40] H. Tomiyasu, H. Fukutomi, G. Gordon, "Kinetics and mechanism of ozone decomposition in basic aqueous solution" *Inorg. Chem.* 24 (**1985**) 2962–2966.

[41] J.L. Acero, U. Von Gunten, "Influence of carbonate on the ozone/hydrogen peroxide based advanced oxidation process for drinking water treatment" *Ozone Sci. Eng.* 22 (**2000**) 305–328.

[42] E. Reisz, W. Schmidt, H.P. Schuchmann, C. Von Sonntag, "Photolysis of ozone in aqueous solutions in the presence of tertiary butanol" *Environ. Sci. Technol.* 37 (**2003**) 1941–1948.

[43] E.M. Rodríguez, G. Márquez, M. Tena, P.M. Álvarez, F.J. Beltrán, "Determination of main species involved in the first steps of TiO_2 photocatalytic

degradation of organics with the use of scavengers: The case of ofloxacin" *Appl. Catal. B Environ.* 178 (**2015**) 44–53.

[44] P.R. Gogate, A.B. Pandit, "A review of imperative technologies for wastewater treatment I: Oxidation technologies at ambient conditions" *Adv. Environ. Res.* 8 (**2004**) 501–551.

[45] F.J. Beltrán, A. Rey, "Free radical and direct ozone reaction competition to remove priority and pharmaceutical water contaminants with single and hydrogen peroxide ozonation systems" *Ozone Sci. Eng.* 40 (**2018**) 1–15.

[46] J. Hoigné, H. Bader, W.R. Haag, J. Staehelin, "Rate constants of reactions of ozone with organic and inorganic compounds in water-III. Inorganic compounds and radicals" *Water Res.* 19 (**1985**) 993–1004.

[47] J. Hoigné, H. Bader, "Rate constants of reactions of ozone with organic and inorganic compounds in water — II disociating organic compounds" *Water Res.* 17 (**1983**) 185–194.

[48] J. Rivera-Utrilla, M. Sánchez-Polo, M.Á. Ferro-García, G. Prados-Joya, R. Ocampo-Pérez, "Pharmaceuticals as emerging contaminants and their removal from water. A review" *Chemosphere*. 93 (**2013**) 1268–1287.

[49] F.J. Beltrán, F.J. Rivas, R. Montero-De-Espinosa, "A TiO_2/Al_2O_3 catalyst to improve the ozonation of oxalic acid in water" *Appl. Catal. B Environ.* 47 (**2004**) 101–109.

[50] M. Sánchez-Polo, E. Salhi, J. Rivera-Utrilla, U. Von Gunten, "Combination of ozone with activated carbon as an alternative to conventional advanced oxidation processes" *Ozone Sci. Eng.* 28 (**2006**) 237–245.

[51] P. Pocostales, P. Álvarez, F.J. Beltrán, "Catalytic ozonation promoted by alumina-based catalysts for the removal of some pharmaceutical compounds from water" *Chem. Eng. J.* 168 (**2011**) 1289–1295.

[52] P.M. Álvarez, J.F. García-Araya, F.J. Beltrán, I. Giráldez, J. Jaramillo, V. Gómez-Serrano, "The influence of various factors on aqueous ozone decomposition by granular activated carbons and the development of a mechanistic approach" *Carbon N. Y.* 44 (**2006**) 3102–3112.

[53] P.M. Álvarez, F.J. Masa, J. Jaramillo, F.J. Beltrán, V. Gómez-Serrano, "Kinetics of ozone decomposition by granular activated carbon" *Ind. Eng. Chem. Res.* 47 (**2008**) 2545–2553.

[54] P.C.C. Faria, J.J.M. Órfão, M.F.R. Pereira, "Activated carbon catalytic ozonation of oxamic and oxalic acids" *Appl. Catal. B Environ.* (**2008**).

[55] F.J. Beltrán, F.J. Rivas, R. Montero-De-Espinosa, "Iron type catalysts for the ozonation of oxalic acid in water" *Water Res.* 39 (**2005**) 3553–3564.

[56] F.J. Beltrá, F.J. Rivas, R.N. Montero-de-Espinosa, "Ozone-enhanced oxidation of oxalic acid in water with cobalt catalysts. 1. Homogeneous catalytic ozonation" (**2003**).

[57] L. Sánchez, X. Domènech, J. Casado, J. Peral, "Solar activated ozonation of phenol and malic acid" *Chemosphere.* 50 (**2003**) 1085–1093.

[58] J.M. Anglada, M. Martins-Costa, M.F. Ruiz-López, J.S. Francisco, "Spectroscopic signatures of ozone at the air-water interface and photochemistry implications." *Proc. Natl. Acad. Sci. U. S. A.* 111 (**2014**) 11618–23.

[59] D. Biedenkapp, L.G. Hartshorn, E.J. Bair, "The $O(^1D) + H_2O$ reaction" *Chem. Phys. Lett.* 5 (**1970**) 379–381.

[60] L. Chu, C. Anastasio, "Formation of hydroxyl radical from the photolysis of frozen hydrogen peroxide" *J. Phys. Chem. A.* 109 (**2005**) 6264–6271.

[61] L. Chu, C. Anastasio, "Formation of hydroxyl radical from the photolysis of frozen hydrogen peroxide. Additions and corrections" *J. Phys. Chem. A.* 112 (**2008**) 2747–2748.

[62] F.J. Beltrán, A. Rey, "Solar or UVA-visible photocatalytic ozonation of water contaminants" *Molecules.* 22 (**2017**) 1177.

[63] D. Bahnemann, E.J. Hart, "Rate constants of the reaction of the hydrated electron and hydroxyl radical with ozone in aqueous solution" *J. Phys. Chem.* 86 (**1982**) 252–255.

[64] T.E. Agustina, H.M. Ang, V.K. Vareek, "A review of synergistic effect of photocatalysis and ozonation on wastewater treatment" *J. Photochem. Photobiol. C*

Photochem. Rev. 6 (**2005**) 264–273.

[65] V. Augugliaro, M. Litter, L. Palmisano, J. Soria, "The combination of heterogeneous photocatalysis with chemical and physical operations: A tool for improving the photoprocess performance" *J. Photochem. Photobiol. C Photochem. Rev.* 7 (**2006**) 127–144.

[66] X. Ao, W. Liu, "Degradation of sulfamethoxazole by medium pressure UV and oxidants: Peroxymonosulfate, persulfate, and hydrogen peroxide" *Chem. Eng. J.* 313 (**2017**) 629–637.

[67] F.J. Beltrán, J. Rivas, P.M. Alvarez, M.A. Alonso, B. Acedo, "A kinetic model for advanced oxidation processes of aromatic hydrocarbons in water: application to phenanthrene and nitrobenzene" *Ind. Eng. Chem. Res.* 38 (**1999**) 4189–4199.

[68] S. Morooka, K. Kusakabe, J. ichiro Hayashi, K. Isomura, K. Ikemizu, "Decomposition and utilization of ozone in water treatment reactor with ultraviolet radiation" *Ind. Eng. Chem. Res.* 27 (**1988**) 2372–2377.

[69] D. Suryaman, K. Hasegawa, S. Kagaya, "Combined biological and photocatalytic treatment for the mineralization of phenol in water" *Chemosphere*. 65 (**2006**) 2502–2506.

[70] S. Mandal, "Reaction rate constants of hydroxyl radicals with micropollutants and their significance in advanced oxidation processes" *J. Adv. Oxid. Technol.* 21 (**2018**) 178–195.

[71] N.F.F. Moreira, J.M. Sousa, G. Macedo, A.R. Ribeiro, L. Barreiros, M. Pedrosa, J.L. Faria, M.F.R. Pereira, S. Castro-Silva, M.A. Segundo, C.M. Manaia, O.C. Nunes, A.M.T. Silva, "Photocatalytic ozonation of urban wastewater and surface water using immobilized TiO_2 with LEDs: micropollutants, antibiotic resistance genes and estrogenic activity" *Water Res.* 94 (**2016**) 10–22.

[72] A. Eduardo, H. Machado, L. Maria, K.A. Borges, S. Batista, V. Alexandre, B. De Paiva, P. Souza, M. Jr, D. Fernanda, D.M. Oliveira, M.D. França, "Potential applications for solar photocatalysis: from environmental remediation to energy conversion" *Sol. Radiat.* (**2012**) 339–378.

[73] R.J. Braham, A.T. Harris, "Review of major design and scale-up considerations

for solar photocatalytic reactors" *Ind. Eng. Chem. Res.* 48 (**2009**) 8890–8905.

[74] A. Pérez-Burgos, J. Bilbao, A. De Miguel, R. Román, "Analysis of solar direct irradiance in Spain" in: "*Energy Procedia*" *Elsevier Ltd*, (**2014**).

[75] A. Alagarasi, P.U. Rajalakshmi, K. Shanthi, P. Selvam, "Solar light photocatalytic activity of mesoporous nanocrystalline TiO_2, SnO_2, and TiO_2-SnO_2 composites" *Mater. Today Sustain.* (**2019**) 100016.

[76] J. Tan, X. Wang, W. Hou, X. Zhang, L. Liu, J. Ye, D. Wang, "Fabrication of Fe_3O_4@graphene/TiO_2 nanohybrid with enhanced photocatalytic activity for isopropanol degradation" *J. Alloys Compd.* (**2019**) 918–927.

[77] S. Dominguez, M. Huebra, C. Han, P. Campo, M.N. Nadagouda, M.J. Rivero, I. Ortiz, D.D. Dionysiou, "Magnetically recoverable TiO_2-WO_3 photocatalyst to oxidize bisphenol A from model wastewater under simulated solar light" *Environ. Sci. Pollut. Res.* 24 (**2017**) 12589–12598.

[78] E. Mena, A. Rey, E.M. Rodríguez, F.J. Beltrán, "Reaction mechanism and kinetics of DEET visible light assisted photocatalytic ozonation with WO_3 catalyst" *Appl. Catal. B Environ.* 202 (**2017**) 460–472.

[79] R.R. Solís, F.J. Rivas, A.M. Chávez, D.D. Dionysiou, "Simulated solar photo-assisted decomposition of peroxymonosulfate. Radiation filtering and operational variables influence on the oxidation of aqueous bezafibrate" *Water Res.* 162 (**2019**) 383–393.

[80] M. Checa, M. Figueredo, A. Aguinaco, F.J. Beltrán, "Graphene oxide/titania photocatalytic ozonation of primidone in a visible LED photoreactor" *J. Hazard. Mater.* 369 (**2019**) 70–78.

[81] S. Mosleh, M.R. Rahimi, M. Ghaedi, K. Dashtian, S. Hajati, "Photocatalytic degradation of binary mixture of toxic dyes by HKUST-1 MOF and HKUST-1-SBA-15 in a rotating packed bed reactor under blue LED illumination: central composite design optimization" *RSC Adv.* 6 (**2016**) 17204–17214.

[82] C. Byrne, G. Subramanian, S.C. Pillai, "Recent advances in photocatalysis for environmental applications" *J. Environ. Chem. Eng.* 6 (**2018**) 3531–3555.

[83] X. Kang, S. Liu, Z. Dai, Y. He, X. Song, Z. Tan, "Titanium dioxide: from engineering to applications" *Catalysts*. 9 (**2019**) 191–223.

[84] X. Zhang, F. Wu, X.W. Wu, P. Chen, N. Deng, "Photodegradation of acetaminophen in TiO_2 suspended solution" *J. Hazard. Mater.* 157 (**2008**) 300–307.

[85] Y. Parent, D. Blake, K. Magrini-Bair, C. Lyons, C. Turchi, A. Watt, E. Wolfrum, M. Prairie, "Solar photocatalytic processes for the purification of water: State of development and barriers to commercialization" *Sol. Energy*. 56 (**1996**) 429–437.

[86] S. Malato, J. Blanco, C. Richter, D. Curcó, J. Giménez, "Low-concentrating CPC collectors for photocatalytic water detoxification: comparison with a medium concentrating solar collector" *Water Sci. Technol.* 35 (**1997**) 157–164.

[87] E. Mena, A. Rey, F.J. Beltrán, "TiO_2 photocatalytic oxidation of a mixture of emerging contaminants: A kinetic study independent of radiation absorption based on the direct-indirect model" *Chem. Eng. J.* 339 (**2018**) 369–380.

[88] S.M. Gupta, M. Tripathi, "A review of TiO_2 nanoparticles" *Chinese Sci. Bull.* 56 (**2011**) 1639.

[89] A. Mills, S. Le Hunte, "An overview of semiconductor photocatalysis" *J. Photochem. Photobiol. A Chem.* 108 (**1997**) 1–35.

[90] A.L. Linsebigler, G. Lu, J.T. Yates, "Photocatalysis on TiO_2 surfaces: Principles, mechanisms, and selected results" *Chem. Rev.* 95 (**1995**) 735–758.

[91] M.R. Hoffmann, S.T. Martin, W. Choi, D.W. Bahnemann, "Environmental applications of semiconductor photocatalysis" *Chem. Rev.* 95 (**1995**) 69–96.

[92] B. Ohtani, O.O. Prieto-Mahaney, D. Li, R. Abe, "What is Degussa (Evonik) P25? Crystalline composition analysis, reconstruction from isolated pure particles and photocatalytic activity test" *J. Photochem. Photobiol. A Chem.* 216 (**2010**) 179–182.

[93] D.H. Quiñones, A. Rey, P.M. Álvarez, F.J. Beltrán, G. Li Puma, "Boron doped TiO_2 catalysts for photocatalytic ozonation of aqueous mixtures of common pesticides: Diuron, o-phenylphenol, MCPA and terbuthylazine" *Appl. Catal. B Environ.* 178 (**2015**) 74–81.

[94] X. Zhou, J. Lu, J. Jiang, X. Li, M. Lu, G. Yuan, Z. Wang, M. Zheng, H. Seo, "Simple fabrication of N-doped mesoporous TiO_2 nanorods with the enhanced visible light photocatalytic activity" *Nanoscale Res. Lett.* 9 (**2014**) 34.

[95] A.C. Mecha, M.S. Onyango, A. Ochieng, C.J.S. Fourie, M.N.B. Momba, "Synergistic effect of UV-vis and solar photocatalytic ozonation on the degradation of phenol in municipal wastewater: A comparative study" *J. Catal.* 341 (**2016**) 116–125.

[96] A. Rey, P. García-Muñoz, M.D. Hernández-Alonso, E. Mena, S. García-Rodríguez, F.J. Beltrán, "WO_3-TiO_2 based catalysts for the simulated solar radiation assisted photocatalytic ozonation of emerging contaminants in a municipal wastewater treatment plant effluent" *Appl. Catal. B Environ.* 154–155 (**2014**) 274–284.

[97] P.M. Álvarez, J. Jaramillo, F. López-Piñero, P.K. Plucinski, "Preparation and characterization of magnetic TiO_2 nanoparticles and their utilization for the degradation of emerging pollutants in water" *Appl. Catal. B Environ.* 100 (**2010**) 338–345.

[98] D. Sudha, P. Sivakumar, "Review on the photocatalytic activity of various composite catalysts" *Chem. Eng. Process.* 97 (**2015**) 112–133.

[99] P. Roy, S. Berger, P. Schmuki, "TiO_2 nanotubes: Synthesis and applications" *Angew. Chemie - Int. Ed.* 50 (**2011**) 2904–2939.

[100] E.M. Rodríguez, A. Rey, E. Mena, F.J. Beltrán, "Application of solar photocatalytic ozonation in water treatment using supported TiO_2" *Appl. Catal. B Environ.* (**2019**) 237–245.

[101] Y. Ao, J. Xu, D. Fu, C. Yuan, "A simple route for the preparation of anatase titania-coated magnetic porous carbons with enhanced photocatalytic activity" *Carbon N. Y.* 46 (**2008**) 596–603.

[102] X. Liu, R. Dang, W. Dong, X. Huang, J. Tang, H. Gao, G. Wang, "A sandwich-like heterostructure of TiO_2 nanosheets with MIL-100(Fe): A platform for efficient visible-light-driven photocatalysis" *Appl. Catal. B Environ.* 209 (**2017**) 506–513.

[103] J. Araña, J.M. Doña-Rodríguez, E. Tello Rendón, C. Garriga I Cabo, O. González-Díaz, J.A. Herrera-Melián, J. Pérez-Peña, G. Colón, J.A. Navío, "TiO2 activation by using activated carbon as a support: Part I. Surface characterisation and decantability study" *Appl. Catal. B Environ.* (**2003**) 161–172.

[104] D.H. Quiñones, P.M. Álvarez, A. Rey, F.J. Beltrán, "Removal of emerging contaminants from municipal WWTP secondary effluents by solar photocatalytic ozonation. A pilot-scale study" *Sep. Purif. Technol.* 149 (**2015**) 132–139.

[105] A.Y. Shan, T.I.M. Ghazi, S.A. Rashid, "Immobilisation of titanium dioxide onto supporting materials in heterogeneous photocatalysis: A review" *Appl. Catal. A Gen.* 389 (**2010**) 1–8.

[106] R.R. Solís, F. Javier Rivas, O. Gimeno, J.L. Pérez-Bote, "Photocatalytic ozonation of pyridine-based herbicides by N-doped titania" *J. Chem. Technol. Biotechnol.* 91 (**2016**) 1998–2008.

[107] N.M. Julkapli, S. Bagheri, "Graphene supported heterogeneous catalysts: An overview" *Int. J. Hydrogen Energy*. (**2015**).

[108] P.S. Karthik, A.L. Himaja, S.P. Singh, "Carbon-allotropes: Synthesis methods, applications and future perspectives" *Carbon Lett.* 15 (**2014**) 219–237.

[109] A. Rey, M. Faraldos, A. Bahamonde, J.A. Casas, J.A. Zazo, J.J. Rodríguez, "Role of the activated carbon surface on catalytic wet peroxide oxidation" *Ind. Eng. Chem. Res.* 47 (**2008**) 8166–8174.

[110] X. Li, J. Yu, S. Wageh, A.A. Al-Ghamdi, J. Xie, "Graphene in photocatalysis: A review" *Small.* 12 (**2016**) 6640–6696.

[111] L. Fu, T. Xia, Y. Zheng, J. Yang, A. Wang, Z. Wang, "Preparation of WO_3-reduced graphene oxide nanocomposites with enhanced photocatalytic property" *Ceram. Int.* 41 (**2015**) 5903–5908.

[112] Q. Li, X. Li, S. Wageh, A.A. Al-Ghamdi, J. Yu, "CdS/Graphene nanocomposite photocatalysts" *Adv. Energy Mater.* 5 (**2015**).

[113] M. Cao, P. Wang, Y. Ao, C. Wang, J. Hou, J. Qian, "Photocatalytic degradation of tetrabromobisphenol A by a magnetically separable graphene-TiO_2 composite

photocatalyst: Mechanism and intermediates analysis" *Chem. Eng. J.* (**2015**).

[114] Q. Xiang, J. Yu, M. Jaroniec, "Graphene-based semiconductor photocatalysts" *Chem. Soc. Rev.* 41 (**2012**) 782–796.

[115] P.J. Johnson, D.J. Setsuda, R.S. Williams, "Activated Carbon for Automotive Applications" in: "*Carbon Materials for Advanced Technologies*" (**1999**).

[116] N. Rey-Raap, E.G. Calvo, J.M. Bermúdez, I. Cameán, A.B. García, J.A. Menéndez, A. Arenillas, "An electrical conductivity translator for carbons" *Meas. J. Int. Meas. Confed.* 56 (**2014**) 215–218.

[117] M. Aliofkhazraei, N. Ali, W.I. Milne, C.S. Ozkan, S. Mitura, J.L. Gervasoni, "Mechanical and Chemical Properties" in: M. Aliofkhazraei, N. Ali, W.I. Milne, C.S. Ozkan, S. Mitura, J.L.G.S.E. - (Eds.), "*Graphene Science Handbook*" 1st edition. *CRC Press*, Boca Raton (**2016**).

[118] X. Wang, D. Wu, X. Song, W. Du, X. Zhao, D. Zhang, "Review on carbon/polyaniline hybrids: Design and synthesis for supercapacitor" *Molecules*. 24 (**2019**).

[119] Y. Liu, X. Zhu, F. Qian, S. Zhang, J. Chen, "Magnetic activated carbon prepared from rice straw-derived hydrochar for triclosan removal" *RSC Adv.* 4 (**2014**) 63620–63626.

[120] A. Celzard, V. Fierro, J.F. Marêché, G. Furdin, "Advanced preparative strategies for activated carbons designed for the adsorptive storage of hydrogen" *Adsorpt. Sci. Technol.* 25 (**2007**) 129–142.

[121] S. Fatima, S.I. Ali, M.Z. Iqbal, S. Rizwan, "The high photocatalytic activity and reduced band gap energy of La and Mn co-doped $BiFeO_3$/graphene nanoplatelet (GNP) nanohybrids" *RSC Adv.* 7 (**2017**) 35928.

[122] H. Jafarlou, K. Hassannezhad, H. Asgharzadeh, G.R. Marami, "Enhancement of mechanical properties of low carbon steel joints via graphene addition" *Mater. Sci. Technol. (United Kingdom)*. 34 (**2018**) 455–467.

[123] S. Mitani, M. Sathish, D. Rangappa, A. Unemoto, T. Tomai, I. Honma, "Nanographene derived from carbon nanofiber and its application to electric

double-layer capacitors" *Electrochim. Acta.* 68 (**2012**) 146–152.

[124] F.J. Rivas, Á. Encinas, B. Acedo, F.J. Beltrán, "Mineralization of bisphenol A by advanced oxidation processes" *J. Chem. Technol. Biotechnol.* 84 (**2009**) 589–594.

[125] R. Yuan, B. Zhou, L. Ma, "Removal of toluene from water by photocatalytic oxidation with activated carbon supported $Fe3^{3+}$-doped TiO_2 nanotubes" *Water Sci. Technol.* 70 (**2014**) 642–648.

[126] A. Rey, D.H. Quiñones, P.M. Álvarez, F.J. Beltrán, P.K. Plucinski, "Simulated solar-light assisted photocatalytic ozonation of metoprolol over titania-coated magnetic activated carbon" *Appl. Catal. B Environ.* 111–112 (**2012**) 246–253.

[127] M. Sheydaei, H.R.K. Shiadeh, B. Ayoubi-Feiz, R. Ezzati, "Preparation of nano N-TiO_2/graphene oxide/titan grid sheets for visible light assisted photocatalytic ozonation of cefixime" *Chem. Eng. J.* 353 (**2018**) 138–146.

[128] G. Liao, D. Zhu, J. Zheng, J. Yin, B. Lan, L. Li, "Efficient mineralization of bisphenol A by photocatalytic ozonation with TiO2-graphene hybrid" *J. Taiwan Inst. Chem. Eng.* 67 (**2016**) 300–305.

[129] M. Pedrosa, L.M. Pastrana-Martínez, M.F.R. Pereira, J.L. Faria, J.L. Figueiredo, A.M.T. Silva, "N/S-doped graphene derivatives and TiO_2 for catalytic ozonation and photocatalysis of water pollutants" *Chem. Eng. J.* 348 (**2018**) 888–897.

[130] D.L. Cunha, A. Kuznetsov, C.A. Achete, A.E. da H. Machado, M. Marques, "Immobilized TiO_2 on glass spheres applied to heterogeneous photocatalysis: photoactivity, leaching and regeneration process" *PeerJ.* 6 (**2018**) e4464.

[131] S.L. James, "Metal-organic frameworks" *Chem. Soc. Rev.* 32 (**2003**) 276.

[132] V. Benoit, R.S. Pillai, A. Orsi, P. Normand, H. Jobic, F. Nouar, P. Billemont, E. Bloch, S. Bourrelly, T. Devic, P.A. Wright, G. de Weireld, C. Serre, G. Maurin, P.L. Llewellyn, "MIL-91(Ti), a small pore metal-organic framework which fulfils several criteria: an upscaled green synthesis, excellent water stability, high CO2 selectivity and fast CO2 transport" *J. Mater. Chem. A.* 4 (**2016**) 1383–1389.

[133] D. Wang, F. Jia, H. Wang, F. Chen, Y. Fang, W. Dong, G. Zeng, X. Li, Q. Yang, X. Yuan, "Simultaneously efficient adsorption and photocatalytic degradation of

tetracycline by Fe-based MOFs" *J. Colloid Interface Sci.* 519 (**2018**) 273–284.

[134] K. Tan, S. Zuluaga, H. Wang, P. Canepa, K. Soliman, J. Cure, J. Li, T. Thonhauser, Y.J. Chabal, "Interaction of acid gases SO_2 and NO with coordinatively unsaturated metal organic frameworks: M-MOF-74 (M = Zn, Mg, Ni, Co)" *Chem. Mater.* 29 (**2017**) 4227–4235.

[135] S.T. Meek, J.A. Greathouse, M.D. Allendorf, "Metal-organic frameworks: A rapidly growing class of versatile nanoporous materials" *Adv. Mater.* 23 (**2011**) 249–267.

[136] X. Liu, B. Tang, J. Long, W. Zhang, X. Liu, Z. Mirza, "The development of MOFs-based nanomaterials in heterogeneous organocatalysis" *Sci. Bull.* 63 (**2018**) 502–524.

[137] P. Horcajada, T. Chalati, C. Serre, B. Gillet, C. Sebrie, T. Baati, J.F. Eubank, D. Heurtaux, P. Clayette, C. Kreuz, J.S. Chang, Y.K. Hwang, V. Marsaud, P.N. Bories, L. Cynober, S. Gil, G. Férey, P. Couvreur, R. Gref, "Porous metal-organic-framework nanoscale carriers as a potential platform for drug deliveryand imaging" *Nat. Mater.* 9 (**2010**) 172–178.

[138] E.A. Kozlova, V.N. Panchenko, Z. Hasan, N.A. Khan, M.N. Timofeeva, S.H. Jhung, "Photoreactivity of metal-organic frameworks in the decolorization of methylene blue in aqueous solution" *Catal. Today*. 266 (**2016**) 136–143.

[139] K. Guesh, C.A.D. Caiuby, Á. Mayoral, M. Díaz-García, I. Díaz, M. Sanchez-Sanchez, "Sustainable preparation of MIL-100(Fe) and its photocatalytic behavior in the degradation of methyl orange in water" *Cryst. Growth Des.* 17 (**2017**) 1806–1813.

[140] J. Yang, X. Niu, S. An, W. Chen, J. Wang, W. Liu, "Facile synthesis of Bi_2MoO_6-MIL-100(Fe) metal-organic framework composites with enhanced photocatalytic performance" *RSC Adv.* 7 (**2017**) 2943–2952.

[141] J. Huang, H. Song, C. Chen, Y. Yang, N. Xu, X. Ji, C. Li, J.-A. You, "Facile synthesis of N-doped TiO_2 nanoparticles caged in MIL-100(Fe) for photocatalytic degradation of organic dyes under visible light irradiation" *J. Environ. Chem. Eng.* 5 (**2017**) 2579–2585.

[142] N.M. Mahmoodi, J. Abdi, M. Oveisi, M. Alinia Asli, M. Vossoughi, "Metal-organic framework (MIL-100(Fe)): Synthesis, detailed photocatalytic dye degradation ability in colored textile wastewater and recycling" *Mater. Res. Bull.* 100 (**2018**) 357–366.

[143] H.U. Rasheed, X. Lv, S. Zhang, W. Wei, N. Ullah, J. Xie, "Ternary MIL-100(Fe)@Fe_3O_4/CA magnetic nanophotocatalysts (MNPCs): Magnetically separable and Fenton-like degradation of tetracycline hydrochloride" *Adv. Powder Technol.* 29 (**2018**) 3305–3314.

[144] D.-D. Chen, X.-H. Yi, C. Zhao, H. Fu, P. Wang, C.-C. Wang, "Polyaniline modified MIL-100(Fe) for enhanced photocatalytic Cr(VI) reduction and tetracycline degradation under white light" *Chemosphere.* 245 (**2020**) 125659.

[145] R. Liang, S. Luo, F. Jing, L. Shen, N. Qin, L. Wu, "A simple strategy for fabrication of Pd@MIL-100(Fe) nanocomposite as a visible-light-driven photocatalyst for the treatment of pharmaceuticals and personal care products (PPCPs)" *Appl. Catal. B Environ.* 176–177 (**2015**) 240–248.

[146] Z. Mohammadifard, R. Saboori, N.S. Mirbagheri, S. Sabbaghi, "Heterogeneous photo-Fenton degradation of formaldehyde using MIL-100(Fe) under visible light irradiation" *Environ. Pollut.* 251 (**2019**) 783–791.

[147] D. Yu, M. Wu, Q. Hu, L. Wang, C. Lv, L. Zhang, "Iron-based metal-organic frameworks as novel platforms for catalytic ozonation of organic pollutant: Efficiency and mechanism" *J. Hazard. Mater.* 367 (**2019**) 456–464.

[148] J. Bedia, V. Muelas-Ramos, M. Peñas-Garzón, A. Gómez-Avilés, J.J. Rodríguez, C. Belver, "A review on the synthesis and characterization of metal organic frameworks for photocatalytic water purification" *Catalysts*. 9 (**2019**) 52.

[149] D. Stewart Robertson, "The function of oxalic acid in the human metabolism" *Clin. Chem. Lab. Med.* 49 (**2011**) 1405–1412.

[150] S.C. Noonan, G.P. Savage, "Oxalate content of foods and its effect on humans" *Asia Pac. J. Clin. Nutr.* 8 (**1999**) 64–74.

[151] L. Mansouri, C. Tizaoui, S.U. Geissen, L. Bousselmi, "A comparative study on ozone, hydrogen peroxide and UV based advanced oxidation processes for

efficient removal of diethyl phthalate in water" *J. Hazard. Mater.* 363 (**2019**) 401–411.

[152] Y. Zhao, G. Yu, S. Chen, S. Zhang, B. Wang, J. Huang, S. Deng, Y. Wang, "Ozonation of antidepressant fluoxetine and its metabolite product norfluoxetine: Kinetics, intermediates and toxicity" *Chem. Eng. J.* 316 (**2017**) 951–963.

[153] F.J. Rivas, R.R. Solís, F.J. Beltrán, O. Gimeno, "Sunlight driven photolytic ozonation as an advanced oxidation process in the oxidation of bezafibrate, cotinine and iopamidol" *Water Res.* 151 (**2019**) 226–242.

[154] S.N.A.M. Yusuf, Y.M. Ng, A.D. Ayub, S.H. Ngalim, V. Lim, "Characterisation and evaluation of trimesic acid derivatives as disulphide cross-linked polymers for potential colon targeted drug delivery" *Polymers (Basel).* 9 (**2017**) 311–327.

[155] S. Fekadu, E. Alemayehu, R. Dewil, B. Van der Bruggen, "Pharmaceuticals in freshwater aquatic environments: A comparison of the African and European challenge" *Sci. Total Environ.* 654 (**2019**) 324–337.

[156] R. Loos, R. Carvalho, D.C. António, S. Comero, G. Locoro, S. Tavazzi, B. Paracchini, M. Ghiani, T. Lettieri, L. Blaha, B. Jarosova, S. Voorspoels, K. Servaes, P. Haglund, J. Fick, R.H. Lindberg, D. Schwesig, B.M. Gawlik, "EU-wide monitoring survey on emerging polar organic contaminants in wastewater treatment plant effluents" *Water Res.* 47 (**2013**) 6475–6487.

[157] T. Deblonde, C. Cossu-Leguille, P. Hartemann, "Emerging pollutants in wastewater: A review of the literature" *Int. J. Hyg. Environ. Health*. 214 (**2011**) 442–448.

[158] J.P. Monk, P.A. Todd, "Bezafibrate" *Drugs*. 33 (**1987**) 539–576.

[159] A. Garcia-Ac, P.A. Segura, C. Gagnon, S. Sauvé, "Determination of bezafibrate, methotrexate, cyclophosphamide, orlistat and enalapril in waste and surface waters using on-line solid-phase extraction liquid chromatography coupled to polarity-switching electrospray tandem mass spectrometry" *J. Environ. Monit.* 11 (**2009**) 830–838.

[160] I. of Medicine, "Food components to enhance performance: An evaluation of

potential performance-enhancing food components for operational rations" *National Academy Press*, Washington D.C. (**1994**).

[161] R. Davis, A. Markham, J.A. Balfour, "Ciprofloxacin" *Drugs*. 51 (**1996**) 1019–1074.

[162] I. Ebert, J. Bachmann, U. Kühnen, A. Küster, C. Kussatz, D. Maletzki, C. Schlüter, "Toxicity of the fluoroquinolone antibiotics enrofloxacin and ciprofloxacin to photoautotrophic aquatic organisms" *Environ. Toxicol. Chem.* 30 (**2011**) 2786–2792.

[163] S.K. Khetan, T.J. Collins, "Human Pharmaceuticals in the Aquatic Environment: A Challenge to Green Chemistry" *Chem. Rev.* 107 (**2007**) 2319–2364.

[164] L. Araujo, M. Troconis, M. Espina, A. Prieto, "Persistence of ibuprofen, ketoprofen, diclofenac and clofibric acid in natural waters" *J. Environ. Hum.* 1 (**2014**) 32–38.

[165] P. Pfluger, D.R. Dietrich, "Effects on pharmaceuticals in the environment — An overview and principle considerations" in: K. Kümmerer (Ed.), "*Pharmaceuticals in the Environment*" *Springer*, Berlin, Heidelberg (**2001**).

[166] M. Saravanan, J.H. Hur, N. Arul, M. Ramesh, "Toxicological effects of clofibric acid and diclofenac on plasma thyroid hormones of an Indian major carp, Cirrhinus mrigala during short and long-term exposures" *Environ. Toxicol. Pharmacol.* (**2014**).

[167] M. Saravanan, S. Karthika, A. Malarvizhi, M. Ramesh, "Ecotoxicological impacts of clofibric acid and diclofenac in common carp (Cyprinus carpio) fingerlings: Hematological, biochemical, ionoregulatory and enzymological responses" *J. Hazard. Mater.* (**2011**).

[168] N.L. Benowitz, F. Kuyt, P. Jacob, R.T. Jones, A.-L. Osman, "Cotinine disposition and effects" *Clin. Pharmacol. Ther.* 34 (**1983**) 604–611.

[169] S.D. Costanzo, A.J. Watkinson, E.J. Murby, D.W. Kolpin, M.W. Sandstrom, "Is there a risk associated with the insect repellent DEET (N,N-diethyl-m-toluamide) commonly found in aquatic environments?" *Sci. Total Environ.* (**2007**).

[170] D. Campos, C. Gravato, C. Quintaneiro, O. Koba, T. Randak, A.M.V.M. Soares,

J.L.T. Pestana, "Are insect repellents toxic to freshwater insects? A case study using caddisflies exposed to DEET" *Chemosphere*. (**2016**).

[171] M. Tisch, P. Schmezer, M. Faulde, A. Groh, H. Maier, "Genotoxicity studies on permethrin, DEET and diazinon in primary human nasal mucosal cells" *Eur. Arch. Oto-Rhino-Laryngology*. 259 (**2002**) 150–153.

[172] N. Petrucci, S. Sardini, "Severe neurotoxic reaction associated with oral ingestion of low-dose diethyltoluamide-containing insect repellent in a child" *Pediatr. Emerg. Care*. 16 (**2000**) 341–342.

[173] L.H. Heckmann, A. Callaghan, H.L. Hooper, R. Connon, T.H. Hutchinson, S.J. Maund, R.M. Sibly, "Chronic toxicity of ibuprofen to Daphnia magna: Effects on life history traits and population dynamics" *Toxicol. Lett.* 172 (**2007**) 137–145.

[174] F. Pomati, A.G. Netting, D. Calamari, B.A. Neilan, "Effects of erythromycin, tetracycline and ibuprofen on the growth of Synechocystis sp. and Lemna minor" *Aquat. Toxicol.* (**2004**) 387–396.

[175] P. Benfield, S.P. Clissold, R.N. Brogden, "Metoprolol" *Drugs*. 31 (**1986**) 376–429.

[176] A.M. Chávez, A.R. Ribeiro, N.F.F. Moreira, A.M.T. Silva, A. Rey, P.M. Álvarez, F.J. Beltrán, "Removal of organic micropollutants from a municipal wastewater secondary effluent by UVA-LED photocatalytic ozonation" *Catalysts*. 9 (**2019**) 472–488.

[177] N.H. Tran, M. Reinhard, K.Y.-H. Gin, "Occurrence and fate of emerging contaminants in municipal wastewater treatment plants from different geographical regions-a review" *Water Res.* 133 (**2018**) 182–207.

[178] R. Rosal, A. Rodríguez, J.A. Perdigón-Melón, A. Petre, E. García-Calvo, M.J. Gómez, A. Agüera, A.R. Fernández-Alba, "Occurrence of emerging pollutants in urban wastewater and their removal through biological treatment followed by ozonation" *Water Res.* 44 (**2010**) 578–588.

[179] A. Massarsky, V.L. Trudeau, T.W. Moon, "β-blockers as endocrine disruptors: the potential effects of human β-blockers on aquatic organisms" *J. Exp. Zool. Part A Ecol. Genet. Physiol.* 315A (**2011**) 251–265.

[180] P.A. Masters, T.A. O'Bryan, J. Zurlo, D.Q. Miller, N. Joshi, "Trimethoprim-sulfamethoxazole revisited" *JAMA Intern. Med.* 163 (**2003**) 402–410.

[181] R.R. Solís, O. Gimeno, F.J. Rivas, F.J. Beltrán, "Simulated solar driven photolytic ozonation for the oxidation of aqueous recalcitrant-to-ozone tritosulfuron. Transformation products and toxicity" *J. Environ. Manage.* 233 (**2019**) 513–522.

EXPERIMENTAL SECTION

CHAPTER III

3.1. CHEMICALS

Reagents, chemicals and solvents in this research were used as received, without any further purification. Chemical name, stoichiometric formula, CAS number, commercial manufacturer and minimum purity grade of each substance used in this work are listed in **Table 3.1**.

Table 3.1. List of chemicals and materials.

Chemical (state)	Formula	CAS	Supplier	Purity
Target compounds				
Bezafibrate (s)	$C_{19}H_{20}ClNO_4$	41859-67	Merck	98.0%
Caffeine (s)	$C_8H_{10}N_4O_2$	58-08-2	Merck	99.0%
Clofibric acid (s)	$C_{10}H_{11}ClO_3$	882-09-7	Merck	97.0%
Ciprofloxacin (s)	$C_{17}H_{18}FN_3O_3$	85721-33-1	A.O.	98.0%
Cotinine (s)	$C_{10}H_{12}N_2O$	486-56-6	Merck	98.0%
N,N-diethyl-meta-toluamide (l)	$C_{12}H_{17}NO$	134-62-3	Merck	97.0%
Ibuprofen sodium salt (s)	$C_{13}H_{17}O_2Na$	31121-93-4	Merck	98.0%
Metoprolol tartrate salt (s)	$C_{34}H_{56}N_2O_{12}$	56392-17-7	Merck	99.0%
Oxalic acid 2-hydrated (s)	$C_2H_6O_4{\cdot}2H_2O$	144-62-7	Merck	99.5%
Sulfamethoxazole (s)	$C_{10}H_{11}N_3O_3S$	723-46-6	Merck	98.0%
Trimesic acid (s)	$C_9H_6O_6$	554-95-0	A.A.	98.0%
Tritosulfuron (s)	$C_{13}H_9F_6N_5O_4S$	142469-14-5	Merck	98.0%
Chemicals for synthetic wastewater effluents				
Ammonium chloride (s)	NH_4Cl	12125-02-9	Panreac	99.0%
Ammonium sulfate (s)	$(NH_4)_2SO_4$	7783-20-2	Merck	99.5%
Arabic acid (s)	$C_5H_{10}O_6$	32609-14-6	Merck	-
Beef extract powder (s)	-	68990-09-0	Merck	-
Calcium chloride (s)	$CaCl_2$	10043-52-4	Panreac	95.0%
D(+)-glucose (s)	$C_6H_{12}O_6$	50-99-7	Panreac	99.0%
Gum arabic from acacia tree (s)	-	9000-01-5	Merck	-
Humic acid (s)	-	1415-93-6	Merck	-
Iron (II) sulfate 7-hydate (s)	$FeSO_4{\cdot}7H_2O$	7782-63-0	Panreac	99.5%
Lignosulfonic acid sodium salt (s)	-	8061-51-6	Merck	-
Magnesium sulfate 7-hydrate (s)	$MgSO_4{\cdot}7H_2O$	10034-99-8	Panreac	99.0%
Manganese (II) sulfate 1-hydrate(s)	$MnSO_4{\cdot}H_2O$	10034-96-5	Panreac	99.0%
Meat peptone (s)	-	91079-38-8	Panreac	-
Sodium lauryl sulfate (s)	$C_{12}H_{25}NaO_4S$	151-21-3	Merck	98.5%
Sodium bicarbonate (s)	$NaHCO_3$	144-55-8	Panreac	99.7%
Sodium carbonate (s)	Na_2CO_3	497-19-8	Merck	99.8%
Tannic acid (s)	$C_{76}H_{52}O_{46}$	1401-55-4	Merck	-
Potassium phosphate dibasic (s)	K_2HPO_4	7758-11-4	Panreac	99.0%
Potassium phosphate monobasic(s)	KH_2PO_4	7778-77-0	Panreac	98.0%
Zinc sulfate 7-hydrate (s)	$ZnSO_4{\cdot}7H_2O$	7733-02-0	Panreac	99.0%

Table 3.1. (continued) List of chemicals and materials.

Chemical (state)	Formula	CAS	Supplier	Purity
Materials and reagents for analysis				
Acetic acid glacial (l)	C_2H_4O	64-19-7	Fischer	99.0%
Acetonitrile (l)	C_2H_3N	75-05-8	Panreac	99.99%
Ammonium fluoride (s)	NH_4F	12125-01-8	Merck	98.0%
tert-butanol (l)	$C_4H_{10}O$	75-65-0	Panreac	99.0%
Cobalt chloride 6-hydrate (s)	$CoCl_2 \cdot 6H_2O$	7791-13-1	Panreac	99.0%
Daphtoxkit F. Magna	-	-	M.B.	-
Dichloroacetic acid (l)	$C_2H_2Cl_2O_2$	2156-56-1	Merck	98.0%
Folin Ciocalteau's phenol reagent (2M with respect to acid) (l)	-	-	Merck	-
Formic acid (l)	CH_2O_2	64-18-6	Panreac	98.0%
Fumaric acid (s)	$C_4H_4O_4$	110-17-8	Merck	99.0%
Hydrochloric acid (l)	HCl	7647-01-0	Fischer	37.0%
Hydrogen peroxide (l)	H_2O_2	7722-84-1	Panreac	33.0%
Iron test, Spectroquant® (l)	-	-	Merck	-
Malonic acid (s)	$C_2H_2O_4$	141-82-2	Merck	99.0%
Mercury (II) sulfate (s)	$HgSO_4$	7783-35-9	Merck	98.0%
Methanol (l)	CH_4O	67-56-1	Panreac	99.99%
Microtox ® toxicity test	-	-	-	-
trans,trans-Muconic acid (s)	$C_6H_6O_4$	3588-17-8	Merck	98.0%
ortho-Phosphoric acid (l)	H_3PO_4	7664-38-2	Panreac	85.0%
Oxalic acid 2-hydrated (s)	$C_2H_6O_4 \cdot 2H_2O$	144-62-7	Merck	99.5%
Perchloric acid (l)	$HClO_4$	7601-90-3	Panreac	70.0%
Phenol (s)	C_6H_6O	108-95-2	Merck	99.5%
Potassium bromide (s)	KBr	7758-02-3	Merck	99.0%
Potassium dichromate (s)	$K_2Cr_2O_7$	7778-50-9	Panreac	99.5%
Potassium hydrogen phthalate (s)	$C_8H_5KO_4$	877-24-7	Merck	99.95%
Potassium indigotrisulfonate (s)	$C_{16}H_7K_3N_2O_{11}S_3$	67627-18-3	Merck	98.0%
Potassium monoacid phosphate(s)	K_2HPO_4	7758-11-4	Panreac	99.0%
Propionic acid (l)	$C_3H_6O_2$	79-09-4	Panreac	99.5%
Pyruvic acid sodium salt (s)	$C_3H_3NaO_3$	113-24-6	Merck	98.0%
Silver sulfate solution (6.6 $g \cdot L^{-1}$ in sulfuric acid) (l)	$Ag_2SO_4 \cdot xH_2SO_4$	-	Panreac	-
Sodium monoacid carbonate (s)	$NaHCO_3$	144-55-8	Panreac	99.7%
Sodium chloride (s)	NaCl	7647-14-5	Panreac	99.0%
Sodium hydroxide (s)	NaOH	1310-73-2	Panreac	98.0%
Sodium nitrite (s)	$NaNO_2$	7632-00-2	Panreac	98.0%
Sodium nitrate (s)	$NaNO_3$	7631-99-4	Panreac	99.0%
Sodium polyphosphate (s)	$Na(PO_3)_n$	50813-16-6	Merck	96.0%
Sodium sulfate (s)	Na_2SO_4	7757-82-6	Panreac	99.0%
Succinic acid (s)	$C_4H_6O_4$	110-15-6	Merck	99.5%
Sulfuric acid	H_2SO_4	7664-93-9	Panreac	98.0%
Titanium (IV) oxysulfate in sulfuric acid solution (l)	$TiSO_5 \cdot xH_2SO_4$	123334-00-9	Merck	27.0%

Table 3.1. (continued) List of chemicals and materials.

Chemical (state)	Formula	CAS	Supplier	Purity
Material and chemicals for catalyst synthesis				
Activated carbon (12-20 mesh) (s)	-	7440-44-0	Merck	-
Ammonia (l)	NH_3	1336-21-6	Panreac	25.0%
Ethylene glycol (l)	$C_2H_6O_2$	107-21-1	Merck	99.8%
Glass rings (s)	-	-	-	-
Graphene nanoplatelets (s)	-	7782-42-5	Merck	-
Iron (II) chloride 4-hydate (s)	$FeCl_2 \cdot 4H_2O$	13478-10-9	Panreac	98.0%
Iron (II) sulfate 7-hydate (s)	$FeSO_4 \cdot 7H_2O$	7782-63-0	Panreac	99.0%
Iron (III) chloride 6-hydate (s)	$FeCl_3 \cdot 6H_2O$	7705-08-0	Panreac	97.0%
Iron (III) nitrate 9-hydrate (s)	$FeN_3O_9 \cdot 9H_2O$	7782-61-8	Panreac	98.0%
Nitric acid (l)	HNO_3	7697-37-2	Fischer	65.0%
2-propanol (l)	C_3H_8O	67-63-0	Panreac	99.5%
Titanium dioxide, Aeroxide P25(s)	TiO_2	13463-67-7	Evonik	-
Titanium (IV) butoxide (l)	$Ti(OC_{16}H_{36})$	5593-70-4	Merck	97.0%
Titanium (IV) isopropoxide (l)	$Ti\ (C_3H_7O)_4$	546-68-9	Merck	97.0%
Trimesic acid (s)	$C_9H_6O_6$	554-95-0	A.A.	98.0%
Gases and solvents				
Acetone (l)	C_3H_6O	67-64-1	Panreac	99.5%
Ethanol (l)	C_2H_6O	64-17-5	Panreac	99.5%
Oxygen (g)	O_2	7782-44-7	Linde	99.5%
Nitrogen (g)	N_2	7727-37-9	Linde	99.99%
Synthetic air (g)	$20\%O_2 + 80\%N_2$	-	Linde	-
Ultrapure water (l)	H_2O	-	Merck	-
Micropollutants for HPLC-MS/MS analysis				
2-Ethylhexyl 4-methoxycinnamate (EHMC) (s)	$C_{18}H_{26}O_3$	5466-77-3	Merck	98.0%
Acetamiprid (s)	$C_{10}H_{11}ClN_4$	160430-64-8	Merck	98.0%
Alachlor (s)	$C_{14}H_{20}ClNO_2$	15972-60-8	Merck	98.0%
Atenolol (s)	$C_{14}H_{22}N_2O_3$	29122-68-7	Merck	98.0%
Atorvastatin calcium salt 3-hydrate (s)	$Ca(C_{33}H_{34}FN_2O_5)_2 \cdot 3H_2O$	134523-03-8	Merck	98.0%
Atrazine (s)	$C_8H_{14}ClN_3$	1912-24-9	Merck	98.0%
Azithromycin 2-hydrate (s)	$C_{38}H_{72}N_2O_{12} \cdot 2H_2O$	117772-70-0	Merck	98.0%
Bezafibrate (s)	$C_{19}H_{20}ClNO_4$	41859-67-0	Merck	98.0%
Carbamazepine (s)	$C_{15}H_{12}N_2O$	298-46-4	Merck	99.0%
Cefalexin (s)	$C_{16}H_{17}N_3O_4S$	15686-71-2	Merck	98.0%
Ceftiofur (s)	$C_{19}H_{17}N_5O_7S_3$	80370-57-6	Merck	95.0%
Ciprofloxacin (s)	$C_{17}H_{18}FN_3O_3$	85721-33-1	Merck	98.0%
Citalopram hydrobromide (l)	$C_{20}H_{21}FN_2O \cdot HBr$	59729-32-7	Merck	98.0%
Clarithromycin (s)	$C_{38}H_{69}NO_{13}$	81103-11-9	Merck	98.0%
Chlorfenvinphos (s)	$C_{12}H_{14}Cl_3O_4P$	470-90-6	Merck	95.0%
Clindamycin hydrochloride (s)	$C_{18}H_{33}ClN_2O_5S \cdot HCl$	21462-39-5	Merck	98.0%
Clofibric acid (s)	$C_{10}H_{11}ClO_3$	882-09-7	Merck	97.0%
Clopidogrel hydrogen sulfate (s)	$C_{16}H_{16}ClNO_2S \cdot H_2SO_4$	135046-48-9	Merck	98.0%

Table 3.1. (continued) List of chemicals and materials.

Chemical (state)	Formula	CAS	Supplier	Purity
Clothianidin (s)	$C_6H_8ClN_5O_2S$	210880-92-5	Merck	98.0%
Diclofenac sodium salt (s)	$C_{14}H_{10}Cl_2NNaO_2$	15307-79-6	Merck	98.5%
Diphenhydramine hydrochloride (s)	$C_{17}H_{21}NO{\cdot}HCl$	147-24-0	Merck	98.0%
Diuron (s)	$C_9H_{10}Cl_2N_2O$	330-54-1	Merck	98.0%
Enrofloxacin (s)	$C_{19}H_{22}FN_3O_3$	93106-60-6	Merck	99.0%
Erythromycin (s)	$C_{37}H_{67}NO_{13}$	114-07-8	Merck	99.0%
Fluoxetine hydrochloride solution (1 mg·mL^{-1} in methanol) (l)	$C_{17}H_{19}ClF_3NO$	56296-78-7	Merck	-
Hydrochlorothiazide solution (1mg·mL^{-1} in methanol) (l)	$C_7H_8ClN_3O_4S$	58-93-5	Merck	-
Imidacloprid solution (100 µg·mL^{-1} in acetonitrile) (l)	$C_9H_{10}ClN_5O_2$	138261-41-3	Merck	-
Isoproturon (s)	$C_{12}H_{18}N_2O$	34123-59-6	Merck	98.0%
Ketoprofen (s)	$C_{16}H_{14}O_3$	22071-15-4	Merck	98.0%
Methiocarb (s)	$C_{11}H_{15}NO_2S$	2032-65-7	Merck	98.0%
Metoprolol tartrate salt (s)	$C_{34}H_{56}N_2O_{12}$	56392-17-7	Merck	99.0%
Norfluoxetine oxalate solution (1 mg·mL^{-1} in methanol) (l)	$C_{18}H_{18}F_3NO_5$	107674-50-0	Merck	-
Ofloxacin (s)	$C_{18}H_{20}FN_3O_4$	82419-36-1	Merck	98.0%
Pentachlorophenol (s)	C_6Cl_5OH	87-86-5	Merck	97.0%
Perfluorooctanesulfonic acid potassium salt (s)	$CF_3(CF_2)_7SO_3K$	2795-39-3	Merck	98.0%
Propranolol hydrochloride (s)	$C_{16}H_{21}NO_2{\cdot}HCl$	318-98-9	Merck	99.0%
Simazine (s)	$C_7H_{12}ClN_5$	122-34-9	Merck	98.0%
Sulfamethoxazole (s)	$C_{10}H_{11}N_3O_3S$	723-46-6	Merck	98.0%
Tetracycline hydrochloride (s)	$C_{22}H_{24}N_2O_8{\cdot}HCl$	64-75-5	Merck	95.0%
Thiacloprid (s)	$C_{10}H_9ClN_4S$	111988-49-9	Merck	98.0%
Thiamethoxam (s)	$C_8H_{10}ClN_5O_3S$	153719-23-4	Merck	98.0%
Tramadol hydrochloride (s)	$C_{16}H_{25}NO_2{\cdot}HCl$	36282-47-0	Merck	99.0%
Trimethoprim (s)	$C_{14}H_{18}N_4O_3$	738-70-5	Merck	98.0%
Venlafaxine hydrochloride solution (1 mg·mL^{-1} in methanol) (l)	$C_{17}H_{28}ClNO_2$	99300-78-4	Merck	-
Warfarin (s)	$C_{19}H_{16}O_4$	81-81-2	Merck	98.0%

A.O.: Acros Organics; A.A.: Alfa Aesar; M.B.: MicroBioTest

In order to obtain ultrapure water, tap water was firstly deionized with a RIOs-ID® device and further purified in a Milli-Q® academic system. Both devices were supplied by Merck-Millipore.

3.2. WATER EFFLUENTS

This work has been carried out using different sort of effluents, though some studies were performed in ultrapure water. This section describes in detail the main characteristics and uses of the wastewater samples employed in this research.

3.2.1. AQUEOUS SOLUTIONS OF CONTAMINANTS

In this Thesis, oxalic acid (OA), bezafibrate (BZF), caffeine, (CAF), ciprofloxacin (CPR), clofibric acid (CA), cotinine (CTN), N,N-diethyl-meta-toluamide (DEET), ibuprofen (IBP), metoprolol (MTP), sulfamethoxazole (SMX), trimesic acid (TMA) and tritosulfuron (TSF) were used as target compounds to test a variety of treatment processes. Aqueous solutions were prepared in ultrapure water and wastewater effluents.

Oxalic acid was chosen to study the decomposition of aqueous ozone in the presence and absence of solar light (see Chapter IV). For that purpose, an aqueous solution of OA (25 $mg \cdot L^{-1}$) at pH 4 (NaOH was used to adjust the pH of the solution) was prepared in ultrapure water.

Cotinine was employed to assess the efficiency of magnetic graphene with TiO_2 (see Chapter VII). A solution of CTN (10 $mg \cdot L^{-1}$) was prepared in ultrapure water.

A mixture of four contaminants of emerging concern (MTP, IBP, DEET and CA, 2 $mg \cdot L^{-1}$ of each compound) was prepared both in a synthetic secondary wastewater effluent and ultrapure water to test the efficiency of some catalysts in ozone and ozone/radiation processes (see Chapters IV and V). Other concentrations of CECs (e.g., 4 or 10 $mg \cdot L^{-1}$ each) were also considered for specific purposes (see Chapters V and IX for more details). Also, another broad mixture of ten contaminants, (CTN, CAF, CPR, MTP, SMX, DEET, CA, BZF, TSF and IBP) was added to a secondary effluent with 0.5 $mg \cdot L^{-1}$ each. This effluent was used to prove the efficiency of the magnetic graphene TiO_2 photocatalyst (see Chapter VII).

3.2.2. SYNTHETIC WASTEWATER EFFLUENTS

In order o simulate typical primary and secondary effluents from municipal WWTPs synthetic wastewater samples were prepared.

A. Synthetic primary wastewater effluent (SPW)

As mentioned in Chapter II, WWTPs are usually designed to have grinding, desanding and degreasing processes prior to a biological treatment. Primary effluents, which are the feed of biological units, are rich in ammonia, phosphates and, primarily, organic matter. Accordingly, SPW was prepared as reported in the literature [1], using meat peptone and D(+)-glucose as organic carbon sources and a mixture of metal and inorganic salts to provide nitrogen, phosphorous and micronutrients. **Table 3.2** shows the composition of the as-prepared SPW as well as some of its main characteristics. In this work, SPW was used as feed for activated sludge culture in biodegradation experiments and as effluent to be mixed with industrial wastewater (see Chapter VI).

Table 3.2. Chemical composition and characterization of the SPW.

Chemical	Concentration	Parameter	Value
D(+)-glucose	216 $mg \cdot L^{-1}$	pH	7.3
Meat peptone	46 $mg \cdot L^{-1}$	Turbidity	13 NTU
K_2HPO_4	138 $mg \cdot L^{-1}$	Conductivity	473 $\mu S \cdot cm^{-1}$
$NaHCO_3$	83 $mg \cdot L^{-1}$	DOC	85 $mg \cdot L^{-1}$
KH_2PO_4	69 $mg \cdot L^{-1}$	IC	12 $mg \cdot L^{-1}$
NH_4Cl	52 $mg \cdot L^{-1}$	COD	172 $mg \cdot L^{-1}$
$MgSO_4 \cdot 7H_2O$	26 $mg \cdot L^{-1}$	BOD_5	135 $mg \cdot L^{-1}$
$CaCl_2$	7 $mg \cdot L^{-1}$	BOD_5/COD	0.78
$FeSO_4 \cdot 7H_2O$	1 $mg \cdot L^{-1}$	UV_{254nm}	0.34
$MnSO_4 \cdot H_2O$	1 $mg \cdot L^{-1}$	SUVA	0.4 $L \cdot mg^{-1} \cdot m^{-1}$
$ZnSO_4 \cdot 7H_2O$	1 $mg \cdot L^{-1}$		

B. Synthetic secondary wastewater effluent (SSE)

Typically, secondary effluents contains a mixture of organic and inorganic substances, such as humic acids, carbonates, phosphates and sulfates [2]. In this work SSE was prepared as described in the recent literature to achieve dissolved organic carbon (DOC) and inorganic carbon (IC) values of about 20 and 40 $mg \cdot L^{-1}$, respectively [3]. **Table 3.3** specifies the chemicals and their corresponding concentration used to prepare the SSE. The main characterization parameters of this effluent are also shown in the table. SSE was spiked with a number of CECs and used to study their degradation by an array of methods.

Table 3.3. Chemical composition and characterization of a typical SSE.

Chemical	Concentration	Parameter	Value
Arabic acid	9.4 $mg \cdot L^{-1}$	pH	7.5
Gum arabic from acacia tree	9.4 $mg \cdot L^{-1}$	Turbidity	6.6 NTU
Humic acid	8.5 $mg \cdot L^{-1}$	Conductivity	140 $\mu S \cdot cm^{-1}$
Tannic acid	8.4 $mg \cdot L^{-1}$	DOC	20 $mg \cdot L^{-1}$
Meat peptone	5.4 $mg \cdot L^{-1}$	IC	42 $mg \cdot L^{-1}$
Lignosulfonic acid sodium salt	4.9 $mg \cdot L^{-1}$	COD	71 $mg \cdot L^{-1}$
Beef extract powder	3.6 $mg \cdot L^{-1}$	BOD_5	10 $mg \cdot L^{-1}$
Sodium lauryl sulfate	1.9 $mg \cdot L^{-1}$	BOD_5/COD	0.14
Na_2CO_3	371.0 $mg \cdot L^{-1}$	UV_{254nm}	0.68
$(NH_4)_2SO_4$	14.2 $mg \cdot L^{-1}$	SUVA	3.4 $L \cdot mg^{-1} \cdot m^{-1}$
K_2HPO_4	9.9 $mg \cdot L^{-1}$		
$MgSO_4 \cdot 7H_2O$	2.9 $mg \cdot L^{-1}$		

In this work SSE was prepared as described elsewhere [3], simulating the characteristics of the effluent at the outlet of Badajoz's WWTP. The influence of water matrix, phosphate or carbonate ions on the degradation of water pollutants (metoprolol, ibuprofen, DEET and clofibric acid) was studied.

3.2.3. REAL WASTEWATER EFFLUENTS AND ACTIVATED SLUDGE

Apart from synthetic effluents, real wastewater samples were also used in order to study the efficiency of some treatment processes. After collection from WWTPs, wastewater samples were either used directly or stored in the freezer at -4 ºC until further use. Activated sludge samples were also taken directly from the biological unit of a WWTP to be used as inoculum in cultivations carried out in the laboratory.

A. Domestic wastewater

Urban wastewaters were collected from municipal WWTPs. Domestic effluents are treated by means of 4 clear stages (pretreatment, primary treatment, secondary treatment and reconditioning), being the conventional activated sludge process the most important one.

Some of the secondary effluent samples were taken from Rincón de Caya WWTP located in Badajoz (Spain). All samples were filtered through a nitrocellulose filter (0.45 µm) and analyzed before being used or stored. In some experiments inorganic carbon was removed to some extent from the samples by acidification followed by air bubbling. The main parameters of different wastewater samples are given in **Table 5.2** and **Table 7.1.**

Other secondary effluent samples were collected from the outlet of Maia WWTP (Porto, Portugal). Effluents were filtered (retention particles of 2 μm) for comparative results. The main characteristic of these effluents are given in **Table S8.1** in the supplementary section of Chapter VIII.

B. Industrial wastewater

Raw industrial wastewater (RIW) was provided by a waste management company located in an industrial site from Catalonia (Spain). RIW consisted of a high-polluted wastewater containing a mixture of effluents from some industrial activities (mainly chemical). A filter paper (Filter Lab 1305) was used to remove suspended solids from RIW to some extent. Filtered industrial wastewater (FIW) was quite recalcitrant to biodegradation, likely because of the presence of metals or organic substances, which might be toxic to microorganisms. For that reason, FIW was mixed with SPW (dilution 1:5, MIW) to make the mixture amenable for biodegradation. Main characteristics of RIW, FIW and MIW effluents are shown in **Table 6.1.**

C. Activated sludge

Activated sludge samples were used in biological treatments. Inoculum samples were obtained from the activated sludge biological unit of the Rincón de Caya WWTP, which works with an average 1.5 $g \cdot L^{-1}$ of mixed liquor volatile suspended solids concentration (MLVSS) and 0.5 of food to microbial ratio (F/M), being the hydraulic retention time (HRT) set in about 7 hours.

3.3. CATALYSTS

3.3.1. TiO_2 ONTO MAGNETIC ACTIVATED CARBON

A TiO_2-Fe_3O_4-activated carbon magnetic composite (TiFeC) was synthesized following a method reported in a previous work [4]. The synthesis of this catalyst comprises three steps: 1) carbon magnetization, 2) TiO_2 sol-gel preparation and 3) impregnation of TiO_2 onto the magnetic carbon. **Figure 3.1** summarizes the synthesis procedure.

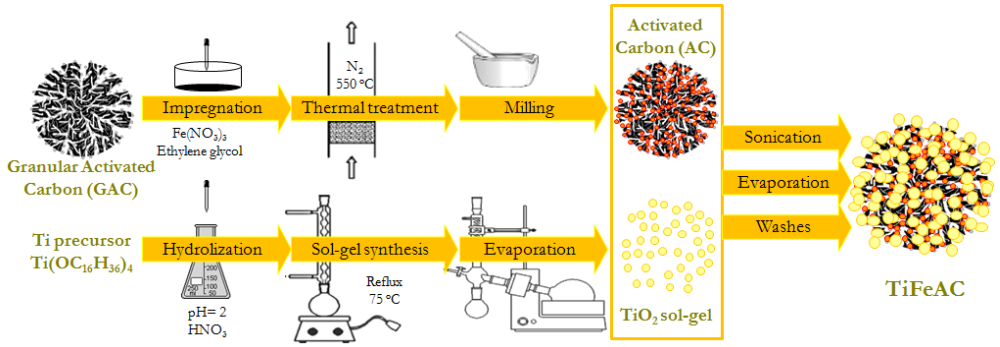

Figure 3.1. Scheme of the procedure for the TiFeAC synthesis.

Firstly, 3 g of commercial granular activated carbon (Darco 12-20 mesh) was impregnated dropwise with 2.61 mL of an iron (III) nitrate ethanol solution of 8.82 M. Once dried, 15 mM of ethylene glycol per gram of activated carbon was added as reducing agent during the thermal treatment in N_2 atmosphere at 550 ºC for 4 h. Afterwards, the granular magnetic carbon was powdered to particle size < 125 µm.

Separately, titanium (IV) butoxide was dropped in acidic ultrapure water (adjusted at pH 2 with HNO_3) and kept under reflux at 75 ºC for 24 h. Then, organic precursors were extracted under vacuum at 80 ºC.

Finally, TiO_2 sol-gel and magnetic particles were dispersed in the nanosol under sonication for 1 hour. Immediately, the product was completely dried under vacuum at 80 ºC and washed thoroughly with ultrapure water to remove impurities.

3.3.2. TiO_2 COATED GLASS RINGS

Samples of commercial titania (Degussa P25, Evonik) supported on borosilicate glass rings (8mm O.D. x 10mm) were prepared by means of a dip-coating method as described elsewhere [5]. Glass rings were first washed with an anionic gel and later with deionized water several times. Dried rings were immersed into a 5% w/v P25ethanolic suspension, previously sonicated for 5 minutes, at a constant rate of 30 $mm \cdot min^{-1}$. The obtained product was coated twice in order to create three homogeneous layers of P25 in rings and was dried overnight at 110 ºC. Finally supported titania was calcined in air atmosphere at 450 ºC for 2 h, thus obtaining the catalyst (named as P25R).

3.3.3. TiO_2 ON MAGNETIC GRAPHENE

The method used to prepare a magnetic graphene-TiO_2 based photocatalysts (MG-Ti) was adapted from literature [6]. The synthesis consisted of: 1) magnetite synthesis, 2) magnetization of graphene, 3) TiO_2 deposition.

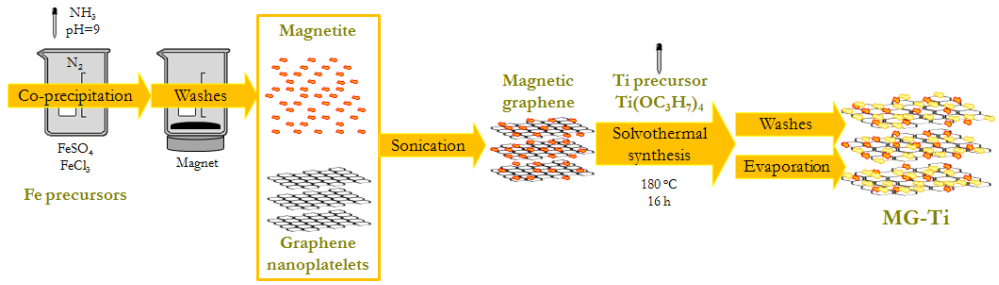

Figure 3.2. Scheme of the procedure for the MG-Ti synthesis.

Magnetite nanoparticles were firstly synthesized. After 30-minute bubbling N_2 in ultrapure water, $FeCl_3 \cdot 6H_2O$ and $FeSO_4 \cdot 7H_2O$ were added at the same molar ratio leading to a simultaneous co-precipitation of Fe (III) and Fe (II) oxides. A concentrated ammonia solution was added dropwise into the solution to reach pH 9. Magnetic particles were thoroughly washed with ultrapure water under stirring and then recovered with a magnet. Then, the obtained solid was dried overnight at 80 ºC.

Secondly, magnetic graphene (MGX) was prepared with different magnetite:graphene (X:1) weight ratios by sonicating a certain amount of the synthesized magnetite and commercial graphene in 200 mL of iso-propanol. The solvent was evaporated at 80 ºC and kept at this temperature overnight.

Thirdly, magnetic-graphene TiO_2 composite was obtained by a solvothermal method in a 200 mL Teflon lined stainless steel autoclave. Thus, 10 mL of titanium (IV) iso-propoxide were dissolved in 50 mL of iso-propanol containing the desired amount of MGX. Precipitation of titanium was accomplished by adding 5 mL of ultrapure water under stirring. Thermal treatment was undergone at 180 ºC for 16 h.

The final product was firstly washed with ethanol to mainly remove organic solvents and then with ultrapure water several times. Finally, the solid was dried under vacuum at 80 ºC and kept overnight at this temperature. The catalyst was labeled as Y-MGX-Ti where Y stands for the mass percentage of MGX in comparison to the theoretical TiO_2 incorporated in the process.

3.3.4. METAL ORGANIC FRAMEWORK: MIL-100(Fe)

MIL-100(Fe) was synthesized following an easy and sustainable method [7] based on the link between deprotonated trimesic acid (TMA) and iron (III) according to the stoichiometric formula of MIL 100(Fe) [8]. Typically, 1.68 g of dissolved TMA in 23.7 g of 1M NaOH solution were added dropwise into a solution containing iron (II) (2.3 g of $FeCl_2 \cdot 4H_2O$ and 97.2 g of H_2O). The green mixture caused by Fe (II) content turned brown after 24 h on stirring at room temperature. The product was recovered by centrifugation (orto-Alresa centrifuge) and washed several times with hot (70 ºC) and cold (room temperature) ultrapure water. Then, the catalyst was dried at 100 ºC overnight.

3.4. EXPERIMENTAL PROCEDURES

3.4.1. BIOLOGICAL OXIDATION

Biological processes (acclimation stage and biological degradation experiments) were adopted using the sequential batch reactor (SBR) cycle: filling, aeration, settle, draw and idle [9]. Experiments were carried out under aerobic conditions in a 2 L cylindrical glass SBR equipped with a diffuser to provide air along the experiments, a mechanical stirrer, thermometer, portable pH meter and dissolved oxygen probe. In addition, pH and temperature were controlled to be kept in the range of 6.5-8.5 and 18-22 ºC, respectively.

To begin with, in the acclimation period, the reactor was initially load (day 0) with 2 L of a mixture of activated sludge and SPW to feed the microorganisms. The following 15 days, MIW was stepwise introduced in the feed up to become a complete acclimated culture to MIW (see **Table 6.5** for details). The duration of the SBR process in every stage was 15 min, 22 h, 30 min, 15 min and 90 min, respectively.

Once the activated sludge was healthily grown (c.a. 1.8 g $MLVSS \cdot L^{-1}$), biological reactions were conducted. The experimental procedure was carried out with the same routine in an optimized reaction time (8 hours). Then, SBR phase times were set now in 15 min, 8 h, 30 min, 15 min and 90 min, respectively.

At time intervals, samples were withdrawn from the reactor, centrifuged (3000 rpm, orto-Alresa centrifuge, 200 W) and/or filtered using a 0.45 μm PVDF membrane filter for further analyses.

3.4.2. PHOTOACTIVITY TESTS WITH SOLAR SIMULATOR

Experiments with solar simulated radiation were carried out in semi-batch mode. **Figure 4.1.** depicts a scheme of the experimental set-up. Typically, a glass reactor equipped with a magnetic stirring device, a gas inlet, a gas outlet and a liquid sampling port was placed in the middle of a chamber of a solar simulator (Suntest CPS+, Atlas). The simulator is provided with a 1500 W air-cooled Xe lamp programmed to emit at 550 $W \cdot m^{-2}$. Quartz and glass cut-off filters were also used so as to select radiation in the range of 300-800 nm. **Figure 3.3.** compares the natural and simulated solar radiation spectra and irradiance distribution.

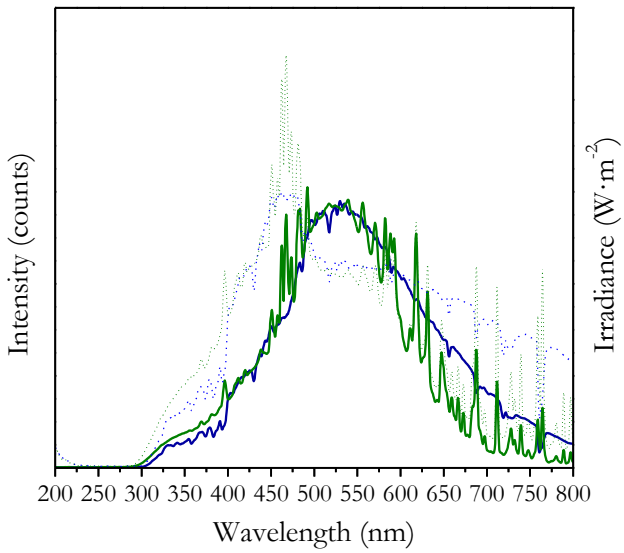

Figure 3.3. Natural and simulated sunlight spectra (solid blue and green lines respectively) and irradiance distribution (dotted blue and green lines respectively). Natural sunlight: 11 am at 07/01/2019, UV-irradiance (300-400 nm): 61.4 $W \cdot m^{-2}$. Simulated sunlight: UV-irradiance (300-400 nm): 62.0 $W \cdot m^{-2}$.

In tests where ozone was used, the gas was generated in situ via oxygen splitting with an electrical shock in a laboratory ozone generator (Anseros Ozomat Com AD-02). Ozone gas concentration at the inlet and outlet streams of the reactor was

monitored with two ozone gas analyzers (Anseros Ozomat GM-OEM and GM-6000 Pro, respectively).

To begin with runs, reactor was first charged with the target solution, adding the pertinent amount of catalyst and kept in the darkness under agitation for 30 min to nearly reach adsorption equilibrium (if required). The solar lamp was switched on and the oxygen or oxygen-ozone mixture flow was continuously supplied to the reactor. The temperature inside the solar chamber was controlled at 35-40 ºC. In non-photolytic processes, the reactor was covered with aluminum foil to avoid radiation reaching its content. During the course of the experiments, samples were taken from the reactor and filtered using a 0.45 μm PVDF membrane filter for analyses.

3.4.3. PHOTOACTIVITY TESTS WITH LEDs DEVICES

Additional studies were carried out using different UVA-LED systems in semi-batch and continuous operation modes. Schemes of the experimental set-up and devices are depicted in **Figure 8.1.** and **8.2.**

Briefly, the experimental set-up for semi-batch mode runs consisted of a reactor enclosed in a square box with four 10 W UVA LEDs with a maximum irradiance at 390 nm and continuously refrigerated with fans. Reactions took place into a cylindrical borosilicate glass reactor charged with 750 mL of Maia's WWTP effluent and 0.375 g of P25 (i.e., catalyst concentration of 0.5 $g \cdot L^{-1}$), keeping the mixture under agitation in the dark for 10 min to achieve adsorption equilibrium. LEDs systems were switched on and a gas stream was bubbled through a ceramic diffuser. When ozone was used, it was produced from pure oxygen in a BMT 802X ozone generator and monitored in a BMT 964 analyzer. Then 10-minute reaction took place. A unique sample was withdrawn at the end of the reaction, being centrifuged afterwards. Remaining dissolved ozone gas was previously removed by air bubbling.

As for continuous operation runs, the experimental set-up was made up of a long borosilicate glass packed bubble column filled with glass rings (uncoated or coated with P25) and eight 10 W UVA LEDs disposed along the column with a maximum wavelength of emission at 381 nm. In a typical experiment, the system was completely filled with distilled water. Then, the wastewater was pumped (15 $mL \cdot min^{-1}$) and the gas was supplied to the column through a porous plate diffuser placed at its bottom. Recirculation flow rate was set at 166 $mL \cdot min^{-1}$ to ensure homogeneous liquid mixture and LEDs were turned on (if required). Ozone gas inlet was produced in situ and

monitored (BMT 802X ozone generator and BMT 964 analyzer). Liquid samples were regularly taken from the outlet stream and immediately bubbled with air to remove residual ozone. Then, the collected samples were centrifuged at 4000 rpm for 5 min prior to analyses.

Positive step input tracer experiments using NaCl aqueous solution (2 $g \cdot L^{-1}$) were carried out to characterize the flow pattern in the reactor. Conductivity was continuously measured in the stream leaving the reactor to obtain the residence time distribution (RTD) curve.

3.5. ANALYTICAL METHODS FOR WATER CHARACTERIZATION

This section gathers the analytical methods employed in this research for the characterization of water samples. **Table 3.4** summarizes the analytical methods and equipment used for each parameter.

3.5.1. ORGANIC MICROPOLLUTANT CONCENTRATION

The concentration of organic micropollutants in water was analyzed by liquid chromatography. Two different techniques were applied for the organic micropollutant determination, taking into account the concentration range. Equipment and analytical conditions are detailed in the following subsections.

A. Liquid chromatography analysis

Model compounds labeled as MTP, IBP, DEET, CA and TMA were analyzed with an Elite LaChrom HPLC (Hitachi) equipped with a programmable high pressure pump (L-2130), degassing unit, autosampler (L-2200), a diode array detector (L-2450) and Phenomenex Gemini C18 column (150 x 3 mm i.d.).

Regarding cotinine solution and the mixture of ten contaminants (i.e. BZF, CLO, CAF, CTN, CPR, DEET, IBP,MTP, SMX and TSF), an UFLC LC-20AD (Shimadzu) provided with a high pressure pump, degassing unit (DGU-20A SR), autosampler (SIL-20 HT), column oven (CTO-10AS VD), fluorescence (RF-20 XS), diode array (SPD-M20A detector) and also a Phenomenex Gemini C18 column (150 x 3 mm i.d.) were employed. **Table 3.5** shows the conditions for the analyses.

Table 3.4. Summary of parameters measured in aqueous samples, methods applied and equipment used in this work.

Parameter	Method	Equipment
Micropollutant concentration in mg·L^{-1} range	Liquid chromatography	HPLC-DAD, Elite LaChrom UFLC-DAD, Shimadzu
Micropollutant concentration in ng·L^{-1} range	Solid phase extraction (SPE) + Ultra-high performance liquid chromatography with tandem mass spectrometry (UHPLC-MS/MS)	HLB cartridges, Oasis + HPLC-MS/MS,Shimadzu
Inorganic anions concentration (F^-, Cl^-, Br^-, NO^{3-}, PO_4^{3-}, SO_4^{2-})	Ionic chromatography	881 Compact IC pro, Metrohm
Anions concentration from short-chain organic acids (acetic, propionic, formic, piruvic, diclhoroacetic, succinic, malonic, oxalic, fumaric and maleic acid)		
Total organic carbon concentration (TOC) **Inorganic carbon concentration (IC)**	Oxidation/acidification + Infrared spectroscopy	TOC-V_{CSH}, Shimadzu TOC-5000A, Shimadzu
Organic compounds identification	Gas chromatography + Mass spectrometry (GC-MS)	CP-3800/Saturn 2200, Varian
Chemical oxygen demand (COD)	Oxidation + Spectrophotometry	Digestor LT200, Hach Spectrophotometer DR2800, Hach
Biological oxygen demand (BOD_5)	Respirometry	OxiTop® respirometer
Dissolved ozone concentration	Oxidation + Spectrophotometry	Ηελιος α, Thermo Spectronic T60, PG Instruments
Dissolved oxygen concentration	Photometry	HQ40D portable meter, Hach

Table 3.4. (continued) Summary of parameters measured in aqueous samples, methods applied and equipment used in this work.

Parameter	Method	Equipment
Hydrogen peroxide concentration	Oxidation-complexation + Spectrophotometry	Helios α, Thermo Spectronic
Total phenolic content (TPC)	Oxidation + Spectrophotometry	Helios α, Thermo Spectronic
Total dissolved iron concentration	Complexation + Spectrophotometry	Spectroquant iron test, Merck Helios α, Thermo Spectronic
UV absorption at 254 nm (A_{254})	Spectrophotometry	Helios α,Thermo Spectronic T60, PG Instruments
Total suspended solids (TSS) **Volatile suspended solids (VSS)**	Filtration + Gravimetry	Scale AB204-S, Mettler Toledo Mufle, Raypa HM
Sludge volumetric index (SVI)	Settleability	Graduated cylinder
Acute toxicity	Luminiscence inhibition Mobility test	Vibrio fischeri luminescence Lumistox 300, Lange Daphnia magna Straus
Turbidity	Nephelometry	Turbidity-meter, HI 93414 Hanna
Conductivity	Conductimetry	Conductivity-meter, 524 Crison Conductivity-meter, GLP31 Crison
pH and temperature	Potenciometry	pH-meter, GLP21+ Crison pH-meter, pH 730 WTW

~ 96 ~

Table 3.5. Analytical conditions for the quantification of organic compounds by liquid chromatography.

Compound	Range ($mg \cdot L^{-1}$)	Condition	λ (nm)/ t_r (min)	LOD ($mg \cdot L^{-1}$)
MTP	< 5	Gradient method (0.6 $mL \cdot min^{-1}$): 1. Ramp from 5% to 50% B in 15 min 2. Hold at 50% B for 10 min 3. Back to 5% B in 3 min 4. Hold at 5% B for 12 min	220/7.8	0.25
DEET			220/16.4	0.22
CA			220/18.0	0.23
IBP			220/22.2	0.29
TMA	< 22		220/8.9	0.3
TMA	< 18	Isoctratic method (0.6 $mL \cdot min^{-1}$): 90% B + 10% A	215/8.3	0.6
CTN	< 2	Gradient method (0.5 $mL \cdot min^{-1}$, thermoregulated at 30 °C): 1. Hold at 95% C for 5 min 2. Ramp from 95% to 5% C in 15 min 3. Hold at 5% C for 1 min 4. Back to 95% C in 9 min	259/2.1	0.05
CAF			274/12.1	0.05
CPR			274/13.0	0.04
MTP			220/13.4	0.07
SMX			270/14.5	0.05
DEET			220/17.3	0.05
CLO			225/17.8	0.03
BZF			228/18.0	0.04
TSF			225/19.2	0.07
IBP			220/19.6	0.06

A: Acetonitrile; B: Acidified water (0.1% formic acid); C: Acidified water (0.1% H_3PO_4).
LOD: Limit of detection

As an example, **Figure 3.4.** shows a chromatogram obtained when analyzing a mixture of ten contaminants.

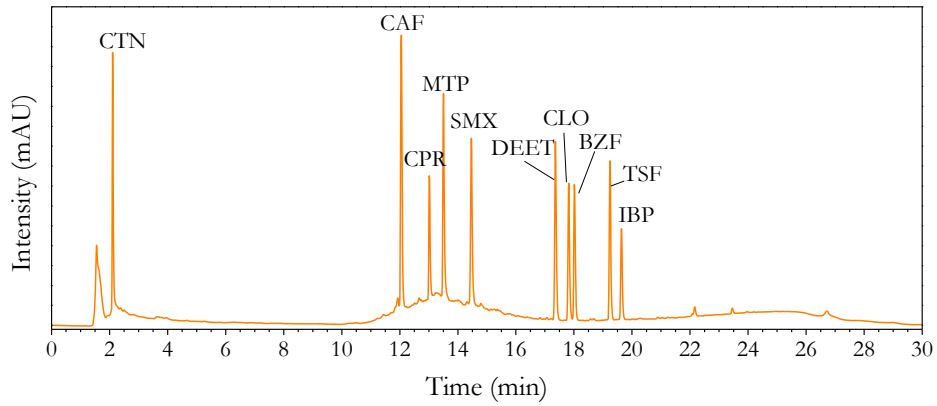

Figure 3.4. Chromatogram at 220 nm of the mixture of 10 contaminants in an urban wastewater effluent. Conditions: CEC_0=0.5 $mg \cdot L^{-1}$ (each).

B. Solid phase extraction and ultra-high performance liquid chromatography-tandem mass spectrometry analysis

The analysis of the organic micropollutants in the secondary effluent from Maia's WWTP was carried out following a fully-validated method of solid phase extraction (SPE) and ultra-high performance liquid chromatography with tandem mass spectrometry (UHPLC-MS/MS) that was adapted from a work published elsewhere [10]. This method is available to determine 45 contaminants, some included in Directive 2013/39/EU and Decision 840/2018/EU (**Table S8.2** in the supplementary information of chapter VIII).

First, 100 mL of sample was filtered through 1.2 µm glass microfiber filter GF/C, 47 mm (Whatman™) and acidified to pH 2 with sulfuric acid. Subsequently, 100 µL of a concentrated internal standard (5 $mg \cdot L^{-1}$) were added to wastewater samples. Afterwards, a 7-step SPE process (cartridges conditioning, sample loading, washing, dryness, elution, evaporation and reconstitution) was followed using Oasis® HLB (Hydrophilic-Lipophilic-Balanced sorbent, 150 mg, 6 mL) cartridges (Waters) and a vacuum extraction unit equipped with a drying unit (LiChrolut®, Merck Millipore) (see scheme of the process in **Figure 3.5**). First, cartridges were sequentially conditioned with 4 mL of ethanol and 4 mL of ultrapure water at a flow rate of 1 $mL \cdot min^{-1}$. Then, samples were continuously loaded under vacuum through the cartridges. After washing with 4 mL of ultrapure water, the cartridges were dried under vacuum aspiration for 30 min. The concentrated cartridges were restored with 4 mL of ethanol at 1 $mL \cdot min^{-1}$ and the eluent was evaporated to dryness in a vacuum concentrator (Centrivap centrifugal concentrator with cold trap, Labconco). The residues were dissolved in 400 µL of ethanol and filtered through 0.22 µm polytetrafluoroethylene (PTFE) syringe filters (Membrane Solutions) for further UHPLC-MS/MS analysis.

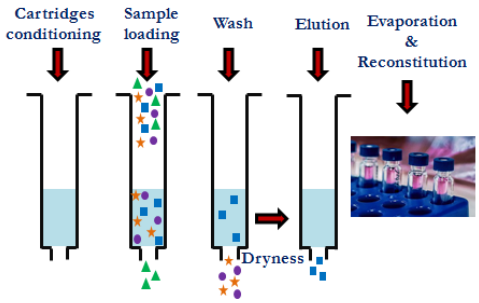

Figure 3.5. Scheme of the SPE process

Chromatographic analysis was performed using a Shimadzu© apparatus consisting of an UHPLC equipment (Nexera) with two pumps (LC-30AD), autosampler (SIL-30AC), oven (CTO-20AC), degasser (DGU-20A 5R), system controller (CBM-20A) and LC Solution Version 5.41SP1 software, coupled to a triple quadrupole mass spectrometer detector (Ultra Fast Mass Spectrometry series LCMS-8040).

A Kinetex™ 1.7 μm XB-C18 100 Å (100 x 2.1 mm i.d.) column was used as stationary phase, while a mixture of 0.1% formic acid and methanol at 0.25 $mL \cdot min^{-1}$ in gradient mode with a total run time of 12 min was employed as the mobile phase. The proportion of aqueous and organic phases (v/v) was as follows: 30/70 for 0.5 min; a linear gradient until reaching 10/90 in 1 min; hold for 6 min; back to 30/70 in 0.5 min and finally an equilibration step for 4 min. The volume required for injection was 5 μL. Column oven and autosampler temperatures were set at 35 °C and 4 °C, respectively. The electrospray ionization source operated in both positive and negative ionization modes. Quantification was performed by selected reaction monitoring (SRM), evaluating the two SRM transitions between the precursor ion and the two most abundant fragment ions for each compound, the most abundant used as quantifier and the second most abundant as qualifier, with a scan time of 100 ms per transition. The capillary voltage, drying gas and nebulizing gas flows, desolvation and source temperatures were, respectively: 4.5 kV, 15 $L \cdot min^{-1}$, 3.0 $L \cdot min^{-1}$; 400 °C and 250 °C. The collision induced dissociation gas (CID) was argon at 230 kPa. Calibration curves were prepared taking into account the two SRM transition.

3.5.2. INORGANIC IONS AND SHORT-CHAIN ORGANIC ACIDS

Inorganic anions and anions from short-chain organic acids (e.g. oxalic acid) were analyzed by ion chromatography.

Analyses were carried out using a 881 Compact IC Pro (Metrohm®) provided with a chemical ion suppressor, a conductivity detector and a dosage unit (800 Dosino) coupled to an 863 Compact autosampler. An ion exchange MetroSep A Supp 7 (150 x 4.0 mm, 5-μm particles of polyvinyl alcohol and quaternary ammonium groups) column thermally controlled at 45 ºC was used as stationary phase. Moreover, data acquisitions were processed with the Magic IC Net™ software.

Aqueous Na_2CO_3 with a gradient program from 0.6 to 14.6 mM in 50 min and 10-min equilibration step at a constant flow rate of 0.7 $mL \cdot min^{-1}$ was applied. A 800 Dosino unit containing concentrated Na_2CO_3 (35.6mM) was also needed.

Chemical suppression was performed with 250 mM H_2SO_4 and 23.6 mM oxalic acid solution for the regeneration of the system. The injection circuit was also reconditioned with sample and washed with methanol-ultrapure water solution (1:1) before sample injection. Then 20 µL of sample was required.

This method is able to separate inorganic anions and some short-chain organic acids. Calibration curves (0.1-10 mg·L^{-1}) were checked with an external standard, as given in **Figure 3.6** as example.

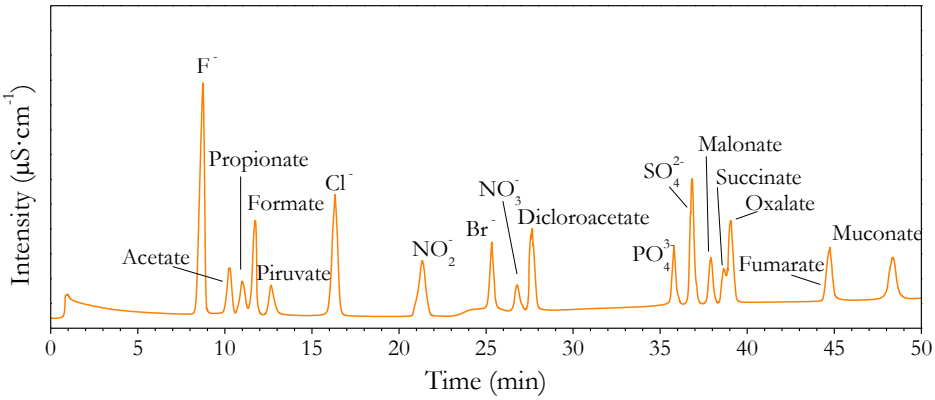

Figure 3.6. Extracted chromatogram of the external standard (5 mg·L^{-1}) from the ion chromatograph.

3.5.3. ORGANIC COMPOUNDS DETECTION: GAS CHROMATOGRAPHY-MASS SPECTROMETRY

Identification of the main organic compounds present in the industrial wastewater was carried out by means of a gas chromatography-mass spectrometry (GC-MS) system operated in electron impact ionization mode. The analyses were performed by gas chromatography/ion trap mass spectrometry (CP-3800/Saturn 2200, Varian, equipped with an automatic injector CP-8200/SPME, solid-phase microextraction). A 30 m length and 0.25 i.d. capillary column (Factor Four VF-5 ms) was used. The carrier gas (helium) flow rate was set at 1 mL·min^{-1}. The SPME was carried out with a fibre cartridge (poly(dimethylsiloxane) red), using adsorption and desorption times of 30 min and 5 min, respectively. The sample injection was conducted at 220 ºC. The temperature program used was as follows: (i) 40 ºC for 5 min; (ii) then from 40 ºC to 300 ºC at 15 ºC·min^{-1}; (iii) held at 300 ºC for 2 min. Compounds identification was assessed using the National Institute of Standards and Technology (NIST) database.

The main organic compounds found in the industrial wastewater are listed in **Table 6.3.**

3.5.4. TOTAL ORGANIC AND INORGANIC CARBON

The total carbon (TC) in a water sample includes the total organic carbon (TOC), from the organic matter, and inorganic carbon (IC), carbonates and bicarbonate ions. TC, TOC and IC were determined in a Shimadzu TOC-V_{CSH} analyzer coupled to an ASI-V automatic sample injector. The data of TC, IC measurements and consequently the TOC values were registered and automatically processed automatically by a TOC-Control V™ software. The model TOC-5000A analyzer (Shimadzu) was also used.

The analysis of TC is first carried out. The aqueous sample is introduced in a quartz combustion tube filled with a catalyst (i.e. platinum supported over alumina balls 5/64", 33g). The air current flow (150 mL·min^{-1}) passing continuously through the reactor heated at 680 ºC allows to oxidize and decompose the TC content of the sample into carbon dioxide. Thus, CO_2 produced in the combustion process, previously cooled and dehumidified, is analyzed by non-dispersive infrared spectroscopy (NDIR). The signal is processed by TOC-Control V software which associates the peak area with an internal calibration curve for quantification purposes.

Likewise, IC concentration is quantified by means of acidification with H_3PO_4 (25%) so that carbonate and bicarbonate ions are transformed into CO_2, to be measured by NDIR spectroscopy. The same as TC analyses, signal processes are correlated with a calibration curve. TOC measurement is subtracted from the difference between TC and IC values.

Finally, to ensure the reliability of the measurement, both combustion tube and catalysts were washed every 15 days with HCl (2 M) in order to prevent from inorganic salt fouling. Additionally, TC and IC calibration curves (0.1-20 mg TC·L^{-1}, 20-100 mg TC·L^{-1} and 0.1-20 mg IC·L^{-1}) were periodically checked using potassium hydrogen phthalate and a mixture of sodium hydrogen carbonate and sodium carbonate as standards, respectively.

3.5.5. CHEMICAL OXYGEN DEMAND (COD)

Chemical oxygen demand (COD) represents the amount of oxygen consumed in order to oxidize both organic and inorganic matter in a water sample. COD was measured following the standard dichromate reflux method [11,12]. The matter is

oxidized with the strong chemical oxidant, $K_2Cr_2O_7$, under acidic conditions at 148 ºC for 2 hours, using $AgSO_4$ as catalyst. The reduction of Cr (VI) (orange) to Cr (III) (green) is spectrophotometrically measured. $HgSO_4$ is also needed to avoid the interference of chloride anions, which precipitate as $HgCl_2$.

COD measurements were conducted with Hach-Lange commercial cuvettes valid for the COD determination in the 100-2000 $mg \cdot L^{-1}$ (LCK 514) and 5-60 $g \cdot L^{-1}$ (LCK 914) ranges. A certain amount of sample (2 or 0.2 mL respectively) is added into the cuvette and directly placed into a preheated COD thermoreactor (LT 200, Hach) at 148 ºC for 2 hours. Then, solution is analyzed at room temperature in a Spectrophotometer DR 2800 (Hach).

3.5.6. BIOLOGICAL OXYGEN DEMAND (BOD_5)

Biological oxygen demand (BOD) is defined as the amount of oxygen consumed by aerobic microorganisms to biodegrade organic matter in a water sample in a specific period. Therefore, this parameter is often used as a surrogate parameter for the biodegradable organic pollution in water.

BOD_5 was analyzed by measuring the oxygen consumption by microorganisms in 5-day period at 20 ºC, using OxiTop® respirometers [13]. The pressure variation caused by the oxygen consumption inside the glass bottle containing the sample and inoculum was continuously registered up to day 5 in the respirometer. The CO_2 generated as a result of the biodegradation process was absorbed by sodium hydroxide pellets placed in a rubber cup at the top of the bottle.

Table 3.6 shows the volume of sample and correction factors used to estimate BOD_5, depending on the expected BOD_5 range.

Table 3.6. Correction factor for different water sample volumes

Total volume (mL)	BOD_5 range	Correction factor
432	0-40	1
365	0-80	2
250	0-200	5
164	0-400	10
97.0	0-800	20
43.5	0-2000	50
22.7	0-4000	100

Every BOD_5 analysis was conducted with the proper volume of sample (pH previously adjusted to 6.5-7.5 if needed and filtered when catalyst was used) and inoculated with BOD microbe capsules (Cole-Parmer). Then, glass bottles provided with cup containg 4-5 NaOH pellets and the OxiTop deviced were kept under stirring in an incubator at 20 ºC. During the incubation period, the pressure sensor gives automatically the oxygen consumption into $mg \cdot L^{-1}$.

3.5.7. OZONE CONCENTRATION IN WATER

The ozone concentration in aqueous solution was measured according to the colorimetric method proposed by Bader and Hoigné [14]. This method is based on the decoloration of the dye potassium 5,5,7,-indigo trisulfonate when it is oxidized with ozone at acidic conditions. Given the fact that the distinctive blue color of indigo dye is easily identifiable at 600 nm, the ozone concentration is evaluated spectrophotometrically from the difference between the blank sample and the partially colorless product from the oxidized sample. The indigo method allows the dissolved ozone concentration to be determined in the range between 1.0×10^{-7} M and 6.3×10^{-4} M with a 2% of deviation.

An indigo stock solution was prepared with 900 mL of buffer solution at pH 2 (containing 35 and 28 $g \cdot L^{-1}$ of H_3PO_4 and KH_2PO_4, respectively) and 100 mL of a concentrated dye stock solution (0.6 and 2.3 $g \cdot L^{-1}$ of indigo trisulfonate and H_3PO_4, respectively).

In a typical test, 4 mL of diluted indigo stock solution were mixed in a vial with 2 mL of ozonized sample. The absorbance of the mixture was measured at 600 nm in a 1-cm plastic cell afterwards. Likewise, a blank sample was prepared replacing the ozonized sample with a 2 mL of non-ozonized sample (e.g. initial sample in ozone reactions). Besides, for experiments in the presence of catalyst, the mixture was filtered through a hydrophilic PVDF 0.45 μm filter prior to spectrophotometric measurement.

According to the Lambert-Beer's law, ozone concentration is directly proportional to the decrease of absorbance, as given in equation (3.1):

$$O_{3,d}\ (mol \cdot L^{-1}) = \frac{A_{blank} - A_{sample}}{\varepsilon_{600} b} \frac{V_{dye} + V_{sample}}{V_{sample}} \qquad (3.1)$$

where, $O_{3,d}$ is the dissolved ozone concentration; A_{blank} and A_{sample} the absorbances at 600 nm of the blank sample and ozonized sample test, respectively; ε_{600} the molar

extinction coefficient of ozone at 600 nm (i.e. 20000 $M^{-1}\cdot cm^{-1}$ [14]); b the cell path length; and V_{dye} and V_{sample} the volumes of dye stock solution and sample, respectively.

3.5.8. OZONE CONCENTRATION IN GAS

Ozone gas concentration was monitored on ozone gas analyzers. A fraction of gas stream is irradiated by a Hg lamp inside of an optical absorption cell. Thus, ozone could be spectrophotometrically measured at 253.7 nm, where the maximum absorbance is found. Inlet stream of ozone was displayed in an Anseros GM-6000-OEM (0-200 $mg\cdot L^{-1}$) analyzer while outlet streams of ozone were analyzed in Anseros GM-PRO (0-200 $mg\cdot L^{-1}$), Anseros GM-OEM (0-200 $mg\cdot L^{-1}$) or Anseros GM-6000-RTI (0-100 $mg\cdot L^{-1}$) analyzers.

3.5.9. DISSOLVED OXYGEN CONCENTRATION

A new photometric technology was used to measure oxygen concentration (DO) in aqueous samples. Specifically, USEPA approved a luminescent method for dissolved oxygen measurements in wastewater treatment processes (e.g., aeration and biological nutrient basins, effluent outfalls and receiving water) [15].

DO measurements were conducted in a HQ40D portable meter provided with an Intellical™ LDO101 Laboratory luminescent/optical dissolved oxygen sensor consisted of an electronic and optical body, and a membrane cap with the luminescent chemical sensor. The sensor is coated with a luminescent material, which becomes excited by a blue LED light. At the same time, a red light is released from the luminescent material and detected by a photo-diode. Thus, when oxygen is brought into contact with the chemical the intensity of the red light is reduced. Therefore, the higher the oxygen concentration, the lesser the red light emitted by the sensor. A red light is also provided in the sensor as an internal standard. The electronics inside the LDO probe immediately calculates the DO concentration in $mg\cdot L^{-1}$ or as percentage which is displayed in the screen.

The oxygen consumed by microorganisms of the activated sludge was determined by measuring continuously the DO of an aqueous sample. Hence, a flask containing 200 mL of a mixed liquor sample was air-bubbled. Afterwards, the LOD sensor was introduced into the water sample up to cover completely the protector cap.

The common method to calibrate the apparatus is using a 100% DO standard. In this case, a BOD bottle was filled with tap water approximately 1 cm and firmly closed

to maintain a water saturated atmosphere. After waiting 30 minutes, LDO is quickly introduced into the bottle and calibrated. The usual oxygen content in drinking water is around 8-9 $mg \cdot L^{-1}$, corresponding to 100% DO.

3.5.10. HYDROGEN PEROXIDE CONCENTRATION

Two methods were employed for hydrogen peroxide quantification depending on the H_2O_2 concentration.

A. Hydrogen peroxide concentration (10^{-3} M > C > 10^{-5} M)

Concentration of H_2O_2 in the range of 10^{-5} M to 10^{-3} M was quantified according to the method proposed by Einsenberg (1993). This is based on the colorimetric determination at 405 nm of the yellow pertitanic acid generated in reaction between hydrogen peroxide and titanium sulfonate reagent [16].

Typically, 0.5 mL of commercial titanium (IV) oxysulfate in sulfuric acid solution was mixed with 4.5 mL of sample. Solutions with higher H_2O_2 concentration were diluted until being in the measurable range. After a few minutes, the mixture was directly transferred into a plastic cell and measured at 405 nm. Equation (3.2) was used to calculate the concentration of H_2O_2:

$$H_2O_2\ (mol \cdot L^{-1}) = \frac{A_{blank} - A_{sample}}{\varepsilon_{405} b} \frac{V_{reagent} + V_{sample}}{V_{sample}} \qquad (3.2)$$

where H_2O_2 is the hydrogen peroxide concentration; A_{blank} and A_{sample} the absorbances at 405 nm of the blank sample and sample test, respectively; ε_{405} the molar extinction coefficient at 405 nm (i.e. 720 $M^{-1} \cdot cm^{-1}$); b the cell path length and V_{regent} and V_{sample} the volume of titanium (IV) oxysulfate reagent and the sample volume, respectively.

B. Hydrogen peroxide concentration (C < 10^{-5} M)

For concentration of H_2O_2 below 10^{-5} M, the cobalt-carbonate method proposed by Maschelein et al. (1977) was chosen [17]. The cation Co (II) is oxidized to Co (III) by the presence of H_2O_2, taking place to Co (III)-bicarbonate complex with maximum absorbances at 260, 440 and 665 nm. The quantification is performed at 260 nm since this is the wavelength with the highest molar extinction coefficient. Detection limit is estimated to be 3×10^{-7} M.

In a typical assay, 1 mL of sample was added to a vial containing 0.5 mL of cobalt (II) chloride 16.1 g $Co_2Cl.6H_2O \cdot L^{-1}$), 0.5 mL of sodium hexamethaphosphate solution (10 $g \cdot L^{-1}$), also named as calgon, and 10 mL of saturated sodium bicarbonate. Since the organic content may cause a positive interference in the determination at 260 nm, it is necessary to prepare another vial with the mixture where the cobalt (II) chloride solution is replaced with ultrapure water. After waiting at least 15 minutes, the mixture is transferred into a 1-cm path quartz cell and the concentration spectrophotometrically measured at 260 nm. In addition, two blank vials were prepared using 1 mL of ultrapure water instead of 1 mL of the sample test. Therefore, according to Lambert-Beer law, the concentration of hydrogen peroxide is deduced form the following equation (3.3):

$$H_2O_2\ (mol \cdot L^{-1}) = \frac{\left(A_{Co}^{sample} - A_{no\ Co}^{sample}\right) - \left(A_{Co}^{blank} - A_{no\ Co}^{blank}\right)}{\varepsilon_{260} b} \frac{V_{chemicals} + V_{sample}}{V_{sample}} \qquad (3.3)$$

being H_2O_2 the hydrogen peroxide concentration; A_{Co}^{sample}, $A_{no\ Co}^{sample}$, A_{Co}^{blank} and $A_{no\ Co}^{blank}$, are absorbance values at 260 nm of sample vials with and without cobalt solution and blank vials with and without cobalt solution, respectively; ε_{260} the molar extinction coefficient at 260 nm (i.e. 26645 $M^{-1} \cdot cm^{-1}$); b the quartz cell path length; $V_{chemicals}$ the volume of bicarbonate cobalt (II) solution (or ultrapure water); sodium hexamethaphospate and saturated sodium bicarbonate; and finally V_{sample} the sample volume.

3.5.11. TOTAL PHENOLIC CONTENT (TPC)

Total phenolic content (TPC) was determined by the colorimetric method proposed by Singleton and Rossi [18]. Accordingly, phenolic compounds are oxidized by Folin-Ciocalteu reagent, composed of phosphotungstic acid ($H_{13}PW_{12}O_{40}$) and phosphomolibdic acid ($H_{13}PMo_{12}O_{40}$), yielding a mixture of blue tungsten oxide (W_8O_{23}) and molybdenum oxide (Mo_8O_{23}), which can be measured spectrophotometrically at 740 nm.

Analyses in the range of TPC_1 (concentration level below 205 $mg \cdot L^{-1}$) were carried out with 0.5 mL Folin Ciocalteau reagent, 6.5 mL of ultrapure water and 0.5 mL of sample in a vial. After waiting some minutes for homogenization, 4.5 mL from Na_2CO_3 solution (7% w/v) were added. The reaction was considered to be completed after 2 h, being able to measure directly the absorbance at 740 nm. The same procedure was used for the quantification of TPC_2 (concentration level below 30 $mg \cdot L^{-1}$), taking 0.5

mL of Folin Ciocalteau reagent, 3.5 mL of ultrapure water, 3.5 mL of sample and followed by 4.5 mL of Na_2CO_3 solution (7% w/v).

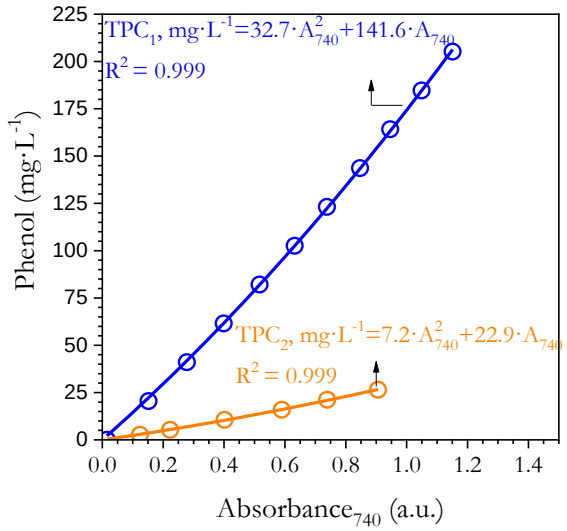

Figure 3.7. Calibration curves for the determination of total phenolic content.

The concentration of poliphenols was determined by means of calibration curves obtained from standard solutions of phenol. As given in **Figure 3.7**, calibration curves at high and low concentration of TPC (TPC_1 and TPC_2 respectively) agreed to a second order polynomial (correlation coefficients R^2=0.999).

3.5.12. TOTAL DISSOLVED IRON CONCENTRATION

Total iron concentration was evaluated spectrophotometrically at 565 nm following the specifications of Spectroquant® iron test (Merck 1.14761.0001), based on the transformation of Fe (III) into Fe (II) and the sudden formation of purple complex between Fe (II) and ferrozine in a thioglycolate-buffered medium. The analysis was performed adding 3 drops of iron test reagent into 5 mL of sample. After waiting 3 minutes, the absorbance at 565 nm was evaluated in a 1-cm plastic cuvette. The concentration in $mg \cdot L^{-1}$ could be directly obtained taking a factor of 2.08 (ε_{Fe}=27044 $M^{-1} \cdot cm^{-1}$). Minimum and maximum quantification limits are 0.05 and 5 $mg \cdot L^{-1}$, respectively.

3.5.13. UV ABSORPTION AT 254nm

Aromatic and unsaturated substances in solution typically absorb radiation in the UV range. Then, the absorption of ultraviolet light by a water sample at 254 nm (UV_{254nm}) is considered as a surrogate parameter representing the presence of aromatic and unsaturated compounds. An increase in the organic content also increases the absorbance in the UV range. The parameter called specific ultraviolet absorbance (SUVA) (equation (3.4)) is defined as the ratio between the absorbance at 254 nm of an aqueous sample and its dissolved organic carbon content (DOC). $SUVA_{254nm}$ gives an idea of aromatic nature of the dissolved organic matter [19].

$$SUVA_{254nm}\ (L \cdot mg^{-1} \cdot m^{-1}) = \frac{UV_{254nm}}{DOC} \times 100 \tag{3.4}$$

Measurements of UV_{254nm} were carried out with a spectrophotometer Helios α (Thermo Spectronic, UEx) or T60 (PG Instruments, FEUP), employing 1-cm quartz cuvettes. When values of UV_{254nm} where higher than 1.5, samples were diluted with ultrapure water.

3.5.14. TOTAL AND VOLATILE SUSPENDED SOLIDS (TSS AND VSS)

Wastewaters frequently contain suspended matter. Total suspended solids (TSS) include both fixed solids (FSS) and volatile suspended solids (VSS) which are determined by separating the solid and liquid phases by evaporation. They are usually analyzed by filtering a certain volume of water sample (Vs) through a glass fiber filter, previously weighted (P_0) and three times conditioned with 50 mL of milli-Q water each time. This glass fiber filter is heated at 110 ºC overnight, weighted (P_0), calcined at 550 ºC 1 h and weighted again (P_2). The loss of mass by calcinations is a measure of the volatile solids, considered as organic matter, while the remaining solids are the fixed solids, consisted of inorganic (mineral) portion. The different parameters showing solid present in wastewater are defined as follows:

$$TSS\ (mg \cdot L^{-1}) = \frac{P_1 - P_0}{V_s} \tag{3.5}$$

$$FSS\ (mg \cdot L^{-1}) = \frac{P_2 - P_0}{V_s} \tag{3.6}$$

$$VSS\ (mg \cdot L^{-1}) = TSS - FSS \tag{3.7}$$

3.5.15. MIXED LIQUOR VOLATILE SUSPENDED SOLIDS (MLVSS)

The biomass solids in biological wastewater reactor are consisted of microorganisms and non-biodegradable suspended matter, this is, mixed liquor suspended solids (MLSS). At the same time, the volatile solids concentration of mixed liquor is approximately equal to the amount of microorganisms referred as the mixed liquor volatile suspended solids (MLVSS). As a result, MLVSS is one of the most important parameters in a biological process since ensures that the available active biomass is able to consume the incoming food at any time.

Suspended solids were measured gravimetrically following standard methods [20]. Typically, 15 mL of sample from the aeration tank was withdrawn and centrifuged at 3500 rpm for 5 min. The supernatant was rejected and the remaining portion was placed in a ceramic capsule to be heated at 110 ºC and subsequently at 550 ºC in a muffle Raypa HM model. Crucibles were weighted emptiness and after each thermal treatment once they were cooling down. MLSS is determined as the mass residue after the first heating and MLVSS the mass loss weight after the calcinations.

3.5.16. SLUDGE VOLUMETRIC INDEX (SVI)

Sludge volumetric index (SVI) is used to characterize the settling properties of biomass in the aeration tank in an activated sludge process. Given the fact that the separation of sludge from the effluent is needed in a conventional treatment, SVI is considered as an indicator to assess the stability of sludge in any aerobic biological system. SVI is defined as the volume occupied by 1 g of biomass after settling the aerated liquid for 30 minutes. Hence, this index is linked to settle volume as well as MLSS through equation (3.8):

$$\text{SVI } (\text{mL}\cdot\text{g}^{-1}) = \frac{\text{Settle sludge volume}}{\text{MLVSS}} \tag{3.8}$$

3.5.17. ACUTE TOXICITY

Acute toxicity was evaluated by two different organisms, bacteria *Vibrio fischeri* and *Daphnia magna.*

A. Vibrio fischeri

The exposure to toxic substances may inhibit the emission of light bacteria *Vibrio fischeri* makes in the visible range (490-505nm). Thus, toxicity of wastewater samples was studied by the inhibition of the bioluminescent bacteria.

Luminiscence tests were performed with Luminotox® to evaluate the inhibition of the marine bacteria *V. fischeri* luminescence (NRRL B-11177) with a luminometer equipment (Lumistox 300, Lange) according to ISO 11348-3 [21]. The bacteria *V. fischeri* was supplied as a liquid-dried solution and then stored at -20 ºC to be re-hydrated prior to the tests.

Previously to toxicity assays, samples must be kept at pH at 7±0.5. Then, 2% NaCl solution was diluted with samples to prepare different volume concentrations (100.0% (undiluted), 50.0%, 25.0%, 12.5% and 6.25%). For each dilution, bioluminescence was measured before and after the exposure period of 15 and 30 min. Afterwards, the inhibition of the bacteria natural light emission was measured against a non-toxic control (2% NaCl solution, 100%). Thus, the inhibiting effect is calculated following equation (3.9):

$$\text{Inhibiting effect (\%)} = \frac{I_0 - I_t}{I_0} \times 100 \qquad (3.9)$$

where I_0 stands for the light intensity at the initial time and I_t the light intensity at certain time "t".

Once the evolution of the inhibiting effect versus dilution was determined, the EC_{50} (%) value (solution of each sample that reduces 50% of the bacteria luminescence) was estimated using LUMISsoft 4 Software™.

B. Daphnia magna

Experiments were conducted with the cladoceran *Daphnia magna* Straus. These organisms are extensively used as a representative freshwater invertebrate species in ecotoxicological studies.

Firstly, a culture of *Daphnids* were continuously obtained at laboratory scale in 800 mL of ASTM hard water [22], enriched with a standard organic extract from the algae *Ascophyllum nodosum* with a density of 3.0×10^5 cell·mL^{-1} Daphnia (TOC c.a. 2.65

$mg \cdot mL^{-1}$) [23]. The culture medium was renewed three times per week, setting to 15 animals per 800 mL, kept in a light–dark photoperiod of 16 and 8 h respectively, at a light intensity of 100-1000 lux and at constant temperature of 20±1 ºC. A reference test with potassium dichromate ($K_2Cr_2O_7$) from Merck® was regularly performed to test the sensitivity of the daphnids.

Acute toxicity test with *D. magna* was performed according to the OECD Guidelines for *Daphnia* acute mobilization test [24]. Then, neonates (< 24 h old) were exposed for 48 h at the different dilutions (100.0% (undiluted), 50.0%, 25.0%, 12.5% and 6.25%) with ASTM medium from undiluted solution and under the same conditions for the culture mentioned above. ASTM hard water was used as a negative control. In this case, immobility of *Daphnids* were observed after 24 and 48 h of exposure to the solutions and the value of EC_{50} (solution of each sample that immobilizes 50% of the *Daphnids* within a stated exposure period, mainly 48 h) was calculated using the Probit analysis (MINITAB STATISTICAL Software™ 2000). A *Daphnia* was considered immobile if it does not move after 15 s of gentle agitation.

3.5.18. TURBIDITY

Tubidity of water is due to suspended solids or salts in an aqueous sample. It is an optical property caused by the absorption and scattering of a light beam instead of being transmitted.

Turbidity values were obtained by a nephelometric method [25] by means of a HI 93414 turbidimeter (Hanna) which is appropriated to be used in drinking water and wastewater up to 1000 NTU (Nephelometric Tubidity Units). Specifically, the HI 93414 turbidimeter is based on an optical system within a tungsten filament to irradiate the cuvette containing sample, detectors to measure the scattered and transmitted light and a microprocessor to calculate the NTU value by an effective algorithm.

The device was calibrated monthly with standards (< 0.1, 15, 100 and 750 NTU) supplied by Hanna.

3.5.19. CONDUCTIVITY

Conductivity of a solution is the measurement of its capacity to drive the electrical current due to the presence of ions.

Conductivity was measured by potentiometry [26] using 524 conductivity-meter (Crison) in the case of wastewater characterization. The instrument consists of a graphite sensor, proper for water samples, microprocessor which displays the value on screen, and automatic compensator of temperature. This instrument was calibrated with standard solutions of 1413 $\mu mS \cdot cm^{-1}$ or 12.88 $mS \cdot cm^{-1}$ for measurements higher than 5 $mS \cdot cm^{-1}$.

On the other hand, the evolution of conductivity during time in the stay in Porto was made using GLP31 conductivity-meter (Crison). This device is provided with a glass-made conductivity cell with Pt1000 sensor, in addition to a temperature sensor, magnetic stirrer, high resolution display, Software ComLabo and automatic compensator of temperature. The GLP31 conductivity-meter was calibrated with standard solutions of 147 $\mu mS \cdot cm^{-1}$ and 1413 $\mu mS \cdot cm^{-1}$ or 12.88 $mS \cdot cm^{-1}$ and 118.8 $mS \cdot cm^{-1}$.

3.5.20. pH AND TEMPERATURE

pH measurements were performed using a GLP 21+ pH-meter, provided with 50 21T electrode, characterized by a frosted diaphragm improving the flow of electrolytes, Ag/AgCl encapsulated crystals, Ag^+ cartridge barrier and temperature sensor. This pH-meter is suitable for wastewater samples and low-conductivity water in a pH range between 0 and 14 and at temperatures from 0 to 60 ºC. The electrode was refilled with KCl electrolyte solution (1 M, Crison) when necessary.

Besides, the device used for pH measurements during FEUP stay was pH 730 WTW with a SenTix glass-made electrode, Ag^+ free and temperature sensor.

Both instruments were calibrated daily with buffered standard solutions of 4.01, 7.00 and 9.21.

3.6. ANALYTICAL METHODS FOR CATALYSTS CHARACTERIZATION

Textural, physical and chemical properties of the catalysts and their surfaces have been widely study in this Thesis, as shown in **Table 3.7**. Analyses were primarily performed by the "Servicio de Análisis y Caracterización de Sólidos y Superficies (SACSS)" and "Servicio de Análisis Elemental y Molecular (SAEM)" belonging to the "Servicio de Apoyo a la Investigación de la Universidad de Extremadura (SAIUEX)",

except the UV-visible diffuse reflectance spectroscopy and magnetometry, which were perfomed by the "Unidad de Apoyo a la Investigación" from the "Instituto de Catálisis y Petroleoquímica (ICP)" of "Consejo Superior de Investigaciones Científicas (CSIC)" and the "Unitat de Mesures Magnètiques" from the "Centres Científics i Tecnològics Universitat de Barcelona (CCiTUB)", respectively. Besides, exceptionally, the XPS analyses of Fe-MOFs were carried out by the "Servicios Centrales de Apoyo a la Investigación (SCAI)" at the "Universidad de Málaga". This section details the techniques for the characterization of catalysts as well as their analyses.

Table 3.7. Summary of properties measured for the characterization of the catalysts, techniques applied and equipment used in this work.

Properties	Technique	Equipment
Crystallinity Structural composition Cristal size	X-Ray Diffraction (XRD)	X-Ray diffractometer D8 Advance, Bruker©
Surface composition Chemical bonds Oxidation state	X-Ray Photoelectron Spectroscopy (XPS)	XPS Kα, Thermo Scientific
Elemental composition	Wavelength Dispersive X-Ray Fluorescence (WDXRF)	S8 Tiger 4K, Bruker©
Elemental composition	Inductively Coupled Plasma Mass Spectrometry (ICP-MS)	NexION 300D ICP-MS, Perkin Elmer
Adsorption-desorption isotherms BET surface area Pore volume	N_2 adsorption-desorption	Autosorb iQ2-C, Quantachrome®
Magnetic properties	SQUID magnetometry	SQUID MPMS XL-7, Quantum Design
Carbon, hydrogen, nitrogen and sulfur determination	Elemental analysis	Elemental analyzer CHNS-932, LECO
Thermal stability Chemical composition	Thermogravimetry and Differential Thermal Analysis (TG-DTA)	SETSYS Evolution-16, Setaram
Functional groups identification Chemical composition Structural features	Fourier Transform Infrared Spectroscopy (FTIR)	Nicolet iS10, Thermo Scientific
	Raman spectroscopy	Nicolet Almega XR dispersive raman spectrometer, Thermo Scientific
UV-vis absorption Band Gap	UV-visible Diffuse Reflectance Spectroscopy (DRUV-VIS)	UV-vis-NIR Cary 5000, Varian
Superficial morphology	Scanning Electron Microscopy (SEM)	SEM 3D, Quanta (FEI)
pH_{PZC}	Mass titration	pH GLP 21+,Crison

3.6.1. X-RAY DIFFRACTION (XRD)

X-ray diffraction analysis relies on the dispersion phenomenon of an incident beam of mono-chromatic X-rays in a certain angle and intensity from a crystalline material, satisfying the Bragg's law. This states that crystals will reflect X-rays of specific wavelengths and incident angles when the wavelengths of the scattered X-rays interfere constructively. Thus, the graphical representation of the radiation intensity versus the diffracted angle constitutes a diffractogram or a XRD pattern, typical of each crystalline material. Usually, most of the materials are composed by microcrystals randomly oriented, also called as polycrystalline aggregate [27]. Therefore, crystalline phases of polycrystalline aggregates could be obtained comparing the experimental XRD pattern with those patterns from single crystals recorded in the database of International Centre for Diffraction Data (ICDD).

Also, the mean size of a crystalline phase may be calculated through the Scherrer equation (3.10) attending to its main peak in the diffractogram [28]:

$$d = \frac{K\lambda}{\beta \cos\theta} \tag{3.10}$$

where d is the crystal size; K is a numerical factor referred to the crystal shape (generally K=0.9 [29]); λ the wavelength employed in the analysis; β the width at half-maximum peak of the main XRD peak in radians; and θ the Bragg angle.

Consequently, XRD is a powerful non-destructive technique widely employed to identify and quantify the crystalline phases, as well as the determination of their crystal sizes.

XRD analysis was conducted with a D8 Advance (Bruker©) microcrystalline powder diffractometer using a Cu Kα radiation (λ=0.1541 nm) and a linear VANTEC detector with aperture up to 12º. During the analysis, beam is falling upon the powered sample and moving around in a clockwise circle, while the detector is scanning counterclockwise. Data were collected among 2º to 80º at scan rate of $0.1^{\circ}\cdot s^{-1}$.

3.6.2. X-RAY PHOTOELECTRON SPECTROSCOPY (XPS)

X-ray photoelectron spectroscopy is a surface quantitative spectroscopic technique to value the surface composition, the chemical state and the oxidation state of an element from a material [30].

XPS is typically accomplished by exciting a sample surface with X-rays causing photoelectrons to be emitted from the surface (effective penetration of 8-10 nm). The photoelectrons possess a specific kinetic energy (KE), that which is able to be measured during the analysis by an electron energy detector. Thus, taking into account the energy of the incident radiation (hν) and KE, the electron binding energy (BE) can be obtained using the following equation (3.11).

$$BE=h\nu-KE \tag{3.11}$$

Therefore, if energy of enough power is applied to ionize many different levels in the sample, a spectrum with every atom level is produced.

The chemical composition, chemical bonds and oxidation states were evaluated with a XPS K-Alpha model (ThermoFisher Scientific) using a Al Kα radiation (hν=1486.68 eV) at vacuum conditions. Voltage and intensity were 12 kV and 6 mA, respectively. Moreover, radiation source was inclined at 30º with respect to the horizontal of the sample. Spectrum energy deviation was 0.9% from the set value in pass energy. Anyway, BE was corrected to the C1s peak at 284.6 eV. The acquired data for specific atomic levels were deconvoluted into different peaks in shape of Gaussian and Lorentzian functions with background of Shirley type by XPSpeak 4.1 software. Surface chemical composition was estimated from peak areas.

3.6.3. WAVELENGTH DISPERSIVE X-RAY FLUORESCENCE (WDXRF)

X-Ray fluorescence (XRF) is an analytic technique to determine the chemical composition of all kinds of materials. The analysis is fast, accurate, non-destructive and does not require a high amount of sample. Two different methods of XRF are distinguished: energy dispersive (EDXRF) and wavelength dispersive (WDXRF) systems [31]. A wider range of elements are detected by means of WDXRF, from beryllium to uranium.

XRF analysis is based on the principle that all elements produce secondary "fluorescent" X-rays of characteristic energy when they are exposed to X-rays of appropriate higher energy. The higher the atomic weight of an element, the higher the energy needed to induce fluorescence energy. WDXRF systems are based on Bragg's law, where photons emitted by the sample are diffracted before hitting the detector.

WDXRF analyses were performed in a Brucker S8 Tiger 4K WDXRF spectrometer, equipped with a rhodium excitation X-ray source at 4 kW operating at maximum

voltage and intensity of 60 kV and 170 mA, respectively. The elemental composition was evaluated in helium atmosphere, using different mask sizes (28 or 8 mm) and crystals (XS-5S, PET and LiF (200)) according to the energy range and the measurable elements. Experimental data were assessed with the Spectra Plus software (version 3).

3.6.4. INDUCTIVELY COUPLED PLASMA MASS SPECTROMETRY (ICP-MS)

Inductively coupled plasma (ICP) analysis deals with the ionization of a sample that decomposes into atomic and polyatomic ions. It is used to detect metals and some non-metals in liquid samples. For that reason, solid samples were digested in acidic media by microwaves prior to analyses. Afterwards, samples were digested into ICP with Ar gas plasma, excited by a magnetic field. In the case of ICP coupled with mass spectrometry (ICP-MS), positive charged ions are generated after the ionization, and the mass spectrometer is able to distinguish the element throughout the mass-to-charge ratio, and as a result, quantify the elements in the sample [32].

The analyses were carried out in ICP-MS NexION 300D (Perkin-Elmer) to determine the iron content of the TiFeC catalyst.

3.6.5. N_2 ADSORPTION-DESORPTION ISOTHERMS. BET SURFACE AREA

Adsorption and desorption of gases allows analyzing the textural properties of a solid, such as the external surface area, pore volume and pore size distribution. This technique relies on the physical phenomenon of adsorption where an adsorbate (commonly N_2 gas) is perfectly distributed onto the adsorbent surface caused by Van der Walls forces among them [27].

The higher the pressure applied, the higher the amount of gas is adsorbed, filling so micropores, mesopores and macropores. Adsorption-desorption isotherms are obtained when representing the adsorbed volume versus the normalized pressure. The isotherms are classified into six types (type I: microporous material, type II, III, VI: non-porous and type IV and V: mesoporous materials) [27]. Therefore, the specific BET surface area (S_{BET}) is determined from the data collected when a monolayer of adsorbed gas is built onto the surface according to the Brunauer, Emmet and Teller's model (equation (3.12)):

$$\frac{1}{V\left[\left(P_0/P\right)-1\right]}=\frac{C-1}{V_m C}\frac{P}{P_0}+\frac{1}{V_m C} \qquad (3.12)$$

where V is the volume of gas adsorbed in $mL \cdot g^{-1}$ at a given relative pressure (P/P_0), V_m the volume of gas in the monolayer $mL \cdot g^{-1}$ and C a constant related to the interaction adsorbate-adsorbent, and consequently, to the adsorption heat.

Hence, V_m and C are obtained from the linear regression of Eq. (3.12) of the monolayer data. Specifically, in this work, a monolayer is reached with relative pressures up to 0.3. Moreover, when N_2 is used as adsorbate gas, S_{BET}, expressed as $m^2 \cdot g^{-1}$, is obtained from the expession (3.13).

$$S_{BET}=4.37V_m \tag{3.13}$$

The external surface (S_{ext}), the standard non-porous solid multilayer thickness (t), and micropore volume (V_{micro}) are firstly assessed by means of the t-plot method [27]. Then, S_{ext} of the microporous sample can be derived from the slope of the gas volume and t values, whereas the intercept of the t-plot is related to V_{micro}.

Analyses of nitrogen adsorption-desorption isotherms of catalysts were perfomed using an Autosorb iQ2-C apparatus (Quantachrome®). Samples were previously outgassed at 150 ºC for 12 hours under vacuum in order to extract eventual adsorbed particles. Afterwards, the amount of adsorbed N_2 is measured at the same time that pressure is increased or decreased. Data are recorded and processed with ASiQwin™ software to obtain S_{BET}, S_{ext} and V_{micro}.

3.6.6. SQUID MAGNETOMETRY

Superconducting quantum interference device (SQUID) magnetometry is one of the most effective and sensitive techniques of measuring magnetic properties. The magnetic signal of the sample is obtained via a superconducting pick-up coil with 4 windings. When the sample is moved up and down it produces an alternating magnetic flux in the pick-up coil, leading to an alternating output voltage of the SQUID. Voltage is later amplified and recorded by the magnetometer's electronics [33].

The magnetization measurements were conducted in a Quantum Design MPMS XL-7 SQUID at room temperature. The maximum magnetization is obtained with the maximum value of the asymptotical curve of the magnetic moment M versus the applied magnetic field (H).

3.6.7. ELEMENTAL ANALYSIS

Generally, the elemental analysis determines the content of carbon, hydrogen, nitrogen and sulphur of a given material. The CHNS analysis requires the combustion of the material in an oxygen-pure atmosphere, giving place to a transformation of C, H, N and S of the materials into CO_2, H_2O, N_2 and SO_2, respectively. Consequently, these gases are measured in a thermal conductivity or high selectivity IR detector.

The analytical determination was performed in a CHNS-932 LECO analyzer at 1100 ºC.

3.6.8. THERMOGRAVIMETRY AND DIFFERENTIAL THERMAL ANALYSIS (TG-DTA)

The thermogravimetric (TG) and diferential thermal analysis (DTA) is included among the thermal analysis techniques, which are based on the measurement of a physical property of a sample at different temperature when they are submitted to a thermal program [27].

Regarding the thermogravimetric analysis, TG curve shows the weigth loss or gain of a substance at different temperatures under a specific atmosphere. Hence, the thermal stability and chemical composition of a sample, intermediates or the final product can be guessed.

DTA is based on the difference between the sample temperature (T_s) and the temperature of a reference (T_r) under a specific atmosphere. As a result, the DTA curve describes the amount of heat absorbed or released by a sample. Thus, exothermic processes (positive changes) or endothermic processes (negatives changes) are recorded in the DTA curve.

If TG and DTA analysis are analyzed together, (TG-DTA), water adsorbed, decomposition and chemical transformations may be analyzed. Both analyses are carried out in a thermobalance which consisted of an oven, an accurate balance device, and a sample carrier (made of platinium, alumina or quartz crucibles) where the sample is placed [27]..

TG-DTA analyses were conducted in a SETARAM thermobalance (SETSYS Evolution-16) at a heating rate of 5 ºC·min^{-1} under 50 mL·min^{-1} of air gas and in the temperature range between 20 to 800 ºC.

3.6.9. FOURIER TRANSFORM INFRARED SPECTROSCOPY (FTIR)

The IR spectroscopy is sensitive to the presence of functional groups in a molecule since a vibrational state of higher energy is generated when a functional group absorb photons belonged to the IR region, that can identify a functional group with the frequency (wavenumber) at the maximum absorbance. Thus, the representation of the intensity (e.g. transmittance) versus the wavenumber gives place to a spectrum, that it is used as a fingerprint of a sample. As any other spectroscopy technique, the intensity of the signal at specific wavenumber is related to the concentration of this specie in the sample [34].

FTIR spectra were obtained on a Nicolet iS10 (Thermo Scientific) spectrometer using KBr wafers or using the attenuated total reflectance accessory (ATR). When KBr was employed, a solid mixture containing 10 mg of sample and KBr powder was prepared. Subsequently, the mixture was homogenized and pressed to obtain a thin pellet. Then the IR light pass through the pellet and the intensity of the transmitted beam is detected and recorded using the OMNIC Software. In the case of the ATR accessory, no previously treatment was needed. The sample is directly located over the ATR plate and the infrared radiation undergoes multiple internal reflections in the crystal. Data were acquired in the range of 400-4000 cm^{-1} (with the KBr pellet) or 550-4000 cm^{-1} (with the ATR) with a resolution of 1 cm^{-1}.

3.6.10. RAMAN SPECTROSCOPY

Raman spectroscopy is a non-destructive technique which provides detailed information about chemical structure, phase and polymorphy, crystallinity and molecular interactions. Raman is often used as a complement of IR spectroscopy results.

The fundamentals of this spectroscopic analysis rely on the interaction of a laser light source with the chemical bonds of a sample. Typically a monochromatic light source from the visible, near IR or UV range is used. Thus, a molecule scatters incident light from the laser, resulting in the energy of the laser photons being shifted up or down and, as consequence, a Raman spectrum is obtained as a fingerprint of a sample. As aforementioned, the intensity of the signal allows to quantify the concentration of this specie in the sample [35].

Raman spectra were recorded in a Nicolet Almega XR dispersive Raman spectrometer (Thermo Scientific) provided with a laser at 633 nm.

3.6.11. UV-VISIBLE DIFFUSE REFLECTANCE SPECTROSCOPY (UV-vis DR)

Diffuse reflection is an optical phenomenon caused when a ray incident on the surface is scattered at many angles. The scattered radiation is collected by an accessory, i.e. integrating sphere. The resulting integrated radiation level is directly proportional to the initial radiation level and may be easily measured using a detector. Diffuse reflectance spectroscopy is commonly used in the UV-visible range, also named as UV-vis DR, for the characterization of semiconductors.

An UV-vis-NIR Varian Cary 5000 spectrophotometer was used for the measurements of UV-vis DR spectra equipped with double beam and shutter synced each other. Deuterium lamp and halogen quartz were employed as radiation sources. Detectors consisted of a photomultiplier and refrigerated PbS (if infrared is used). Spectra were recorded in the range of 200-900 nm.

Band gap indicates the difference in energy between the top of the valence band filled with electrons and the bottom of the conduction band devoid of electrons. Hence, band gap energies in catalysts were calculated using the widely-known Tauc's plot method using the UV-vis DR spectra. The following expression was proposed [36,37]:

$$(h\nu\alpha)^{1/n} = A(h\nu - E_g) \tag{3.14}$$

where h stands for the Planck's constant (4.14×10^{-15} eV·s), ν the frequency of incident photons, α as the absorption coefficient, A a proportional constant and E_g the band gap energy of the semiconductor.

Regarding the value of the exponent, n denotes the nature of the sample transition, with n=1/2 for direct transition, n=3/2 for direct forbidden transition, n=2 for indirect allowed transition or n=3 for indirect forbidden transition. A value of 2 was taken for semiconductors [38].

Typically, the unit for hν is eV (electron volts), and its relationship to the wavelength λ (nm) becomes hν=1239.7/ λ. Moreover, the absorption coefficient is obtained using the reflectance values (R) of the UV-vis DR measurement attending to equation (3.15) or directly from Kubelka-Munk function, also labeled as $F(R_\alpha)$.

$$\alpha = \ln(R) \tag{3.15}$$

Therefore, according to equation (3.14) a plot of $(h\nu\alpha)^{1/n}$ versus $h\nu$, allows to determine E_g in the linear range when $(h\nu\alpha)^2=0$ [28,38].

3.6.12. SCANNING ELECTRON MICROSCOPY (SEM)

Scanning electron microscopy (SEM) is a common technique used to determine the morphology of a sample. The principle of this technique relies on an incident electron beam scans across the sample surface and interactions with the sample, generating various types of signals: secondary electrons (SE), reflected or backscattered electrons (BSE), characteristic X-rays, Auger electrons, light photons, inelastically and elastically scattered electrons and transmitted electrons (see **Figure 3.8**).

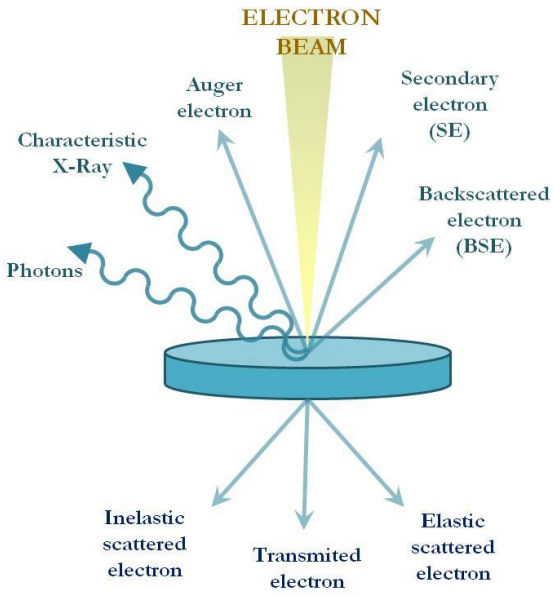

Figure 3.8. Scheme of generated electrons when irradiated a sample with an electron beam in a SEM analysis.

Thus, depending on the selected signal, different information can be obtained. For instance, BSE are commonly used to depict a 2-D image with a contrast in composition, while SE are useful to show the morphology of the sample. Moreover, the characteristic X-rays can also be detected in the SEM device for an energy-dispersive X-ray (EDX) spectroscopy, which allows to determine semi-quantitatively the abundance of differents elements in the sample.

In this way, SEM images were taken in a SEM Hitachi S-4800 device working at 20 kV of accelerating voltage and 120-10000x of magnification. Eventually, catalysts were examined by means of EDX to essay the surface chemical composition. For that purpose, a SSD detector XFlash 5010 (Bruker) was employed.

3.6.13. pH OF POINT OF ZERO CHARGE

The pH of a solution (pH_s) varies in relation to the amount of solid added into. Therefore, the pH at point of zero charge (pH_{PZC}) of a material represents the pH value when solid immersed in an aqueous solution exhibits net electrical charge on the surface. Consequently, if $pH_s > pH_{PZC}$ the solid surface would be negatively charged due to the ability of the solid to attract H^+ ions, and on the contrary, for $pH_s < pH_{PZC}$, the surface of the material would be positively charged caused of its captation of OH^- ions [39].

The estimation of pH_{PZC} was performed by mass titration method [40]. Typically, different mass percentages were added into vial containing ultrapure water. The vials were sealed and kept under magnetic stirring during 24 h to reach the equilibrium. Afterwards, the pH of the resulting solution was measured. The plot of the pH versus the amount of solid added (%) gives a trend at certain pH, which corresponds with the pH_{PZC}.

REFERENCES

[1] F.J. Rivas, F.J. Beltrán, O. Gimeno, "Joint treatment of wastewater from table olive processing and urban wastewater. Integrated ozonation - aerobic oxidation" *Chem. Eng. Technol.* 23 (**2000**) 177–181.

[2] H.K. Shon, S. Vigneswaran, J. Kandasamy, J. Cho, "Characteristics of Effluent Organic Matter in Wastewater" in: "*Water and Wastewater Treatment Technologies - Vol 1*" *UNESCO-United Nations Educational, Scientific and Cultural Organization*, (**2009**).

[3] L. Erdei, N. Arecrachakul, S. Vigneswaran, "A combined photocatalytic slurry reactor-immersed membrane module system for advanced wastewater treatment" *Sep. Purif. Technol.* 62 (**2008**) 382–388.

[4] D.H. Quiñones, A. Rey, P.M. Álvarez, F.J. Beltrán, P.K. Plucinski, "Enhanced activity and reusability of TiO_2 loaded magnetic activated carbon for solar photocatalytic ozonation" *Appl. Catal. B Environ.* 144 (**2014**) 96–106.

[5] M.J. Sampaio, C.G. Silva, A.M.T. Silva, V.J.P. Vilar, R.A.R. Boaventura, J.L. Faria, "Photocatalytic activity of TiO_2-coated glass raschig rings on the degradation of phenolic derivatives under simulated solar light irradiation" *Chem. Eng. J.* 224 (**2013**) 32–38.

[6] M. Cao, P. Wang, Y. Ao, C. Wang, J. Hou, J. Qian, "Photocatalytic degradation of tetrabromobisphenol A by a magnetically separable graphene-TiO_2 composite photocatalyst: Mechanism and intermediates analysis" *Chem. Eng. J.* (**2015**).

[7] K. Guesh, C.A.D. Caiuby, Á. Mayoral, M. Díaz-García, I. Díaz, M. Sanchez-Sanchez, "Sustainable preparation of MIL-100(Fe) and its photocatalytic behavior in the degradation of methyl orange in water" *Cryst. Growth Des.* 17 (**2017**) 1806–1813.

[8] I. Bezverkhyy, G. Weber, J.P. Bellat, "Degradation of fluoride-free MIL-100(Fe) and MIL-53(Fe) in water: Effect of temperature and pH" *Microporous Mesoporous Mater.* 219 (**2016**) 117–124.

[9] S. Mace, J. Mata-Alvarez, "Utilization of SBR technology for wastewater

treatment: An overview" *Ind. Eng. Chem. Res.* 41 (**2002**) 5539–5553.

[10] A.R. Ribeiro, M. Pedrosa, N.F.F. Moreira, M.F.R. Pereira, A.M.T. Silva, "Environmental friendly method for urban wastewater monitoring of micropollutants defined in the Directive 2013/39/EU and Decision 2015/495/EU" *J. Chromatogr. A.* 1418 (**2015**) 140–149.

[11] W.A. Moore, R.C. Kroner, C.C. Ruchhoft, "Dichromate reflux method for determination of oxygen consumed" *Anal. Chem.* 21 (**1949**) 953–957.

[12] E.W. Rice, R.B. Baird, A.D. Eaton, "5220 COD" in: A.W.W.A. and W.E.F. American Public Health Association (Ed.), "*Standard Methods for the Examination of Water and Wastewater*" 23rd edition. Washington D.C. (**2017**).

[13] E.W. Rice, R.B. Baird, A.D. Eaton, "5210 BOD" in: "*Standard Methods for the Examination of Water and Wastewater*" 23rd edition. *American Public Health Association, American Water Works Association and Water Environment Federation*, Washington D.C. (**2017**).

[14] H. Bader, J. Hoigné, "Determination of ozone in water by the indigo method" *Water Res.* 15 (**1981**) 449–456.

[15] ASTM-American Society for Testing and Materials, "Standard Test Methods for Dissolved Oxygen in Water proposed by U. S. Environmental Protection Agency" D888-09 (**2009**).

[16] G. Eisenberg, "Colorimetric determination of hydrogen peroxide" *Ind. Eng. Chem. Anal. Ed.* 15 (**1943**) 327–328.

[17] W. Masschelein, M. Denis, R. Ledent, "Spectrophotometric determination of residual hydrogen peroxide" *Water Sew. Work.* 124 (**1977**) 69–72.

[18] V.L. Singleton, J.A. Rossi Jr., "Colorimetry of total phenolics with phosphomolybdic-phosphotungstic acid reagents" *Am. J. Enol. Vitic.* 16 (**1965**) 144–158.

[19] C. Bahr, J. Schumacher, M. Ernst, F. Luck, B. Heinzmann, M. Jekel, "SUVA as control parameter for the effective ozonation of organic pollutants in secondary effluent" *Water Sci. Technol.* 55 (**2007**) 267–274.

[20] E.W. Rice, R.B. Baird, A.D. Eaton, "Standard Methods for the Examination of Water and Wastewater" 23rd edition *American Public Health Association, American Water Works Association and Water Environment Federation*, Washington D.C. (**2017**).

[21] ISO-International Organization for Standardization, "Water Quality: Determination of the inhibitory effect of water samples on the light emission of Vibrio fischeri (Luminescent bacteria test)—Part 3: method using freeze-dried bacteria" 11348–3 (**2007**).

[22] ASTM-American Society for Testing and Materials, "Standard guide for conducting acute toxicity tests on test materials with fishes, macroinvertebrates, and amphibians" E729-96 (**2004**) 1–22.

[23] D.J. Baird, I. Barber, M. Bradley, P. Calow, A.M.V.M. Soares, "The Daphnia bioassay: a critique" *Hydrobiologia*. 188 (**1989**) 403–406.

[24] OECD-Organization for Economic Co-operation and Development, "OECD Guidelines for Testing of Chemicals, Section 2, Guideline 202, Test No. 202: Daphnia sp., acute immobilisation test" (**2004**) 1–12.

[25] E.W. Rice, R.B. Baird, A.D. Eaton, "2130 Turbidity" in: "*Standard Methods for the Examination of Water and Wastewater*" 23rd edition. *American Public Health Association, American Water Works Association and Water Environment Federation*, Washington D.C. (**2017**).

[26] E.W. Rice, R.B. Baird, A.D. Eaton, "2510 Conductivity" in: "*Standard Methods for the Examination of Water and Wastewater*" 23rd edition. *American Public Health Association, American Water Works Association and Water Environment Federation*, Washington D.C. (**2017**).

[27] C. Goberna, M. Faraldos, "Técnicas de análisis y caracterización de materiales" 2nd edition *Consejo Superior de Investigaciones Científicas (CSIC)*, Madrid (**2011**).

[28] B. Ohtani, "Photocatalysis A to Z-What we know and what we do not know in a scientific sense" *J. Photochem. Photobiol. C Photochem. Rev.* 11 (**2010**) 157–178.

[29] H.P. Klug, L.E. Alexander, "X-ray diffraction procedures for polycrystalline and amorphous materials." *John Wiley & Sons*, New York (**1974**).

[30] J. Sharma, B.C. Beard, "Fundamentals of X-ray Photoelectron Spectroscopy (XPS) and its applications to explosives and propellants" in: S.N. Bulusu (Ed.), "*Chemistry and Physics of Energetic Materials*" *Springer Netherlands*, Dordrecht (**1990**).

[31] P. Brouwer, "Theory of XRF" 3rd edition *PANalytical B.V.*, The Netherlands (**2010**).

[32] R. Thomas, "Practical Guide to ICP-MS" in: "*Practical Spectroscopy*" *Marcel Dekker, Inc*, New York (**2004**).

[33] J. Clarke, A.I. Braginski, "Fundamentals and technology of SQUIDs and SQUID systems" in: "*The SQUID Handbook*" *WILEY-VCH*, Weinheim (**2004**).

[34] B.C. Smith, "Fundamentals of Fourier Transform Infrared Spectroscopy" 2nd edition *Taylor & Francis*, Boca Raton (**2011**).

[35] B. Dietzek, D. Cialla, M. Schmitt, J. Popp, "Introduction to the fundamentals of raman spectroscopy" in: T. Dieing, O. Hollricher, J. Toporski (Eds.), "*Confocal Raman Microscopy*" *Springer*, Berlin, Heidelberg (**2010**).

[36] J. Tauc, R. Grigorovici, A. Vancu, "Optical properties and electronic structure of amorphous germanium" *Phys. Status Solidi*. 15 (**1966**) 627–637.

[37] E.A. Davis, N.F. Mott, "Conduction in non-crystalline systems V. Conductivity, optical absorption and photoconductivity in amorphous semiconductors" *Philos. Mag. A J. Theor. Exp. Appl. Phys.* 22 (**1970**) 903–922.

[38] A.B. Murphy, "Band-gap determination from diffuse reflectance measurements of semiconductor films, and application to photoelectrochemical water-splitting" *Sol. Energy Mater. Sol. Cells*. 91 (**2007**) 1326–1337.

[39] S. Subramanian, J.S. Noh, J.A. Schwarz, "Determination of the point of zero charge of composite oxides" *J. Catal.* 114 (**1988**) 433–439.

[40] J.S. Noh, J.A. Schwarz, "Estimation of the point of zero charge of simple oxides by mass titration" *J. Colloid Interface Sci.* 130 (**1989**) 157–164.

PAPER 1

SOLAR PHOTO-OZONATION: A NOVEL TREATMENT METHOD FOR THE DEGRADATION OF WATER POLLUTANTS

Journal of Hazardous Materials 317 (2016) 36-43

Ana M. Chávez, Ana Rey, Fernando J. Beltrán, Pedro M. Álvarez*

Departamento de Ingeniería Química y Química Física, Universidad de Extremadura, Avenida de Elvas S/N, 06006 Badajoz, Spain

CHAPTER IV

GRAPHICAL ABSTRACT

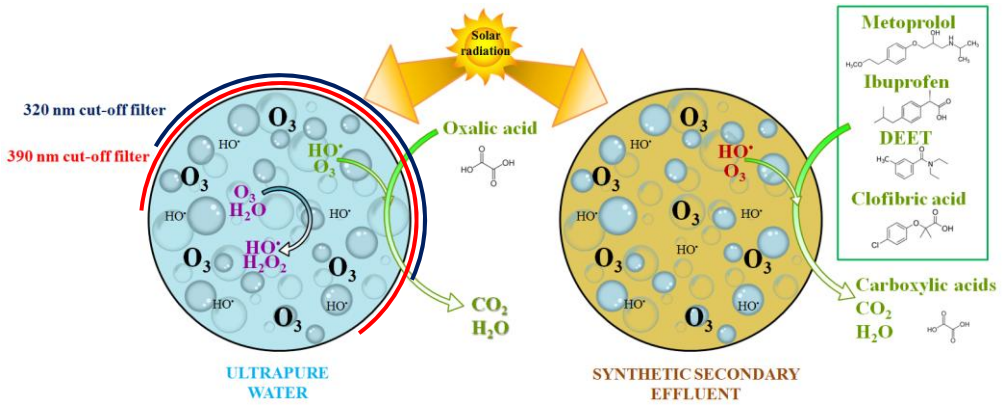

ABSTRACT

The decomposition of aqueous ozone by UV-vis radiation has been investigated with focus on the impact of ozone photolysis on the degradation of water pollutants during solar ozonation processes. The apparent first-order rate constants of the decomposition of ozone (k_{obs}) have been determined at various pHs in the 4-9 range using radiation of different wavelengths in the UV-vis range. It was found that UVA-visible radiation (λ > 320 nm) highly enhanced ozone decomposition, especially at pH 4, for which k_{obs} was three-folded with respect to the process in the absence of radiation. Hydrogen peroxide was identified as a main intermediate of ozone photo-decomposition at pH 4. Experiments of degradation of oxalic acid by ozone showed that solar irradiation brings about an increase in the hydroxyl radical to ozone exposures ratio (R_{ct}). Finally, photo-ozonation (λ > 300 nm) was shown advantageous over single ozonation in the mineralization of a selection of emerging contaminants (metoprolol, ibuprofen, N,N-diethyl-meta-toluamide and clofibric acid) in both ultrapure water and a synthetic secondary effluent. Thus, TOC removal in 2-h treatments increased from 10 to 25% in the absence of radiation to about 50% in the presence of radiation.

Keywords: AOP, emerging contaminants, photo-ozonation, UVA-visible radiation, water treatment

4.1. INTRODUCTION

Ozone has been extensively used in water treatment since long due to its great oxidizing power (2.1 eV) which enables it to selectively oxidize many organic and inorganic species in aqueous solution. The reactions between ozone and organic compounds, however, usually lead to the formation of intermediates, many of which are recalcitrant to the ozone attack and, therefore, accumulate in water. In some advanced oxidation processes (AOPs), aqueous ozone can be transformed into free-radical oxygen species (ROS), such as the hydroxyl radical ($HO^{\bullet}$) which exhibits an oxidizing power (2.8 eV) even higher than that of the ozone molecule. As consequence, these AOPs are preferred over single ozonation when the goal is to clean water avoiding the accumulation of refractory intermediates [1].

Much research has been devoted to study methods to effectively decompose ozone in water leading to the formation of ROS in order to improve oxidation efficiency. Methods to decompose aqueous ozone in alkaline solution and/or in the presence of hydrogen peroxide or UV radiation are well known [2]. In addition to those classical methods, the use of different catalysts in combination with ozone in the presence or absence of UV-vis radiation has attracted a great deal of research interest. Thus, it has been found that the transformation of aqueous ozone into hydroxyl radicals is accelerated by materials such as activated carbon, carbon nanotubes, alumina or zeolites amongst others [3–6]. Also, the combination of ozone, UV-vis radiation and some catalysts destroys organic compounds by photosensitized oxidation involving ROS [7]. Both, catalytic and photocatalytic ozonation have been proven as efficient methods to deal with water contaminants of special concern, such as emerging contaminants (ECs). Particularly, photocatalytic ozonation is a technology where synergistic effects of a number of oxidation pathways that take place simultaneously are observed [8]. However, photocatalytic ozonation is regarded as an expensive treatment technology so its applications at full-scale are scarce [7]. To overcome this drawback, solar photocatalytic ozonation has recently been investigated as a cost-effective method where the operating cost of UV lamps can be partly avoided by the use of sun-light as radiation source [9,10]. One of the first steps of the solar photocatalytic ozonation mechanism is the photolysis of ozone under solar illumination [8]. According to previous works, this step might highly contribute to the overall degradation of water pollutants. Thus, for example, it has been found that solar irradiation of a mixture of ECs (acetaminophen, antipyrine, bisphenol A, caffeine, metoprolol and testosterone) while treating it by ozone greatly improved EC removal rates and the mineralization

efficiency [9]. This might likely be due to the partial decomposition of ozone under solar radiation eventually yielding hydroxyl radicals and other ROS [11]. To our knowledge, the effect of solar radiation on the kinetics and mechanism of aqueous ozone decomposition has not been fully investigated yet.

This work is focused on the study of the effect of UV-vis radiation of different wavelengths ($\lambda > 300$ nm, $\lambda > 320$ nm and $\lambda > 390$ nm) on the rate of decomposition of aqueous ozone and the formation of hydrogen peroxide and hydroxyl radicals. In addition, the degradation of a mixture of ECs (metoprolol, N,N-diethyl-meta-toluamide (DEET) and clofibric acid) in ultrapure water and in a typical secondary effluent of municipal wastewater treatment plant (MWWTP) by photo-ozonation has been studied.

4.2. MATERIALS and METHODS

4.2.1. CHEMICALS AND SOLUTIONS

Four ECs were used in this research: metoprolol tartrate (CAS number: 56392-17-7), ibuprofen (CAS number: 15687-27-1), N,N-diethyl-m-toluamide (DEET, CAS number: 134-62-3) and clofibric acid (CAS number: 882-09-7). All of them (> 97%) were purchased from Sigma-Aldrich Chemical Co. (Spain) and used without further purification. In addition, oxalic acid (99%) (CAS number 144-62-7) was also obtained from Sigma-Aldrich Chemical Co. and used as target compound in degradation experiments. An aqueous solution was prepared to simulate a typical secondary effluent discharged from a MWWTP. ECs were added to the solution to reach a concentration of 2 $mg \cdot L^{-1}$ each.

The composition of the solution, after addition of ECs, is given in **Table 4.1**. Total organic carbon (TOC) of the mixture was c.a. 20 $mg \cdot L^{-1}$. All the reagents used to obtain this synthetic aqueous solution, except ECs, were provided by Panreac (Spain).

Table 4.1. Chemical composition of the synthetic effluent used in this work.

Chemical	Concentration mg·L^{-1}
Beef extract powder	3.6
Meat peptone	5.4
Humic acid	8.5
Tannic acid	8.4
Lignosulfonic acid sodium salt	4.9
Sodium lauryl sulfate	2.0
Arabic acid	9.4
Gum Arabic from acacia tree	9.4
Magnesium sulfate 7-hydrate	2.9
Ammonium sulfate	14.2
Metropolol tartrate	2.0
Ibuprofen	2.0
N,N-diethyl-meta-toluamide (DEET)	2.0
Clofibric acid	2.0
TOC	20

4.2.2. PHOTO-OZONATION EXPERIMENTAL SET-UP

Photo-ozonation experiments were carried out in an experimental set-up as that shown in **Figure 4.1**. It consisted of a reactor and a commercial solar simulator (Suntest CPS, Atlas). The spherical, glass-made reactor had a working volume of 0.5 L and it was provided with a gas inlet, a gas outlet and a liquid sampling port. The reactor was thermoregulated to keep temperature at 37 ºC throughout the experiments. This temperature was chosen as it is the temperature actually reached inside the solar simulator with the lamp switched on. Agitation was provided by means of a magnetic device. The reactor was placed in the chamber of the solar simulator, which was equipped with a 1500 W air-cooled Xe arc lamp.

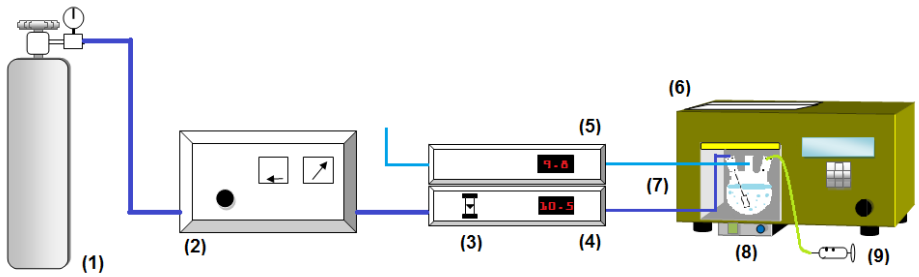

Figure 4.1. Experimental set-up used to carry out photo-ozonation experiments. (1) Oxygen bottle, (2) ozone generator, (3) flow meter, (4) ozone analyzer (inlet stream), (5) ozone outlet analyzer (outlet stream), (6) solar simulator, (7) agitated reactor, (8) magnetic stirrer, (9) sampling port.

To carry out the experiments, radiation was restricted to wavelengths over 300 nm (filter A), 320 nm (filter A + B) or 390 nm (filters A + C). Filter A, made of a coated quartz glass plus a window glass (Solar Standard, Atlas), was fixed on the equipment by the manufacturer to simulate outdoors solar radiation according to DIN 67501:1999. Cut-off polyester filters B (Unipapel) or C (Edmund Optics) were additionally used to provide UVA-visible or visible radiation, respectively. **Table 4.2** shows spectral irradiances as measured with a UV-vis spectrometer (Black Comet C model, Stellar Net, USA) while operating with the different filters. As can be seen in **Table 4.2**, the overall irradiance (λ=300-800 nm) was in the range 448-550 $W \cdot m^{-2}$. Ozone was produced from dry oxygen in a laboratory ozone generator (Anseros COM) and the concentration of ozone in gaseous streams entering and leaving the reactor was continuously monitored by ozone analyzers (Anseros GM-OEM and Anseros GM-PRO models, respectively).

Table 4.2. Irradiance distribution produced by the lamp and cut-off filters used in this work.

Cut-off filters	Irradiance ($W \cdot m^{-2}$)			
	λ=300-320 nm	λ=320-390 nm	λ=390-800 nm	λ=300-800 nm
A	0.1	50.6	499.3	550.0
A+B	<0.01	40.5	469.3	509.8
A+C	<0.01	<1.0	447.4	448.4

4.2.3. OZONE PHOTO-DECOMPOSITION EXPERIMENTS

A duplicate set of ozone decomposition experiments was first carried out in batch mode. In a typical experiment, ozone was produced from a 30 $L \cdot h^{-1}$ dry oxygen flow in a laboratory ozone generator (Anseros COM). The gas from the ozone generator, containing about 50 mg $O_3 \cdot L^{-1}$ was bubbled through a porous plate into the reactor previously loaded with 500 mL of 10 mM phosphate-buffered organic-free water (Milli-Q Millipore system). Gaseous ozone was fed to the reactor for 30 min to saturate the water with ozone and, at the same time, remove any trace of organic matter that could further affect the ozone stability significantly. The dissolved ozone concentration after this stage was about 7 $mg \cdot L^{-1}$. Then, the gas flow was stopped and the lamp of the solar simulator was switched on (in blank experiments the lamp was kept off). At intervals of time, aqueous samples were withdrawn from the reactor through a dispenser and immediately analyzed for dissolved ozone concentration. Another duplicate set of ozone decomposition experiments was carried out in semi-batch mode in order to follow the formation of hydrogen peroxide as a product of the aqueous ozone decomposition. In these experiments, a continuous stream of an oxygen-ozone

mixture (30 $L \cdot h^{-1}$ flow rate, 50 $mg \cdot L^{-1}$ ozone concentration) was continuously supplied to the reactor, which was previously charged with 500 mL of 10 mM phosphate-buffered organic-free water (Milli-Q Millipore system). The solar simulator lamp was kept on throughout the experiment except in blank experiments for which the lamp was always off. At different times, aqueous samples were taken from the reactor to be analyzed for dissolved ozone and hydrogen peroxide concentrations.

4.2.4. OXALIC ACID REMOVAL EXPERIMENTS

Oxalic acid was chosen as a probe compound to test the ability of solar radiation to decompose aqueous ozone into hydroxyl radicals. Photo-ozonation experiments were carried out in semi-batch mode as described above. The reactor was first loaded with an aqueous solution of oxalic acid (pH 4, initial concentration 25 $mg \cdot L^{-1}$) in organic-free water (Milli-Q Millipore system). The gas flow rate and the concentration of ozone in the inlet gaseous stream were set at 15 $L \cdot h^{-1}$ and 10 $mg \cdot L^{-1}$, respectively. Samples from the reactor were analyzed at different reaction times for oxalic acid concentration and TOC. Also, the evolution of the pH was followed with the reaction time.

4.2.5. EC DEGRADATION EXPERIMENTS

Photo-ozonation of a mixture of ECs (metoprolol, ibuprofen, DEET and clofibric acid) both in unbuffered organic-free water (Milli-Q Millipore system) and in a synthetic aqueous effluent (see **Table 4.1**) was carried out in semi-batch mode as described above for oxalic acid removal experiments. The reactor was charged with the aqueous solution containing the mixture of ECs and subjected to ozonation (gas flow rate 20 $L \cdot h^{-1}$, ozone concentration in the inlet gas 10 $mg \cdot L^{-1}$) in the presence and absence of radiation. A blank experiment was also carried out under illumination but in the absence of ozone to account for the direct photolysis of ECs. Samples from the reactor at different reaction times were analyzed for the concentration of ECs, short-chain carboxylic acids and TOC. pH was also followed throughout the experiments.

4.2.6. ANALYTICAL METHODS

Aqueous ozone concentration was measured by the indigo method based on the decolorization of indigo trisulfonate (600 nm, pH < 4) by ozone [12]. Hydrogen peroxide was analyzed following the cobalt colorimetric method [13]. UV-vis absorbance was recorded on a spectrophotometer (Thermo Spectronic Helios α) using a 1 cm quartz cell. Measurements of pH were made with a pH-meter (Crison

GLP21+). Oxalic acid and other short-chain carboxylic acids were analyzed by ion chromatography using a Metrohm apparatus (881 Compact IC Pro model) provided with an ion suppressor and a conductivity detector. A MetroSep A Supp 5 (150 × 4.0 mm) column thermoregulated at 45 ºC was used as stationary phase. Aqueous Na_2CO_3 with a gradient program from 0.6 to 14.6 mM in 50 min and 10 min post-time equilibration and a flow rate set at 0.7 mL·min^{-1} was the mobile phase. Concentrations of ECs were analyzed by HPLC with a Hitachi Elite LaChrom HPLC system provided with a diode array detector (Hitachi L-2455). A Phenomenex Gemini C18 column (150 x 3 mm, 5 μm) was used as stationary phase while a mixture of acidified ultrapure water (0.1% vol. formic acid) (A) and acetonitrile (B) was used as mobile phase. All solvents were degassed prior to the HPLC analysis. The mobile phase flowrate was set at 0.6 mL·min^{-1}. The gradient program used was as follows: start at 5% B, ramp to 50% B in 15 min, hold at 50% B for 10 min, back to 5% B in 3 min and hold at 5% B for 12 min. Detection was made at 220 nm. Retention times were as follows: metoprolol (7.5 min), DEET (16.5 min), clofibric acid (18 min) and ibuprofen (22 min). TOC was analyzed with a Shimazdu apparatus (TOC-V CSH model).

4.3. RESULTS and DISCUSSION

4.3.1. EFFECT OF UV-VIS RADIATION AND pH ON THE DECOMPOSITION OF AQUEOUS OZONE

Figure 4.2 shows, in a semi-log graph, the profiles of ozone concentration during the course of batch experiments of ozone decomposition in buffered ultrapure water (pH 4). As it can be seen, the presence of visible radiation (λ > 390 nm) did not accelerate the decomposition of ozone with respect to that took place in the darkness (no radiation). However, the application of radiation belonging to the entire solar spectrum (λ > 300 nm) highly increased the ozone decomposition rate. Moreover, such acceleration was mainly due to UVA radiation (λ=320-390 nm) as deduced from **Figure 4.2.** However, it is worth noticing that the irradiance produced by the lamp of the solar simulator in the 300-320 nm wavelength range was very limited (0.1 W·m^{-2} when only filter A was used, see **Table 4.2**), which may explain the little effect observed when applying this type of radiation.

Figure 4.3 shows the absorption spectrum of aqueous ozone (pH 4) in the 300-800 nm wavelength range. As it can be seen, the absorption of radiation greatly increases from 340 to 300 nm while absorption above 340 nm is low. Accordingly, UV radiation

in the 300-340 nm range may be pointed out as responsible for the activation of ozone decomposition.

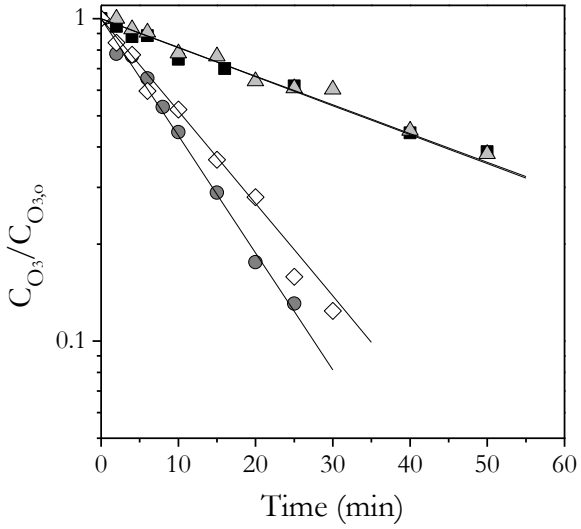

Figure 4.2. Time-evolution of normalized aqueous ozone concentration during the course of batch ozone decomposition experiments. Experimental conditions: V=500 mL, pH=4 (10 mM phosphate buffer), $CO_{3,o}$=1.5·10^{-4} M, T=37ºC. Symbols: ■ No radiation, ● hν (λ > 300 nm) filter A, ◇ hν (λ > 320 nm) filter A+B, ▲ hν (λ > 390 nm) filter A+C. See **Table 4.2** for irradiance distribution.

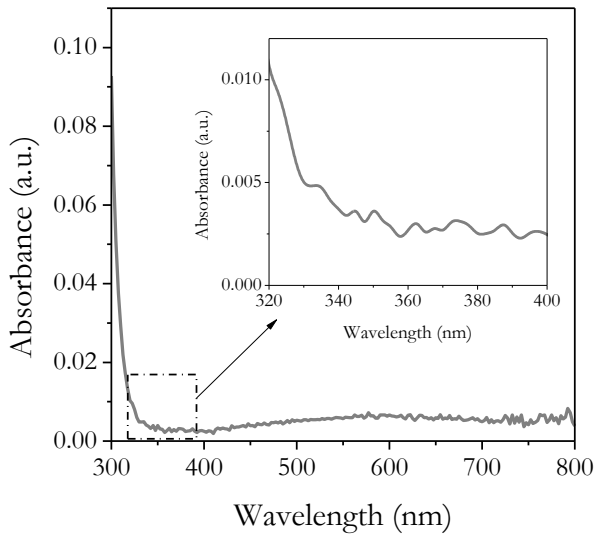

Figure 4.3. Absorption spectrum of aqueous ozone in the wavelength range 300-800 nm. Conditions: pH=4 (10 mM phosphate buffer), $CO_{3,o}$=1.5 x 10^{-4} M.

This would be likely due to the combined effect of ozone decomposition processes leading to the formation of $O(^1D)$ and, possibly, $O(^3P)$, which would rapidly react with water to yield hydroxyl radicals ($HO^{\bullet}$) [14]:

$$O_3 \xrightarrow{h\nu(\lambda<310nm)} O(^1D)+O_2(a_1\Delta_g) \quad (4.1)$$

$$O_3 \xrightarrow{h\nu(\lambda<411nm)} O(^1D)+O_2(X^3\textstyle\sum_g^{-1}) \quad (4.2)$$

$$O_3 \xrightarrow{h\nu(\lambda<1180nm)} O(^3P)+O_2(a_1\Delta_g) \quad (4.3)$$

$$O(^1D)+H_2O \longrightarrow 2HO^{\bullet} \quad (4.4)$$

$$O(^3P)+H_2O \longrightarrow 2HO^{\bullet} \quad (4.5)$$

Once $HO^{\bullet}$ is formed through reactions (4.4) and (4.5), decomposition of ozone is accelerated by a series of well-known reactions leading to the formation of hydrogen peroxide and ROS, such as the superoxide ion radical ($O_2^{\bullet-}$) and the ozonide ion radical ($O_3^{\bullet-}$)[15].

To quantitatively evaluate the effect of the UV-vis radiation on the ozone decomposition rate, the first-order kinetic approach was considered. Accordingly, the observed rate coefficient of ozone decay (k_{obs}) was obtained from the slope of plots such as those shown in **Figure 4.2**. **Table 4.3** presents the values of k_{obs} for the decomposition of ozone under different conditions of radiation and pH of the aqueous solution. In all cases $R^2 > 0.93$ was found, which makes valid the assumption of first-order kinetics.

Table 4.3. Apparent first-order rate constant of aqueous ozone decomposition at various pHs and irradiation wavelength ranges.

Irradiation	pH=4		pH=7		pH=9	
	k_{obs} (min^{-1})	R^2	k_{obs} (min^{-1})	R^2	k_{obs} (min^{-1})	R^2
No radiation	0.021	0.978	0.181	0.967	0.940	0.996
hν (λ>390 nm)	0.020	0.974	0.259	0.910	1.181	0.947
hν (λ>320 nm)	0.066	0.985	0.272	0.976	1.030	0.938
hν (λ>300 nm)	0.084	0.990	0.273	0.974	1.152	0.935

As can be seen in **Table 4.3**, in the absence of radiation k_{obs} greatly increased with pH from 0.021 min^{-1} (pH 4) to 0.940 min^{-1} (pH 9). This pH effect has been extensively reported in the literature [16] and it is attributed to the initiation reaction (4.6) where hydrogen peroxide in its anionic form (HO_2^-) is generated. This triggers the decomposition of ozone through a radical-chain mechanism where a number of ROS such as $HO^{\bullet}$, $HO_2^{\bullet}/O_2^{\bullet-}$ and $HO_3^{\bullet}/O_3^{\bullet-}$ are involved [15]:

$$O_3 + OH^- \xrightarrow{k= 70\ M^{-1}\cdot s^{-1}} HO_2^- + O_2 \quad (4.6)$$

The effect of radiation on the rate of aqueous ozone decomposition was strong at pH 4. Thus, in the presence of radiation of $\lambda > 300$ nm (see **Table 4.1** for irradiance distribution) k_{obs} was four folded compared to the value achieved in the absence of any radiation. At pH 7 and 9 the effect of radiation was of less significance (k_{obs} increased by factors of 1.5 and 1.2 at pH 7 and 9, respectively). This result suggests that at neutral and alkaline conditions, reaction (4.6) is the main initiation step, which hinders the contributions of reactions (4.1)-(4.5). At pH < 7, however, the contribution of ozone photolysis to the initiation of the radical-chain mechanism of ozone decomposition must be taken into consideration.

4.3.2. HYDROGEN PEROXIDE AS INTERMEDIATE OF OZONE DECOMPOSITION

Hydrogen peroxide is an initiator and promoter of the aqueous ozone decomposition as it can react with both ozone and $HO^{\bullet}$ to form other ROS such as the pairs $HO_2^{\bullet}/O_2^{\bullet-}$ and $HO_3^{\bullet}/O_3^{\bullet-}$, which accelerate the transformation of ozone into $HO^{\bullet}$. **Figure 4.4** shows the concentration of hydrogen peroxide during the course of some semi-batch ozone decomposition experiments. From **Figure 4.4** it is apparent that, at pH 4, the net formation of hydrogen peroxide during ozone decomposition is favored by radiation ($\lambda < 300$ nm), suggesting that, at this condition, hydrogen peroxide is an intermediate of reactions (4.4) and (4.5). At higher pH (i.e., pH 7 and 9), however, the profiles of hydrogen peroxide concentration were quite similar both in the presence and absence of radiation. Although formation of hydrogen peroxide at high pH might be also enhanced by radiation, it could not accumulate in solution to a high degree because it would rapidly react with ozone and $HO^{\bullet}$ mainly through reactions (4.7) and (4.8) [15]:

$$O_3 + HO_2^- \xrightarrow{k=2.2\times10^6 M^{-1}s^{-1}} O_3^{\bullet-} + HO_2^{\bullet} \quad (4.7)$$

$$HO^{\bullet} + HO_2^- \xrightarrow{k=7.5\times10^9 M^{-1}s^{-1}} O_2^{\bullet-} + H_2O \quad (4.8)$$

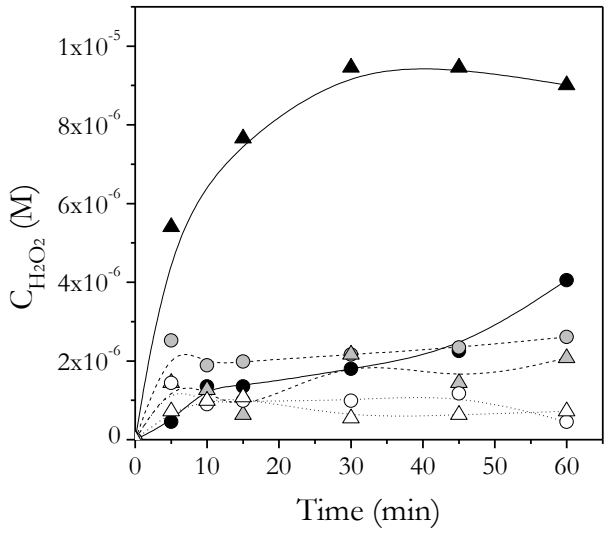

Figure 4.4. Time-evolution of hydrogen peroxide concentration during the course of semi-batch ozone absorption-decomposition experiments. Influence of pH and radiation. Experimental conditions: V=500 mL, T=37 ºC, phospate buffer=10 mM, ozone dosage=25 mg·min^{-1}. Symbols: pH=4 [● O_3, ▲Photo-ozonation (λ > 300 nm)], pH=7 [◍ O_3, ◬Photo-ozonation (λ > 300 nm)], pH=9 [○ O_3, △Photo-ozonation (λ > 300 nm)].

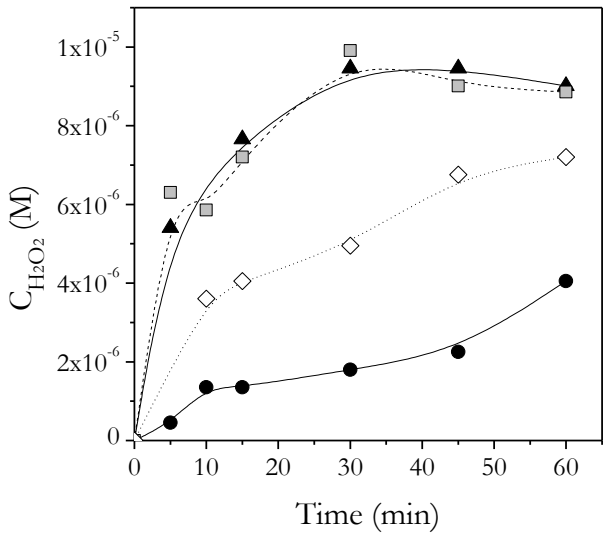

Figure 4.5. Time-evolution of hydrogen peroxide concentration during the course of semi-batch ozone absorption-decomposition experiments. Influence of radiation wavelength. Experimental conditions: V=500 mL, pH=4, C_{O3ge}=50 mg·L^{-1}, Q=30 L h^{-1}, T=37ºC, phosphate buffer=10 mM. Symbols: ● O_3, ▲ O_3+hν (λ>300 nm), ■ O_3+hν (λ > 320 nm), ◇ O_3+hν (λ > 390 nm).

To further explore the effect of radiation on the net formation of hydrogen peroxide during decomposition of ozone at pH 4, a new set of semi-batch experiments was carried out applying radiation of different wavelength ranges. **Figure 4.5** shows the concentration profiles of hydrogen peroxide during the course of these experiments. It can be observed that hydrogen peroxide concentration in solution increased fast from the beginning of any experiment. However, the initial rate of hydrogen peroxide formation depended on the type of radiation applied. Thus, when radiation $\lambda > 300$ nm or $\lambda > 320$ nm was used, hydrogen peroxide concentration reached concentrations of c.a. 9×10^{-6} M in about 30 min while when only visible radiation was applied ($\lambda > 390$ nm) half that concentration was analyzed in water after 30 min. In the blank experiment, carried out without radiation, the concentration of hydrogen peroxide was even lower ($< 2 \times 10^{-6}$ M after 30 min). If **Figures 4.2** and **4.5** are analyzed together, it can be easily deduced that the use of radiation accelerates both ozone decomposition and hydrogen peroxide generation following the same trend.

This result suggests that, at pH 4, the generated hydrogen peroxide may play an important role on ozone decomposition, especially at wavelengths in the 300-390 nm range. At $\lambda > 390$ nm, hydrogen peroxide, though formed to some extent, is not expected to undergo photolysis and, therefore, accelerate ozone transformation into ROS. In accordance with this, Chu and Anastasio [17] found that the absorption coefficient of aqueous hydrogen peroxide at slightly acidic conditions decreased with the increasing wavelength from c.a. 1 $M^{-1} \cdot cm^{-1}$ at 300 nm to nearly 0 at 360 nm. Therefore, it is plausible to consider that hydrogen peroxide is a primary intermediate of ozone decomposition that may further decompose into ROS both by radiation ($\lambda <$ 360 nm) and by the well-known mechanism of ozone decomposition in water [9].

4.3.3. KINETIC MODEL FOR AQUEOUS OZONE DECOMPOSITION AT PH 4 UNDER ILLUMINATION

An attempt to model the kinetics of aqueous ozone decomposition under illumination was carried out. Considering the findings above, reactions (4.9) and (4.10) were assumed as main photolytic steps:

$$O_3 + H_2O \xrightarrow{k_{rad\text{-}O_3}} O_2 + H_2O_2 \quad (4.9)$$

$$H_2O_2 \xrightarrow{k_{rad\text{-}H_2O_2}} 2HO^{\bullet} \quad (4.10)$$

In addition, reactions in **Table 4.4.** were considered to develop a mathematical model aimed to simulate the kinetics of ozone decay in batch experiments. Rate

constant data in **Table 4.4.** were taken or adapted from the literature [18–20]. The mathematical model, which considers a set of differential equations for ozone, hydrogen peroxide and free-radical species, was numerically solved by a fourth-order Runge-Kutta method (Micromath Sicentist 3.0) to obtain the ozone concentration profile. The values of the rate constants of reactions (4.9) and (4.10) were found matching the experimental profiles of ozone concentration and the simulated ones.

Table 4.4. Reactions and rate constants considered in the mechanism of ozone decomposition under illumination.

Reaction	Rate constant (T=37 ºC)
$O_3 + OH^- \longrightarrow HO_2^- + O_2$	k=390 $M^{-1}\cdot s^{-1}$
$O_3 + HO_2^- \longrightarrow O_3^{\bullet-} + HO_2^{\bullet}$	k=1.09 x 10^7 $M^{-1}\cdot s^{-1}$
$O_3 + O_2^{\bullet-} \longrightarrow O_3^{\bullet-} + O_2$	k=1.6 x 10^9 $M^{-1}\cdot s^{-1}$
$HO_3^{\bullet} \longrightarrow HO^{\bullet} + O_2$	k=1.4 x 10^5 $M^{-1}\cdot s^{-1}$
$O_3 + HO^{\bullet} \longrightarrow HO_2^{\bullet} + O_2$	k= 3 x 10^9 $M^{-1}\cdot s^{-1}$
$H_2O_2 + HO^{\bullet} \longrightarrow HO_2^{\bullet} + H_2O$	k=2.7 x 10^7 $M^{-1}\cdot s^{-1}$
$HO_2^- + HO^{\bullet} \longrightarrow O_2^{\bullet-} + H_2O$	k=7.5 x 10^9 $M^{-1}\cdot s^{-1}$
$O_3 \longrightarrow O + O_2$	k=1.69 x 10^{-6} s^{-1}
$O + O_2 \longrightarrow O_3$	k=4 x 10^9 $M^{-1}s^{-1}$
$O + H_2O \longrightarrow 2HO^{\bullet}$	k=2520 s^{-1}
$H_3PO_4 + HO^{\bullet} \longrightarrow P_2$	k=2.6 x 10^6 $M^{-1}\cdot s^{-1}$
$H_2PO_4^- + HO^{\bullet} \longrightarrow P_1$	k=2 x 10^4 $M^{-1}\cdot s^{-1}$
$HPO_4^{2-} + HO^{\bullet} \longrightarrow P_3$	k=7.9 x 10^5 $M^{-1}\cdot s^{-1}$
$O_3 + H_2O \xrightarrow{k_{rad\text{-}O_3}} O_2 + H_2O_2$	k_{O_3}-rad s^{-1}
$H_2O_2 \xrightarrow{k_{rad\text{-}H_2O_2}} 2HO^{\bullet}$	$k_{H_2O_2}$-rad s^{-1}
$HO_2^- + H^+ \rightleftharpoons H_2O_2$	pK_1=11.3
$HO_2^{\bullet} \rightleftharpoons O_2^{\bullet-} + H^+$	pK_2=4.8
$O_3^{\bullet-} + H^+ \rightleftharpoons HO_3^{\bullet-}$	pK_3=8.2
$H_3PO_4 \rightleftharpoons H^+ + H_2PO_4^-$	pK_4=2.2
$H_2PO_4^- \rightleftharpoons H^+ + HPO_4^{2-}$	pK_5=7.2
$HPO_4^{2-} \rightleftharpoons H^+ + PO_4^{3-}$	pK_6=12.3

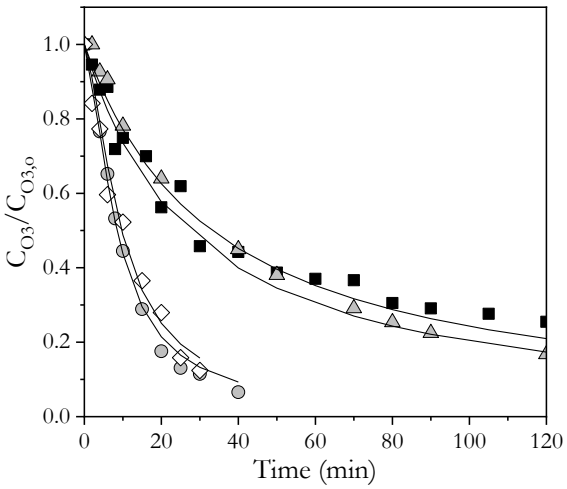

Figure 4.6. Time-evolution of normalized aqueous ozone concentration during the course of batch ozone decomposition experiments. Experimental conditions: V=500 mL, pH=4 (10 mM phosphate buffer), $CO_{3,o}$=1.5 x 10^{-4} M, T=37ºC. Symbols: ■ No radiation, ● hν (λ > 300 nm) filter A, ◇ hν (λ > 320 nm) filter A+B, △ hν (λ > 390 nm) filter A+C. See **Table 4.2** for irradiance distribution. Solid lines represents fitting results according to the model in **Table 4.4**.

Figure 4.6 shows the actual ozone concentration profiles and those simulated for experiments in the absence and presence of radiation. As can be seen, good agreement (R^2 > 0.99) was observed between the experimental and calculated values, which validates the model used. Therefore, the computational method allowed the estimation of the rate constants of reactions (4.9) and (4.10) as shown in **Table 4.5**. As expected, both rate constants were much lower for λ > 390 nm than for λ > 300 nm or λ > 320 nm.

Table 4.5. Rate constants of photolytic decomposition of ozone and hydrogen peroxide at pH 4 according to the reactions model shown in Table 4.4.

Radiation	$k_{rad\text{-}O_3}$ (s^{-1})	$k_{rad\text{-}H_2O_2}$ (s^{-1})	R^2
hν (λ>390 nm)	1.01 x 10^{-9}	1.15 x 10^{-10}	0.997
hν (λ>320 nm)	1.05 x 10^{-7}	9.53 x 10^{-4}	0.993
hν (λ>300 nm)	1.13 x 10^{-7}	9.98 x 10^{-4}	0.990

4.3.4. EFFECT OF RADIATION ON THE DEGRADATION OF OXALIC ACID BY OZONATION: R_{CT} RATIOS

Oxalic acid was chosen as a probe compound to test the ability of UV-vis radiation (λ > 300 nm) to decompose aqueous ozone into ROS, mainly hydroxyl radical.

Aqueous oxalic acid (pH 4) does not absorb radiation of λ>300 nm as it was deduced from the absorption spectrum acquired (results not shown). Also, oxalic acid reacts very slowly with molecular ozone ($k < 0.04$ $M^{-1}s^{-1}$ at pH 4 as obtained from [21]) while does react fast with the hydroxyl radical ($k=2.3 \times 10^7$ $M^{-1}s^{-1}$ at pH 4 as obtained from [22]) leaving no intermediates in solution as it is transformed directly to CO_2. This latter is corroborated by results in **Figure 4.7** where residual normalized concentration of oxalic acid and TOC during the course of ozonation and photo-ozonation experiments at pH 4 are plotted together. It can be seen that for given reaction conditions oxalic acid and TOC profiles are close to each other.

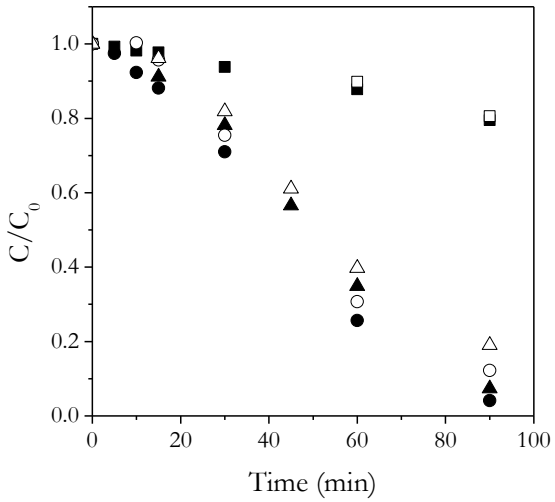

Figure 4.7. Time-evolution of normalized oxalic acid concentration and normalized TOC during the course of semi-batch ozonation and photo-ozonation experiments. Experimental conditions: V=500 mL, $C_{OX,0}$=25 mg·L^{-1}, pH_0=4, T=37ºC, Ozone dosage=2.5 mg·min^{-1}. Symbols: ■,□ O_3; ●,○ Photo-ozonation (λ > 300 nm); ▲,△ Photo-ozonation (λ > 320 nm). Solid symbols for oxalic acid, open symbols for TOC.

The effect of radiation on the removal of oxalic acid is clear from the results in **Figure 4.7**. Thus, oxalic acid removal rate was greatly enhanced by using UV-vis radiation (λ > 300 nm or λ > 320 nm). Little differences were observed between the oxalic acid concentration profiles from photo-ozonation experiments carried out with filters A (λ > 300 nm) and A+B (λ > 320 nm). These results suggest that ozone decomposition in the presence of UV-vis radiation involves a greater generation of secondary oxidants (i.e., ROS) able to remove oxalic acid.

As the rate constants of the reactions between oxalic acid and ROS other than HO• are much lower than that reported for the reaction oxalic acid-HO• [23], one can consider that oxalic acid depletion during ozonation is primarily due to hydroxyl radical reactions. Accordingly, it can be assumed that the degradation of oxalic acid by ozonation or photo-ozonation obeys a second order kinetic law as follows:

$$-\frac{dC_{OX}}{dt} = k_{HO^\bullet} \cdot C_{OX} \cdot C_{HO^\bullet} \quad (4.11)$$

In Eq. (4.11), C_{OX} stands for the concentration of oxalic acid, $C_{HO^\bullet}$ for the concentration of hydroxyl radicals in solution and $k_{HO^\bullet}$ for the second-order rate constant of the reaction between oxalic acid and hydroxyl radicals. Rearranging Eq. (4.11) and integrating:

$$\ln \frac{C_{OX,0}}{C_{OX,t}} = k_{HO^\bullet} \cdot \int_0^t C_{HO^\bullet} \cdot dt \quad (4.12)$$

This allows one to determine the ratio of exposures of HO• and ozone (R_{ct}) during ozonation experiments as follows [24]:

$$R_{ct} = \frac{C_{HO^\bullet}}{C_{O_3}} = \frac{\int_0^t C_{HO^\bullet} \cdot dt}{\int_0^t C_{O_3} dt} = \frac{\ln \frac{C_{OX,0}}{C_{OX,t}}}{k_{HO^\bullet} \cdot \int_0^t C_{O_3} dt} \quad (4.13)$$

Figure 4.8 shows plots of ln ($C_{OX,o}/C_{OX,t}$) versus the ozone exposure ($\int CO_3 \cdot dt$) measured in some ozonation and photo-ozonation experiments. **Figure 4.8** demonstrates a strong dependence of R_{ct} on the presence of radiation ($\lambda > 300$ nm). Thus, R_{ct}, which was constant throughout the experiments ($R^2 > 0.98$), took an average value of 6.2×10^{-8} for the single ozonation experiment while in the presence of radiation the HO• exposure increased dramatically leading to much higher values of R_{ct} (average values of 1.4×10^{-5} and 6.5×10^{-6} for experiments carried out with radiation $\lambda > 300$ nm and $\lambda > 320$ nm, respectively).

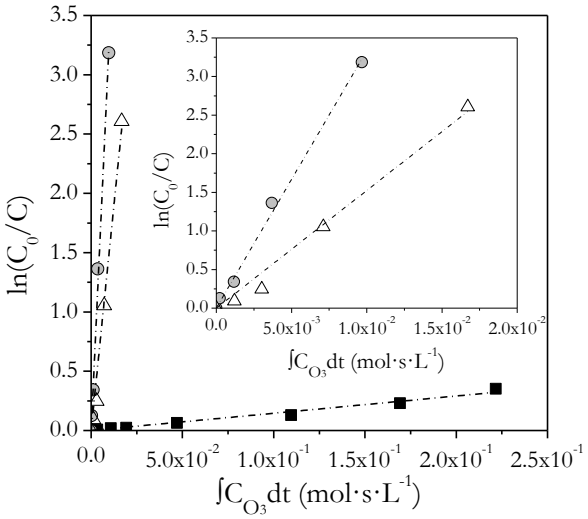

Figure 4.8. Rct plots for ozonation and photo-ozonation semi-batch experiments. Operating conditions: V=500 mL, $C_{OX,0}$=25 mg·L^{-1}, pH_0=4, T=37ºC, ozone dosage=2.5 mg·min^{-1}. Symbols: ■ O_3; ● O_3+hν (λ > 300 nm); △ O_3+hν (λ > 320 nm).

4.3.5. DEGRADATION OF A MIXTURE OF ECS BY PHOTO-OZONATION

Finally, a set of experiments was primarily designed to elucidate the effect of solar photo-ozonation on the mineralization of organic compounds of special concern, such as ECs. For that purpose, four ECs were selected: metoprolol, ibuprofen, DEET and clofibric acid. Blank experiments (in the absence of ozone) demonstrated that none of these compounds could be removed significantly by direct photolysis at λ > 300 nm (not shown). Thus, EC removal percentages after 2-h treatment were below 1%. Semi-batch ozonation experiments were carried out both in ultrapure water and in a synthetic effluent prepared to simulate a typical secondary effluent from a MWWTP (see **Table 1**). **Figure 4.9** shows the degradation of ECs sin terms of overall removal and mineralization (i.e., TOC removal).

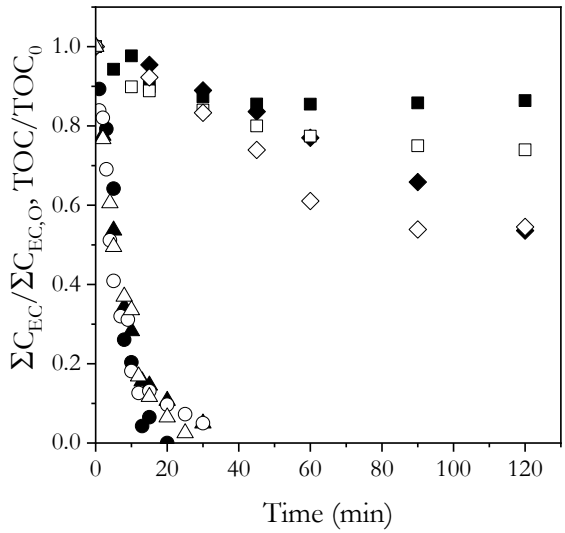

Figure 4.9. Time-evolution of normalized overall ECs concentration and normalized TOC during the course of semi-batch ozonation and photo-ozonation (λ > 320 nm) experiments. Experimental conditions: V=500 mL, $C_{EC,0}$=2 mg·L^{-1} each, TOC_0=4 mg·L^{-1} (ultrapure water spiked with ECs) or 20 mg·L^{-1} (synthetic effluent), pH_0=7, T=37 ºC, ozone dosage=3.3 mg·min^{-1}. Symbols: ■,□ O_3, TOC profile; ●,○ O_3, ECs concentration profile; ◆,◇ Photo-ozonation, TOC profile; ▲,△ Photo-ozonation, ECs concentration profile. Solid symbols for experiments with the synthetic effluent (see **Table 4.1**), open symbols for experiments carried out in ultrapure water spiked with ECs.

It is apparent that single ozonation (in the absence of radiation) was able to completely remove the four ECs in less than 20 min regardless of the water matrix used. Moreover, no effect of radiation was observed on the removal rate of ECs. However, the impact of radiation on TOC removal was considerable. Thus, while single ozonation (i.e., absence of radiation) led to only about 25% TOC removal after 2 h of ozonation of the aqueous solution of ECs (ultrapure water), 50% TOC removal was achieved by photo-ozonation. The impact of radiation on mineralization was also evident in the experiments carried out with the synthetic effluent. Thus, while single ozonation barely removed 10% of the initial TOC in 2 h of treatment, about 45% TOC removal was achieved within this time in the photo-ozonation experiment. These results suggest that, once the ECs were transformed into ozone-refractory intermediates, radiation (λ > 300 nm) promoted an ozone decomposition free-radical mechanism leading to the overall degradation of ECs and partial mineralization of the synthetic effluent. This finding could be useful to design photo-ozonation processes aimed to degrade pollutants in water which are difficult to mineralize by single ozonation.

Partial oxidation of ECs in the ozonation experiments carried out with the synthetic effluent (i.e., TOC removal was not complete) suggests the accumulation of reaction intermediates. As pH decreased from c.a. 7 to about 4.5-5 as a result of ozonation, the formation of some carboxylic acid was analyzed by ion chromatography. Oxalic acid was the main reaction intermediate though noticeable amounts of formic and acetic acids were also formed. Succinic and malonic acids were also detected as reaction intermediates in some instances. **Figure 4.10** presents the evolution with time of these carboxylic acids, considered as a whole in terms of organic carbon (TOC_{carbx}), during ozonation experiments in the presence and absence of radiation.

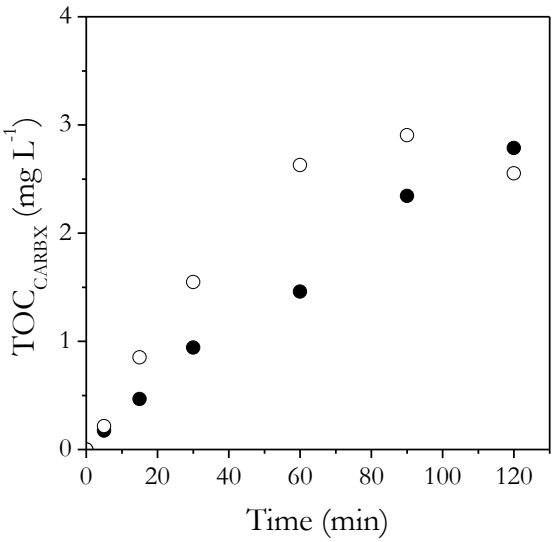

Figure 4.10. Time-evolution of short-chain carboxylic acids (measured as organic carbon) accumulated during ozonation and photo-ozonation semi-batch experiments carried out with the synthetic effluent. Experimental conditions: V=500 mL, $C_{EC,0}$=2 mg·L^{-1} each TOC_0=20 mg L^{-1}, pH_0=7, C_{O3ge}=10 mg·L^{-1}, Q=20 L·h^{-1},T=37 ºC, ozone dosage=3.3 mg·min^{-1}. Symbols: ● O_3, ○ Photo-ozonation (λ > 300 nm).

It can be seen that the production rate of carboxylic acids was almost constant during the 2-h single ozonation experiment while the TOC_{carbx} increased to reach a maximum at 90 min in the photo-ozonation experiment and decreased afterwards. A TOC balance revealed that after 2 h of treatment, the residual TOC was partly due to the accumulation of carboxylic acids. Thus, the TOC_{carbx}/TOC ratio at 2 h was 16.7% in the single ozonation experiment (no radiation) and 45.7% in the photo-ozonation experiment. This points out the photo-ozonation process as a more efficient one in terms of overall organic matter degradation.

4.4. CONCLUSIONS

In this study the experimental results show that aqueous ozone transformation into ROS can be accelerated by solar radiation (λ > 300 nm). The acceleration is higher at pH 4 than at pH 7 or 9. At pH 4 and considering other experimental conditions used in this work, ozone photo-decomposition is mainly due to radiation in the 320-390 wavelength range. Hydrogen peroxide was identified as an intermediate of ozone photo-decomposition, which eventually yields a higher concentration of hydroxyl radicals than single ozonation (in the absence of radiation). Thus, it was found that the hydroxyl radical-to-ozone exposure ratio (R_{ct}) could be more than 100 folded by using UVA-vis radiation (λ > 320 nm). In this work, it has been shown that photo-ozonation is a more efficient process than single ozonation to mineralize a mixture of four selected ECs, both in aqueous solution (ultrapure water) and in a synthetic effluent prepared to simulate a secondary effluent from a MWWTP. Accordingly, solar photo-ozonation could be regarded as an efficient oxidation method of water pollutants which are difficult to mineralize.

REFERENCES

[1] R. Andreozzi, V. Caprio, A. Insola, R. Marotta, "Advanced oxidation processes (AOP) for water purification and recovery" *Catal. Today*. 53 (**1999**) 51–59.

[2] W.H. Glaze, J.-W. Kang, D.H. Chapin, "The chemistry of water treatment processes involving ozone, hydrogen peroxide and ultraviolet radiation" *Ozone Sci. Eng.* 9 (**1987**) 335–352.

[3] P.M. Álvarez, J.F. García-Araya, F.J. Beltrán, I. Giráldez, J. Jaramillo, V. Gómez-Serrano, "The influence of various factors on aqueous ozone decomposition by granular activated carbons and the development of a mechanistic approach" *Carbon N. Y.* 44 (**2006**) 3102–3112.

[4] A. Ikhlaq, D.R. Brown, B. Kasprzyk-Hordern, "Mechanisms of catalytic ozonation: An investigation into superoxide ion radical and hydrogen peroxide formation during catalytic ozonation on alumina and zeolites in water" *Appl. Catal. B Environ.* 129 (**2013**) 437–449.

[5] R. Oulton, J.P. Haase, S. Kaalberg, C.T. Redmond, M.J. Nalbandian, D.M. Cwiertny, "Hydroxyl radical formation during ozonation of multiwalled carbon nanotubes: performance optimization and demonstration of a reactive CNT filter" *Environ. Sci. Technol.* 49 (**2015**) 3687–3697.

[6] J. Nawrocki, L. Fijołek, "Catalytic ozonation — Effect of carbon contaminants on the process of ozone decomposition" *Appl. Catal. B Environ.* 142–143 (**2013**) 307–314.

[7] M. Mehrjouei, S. Müller, D. Möller, "A review on photocatalytic ozonation used for the treatment of water and wastewater" *Chem. Eng. J.* 263 (**2015**) 209–219.

[8] E.M. Rodríguez, G. Fernández, P.M. Álvarez, F.J. Beltrán, "TiO_2 and Fe (III) photocatalytic ozonation processes of a mixture of emergent contaminants of water" *Water Res.* 46 (**2012**) 152–166.

[9] D.H. Quiñones, P.M. Álvarez, A. Rey, S. Contreras, F.J. Beltrán, "Application of solar photocatalytic ozonation for the degradation of emerging contaminants in water in a pilot plant" *Chem. Eng. J.* 260 (**2015**) 399–410.

[10] D.H. Quiñones, P.M. Álvarez, A. Rey, F.J. Beltrán, "Removal of emerging contaminants from municipal WWTP secondary effluents by solar photocatalytic ozonation. A pilot-scale study" *Sep. Purif. Technol.* 149 (**2015**) 132–139.

[11] L. Sánchez, X. Domènech, J. Casado, J. Peral, "Solar activated ozonation of phenol and malic acid" *Chemosphere*. 50 (**2003**) 1085–1093.

[12] H. Bader, J. Hoigné, "Determination of ozone in water by the indigo method" *Water Res.* 15 (**1981**) 449–456.

[13] W. Masschelein, M. Denis, R. Ledent, "Spectrophotometric determination of residual hydrogen peroxide" *Water Sew. Work.* 124 (**1977**) 69–72.

[14] J.M. Anglada, M. Martins-Costa, M.F. Ruiz-López, J.S. Francisco, "Spectroscopic signatures of ozone at the air-water interface and photochemistry implications." *Proc. Natl. Acad. Sci. U. S. A.* 111 (**2014**) 11618–23.

[15] J. Staehelin, R.E. Bühler, J. Hoigné, "Ozone decomposition in water studied by pulse radiolysis. 2. Hydroxyl and hydrogen tetroxide (HO_4·) as chain intermediates" *J. Phys. Chem.* 88 (**1984**) 5999–6004.

[16] J.L. Sotelo, F.J. Beltrán, F.J. Benítez, J. Beltrán-Heredia, "Ozone decomposition in water: kinetic study" *Ind. Eng. Chem. Res.* 26 (**1987**) 39–43.

[17] L. Chu, C. Anastasio, "Formation of hydroxyl radical from the photolysis of frozen hydrogen peroxide" *J. Phys. Chem. A.* 109 (**2005**) 6264–6271.

[18] F.J. Beltrán, J. Rivas, P.M. Alvarez, M.A. Alonso, B. Acedo, "A kinetic model for advanced oxidation processes of aromatic hydrocarbons in water: application to phenanthrene and nitrobenzene" *Ind. Eng. Chem. Res.* 38 (**1999**) 4189–4199.

[19] J. Lin, T. Nakajima, "An AM1 study of decomposition of aqueous ozone" *J. Mol. Struct. Theochem*. 625 (**2003**) 161–167.

[20] P. Maruthamuthu, P. Neta, "Phosphate radicals. Spectra, acid-base equilibriums, and reactions with inorganic compounds" *J. Phys. Chem.* 82 (**1978**) 710–713.

[21] J. Hoigné, H. Bader, "Rate constants of reactions of ozone with organic and inorganic compounds in water — II disociating organic compounds" *Water Res.* 17 (**1983**) 185–194.

[22] G. V. Buxton, C.L. Greenstock, W.P. Helman, A.B. Ross, "Critical review of rate constants for reactions of hydrated electrons, hydrogen atoms and hydroxyl radicals in aqueous solution" *J. Phys. Chem.* 17 (**1988**) 513–886.

[23] T. Garoma, M.D. Gurol, "Modeling aqueous ozone/UV process using oxalic acid as probe chemical" *Environ. Sci. Technol.* 39 (**2005**) 7964–7969.

[24] M.S. Elovitz, U. Von Gunten, "Hydroxyl radical/ozone ratios during ozonation processes. I. The R(ct) concept" *Ozone Sci. Eng.* 21 (**1999**) 239–260.

PAPER 2

SOLAR PHOTOCATALYTIC OZONATION OF CONTAMINANTS OF EMERGING CONCERN AND EFFLUENT ORGANIC MATTER (EfOM) IN SECONDARY EFFLUENTS BY REUSABLE MAGNETIC CATALYST

Chemical Engineering Journal (2020)

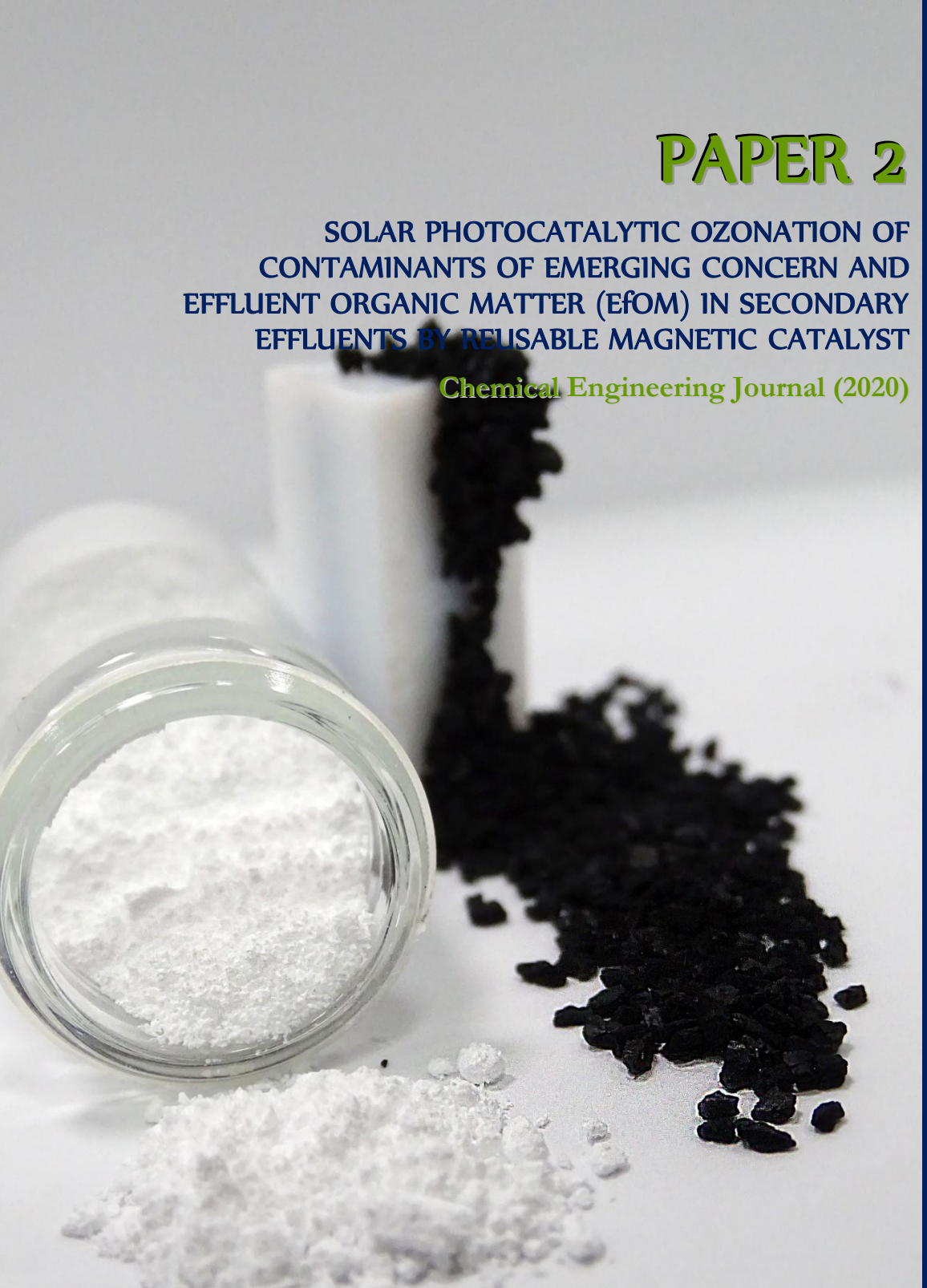

Ana M. Chávez, Diego H. Quiñones, Ana Rey, Fernando J. Beltrán, Pedro M. Álvarez*

Departamento de Ingeniería Química y Química Física, Instituto Universitario de Investigación del Agua, Cambio Climático y Sostenibilidad (IACYS), Universidad de Extremadura, Av. de Elvas s/n, 06006 Badajoz (Spain)

CHAPTER V

GRAPHICAL ABSTRACT

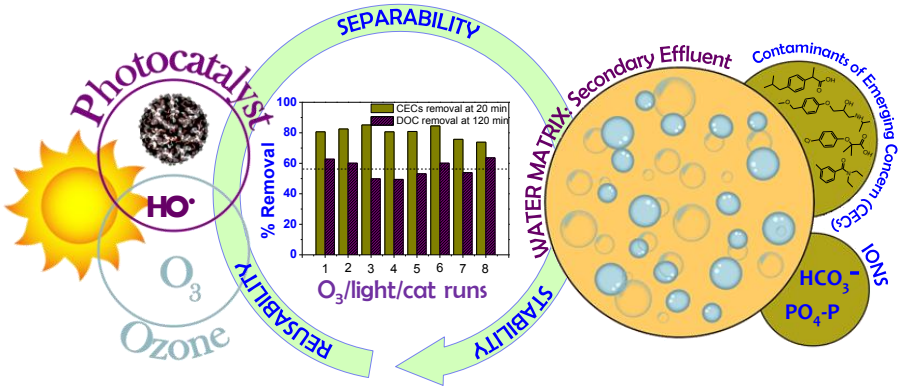

ABSTRACT

A magnetic TiO_2/Fe_3O_4/activated carbon composite was used as a photocatalyst for the removal of contaminants of emerging concern (CECs) and effluent organic matter (EfOM) of real and simulated effluents from municipal wastewater treatment plants (MWWTPs). While the catalyst showed limited activity under solar irradiation in the absence of ozone, the ECs were completely eliminated and dissolved organic carbon (DOC) removal efficiencies reached up to more than 75% by solar photocatalytic ozonation. The influence of the EfOM (0-30 mg·L^{-1} DOC), carbonate/bicarbonate (0-60 mg·L^{-1} IC) and PO_4-P (0-3.5 mg·L^{-1} PO_4-P) concentration of the secondary effluent on the photocatalytic activity was studied. Both EfOM and carbonate/bicarbonate concentration accelerated the DOC removal in single ozonation experiments (i.e., absence of catalyst and radiation) due to the presence of initiators of the hydroxyl radical chain, the formation of secondary oxidants (i.e., hydrogen peroxide and carbonate radical) and the buffering capacity of the effluent. However, the interaction of EfOM and carbonate/bicarbonate with the catalyst brought about a decrease of its photocatalytic activity. Phosphates, in the concentration range studied, did not influence appreciably the catalytic activity. The reusability of the catalyst was evaluated through eight consecutive solar phototacalytic ozonation runs. Samples of fresh and reused catalysts were examined by bulk composition analysis, N_2 adsorption-desorption isotherms, XRD, XPS, SQUID magnetometry and the pH_{PZC}. Despite some changes in the porous structure and the fixation of some oxygen groups on the carbon surface as a result of ozonation, the catalyst showed good stability and the oxidation efficiency was maintained through runs.

Keywords: contaminants of emerging concern, magnetic photocatalyst, secondary effluent, solar photocatalytic ozonation

5.1. INTRODUCTION

Nowadays, there is a great deal of interest about the occurrence of contaminants of emerging concern (CECs) in effluents from municipal wastewater treatment plants (WWTPs). These CECs include a wide variety of micropollutants such as drugs, pesticides, pharmaceuticals, personal care products, industrial chemicals, food additives or engineered nanomaterials [1]. Generally, conventional WWTPs comprise primary and secondary treatment systems with a limited capacity to safely remove CECs from wastewater [2]. Some advanced treatments have been proposed to remove CECs from wastewater, including adsorption onto activated carbon and carbon nanotubes, membrane technologies and advanced oxidation processes (AOPs) [3]. However, the application of these methods as tertiary treatment of wastewater at full-scale is still very limited due to their high cost and relatively low selectivity [4].

Recently, an emerging AOP based on the combination of ozone, sunlight and a semiconductor photocatalyst, the so-called solar photocatalytic ozonation, has attracted significant research attention [5]. The process takes advantage of the selective molecular ozone reactions and the non-selective photocatalytic reactions. On one hand, ozone is able to remove most of the recalcitrant CECs but does not mineralize them to a high extent, leaving ozonation by-products in water [6]. On the other hand, photocatalytic oxidation reactions can mineralize most of these ozonation products though it is usually a slow process [7]. Photocatalytic ozonation takes advantage of both processes, showing also synergistic effects between them. Thus, ozone could trap electrons, decreasing the recombination of photo-generated electrons and holes, and promotes the formation of free-radical oxygen species (ROS) such as the hydroxyl radical ($HO^{\bullet}$), which shows high, non-selective oxidation power [8–10]. As a result, solar photocatalytic ozonation has been shown to efficiently produce $HO^{\bullet}$, enhancing the mineralization of a broad spectrum of CECs present in WWTP effluents, such as pharmaceuticals [11,12], pesticides [13] or plasticizers [14]. Solar photocatalytic ozonation has also been proved effective for the disinfection of municipal wastewater, preventing bacterial regrowth [15]. The use of sunlight instead of UV lamps makes the photocatalytic ozonation treatment cheaper and, consequently, a promising approach to be scaled up at industrial level [16]. Another key factor in the development of solar photocatalytic ozonation for the removal of CECs from municipal wastewater is the effect of the background water matrix, which might compete with the CECs for catalytic sites and the oxidizing species. Thus, secondary effluents from MWWTPs, in addition to some CECs at $\mu g \cdot L^{-1}$-$ng \cdot L^{-1}$ levels, contain organic matter (EfOM),

inorganic ions (e.g., carbonate/bicarbonate and phosphate) and microorganisms, which can greatly affect the efficiency of an AOP to degrade the CECs. Therefore, the effect of these effluent components on the performance of solar photocatalytic ozonation should be studied.

Recent research on photocatalytic removal of CECs from water focuses primarily on the catalyst suitability. The most widely investigated catalyst so far has been nanosized TiO_2 because of its high catalytic activity, good stability and low toxicity. Among the various photocatalytic reactors, the slurry reactor with suspended TiO_2 nanoparticles is the most often used in the laboratory due to its high catalyst surface area, simple operation and low cost [17]. However, a main drawback of this approach is the impractical separation of TiO_2 particles. The use of TiO_2-containing magnetic nanoparticles and composites, which are easily separable from the treated water by applying an external magnetic field, have been proposed to overcome this problem [18]. In a previous work, an easily prepared TiO_2-magnetic carbon composite showed high catalytic efficiency in the solar photocatalytic ozonation of an aqueous solution of metoprolol [19]. As part of our ongoing research on solar photocatalytic ozonation, this paper addresses the use of a TiO_2-magnetic carbon photocatalyst to degrade a mixture of four CECs usually detected in municipal secondary effluents, namely metoprolol (MTP), ibuprofen (IBP), *N,N*-diethyl-*meta*-toluamide (DEET) and clofibric acid (CA). The effects of the background water matrix on the photocatalytic activity and the separability, stability and reusability of the catalyst have been investigated.

5.2. MATERIALS and METHODS

5.2.1. CECs SELECTION AND SECONDARY EFFLUENTS PREPARATION

The CECs selected for this study (MTP, IBP, DEET and CA) were purchased from Sigma-Aldrich with purity > 97% and used without further treatment. **Table 5.1** shows their chemical structures, common uses, occurrence in MWWTPs and reactivity with O_3 and $HO^{\bullet}$. It is interesting to point out that all these CECs are photo-resistant to sunlight and show rather similar reactivity towards $HO^{\bullet}$ ($k_{HO^{\bullet}} \sim 5 \times 10^9$ $M^{-1} \cdot s^{-1}$) but quite different towards molecular ozone (k_{O_3} ranged from 0.1 to 1.4×10^2 $M^{-1} \cdot s^{-1}$).

Table 5.1. Chemical structures, common uses, occurrence in secondary effluents and reactivity towards ozone and hydroxyl radical of the CECs selected in this work.

CEC	Chemical structure	Common uses	Occurrence	k_{O3} ($M^{-1}\cdot s^{-1}$)	Ref.	$k_{HO^{\bullet}} \times 10^{-9}$ ($M^{-1}\cdot s^{-1}$)	Ref.
Metoprolol (MTP)	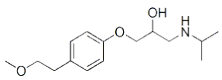	β-blocker	MWWTP influent (average conc. 1535 ng·L^{-1}), MWWTP effluent (average conc. 679 ng·L^{-1}) [20] and water rivers (maximum concentration 33 ng·L^{-1}) [21].	1400	[22]	6.8	[22]
Ibuprofen (IBP)	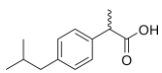	Anti-inflammatory	MWWTP effluent (max. conc. 2400 ng·L^{-1}), water rivers (max conc.185 ng·L^{-1}) [23] and groundwater (average conc. 1491 ng·L^{-1}) [24].	9.1	[25]	7.4	[25]
DEET	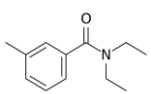	Insect repellent	MWWTP effluent (max. conc. 15800 ng·L^{-1} and average conc. 678 ng·L^{-1}) [26] and groundwater (average conc. 2251 ng·L^{-1}) [24].	0.126	[27]	4.95	[28]
Clofibric acid (CA)	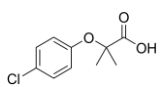	Herbicide	MWWTP influent (average conc. 251 ng·L^{-1}), MWWTP effluent (average conc. 131 ng·L^{-1}) [20], water rivers (max. conc. 104 ng·L^{-1}) [23] and groundwater (average conc. 1113 ng·L^{-1}) [24].	<20	[25]	4.7	[25]

A real secondary effluent (SE) taken from a MWWTP at Badajoz (Spain) was used in this investigation. SE samples were collected from the outlet of the activated sludge treatment of the plant and used within one day. Also, a synthetic secondary effluent (SSE) was typically prepared by dissolving the following components in distilled water: beef extract powder (3.6 $mg \cdot L^{-1}$), meat peptone (5.4 $mg \cdot L^{-1}$), humic acid (8.5 $mg \cdot L^{-1}$), tannic acid (8.4 $mg \cdot L^{-1}$), lignosulphonic acid sodium salt (4.9 $mg \cdot L^{-1}$), sodium lauryl sulphate (2.0 $mg \cdot L^{-1}$), arabic acid (9.4 $mg \cdot L^{-1}$), gum arabic from acacia tree (9.4 $mg \cdot L^{-1}$), magnesium sulphate 7-hydrate (2.9 $mg \cdot L^{-1}$), ammonium sulphate (14.2 $mg \cdot L^{-1}$), sodium carbonate (370 $mg \cdot L^{-1}$) and dibasic potassium phosphate (10 $mg \cdot L^{-1}$). Some variations in the composition of the SSE were also considered to provide effluents with different inorganic carbon (IC), P-PO_4^{3-} and DOC contents. The pH of the SEE was adjusted to about 7.5 with hydrochloric acid (37%, technical grade) or NaOH (1M) if needed. All the reagents used to prepare the SSE were provided either by Panreac or Sigma-Aldrich. The CECs were added to SE and SSE samples to reach a concentration of 2 $mg \cdot L^{-1}$ each. Some average characteristics of the secondary effluents after the addition of the CECs are given in **Table 5.2.**

Table 5.2. Some average characteristics of the secondary effluents after the addition of the CECs.

Parameter	SE	SSE (*)
pH	7.8	7.5
Conductivity ($\mu S \cdot cm^{-1}$)	712	870
Turbidity (NTU)	15	7
COD ($mg \cdot L^{-1}$)	78	89
BOD_5 ($mg \cdot L^{-1}$)	14	10
DOC ($mg \cdot L^{-1}$)	20	20
$SUVA_{254}$ ($L \cdot mg^{-1} \cdot m^{-1}$)	2.05	3.40
IC ($mg \cdot L^{-1}$)	43	42
PO_4-P ($mg \cdot L^{-1}$)	1.3	1.1
Total Nitrogen ($mg \cdot L^{-1}$)	2.4	3.3

(*) Some experiments were carried out with different DOC, IC and PO_4-P contents.

5.2.2. CATALYST PREPARATION AND CHARACTERIZATION

Samples of the TiO_2-magnetic carbon composite (TiFeC) used as catalyst in this study were synthesized following the three-step method described in a previous work [19]. First, magnetic carbon particles were obtained by impregnation of a commercial activated carbon (Darco 12-20, Sigma Aldrich) with an iron (III) nitrate ethanol solution followed by iron reduction with ethylene glycol and heat treatment at 550 ºC for 4 h. Second, a TiO_2 nanosol was produced from titanium (IV) butoxide (Sigma-

Aldrich Co, Spain). Finally, the magnetic carbon particles were dispersed in the TiO_2 nanosol under sonication for 1 h. The product was dried under vacuum at 80 ºC and washed thoroughly with distilled water to remove impurities.

Samples of fresh and used catalysts were analyzed for bulk composition and also characterized by nitrogen adsorption-desorption, X-ray diffraction (XRD), X-ray photoelectron spectroscopy (XPS), SQUID magnetometry and the pH at the point of zero charge (pH_{PZC}). Bulk catalyst composition was quantified analyzing Fe, C and TiO_2 contents. Iron was measured on digested samples using a Perkin Elmer ICP-MS-NexION 300D apparatus provided with external calibration curve of Fe. Carbon was analyzed with a LECO CHNS628 elemental analyzer. TiO_2 content was estimated from the residue after sample combustion in air at 900 ºC. Nitrogen adsorption-desorption isotherms at -196 ºC were obtained using an Autosorb iQ2-C apparatus (Quantachrome). Samples were outgassed at 150 ºC for 12 h under high vacuum (< 10^{-4} Pa) prior the analysis. Isotherm data were used to obtain BET surface area, external surface area and micropore volume (t-plot method). Also, the total pore volume was determined as the volume of nitrogen corresponding to the 0.96 P/P_0 point of the desorption branch of the isotherm, which corresponds to the filling of pores with diameter lower than 50 nm. XRD diffraction patters were recorded on a Bruker D8 Advance XRD diffractometer with a Cu Kα radiation (λ=0.1541 nm). Data were collected from 2θ=20º to 70º at a scan rate of 0.02 s^{-1}. The identification of the crystalline phases was performed by means of an EVA v.14 software (Bruker-AXS). The crystallite sizes were calculated using the Scherrer equation. XPS spectra were obtained on a Kα Thermo Scientific apparatus with an Al Kα (hν=1486.68 eV) X-ray source using a voltage of 12 kV under vacuum (2 x 10^{-7} mbar). Binding energies were calibrated relative to the C1s peak at 284.6 eV. The obtained spectra were curve-fitted using the software XPSpeak 4.1 taking into account parameter constraints on the binding energy and full width at half maximum. Atomic surface composition was obtained from XPS peak areas and Wagner atomic sensitivity factors [29]. Magnetic properties of samples were tested on a Quantum Design MPMS XL-7 Superconducting Quantum Interference Device (SQUID). The magnetic moment was measured as function of the applied magnetic field at room temperature. The pH_{PZC} was determined by mass titration [30]. Bulk composition, crystallite size, pH_{PZC} and some textural and magnetic properties of fresh and reused catalyst samples are summarized in **Table 5.3.**

Table 5.3. Some properties of the fresh and reused catalysts.

Parameter	Fresh catalyst	Reused catalyst(*)
Fe (wt.%)	7.5	7.3
C (wt.%)	18.5	18.2
TiO_2 (wt.%)	70.0	69.8
d_A (nm)	5.3	5.4
d_M (nm)	14.6	15.1
pH_{PZC}	5.7	4.9
S_{BET} ($m^2 \cdot g^{-1}$)	277	218
S_{ext} ($m^2 \cdot g^{-1}$)	36	50
V_{micro}($cm^3 \cdot g^{-1}$)	0.255	0.187
V_T ($cm^3 \cdot g^{-1}$)	0.326	0.292
M_S (emu·g^{-1})	4.2	4.1

d_A= anatase crystallite size; d_M= magnetite crystallite size
S_{BET} = BET surface area; S_{ext} = External surface area
V_{micro}= micropore volume; V_T= total pore volume (mesopore+micropore)
M_S= saturation magnetization
(*) Catalyst sample reused in a cycle experiment comprising eight consecutive solar photocatalytic ozonation runs.

5.2.3. PHOTOCATALYTIC ACTIVITY TESTS

Photocatalytic ozonation experiments were carried out in semi-batch mode using a cylindrical glass reactor equipped with a magnetic stirring system, a thermostatic water bath, a gas inlet, a gas outlet and a liquid sampling port. The reactor was placed in the chamber of a solar box (Suntest CPS, Atlas), which was equipped with a 1500 W air-cooled Xe lamp working at 550 $W \cdot m^{-2}$ and provided with quartz and glass cut-off filters. Spectral irradiance of the device is shown in **Figure 5.S1**. Ozone was provided by a laboratory ozone generator (Anseros Ozomat Com AD-02). In a typical test the reactor was first charged with 750 mL of the solution to be treated. The photocatalyst was then added to the reactor to achieve a catalyst loading of 0.4 $g \cdot L^{-1}$, which was found optimal for the purpose of the experiments (**Figure 5.S2**). The reactor content was kept in the darkness under agitation for 30 min to nearly reach adsorption equilibrium onto the catalyst (see **Figure 5.S3**). Then, the Xe-lamp was switched on and a continuous stream of an oxygen-ozone mixture (20 $L \cdot h^{-1}$ flow rate, 10 $mg \cdot L^{-1}$ ozone concentration) was continuously supplied to the reactor. The reactor was maintained agitated and the temperature was regulated at 35-40ºC throughout the experiment. At interval times, aqueous samples were withdrawn from the reactor to be analyzed for the concentration of CECs, DOC, UV-vis absorbance, short-chain organic acids (SCOAs), inorganic anions, dissolved ozone, hydrogen peroxide, Fe, Ti and pH. Once the time programmed for the experiment (typically 2 h) elapsed, the catalyst was magnetically recovered, washed with distilled water, dried and stored for reuse. In

addition to photocatalytic ozonation experiments (O_3/light/cat), adsorption (Ads), photolysis (light), dark ozonation (O_3), photo-ozonation (O_3/light), catalytic ozonation (O_3/cat) and photocatalytic oxidation (O_2/light/cat) runs were carried out for comparative purposes.

5.2.4. ANALYTICAL METHODS

Turbidity, pH and conductivity were measured with a Hanna HI 93414 turbidity-meter, a Crison GLP21+ pH-meter and a Crison 524 conductivity-meter, respectively. UV_{254nm} absorbance was determined with an Evolution 201 spectrophotometer (Thermo Spectronic) using 1 cm quartz cells. Chemical oxygen demand (COD), total nitrogen and total phosphorous measurements were conducted with Hach-Lange commercial kits (LCK 1414, LCK 138 and LCK 349) and Hach DR2800 spectrophotometer. Biological oxygen demand (BOD_5) tests were carried out on OxiTop® respirometers inoculated with activated sludge from a MWWTP. Dissolved organic carbon (DOC) and inorganic carbon (IC) were analyzed with a TOC-V_{CSH} Shimadzu analyzer. Anions from short-chain organic acids (SCOAs) (acetate, pyruvate, formate, succinate and malonate) and phosphate (PO_4-P) were analyzed by ion chromatography, using a Metrohm 881 Compact IC Pro model provided with an ion suppressor, a conductivity detector and a MetroSep A Supp 5 column (150 x 4 mm i.d.). Analyses were performed at 45 ºC with a constant flow rate of 0.7 mL·min^{-1} and a gradient program from 0.6 to 14.6 mM of Na_2CO_3 solution during 50 min with a previous 10-min equilibration step. Concentrations of CECs were analyzed with a Hitachi Elite LaChrom HPLC system provided with a diode array detector (Hitachi L-2455) and a Phenomenex Gemini C18 column (150 x 3 mm i.d.). Analyses were carried out at 0.6 mL·min^{-1} in gradient program using acidified ultrapure water (0.1% vol formic acid) (A) and acetonitrile (B) as follows: 15-minute ramp from 5% to 50% B, 10-minute keeping at 50% B, back to 5% B in 3 min and finally 12-minute equilibration at 5% B. CECs were detected at 220 nm, being their retention times: MTP (7.5 min), DEET (16.5 min), CA (18 min) and IBP (22 min). A 201 spectrophotometer (Thermo Spectronic) was used to analyze aqueous ozone by the indigo method [31] and hydrogen peroxide by the cobalt/bicarbonate method [32]. Ozone concentration in the gaseous streams entering and leaving the reactor was continuously monitored with ozone gas analyzers (Anseros Ozomat GM-OEM and GM-6000 Pro, respectively). Iron and titanium in solution were analyzed with a Perkin-Elmer NexION 300D ICP-MS apparatus.

5.3. RESULTS and DISCUSSION

5.3.1. COMPARISON OF AOPS: CECs AND DOC REMOVAL EFFICIENCIES

Firstly, a comparison of seven treatment processes (photolysis, adsorption, single ozonation, photo-ozonation, catalytic ozonation, photocatalytic oxidation and photocatalytic ozonation) to degrade the CECs in real and synthetic secondary effluents (SE and SSE, respectively) was carried out. It should be pointed out that initial DOC, IC and PO_4-P concentrations were practically the same in both effluents though the nature of the EfOM was different as revealed by $SUVA_{254}$ values (see **Table 5.2**). The evolution of the concentration of the CECs during the treatments was followed (**Figure 5.1**). Also, as the ultimate objective of a wastewater treatment technology is the conversion of specific contaminants and natural organic matter of EfOM to CO_2, the removal of DOC was examined (**Figure 5.2**). From these figures, it is apparent that, regardless of the type of secondary effluent, the CECs and EfOM were stable under solar irradiation in the absence of catalyst and ozone (photolysis runs) with less than 10% and 5% CECs and DOC removals, respectively. On the other hand, the uptakes of the CECs and DOC by the catalyst during adsorption runs were significant with removal percentages in the 25-35% range. Adsorption of the CECs from an aqueous solution (Milli-Q ultrapure water) onto the TiFeC catalyst led to about 40% DOC removal after 2 h (not shown), which suggests that the water matrices of the SE and SSE had a little negative effect on the CECs removal efficiency by adsorption onto TiFeC. Moreover, the catalyst showed distinct capacity for the adsorption of the four CECs, which obeyed the following order of affinity: MTP >>DEET > IBP > CA (**Figure 5.S3**). Thus, nearly 80% of MTP was adsorbed onto the catalyst while negligible uptake of CA was observed (< 5% removal). Adsorption of the selected CECs onto the catalyst is likely dominated by electrostatic attraction and repulsion forces. At pH 7.5-8.5 the catalyst surface is negatively charged ($pH>pH_{PZC}$). Accordingly, attraction forces take place between the catalyst surface and positive charged species in solution as it is the case of MTP (pK_a=9.5). In contrast, IBP (pK_a=5.3) and, specially, CA (pK_a=3.2) are repulsed by the catalyst as they are negatively charged in alkaline solution.

The CECs were not effectively degraded by solar photocatalytic oxidation in the absence of ozone (i.e., O_2/light/cat) since after 30 min of adsorption followed by 2 h of irradiation only 56% of the initial mass of the CECs in the SE was removed while this figure dropped to 45% in the SSE. Moreover, DOC removals from the SE and SSE were limited to about 45% and 35%, respectively.

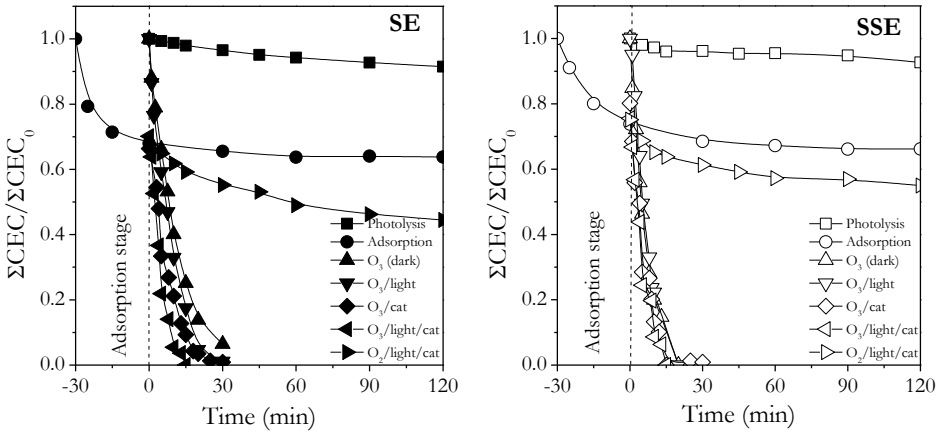

Figure 5.1. CECs removal from SE and SSE by different treatment processes. Experimental conditions: Volume=0.75 L; pH=7.5-8.5; T=35-40ºC; Simulated solar irradiance (if applied)=550 W·m^2; Catalyst dose (if applied)=0.4 g·L^{-1}; Ozone dosage (if applied)=3.3 mg·min^{-1}.

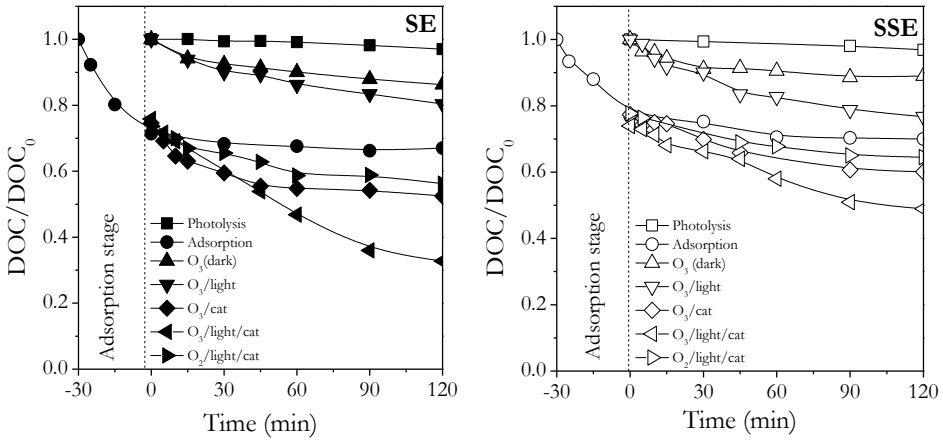

Figure 5.2. DOC removal from SE and SSE by different treatment processes. Experimental conditions: Volume=0.75 L; pH=7.5-8.5; T=35-40ºC; Simulated solar irradiance (if applied)=550 W·m^2; Catalyst dose (if applied)=0.4 g·L^{-1}; Ozone dosage (if applied)=3.3 mg·min^{-1}.

These results contrast with those obtained in Milli-Q ultrapure water where almost complete conversion of the CECs and more than 65% DOC removal were achieved in 2 h (not shown). Also, literature reports efficient removal of the selected ECs from aqueous solution (i.e., ultrapure water or deionized water) by TiO_2-mediated solar photocatalytic oxidation, being $HO^{\bullet}$ and $O_2^{\bullet-}$ the predominant oxidizing species [33–36]. Consequently, the presence of EfOM and/or some ions in the SE and SSE has a detrimental effect on the CECs photodegadation efficiency. This inhibitory effect could be a result of a number of effects including competitive adsorption of EfOM, the $HO^{\bullet}$ scavenging nature of some wastewater constituents and the modification of the catalyst-

pollutant interactions due to the adsorption of species and changes in the aqueous pH [37].

Regarding ozone-based processes, complete conversion of the CECs was achieved in less than 40 min though the removal was faster in the SSE than in the SE as it can be seen in **Figure 5.1**. In general, the removal rate of the CECs by any ozone process (i.e., O_3, O_3/light, O_3/cat and O_3/light/cat) followed the reactivity order MTP> IBP >CA>DEET, which is in agreement with the reported rate constants for O_3 and $HO^{\bullet}$ reactions (see **Table 5.1**). Both the TiFeC catalyst and simulated solar radiation accelerated the conversion of the CECs to some extent, more appreciably in the SE. These positive effects of the catalyst and solar radiation on the organic matter degradation rate can be better appreciated in **Figure 5.2**, where it can be observed that single ozonation led to barely 10-15% DOC removal while photo-ozonation (O_3/light), catalytic ozonation (O_3/cat) and photocatalytic ozonation (O_3/light/cat) brought about DOC removals of 20-25%, 40-50% and 55-70%, respectively. Such improvements in the oxidation efficiency are thought to be primarily due to the increase of $HO^{\bullet}$ exposure [9,19]. $HO^{\bullet}$ production may arise from the interplay of several reaction mechanisms, including (1) hydroxide ion-initiated decomposition of ozone, which was favored along the ozonation as the pH rose from 7.5 up to about 8.5; (2) decomposition of ozone by organic solutes of EfOM acting as initiators (i.e., the compound reacts directly with O_3 to form $O_2^{\bullet-}/HO_2^{\bullet}$ or $O_3^{\bullet-}/HO_3^{\bullet}$) and promoters (i.e., the compound reacts with $HO^{\bullet}$ to yield an intermediate species that propagates the radical chain eventually leading to the formation of $HO^{\bullet}$) [38]; (3) photolytic decomposition of ozone at wavelengths between 300 and 320 nm [9]; (4) catalytic transformation of ozone into $HO^{\bullet}$ on the surface of the catalyst, which contains three potential catalytic constituents: activated carbon, iron oxide and TiO_2 [19]; (5) classical TiO_2 photocatalytic oxidation mechanism, enhanced by the presence of ozone, which would act as electron acceptor on the TiO_2 surface avoiding electron-hole recombination to some extent; (6,7) transformation of hydrogen peroxide into $HO^{\bullet}$ by ozone (peroxone process) [39] and Fenton-like reactions over the catalyst [40]. Hydrogen peroxide arose mainly from reactions of the CECs and EfOM with ozone though it was also produced to some degree from the photolysis of ozone (**Figure 5.S4**). During single ozonation only pathways (1), (2) and (6) could develop while during photo-ozonation (O_3/light) the pathway (3) might significantly contribute to $HO^{\bullet}$ formation. In catalytic ozonation (O_3/cat) $HO^{\bullet}$ can be produced by steps (4) and (7) in addition to (1), (2) and (6). Finally, during photocatalytic ozonation (O_3/light/cat) all the seven steps might take place simultaneously to bring about high $HO^{\bullet}$ exposure in the reaction medium, which

can explain the great removal efficiencies of the CECs and DOC observed in **Figure 5.1** and **Figure 5.2**. Nevertheless, some ions and constituents of EfOM might act as free radical scavengers reducing the availability of HO• to react with CECs to some extent [41].

5.3.2. EFFECT OF SECONDARY EFFLUENT CONSTITUENTS ON THE PHOTOCATALYST ACTIVITY DURING OZONATION

Despite the fairly good catalytic activity exhibited by TiFeC in the solar photocatalytic ozonation of the secondary effluents, some ions and EfOM of the water matrix might impact on the catalytic activity to some degree. To explore this issue, the effect of the DOC level and concentration of prevalent anions (i.e., carbonate/bicarbonate and phosphates) on the efficiency of solar photocatalytic ozonation of SSE was studied. The comparison was done in terms of enhancement factors defined as the ratio between the pseudo first-order degradation rate constants of the photocatalytic and single ozonation processes (**Figure 5.S5, Table 5.S1**):

$$E_{CEC} = \frac{k_{app(O_3/light/cat),CEC}}{k_{app(O_3),CEC}} \quad (5.1)$$

$$E_{DOC} = \frac{k_{app(O_3/light/cat),DOC}}{k_{app(O_3),DOC}} \quad (5.2)$$

Table 5.4 shows the calculated enhancement factors for synthetic effluents of different composition. Besides, results of the overall DOC removal and the percentage of DOC transformed into SCOAs after 2 h of solar photocatalytic ozonation runs are summarized. SCOAs were identified as the main products of incomplete oxidation of the CECs and EfOM. In particular, oxalic acid was found prominent among the detected SCOAs (**Table 5.S2**).

From **Table 5.4** it can be observed that E_{CEC} was close to 1 in all the cases studied, suggesting that the catalytic effect of TiFeC was little as far as the removal of the CECs is concerned, regardless of the concentration of DOC, IC and PO_4-P in the SSE. However, the enhanced generation of ROS promoted by the catalyst was reflected in E_{DOC} values greater than 1 under all the conditions explored. As seen in **Table 5.4**, DOC exerted a dramatic effect on E_{DOC}. In fact, as shown in **Figure 5.3**, $k_{app(O3),DOC}$ increased while $k_{app(O3/light/cat),DOC}$ diminished with the increasing DOC concentration in the 10-30 mg·L^{-1} range. This suggests that EfOM contains HO• reacting species acting as initiators and promoters in addition to inhibitors, thus increasing the HO• exposure

in single ozonation runs [38]. However, increasing DOC concentration had a negative impact on the photo-catalytic generation of HO•, leading to a lower percentage of DOC mineralization and a larger accumulation of refractory SCOAs as shown in **Table 5.4**.

Table 5.4. Effect of some constituents of the SSE water matrix on the photocatalytic activity of TiFeC.

Effluent characteristics	E_{CEC}	E_{DOC}	% DOC removal	% SCOAs
DOC=10 mg·L^{-1} (IC=0; PO_4-P =0)	1.0	28.4	76.7	6.3
DOC=20 mg·L^{-1} (IC=0; PO_4-P =0)	1.1	13.6	64.8	10.1
DOC=30 mg·L^{-1} (IC=0; PO_4-P =0)	1.2	4.6	59.1	14.0
IC=20 mg·L^{-1} (PO_4-P=0; DOC=20 mg·L^{-1})	1.2	1.4	47.2	26.2
IC=40 mg·L^{-1} (PO_4-P=0; DOC=20 mg·L^{-1})	1.1	1.4	33.3	28.1
IC=60 mg·L^{-1} (PO_4-P=0; DOC=20 mg·L^{-1})	1.1	1.3	24.8	37.4
PO_4-P=0.8 mg·L^{-1} (IC=0; DOC=20 mg·L^{-1})	1.1	20.7	68.3	13.9
PO_4-P=3.5 mg·L^{-1} (IC=0; DOC=20 mg·L^{-1})	0.9	19.1	64.1	15.4

Carbonate alkalinity (i.e., IC) also brought about a loss of TiFeC catalytic activity as reflected by the decreasing E_{DOC} and % DOC removal as IC was varied from 0 to 60 mg·L^{-1}. The influence of carbonate/bicarbonate concentration in the ozonation of secondary effluents is not a straightforward matter and literature reports opposing effects [42]. On one hand, carbonate and bicarbonate scavenge HO• through reactions (5.3) and (5.4), where the carbonate radical ($CO_3^{\bullet-}$) is formed [43]:

$$HO^{\bullet} + CO_3^{2-} \xrightarrow{k=3.2\times10^{8}\ M^{-1}\cdot s^{-1}} OH^{-} + CO_3^{\bullet-} \quad (5.3)$$

$$HO^{\bullet} + HCO_3^{-} \xrightarrow{k=8.5\times10^{6}\ M^{-1}\cdot s^{-1}} H_2O + CO_3^{\bullet-} \quad (5.4)$$

On the other hand, carbonate and bicarbonate ions are responsible for the buffering capacity of secondary effluents (pH 7.5-8.5), which favors the decomposition of ozone into HO• initiated by OH^-. Moreover, $CO_3^{\bullet-}$, which under sunlight can also be generated by the reaction of carbonate/bicarbonate with excited triplet state of dissolved organic matter [44], is a strong selective oxidizing species that can react with organic compounds in water with rate constants in the range of 10^2-10^9 $M^{-1}\cdot s^{-1}$. As seen in **Figure 5.3**, IC had a positive effect on the removal rate of DOC by single ozonation. During IC-free ozonation runs, aqueous pH decreased from 7.5 to about 5 as a result of the formation of acidic products while in the presence of carbonate alkalinity (IC ≥ 20 mg·L^{-1}) the pH was kept at 7.5-8.5. This effect, in addition to $CO_3^{\bullet-}$ reactions, would explain the enhancement of DOC removal rate observed in the single

ozonation of SSE with the increasing IC. Contrarily, IC concentration exerted a negative effect on the DOC removal rate achieved by solar photocatalytic ozonation. Also, as a consequence of the decline of catalytic efficiency, an increasing accumulation of SCOAs in solution was observed. Such a loss of catalytic activity might be attributed to the interaction of carbonate/bicarbonate with the catalyst surface rather than to the quenching of HO• through bulk reactions (5.3) and (5.4) [45].

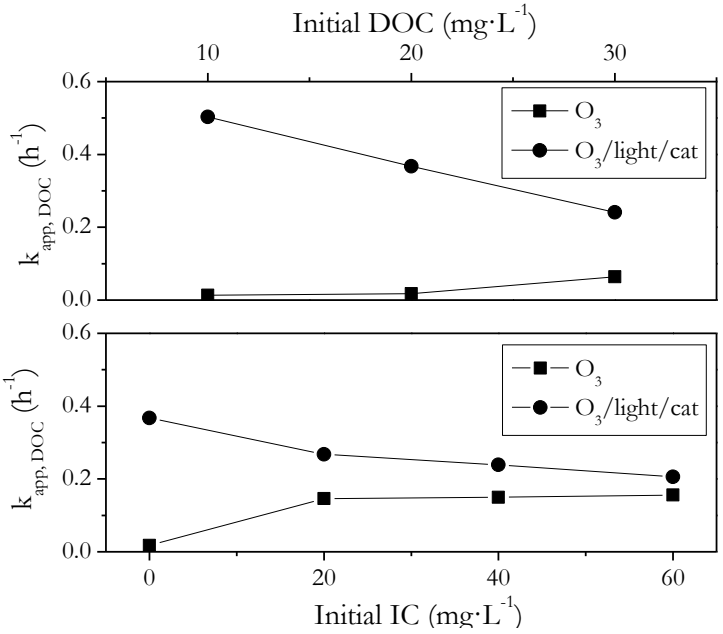

Figure 5.3. Effect of DOC and IC on the pseudo-first order rate constant for DOC removal during ozonation and solar photocatalytic ozonation of SSE. Experimental conditions: Volume=0.75 L; T=35-40ºC; Simulated solar irradiance (if applied)=550 W·m^2; Catalyst dose (if applied)=0.4 g·L^{-1}; Ozone dosage=3.3 mg·min^{-1}.

Contrarily to DOC and IC, PO_4-P, in the concentration range here studied, did not show any relevant effect on the DOC removal efficiency attained by solar photocatalytic ozonation. As a result, E_{DOC}, %DOC removal and %SCOAs did not change appreciably with PO_4-P concentration.

5.3.3. CATALYST SEPARABILITY, STABILITY AND REUSABILITY

The reusability of the TiFeC catalyst was tested in a cycle experiment comprising eight consecutive solar photocatalytic ozonation runs. After each run, the catalyst was easily separated by a magnet and reused in the next run without further treatment. **Figure 5.4** shows that the catalyst retained stable performance in terms of CECs and DOC removals. For the sake of comparison, results from O_3 and O_3/light experiments

are also shown. The catalytic effect is clearly deduced from the higher removal efficiencies achieved in O_3/light/cat experiments. The CECs were completely eliminated in less than 30 min in all the consecutive O_3/light/cat runs, being the percentage of removal after 20 min found as 82.47 ± 6.0% ($k_{app(O_3/light/cat),CEC}$=3.2 ± 1.1 h^{-1}) while the %DOC removal after 2 h was 56.6 ± 5.7% ($k_{app(O_3/light/cat),DOC}$=0.33 ± 0.06 h^{-1}). Accordingly, there was no evident loss of catalytic activity, which demonstrates good reusability of TiFeC.

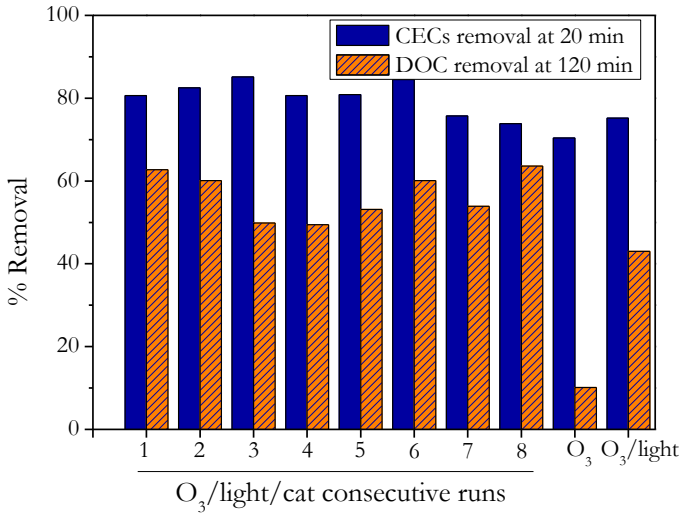

Figure 5.4. CECs and DOC removals from SSE in O_3, O_3/light and consecutive O_3/light/cat runs. Experimental conditions: Volume=0.75 L; T=35-40ºC; Simulated solar irradiance (if applied)=550 W·m²; Catalyst dose (if applied)=0.4 g·L^{-1}; Ozone dosage=3.3 mg·min^{-1}.

Samples of fresh (TiFeC) and reused catalysts (TiFeC-R) were characterized by a number of techniques and the results compared to examine the stability of the catalyst. As seen in **Table 5.2**, the bulk composition of the catalyst did not change appreciably with its use in the solar photocatalytic ozonation cycle experiment. In this sense, it must be pointed out that the mass of Fe and Ti leached out from the catalyst in each run as measured by ICP were negligible, amounting to less than 0.5% Fe and Ti mass losses after the eight runs.

Nitrogen adsorption-desorption isotherms of both fresh and reused catalyst samples could be classified as type I isotherms with H4 hysteresis loop (**Figure 5.S6**), typical of some complex materials containing both micropores and mesopores [46]. As shown in **Table 5.2**, S_{BET} and micropore volume of the catalyst significantly decreased while S_{ext} and mesopore volume increased upon its use in the reutilization experiment. This pore

widening effect is likely due to the ozone attack to the porous structure of the activated carbon [47] though micropore blockage due to adsorbed EfOM and/or reaction products might also take place. The interaction of ozone and the activated carbon also caused a moderate decrease of the pH_{PZC} of the catalyst as a consequence of the formation of acidic surface oxygen groups on the carbon structure [48]. These changes of textural and surface chemical characteristics of the catalyst might affect its adsorption behavior to some extent. To examine this effect, samples of catalyst were suspended in ultrapure water and subjected to ozone with doses equivalent to those applied in three-run and seven-run cycle experiments (i.e., TiFeC-R3 and TiFeC-R7, respectively). The catalyst samples were recovered magnetically and examined for their adsorption capacity for CECs and EfOM from SSE. **Figure 5.5** shows the adsorption performance of these samples and they are compared to that of a sample of catalyst through an eight-run solar photocatalytic ozonation cycle experiment. It can be observed that the adsorption of the CECs and DOC onto the catalyst decreased steadily with its repetitive use in the cycle experiment. It is interesting to note that the adsorption of catalyst samples after 3 and 7 runs in the cycle experiment were close to those of samples TiFeC-R3 and TiFeC-R7, respectively. Accordingly, the loss in the adsorption capacity can be attributed to changes induced in the catalyst by ozone rather than to organic matter remaining on the catalyst surface after each run.

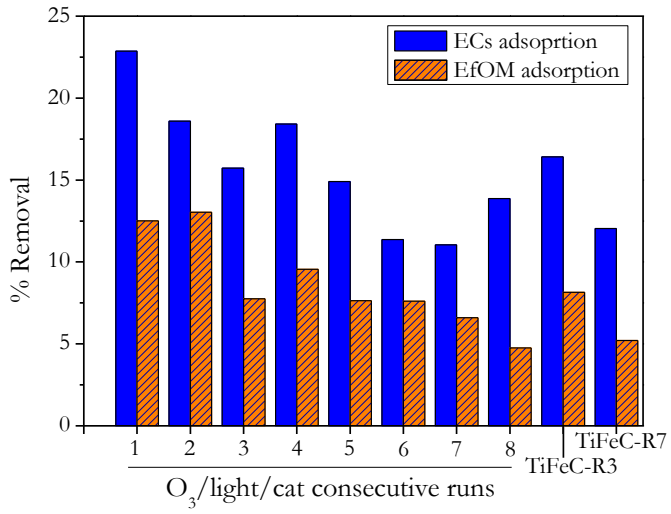

Figure 5.5. CECs and EfOM removals from SSE by adsorption onto catalyst samples. Experimental conditions: Volume=0.75 L; T=35-40ºC; Catalyst dose=0.4 $g \cdot L^{-1}$; Contact time=30 min.

Regarding the characterization results of the fresh and reused catalysts, both showed very similar XRD patterns, being anatase and magnetite/maghemite the crystalline phases identified (**Figure S7**). As shown in **Table 5.2**, the crystallite sizes did not vary appreciably upon solar photocatalytic ozonation.

Both the fresh and reused catalysts exhibited excellent magnetic separation performance owing to the presence of magnetite. In fact, both samples presented similar magnetic hysteresis loops (**Figure 5.S8**), which suggest superparamagnetic behavior of the particles. Accordingly, particle aggregation did not occur significantly and they could be easily separated by a magnet and re-dispersed in solution for reuse purpose. Saturation magnetization (M_S) remained almost the same for fresh and reused catalyst samples (**Table 5.2**).

The XPS survey spectra of samples of fresh and reused catalysts confirmed the presence of surface Ti, Fe, C and O in both materials (**Figure 5.S9**). The exposure of the catalyst to solar radiation and ozone led to small changes in the atomic composition of the surface as revealed by quantitative XPS peak analysis (**Table 5.S3**). **Figure 5.6** shows the high-resolution spectra of individual Ti2p, Fe2p, C1s and O1s spectral regions. The XPS spectra of Ti2p and Fe2p regions remained unchanged after the use of the catalyst in the photo-ozonation cycle experiment while noticeable changes were observed in the spectral regions of C1s and O1s. Ti2p spectra show two peaks at 465.0 eV and 459.3 eV (peak separation of 5.7 eV) corresponding to $Ti2p_{1/2}$ and $Ti2p_{3/2}$ core levels of Ti^{4+} in TiO_2 [49]. The obtained Fe2p spectra show two main asymmetric peaks at binding energies of 710.7-711.2V and 723.9-724.7 eV attributed to $Fe2p_{3/2}$ and $Fe2p_{1/2}$, respectively, which is consistent with the existence of magnetite nanoparticles [50]. The high resolution C1s and O1s spectra were deconvoluted in order to study the oxygen speciation in TiFeC and TiFeC-R samples. As seen, substantial changes in peak shapes and areas were observed after the reuse of the catalyst. **Table 5.5** summarizes the peak assignation and relative percentages of these functionalities as deduced from peak areas. Accordingly, the repetitive use of the catalyst brought about an increase in the concentration of acidic oxygen surface groups such as C–O in alcohol and ether structures, carbonyl, hydroxyl, carboxyl and ester groups. This finding is in complete agreement with the changes produced on activated carbon by aqueous ozone [48]. However, it should be pointed out that despite the changes in the surface properties of the activated carbon used as support for the TiFeC catalyst, this maintained its catalytic performance.

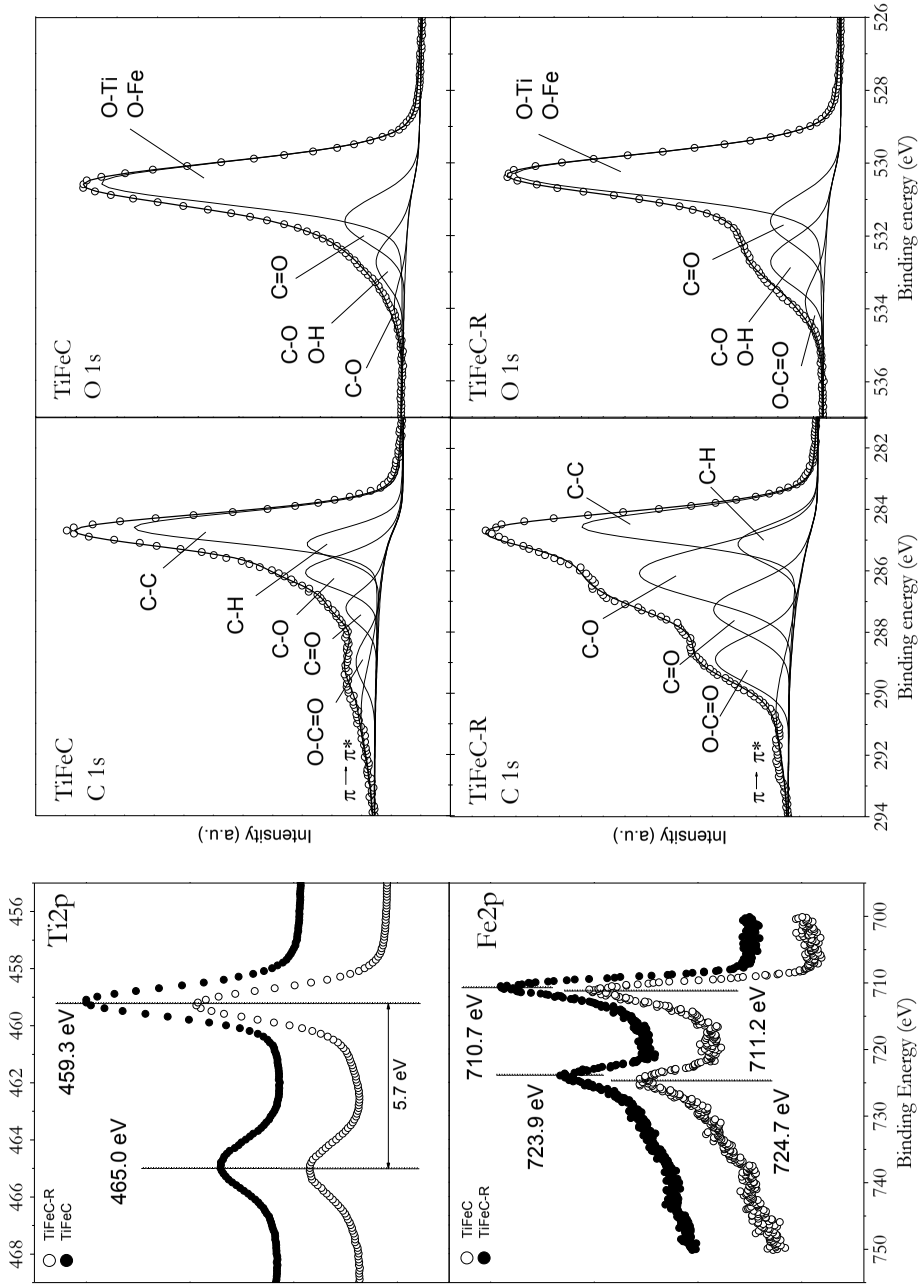

Figure 5.6. High-resolution XPS spectra of fresh and reused TiFeC samples.

Table 5.5. Surface oxygen groups and bond distributions obtained from deconvolution of C1s and O1s XPS regions of samples of fresh and reused catalyst.

Region	Peak position (eV)	Bond assignment	% Abundance	
			TiFeC	TiFeC-R
C1s	284.5	C–C	48.7	30.0
	285.1	C–H	15.2	9.3
	286.0	C–O	15.2	30.0
	287.2	C=O	6.9	13.8
	288.9	O–C=O	5.4	12.1
	290.5	π→π*	8.6	4.7
O1s	530.4	O–Ti and O–Fe	75.0	70.1
	531.6	C=O	15.4	12.9
	532.7	O–H and/or C–O	7.2	12.3
	533.9	O–C=O	2.5	4.7

5.4. CONCLUSIONS

Solar photocatalytic ozonation is a powerful AOP for the treatment of secondary effluents from MWWTPs. The magnetic TiO_2/Fe_3O_4/activated carbon prepared in this work was successfully applied as photocatalyst for the removal of four CECs and EfOM from two types of secondary effluents. The performance of solar photocatalytic ozonation was found superior to those of other alternative AOPs. Photocatalytic oxidation in the absence of ozone showed limited capacity for the removal of the CECs (<55%) and DOC (<45%) while ozone alone was able to completely remove the CECs but poor DOC removal was observed (<15%). In addition to complete conversion of the CECs, solar photocatalytic ozonation led to efficient organic matter mineralization (i.e., 55-70% removal) and lower accumulation of intermediates (e.g. SCOAs). The DOC and carbonate/bicarbonate content of the secondary effluent had negative impacts on the photocatalytic activity of due to interactions on the surface of the catalyst. However, PO_4-P in concentration up to 3.5 $mg \cdot L^{-1}$ did not affect significantly the photocatalytic performance. The catalyst could be easily separated from the reaction medium owing to its excellent magnetic properties and efficiently reused in eight consecutive solar photocatalytic ozonation runs. The repetitive use of the catalyst provoked a loss of surface area and microporosity and the fixation of acidic surface oxygen groups as a result of the interaction between ozone and the activated carbon used as catalyst support. However, bulk composition, crystalline phases and magnetic properties of the catalyst did not change appreciably with its use.

From the results of this study, it can be concluded that solar photocatalytic ozonation with a reusable magnetic catalyst might be a promising tertiary treatment method of secondary effluents from WWTPs.

REFERENCES

[1] N.H. Tran, M. Reinhard, K.Y.-H. Gin, "Occurrence and fate of emerging contaminants in municipal wastewater treatment plants from different geographical regions-a review" *Water Res.* 133 (**2018**) 182–207.

[2] Y. Luo, W. Guo, H.H. Ngo, L.D. Nghiem, F.I. Hai, J. Zhang, S. Liang, X.C. Wang, "A review on the occurrence of micropollutants in the aquatic environment and their fate and removal during wastewater treatment" *Sci. Total Environ.* 473–474 (**2014**) 619–641.

[3] O.M. Rodríguez-Narveez, J.M. Peralta-Hernández, A. Goonetilleke, E.R. Bandala, "Treatment technologies for emerging contaminants in water: A review" *Chem. Eng. J.* 323 (**2017**) 361–380.

[4] M.B. Ahmed, J.L. Zhou, H.H. Ngo, W. Guo, N.S. Thomaidis, J. Xu, "Progress in the biological and chemical treatment technologies for emerging contaminant removal from wastewater: A critical review" *J. Hazard. Mater.* 323 (**2017**) 274–298.

[5] M. Mehrjouei, S. Müller, D. Möller, "A review on photocatalytic ozonation used for the treatment of water and wastewater" *Chem. Eng. J.* 263 (**2015**) 209–219.

[6] R.R. Solís, O. Gimeno, F.J. Rivas, F.J. Beltrán, "Simulated solar driven photolytic ozonation for the oxidation of aqueous recalcitrant-to-ozone tritosulfuron. Transformation products and toxicity" *J. Environ. Manage.* 233 (**2019**) 513–522.

[7] A.C. Mecha, M.S. Onyango, A. Ochieng, C.J.S. Fourie, M.N.B. Momba, "Synergistic effect of UV-vis and solar photocatalytic ozonation on the degradation of phenol in municipal wastewater: A comparative study" *J. Catal.* 341 (**2016**) 116–125.

[8] E.M. Rodríguez, G. Fernández, P.M. Álvarez, F.J. Beltrán, "TiO_2 and Fe (III) photocatalytic ozonation processes of a mixture of emergent contaminants of water" *Water Res.* 46 (**2012**) 152–166.

[9] A.M. Chávez, A. Rey, F.J. Beltrán, P.M. Álvarez, "Solar photo-ozonation: A novel treatment method for the degradation of water pollutants" *J. Hazard.*

Mater. 317 (**2016**) 36–43.

[10] F.J. Beltrán, A. Rey, "Solar or UVA-Visible photocatalytic ozonation of water contaminants" *Molecules*. 22 (**2017**) 1177.

[11] G. Márquez, E.M. Rodríguez, M.I. Maldonado, P.M. Álvarez, "Integration of ozone and solar TiO_2-photocatalytic oxidation for the degradation of selected pharmaceutical compounds in water and wastewater" *Sep. Purif. Technol.* 136 (**2014**) 18–26.

[12] D.H. Quiñones, P.M. Álvarez, A. Rey, F.J. Beltrán, "Removal of emerging contaminants from municipal WWTP secondary effluents by solar photocatalytic ozonation. A pilot-scale study" *Sep. Purif. Technol.* 149 (**2015**) 132–139.

[13] D.H. Quiñones, A. Rey, P.M. Álvarez, F.J. Beltrán, G. Li Puma, "Boron doped TiO_2 catalysts for photocatalytic ozonation of aqueous mixtures of common pesticides: Diuron, o-phenylphenol, MCPA and terbuthylazine" *Appl. Catal. B Environ.* 178 (**2015**) 74–81.

[14] G. Liao, D. Zhu, C. Li, B. Lan, L. Li, "Degradation of oxalic acid and bisphenol A by photocatalytic ozonation with g-C3N4 nanosheet under simulated solar irradiation" *Ozone Sci. Eng.* 38 (**2016**) 312–317.

[15] A.C. Mecha, M.S. Onyango, A. Ochieng, M.N.B. Momba, "Evaluation of synergy and bacterial regrowth in photocatalytic ozonation disinfection of municipal wastewater" *Sci. Total Environ.* 601–602 (**2017**) 626–635.

[16] A.C. Mecha, M.S. Onyango, A. Ochieng, M.N.B. Momba, "Ultraviolet and solar photocatalytic ozonation of municipal wastewater: Catalyst reuse, energy requirements and toxicity assessment" *Chemosphere*. 186 (**2017**) 669–676.

[17] C. Byrne, G. Subramanian, S.C. Pillai, "Recent advances in photocatalysis for environmental applications" *J. Environ. Chem. Eng.* 6 (**2018**) 3531–3555.

[18] P.M. Álvarez, J. Jaramillo, F. López-Piñero, P.K. Plucinski, "Preparation and characterization of magnetic TiO_2 nanoparticles and their utilization for the degradation of emerging pollutants in water" *Appl. Catal. B Environ.* 100 (**2010**) 338–345.

[19] D.H. Quiñones, A. Rey, P.M. Álvarez, F.J. Beltrán, P.K. Plucinski, "Enhanced activity and reusability of TiO_2 loaded magnetic activated carbon for solar photocatalytic ozonation" *Appl. Catal. B Environ.* 144 (**2014**) 96–106.

[20] T. Deblonde, C. Cossu-Leguille, P. Hartemann, "Emerging pollutants in wastewater: A review of the literature" *Int. J. Hyg. Environ. Health*. 214 (**2011**) 442–448.

[21] B. Shao, D. Chen, J. Zhang, Y. Wu, C. Sun, "Determination of 76 pharmaceutical drugs by liquid chromatography-tandem mass spectrometry in slaughterhouse wastewater" *J. Chromatogr. A*. 1216 (**2009**) 8312–8318.

[22] F.J. Benítez, J.L. Acero, F.J. Real, G. Roldán, "Ozonation of pharmaceutical compounds: rate constants and elimination in various water matrices" *Chemosphere*. 77 (**2009**) 53–59.

[23] M. Gros, M. Petrović, A. Ginebreda, D. Barceló, "Removal of pharmaceuticals during wastewater treatment and environmental risk assessment using hazard indexes" *Environ. Int.* 36 (**2010**) 15–26.

[24] D.J. Lapworth, N. Baran, M.E. Stuart, R.S. Ward, "Emerging organic contaminants in groundwater: a review of sources, fate and occurrence" *Environ. Pollut.* 163 (**2012**) 287–303.

[25] M.M. Huber, A. Göbel, A. Joss, N. Hermann, D. Löffler, C.S. McArdell, A. Ried, H. Siegrist, T.A. Ternes, U. Von Gunten, A. Go, "Oxidation of pharmaceuticals during ozonation of municipal wastewater effluents: a pilot study" *Environ. Sci. Technol.* 39 (**2005**) 4290–4299.

[26] R. Loos, R. Carvalho, D.C. António, S. Comero, G. Locoro, S. Tavazzi, B. Paracchini, M. Ghiani, T. Lettieri, L. Blaha, B. Jarosova, S. Voorspoels, K. Servaes, P. Haglund, J. Fick, R.H. Lindberg, D. Schwesig, B.M. Gawlik, "EU-wide monitoring survey on emerging polar organic contaminants in wastewater treatment plant effluents" *Water Res.* 47 (**2013**) 6475–6487.

[27] F.J. Benítez, J.L. Acero, J.F. García-Reyes, F.J. Real, G. Roldán, E. Rodríguez, A. Molina-Díaz, "Determination of the reaction rate constants and decomposition mechanisms of ozone with two model emerging contaminants: DEET and nortriptyline" *Ind. Eng. Chem. Res.* 52 (**2013**) 17064–17073.

[28] W. Song, W.J. Cooper, B.M. Peake, S.P. Mezyk, M.G. Nickelsen, K.E. O'Shea, "Free-radical-induced oxidative and reductive degradation of N,N'-diethyl-m-toluamide (DEET): Kinetic studies and degradation pathway" *Water Res.* 43 (**2009**) 635–642.

[29] C.D. Wagner, L.E. Davis, M. V Zeller, J.A. Taylor, R.H. Raymond, L.H. Gale, "Empirical atomic sensitivity factors for quantitative analysis by electron spectroscopy for chemical analysis" *Surf. Interface Anal.* 3 (**1981**) 211–225.

[30] J.S. Noh, J.A. Schwarz, "Estimation of the point of zero charge of simple oxides by mass titration" *J. Colloid Interface Sci.* 130 (**1989**) 157–164.

[31] H. Bader, J. Hoigné, "Determination of ozone in water by the indigo method; a submitted standard method" *Ozone Sci. Eng.* 4 (**1982**) 169–176.

[32] W. Masschelein, M. Denis, R. Ledent, "Spectrophotometric determination of residual hydrogen peroxide" *Water Sew. Work.* 124 (**1977**) 69–72.

[33] M. Antonopoulou, A. Giannakas, Y. Deligiannakis, I. Konstantinou, "Kinetic and mechanistic investigation of photocatalytic degradation of the N,N-diethyl-m-toluamide" *Chem. Eng. J.* (**2013**).

[34] A. Achilleos, E. Hapeshi, N.P. Xekoukoulotakis, D. Mantzavinos, D. Fatta-Kassinos, "UV-A and solar photodegradation of ibuprofen and carbamazepine catalyzed by TiO2" *Sep. Sci. Technol.* 45 (**2010**) 1564–1570.

[35] T.E. Doll, F.H. Frimmel, "Kinetic study of photocatalytic degradation of carbamazepine, clofibric acid, iomeprol and iopromide assisted by different TiO_2 materials—determination of intermediates and reaction pathways" *Water Res.* 38 (**2004**) 955–964.

[36] R.P. Cavalcante, R.F. Dantas, B. Bayarri, O. González, J. Giménez, S. Esplugas, A. Machulek, "Photocatalytic mechanism of metoprolol oxidation by photocatalysts TiO_2 and TiO_2 doped with 5% B: Primary active species and intermediates" *Appl. Catal. B Environ.* 194 (**2016**) 111–122.

[37] J. Carbajo, M. Jiménez, S. Miralles, S. Malato, M. Faraldos, A. Bahamonde, "Study of application of titania catalysts on solar photocatalysis: Influence of type of pollutants and water matrices" *Chem. Eng. J.* 291 (**2016**) 64–73.

[38] M.-J. Cai, Y.-P. Lin, "Effects of effluent organic matter (EfOM) on the removal of emerging contaminants by ozonation" *Chemosphere*. 151 (**2016**) 332–338.

[39] J. Staehelin, J. Hoigné, "Decomposition of ozone in water: rate of initiation by hydroxide ions and hydrogen peroxide" *Environ. Sci. Technol.* 16 (**1982**) 676–681.

[40] K. Rusevova, F.-D. Kopinke, A. Georgi, "Nano-sized magnetic iron oxides as catalysts for heterogeneous Fenton-like reactions — Influence of Fe(II)/Fe(III) ratio on catalytic performance" *J. Hazard. Mater.* 241–242 (**2012**) 433–440.

[41] T. Nöthe, H. Fahlenkamp, C. von Sonntag, "Ozonation of wastewater: rate of ozone consumption and hydroxyl radical yield" *Environ. Sci. Technol.* 43 (**2009**) 5990–5995.

[42] A.R. Lado Ribeiro, N.F.F. Moreira, G. Li Puma, A.M.T. Silva, "Impact of water matrix on the removal of micropollutants by advanced oxidation technologies" *Chem. Eng. J.* 363 (**2019**) 155–173.

[43] G. V. Buxton, A.J. Elliot, "Rate constant for reaction of hydroxyl radicals with bicarbonate ions" *Int. J. Radiat. Appl. Instrumentation. Part C. Radiat. Phys. Chem.* 27 (**1986**) 241–243.

[44] S. Canónica, T. Kohn, M. Mac, F.J. Real, J. Wirz, U. von Gunten, "Photosensitizer method to determine rate constants for the reaction of carbonate radical with organic compounds" *Environ. Sci. Technol.* 39 (**2005**) 9182–9188.

[45] J.F. Budarz, A. Turolla, A.F. Piasecki, J.Y. Bottero, M. Antonelli, M.R. Wiesner, "Influence of Aqueous Inorganic Anions on the Reactivity of Nanoparticles in TiO2 photocatalysis" *Langmuir*. 33 (**2017**) 2770–2779.

[46] K.S.W. Sing, D.H. Everett, R.A.W. Haul, L. Moscou, R.A. Pierotti, J. Rouquérol, T. Siemieniwska, "Reporting physisorption data for gas/solid systems with special reference to the determination of surface area and porosity" *Pure Appl. Chem.* 57 (**1985**) 603–619.

[47] P.M. Álvarez, F.J. Beltrán, F.J. Masa, J.P. Pocostales, "A comparison between catalytic ozonation and activated carbon adsorption/ozone-regeneration processes for wastewater treatment" *Appl. Catal. B Environ.* 92 (**2009**) 393–400.

[48] P.M. Álvarez, J.F. García-Araya, F.J. Beltrán, I. Giráldez, J. Jaramillo, V. Gómez-Serrano, "The influence of various factors on aqueous ozone decomposition by granular activated carbons and the development of a mechanistic approach" *Carbon N. Y.* 44 (**2006**) 3102–3112.

[49] P. Fu, Y. Luan, X. Dai, "Preparation of activated carbon fibers supported TiO_2 photocatalyst and evaluation of its photocatalytic reactivity" *J. Mol. Catal. A Chem.* 221 (**2004**) 81–88.

[50] T. Radu, C. Iacovita, D. Benea, R. Turcu, "X-ray photoelectron spectroscopic characterization of iron oxide nanoparticles" *Appl. Surf. Sci.* 405 (**2017**) 337–343.

SUPPLEMENTARY MATERIAL

Solar photocatalytic ozonation of contaminants of emerging concern and effluent organic matter (EfOM) in secondary effluents by reusable magnetic catalyst

Ana M. Chávez, Diego H. Quiñones, Ana Rey, Fernando J. Beltrán, Pedro M. Álvarez*

Departamento de Ingeniería Química y Química Física, Instituto Universitario de Investigación del Agua, Cambio Climático y Sostenibilidad (IACYS), Universidad de Extremadura, Av. de Elvas s/n, 06006 Badajoz (Spain)

1. Spectral irradiance of the solar simulator device used in solar photodegradation experiments

Figure 5.S1 shows the spectral irradiance for the solar simulator Suntest CPS+ (Atlas Material Testing Technology LLC, USA) provided with quartz and glass cut-off filters as measured at the solution level with a UV-vis spectrometer (Black Comet C, Stellarwet, USA).

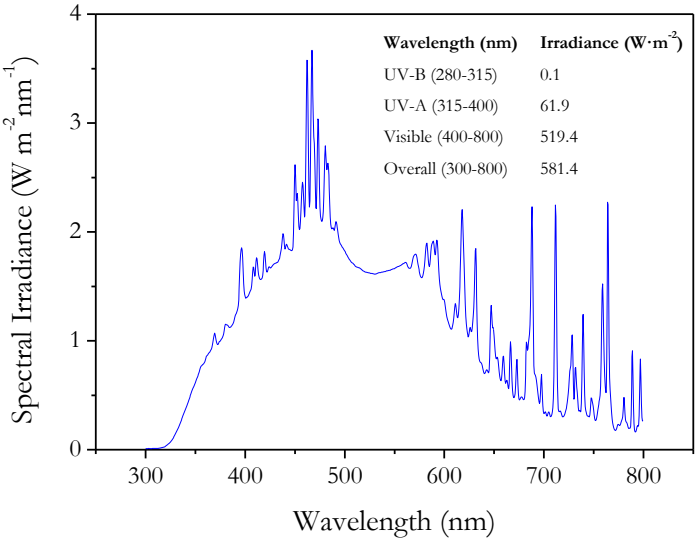

Figure 5.S1. Spectral irradiance for the solar simulator used in this work.

2. Effect of radiation and catalyst loading on solar photocatalytic ozonation of SSE.

Figure 5.S2 shows the evolution of the normalized DOC of a mixture of CECs (MTP, DEET, CA and IBP, 2 mg·L^{-1} each) in the synthetic secondary effluent (SSE) during the course of solar photocatalytic ozonation experiments carried out with different catalyst (TiFeC) loadings from 0.1 to 0.8 g·L^{-1}. It can be observed that ozonation in the absence of catalyst and light (single ozonation in the dark) led to less than 10% DOC removal over the course of the experiment while about 45% DOC removal was achieved by photo-ozonation in the absence of catalyst (O_3/light). The addition of the catalyst to the reaction medium led to further DOC removal due to adsorption onto the catalyst surface and photocatalytic ozonation of the CECs and other organic matter of the effluent (i.e., EfOM). However, it is worth noting that a catalyst loading of 0.4 g·L^{-1}

brought about the highest DOC removal within the ozonation stage. Therefore, this catalyst loading was considered optimal for the use in solar photocatalytic ozonation experiments in this work. A higher catalyst loading (e.g., 0.8 $g \cdot L^{-1}$) increased turbidity, which was detrimental to the distribution of the radiation flux in the reactor and, therefore, to the oxidation efficiency. At the optimal catalyst loading of 0.4 $g \cdot L^{-1}$ complete removal of the CECs was achieved in less than 30 min of ozonation.

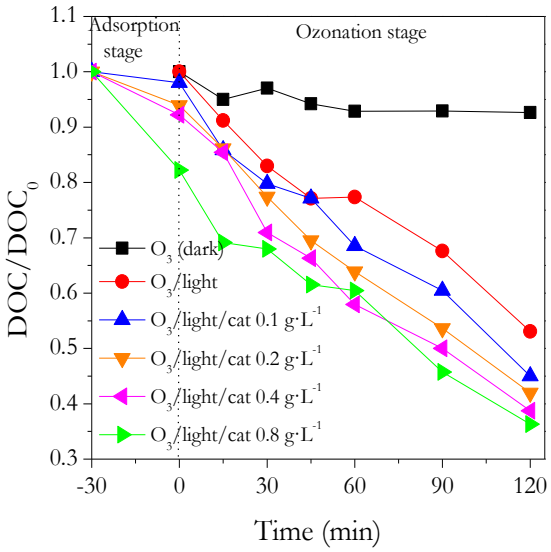

Figure 5.S2. Effect of the catalyst loading on the removal of DOC by solar photocatalytic ozonation. Experimental conditions: Secondary effluent=SSE; Volume=0.75 L; pH=7.5–8.5; T=35-40ºC; Simulated solar irradiance (if applied =550 $W \cdot m^2$; Ozone dosage=3.3 $mg \cdot min^{-1}$.

3. Adsorption of CECs and DOC of SSE onto the catalyst.

Figure 5.S3 shows the evolution of the concentration of the CECs and DOC during the course of a batch adsorption experiment carried out with SSE using a catalyst loading of 0.4 $g \cdot L^{-1}$. As it can be seen, the catalyst showed different adsorption capacity for the four CECs. Thus, CA was the most poorly adsorbed CEC, followed by IBP and DEET while MTP was the most effectively adsorbed. From the profiles shown in **Figure 5.S3**, it is apparent that adsorption equilibria were achieved within the 150 min of the experiment. Equilibrium adsorption capacities, calculated as mg of CEC adsorbed per gram of catalyst after 2 h of contact between the catalyst and the aqueous solution were 3.80, 1.69, 1.01 and 0.31 for MTP, DEET, IBP and CA, respectively. For DOC an equilibrium adsorption capacity of 14.3 $mg \cdot g^{-1}$ was calculated. Taking into account this figures and the carbon composition of each CEC an adsorption capacity of EfOM of 9.8 mg $C \cdot g^{-1}$ was estimated. At 30 min adsorption time, more than 75% of these adsorption capacities were reached.

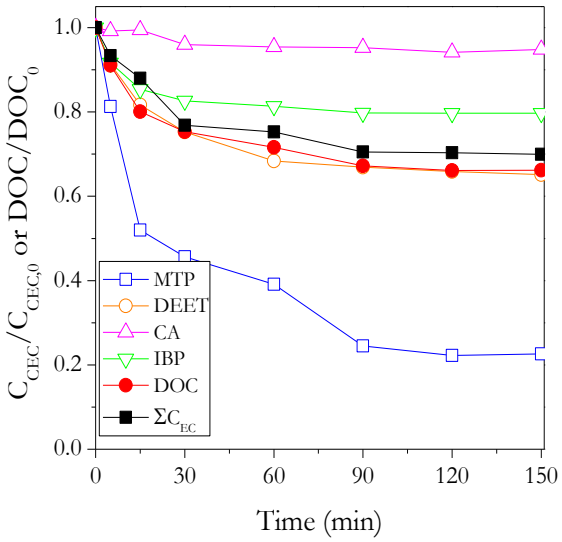

Figure 5.S3. Removal of the CECs and DOC by adsorption onto the catalyst used in this work. Experimental conditions: Secondary effluent=SSE; Volume=0.75 L; pH=7.5-8.5; T=35-40ºC; Catalyst loading=0.4 $g \cdot L^{-1}$.

4. Formation of hydrogen peroxide during ozonation.

Fig 5.S4 shows the evolution of the concentration of hydrogen peroxide during the course of some ozonation runs carried out in Milli-Q ultrapure water and SSE. It is observed that the net formation of hydrogen peroxide during single ozonation was favoured by the presence of CECs and EfOM. In addition the photolysis of ozone during photo-ozonation (O_3/light) also gave rise to the formation of hydrogen peroxide. No hydrogen peroxide was detected in solution during the irradiation of SSE in the absence of ozone (not shown). In the presence of the catalyst (O_3/light/cat) the accumulation of hydrogen peroxide in solution was low likely due to the decomposition of ozone and H_2O_2 over the catalyst.

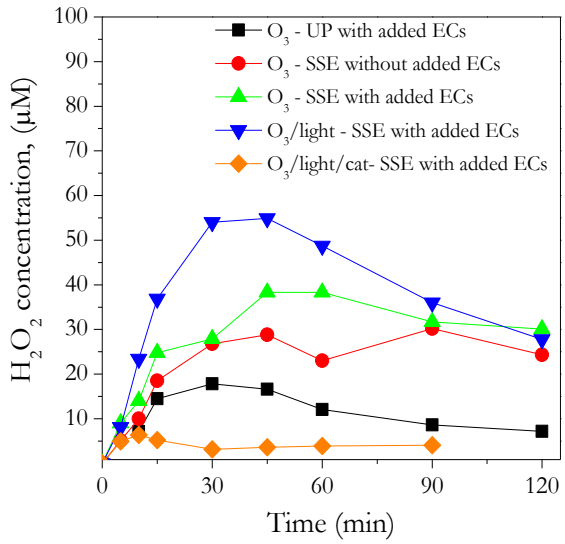

Figure 5.S4. Formation of hydrogen peroxide during some ozonation runs. Experimental conditions: Volume=0.75 L; pH=7.5-8.5; T=35-40ºC; Simulated solar irradiance (if applied)=550 W·m^2; Catalyst loading (if applied)=0.4 g·L^{-1}; Ozone dosage (if applied)=3.3 mg·min^{-1}.

5. Apparent first-order rate constant determination for the removal of CECs and DOC by single ozonation and solar photocatalytic ozonation.

The removal of the CECs, considered as a whole, and DOC by ozonation followed a pseudo first order kinetics as shown in **Figure 5.S5** and **Table 5.S1**.

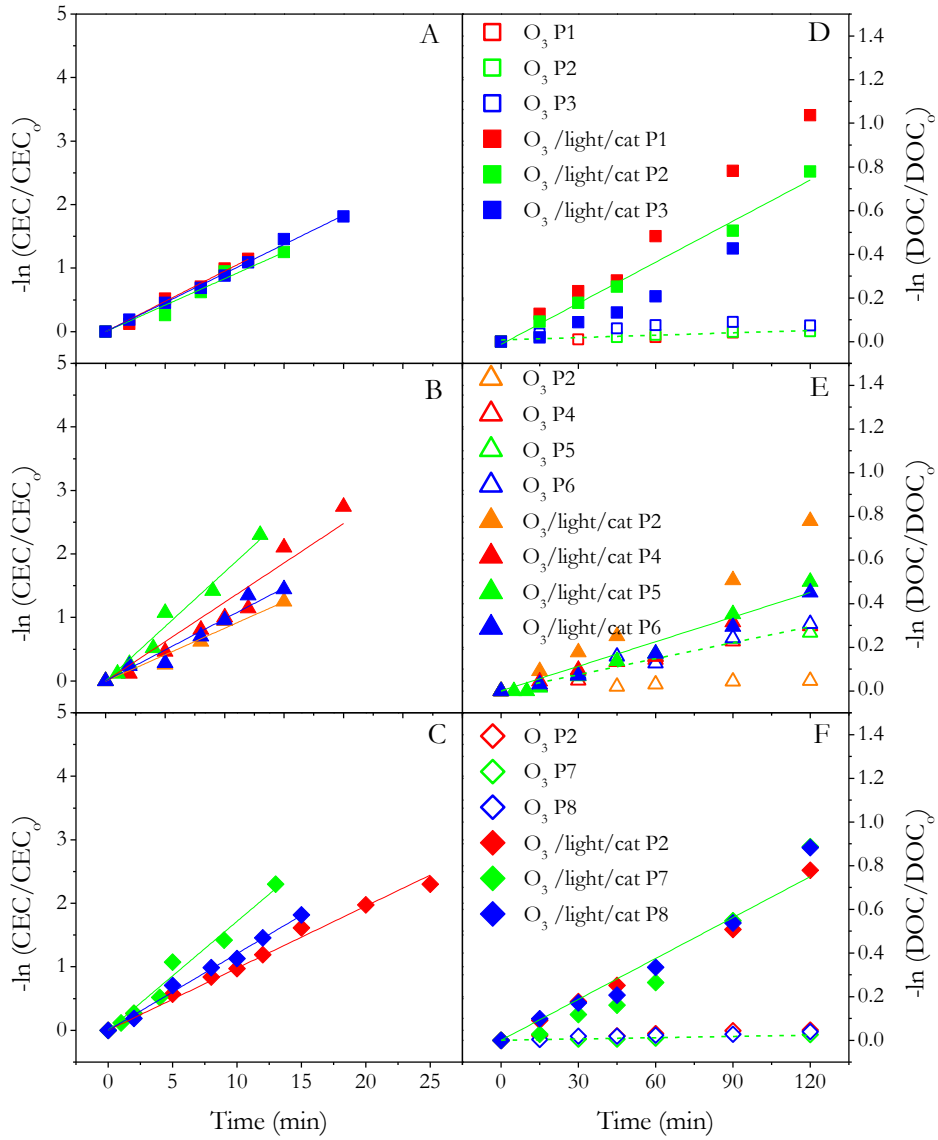

Figure 5.S5. Plots for the determination of pseudo-first order rate constant of the CECs removal (A-C), DOC removal (D-F) in solar photocatalytic ozonation and DOC removal (D-F) in single ozonation treatments of SSE. A, D: Effect of initial DOC (P1=10 mg DOC·L^{-1}; P2=20 mg DOC·L^{-1}; P3=30 mg DOC·L^{-1}); B, E: Effect of initial IC (P2=0 mg IC·L^{-1}; P4=20 mg IC·L^{-1}; P5=40 mg IC·L^{-1}; P6=60 mg IC·L^{-1}); C, F: Effect of PO_4-P concentration (P2=0 mg PO_4-P·L^{-1}; P7=0.8 mg PO_4-P·L^{-1}; P8=3.5 mg PO_4-P·L^{-1}).

Table 5.S1. Pseudo-first order rate constant of the CECs and DOC removal by ozonation and solar photocatalytic ozonation

Effluent characteristics	$k_{app(O_3),CECs}$ h^{-1}	R^2	$k_{app(O_3/light/cat),CECs}$ h^{-1}	R^2
DOC=10 mg·L^{-1} (IC=0; PO_4-P =0)	5.9	0.988	5.7	0.993
DOC=20 mg·L^{-1} (IC=0; PO_4-P =0)	4.6	0.931	5.0	0.962
DOC=30 mg·L^{-1} (IC=0; PO_4-P =0)	4.4	0.994	5.5	0.996
IC=20 mg·L^{-1} (PO_4-P=0; DOC=20 mg·L^{-1})	6.3	0.994	7.4	0.941
IC=40 mg·L^{-1} (PO_4-P=0; DOC=20 mg·L^{-1})	10.4	0.975	11.2	0.961
IC=60 mg·L^{-1} (PO_4-P=0; DOC=20 mg·L^{-1})	5.5	0.947	5.9	0.957
PO_4-P=0.8 mg·L^{-1} (IC=0; DOC=20 mg·L^{-1})	5.5	0.956	5.9	0.988
PO_4-P=3.5 mg·L^{-1} (IC=0; DOC=20 mg·L^{-1})	7.8	0.996	7.2	0.992
Effluent characteristics	$k_{app(O_3),DOC}$ h^{-1}	R^2	$k_{app(O_3/light/cat),DOC}$ h^{-1}	R^2
DOC=10 mg·L^{-1} (IC=0; PO_4-P =0)	0.025	0.977	0.503	0.986
DOC=20 mg·L^{-1} (IC=0; PO_4-P =0)	0.027	0.805	0.367	0.989
DOC=30 mg·L^{-1} (IC=0; PO_4-P =0)	0.052	0.905	0.241	0.915
IC=20 mg·L^{-1} (PO_4-P=0; DOC=20 mg·L^{-1})	0.146	0.987	0.208	0.970
IC=40 mg·L^{-1} (PO_4-P=0; DOC=20 mg·L^{-1})	0.145	0.969	0.202	0.932
IC=60 mg·L^{-1} (PO_4-P=0; DOC=20 mg·L^{-1})	0.156	0.961	0.206	0.970
PO_4-P=0.8 mg·L^{-1} (IC=0; DOC=20 mg·L^{-1})	0.012	0.940	0.241	0.986
PO_4-P=3.5 mg·L^{-1} (IC=0; DOC=20 mg·L^{-1})	0.020	0.925	0.390	0.857

6. CECs and EfOM transformation into SCOAs in single ozonation and solar photocatalytic ozonation.

The formation of short-chain organic acids (SCOAs) upon ozonation of the SSE was followed and the effect of some EfOM constituents was investigated. Among the detected anions from SCOAs, oxalate was prominent accounting in most cases for more than 50% of SCOAs concentration. Other formed SCOAs were acetate, pyruvate, formate, succinate and malonate. **Table 5.S2** shows the percentage of DOC converted into CO_2, SCOAs and oxalate after ozonation treatments of the SSE.

Table 5.S2. DOC conversion into CO_2,SCOAs and oxalate after 2 h of ozonation of the SSE.

Single ozonation			
Effluent characteristics	$\%DOC_{CO2}$	$\%DOC_{SCOAs}$	$\%DOC_{Oxalate}$
DOC=10 mg·L^{-1} (IC=0; PO_4-P =0)	0.5	14.9	7.4
DOC=20 mg·L^{-1} (IC=0; PO_4-P =0)	4.5	16.0	5.9
DOC=30 mg·L^{-1} (IC=0; PO_4-P =0)	8.6	19.9	10.7
IC=20 mg·L^{-1} (PO_4-P=0; DOC=20 mg·L^{-1})	34.8	34.4	22.5
IC=40 mg·L^{-1} (PO_4-P=0; DOC=20 mg·L^{-1})	30.6	33.2	22.1
IC=60 mg·L^{-1} (PO_4-P=0; DOC=20 mg·L^{-1})	26.9	27.9	16.4
PO_4-P=0.8 mg·L^{-1} (IC=0; DOC=20 mg·L^{-1})	3.3	16.6	8.6
PO_4-P=3.5 mg·L^{-1} (IC=0; DOC=20 mg·L^{-1})	15.7	18.1	10.2
Solar photocatalytic ozonation			
Effluent characteristics	$\%DOC_{CO2}$	$\%DOC_{SCOAs}$	$\%DOC_{Oxalate}$
DOC=10 mg·L^{-1} (IC=0; PO_4-P =0)	76.7	6.3	2.9
DOC=20 mg·L^{-1} (IC=0; PO_4-P =0)	64.8	10.1	3.1
DOC=30 mg·L^{-1} (IC=0; PO_4-P =0)	59.1	14.0	5.6
IC=20 mg·L^{-1} (PO_4-P=0; DOC=20 mg·L^{-1})	47.2	26.2	19.6
IC=40 mg·L^{-1} (PO_4-P=0; DOC=20 mg·L^{-1})	33.3	28.1	22.2
IC=60 mg·L^{-1} (PO_4-P=0; DOC=20 mg·L^{-1})	24.8	37.4	19.7
PO_4-P=0.8 mg·L^{-1} (IC=0; DOC=20 mg·L^{-1})	68.3	13.9	7.6
PO_4-P=3.5 mg·L^{-1} (IC=0; DOC=20 mg·L^{-1})	64.1	15.4	12.9

7. N_2 adsorption-desorption isotherms of samples of fresh and reused catalyst.

Figure 5.S6 shows the N_2 adsorption-desorption isotherms of samples of fresh catalyst (TiFeC) and that reused in an eight-run solar photocatalytic ozonation cycle experiment (TiFeC-R).

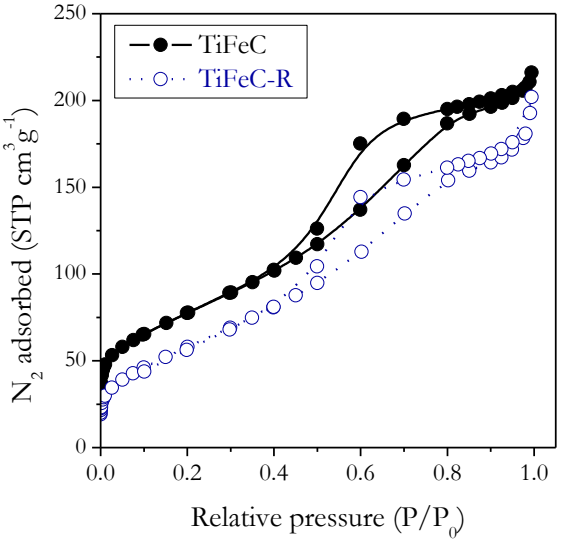

Figure 5.S6. Nitrogen adsorption-desorption isotherms at 77 K of fresh and reused TiFeC samples.

8. XRD patterns of samples of fresh and reused catalyst.

Figure 5.S7 shows the XRD patters of samples of fresh catalyst (TiFeC) and that reused in an eight-run solar photocatalytic ozonation cycle experiment (TiFeC-R). Anatase (A) and magnetite and/or maghemite (M) characteristics peaks can be distinguished.

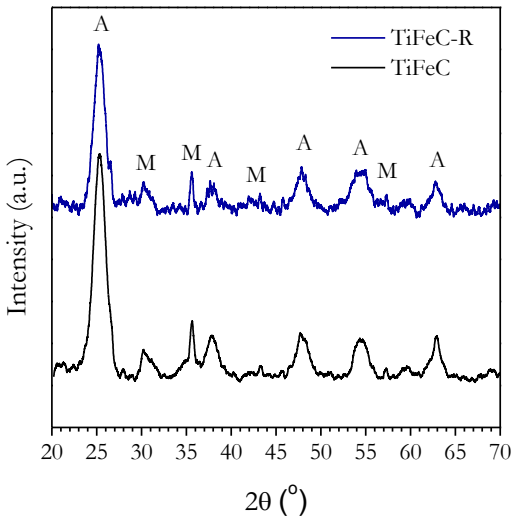

Figure 5.S7. XRD patterns of fresh and reused catalysts. Crystalline phases detected: anatase (A), magnetite/maghemite (M).

9. Magnetic (SQUID) hysteresis loops of samples of fresh and reused catalyst.

Figure 5.S8 shows the magnetization curves of samples of fresh catalyst(TiFeC) and that reused in an eight-run solar photocatalytic ozonation cycle experiment (TiFeC-R).

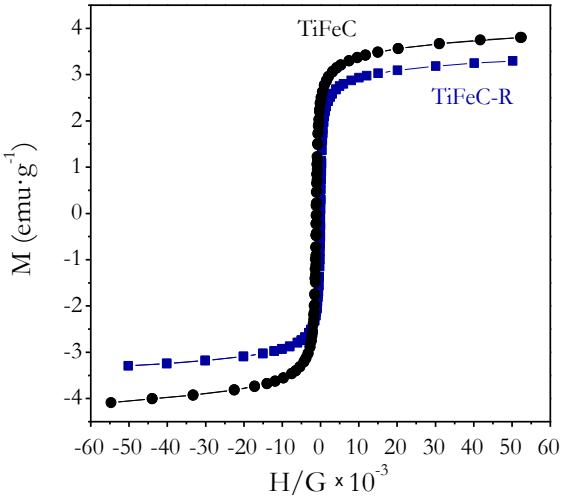

Figure 5.S8. Magnetic hysteresis loops of samples of fresh and reused catalysts obtained by a SQUID magnetometer

10. XPS full spectra of samples of fresh and reused catalyst.

Figure 5.S9 shows the XPS survey spectra of samples of the fresh catalyst (TiFeC) and that reused in an eight-run solar photocatalytic cycle experiment (TiFeC-R). **Table 5.S3** presents the relative atomic surface composition of both samples.

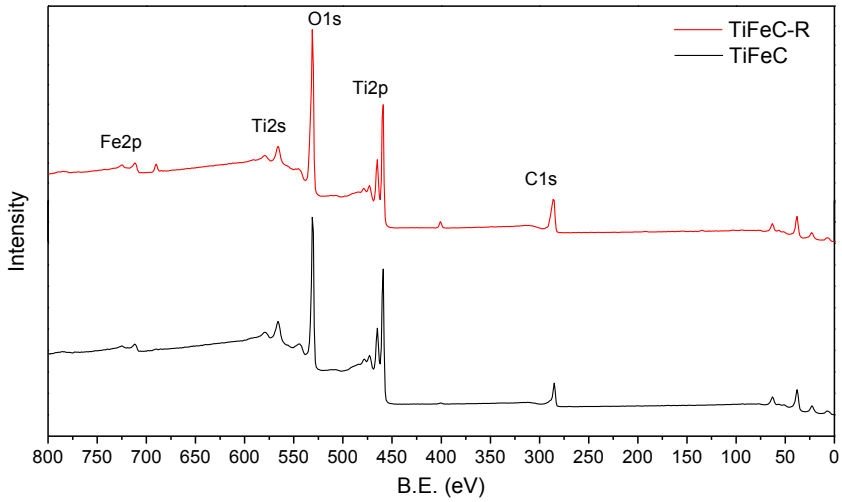

Figure 5.S9. XPS survey spectra of samples of fresh and reused catalysts. Main spectral regions identified.

Table 5.S3 Atomic surface composition of fresh and reused TiFeC samples

Sample	Ti (%)	Fe (%)	C (%)	O (%)
TiFeC	19.7	2.0	25.0	53.2
TiFeC-R	13.9	2.0	35.1	48.9

PAPER 3

TREATMENT OF HIGHLY POLLUTED INDUSTRIAL WASTEWATER BY MEANS OF SEQUENTIAL AEROBIC BIOLOGICAL OXIDATION-OZONE BASED AOPs

Chemical Engineering Journal 361 (2019) 89-98

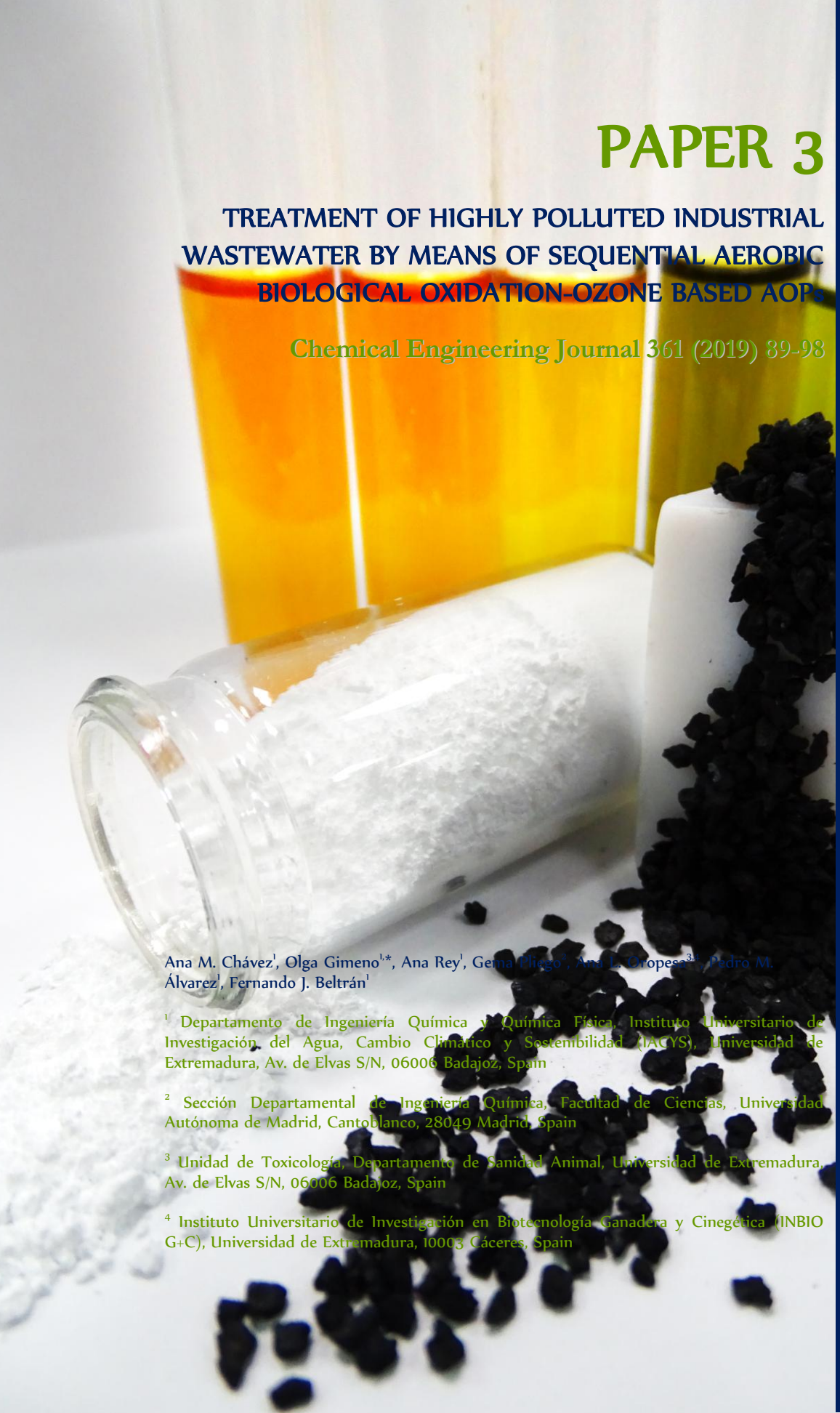

Ana M. Chávez[1], Olga Gimeno[1,*], Ana Rey[1], Gema Pliego[2], Ana L. Oropesa[3,4], Pedro M. Álvarez[1], Fernando J. Beltrán[1]

[1] Departamento de Ingeniería Química y Química Física, Instituto Universitario de Investigación del Agua, Cambio Climático y Sostenibilidad (IACYS), Universidad de Extremadura, Av. de Elvas S/N, 06006 Badajoz, Spain

[2] Sección Departamental de Ingeniería Química, Facultad de Ciencias, Universidad Autónoma de Madrid, Cantoblanco, 28049 Madrid, Spain

[3] Unidad de Toxicología, Departamento de Sanidad Animal, Universidad de Extremadura, Av. de Elvas S/N, 06006 Badajoz, Spain

[4] Instituto Universitario de Investigación en Biotecnología Ganadera y Cinegética (INBIO G+C), Universidad de Extremadura, 10003 Cáceres, Spain

CHAPTER VI

GRAPHICAL ABSTRACT

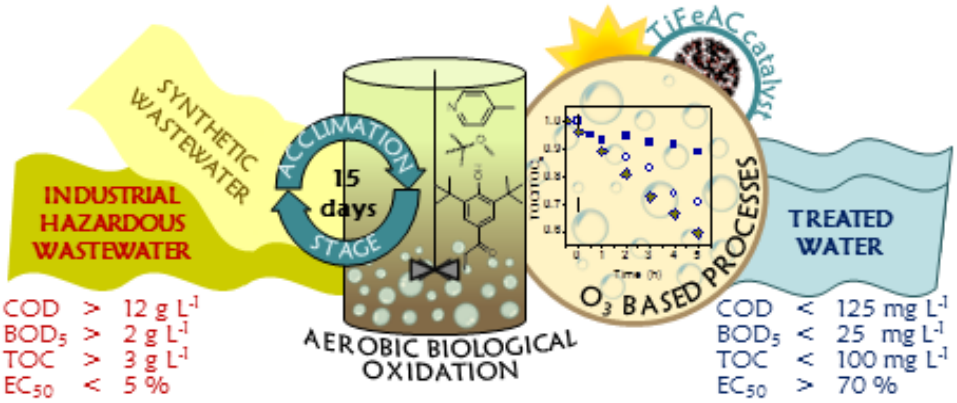

ABSTRACT

The feasibility of the treatment of a complex industrial wastewater by aerobic biodegradation in a sequential batch reactor (SBR) followed by ozone-based advanced oxidation processes (AOPs) has been studied. The industrial wastewater had high organic load (TOC > 3 g·L^{-1}, COD > 12 g·L^{-1}, BOD_5 > 2 g·L^{-1}) including some toxic/harmful compounds and high concentration of metal and other inorganic species. SBR treatment of the industrial wastewater diluted with urban wastewater (dilution 1:5) was successful after complete acclimation of the mixed culture (i.e., > 50% COD and TOC removals). Nevertheless, the SBR effluent was still not acceptable to be disposed into the environment (c.a. COD 850 mg·L^{-1}) so ozonation, solar photo-ozonation and solar photocatalytic ozonation processes were investigated as further polishing treatments. Thus, the sequential combination of aerobic biodegradation and solar photocatalytic ozonation with a TiO_2-based catalyst led to an effluent suitable for discharge into the aquatic environment according to environmental regulations (COD < 125 mg·L^{-1}, BOD_5 < 25 mg·L^{-1}).

Keywords: hazardous wastewater, integrated treatment, biological oxidation, photocatalytic ozonation.

6.1. INTRODUCTION

The management and treatment of wastewater from residential and industrial sites is critical to the sustainability of water systems. It is crucial for treatment technologies to be as much efficient and economically feasible as possible [1]. To deal with hazardous effluents from some industrial sites, such as chemical multi-product plants with diverse toxic wastewater streams, incineration is sometimes considered as the preferred option [2]. However, depending on the characteristics of the effluent, toxic compounds (e.g, VOCs) and metal salts can be formed or remain during incineration. Moreover, incineration facilities are expensive to build, operate, and maintain, being a major cost factor the equipment needed for the flue gas treatment in order to obey international and local environmental regulations [3]. The high cost associated with incineration urges waste generators to seek other alternatives. In this sense, biological treatment is nowadays considered to be among the best available technologies for wastewater treatment because of its low operating and capital costs. However, conventional biological treatments have long retention times and usually fail to degrade high strength wastewater or bio-refractory compounds [4]. Nevertheless, through acclimation, microbes can undergo physiological transformations, resulting in the selection and multiplication of specialized microorganisms capable to resist toxic substances and/or biodegrade recalcitrant substrates. [5]. Even so, biological treatment of hazardous wastewaters usually does not lead to an effluent suitable for permitted direct reuse or discharge and for this reason, it has to be assisted by other non-biological technologies, such as advanced oxidation processes (AOPs). Although, the latter imply higher cost, coupling AOPs with biological treatment could be proposed as an appropriate treatment strategy for recalcitrant wastewaters. For instance, Blanco et al. (2012) could efficiently treat a textile wastewater by combining an aerobic SBR with a Fenton process, reducing the influent COD by about 85% [6].

Among AOPs, heterogeneous photocatalytic oxidation has been proven as an efficient one for the degradation of complex organic contaminants [7,8]. However, it is usually a slow process when treating high organic load wastewaters [9]. To enhance the oxidation rate, proper selection of the photocatalyst and the use of oxidizing species as electron scavengers and co-oxidants are key factors. Thus, photocatalytic oxidation in the presence of TiO_2-based catalysts and ozone (i.e. photocatalytic ozonation) has been demonstrated beneficial in some instances [10]. However, to the best of our knowledge, no work on the integrated biological – photocatalytic ozonation treatment of industrial wastewater is reported in the literature.

In this work, the feasibility of a SBR - solar photocatalytic ozonation treatment at lab scale for the purification of a hazardous wastewater from petrochemical and cosmetic products manufacture has been examined. For the photocatalytic ozonation stage, a magnetically separable TiO_2 photocatalyst (TiO_2 loaded magnetic activated carbon, TiFeAC) with high activity under solar illumination has been used owing to its success in degrading some wastewater contaminants [11,12].

6.2. MATERIALS and METHODS

6.2.1. INDUSTRIAL WASTEWATER

Raw industrial wastewater (RIW) was provided by a waste management company located in Catalonia (Spain). RIW consisted of a mixture of effluents from some industrial sites (manufacture of petrochemical and cosmetic products), making a high-polluted wastewater. RIW was filtered through filter paper (Filter Lab 1305) to remove suspended solids to some extent. Preliminary experiments showed that the filtered industrial wastewater (FIW) was quite recalcitrant to biodegradation, likely because of the presence of metals and organic compounds, which might be toxic to microbes hence inhibiting biodegradation. To assist biodegradation, a synthetic urban wastewater (SUW) was used as growth substrate. SUW was prepared using peptone and glucose as carbon sources [13]. Average chemical oxygen demand (COD), total organic carbon (TOC) and inorganic carbon (IC) of SUW were 172, 85 and 47 $mg \cdot L^{-1}$, respectively. RIW was mixed with SUW (dilution 1:5) to prepare a mixed industrial wastewater (MIW), which was further subjected to biodegradation and chemical oxidation experiments. RIW, FIW and MIW were fully characterized. Analyses were carried out in duplicate with mean values shown in **Table 6.1** and **Table 6.2.**

6.2.2. BIOLOGICAL TREATMENT

The activated sludge sample used as starting inoculum was collected from a municipal wastewater treatment plant (MWWTP) at Badajoz city (Spain), which treats domestic wastewater using a conventional activated sludge process. At the time of sampling, the process at the MWWTP operated at average food to microbial ratio (F/M) of 0.5, hydraulic retention time (HRT) of 7 h and mixed liquor volatile suspended solids concentration (MLVSS) of 1.5 $g \cdot L^{-1}$.

Table 6.1. Main characteristics of RIW, FIW and MIW effluents.

Parameter	RIW	FIW	MIW
pH	5.8	5.8	6.6
Turbidity (NTU)	520	420	105
Conductivity ($mS \cdot cm^{-1}$)	4.44	4.36	1.28
PO_4^{3-} ($mg \cdot L^{-1}$)	2.6	2.5	99
SO_4^{2-} ($mg \cdot L^{-1}$)	585	576	124
Cl^- ($mg \cdot L^{-1}$)	1385	1379	307
Bicarbonate alkalinity (g $CaCO_3 \cdot L^{-1}$)	3.56	3.36	0.92
TSS ($mg \cdot L^{-1}$)	674	518	< 0.15
VSS ($mg \cdot L^{-1}$)	650	508	< 0.15
COD ($g \cdot L^{-1}$)	12.2	10.3	2.1
BOD_5 ($g \cdot L^{-1}$)	2.2	1.8	0.8
TOC ($g \cdot L^{-1}$)	3.4	3.3	0.6
TPC ($mg \cdot L^{-1}$)	113	113	23
A_{465nm}	0.58	0.58	0.36
UV_{254nm} (samples diluted 1:10)	1.24	1.19	0.25
BOD_5/COD	0.18	0.17	0.38

Table 6.2. Metal composition of industrial wastewater before and after treatments.

Element	FIW	MIW	BW	O_3	O_3-solar	O_3-solar-cat
Mg ($mg \cdot L^{-1}$)	23.6	6.8	7.3	6.8	7.9	6.9
K ($mg \cdot L^{-1}$)	61.1	52.8	69.4	61.1	74.5	69.7
Ca ($mg \cdot L^{-1}$)	277.0	57.4	32.7	51.6	67.7	40.6
Fe (mgL^{-1})	1.42	0.45	< 0.05	< 0.05	< 0.05	< 0.05
Zn ($mg \cdot L^{-1}$)	2.77	0.54	0.21	0.24	0.23	0.11
Mo ($mg \cdot L^{-1}$)	2.56	0.51	0.69	0.56	0.59	0.43
Ni ($mg \cdot L^{-1}$)	0.20	0.04	0.04	0.04	0.04	0.02
Cr ($\mu g \cdot L^{-1}$)	75.3	15.1	7.1	9.1	15.7	4.8
Cu ($\mu g \cdot L^{-1}$)	6.6	1.3	1.4	1.7	1.9	1.6
As ($\mu g \cdot L^{-1}$)	9.4	1.9	2.1	1.8	2.0	1.0
Se ($\mu g \cdot L^{-1}$)	11.3	2.3	1.9	1.6	1.8	2.2
Cd ($\mu g \cdot L^{-1}$)	0.48	0.01	n.d.	n.d.	n.d.	n.d.
Sn ($\mu g \cdot L^{-1}$)	1.41	0.28	0.30	0.31	0.28	0.33.
Hg ($\mu g \cdot L^{-1}$)	0.42	0.08	n.d.	n.d.	n.d.	n.d.
Pb ($\mu g \cdot L^{-1}$)	1.33	0.27	n.d.	n.d.	n.d.	n.d.

n.d.: not detected (below quantification limit)

After collection, the activated sludge sample was allowed to settle at room temperature for 30 min and the supernatant was removed. The bio-solids were transferred to a cylindrical aerobic batch bioreactor (2 L working volume) provided with temperature, pH and dissolved oxygen concentration (DO) controllers. The bioreactor was operated as a sequencing batch reactor (SBR) with fill, reaction, settle, extract and idle stages [14]. The duration of these phases was 15 min, 22 h, 30 min, 15 min and 60 min, respectively. The system was initially fed with SUW only for two days in order to develop a healthy culture. Then, MIW was stepwise introduced in the feed. Thus, at the beginning of each cycle the bioreactor was fed with an increasing volume of MIW and filled up to 2 L with SUW. At the reaction stage, temperature, pH and DO were controlled at 20±2 ºC, 7.5±1.0 and 3.5±0.5 $mg \cdot L^{-1}$, respectively. Oxygen uptake rate (OUR), sludge volume index (SVI) and effluent COD were measured and used as indicators of the acclimation process success. Once a healthy culture was adapted to MIW, biodegradation experiments were carried out for 10 h (8 h reaction time) to follow COD, TOC, UV_{254nm} and chroma depletion with time.

Thus, at time intervals, samples were withdrawn from the reactor for analysis. MLSS and MLVSS were measured in the mixed liquor while COD, TOC and UV_{254nm} and A_{465nm} absorbance were analyzed in samples after solids removal by centrifugation (3000 rpm, Alresa centrifuge, 200 W) and subsequent filtration through 0.45 μm PVDF membrane filters. Some short-chain carboxylic acids and ecotoxicity towards *Daphnia magna* and *Vibrio fischeri* were also analyzed on MIW before and after the biological treatment. Biodegradation experiments were carried out five times to check for reproducibility.

6.2.3. ADVANCED OXIDATION PROCESSES

The biologically treated wastewater (BW) was further subjected to different ozone-based AOPs such as single ozonation (O_3), solar photo-ozonation (O_3-solar) and photocatalytic ozonation (O_3-solar-cat). All the experiments were carried out in semi-batch mode, using a cylindrical glass-made reactor equipped with a magnetic stirring system, a gas diffuser and gas inlet, gas outlet and liquid sampling ports. A solar box (Suntest CPS, Atlas) provided with a 1500 W Xe lamp and cut-off filters (λ=300-800 nm, irradiation intensity 550 $W \cdot m^2$) was also used. In a typical experiment, the reactor was first loaded with 0.65 L of BW and the required amount of catalyst. If required (experiments in the dark), the reactor was covered with aluminum foil. The reactor content was stirred for 30 min before switching on the Xe lamp and providing a continuous flow (20 $L \cdot h^{-1}$) of an ozone-oxygen mixture (20-30 mg $O_3 \cdot L^{-1}$) to the

reactor. Ozone concentration at the entrance and exit of the reactor was monitored with in-line ozone analyzers (Anseros GM-6000-OEM and GM-6000-PRO models, respectively) Also, ozone concentration in solution was measured. Experiments lasted for 5-8 h and samples were withdrawn from the reactor at time intervals to follow parameters such as pH, UV_{254nm}, COD, TOC and phenolic compounds (TPC). The temperature was kept constant at 37 ± 2 ºC throughout the experiments.

To assess the impact of carbonate/bicarbonate ions present in BW on the efficiency of ozone-based AOPs, some experiments were carried out in the absence of inorganic carbon. To do so, prior to the degradation experiments carbonate/bicarbonate ions were removed from BW by means of air-striping at acid pH. Once the striping operation was completed, the pH was restored to circumneutral conditions.

The catalyst used in photocatalytic experiments was a TiO_2-Fe_3O_4-activated carbon magnetic composite (TiFeAC) synthesized according to a previous work [12]. Briefly, magnetic carbon particles were obtained by impregnation of a commercial activated carbon (Darco 12-20, Sigma Aldrich) with an iron (III) nitrate ethanol solution followed by iron reduction with ethylene glycol and heat treatment at 550 ºC for 4 h. Separately, a TiO_2 nanosol was produced from titanium (IV) butoxide. Finally, the magnetic carbon particles were dispersed in the TiO_2 nanosol under sonication for 1 h. The product was dried under vacuum at 80 ºC and washed thoroughly with distilled water to remove impurities.

TiFeAC composition was 70.0 wt.% TiO_2 (anatase), 7.5 wt.% Fe (mainly as magnetite and maghemite) and 18.5 wt.% activated carbon. This catalyst was chosen because of its good photocatalytic activity, stability and facile recovery using a magnet [12]. To assess the stability and reusability of the photocatalyst, a series of five consecutive solar ozonation experiments was carried out. After each run, the catalyst was separated with a magnet, washed with distilled water and used to treat fresh BW in the next run. TOC, COD, UV_{254nm} and Fe were measured in the treated effluent.

6.2.4. ANALYTICAL METHODS

Turbidity, pH, conductivity and dissolved oxygen were measured with a Hanna HI 93414 turbidity-meter, a Crison GLP21+ pH-meter, a 524 Crison conductivity-meter and an HQd Portable Hach meter, respectively. Total and volatile suspended solids (TSS and VSS, respectively) were measured gravimetrically following standard methods [15]. Short-chain organic acids (oxalic, acetic, pyruvic, formic, succinic and maleic

acids) and some inorganic anions (phosphate, sulfate and chloride) were analyzed with by suppressed ion chromatography (Metrohm 881 Compact IC Pro model provided with an ion suppressor and a conductivity detector). A MetroSep A Supp 5 column (150 mm length, 4 mm diameter) at 45 ºC was used as stationary phase. Aqueous Na_2CO_3 was used as mobile phase with a gradient program from 0.6 to 14.6 mM in 50 min and 10 min equilibration time with a flow rate set at 0.7 mL·min^{-1}. Some metallic elements were analyzed by ICP-MS with a Perkin Elmer NexION 300 apparatus. COD was measured following the standard dichromate reflux method using Hach-Lange commercial cuvettes and a Hach DR2800 spectrophotometer [16]. BOD_5 tests were carried out on 500 mL OxiTop® respirometers inoculated with BOD microbe capsules (Cole-Parmer). TOC and IC were determined with a TOC-VCSH Shimadzu analyzer. UV_{254nm} and A_{465nm} were determined with an Evolution 201 spectrophotometer from ThermoSpectronic using 1 cm quartz cells. Total phenolic content (TPC) was evaluated by the Folin-Ciocalteau colorimetric method and expressed as phenol equivalents [17]. Identification of the main organic compounds present in wastewater was carried out by means of gas chromatography-mass spectrometry (GC-MS) system operated in electron impact ionization mode to identify the organic compounds present in the effluents. The analyses were performed by gas chromatography/ion trap mass spectrometry (CP-3800/Saturn 2200, Varian, equipped with an automatic injector CP-8200/SPME, solid-phase microextraction). A 30 m length and 0.25 i.d. capillary column (Factor Four VF-5 ms) was used. The carrier gas (helium) flow rate was set at 1 mL·min^{-1}. The SPME was carried out with a fiber cartridge (poly(dimethylsiloxane) red), using adsorption and desorption times of 30 min and 5 min, respectively. The sample injection was conducted at 220 ºC. The temperature program used was as follows: (i) 40 ºC for 5 min; (ii) then from 40 ºC to final temperature of 300 ºC at 15 ºC min^{-1}; (iii) held at 300 ºC for 2 min. Compounds identification was assessed using the National Institute of Standards and Technology (NIST) database.

Acute toxicity tests with *Vibrio fischeri* and *Daphnia magna* were also carried out. Luminotox® was used to evaluate the bioluminiscence inhibition of the marine bacteria *V. fischeri* (LUMIStox 300, Dr. Lange) following ISO 11348-2 [18]. *D magna* acute toxicity tests were conducted with the cladoceran *D. magna Straus* following the protocols given by Baird et al. [19] and the OECD Guideline 202 [20]. Toxicity results were expressed in terms of EC_{50} (%) and TU (Equitox·m^{-3}). Values of EC_{50} (%) were calculated using LUMISsoft 4 Software™ for *V. fischeri* tests and using a probit analysis (MINITAB STATISTICAL Software™ 2000) for *D. magna* tests.

Mixed liquor samples from the bioreactor were tested for mixed liquor suspended solids (MLSS), mixed liquor volatile suspended solids (MLVSS), sludge volume index (SVI) and specific oxygen uptake rate (sOUR) following standard methods [15]. In ozone-based AOPs, ozone concentration in aqueous solution was determined by the indigo method [21].

6.3. RESULTS and DISCUSSION

6.3.1. INDUSTRIAL WASTEWATER CHARACTERIZATION

Table 6.1 shows the main characteristics of RIW, FIW and MIW samples used in this study. RIW could be classified as a high strength effluent in terms of organic load because of high COD, TOC and TPC values. In addition, the industrial wastewater showed high conductivity mainly as a result of the presence of large concentrations of bicarbonate, sulfate, chloride and phosphate ions. The biodegradability index, measured as the BOD_5/COD ratio, was below 0.2, which means poor biodegradability [22]. Upon filtration of RIW, suspended solids and particulate organic matter were removed to some extent (note lower values of TSS, COD, BOD_5 and TOC in FIW in comparison to RIW). However, the concentrations of inorganic ions, conductivity and the biodegradability index remained practically unchanged from RIW to FIW. Low biodegradability of the wastewater can be attributed to the high organic load and conductivity and to the presence of toxic organic compounds such as TPC. In addition, noticeably concentration of some heavy metals was measured in FIW as shown in **Table 6.2,** being Fe (1.42 $mg \cdot L^{-1}$), Zn (2.77 $mg \cdot L^{-1}$) and Mo (2.56 $mg \cdot L^{-1}$) the most abundant ones. UV_{254nm} absorbance of RIW and FIW was high (note that UV_{254nm} values shown in **Table 6.1** were obtained on diluted samples), which suggests the presence of aromatic and unsaturated compounds in the effluent. In fact, some of these chemical structures were detected in FIW by GC-MS as shown in **Figure 6.1** and **Table 6.3**. The GC-MS results reveal the presence of a number of compounds related to petrochemical and cosmetic industries, which agrees with the origin of the industrial wastewater. **Table 6.4** shows results of the industrial wastewater toxicity towards *Vibrio fisheri* and *Daphnia magna*. Low EC_{50} and high TU values were obtained in the toxicity tests of FIW, indicating that the industrial wastewater was toxic to both organisms [23].

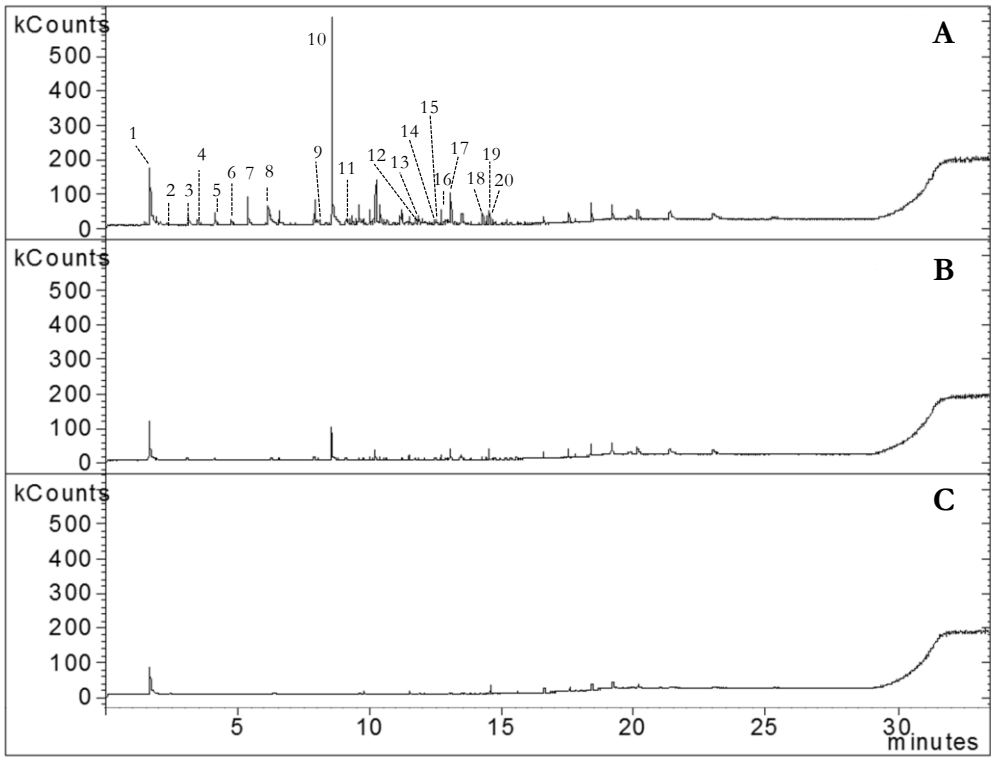

Figure 6.1. Total ion current GC-MS chromatogram of (A) FIW, (B) MIW and (C) BW. For main wastewater characteristics see **Table 6.1.**

The characteristics of the industrial wastewater discussed above make it unsuitable for discharge into the municipal sewer system. According to local regulations, maximum allowable limits for discharge are established at: COD=1.5 $g \cdot L^{-1}$; BOD_5 =0.75 $g \cdot L^{-1}$; TPC=2 $mg \cdot L^{-1}$; Toxicity towards *V. fischeri* = 25 Equitox m^{-3} among other parameters [24]. Therefore, wastewater treatment is compulsory. Given the low wastewater biodegradability, direct biological treatment cannot be recommended. As a cost-effective treatment, dilution of the industrial wastewater with urban wastewater and a sequential biological - chemical treatment of the combined effluent is proposed in this work in order to fulfil environmental regulations for discharge into the aquatic environment (pH= 6-8; COD=125 $mg \cdot L^{-1}$; BOD_5 =25 $mg \cdot L^{-1}$). Dilution of FIW with SUW resulted in the MIW effluent, which presented reduced COD, BOD_5 and TPC values compared to FIW but still did not meet limit regulations for discharge. However, it is important to note that the biodegradability index (i.e., BOD_5/COD) of the industrial wastewater increased as a result of dilution (see **Table 6.1**), thus making the MIW effluent more amenable to biological degradation. Also MIW toxicity towards *V. fisheri* and *D. magna* was much lower than that of FIW (see **Table 6.2**).

Table 6.3. Main organic compounds in FIW, MIW and BW as detected by GC-MS

Compound	t_R (min)	Molecular formula	Molecular weight	Tentative structure	Samples[1]
Peak 1 C-88	1.674	$C_5H_{12}O$	88	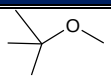 Methyl-tert-butyl-ether	FIW MIW BW
Peak 2 C-102	2.313	$C_5H_{10}O_2$	102	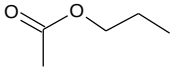 Propyl acetate	FIW MIW
Peak 3 C-116	3.115	$C_6H_{12}O_2$	116	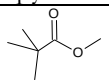 Methyl trimethylacetate	FIW MIW
Peak 4 C-100	3.487	$C_6H_{12}O$	100	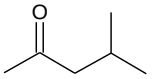 Methyl isobutyl ketone	FIW MIW
Peak 5 C-92	4.117	C_7H_8	92	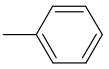 Toluene	FIW MIW
Peak 6 C-160	4.743	$C_9H_{20}O_2$	160	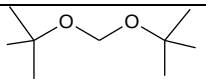 2,2'-[Methylenebis(oxy)]bis(2-methylpropane)	FIW MIW
Peak 7 C-116	5.385	$C_6H_{12}O_2$	116	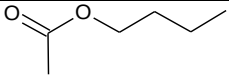 Butyl acetate	FIW MIW
Peak 8 C-93	6.154	C_6H_7N	93	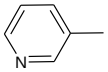 m-methyl pyridine (3-picoline, 3 Mepy)	FIW MIW BW
Peak 9 C-120	8.101	C_9H_{12}	120	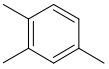 1,2,4-trimethylbenzene	FIW MIW
Peak 10 C-130	8.577	$C_8H_{18}O$	130	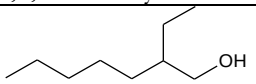 2-ethyl-1-hexanol	FIW MIW
Peak 11 C-152	9.091	$C_8H_8O_3$	152	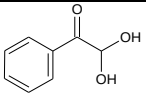 2,2-dihydroxy-1-phenyl-ethanone	FIW MIW

[1] Samples where compounds were detected; [2] Isomers

Table 6.3.(continued) Main organic compounds in FIW, MIW and BW as detected by GC-MS

Compound	t_R (min)	Molecular formula	Molecular weight	Tentative structure	Samples[1]
Peak 12 C-142	11.711	$C_{11}H_{10}$	142	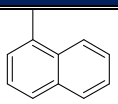 1-methyl-naphthalene	FIW MIW
Peak 13 C-142	11.874	$C_{11}H_{10}$	142	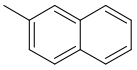 2-methyl-naphthalene	FIW MIW
Peak 14 C-166	12.440	$C_9H_{10}O_3$	166	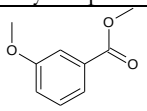 3-methoxy-benzoic acid methyl ester	FIW MIW
Peak 15 C-154	12.526	$C_{12}H_{10}$	154	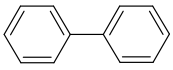 Biphenyl	FIW MIW
Peak 16 C-170	12.717	$C_{12}H_{10}O$	170	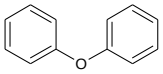 Diphenyl oxide	FIW MIW
Peak 17 C-192	13.051	$C_{12}H_{16}O_2$	192	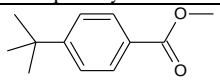 Methyl 4-tert-butylbenzoate	FIW MIW
Peak 18[2] C-226	14.278	$C_{16}H_{18}O$	226	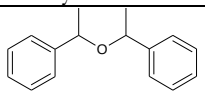 Bis(1-phenylethyl) ether	FIW MIW
Peak 19 [2] C-226	14.450	$C_{16}H_{18}O$	226	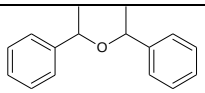 Bis(1-phenylethyl) ether	FIW MIW
Peak20 C-262	14.543	$C_{17}H_{26}O_2$	262	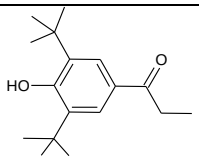 2,6-Bis(1,1-imethylethyl) -4-(1-oxopropyl)phenol	FIW MIW BW

[1] Samples where compounds were detected; [2] Isomers

Table 6.4. Ecotoxicity results of *Vibrio fischeri* inhibition and *Daphnia magna* immobilization tests after exposure to treated and untreated industrial wastewater.

Sample	*Vibrio fischeri*		*Daphnia magna*	
	EC_{50} (%)	TU (Equitox·m^{-3})	EC_{50} (%)	TU (Equitox·m^{-3})
FIW	1.6	62.5	3.2	31.2
MIW	9.2	10.9	25.3	3.9
BW	17.1	5.8	24.0	4.2
O_3	13.3	7.5	46.9	2.1
O_3-solar	5.7	17.5	50.5	2.0
O_3-solar-cat	12.3	8.1	74.8	1.3

6.3.2. AEROBIC BIOLOGICAL OXIDATION

A. Activated sludge acclimation

A 15-day acclimation phase was considered in this study to adapt the microorganisms of the activated sludge sample taken from the MWWTP to the industrial wastewater. MIW was included in the feed of the activated sludge system from day 1 and its concentration was gradually increased throughout the acclimation phase, revealing the acclimation of microorganisms to the industrial effluent. The MLVSS/MLSS ratio was kept within a typical range of 0.75-0.9 [25]. **Table 6.5** shows the SBR process performance during the acclimation stage. As seen in **Table 6.5,** when the activated sludge sample was brought into contact with FIW for the first time (day 1) an abrupt decrease in the aerobic biological activity was observed as sOUR fell from 52 to 9.1 mg O_2 g VSS^{-1}·h^{-1}. OUR inhibition was calculated as follows [26]:

$$\text{Inhibition}=\left(1-\frac{\text{sOUR}}{\text{sOUR}_b}\right)\times 100 \qquad (6.1)$$

where sOUR and $sOUR_b$ are referred to the sample exposed to industrial wastewater and the sample exposed to SUW (used as blank wastewater). $sOUR_b$ was in the 47-55 mg O_2·g VSS^{-1}·h^{-1} range. For 12.5% FIW influent wastewater, high inhibition values (82.5% and 80.6%, respectively) were recorded in days 1 and 2 of acclimation. However, inhibition was drastically reduced from day 2 to 3 (48.8%), indicating a better performance of the activated sludge process. As a general rule, for a given percentage of MIW in the influent wastewater, increasing the time of acclimation resulted in higher sOUR (decreasing inhibition). At the end of the acclimation stage (day 15, 100% MIW), relatively low OUR inhibition (c.a. 30%) was found.

Table 6.5. Activated sludge process performance during the acclimation stage.

Day	% MIW in the influent wastewater	MLSS (mg L^{-1})	MLVSS (mg·L^{-1})	sOUR ($mgO_2 \cdot gVSS^{-1}\ h^{-1}$)	% Inhibition	% COD_{8h} removal	% COD_{22h} removal	SVI (mL·g^{-1})
0	0	1093	872	52.0	0	-	30.1	100
1	12.5	1107	928	9.1	82.5	-	26.0	163
2	12.5	1115	898	10.1	80.6	-	35.4	161
3	12.5	1100	847	26.6	48.8	-	63.1	164
4	25	1087	855	36.7	29.2	-	44.9	146
5	25	1078	862	38.5	25.9	-	59.2	158
6	37.5	1247	962	38.4	26.1	-	49.6	104
7	37.5	1057	932	39.8	23.4	-	54.6	123
8	50	1207	1065	40.7	21.6	460	56.2	108
9	50	1123	955	43.5	16.3	44.6	53.8	116
10	75	1327	1148	32.6	37.1	51.2	61.1	98
11	75	1330	1165	40.0	22.9	49.1	62.8	68
12	100	1678	1478	25.4	51.2	46.6	59.9	60
13	100	1910	1787	30.0	42.1	48.4	64.3	58
14	100	2098	1785	35.8	31.1	56.1	61.9	55
15	100	2033	1780	35.9	30.8	57.0	61.3	54

The process performance during the acclimation stage was also followed by COD removal. As it is apparent in **Table 6.5**, the percentage of COD removal was relatively low at the beginning of the acclimation phase (< 40 % removal in days 1 and 2) but increased up to about 60% with the acclimation time. An adapted population was consistent with the effluent COD concentration reaching constant values and the MLVSS concentration gradually increasing [27].

SVI was used to characterize the settling properties of the activated sludge during the acclimation stage. In practice, SVI can vary from 30 to 400 $mL \cdot g^{-1}$ [28]. As a rule, a proper SVI value, typically below 100 $mL \cdot g^{-1}$, is an indicator of good settling properties of the sludge [29]. Therefore, keeping SVI below 100 $mL \cdot g^{-1}$ is crucial for the optimal operation of an activated sludge process. As seen in **Table 6.5**, SVI values obtained during the acclimation phase varied from 163 to 54 $mL \cdot g^{-1}$ from day 1 to 15. The presence of metals and hazardous compounds resulted in poor sludge settling behavior from day 1 to 5 (SVI > 150 $mL \cdot g^{-1}$). However, SVI was kept below 100 $mL \cdot g^{-1}$ from day 10 onwards. This also reveals the success of the sludge acclimation to MIW.

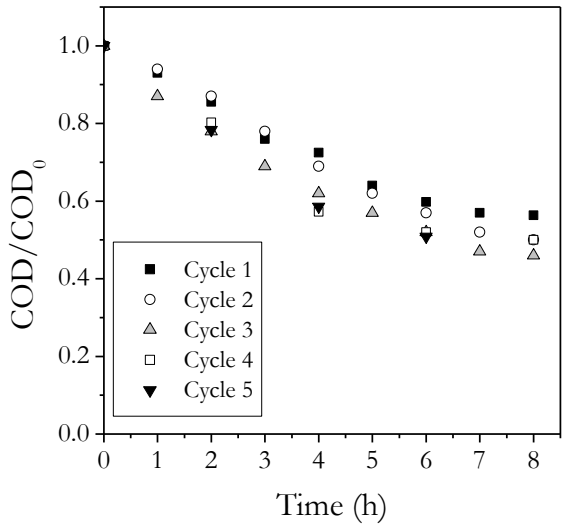

Figure 6.2. Evolution of normalized residual COD during biodegradation of MIW in a SBR. Experimental conditions: pH=7; T=20 ºC; Initial MLVSS=1.8 $g \cdot L^{-1}$. For main MIW characteristics see **Table 6.1**.

B. MIW biodegradation

Additional MIW biodegradation experiments were carried out in the SBR using acclimated activated sludge. **Figure 6.2** shows the evolution of residual COD during

the biodegradation stage of five consecutive SBR cycles (reaction time 8 h) where the biomass concentration was adjusted at the beginning of each cycle to about 1.8 g VSS·L^{-1}. The gradual decline of COD indicates good degrading activity of the acclimated sludge. The evolution of TOC also followed a similar trend (results not shown). On average, COD and TOC removals after the 8-hour biodegradation stage were about 50±5% and 53±4%, respectively. Chroma removal, which was determined as the percentage of A_{465nm} disappearance upon the treatment, was about 90%, suggesting the biodegradation of coloring substances. Regarding metals, only Fe and Zn have been removed to some extent after the biotreatment, probably due to adsorption onto activated sludge [30]. GC-MS analysis of biotreated samples (BW) showed that only three out of twenty compounds detected in MIW were present in BW. As shown in **Table 6.3**, the compounds that were not biodegraded by the acclimated culture were C-88 (metyl-tert-butyl-ether), C-9 (m-methyl pyridine) and C-262 (2,6-bis(1,1-dimethylethyl)-4-(1-oxopropyl)phenol). Likely as a result of this, toxicity of BW towards *V.fisheri* was reduced significantly with regard to MIW. However, little changes were observed in the ecotoxicity tests conducted with *D. magna* on MIW and BW (**Table 6.3**).

Table 6.6. Main characteristic of BW and the O_3-solar-cat effluent and maximum allowable limits for effluent discharge into the municipal sewer system (A) and into the aquatic environment (B).

Parameter	BW	O3-solar-cat	Maximum allowable limit A	Maximum allowable limit B
pH	7.2	6.7	6-10	6-8
COD (mg L^{-1})	850	118	1500	125
BOD_5 (mg L^{-1})	100	< 20	750	25
TOC (mg L^{-1})	280	67	-	-
TPC (mg L^{-1})	15	0.7	2	-
UV_{254nm} (dil. 1:10)	0.113	0.013	-	-

C. Advanced oxidation processes

Although the biotreatment of MIW was satisfactory to some extent, BW presented pollution in terms of TPC (15 mg·L^{-1} on average) and, COD (850 mg·L^{-1} on average) and BOD_5 (100 mg·L^{-1}) well above the allowable discharge limit into the aquatic environment (**Table 6.6**). In order to further remove COD, TOC and TPC from BW, various ozone AOPs were tested: single ozonation (O_3), solar photo-ozonation (O_3-solar) and solar photocatalytic ozonation (O_3-solar-cat). A comparison of processes performance in terms of COD, TOC and TPC removals is presented in **Figure 6.3**.

The highest COD and TOC depletion rates were observed in photocatalytic ozonation. Single ozonation gave rise to a poor mineralization degree (TOC removal < 15%) and COD removal (< 25%) after 5 h reaction time. On the other hand, photo-ozonation (O_3-solar) and, especially, photocatalytic ozonation led to significant TOC and COD removal percentages (25-45% and 40-50%, respectively). This can be attributed to the increased generation of secondary oxidizing species (e.g., hydroxyl free radicals) in the photo-treatments compared to single ozonation. In fact, dissolved ozone observed during O_3-solar and O_3-solar-cat treatments was around 5 μM compared to 30 μM reached in single ozonation runs, which suggests the efficient photo-decomposition of O_3 into HO· radicals [31]. The photocatalytic treatment (O_3-solar-cat) showed a superior power in terms of TOC and COD removals, due to the promotion of different catalytic pathways of HO· radicals production as shown in a previous work [12]. The evolution of TPC (**Figure 6.3(C)**) was similar in all the treatments with nearly 90% TPC removal after 5 h of treatment. In connection with this, UV_{254nm} was also removed to a great extent (> 90%) and complete elimination of the organic compounds detected by GC-MS in BW was achieved with all the ozonation treatments. Some short-chain organic acids were identified in ozone-treated samples. Oxalic, pyruvic, acetic and formic acids accounted for around 10%, 25% and 30% of the overall TOC remaining after the O_3, O_3-solar and O_3-solar-cat processes, respectively, being major by-products of the treatments. In addition to COD, TOC and TPC, chroma was also removed to a high extent by the AOPs applied. Thus, chroma removal efficiencies achieved in the sequential SBR-AOP processes were higher than 99% regardless of ozone-based AOP considered. The toxicity of the final effluent was also evaluated and results are shown in **Table 6.4**. For *V. fischeri*, EC_{50} values did not follow a clear trend in any case. However, for *D. magna* a clear decrease of the toxicity was observed when the AOPs were applied (especially for O_3-solar-cat), indicating the efficiency of the sequential biological-chemical treatment in the detoxification of MIW.

It is well known that carbonate or bicarbonate ions may act as HO· scavengers in AOPs ($k_{CO_3^{2-}\text{-}HO^{\cdot}} = 3.7 \times 10^8\ M^{-1}\cdot s^{-1}$; $k_{HCO_3^{-}\text{-}HO^{\cdot}} = 2 \times 10^7\ M^{-1}\cdot s^{-1}$ [32]). Since IC was high in BW (90 $mg\cdot L^{-1}$ on average), the effect of carbonate/bicarbonate ions removal was studied to analyze the impact of these species on the efficiency of the photo-ozonation and photocatalytic ozonation treatments. **Figure 6.4** compares COD and TOC removals and pH evolution during experiments carried out with as-obtained BW and IC-free BW. From **Figure 6.4(A)** and **(B)** it is apparent that, contrary to what was expected, the presence of bicarbonate in BW had a beneficial impact on the photo-ozonation process performance in terms of COD and TOC removals.

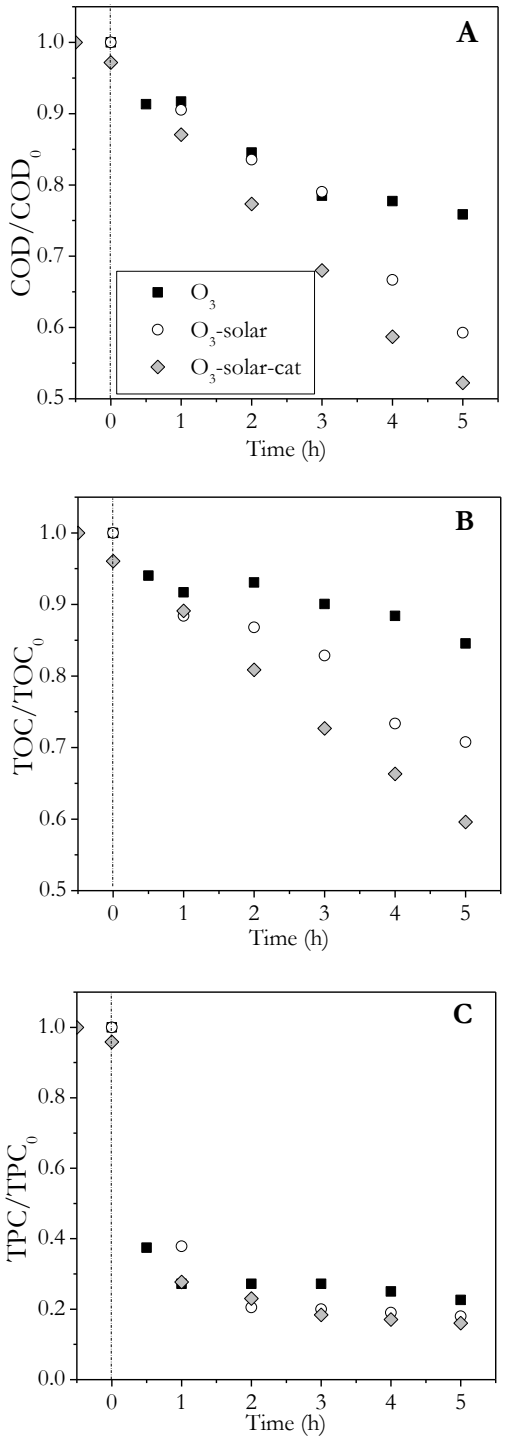

Figure 6.3. Evolution of normalized residual COD (a), TOC (b) and TPC (c) during the application of various AOPs to treat BW. Experimental conditions: T=37 ºC; V=0.65 L; Q_g=20 $L \cdot h^{-1}$; C_{O3g}=20 $mg \cdot L^{-1}$; I=550 $W \cdot m^{-2}$ (λ=300-800 nm) (if radiation applied); C_{cat}=0.375 $g \cdot L^{-1}$ (if catalyst applied). For main BW characteristics see **Table 6.6**

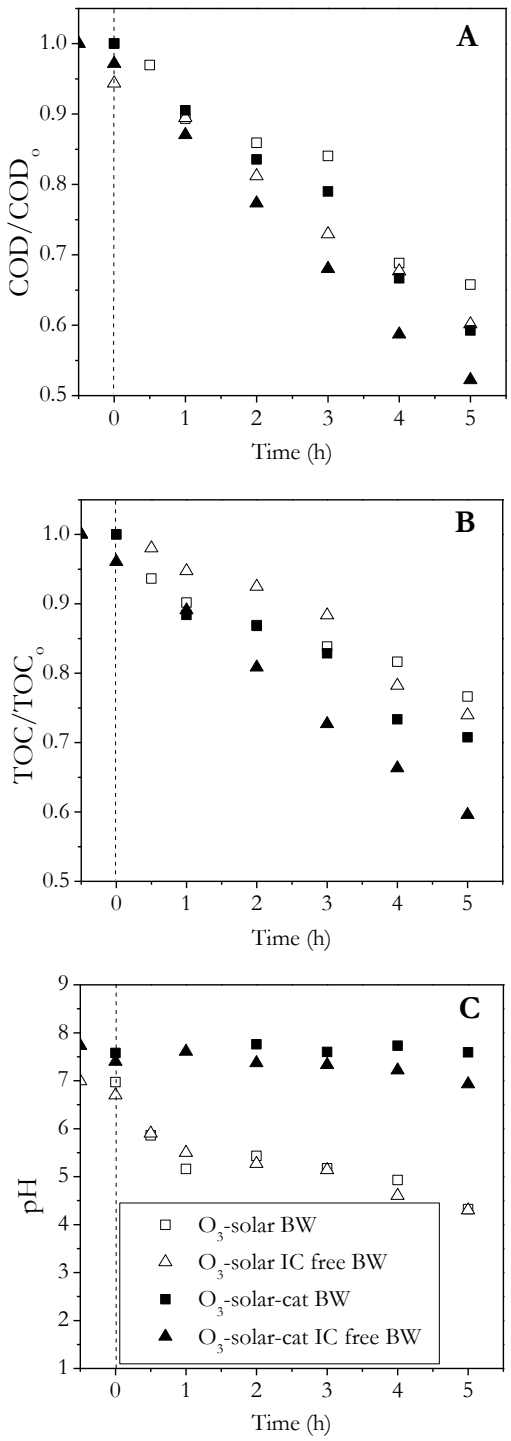

Figure 6.4. Effect of inorganic carbon on the evolution of normalized COD (A), TOC (B) and pH (C) during ozone-solar radiation based AOPs. Experimental conditions: T=37 ºC; V=0.65 L; Q_g=20 L·h^{-1}; $C_{O3,g}$=20 mg·L^{-1}; I=550 W·m^{-2} (λ=300-800 nm); C_{cat}=0.375 g·L^{-1} (if catalyst applied). For main BW characteristics see **Table 6.6**.

As seen in **Figure 6.4(C),** where the evolution of pH throughout the experiments is presented, the removal of IC from BW avoided the buffering effect observed in the as-obtained BW. In fact, pH values were in the range 7.5-8 during the entire reaction time in experiments completed with as-obtained BW in contrast to those with IC-free BW, where pH varied from 7 to 4.3. Therefore, despite the hydroxyl radical scavenging effect of bicarbonate, it seems that neutral-basic pH, which favors indirect ozonation reactions with organics, plays a more important role than bicarbonate itself [33]. TOC was about three times higher than IC in BW. Then, assuming an average rate constant for any organic compound in the range $k_{HO\cdot}=10^7$-10^9 $M^{-1}\cdot s^{-1}$, the apparent reaction rate of HO· radicals with the organic compounds is expected to be higher than that of the bicarbonate-HO· reaction. Moreover, the rate of some direct ozone-organic compounds reactions is favored with increasing pH, which also contributes to BW degradation [34,35].

Additionally, a series of five consecutive runs was carried out reusing the TiFeAC photocatalyst. **Figure 6.5** shows the TOC and COD removal percentages after the reusability runs. As it is apparent, the photocatalyst kept its activity throughout the entire series of runs (67% and 74% TOC and COD removals on average). Furthermore, the concentration of iron found in solution was below 0.05 $mg\cdot L^{-1}$ which demonstrates the stability of the photocatalyst under the reaction conditions.

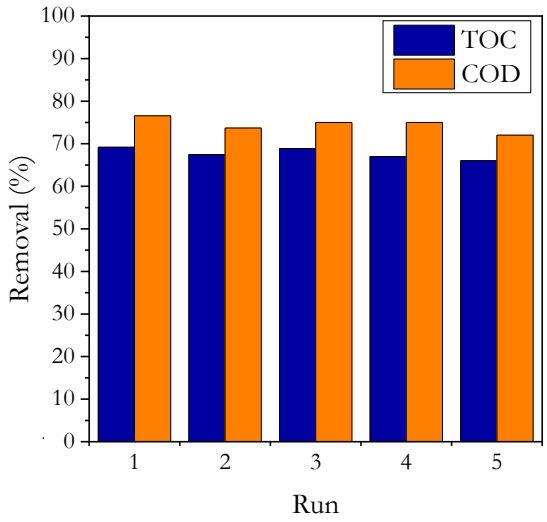

Figure 6.5. Photocatalyst reusability in O_3-solar-cat treatment. Experimental conditions: t= 5h; T=37 ºC; Q_g=20 $L\cdot h^{-1}$; Ozone dose (each run)=4$g\cdot L^{-1}$ h^{-1}; I=550 $W\cdot m^{-2}$ (λ=300-800 nm); C_{cat}=0.375 $g\cdot L^{-1}$. For main BW characteristics see **Table 6.6.**

Finally, to improve the COD and TOC removals achieved by solar photocatalytic ozonation, additional experiments were carried out with higher loading of the photocatalyst and higher ozone dose. Results in terms of COD and TOC removal are depicted in **Figure 6.6(A)** and **Figure 6.6(B)**, respectively. A slight increase in process performance was observed when the catalyst loading was two-folded, achieving a higher COD conversion (74% vs. 64%) though no clear improvement was observed in TOC removal. Regarding the ozone dose, an increase in the ozone applied from 0.6 to 0.9 $g \cdot L^{-1} \cdot h^{-1}$ led to an enhancement in both the COD (from 64 to 84%) and TOC (from 60 to 70%) removals. As a result of the photocatalytic treatment a number of short-chain carboxylic acids were generated, which accounted for 30%, 40% and 48% of overall TOC in the final effluent after 8 h of treatment at the conditions (a) 20 $mg \cdot L^{-1}$ O_3, 0.375 $g \cdot L^{-1}$ catalyst; (b) 20 $mg \cdot L^{-1}$ O_3, 0.750 $g \cdot L^{-1}$ catalyst; and (c) 30 $mg \cdot L^{-1}$ O_3, 0.375 $g \cdot L^{-1}$ catalyst, respectively.

At the most stringent oxidation conditions of those studied here (O_3-solar-cat, 30 $mg \cdot L^{-1}$ O_3, 0.375 $g \cdot L^{-1}$ catalyst) final values of the main characteristic parameters of treated wastewater are summarized in **Table 6.6**. It can be seen that the effluent after the sequential treatment fulfils legal conditions for direct discharge into the environment in terms of pH, COD and BOD. Also, TOC, TPC and UV_{254nm} were satisfactory. In addition, no important concentration of heavy metals was present in the treated effluent (see **Table 6.2**) and all the organic compounds detected by GC-MS in FIW were completely removed (see **Table 6.3**).

Blanco et al. (2012) also found successful an integrated aerobic SBR-Fenton process to treat a textile industrial wastewater, with similar organic load than that considered in this work. They also achieved high overall COD and TOC removals, averaging 86% and 92%, respectively, which are similar percentages than those found in this work (94% and 89%, respectively at conditions of **Table 6.6**) [6]. In the same line than this work, Gimeno et al (2016) applied an aerobic SBR-photocatalytic ozonation treatment (commercial TiO_2/P25 as photocatalyst) to a primary wastewater effluent with spiked pharmaceutical compounds in a pilot plant. They observed about 80% and 70% COD and TOC removals in the overall process leading to a suitable effluent for discharge [36].

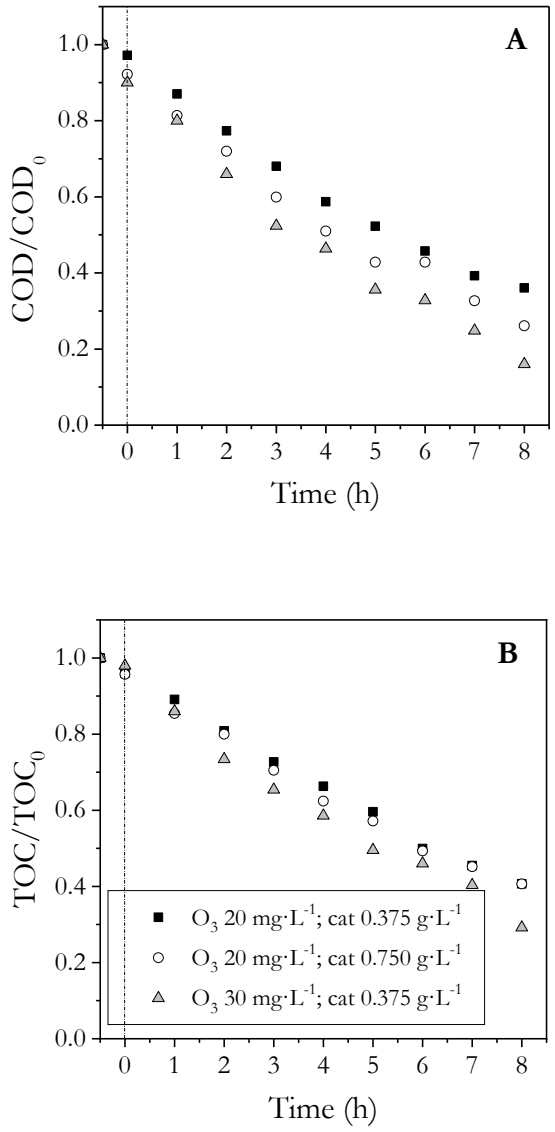

Figure 6.6. Effect of ozone concentration and catalyst loading on the evolution of normalized residual COD (a) and TOC (b) during photocatalytic ozonation runs to treat BW. Experimental conditions: T=37 ºC; V=0.65 L; Q_g=20 L·h^{-1}; C_{O3g}=20-30 mg·L^{-1}; I=550 W·m^{-2} (λ=300-800 nm); C_{cat}=0.375-0.750 g·L^{-1}. For main BW characteristics see **Table 6.6**.

6.4. CONCLUSIONS

A sequential combination of aerobic biodegradation (SBR) followed by ozone-based AOPs has been successfully used to degrade a high-polluted wastewater from petrochemical and cosmetic industries. The SBR treatment could be successfully applied after dilution of the industrial wastewater with urban wastewater (MIW wastewater). Besides, an acclimation stage was needed to develop an appropriate mixed culture able to biodegrade the components of the industrial wastewater. Thus, while biodegradation of MIW was highly inhibited when using non-acclimated activated sludge (> 80% inhibition), after 15 days of acclimation the activated sludge was able to biodegrade the effluent to high extent. Ozone in combination with solar radiation and a TiO_2-based photocatalyst (TiFeAC) could further remove recalcitrant compounds remaining after biodegradation as well as to considerably reduce the toxicity of the wastewater, thus obtaining an effluent suitable for direct discharge into the environment. In addition, the photocatalyst was quite stable and could be reused. Therefore, the combination of biological oxidation using acclimated sludge with solar photocatalytic ozonation AOP is a promising approach to decontaminate the hazardous wastewater studied in this work. Further studies at larger scale about the environmental impact and cost estimation of the integrated process would be necessary to definitively establish its feasibility vs. incineration, which is the treatment method currently applied at the industrial site.

REFERENCES

[1] I. Alyaseri, J. Zhou, "Towards better environmental performance of wastewater sludge treatment using endpoint approach in LCA methodology" *Heliyon*. 3 (**2017**) e00268.

[2] C.R. Dempsey, E.T. Oppelt, "Incineration of hazardous waste: a critical review update" *Air Waste*. 43 (**1993**) 25–73.

[3] A. Poggio, E. Grieco, "Influence of flue gas cleaning system on the energetic efficiency and on the economic performance of a WTE plant" *Waste Manag.* 30 (**2010**) 1355–1361.

[4] B. Guieysse, Z.N. Norvill, "Sequential chemical-biological processes for the treatment of industrial wastewaters: Review of recent progresses and critical assessment" *J. Hazard. Mater.* 267 (**2014**) 142–152.

[5] A.M. Maszenan, Y. Liu, W.J. Ng, "Bioremediation of wastewaters with recalcitrant organic compounds and metals by aerobic granules" *Biotechnol. Adv.* 29 (**2011**) 111–123.

[6] J. Blanco, F. Torrades, M. De la Varga, J. García-Montaño, "Fenton and biological-Fenton coupled processes for textile wastewater treatment and reuse" *Desalination*. 286 (**2012**) 394–399.

[7] D. Sudha, P. Sivakumar, "Review on the photocatalytic activity of various composite catalysts" *Chem. Eng. Process.* 97 (**2015**) 112–133.

[8] G. Singh, J. Singh, S.S. Jolly, R. Rawat, D. Kukkar, S. Kumar, S. Basu, M. Rawat, "Fructose modified synthesis of ZnO nanoparticles and its application for removal of industrial pollutants from water" *J. Mater. Sci. Mater. Electron.* 29 (**2018**) 7364–7371.

[9] M.S. Lucas, R. Mosteo, M.I. Maldonado, S. Malato, J.A. Peres, "Solar photochemical treatment of winery wastewater in a CPC reactor" *J. Agric. Food Chem.* 57 (**2009**) 11242–11248.

[10] D.H. Quiñones, P.M. Álvarez, A. Rey, S. Contreras, F.J. Beltrán, "Application of solar photocatalytic ozonation for the degradation of emerging contaminants

in water in a pilot plant" *Chem. Eng. J.* 260 (**2015**) 399–410.

[11] A. Rey, D.H. Quiñones, P.M. Álvarez, F.J. Beltrán, P.K. Plucinski, "Simulated solar-light assisted photocatalytic ozonation of metoprolol over titania-coated magnetic activated carbon" *Appl. Catal. B Environ.* 111–112 (**2012**) 246–253.

[12] D.H. Quiñones, A. Rey, P.M. Álvarez, F.J. Beltrán, P.K. Plucinski, "Enhanced activity and reusability of TiO_2 loaded magnetic activated carbon for solar photocatalytic ozonation" *Appl. Catal. B Environ.* 144 (**2014**) 96–106.

[13] F.J. Rivas, F.J. Beltrán, O. Gimeno, "Joint treatment of wastewater from table olive processing and urban wastewater. Integrated ozonation-aerobic oxidation" *Chem. Eng. Technol.* 23 (**2000**) 177–181.

[14] S. Mohini, S.R. K., "Sequencing batch reactor technology for biological wastewater treatment: a review" *Asia-Pacific J. Chem. Eng.* 6 (**2010**) 3–13.

[15] E.W. Rice, R.B. Baird, A.D. Eaton, "Standard Methods for the Examination of Water and Wastewater" 23rd edition *American Public Health Association, American Water Works Association and Water Environment Federation*, Washington D.C. (**2017**).

[16] W.A. Moore, R.C. Kroner, C.C. Ruchhoft, "Dichromate reflux method for determination of oxygen consumed" *Anal. Chem.* 21 (**1949**) 953–957.

[17] V.L. Singleton, J.A. Rossi Jr., "Colorimetry of total phenolics with phosphomolybdic-phosphotungstic acid reagents" *Am. J. Enol. Vitic.* 16 (**1965**) 144–158.

[18] ISO-International Organization for Standardization, "Water Quality: Determination of the inhibitory effect of water samples on the light emission of *Vibrio fischeri* (Luminescent bacteria test)—Part 3: method using freeze-dried bacteria" 11348–3 (**2007**).

[19] D.J. Baird, I. Barber, M. Bradley, P. Calow, A.M.V.M. Soares, "The *Daphnia* bioassay: a critique" *Hydrobiologia*. 188 (**1989**) 403–406.

[20] OECD-Organization for Economic Co-operation and Development, "OECD Guidelines for Testing of Chemicals, Section 2, Guideline 202, Test No. 202:

Daphnia sp., acute immobilisation test" (**2004**) 1–12.

[21] H. Bader, J. Hoigné, "Determination of ozone in water by the indigo method; a submitted standard method" *Ozone Sci. Eng.* 4 (**1982**) 169–176.

[22] R.W. Capps, G.N. Mantelli, M.L. Bradford, "Design concepts for biological treatment of industrial wastewater" *Environ. Prog.* 14 (**1995**) 1–8.

[23] P. Guido, M. Blahoslav, B. Irina, T. Andrea, Z. Dzidra, M. Levonas, N.-J. Grzegorz, T. Lucica, S. Nadejda, T. Livia, K. Boris, "A practical and user-friendly toxicity classification system with microbiotests for natural waters and wastewaters" *Environ. Toxicol.* 18 (**2003**) 395–402.

[24] "Decreto 130/2003, de 13 de mayo, por el que se aprueba el Reglamento de los servicios públicos de saneamiento. Diari Oficial de la Generalitat de Catalunya" Catalonia, Spain (**2003**).

[25] F.L. Tchobanoglous, George Burton, H.D. Stensel, "Wastewater engineering. Treatment and reuse, 4th edition" *Mc GrawHill*, (**2002**).

[26] P. Madoni, D. Davoli, L. Guglielmi, "Response of sOUR and AUR to heavy metal contamination in activated sludge" *Water Res.* 33 (**1999**) 2459–2464.

[27] F. Morgan-Sagastume, D.G. Allen, "Effects of temperature transient conditions on aerobic biological treatment of wastewater" *Water Res.* 37 (**2003**) 3590–3601.

[28] W. Janczukowicz, M. Szewczyk, M. Krzemieniewski, J. Pesta, "Settling properties of activated sludge from a sequencing batch reactor (SBR)" *Polish J. Environ. Stud.* 10 (**2001**) 15–20.

[29] J.C. Palm, D. Jenkins, D.S. Parker, "Relationship between organic loading, dissolved oxygen concentration and cludge settleability in the completely-mixed activated sludge process" *J. Water Pollut. Control Fed.* 52 (**1980**) 2484–2506.

[30] A. Hammaini, F. González, A. Ballester, M.L. Blázquez, J.A. Muñoz, "Biosorption of heavy metals by activated sludge and their desorption characteristics" *J. Environ. Manage.* 84 (**2007**) 419–426.

[31] A.M. Chávez, A. Rey, F.J. Beltrán, P.M. Álvarez, "Solar photo-ozonation: A novel treatment method for the degradation of water pollutants" *J. Hazard.*

Mater. 317 (**2016**) 36–43.

[32] G. V. Buxton, C.L. Greenstock, W.P. Helman, A.B. Ross, "Critical review of rate constants for reactions of hydrated electrons, hydrogen atoms and hydroxyl radicals in aqueous solution" *J. Phys. Chem.* 17 (**1988**) 513–886.

[33] H. Barndõk, H. Daphne, C. Luis, N. Carlos, B. Ángeles, "Assessing the effect of inorganic anions on TiO_2-photocatalysis and ozone oxidation treatment efficiencies" *J. Adv. Oxid. Technol.* 15 (**2012**) 125–132.

[34] F.J. Beltrán, "Ozone reaction kinetics for water and wastewater systems" *Lewis Publishers*, Florida (**2004**).

[35] J. Hoigné, H. Bader, "Rate constants of reactions of ozone with organic and inorganic compounds in water—II disociating organic compounds" *Water Res.* 17 (**1983**) 185–194.

[36] O. Gimeno, J.F. García-Araya, F.J. Beltrán, F.J. Rivas, A. Espejo, "Removal of emerging contaminants from a primary effluent of municipal wastewater by means of sequential biological degradation-solar photocatalytic oxidation processes" *Chem. Eng. J.* 290 (**2016**) 12–20.

PAPER 4

MAGNETIC GRAPHENE TiO_2-BASED PHOTOCATALYST FOR THE REMOVAL OF POLLUTANTS OF EMERGING CONCERN IN WATER BY SIMULATED SUNLIGHT AIDED PHOTOCATALYTIC OZONATION

Applied Catalysis B: Environmental 262 (2020) 118275

Ana M. Chávez[1,2], Rafael R. Solís[3*], Fernando J. Beltrán[1,2]

[1] Departamento de Ingeniería Química y Química Física, Facultad de Ciencias, Universidad de Extremadura, Avda. Elvas s/n, 06006 Badajoz (Spain)

[2] Instituto Universitario del Agua, Cambio Climático y Sostenibilidad (IACYS), Universidad de Extremadura, Avda. de la Investigación s/n, 06006 Badajoz (Spain)

[3] Department Chemical & Environmental Engineering, College of Engineering & Environmental Science (CEAS), Engineering Research Centre (ERC), University of Cincinnati, Cincinnati OH 45221-0012 (USA)

CHAPTER VII

GRAPHICAL ABSTRACT

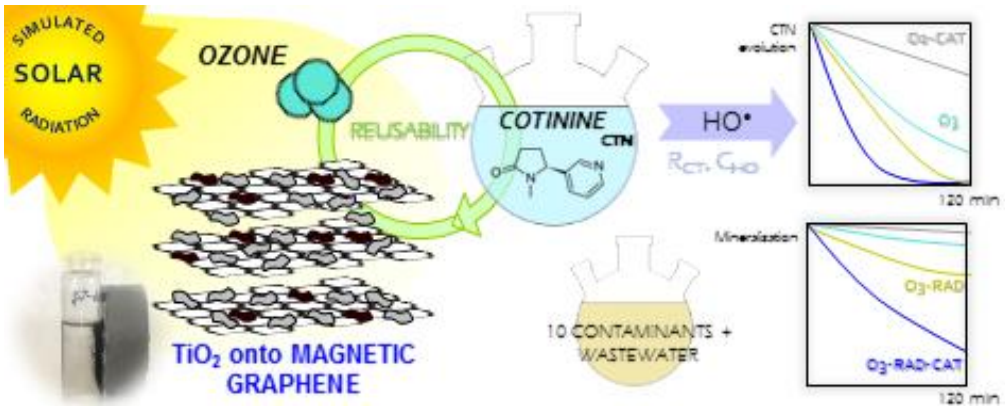

ABSTRACT

Magnetite and titania have been supported onto graphene for the photocatalytic ozonation removal of aqueous micropollutants. Titania and magnetite were successfully attached to graphene nanoparticles keeping with a reasonable separation and photocatalytic activity. Although the presence of graphene did not enhance the photoactivity of bare titania, graphene acted as a good support of magnetite nanoparticles and removed the leaching of iron, a problem observed with the graphene free composite. The synthesized photocatalysts were characterized by diverse techniques. The efficiency of the processes involving ozone was assessed by different tools such as $HO^{\bullet}$ exposure vs time, R_{ct} and $R_{HO^{\bullet},O3}$ ratios. Photocatalytic ozonation was the most efficient for the removal of the target compound and mineralization. No loss of activity was registered after reusing or appreciable iron leaching. Finally, the catalyst was also tested in a real secondary effluent from a wastewater treatment plant containing ten micropollutants of emerging concern.

Keywords: magnetic graphene, titania, photocatalytic ozonation, solar light, water treatment.

7.1. INTRODUCTION

The high standard of life reached by current society demands the use of a huge number of organic substances that are still under research and development every day. However, the concern related to the presence of these organics in the environment is raising among the research community due to the harmful properties and their impact in the natural ecosystems [1]. Concretely, contaminants of emerging concern (CECs) are organic micropollutants, i.e. reported at very low concentration, from diverse families of organics: pharmaceuticals, personal care products, plasticizers, perfluorochemicals, food additives, legal and illegal drugs, pesticides, etc. [2–4]; that have been detected in diverse aqueous ecosystems for the last decades. Furthermore, these substances generate some stable degradation products named as metabolites. The acute toxicity of CECs is not always alarming as the concentration they are reported is below $\mu g \cdot L^{-1}$, commonly in the $ng \cdot L^{-1}$ range. In addition, their interaction with human life and the environment is not well understood. No studies of how they affect the life cycle in the long term are available [5]. Nevertheless, some groups of these substances do generate a concern impact in the short term. For example, the presence of antibiotics in the environment is making microbes to be more resilient as they adapt themselves against the antibacterial properties [6,7].

Although drinking water treatment plants generally are designed to remove specific organic pollutants when required, conventional urban wastewater treatment plants (UWWTPs) do not consider specific stages for that purpose. This makes UWWTPs to be a hotspot of CECs release into aquatic ecosystems [8,9]. Thus, new technologies to face the problematic of CECs are needed.

Advanced oxidation processes (AOPs) have demonstrated to be efficient in the oxidation of almost all kind of organics in water [10–12]. AOPs rely on the production of hydroxyl radicals in enough concentration to oxidize organics, approaching in some cases high mineralization extent as the oxidation is focused on the production of carbon dioxide and inorganic anions. Ozone is a versatile and moderate oxidant that does not produce residues when used in water treatment. Ozone can react, first, selectively by direct attack of the O_3 molecule to e.g. unsaturated bonds or aromatic rings; and secondly, by triggering a decomposition mechanism into hydroxyl radical as the main oxidant species. However, ozonation by itself poses low potential of mineralization [13]. That is why different technologies that enhance the decomposition of aqueous ozone into $HO^{\bullet}$ have gained the attention of researchers. Among all envisaged technologies, photocatalytic ozonation is one of the most powerful due to

the high mineralization extent capability [14–18]. That means, that not only the targeted compounds are oxidized, but also the intermediates and a great extent of the final oxidation products such as organic acids.

Titanium dioxide, activated with radiation below 387 nm [19], has led to the study of photocatalytic ozonation processes due to its high stability, low toxicity and price, if compared to other photoactive catalysts. Although the solid frequently has been displayed in slurry reactors; this disposition lacks interest since further recovery of the catalyst is required, which is economically low attractive. The immobilization of the solid is one strategy trying to deal with this problem [20], even though some radiation adsorption effectiveness is reduced if compared to slurry setup [21]. Alternatively, magnetization of the catalyst has been proved to be an efficient strategy to take advantage of the high radiation adsorption in slurry disposition and easy recovery by applying and external magnetic field after use [22,23]. In this sense, for TiO_2 photocatalysis, some magnetic solids containing Fe_3O_4 with high photocatalytic activity have been proposed [24]. Different high specific surface area supports have been previously tested for magnetic-based TiO_2 using carbonaceous materials such as activated carbon [25,26] or multi-walled carbon nanotubes [27,28]. Graphene, which is defined as a single monolayer of hexagonal carbon, is also a high surface material with delocalization of π electrons, which confers on it promising properties as nano-adsorbent [29] and nano-catalyst [30–33].

This work reports the study of magnetic titania photocatalysts using graphene as support for the photocatalytic ozonation process, under solar simulated radiation, of aqueous contaminants of emerging concern. Different photocatalysts varying the ratios of the photocatalytic specie (TiO_2), magnetic component (Fe_3O_4) and support (graphene) have been tested using preliminary studies in ultrapure water with cotinine, which is a nicotine metabolite recalcitrant to oxidation [34], frequently reported in wastewater effluents [35–38]. Different techniques have been used for the characterization of the synthesized materials (i.e. SEM-EDX, TEM, XRD, FTIR, Raman, N_2 isotherm, XPS, WDXRF, DRS-Vis, SQUID, etc.) in order to analyze the influence of superficial and textural properties on the photocatalytic activity. The material with higher activity was tested for stability in consecutive recycling. Finally, deeper testing for oxidation of a mixture of CECs (bezafibrate, caffeine, ciprofloxacin, clofibric acid, cotinine, DEET, ibuprofen, metoprolol, sulfamethoxazole and tritosulfuron) at low concentration and dissolved in a real urban wastewater (UWW) effluent is accomplished.

7.2. MATERIALS and METHODS

7.2.1. CHEMICALS AND MATERIALS

Cotinine analytical standard (CTN, $C_{10}H_{12}N_2O$, CAS: 486-56-6, ≥ 98%), bezafibrate (BZF, $C_{19}H_{20}ClNO_4$, CAS: 41859-67, ≥98%), caffeine (CAF, $C_8H_{10}N_4O_2$, CAS: 58-08-2, ≥99%), clofibric acid (CA, $C_{10}H_{11}ClO_3$, CAS: 882-09-07, 97%), ibuprofen sodium salt (IBP, $C_{13}H_{17}O_2Na$, CAS: 31121-93-4, ≥98%), metoprolol tartrate (MTP, $(C_{15}H_{25}NO_3)_2 \cdot C_4H_6O_6$, CAS: 56392-17-7, 99%), N,N-diethyl-m-toluamide (DEET, $C_{12}H_{17}NO$, CAS: 134-62-3, 97%), sulfamethoxazole (SMX, $C_{10}H_{11}N_3O_3S$, CAS: 723-46-6, ≥98%) and tritosulfuron (TSF, $C_{13}H_9F_6N_5O_4S$, CAS: 142469-14-5, ≥98%) were acquired from Sigma-Aldrich®. Ciprofloxacin (CPR, $C_{17}H_{18}FN_3O_3$, CAS: 85721-33-1, 98%) was supplied by Acros Organics®.

For catalyst synthesis, commercial xGnP® graphene nanoplatelets from Sigma-Aldrich® was used (particle size < 2μm, thickness few nm, specific surface area 750 $m^2 \cdot g^{-1}$). Titanium (IV) iso-propoxide (Sigma-Aldrich®) and pure *iso*-propanol (Panreac®) were used in the TiO_2 solvothermal synthesis. All chemicals were used as-obtained without any further purification.

Table 7.1. Characterization parameters of the UWW effluent

Parameter (units)	Mean value ± error
pH	8.4 ± 0.1
Conductivity ($\mu S \cdot cm^{-1}$)	960 ± 5
Turbidity (NTU)	5.2 ± 0.1
Total Organic Carbon, TOC ($mg \cdot L^{-1}$)	20.2 ± 0.7
Inorganic Carbon, IC ($mg \cdot L^{-1}$)	58 ± 2
Chloride ($mg \cdot L^{-1}$)	104 ± 9
Nitrate ($mg \cdot L^{-1}$)	0.41 ± 0.02
Phosphate ($mg \cdot L^{-1}$)	0.24 ± 0.02
Sulfate ($mg \cdot L^{-1}$)	60 ± 3

The rest of the chemicals used for analytical purposes were analytical grade and purchased from Panreac®. HPLC-grade acetonitrile (Panreac®) was used in liquid chromatography. Ultrapure Milli-Q® from an Integral 5 system (resistivity 18.2 MΩ cm) was used for the preparation of all the solutions. Urban wastewater (UWW) coming from a secondary clarifier after biological treatment was collected from the local wastewater treatment plant (WWTP of the city of Badajoz in the spring of 2019 (capacity for 160,000 equivalent inhabitants), filtered with paper filters (>11 μm) and stored at -4 ºC until further use. **Table 7.1** summarizes the main characterization parameters of the UWW.

7.2.2. CATALYST SYNTHESIS AND CHARACTERIZATION

The synthesis of magnetic graphene-TiO_2 based photocatalysts was adapted from literature [39]. Briefly, the procedure was as follows. Firstly, magnetite nanoparticles were obtained by simultaneous co-precipitation of Fe (III) and Fe (II) at the same molar ratio under alkaline conditions. Thus, 20 mmol of $FeCl_3 \cdot 6H_2O$ and 20 mmol of $FeSO_4 \cdot 7H_2O$ were dissolved in 200 mL of ultrapure water under N_2 bubbling and magnetic stirring. Solution pH was raised until the value of ~9.0 by dropwise of concentrated aqueous NH_3 solution. The magnetic particles were washed with water under stirring, recovering the particles with the help of a magnet. The washed solid was dried overnight at 80 °C. Secondly, magnetic graphene was prepared by sonicating a certain amount of the previously obtained magnetite and commercial graphene in 200 mL of *iso*-propanol. Different weight ratios of magnetite:graphene (X:1) were considered, labeling them as MGX. Thirdly, TiO_2 was incorporated to the magnetic-graphene substrate by solvothermal method. For that purpose, 10 mL of titanium (IV) *iso*-propoxide were dissolved in 50 mL of *iso*-propanol and a desired amount of MGX was added to the solution. The catalyst was labeled as Y-MGX-Ti where Y stands the mass percentage of MGX in comparison to the theoretical TiO_2 incorporated in the process. Precipitation of titanium was accomplished by adding 5 mL of ultrapure water and the solution was transferred to a 200 mL autoclave. Thermal treatment was undergone at 180 °C during 16 h. The final solid was washed with ethanol and ultrapure water several times. Finally, the solid was dried under vacuum at 80 °C and kept overnight at 80 °C.

Graphene percentage was thermogravimetrically obtained by calcination at 800 °C. The ratio Fe/Ti was quantified by wavelength dispersive X ray fluorescence (WDXRF) in a S8 TIGER® device (Bruker), equipped with Rh X-ray source (4 kW).

Morphology of the solid was studied by scanning electron microscopy (SEM) in a QUANTA 3D FEG (FEI Company) device, equipped with BSED (backscattered electron diffraction) and EDX (energy dispersive X-ray) analysis.

N_2 adsorption isotherm technique was conducted to evaluate the textural properties, using a Quadrasorb EvoTM apparatus (Quantachrome Instruments). Autosorb IQ-c software was used to obtain BET surface area ($0.05 < P/P_0 < 0.35$), as well as analysis of external surface area and micropore volume distribution. Samples were previously outgassed at 150 °C for 12 h under vacuum.

Microcrystalline structure was analyzed by X-Ray diffraction (XRD), performed in a D8 ADVANCE device (Bruker) equipped with Vårio-1 Ge111 monochromator (Cu $K\alpha_1$, radiation 1.5406 Å), registering within an angle range (2θ) 5-70°.

Raman spectra were obtained in a Nicolet™ Almega XR Dispersive Raman Spectrometer (Thermo Scientific™) provided with a laser at 633 nm. Fourier transformed infrared (FTIR) spectra were registered in a Nicolet™ iS10 FTIR spectrometer (Thermo Scientific™) in the range 7800-350 cm^{-1}.

Superficial oxidation states and surface oxygenated groups were analyzed by X-ray photoelectron spectroscopy (XPS) in a Kratos Axis Ultra DLD device operating with monochromatic Al Kα radiation (1486.6 eV) and a selected X-ray power of 150 W. Spectra were corrected to 284.6 eV for C–C bounding in C1s peak. The deconvolution of the peaks was carried out with help of XPSPeak 4.1 software, adopting a Shirley type background correction.

Optical properties were studied in a diffuse reflectance UV-vis spectrophotometer (DR-UV-vis), UV-vis-NIR Cary-5000 (Varian Technologies), equipped with an integrating sphere device. Band gap was calculated following Tauc's method [40].

Magnetic properties were measured using a 7 Tesla Quantum Design MPMS XL Superconducting Quantum Interference Device (SQUID). The magnetic moment, M_s, was measured as function of applied magnetic field (from 0 to 7 T) at room temperature (25 ºC).

7.2.3. PHOTOCATALYTIC OZONATION TESTS

Photocatalytic tests were carried out in a solar box SUNTEST CPS+ (Atlas) equipped with a Xe arc lamp and emitting radiation at > 300 nm. A glass borosilicate spherical reactor, with 500 mL of water solution, was placed in the center of the solar simulator and kept under magnetic stirring. Pure O_2 or O_2-O_3 gas mixture, with ozone generated in a Anseros COM-AD-01 apparatus, was bubbled at a rate of 30 $L \cdot h^{-1}$, containing 10 mg $O_3 \cdot L^{-1}$ (when needed). Ozone concentration in the gas phase was continuously monitored by means of an Anseros GM device (spectrophotometric measurement at 254 nm), connected to the gas outlet/inlet of the reactor. A detailed experimental setup scheme can be checked in a previous work [41].

Experiments started with a 30 min adsorption period, when required, to ensure the adsorption equilibria on the catalyst surface. Photocatalytic ozonation started by

simultaneously application of radiation and ozone bubbling. In experiments in which radiation was not necessary, for temperature profiles comparison, radiation was supplied but the reactor was prevented from radiation by covering it with aluminum foil. At different times aqueous samples were withdrawn, removing residual dissolved ozone by bubbling air and filtering the catalyst with Millex®-HA syringe filters (0.45 μm, Millipore), when required.

7.2.4. ANALYSIS OF AQUEOUS SAMPLES

The concentration of organic pollutants was analyzed in a UFLC Shimadzu Prominence LC-20AD device equipped with Diode-Array detection. The column used for the chromatographic separation was a core-shell Kinetex® (C18, 2.6 μm, 2.1^{x}30 cm), kept at 30 °C. For individual analysis of cotinine, a mixture A:B 5:95 acetonitrile: acidified water (0.1 % H_3PO_4), was pumped at a rate of 0.5 mL·min^{-1}. Quantification was conducted at 259 nm. The method followed for the mixture of the contaminants was a gradient, with the same flow rate, starting with A:B 5:95 during 5 min, thereafter the A proportion was raised until 95:5 in 15 min, and hold during 1 min to go back to the initial conditions in 9 min. Detailed information of quantification wavelength and retention times is provided in **Table 7.S1.**

Dissolved ozone in the aqueous phase was determined by the colorimetric method based on the discoloration of indigo trisulfonate [42]. Total organic and inorganic carbon was quantified in a Shimadzu® TOC-VCSH coupled to ASI-V automatic injector.

Short-chain organic acids (acetic, propionic, formic and oxalic acids) and inorganic anions (chloride, nitrate, phosphate and sulfate) were analyzed by ionic chromatography in a Methrom® 881 Compact IC pro equipped with chemical suppression. The mobile phase program was a gradient of 0.7 mL·min^{-1} of Na_2CO_3 from 0.6 mM to 14.6 mM in 50 min, with 10 min of equilibration.

The released iron into solution was quantified spectrophotometrically as total iron by ferrozine method (Spectroquant®, Merck).

7.3. RESULTS and DISCUSSION

7.3.1. CHARACTERIZATION OF THE PHOTOCATALYSTS

The composition of the synthetized photocatalysts was studied by combining different techniques. The carbon percentage was calculated by calcination and the ratio of Fe:Ti by WDXRF analysis. **Table 7.2** summarizes the results. As shown, the proportion of MG1 was close to 1:1. The percentage of the incorporated titania was slightly lower to the expected, but matching quite well with the theoretically desired. However, the amount of magnetite was generally inferior to a ratio 1:1 graphene magnetite in Y-MG1-Ti solids. There was a clear loss of magnetic particles during the washing step of the catalyst preparation. This latter aspect is even more obvious when the proportion graphene-magnetite was increased two and three times in the 10-MG2-Ti and 10-MG3-Ti. The loss of magnetite particles during the synthesis process could be attributed to a lack of real affixing during the thermal treatment in the solvothermal method.

The morphology of the photocatalytic particles was also studied by SEM technique. From the micrographs in **Figure 7.S1**, a wide variety of particle sizes within 10 and 50 μm was appreciated. An EDX mapping confirmed the presence of titanium and iron on the surface, as well as verified the distribution of magnetite and titania particles. The superficial composition estimated by EDX was in good agreement with the composition calculated by WDXRF, as shown in **Table 7.2.** From the distribution of carbon in EDX scanning, it can be observed that graphene acts as support of titania and magnetite particles.

Textural properties were analyzed by N_2 adsorption isotherm (graphs available in **Figure 7.S2**). The raw commercial graphene presented a BET specific area of 669 $m^2 \cdot g^{-1}$, which is close to the value available from the manufacturer (750 $m^2 \cdot g^{-1}$). The solvothermal prepared TiO_2 had a good surface area, 146 $m^2 \cdot g^{-1}$, if compared to other nanosynthesized titania. The addition of magnetic graphene support did not affect significantly the final surface area, being in all the cases in between 150-200 $m^2 \cdot g^{-1}$.

Table 7.2. Elemental, superficial, optical and magnetic properties of the synthesized photocatalysts

Catalyst	Composition (wt. %)			Textural properties		Optical properties	Magnetic properties	
	C	Fe_3O_4	TiO_2	BET area ($m^2 \cdot g^{-1}$)	Pore volume[3] ($cm^3 \cdot g^{-1}$)	Band gap (eV)	Saturation Moment ($emu \cdot g^{-1}$)	Theoretical saturation Moment[4] ($emu \cdot g^{-1}$)
Graphene	100	-	-	669	0.856	n.m.	n.m.	n.m.
MG1	53.6	45.0	-	56	0.516	n.m.	34.5	31.5
10-MG1-Ti	9.9[1]/ 6.5[2]	4.2[1]/ 4.5[2]	85.9[1]/ 88.8[2]	171	0.374	2.66	2.74	2.94
10-MG1-Ti re	2.1	4.4	92.6	142	0.322	n.m.	n.m.	n.m.
20-MG1-Ti	14.1[1]/ 9.5[2]	8.5[1]/ 9.0[2]	77.1[1]/ 81.5[2]	178	0.313	2.59	5.53	5.95
30-MG1-Ti	17.6[1]/ 14.3[2]	13.2[1]/ 12.8[2]	69.2[1]/ 72.9[2]	200	0.352	2.69	8.89	9.24
10-MG2-Ti	10.7	5.3	84.0	146	0.379	2.74	3.72	3.71
10-MG3-Ti	7.5	6.8	85.7	150	0.327	2.61	4.55	4.76
TiO_2	-	-	100.0	146	0.320	3.19	n.m.	n.m.

[1]Carbon thermogravimetrically quantified (calcination 800 ºC). Magnetite and titania by WDXRF
[2]Measured by EDX analysis in SEM
[3]Obtained through Density Functional Theory (DFT) methodology
[4]Calculated according to the Fe_3O_4 composition and the saturation magnetization measured for pure Fe_3O_4 (70 $emu \cdot g^{-1}$)
n.m. not measured

Nevertheless, there is a correlation of the amount of graphene, e.g. with the highest graphene:magnetite ratio, and the increase of the superficial area in the Y-MG1-Ti photocatalysts. Additionally, the pore volume and its distribution (see **Figure 7.S2**) were analyzed by Density Functional Theory (DFT), concluding that graphene support was the most porous material. All the photocatalysts had similar pore volume (in the proximity of 0.320-0.374 $cm^3 \cdot g^{-1}$) and similar pore distribution as it is highly influenced by the predominant content of titania.

The crystalline composition of the different photocatalysts was qualitatively studied by X-ray diffraction (XRD) technique. **Figure 7.1** depicts diverse diffractograms of some studied photocatalysts. Graphene XRD pattern was characterized by the presence of hexagonal graphitic peaks, *i.e.* mean peak at 26.7º and residual at 44.3º. After incorporating magnetite to obtain MG1, diverse peaks of cubic magnetite were observed, the most important located at 35.5º (minor peaks 30.1, 35.5, 43.1, 53.7, 57.2 and 62.8º). Moreover, MG1 showed a small contribution of graphene peak (26º). The synthesized bare titania was also analyzed, confirming the presence of anatase with a main peak located at 25.2º (minor peaks at 37.7, 47.8, 53.7, 54.8 and 62.4º). The XRD diffractogram of 10-MG1-Ti is characterized by the presence of the peaks of anatase, whose relative intensity was higher than magnetite, i.e. only the peak at 35.5º of cubic magnetite was appreciated. This peak increased as the proportion of MG1 was raised. Therefore, the presence of anatase and magnetite was confirmed in all Y-MGX-Ti photocatalysts, showing a relative increase in the magnetite peak (i.e. 35.5º) when its proportion was increased. The presence of graphene in Y-MGX-Ti could not be confirmed by this technique due to the higher relative intensity of anatase peak.

Thus, the presence of graphene was confirmed by Raman spectroscopy for the 10-MG1-Ti photocatalyst (see **Figure 7.S3(A)**). Raman patterns for titania, magnetite and graphene were also accomplished for comparison purposes. Particular information can be extracted from the Raman spectrum of graphene in which three peaks are usually observed. The peak around 1350 cm^{-1} (D) is referred to disordered carbon, the G peak at ca. 1580 cm^{-1} is attributed to the hexagonal carbon present in graphene and the 2D-band, which gives information of the stacking order of graphene layers. The thickness of graphene nanoplatelets can be estimated by the relative intensity of 2D and G peak. A value up to 2 has been reported in the literature for monolayer graphene [43]. The Raman pattern for the commercial graphene showed that I_{2D}/I_G=2.4. Alternatively, the full width at half maximum (FWHM) for 2D peak has also been studied for graphene

materials of different layers [44]. A value of 25.6 cm^{-1} was estimated in this study, which coincides with the proposed value for monolayer graphene (FWHM=26 cm^{-1} [44]).

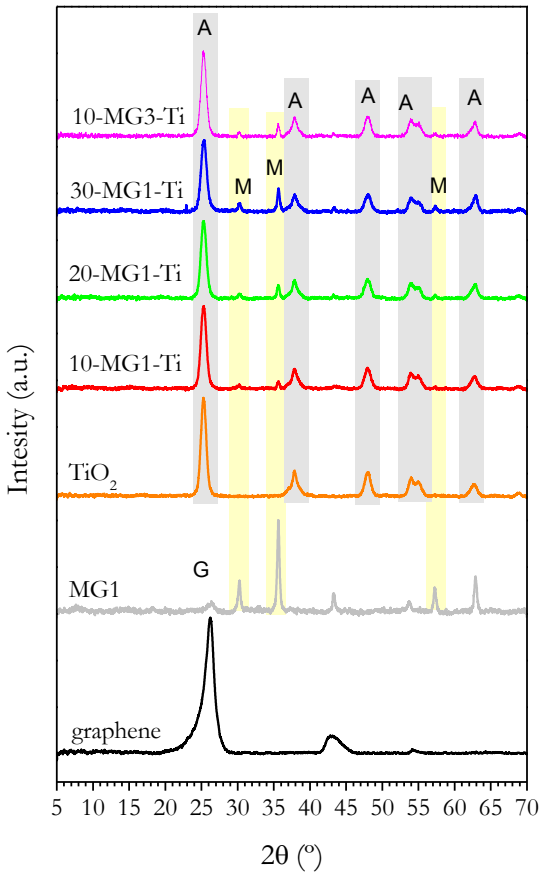

Figure 7.1. XRD pattern of Y-MGX-Ti photocatalysts

Additionally, FTIR was used to evaluate the presence of oxygenated superficial groups (**Figure 7.S3(B)**). A wide band at ca. 3400 cm^{-1}, attributed to the stretching vibration of the hydroxyl group was observed in all the solids analyzed which qualitative justified the presence of coordinated −OH surface groups or molecules of H_2O adsorbed. Hydroxylated groups also presented a deformation vibration at around 1600 cm^{-1}. It is also observed a peak at around 1400 cm^{-1} that is usually identified as vibrations of C–O bounding that could be attributed to C–O in the surface of graphene or due to atmospheric CO_2 adsorbed in the surface.

Surface oxidation states were studied by XPS technique. **Figure 7.2** depicts the high resolution spectra of O1s peak for the different synthesized solids. For graphene

material compounds, the following surface oxygenated species have been considered [45]: oxide state typically recorded in oxides (~530 eV), O-C=O bounding (~531 eV), C=O groups (~532 eV), C–OH (~533 eV) and C–O–C binding (~534 eV). In titania and magnetite, hydroxylated groups were detected at around 532 eV. Raw graphene was characterized by the presence of hydroxylated and carbonyl group, and very low proportion of carboxylic groups. Magnetic graphene (MG) presented higher proportion of carboxylic groups than graphene, probably due to a slight oxidation during the synthesis process. The incorporation of titania, with a low proportion of hydroxylated groups (i.e. around 5.6% of total oxygen) and MG support, led the enrichment of oxygenated groups. Actually, 10-MG-Ti fresh catalyst had 9.4% of carbonyl groups (C=O) and 19.6% of hydroxylated groups. After the 5th use of the catalyst an important decrease of oxygenated groups was recorded (only 10.7% of carbonyl group).

Optical properties of Y-MGX-Ti photocatalysts were studied by DR-UV–vis spectroscopy. Band gap energy was determined by Tauc's plot method (see **Table 7.2** and **Figure 7.S4**). The presence of graphene oxide [33] or reduced graphene oxide in titania has been reported as a good strategy to reduce the band gap of photocatalysts [46] and, therefore, to enhance the activity in the visible region of the solar spectrum. The lab-made photocatalysts presented absorption of radiation up to 340 nm (see **Figure 7.S4(A)**). The determined bandgap for bare TiO_2 was 3.19 eV while the addition of magnetic graphene led to lower values in the range of 2.59-2.74 eV. Experiments filtering the radiation source to the visible region, i.e. 390-800 nm (results not shown), did not change this behavior. A plausible explanation of this effect may be the higher recombination of the photo-induced species as graphene was used as support for titania and magnetite, and not as dopant agent to enhance photocatalytic activity [46].

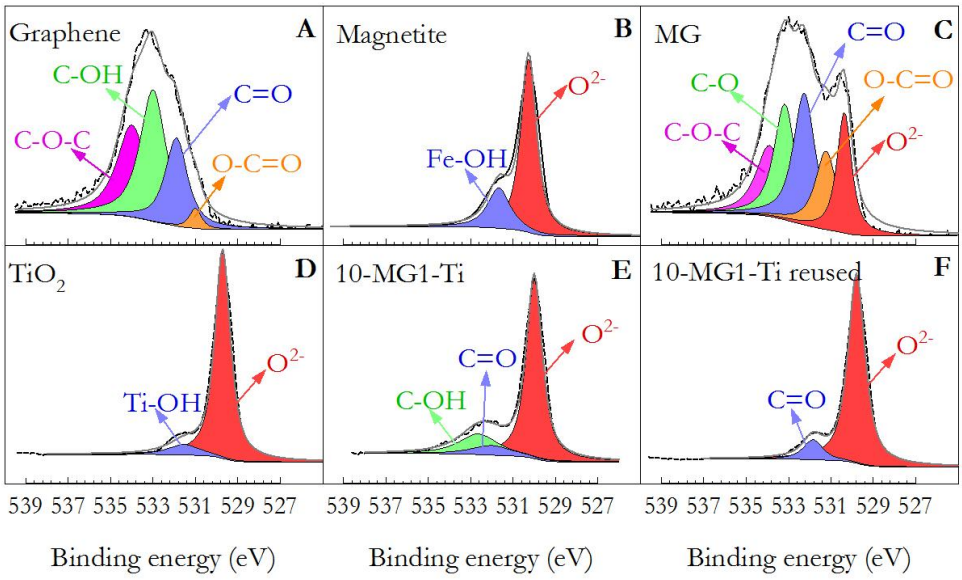

Figure 7.2. High resolution XPS spectra for O1s region of graphene (A), magnetite (B), magnetic graphene MG (C), bare TiO_2 (D), 10-MG1-Ti (E) and reused 10-MG1-Ti photocatalysts (F).

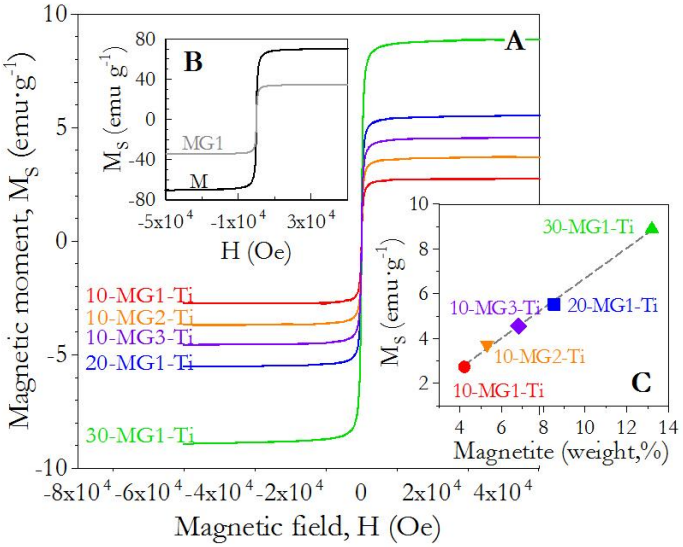

Figure 7.3. Magnetic moment (M_s) *versus* applied magnetic field (H). Figure A, magnetization in graphene-based TiO_2 photocatalysts. Figure B, magnetization of magnetite (M) and magnetic graphene (MG1). Figure C, magnetic moment *vs.* magnetite composition in graphene-based TiO_2 photocatalysts

Magnetic properties were analyzed by means of SQUID technique. **Figure 7.3** shows the results of magnetization of the synthesized photocatalysts. The magnetic moment, M_s, increased according to the proportion of magnetite. Actually, the maximum value was recorded for raw magnetite, M_s=70 emu·g^{-1} (**Figure 7.3(B)**). Although M_s values depend also on the magnetite particle size, values within 60–70 emu·g^{-1} are frequently reported for magnetite nanoparticles. A plot of M_s *versus* the amount of iron, expressed as magnetite, in each sample led to a linear plot, see **Figure 7.3(**C), which confirms the presence of magnetite. Magnetite can undergo oxidation to the less magnetic maghemite (γ-Fe_3O_2). Nevertheless, it was not the case during the synthesis process of the lab made photocatalysts. The M_s values obtained matched the expected ones according to the M_s recorded for pure magnetite and the calculated amount of iron from WDXRF analysis, considering all the presented iron as magnetite. The M_s for the solid 10-MG1-Ti was 2.74 emu·g^{-1}. Similar values have been reported as suitable for photocatalytic ozonation treatment [25,26,47]. Although higher percentages of magnetite enhance the separation by increasing M_s, the photocatalytic activity would be reduced as it is shown in next section.

7.3.2. EFFICIENCY OF PHOTOCATALYTIC OZONATION WITH 10-MG1-Ti. COMPARISON TO SIMPLER TECHNOLOGIES

A series of experiments to assess the efficiency on the removal of cotinine (CTN) as target pollutant were first carried out. Different technologies involving solar simulated radiation, ozone and the 10-MG1-Ti photocatalytic solid, selected in a first approach, were accomplished. Results are depicted in **Figure 7.4**.

Although adsorption onto graphene has been reported in literature for a wide range of aqueous organic pollutants, even at low graphene dose [48]; no adsorption of cotinine was appreciated using 10-MG1-TiO_2 whose percentage of graphene is, theoretically, 5% of total weight. Photolysis produced negligible effect in the removal of the compound, *i.e.* less than 10% removal, as it could be deduced from its absorption UV-vis spectrum (no radiation absorption over 290 nm).

Photocatalysis is a well-known oxidative process in which reactive oxygen species (ROS), mainly HO•, are generated due to the photo-activation of a semiconductor. The photocatalysis with 10-MG1-Ti in presence of oxygen was not capable of generating enough oxidative species to produce an efficient oxidation of the target pollutant (30% of cotinine removal). Consequently, more oxidizing systems adding ozone were assessed.

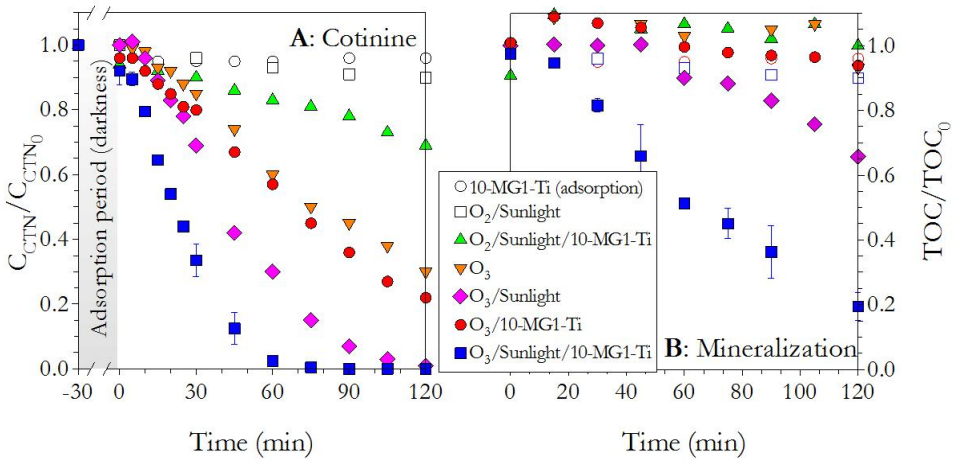

Figure 7.4. Comparison of different technologies combining simulated sunlight, ozone and the photocatalyst 10-MG1-Ti in the oxidation (A) and mineralization (B) of cotinine (CTN). Experimental conditions: V=500 mL; pH_0=free (initially 5.7±0.4); Q_{GAS}=30 L·h^{-1}; $C_{O3inlet}$=10 mg·L^{-1} (if required); $C_{10\text{-}MG1\text{-}Ti}$=0.5 g·L^{-1} (if required); $C_{CTN,o}$=10 mg·L^{-1}.

Cotinine is a recalcitrant-to-oxidation organic with very low reactivity towards molecular ozone [49]. Actually, the second-order rate constant is estimated between 0.5-3.8 M^{-1}·s^{-1} in a pH range within 4-9 [45]. That is the reason why hydroxyl radical plays an important role in ozone-based systems for this kind of recalcitrant organic [49]. As can be appreciated in **Figure 7.4**, single ozonation was capable to remove almost 70% of CTN in 2 h under the experimental conditions tested. However, no mineralization was observed. Catalytic ozonation (O_3+10-MG1-Ti) poorly improved the results (removal circa 80% in 2 h). In fact, poor enhancement on the organic micropollutant removal rate is usually registered in catalytic ozonation using titania [26,50,51]. When combining ozone and radiation, higher efficiencies in the degradation of CTN were observed. A complete degradation of cotinine was observed after 75 min of photocatalytic ozonation (radiation > 300 nm). Furthermore, this technology demonstrated to be the most efficient not only in the oxidation rate and extent of CTN, but also in the mineralization extent reached that was almost 80% in 2 h. Photolytic ozonation reached 30% of TOC removal whereas the rest of oxidative systems were inefficient to further oxidize the generated byproducts. The mineralization extent registered during photocatalytic ozonation (80% of TOC elimination), suggests important oxidation of intermediates and final organic acids oxidation.

Monitoring organic acids, *i.e.* oxalic and formic acid, and nitrate (the structure of cotinine contains 2 N atoms) gave evidence of the efficiency of oxidation of the final

products (see **Figure 7.5**). Single ozonation led to a constant release of nitrate, formic and oxalic acids, this later inhibited during the first hour of oxidation. Only formic acid was detected during catalytic ozonation. The combination of ozone and radiation improved the release of formic acid and oxalic acid, diminishing also the inhibition period to 30 min. The application of photocatalytic ozonation was the most efficient process with the highest concentration of nitrate (approximately 35% of the total amount expected from the N contained in CTN molecule). It should be highlighted that no oxalic acid was registered during this process; the profile of formic acid reached a maximum at 30 min and decreased as the oxidation proceeded. Photocatalytic ozonation has been frequently reported as the most efficient system for the removal of short chain organic acids if compared to other simpler technologies involving ozone, radiation and photocatalysis [52].

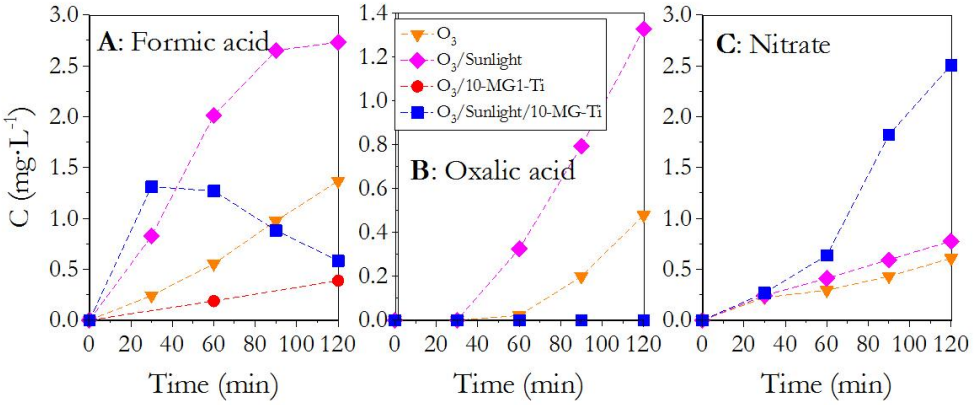

Figure 7.5. Evolution of the released formic acid (A), oxalic acid (B) and nitrate (C) during the oxidation of cotinine by means of different technologies combining simulated sunlight, ozone and the photocatalyst 10-MG1-Ti. Experimental conditions as shown in **Figure 7.4.**

The kinetic depletion of organic compounds in ozone-based systems can be described as a second-order irreversible reaction with molecular ozone and HO• as the main oxidative specie, which could be simplified to a pseudo-first order kinetics. The molar balance of a target pollutant i in the perfectly mixed semi-batch photoreactor used is:

$$-\frac{dC_i}{dt} = \left(k_{HO^\bullet,i} C_{HO^\bullet} + k_{O_3,i} C_{O_3,dis}\right) C_i \approx k_{obs} C_i \qquad (7.1)$$

where C_i, $C_{HO\cdot}$ and $C_{O3,dis}$ stand for the concentration of the target pollutant, hydroxyl radical and dissolved ozone, respectively; $k_{HO,i}$ and k_{O3} are the respective second-order

rate constant of the reaction of the target pollutant with hydroxyl radical and molecular ozone; and k_{Obs} the pseudo-first order rate constant of the process.

The presence of radiation or catalysts in ozonation involves extra promotion routes for the generation of multiple ROS, primarily HO• [53,54]. Direct reaction of CTN with molecular ozone can be disregarded and the contribution of photolysis with the radiation used is negligible (see **Figure 7.4**). Therefore, it can be considered that CTN is exclusively oxidized by the action of hydroxyl radicals. Thus, different tools can be used to evaluate the ability of each technology to decompose dissolved ozone into hydroxyl radicals.

The representation of the HO• exposure *versus* time provides information about the evolution of the concentration of HO•. The exposure HO• can be estimated by the following expression:

$$\int C_{HO^\bullet} \cdot dt = \frac{\ln\left(C_{i_0} / C_i\right)}{k_{HO^\bullet,i}} \qquad (7.2)$$

The temporal evolution of HO• concentration can be calculated by numerical derivation of the represented curve for Equation 7.2.

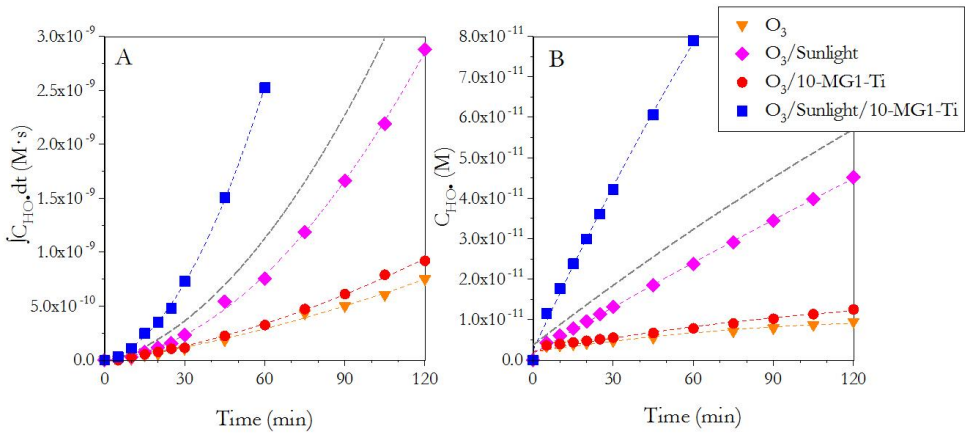

Figure 7.6. Evolution with time of the hydroxyl radical exposure (A) and concentration (B) for different technologies combining simulated sunlight, ozone and the photocatalyst 10-MG1-Ti. Experimental conditions as shown in **Figure 7.4.** Dashed grey line: sum of photolytic and catalytic ozonation.

Figure 7.6(A) depicts the HO• exposure *vs* time for the tested technologies. As observed, the combination of photocatalysis and ozone improved the production of

hydroxyl radical if compared to catalytic or photolytic ozonation. **Figure 7.6(B)** proves the synergistic effect of photocatalytic ozonation process which cannot be explained by the contribution of simpler technologies, i.e. photolytic ozonation and catalytic ozonation (see dashed grey line in **Figure 7.6**).

The yield of $HO^{\bullet}$ production respect to the dissolved ozone exposure can be estimated by calculating the hydroxyl radical ratio to dissolve ozone through the R_{ct} concept [55]:

$$R_{ct} = \frac{\int C_{HO^{\bullet}} dt}{\int C_{O_3,dis} dt} = \frac{1}{k_{HO^{\bullet},i}} \left[\frac{\ln\left(C_{i,o}/C_i\right)}{\int C_{O_3,dis} dt} - k_{O_3,i} \right] \approx \frac{\ln\left(C_{i,o}/C_i\right)}{k_{HO^{\bullet},i} \int C_{O_3,dis} dt} \quad (7.3)$$

Equation 7.3 is usually simplified disregarding the direct reaction between the organic pollutant and molecular ozone if the second-order rate constant for the direct reaction is low or negligible, which is the case of CTN. Monitoring the concentration of dissolved ozone *versus* time, it is possible to deduce the R_{ct} value from Equation 7.3 by quantifying the ozone exposure numerically.

From **Figure 7.7(A)**, a variation of R_{ct} values in two phases during photolytic, photocatalytic, and in minor extent, catalytic ozonation can be observed. The variation of R_{ct} has been frequently reported due to changes in initial O_3 dose, pH, temperature, alkalinity, presence of organic matter, etc. No changes in R_{ct} where registered during the use of ozone alone. As shown in **Table 7.3**, R_{ct} values follows the order photocatalytic ozonation $\gg$ photolytic ozonation $>$ catalytic ozonation~single ozonation. This behavior also provides evidence of a higher production of hydroxyl radical during photocatalytic ozonation. Actually, if compared to single ozonation, photocatalytic ozonation registered 13-38 folded R_{ct}, during the first and second stage, respectively.

Alternatively to R_{ct} parameter, a new concept was proposed by Kwon et al. [56] as the exposure of hydroxyl radical per O_3 consumed (transferred ozone dose, TOD), $R_{HO^{\bullet},O3}$, that can be quantified for compounds that reacts slow with molecular ozone as:

$$R_{HO^{\bullet},O_3} = \frac{\int C_{HO^{\bullet}} dt}{TOD} \approx \frac{\ln\left(C_{i,o}/C_i\right)}{k_{HO^{\bullet},i} TOD} \quad (7.4)$$

TOD stands the ozone consumption, understood as the ozone that is transferred to the liquid bulk per unit of volume:

$$TOD=\frac{1}{V}\int\left(F_{O_3,inlet}-F_{O_3,outlet}\right)dt=\frac{Q_{GAS}}{V}\int\left(C_{O_3,inlet}-C_{O_3,outlet}\right)dt \quad (7.5)$$

where V is the liquid volume of the semi-batch reactor, F_{O3} means the molar flow rate in the inlet or outlet of the reactor (respectively), Q_{GAS} is the volumetric flow rate of the O_2-O_3 gas mixture and C_{O3} the O_3 concentration in the gas phase. A monitoring of the ozone concentration before and after passing the liquid phase allows to quantify the accumulated TOD by resolving Equation (7.5) numerically.

$R_{HO\cdot,O3}$ was proposed as an alternative to R_{ct} to model ozonation process in one unique stage, in an attempt of avoiding the determination of the time in which R_{ct} changes, which strongly depends on the operational conditions and design of the setup [56]. However, as recently reported by Cruz-Alcalde et al. [57], the graphical representation of Equation (7.4) (see **Figure 7.7(B)** and **7(B')**) led to 2 clearly differentiated stages of $R_{HO\cdot,O3}$ during photolytic and photocatalytic ozonation, repeating the behavior observed in R_{ct}. Considering the physical meaning of this concept, $R_{HO\cdot,O3}$ informs about the production of hydroxyl radical per unit of ozone consumed according to a mass balance in the gas phase. From a system comparison, photocatalytic ozonation demonstrated to be an enhanced oxidation technology if compared to the simpler photolytic, catalytic or single ozonation. **Table 7.3** summarizes the different values appreciated for all the systems in their two stages, or just one. The application of photocatalytic ozonation led to 3.3-7.6 times higher $R_{HO\cdot,O3}$ if compared to single ozonation. The second most efficient system, photolytic ozonation, improved folded $R_{HO\cdot,O3}$ parameter 1.9-5.6 times if compared to single ozonation.

Table 7.3 also includes the parameter η, defined as the ratio of the hydroxyl radical rate versus the direct reaction rate:

$$\eta=\frac{k_{HO\cdot,i}C_{HO\cdot}C_i}{k_{O_3,i}C_{O_3}C_i}=\frac{k_{HO\cdot,i}}{k_{O_3,i}}R_{ct} \quad (7.6)$$

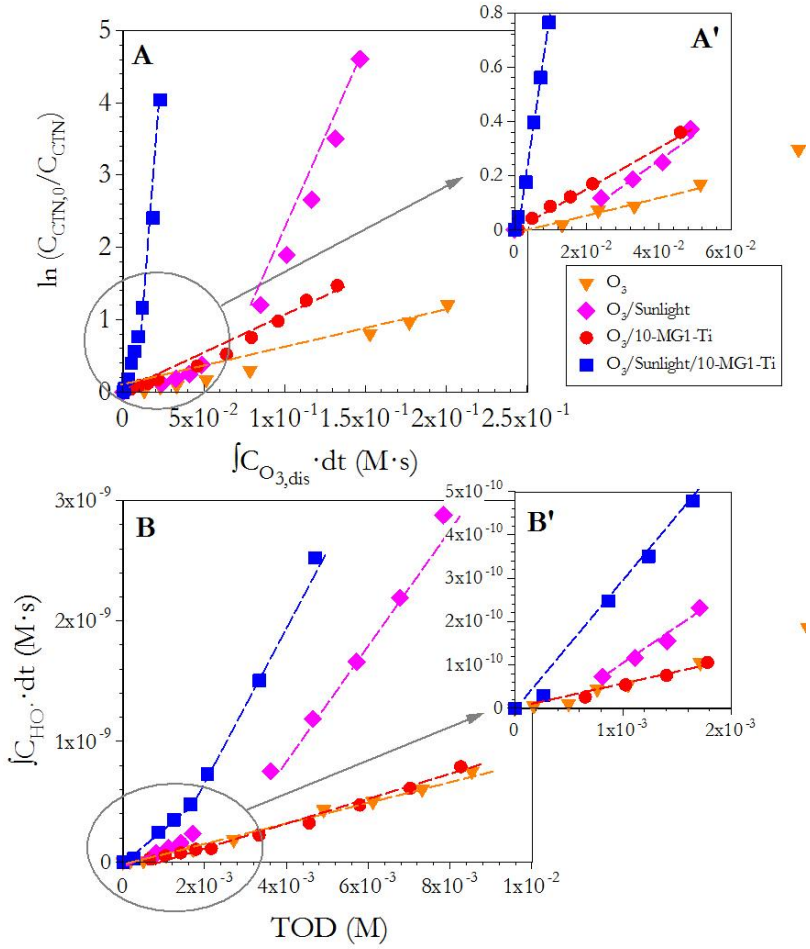

Figure 7.7. Graphical representation of R_{ct} (A) and $R_{HO^\bullet,O3}$ (B) values according to Equations (7.3) and (7.4), respectively, during different ozone-based oxidation systems for cotinine abatement. Experimental conditions as shown in **Figure 7.4.**

Table 7.3. Photocatalytic (10-MG1-Ti) ozonation derived systems. Modelled parameters of the processes: k_{Obs}, R_{ct}, $R_{HO^\bullet,O3}$ and η

System	k_{Obs}, h^{-1} (R^2)	R_{ct} (R^2)		$R_{HO^\bullet,O3}$, s (R^2)		η
		1st phase	2nd phase	1st phase	2nd phase	
Photocatalysis (O_2/Sunlight/10-MG1-Ti)	0.126 (0.997)	- - -		- - -		- - -
Single ozonation (O_3)	0.595 (0.993)	3.88×10^{-9} (0.99)		8.85×10^{-8} (0.99)		4.61
Catalytic ozonation (O_3/10-MG1-Ti)	0.596 (0.999)	4.43×10^{-9} (0.97)	8.38×10^{-9} (0.99)	9.86×10^{-8} (0.98)		9.20
Photolytic ozonation (O_3/Sunlight)	1.031 (0.996)	3.73×10^{-9} (0.98)	3.71×10^{-8} (0.99)	1.73×10^{-7} (0.97)	4.96×10^{-7} (0.99)	38.4
Photocatalytic ozonation (O_3/Sunlight/10-MG1-Ti)	2.356 (0.998)	5.14×10^{-8} (0.99)	1.47×10^{-7} (0.97)	2.99×10^{-7} (0.96)	6.69×10^{-7} (0.99)	63.3

The second-order rate constant for the reaction of cotinine with hydroxyl radical and molecular ozone were respectively 1.6×10^9 $M^{-1} \cdot s^{-1}$ and 1.282 $M^{-1} \cdot s^{-1}$ at pH 6, according to a previous work [58].

From the results in **Table 7.3** it can be observed that ozone-based processes are stronger oxidation systems than photocatalysis by itself, with photocatalytic ozonation as the most efficient process. In fact, the pseudo-first order rate constant of photocatalytic ozonation was almost 17-folded if compared to photocatalysis, or 8 times higher than single ozonation. The sum of these two processes does not explain the higher k_{Obs} value obtained for the combined technology. A synergism [59] of almost 70% is appreciated. Furthermore, the R_{ct} and $R_{HO^{\cdot},O3}$ values also evidenced the higher production of $HO^{\cdot}$ in the order photocatalytic ozonation > photolytic ozonation > catalytic ozonation~ ozonation. Finally, the assessment of the importance of radical pathway (η) also evidenced a considerably higher importance of $HO^{\cdot}$ in photolytic and, specially, photocatalytic ozonation processes. Consequently, photocatalytic ozonation process was the selected technology for further research.

7.3.3. PHOTOCATALYTIC OZONATION WITH Y-MGX-Ti. INFLUENCE OF TITANIA AND GRAPHENE/MAGNETITE RATIO IN THE ACTIVITY

The influence of titania percentage (100-Y), considering the support MG1 (weight ratio magnetite:graphene 1:1), was first evaluated. Different percentages of titania MG1 were selected, in order to increase the magnetite content and, therefore, to improve the separation properties of the initial selected 10-MG1-Ti. Also, for comparison purposes a non-magnetic TiO_2, synthesized following the same procedure, was included. **Figure 7.8** depicts the evolution with time of CTN normalized concentration and mineralization.

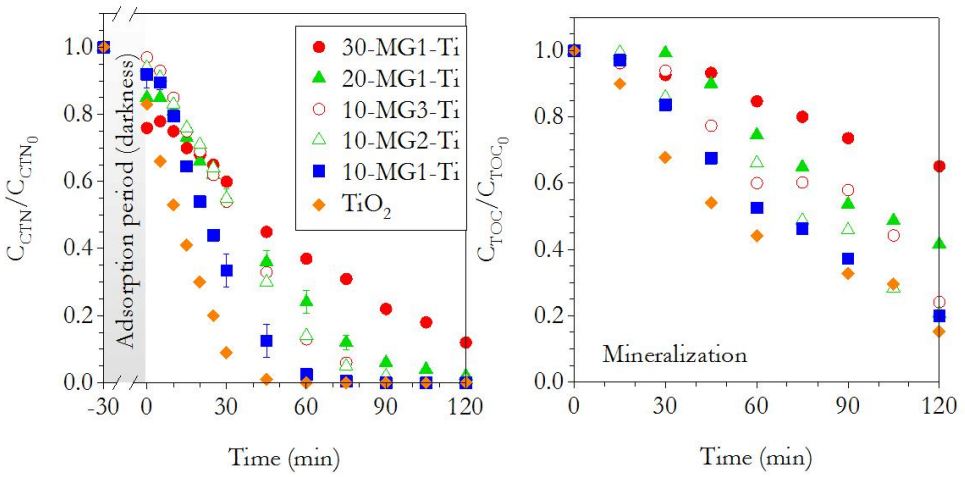

Figure 7.8. Titania and magnetite ratio influence on the photocatalytic ozonation of cotinine (CTN) using Y-MGX-Ti photocatalysts. Normalized evolution of cotinine (A), observed pseudo-first order rate constant vs the proportion of titania in the solid (B) and mineralization evolution (C). Experimental conditions: V=500 mL; pH=free (initially 5.8±0.5); Q_{GAS}=30 L·h^{-1}; $C_{O3inlet}$=10 mg·L^{-1}; $C_{photocatalyst}$=0.5 g·L^{-1} (0.4 g·L^{-1} for TiO_2 series); $C_{CTN,o}$=10 mg·L^{-1}.

As observed in **Figure 7.8**, TiO_2 is the active species responsible for the photocatalytic activity. An analysis of the k_{Obs} *versus* the amount of titania present in the solid, according to the characterization results presented in the previous section, gives evidence of this behavior. The higher amount of TiO_2, the better kinetic rate performance of CTN removal. The k_{Obs}, R_{ct}, $R_{HO\cdot,O3}$ and importance of hydroxyl radical pathway (η) were assessed for the different photocatalytic solids (see **Table 7.4**). In comparison with the non-magnetic photocatalyst, the decrease of titania using MG1 support reduced the photocatalytic activity of the solid. On the other hand, when the percentage of titania was fixed to 90%, and the ratio of magnetite:graphene increased to 2:1 and 3:1 in the support, a negative effect was also registered. However, the photocatalyst 10-MG1-Ti performed acceptable photocatalytic results with still high recovery when applying an external magnetic field. Higher percentages of titania in MG1 were discarded due to the poor magnetic properties, which negatively impacted in the separation ability. Mineralization efficiency was also proportional to the amount of titania in the photocatalysts. Actually, the following mineralization efficiency was monitored: bare TiO_2 > 10-MG1-Ti > 20-MG1-Ti > 30-MG1-Ti.

Table 7.4. Photocatalytic ozonation of CTN with Y-MGX-Ti: k_{Obs}, R_{ct} ratio and η

Photocatalyst	k_{Obs}, h^{-1} (R^2)	R_{ct} (R^2)		$R_{HO^{\bullet},O3}$, s (R^2)		η
		1st phase	2nd phase	1st phase	2nd phase	
10-MG1-Ti	2.356 (0.998)	5.14×10^{-8} (0.99)	1.47×10^{-7} (0.97)	2.99×10^{-7} (0.96)	6.69×10^{-7} (0.99)	63.3
20-MG1-Ti	1.003 (0.999)	3.06×10^{-8} (0.99)	5.31×10^{-8} (0.99)	2.40×10^{-7} (0.99)		26.8
30-MG1-Ti	0.928 (0.995)	1.36×10^{-8} (0.9)	2.60×10^{-8} (0.99)	1.21×10^{-7} (0.99)		19.0
10-MG2-Ti	1.018 (0.997)	2.49×10^{-8} (0.99)	6.91×10^{-8} (0.97)	$1.80 \cdot 10^{-7}$ (0.98)	4.74×10^{-7} (0.99)	31.1
10-MG3-Ti	1.334 (0.989)	2.94×10^{-8} (0.99)	7.01×10^{-8} (0.97)	1.85×10^{-7} (0.99)	5.37×10^{-7} (1.00)	38.2
TiO_2	3.018 (0.995)	8.89×10^{-8} (0.99)	2.09×10^{-7} (1.00)	3.23×10^{-7} (0.99)	1.20×10^{-6} (1.00)	108.8

7.3.4. STABILITY AND REUSABILITY OF THE 10-MG1-Ti CATALYST UNDER PHOTOCATALYTIC OZONATION PROCESS

The photocatalyst 10-MG1-Ti was selected due to the highest activity of all the magnetic solids for the photocatalytic ozonation process, and also because of the reasonable magnetic properties to be recovered after the application of an external magnetic field. The reusability and activity behavior after consecutive cycles was studied by recovering the solid with the help of a magnet. **Figure 7.9** (top) depicts the evolution of the normalized cotinine concentration in each run. Also the mineralization degree after 120 min of treatment was studied (see **Figure 7.9** down right). No activity loss was recorded after 5 runs of use. Cotinine was completely removed before 90 min in all cases. The evolution of k_{Obs} in each run shows no significant catalytic loss of the solid. 81 ± 3% of mineralization degree was observed after 120 min of photocatalytic ozonation.

The leaching of iron was also studied by analyzing the concentration of total iron species in solution. **Figure 7.S5** depicts the temporal evolution of total iron release at different pH values for different titania ratios. Also, a magnetic photocatalyst without graphene and 90% of titania was prepared to elucidate the influence of graphene on the iron release. Neither the fresh 10-MG1-Ti photocatalyst nor after 5 times of reusing led to iron release up the detection limit of the spectrophotometric method (50 $\mu g \cdot L^{-1}$), at pH values of 4, 7 or 9. In absence of graphene, the release of iron was higher than the limit of detection, 90-450 $\mu g \cdot L^{-1}$ in 2 h depending on the pH. The release for this solid was lower at pH 4 < pH 9 < pH 7. Therefore, the presence of graphene minimized the release of iron improving the stability of the magnetic properties.

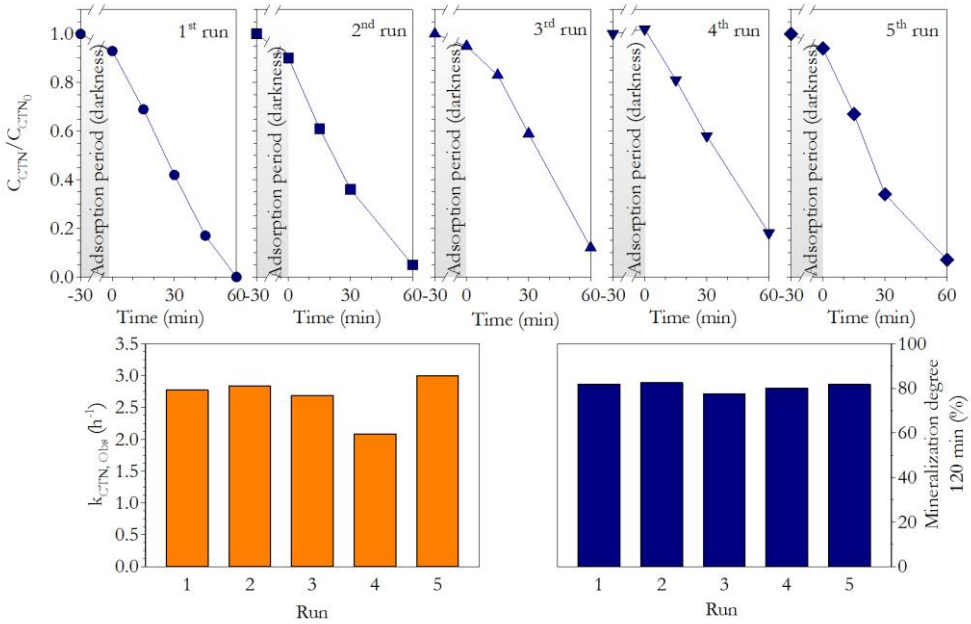

Figure 7.9. Stability study of 10-MG1-Ti under photocatalytic ozonation for the oxidation of cotinine. Experimental conditions: V=500 mL; pH=free (initially 6.2±0.3); Q_{GAS}=30 L·h^{-1}; $C_{O3inlet}$=10 mg·L^{-1}; $C_{10\text{-}MG1\text{-}Ti}$=0.5 g·L^{-1}; $C_{CTN,o}$=10 mg·L^{-1}. Top, evolution of remaining CTN normalized concentration during the recycling. Down left, pseudo-first order rate constant for CTN evolution. Down right, mineralization degree after 120 min.

From the characterization analyses, it is appreciated an important loss of carbon after the 5th reuse, and consequently a reduction on the external surface (**Table 7.2**). In addition, the hydroxylated groups in surface were oxidized into carbonyl groups (see **Table 7.2**). However, this carbon loss did not affect the activity of the catalyst nor compromise the release of iron into the solution.

7.3.5. A CASE OF STUDY: PHOTOCATALYTIC OZONATION OF A MIXTURE OF CECs IN UWW MATRIX USING MAGNETIC 10-MG1-Ti

To further test the activity of the 10-MG1-Ti catalyst in a real scenario, an effluent of an UWWTP, was used as water matrix. A total of 10 micropollutants of emerging concern (CTN, cotinine; CAF, caffeine; CPR, ciprofloxacin; MTP, metroprolol; SMX, sulfamethoxazole; DEET, *N,N*-Diethyl-*m*-toluamide; CLO, clofibric acid; BZF, bezafibrate; TSF, tritosulfuron; IBP, ibuprofen) were added at low concentration, i.e. 500 µg·L^{-1}. Different scenarios (pH and removal of inorganic carbon, IC) were tested in order to evaluate the removal of the 10 CECs and the mineralization by means of ozonation, photolytic and photocatalytic ozonation technologies. **Figure 7.10** (left subfigures) depicts the observed pseudo-first order rate constant, $k_{Obs,i}$, for the

different processes and compounds at pH 4 (**Figure 7.10(A)**), the pH of the UWW effluent, that means ~8.4 (**Figure 7.10(C)**) and after the removal of IC at the received pH (**Figure 7.10(E)**). Also, the mineralization and oxalic acid concentration evolution are presented in **Figure 7.10** (right subfigures).

The rate constant k_{Obs} has been used as a mere tool for comparison purposes and depends on the operational conditions and UWW matrix in which tests were carried out. The behavior of the CECs under the three oxidative technologies can be grouped according to their reactivity towards molecular ozone. Generally, k_{Obs} values are closely related to the direct ozone rate constant (see **Table 7.S1**). An increase of k_{Obs} was registered when applying photocatalytic ozonation for those compounds with low reactivity towards molecular ozone, i.e. direct rate constant with O_3 within the range 0.1-10 $M^{-1}\cdot s^{-1}$. This is the case of CTN, DEET, CA, TSF and IBP. These compounds are eliminated *via* hydroxyl radical reaction; therefore, the application of radiation or photocatalysis improved, to a greater or lesser extent, their rate constant (k_{Obs}) as a higher production of $HO^{\bullet}$ took place. Compounds with a moderate value for the direct reaction with ozone, that means reactivity in the order of 100-1000 $M^{-1}\cdot s^{-1}$, are removed by both direct reactions with O_3 and free radical reactions [60], competing both theoretically in the process. This is the case of CAF, BZF and MTP. For those compounds the k_{Obs} during photocatalytic ozonation is slightly higher or similar to the registered one during single ozonation or photolytic ozonation (excepting some particular case due to the complexity of the UWW matrix or errors in the operational conditions). Finally, SMX and CPR present high reactivity towards O_3 (rate constant > 10^3 $M^{-1}\cdot s^{-1}$). For these two compounds photolytic and photocatalytic ozonation improved the value of k_{Obs} if compared to O_3, specially and surprisingly in the case of sulfamethoxazole at basic pH (rate constant with O_3 4.7-5.7 10^4 $M^{-1}\cdot s^{-1}$), even though the preferential reaction pathway is the reaction with molecular O_3.

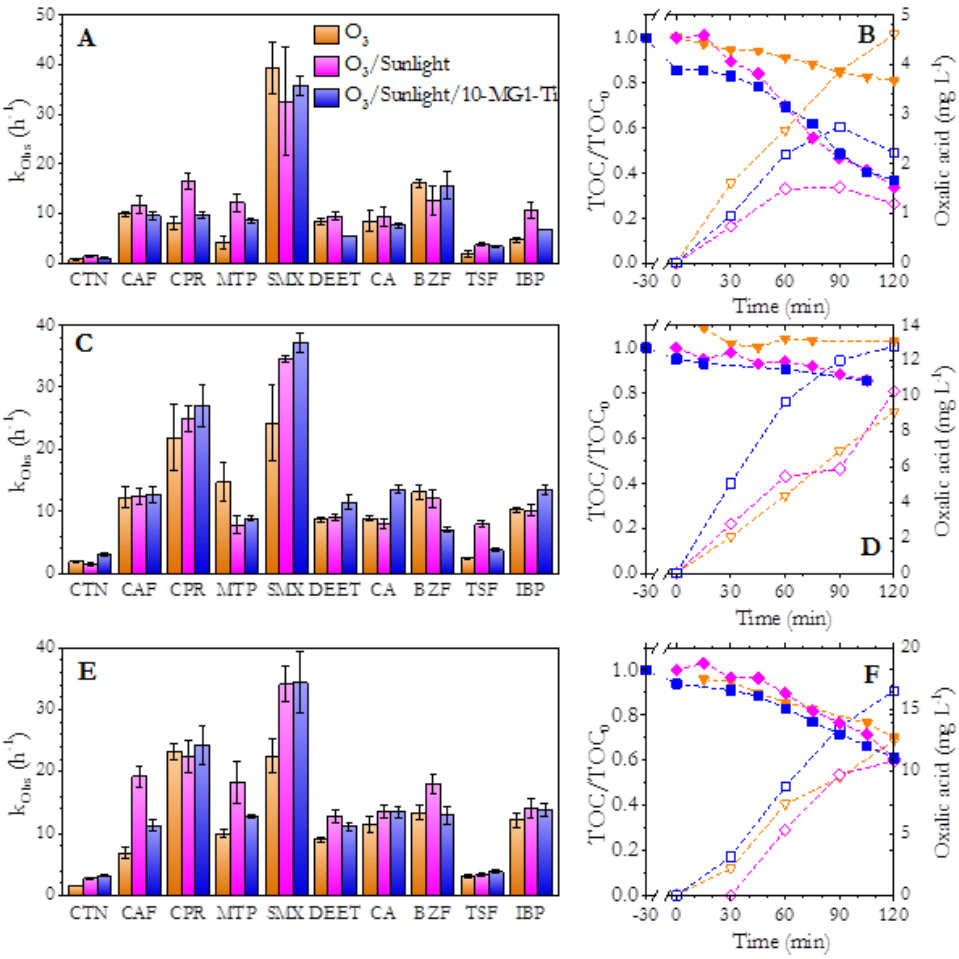

Figure 7.10. Ozonation, photolytic ozonation and photocatalytic ozonation of a mixture of 10 compounds in a secondary effluent of UWW. Experimental conditions: V=500 mL; Q_{GAS}=30 L·h^{-1}; $C_{O3inlet}$=10 mg·L^{-1}; $C_{10\text{-}MG1\text{-}Ti}$=0.5 g·L^{-1} (if required); $C_{CEC,0}$=500 µg·L^{-1} (each); H_3PO_4=6 mM (if required). Pseudo-first order rate constant for the degradation of each contaminant at pH 4 (A), natural pH with inorganic carbon (C) and natural pH without inorganic carbon (E). Mineralization (filled symbols) and evolution of oxalic (open symbols) acid at pH 4 (B), natural pH with inorganic carbon (D) and natural pH without inorganic carbon (F).

pH affects considerably ozone-based AOPs since the anion HO^- catalyzes O_3 decomposition into $HO^{\bullet}$, minimizing the improvement of other radical pathway promoters such as light or catalysts. If the results at pH 4 and pH~8.4 are compared (**Figure 7.10(A)** and **7.10(E)**); in general terms, k_{Obs} for single ozonation is lower at acidic conditions. Some compounds have a substantial change with pH due to the reactivity of the dissociated and non-dissociated species towards molecular ozone. This is the case of ciprofloxacin. This compound is highly reactive to O_3 (> 10^4 $M^{-1}\cdot s^{-1}$) at

basic pH but moderately reactive at acidic conditions (400 $M^{-1}\cdot s^{-1}$) [61]. This fact explains why the k_{Obs} was discreetly lower at pH 4 in the three systems applied.

Carbonates, which are a well-known HO• scavenger [62], were removed by stripping with phosphoric acid, air bubbling and pH was restored to the UWW received value. As shown in **Figure 7.10(C)** and **7.10(E)**, the presence of inorganic carbon does not necessarily mean a negative effect in terms of contaminants removal rate. Only in the case of DEET, CA acid BZF and IBP the removal of IC content was translated into higher k_{Obs} values, regarding the technology applied (photocatalytic, photolytic or single ozonation).

By analyzing the evolution of TOC and oxalic acid, different behavior was observed with the different technologies at the conditions analyzed. Thus, photocatalytic ozonation was the most efficient of all the technologies, especially at pH 4, as 70% of TOC removal was reached in 2 h. At the natural pH of the UWW effluent only 40% of mineralization after 2 h was recorded and no differences between the addition or not of radiation is observed. From all the organic acids released during the oxidative treatments; i.e. formic, acetic, pyruvic, succinic and oxalic acids, the evolution of oxalic acid concentration deserves special attention since this organic is recalcitrant to the direct reaction with molecular ozone ($< 0.04\ M^{-1}\cdot s^{-1}$ [63]). At the natural pH of the UWW effluent (~8.4), photocatalytic ozonation lead to the highest release of oxalic acid. Besides, if the total amount of TOC regarding the carboxylic acid detected is analyzed, photocatalytic ozonation led to a higher conversion of the TOC (not shown), which claims an enhancement in the effectiveness. It is noteworthy the lack of a really negative effect of IC in the formation of oxalic acid, as can be observed in **Figure 7.10(D)** and **7.10(F)**. Under acidic conditions, where the highest rate of mineralization was appreciated, oxalic acid was accumulated during single ozonation; however, photolytic and photocatalytic ozonation were capable of oxidizing it after reaching a maximum in concentration.

7.4. CONCLUSIONS

Commercial graphene was successfully applied as a support for titania and magnetite particles with high photocatalytic activity in presence of ozone and magnetic properties for the solid separation after the treated aqueous solution. The photocatalytic ozonation process proved to be more efficient if compared to simpler technologies (photolytic, catalytic or single ozonation) applied to the degradation of a model pollutant recalcitrant to the direct reaction with molecular ozone, i.e. cotinine. From the analysis of diverse kinetic parameters ($HO^{\bullet}$ exposure vs time, R_{ct} and $R_{HO^{\bullet},O3}$ ratios), a synergistic effect in the production of hydroxyl radicals for the combination of ozone and photocatalysis was registered. The study of the influence of magnetic-graphene: titania ratio on the photocatalytic activity suggests that titania particles are responsible for the photocatalytic activity; with the highest activity registered in the case of bare titania.

Characterization of the solid proved the presence of titania and magnetite particles homogeneously distributed in the graphene surface, acting graphene as a carbonaceous support. Although the presence of magnetic graphene compromised the photoactivity of the solid (it was lower than bare titania), this loss of activity was balanced by the incorporation of magnetic properties that facilitate the recovery after the treatment. The attachment of magnetic particles in graphene remained stable enough after 5 reuses with no appreciable iron leaching in the solution and no significant loss of photocatalytic activity.

The study was extended to a real scenario for the oxidation of a mixture of 10 well-known micropollutants of emerging concern in a real water matrix from a local wastewater treatment plant. The application of photocatalytic ozonation with the magnetic graphene-based titania successfully oxidized the pollutants with an increase in the pseudo-first order rate constant of recalcitrant to ozonation compounds; and also the mineralization extent if compared to simpler technologies.

REFERENCES

[1] B. Petrie, R. Barden, B. Kasprzyk-Hordern, "A review on emerging contaminants in wastewaters and the environment: Current knowledge, understudied areas and recommendations for future monitoring" *Water Res.* 72 (**2015**) 3–27.

[2] A. Gogoi, P. Mazumder, V.K. Tyagi, G.G. Tushara Chaminda, A.K. An, M. Kumar, "Occurrence and fate of emerging contaminants in water environment: A review" *Groundw. Sustain. Dev.* 6 (**2018**) 169–180.

[3] S. Fekadu, E. Alemayehu, R. Dewil, B. Van der Bruggen, "Pharmaceuticals in freshwater aquatic environments: A comparison of the African and European challenge" *Sci. Total Environ.* 654 (**2019**) 324–337.

[4] M. Gavrilescu, K. Demnerová, J. Aamand, S. Agathos, F. Fava, "Emerging pollutants in the environment: present and future challenges in biomonitoring, ecological risks and bioremediation" *N. Biotechnol.* 32 (**2015**) 147–156.

[5] E. Nilsen, K.L. Smalling, L. Ahrens, M. Gros, K.S.B. Miglioranza, Y. Picó, H.L. Schoenfuss, "Critical review: Grand challenges in assessing the adverse effects of contaminants of emerging concern on aquatic food webs" *Environ. Toxicol. Chem.* 38 (**2019**) 46–60.

[6] A. Zarei-Baygi, M. Harb, P. Wang, L.B. Stadler, A.L. Smith, "Evaluating antibiotic resistance gene correlations with antibiotic exposure conditions in anaerobic membrane bioreactors" *Environ. Sci. Technol.* 53 (**2019**) 3599–3609.

[7] A. Christou, A. Agüera, J.M. Bayona, E. Cytryn, V. Fotopoulos, D. Lambropoulou, C.M. Manaia, C. Michael, M. Revitt, P. Schröder, D. Fatta-Kassinos, "The potential implications of reclaimed wastewater reuse for irrigation on the agricultural environment: The knowns and unknowns of the fate of antibiotics and antibiotic resistant bacteria and resistance genes – A review" *Water Res.* 123 (**2017**) 448–467.

[8] I. Michael, L. Rizzo, C.S. McArdell, C.M. Manaia, C. Merlin, T. Schwartz, C. Dagot, D. Fatta-Kassinos, "Urban wastewater treatment plants as hotspots for the release of antibiotics in the environment: A review" *Water Res.* 47 (**2013**) 957–995.

[9] P. Krzeminski, M.C. Tomei, P. Karaolia, A. Langenhoff, C.M.R. Almeida, E. Felis, F. Gritten, H.R. Andersen, T. Fernandes, C.M. Manaia, L. Rizzo, D. Fatta-Kassinos, "Performance of secondary wastewater treatment methods for the removal of contaminants of emerging concern implicated in crop uptake and antibiotic resistance spread: A review" *Sci. Total Environ.* 648 (**2019**) 1052–1081.

[10] A.R. Ribeiro, O.C. Nunes, M.F.R. Pereira, A.M.T. Silva, "An overview on the advanced oxidation processes applied for the treatment of water pollutants defined in the recently launched Directive 2013/39/EU" *Environ. Int.* 75 (**2015**) 33–51.

[11] I. Gültekin, N.H. Ince, "Synthetic endocrine disruptors in the environment and water remediation by advanced oxidation processes" *J. Environ. Manage.* 85 (**2007**) 816–832.

[12] M.A. Oturan, J.-J. Aaron, "Advanced oxidation processes in water/wastewater treatment: principles and applications. A review" *Crit. Rev. Environ. Sci. Technol.* 44 (**2014**) 2577–2641.

[13] I.C. Iakovides, I. Michael-Kordatou, N.F.F. Moreira, A.R. Ribeiro, T. Fernandes, M.F.R. Pereira, O.C. Nunes, C.M. Manaia, A.M.T. Silva, D. Fatta-Kassinos, "Continuous ozonation of urban wastewater: Removal of antibiotics, antibiotic-resistant Escherichia coli and antibiotic resistance genes and phytotoxicity" *Water Res.* 159 (**2019**) 333–347.

[14] T.E. Agustina, H.M. Ang, V.K. Vareek, "A review of synergistic effect of photocatalysis and ozonation on wastewater treatment" *J. Photochem. Photobiol. C Photochem. Rev.* 6 (**2005**) 264–273.

[15] V. Augugliaro, M. Litter, L. Palmisano, J. Soria, "The combination of heterogeneous photocatalysis with chemical and physical operations: A tool for improving the photoprocess performance" *J. Photochem. Photobiol. C Photochem. Rev.* 7 (**2006**) 127–144.

[16] F.J. Beltrán, A. Rey, "Solar or UVA-visible photocatalytic ozonation of water contaminants" *Molecules.* 22 (**2017**) 1177.

[17] M. Mehrjouei, S. Müller, D. Möller, "A review on photocatalytic ozonation used

for the treatment of water and wastewater" *Chem. Eng. J.* 263 (**2015**) 209–219.

[18] J. Xiao, Y. Xie, H. Cao, "Organic pollutants removal in wastewater by heterogeneous photocatalytic ozonation" *Chemosphere*. 121 (**2015**) 1–17.

[19] N. Serpone, "Is the band gap of pristine TiO_2 narrowed by anion- and cation-doping of titanium dioxide in second-generation photocatalysts?" *J. Phys. Chem. B*. 110 (**2006**) 24287–24293.

[20] E.M. Rodríguez, A. Rey, E. Mena, F.J. Beltrán, "Application of solar photocatalytic ozonation in water treatment using supported TiO_2" *Appl. Catal. B Environ.* (**2019**) 237–245.

[21] M.A. Lazar, S. Varghese, S.S. Nair, "Photocatalytic water treatment by titanium dioxide: Recent updates" *Catalysts*. 2 (**2012**) 572–601.

[22] N.M. Mahmoodi, "Photocatalytic ozonation of dyes using copper ferrite nanoparticle prepared by co-precipitation method" *Desalination*. 279 (**2011**) 332–337.

[23] N.M. Mahmoodi, M. Bashiri, S.J. Moeen, "Synthesis of nickel–zinc ferrite magnetic nanoparticle and dye degradation using photocatalytic ozonation" *Mater. Res. Bull.* 47 (**2012**) 4403–4408.

[24] L. Ciccotti, L.A.S. do Vale, T.L.R. Hewer, R.S. Freire, "Fe_3O_4 @TiO_2 preparation and catalytic activity in heterogeneous photocatalytic and ozonation processes" *Catal. Sci. Technol.* 5 (**2015**) 1143–1152.

[25] A. Rey, D.H. Quiñones, P.M. Álvarez, F.J. Beltrán, P.K. Plucinski, "Simulated solar-light assisted photocatalytic ozonation of metoprolol over titania-coated magnetic activated carbon" *Appl. Catal. B Environ.* 111–112 (**2012**) 246–253.

[26] D.H. Quiñones, A. Rey, P.M. Álvarez, F.J. Beltrán, P.K. Plucinski, "Enhanced activity and reusability of TiO_2 loaded magnetic activated carbon for solar photocatalytic ozonation" *Appl. Catal. B Environ.* 144 (**2014**) 96–106.

[27] L. Yu, D. Wang, D. Ye, "Solar photocatalytic ozonation of emerging contaminants detected in municipal wastewater treatment plant effluents by magnetic MWCNTs/TiO_2 nanocomposites" *RSC Adv.* 5 (**2015**) 96896–96904.

[28] P.M. Álvarez, D.H. Quiñones, I. Terrones, A. Rey, F.J. Beltrán, "Insights into the removal of terbuthylazine from aqueous solution by several treatment methods" *Water Res.* 98 (**2016**) 334–343.

[29] S. Chowdhury, R. Balasubramanian, "Recent advances in the use of graphene-family nanoadsorbents for removal of toxic pollutants from wastewater" *Adv. Colloid Interface Sci.* 204 (**2014**) 35–56.

[30] J. Xiao, Y. Xie, H. Cao, Y. Wang, Z. Guo, Y. Chen, "Towards effective design of active nanocarbon materials for integrating visible-light photocatalysis with ozonation" *Carbon N. Y.* 107 (**2016**) 658–666.

[31] G. Liao, D. Zhu, J. Zheng, J. Yin, B. Lan, L. Li, "Efficient mineralization of bisphenol A by photocatalytic ozonation with TiO2-graphene hybrid" *J. Taiwan Inst. Chem. Eng.* 67 (**2016**) 300–305.

[32] M. Sheydaei, H.R.K. Shiadeh, B. Ayoubi-Feiz, R. Ezzati, "Preparation of nano N-TiO_2/graphene oxide/titan grid sheets for visible light assisted photocatalytic ozonation of cefixime" *Chem. Eng. J.* 353 (**2018**) 138–146.

[33] M. Checa, M. Figueredo, A. Aguinaco, F.J. Beltrán, "Graphene oxide/titania photocatalytic ozonation of primidone in a visible LED photoreactor" *J. Hazard. Mater.* 369 (**2019**) 70–78.

[34] L. Lian, S. Yan, B. Yao, S.-A. Chan, W. Song, "Photochemical transformation of nicotine in wastewater effluent" *Environ. Sci. Technol.* 51 (**2017**) 11718–11730.

[35] J. Chen, A.K. Venkatesan, R.U. Halden, "Alcohol and nicotine consumption trends in three U.S. communities determined by wastewater-based epidemiology" *Sci. Total Environ.* 656 (**2019**) 174–183.

[36] R. Kumar, B. Tscharke, J. O'Brien, J.F. Mueller, C. Wilkins, L.P. Padhye, "Assessment of drugs of abuse in a wastewater treatment plant with parallel secondary wastewater treatment train" *Sci. Total Environ.* 658 (**2019**) 947–957.

[37] J. Antonio Baz-Lomba, S. Salvatore, E. Gracia-Lor, R. Bade, S. Castiglioni, E. Castrignanò, A. Causanilles, F. Hernandez, B. Kasprzyk-Hordern, J. Kinyua, A.-K. Mccall, A. Van Nuijs, C. Ort, B.G. Plósz, P. Ramin, M. Reid, N.I. Rousis, Y. Ryu, P. De Voogt, J. Bramness, K. Thomas, "Comparison of pharmaceutical,

illicit drug, alcohol, nicotine and caffeine levels in wastewater with sale, seizure and consumption data for 8 European cities" *BMC Public Health*. 16 (**2016**) 1035.

[38] M. Huerta-Fontela, M.T. Galceran, J. Martin-Alonso, F. Ventura, "Occurrence of psychoactive stimulatory drugs in wastewaters in north-eastern Spain" *Sci. Total Environ.* 397 (**2008**) 31–40.

[39] M. Cao, P. Wang, Y. Ao, C. Wang, J. Hou, J. Qian, "Photocatalytic degradation of tetrabromobisphenol A by a magnetically separable graphene-TiO_2 composite photocatalyst: Mechanism and intermediates analysis" *Chem. Eng. J.* (**2015**).

[40] J. Tauc, "Optical properties and electronic structure of amorphous Ge and Si" *Mater. Res. Bull.* 3 (**1968**) 37–46.

[41] R.R. Solís, O. Gimeno, F.J. Rivas, F.J. Beltrán, "Simulated solar driven photolytic ozonation for the oxidation of aqueous recalcitrant-to-ozone tritosulfuron. Transformation products and toxicity" *J. Environ. Manage.* 233 (**2019**) 513–522.

[42] H. Bader, J. Hoigné, "Determination of ozone in water by the indigo method" *Water Res.* 15 (**1981**) 449–456.

[43] L. Escobar-Alarcón, M.E. Espinosa-Pesqueira, D.A. Solis-Casados, J. Gonzalo, J. Solis, M. Martinez-Orts, E. Haro-Poniatowski, "Two-dimensional carbon nanostructures obtained by laser ablation in liquid: effect of an ultrasonic field" *Appl. Phys. A.* 124 (**2018**) 124–141.

[44] Y. Hao, Y. Wang, L. Wang, Z. Ni, Z. Wang, R. Wang, C.K. Koo, Z. Shen, J.T.L. Thong, "Probing layer number and stacking order of few-layer graphene by Raman spectroscopy" *Small.* 6 (**2010**) 195–200.

[45] R. Al-Gaashani, A. Najjar, Y. Zakaria, S. Mansour, M.A. Atieh, "XPS and structural studies of high quality graphene oxide and reduced graphene oxide prepared by different chemical oxidation methods" *Ceram. Int.* 45 (**2019**) 14439–14448.

[46] A. Tayel, A. Ramadan, O. El Seoud, A. Tayel, A.R. Ramadan, O.A. El Seoud, "Titanium dioxide/graphene and titanium dioxide/graphene oxide

nanocomposites: Synthesis, characterization and photocatalytic applications for water decontamination" *Catalysts*. 8 (**2018**) 491.

[47] L. de Oliveira Pereira, I. Marques Sales, L. Pereira Zampiere, S. Silveira Vieira, I. do Rosário Guimarães, F. Magalhães, "Preparation of magnetic photocatalysts from TiO_2, activated carbon and iron nitrate for environmental remediation" *J. Photochem. Photobiol. A Chem.* 382 (**2019**) 111907.

[48] G. Ersan, O.G. Apul, F. Perreault, T. Karanfil, "Adsorption of organic contaminants by graphene nanosheets: A review" *Water Res.* 126 (**2017**) 385–398.

[49] R. Rosal, A. Rodríguez, J.A. Perdigón-Melón, A. Petre, E. García-Calvo, M.J. Gómez, A. Agüera, A.R. Fernández-Alba, "Occurrence of emerging pollutants in urban wastewater and their removal through biological treatment followed by ozonation" *Water Res.* 44 (**2010**) 578–588.

[50] F.J. Beltrán, A. Aguinaco, J.F. García-Araya, A. Oropesa, "Ozone and photocatalytic processes to remove the antibiotic sulfamethoxazole from water" *Water Res.* 42 (**2008**) 3799–3808.

[51] R.R. Solís, F.J. Rivas, J.L. Pérez-Bote, O. Gimeno, "Photocatalytic ozonation of 4-chloro-2-methylphenoxyacetic acid and its reaction intermediate 4-chloro-2-methyl phenol" *J. Taiwan Inst. Chem. Eng.* 46 (**2015**) 125–131.

[52] R.R. Solís, F.J. Rivas, A. Martínez-Piernas, A. Agüera, "Ozonation, photocatalysis and photocatalytic ozonation of diuron: Intermediates identification" *Chem. Eng. J.* 292 (**2016**) 72–81.

[53] G.R. Peyton, W.H. Glaze, "Destruction of pollutants in water with ozone in combination with ultraviolet radiation. 3. Photolysis of aqueous ozone" *Environ. Sci. Technol.* 22 (**1988**) 761–767.

[54] J. Nawrocki, B. Kasprzyk-Hordern, "The efficiency and mechanisms of catalytic ozonation" *Appl. Catal. B Environ.* 99 (**2010**) 27–42.

[55] M.S. Elovitz, U. Von Gunten, "Hydroxyl radical/ozone ratios during ozonation processes. I. The R(ct) concept" *Ozone Sci. Eng.* 21 (**1999**) 239–260.

[56] M. Kwon, H. Kye, Y. Jung, Y. Yoon, J.-W. Kang, "Performance characterization and kinetic modeling of ozonation using a new method: ROH,O3 concept" *Water Res.* 122 (**2017**) 172–182.

[57] A. Cruz-Alcalde, S. Esplugas, C. Sans, "Abatement of ozone-recalcitrant micropollutants during municipal wastewater ozonation: Kinetic modelling and surrogate-based control strategies" *Chem. Eng. J.* 360 (**2019**) 1092–1100.

[58] F.J. Rivas, R.R. Solís, F.J. Beltrán, O. Gimeno, "Sunlight driven photolytic ozonation as an advanced oxidation process in the oxidation of bezafibrate, cotinine and iopamidol" *Water Res.* 151 (**2019**) 226–242.

[59] R.R. Solís, F.J. Rivas, O. Gimeno, J.L. Pérez-Bote, "Photocatalytic ozonation of clopyralid, picloram and triclopyr. Kinetics, toxicity and influence of operational parameters" *J. Chem. Technol. Biotechnol.* 91 (**2016**) 51–58.

[60] F.J. Beltrán, A. Rey, "Free radical and direct ozone reaction competition to remove priority and pharmaceutical water contaminants with single and hydrogen peroxide ozonation systems" *Ozone Sci. Eng.* 40 (**2018**) 1–15.

[61] M.C. Dodd, M.O. Buffle, U. Von Gunten, "Oxidation of antibacterial molecules by aqueous ozone: moiety-specific reaction kinetics and application to ozone-based wastewater treatment" *Environ. Sci. Technol.* 40 (**2006**) 1969–1977.

[62] J.L. Acero, U. Von Gunten, "Influence of carbonate on the ozone/hydrogen peroxide based advanced oxidation process for drinking water treatment" *Ozone Sci. Eng.* 22 (**2000**) 305–328.

[63] J. Hoigné, H. Bader, "Rate constants of reactions of ozone with organic and inorganic compounds in water — II disociating organic compounds" *Water Res.* 17 (**1983**) 185–194.

SUPPLEMENTARY MATERIAL

Magnetic graphene TiO_2-based photocatalyst for the removal of pollutants of emerging concern in water by simulated sunlight aided photocatalytic ozonation

Ana M. Chávez[1,2], Rafael R. Solís[3]*, Fernando J. Beltrán[1,2]

[1] Departamento de Ingeniería Química y Química Física, Facultad de Ciencias, Universidad de Extremadura, Avda. Elvas s/n, 06006 Badajoz (Spain)

[2] Instituto Universitario del Agua, Cambio Climático y Sostenibilidad (IACYS), Universidad de Extremadura, Avda. de la Investigación s/n, 06006 Badajoz (Spain)

[3] Department Chemical & Environmental Engineering, College of Engineering & Environmental Science (CEAS), Engineering Research Centre (ERC), University of Cincinnati, Cincinnati OH 45221-0012 (USA)

Table 7.S1. List of contaminants of emerging concern (CECs), chemical structures, HPLC conditions analysis, physical properties and chemical reactivity toward molecular ozone and hydroxyl radical.

CECs (abbreviation)	Chemical structure	HPLC analysis		Physical properties [1]		Chemical reactivity towards molecular O_3 and $HO^{\bullet}$			
		λ (nm)	Retention time (min)	pK_a	Water solubility ($mg \cdot L^{-1}$)	k_{O3} ($M^{-1} \cdot s^{-1}$)	Ref.	$k_{HO} \times 10^{-9}$ ($M^{-1} \cdot s^{-1}$)	Ref.
Cotinine (CTN)	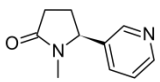	261	2.1	-	10^6 [2]	0.92 (pH 5) 1.48 (pH 7) 3.81 (pH 9)	[3]	1.6	[3]
Caffeine (CAF)	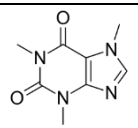	274	12.1	10.4	2.16×10^4	650 (pH 8.1)	[4]	6.9	[4]
Ciprofloxacin (CPR)	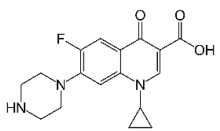	274	13.0	6.1 8.8 [5]	3×10^4	4.0×10^2 ($pH < pK_1$) 7.5×10^3 ($pK_1 < pH < pK_2$) 9.0×10^5 ($pK_2 < pH$)	[5]	4.1	[5]
Metoprolol (MTP)	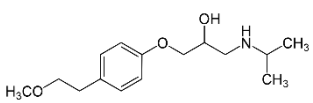	220	13.4	9.7 14.1	402	239 ($pH < pK_1$) 1.4×10^3 ($pK_1 < pH$)	[6]	6.8	[6]
Sulfamethoxazole (SMX)	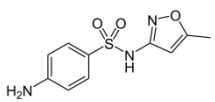	270	14.5	1.7 5.6 [5]	459	4.7×10^4 ($pK_1 < pH < pK_2$) 5.7×10^5 ($pK_2 < pH$)	[5]	5.7	[5]

Table 7.S1. (continued) List of contaminants of emerging concern (CECs), chemical structures, HPLC conditions analysis, physical properties and chemical reactivity toward molecular ozone and hydroxyl radical.

CECs (abbreviation)	Chemical structure	HPLC analysis		Physical properties [1]		Chemical reactivity towards molecular O_3 and $HO^{\bullet}$			
		λ (nm)	Retention time (min)	pK_a	Water solubility ($mg \cdot L^{-1}$)	k_{O3} ($M^{-1} \cdot s^{-1}$)	Ref.	$k_{HO} \times 10^{-9}$ ($M^{-1} \cdot s^{-1}$)	Ref.
N,n-diethyl-m-toluamide (DEET)	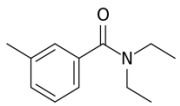	220	17.3	-	1680	0.12 (2 < pH < 9) 2.5-7.0 (T=15-40 ºC)	[7] [8]	4.9	[9]
Clofibric acid (CLO)	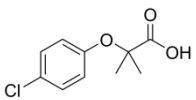	225	17.8	3.2 [10]	583 [10]	< 20 (pH 7)	[11]	6.8	[12]
Bezafibrate (BZF)	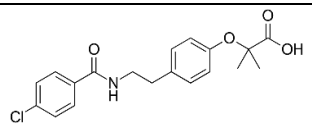	228	18.0	3.8	> 54.3 [2]	590 (pH > pK) $4.2 \cdot 10^3$ (pH 7)	[11] [13]	8.0	[12]
Tritosulfuron (TSF)	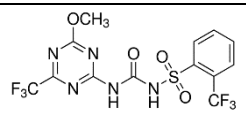	225	19.2	4.7 [10]	78.3 [10]	0.1 (pH 5) 1.9 (pH 7) 2.6 (pH 8)	[14]	2.45	[14]
Ibuprofen (IBP)	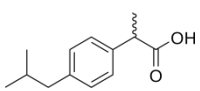	220	19.6	5.3	21	9.1 (pH 7)	[11]	7.4	[11]

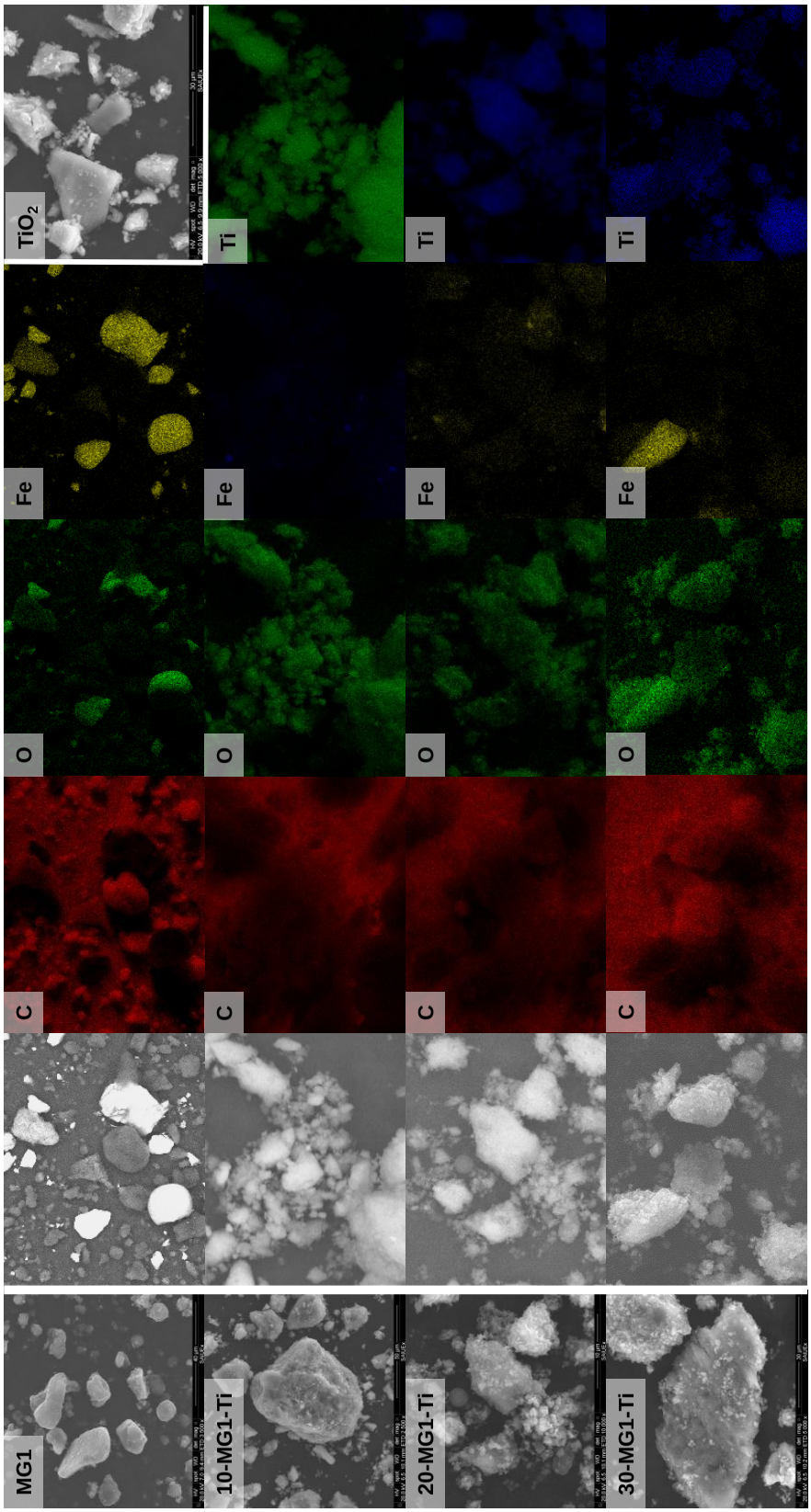

Figure 7.S1. SEM micrographs of Y-MG1-Ti photocatalysts and elemental composition EDX mapping

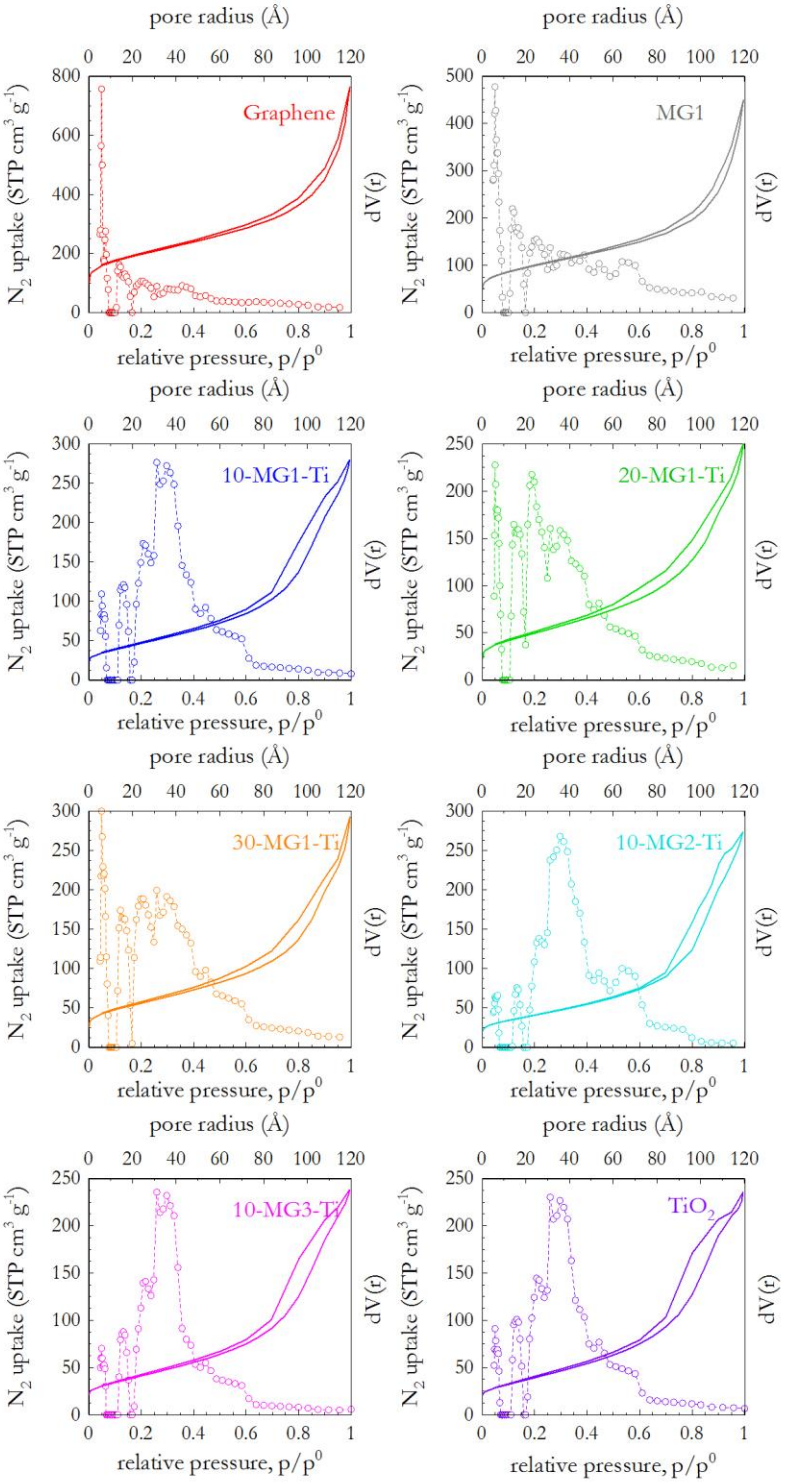

Figure 7S.2. N_2 isotherm and DFT pore size distribution of the synthesized Y-MGX-Ti photocatalysts

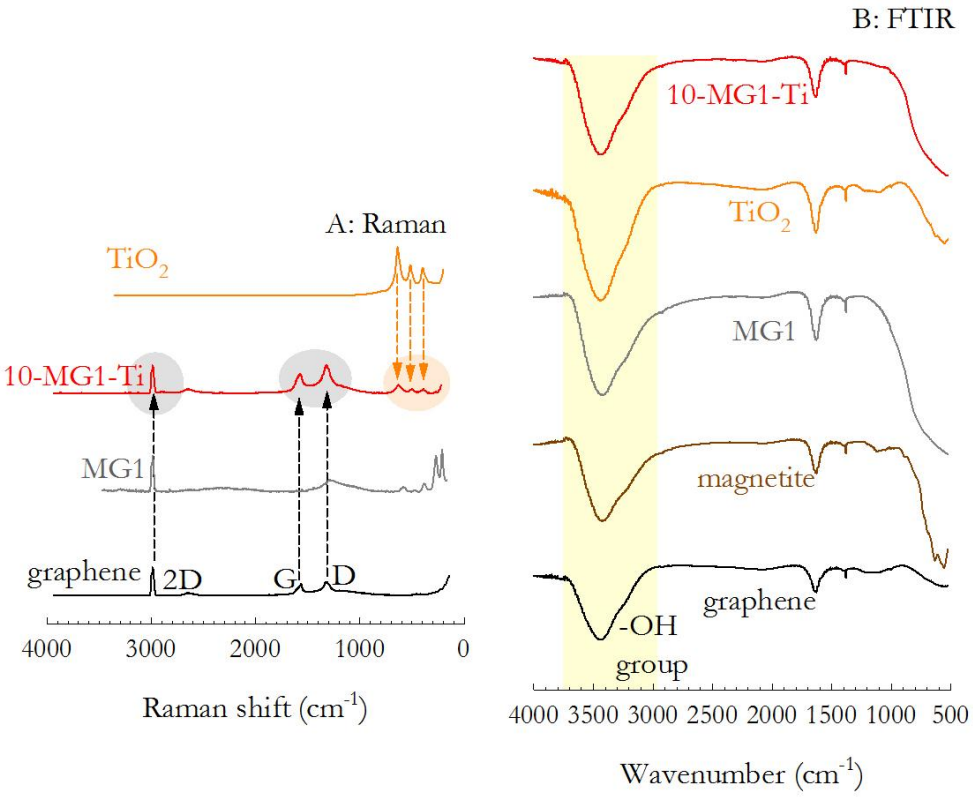

Figure 7.S3. Raman (A) and FTIR (B) spectra of Y-MGX-Ti photocatalysts

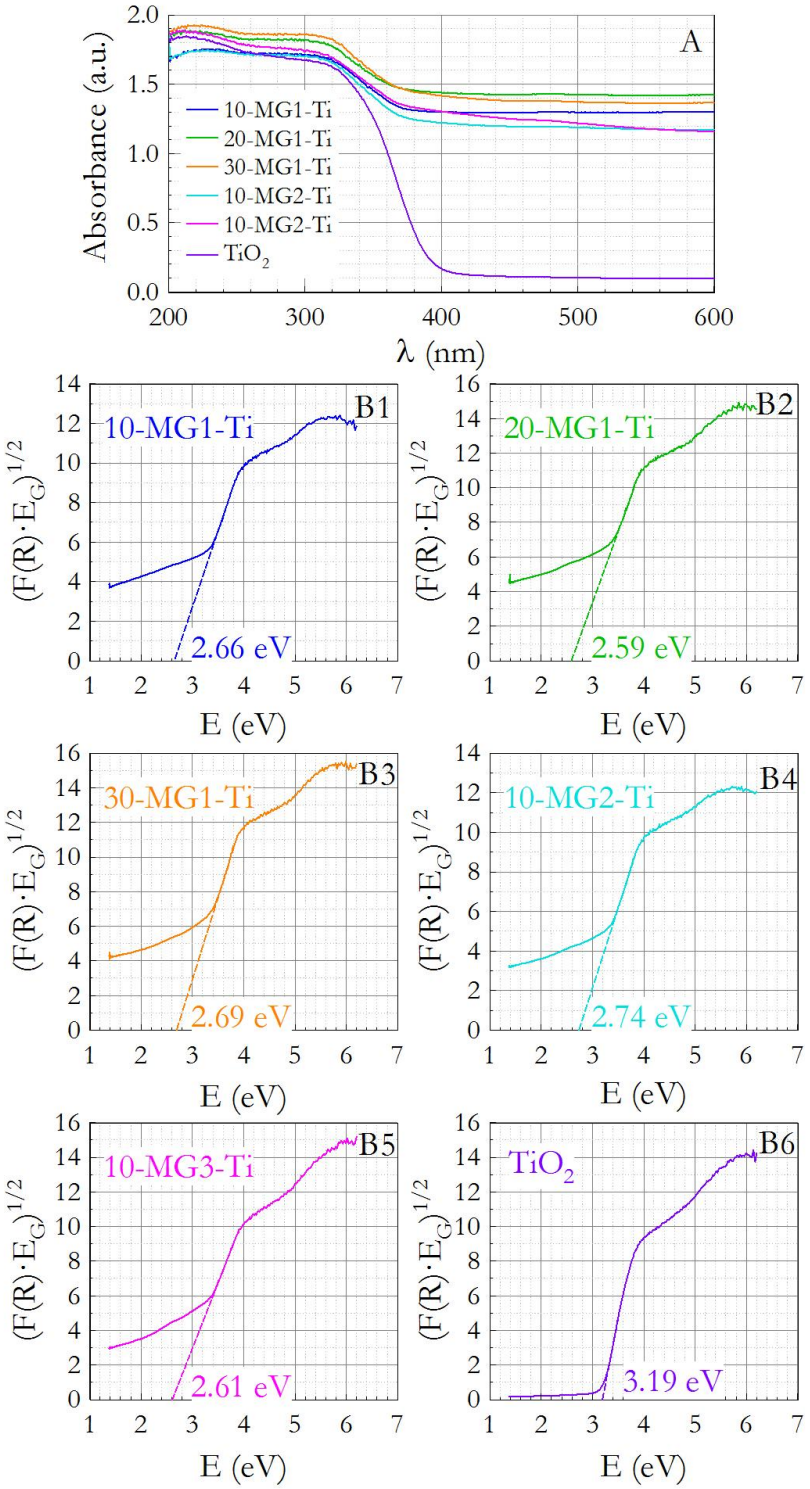

Figure 7.S4. DR-UV-vis spectra of the synthesized Y-MGX-Ti photocatalysts (A) and Tauc's plot for band gap calculation (B1 to B6)

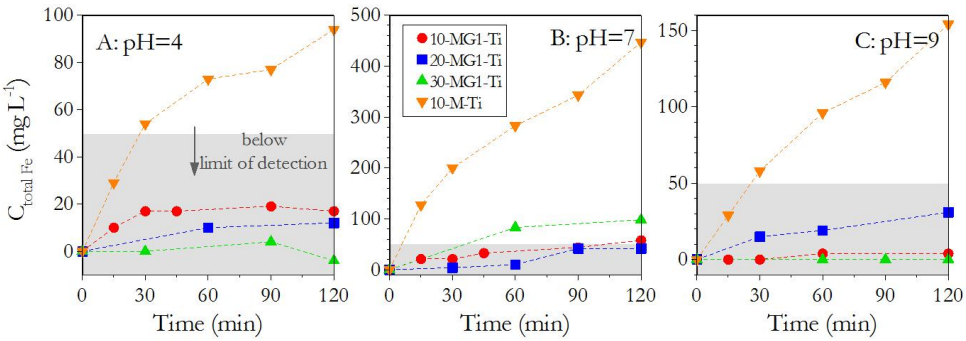

Figure 7.S5. Iron leaching tests at pH 4 (A), pH 7 (B) and pH 9 (C). Influence of graphene presence of Y-MG1-Ti photocatalysts on iron release. Experimental conditions: V=250 mL; $C_{photocatalyst}$=0.5 g·L^{-1}, pH buffered with H_3PO_4 10 mM

REFERENCES

[1] D.S. Wishart, Y.D. Feunang, A.C. Guo, E.J. Lo, A. Marcu, J.R. Grant, T. Sajed, D. Johnson, C. Li, Z. Sayeeda, N. Assempour, I. Iynkkaran, Y. Liu, A. Maciejewski, N. Gale, A. Wilson, L. Chin, R. Cummings, D. Le, A. Pon, C. Knox, M. Wilson, "DrugBank 5.0: a major update to the DrugBank database for 2018" *Nucleic Acids Res.* 46 (**2018**) D1074–D1082.

[2] S. Kim, J. Chen, T. Cheng, A. Gindulyte, J. He, S. He, Q. Li, B.A. Shoemaker, P.A. Thiessen, B. Yu, L. Zaslavsky, J. Zhang, E.E. Bolton, "PubChem 2019 update: improved access to chemical data" *Nucleic Acids Res.* 47 (**2019**) D1102–D1109.

[3] F.J. Rivas, R.R. Solís, F.J. Beltrán, O. Gimeno, "Sunlight driven photolytic ozonation as an advanced oxidation process in the oxidation of bezafibrate, cotinine and iopamidol" *Water Res.* 151 (**2019**) 226–242.

[4] R. Broséus, S. Vincent, K. Aboulfadl, A. Daneshvar, S. Sauvé, B. Barbeau, M. Prévost, "Ozone oxidation of pharmaceuticals, endocrine disruptors and pesticides during drinking water treatment" *Water Res.* 43 (**2009**) 4707–4717.

[5] M.C. Dodd, M.O. Buffle, U. Von Gunten, "Oxidation of antibacterial molecules by aqueous ozone: moiety-specific reaction kinetics and application to ozone-based wastewater treatment" *Environ. Sci. Technol.* 40 (**2006**) 1969–1977.

[6] F.J. Benítez, J.L. Acero, F.J. Real, G. Roldán, "Ozonation of pharmaceutical compounds: rate constants and elimination in various water matrices" *Chemosphere.* 77 (**2009**) 53–59.

[7] F.J. Benítez, J.L. Acero, J.F. García-Reyes, F.J. Real, G. Roldán, E. Rodríguez, A. Molina-Díaz, "Determination of the reaction rate constants and decomposition mechanisms of ozone with two model emerging contaminants: DEET and nortriptyline" *Ind. Eng. Chem. Res.* 52 (**2013**) 17064–17073.

[8] E. Mena, A. Rey, E.M. Rodríguez, F.J. Beltrán, "Reaction mechanism and kinetics of DEET visible light assisted photocatalytic ozonation with WO_3 catalyst" *Appl. Catal. B Environ.* 202 (**2017**) 460–472.

[9] W. Song, W.J. Cooper, B.M. Peake, S.P. Mezyk, M.G. Nickelsen, K.E. O'Shea, "Free-radical-induced oxidative and reductive degradation of N,N'-diethyl-m-toluamide (DEET): Kinetic studies and degradation pathway" *Water Res.* 43 (**2009**) 635–642.

[10] K.A. Lewis, J. Tzilivakis, D.J. Warner, A. Green, "An international database for pesticide risk assessments and management" *Hum. Ecol. Risk Assess. An Int. J.* 22 (**2016**) 1050–1064.

[11] M.M. Huber, A. Göbel, A. Joss, N. Hermann, D. Löffler, C.S. McArdell, A. Ried, H. Siegrist, T.A. Ternes, U. Von Gunten, A. Go, "Oxidation of pharmaceuticals during ozonation of municipal wastewater effluents: a pilot study" *Environ. Sci. Technol.* 39 (**2005**) 4290–4299.

[12] B. Razavi, W. Song, W.J. Cooper, J. Greaves, J. Jeong, "Free-radical-induced oxidative and reductive degradation of fibrate pharmaceuticals: Kinetic studies and degradation mechanisms" *J. Phys. Chem. A.* 113 (**2009**) 1287–1294.

[13] R.F. Dantas, M. Canterino, R. Marotta, C. Sans, S. Esplugas, R. Andreozzi, "Bezafibrate removal by means of ozonation: Primary intermediates, kinetics, and toxicity assessment" *Water Res.* 41 (**2007**) 2525–2532.

[14] R.R. Solís, O. Gimeno, F.J. Rivas, F.J. Beltrán, "Simulated solar driven photolytic ozonation for the oxidation of aqueous recalcitrant-to-ozone tritosulfuron. Transformation products and toxicity" *J. Environ. Manage.* 233 (**2019**) 513–522.

PAPER 5

REMOVAL OF ORGANIC MICROPOLLUTANTS FROM A MUNICIPAL WASTEWATER SECONDARY EFFLUENT BY UVA-LED PHOTOCATALYTIC OZONATION

Catalysts 9 (5) (2019) 472

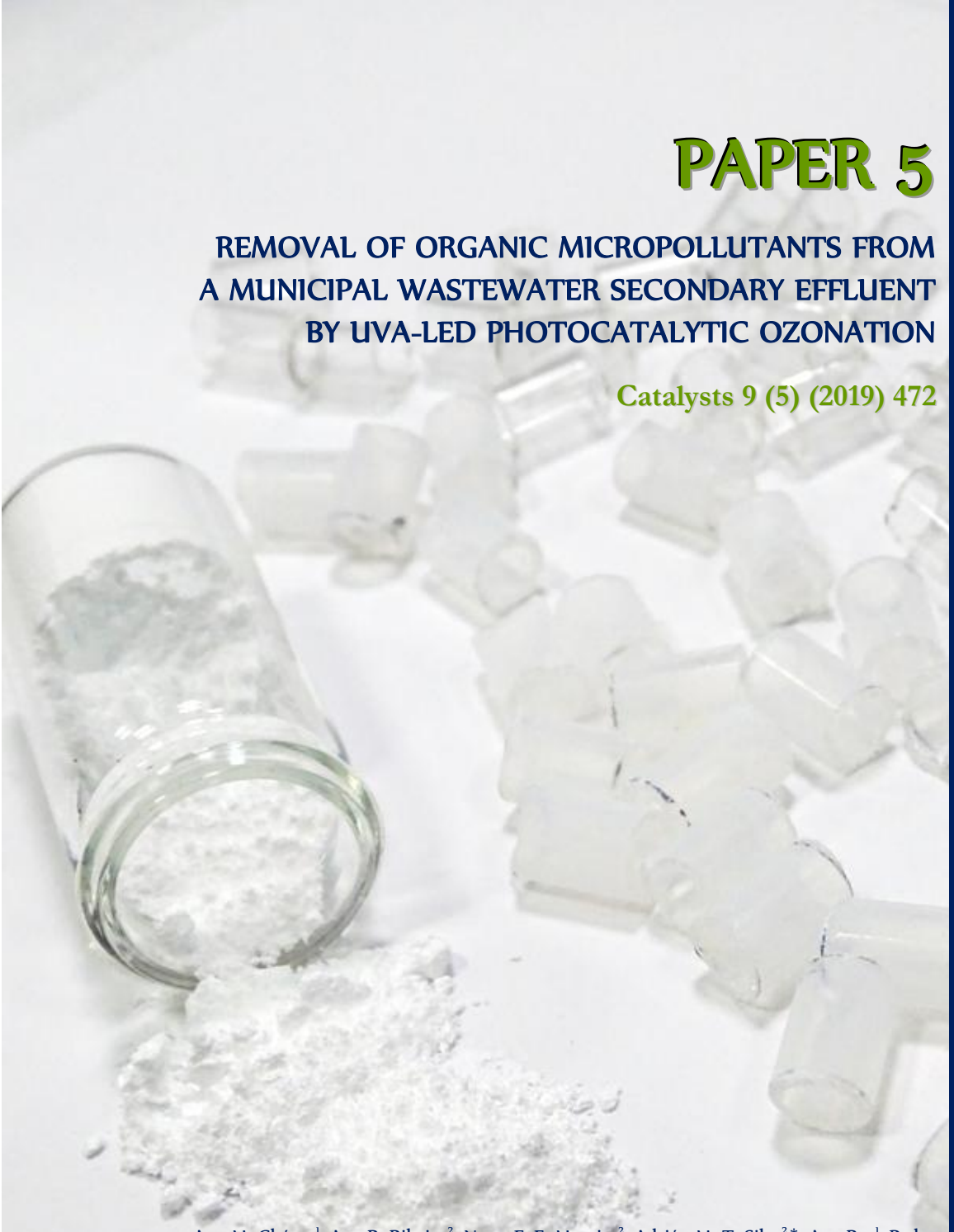

Ana M. Chávez[1], Ana R. Ribeiro[2], Nuno F. F. Moreira[2], Adrián M. T. Silva[2,*], Ana Rey[1], Pedro M. Álvarez[1] and Fernando J. Beltrán[1,*]

[1] Departamento de Ingeniería Química y Química Física, Instituto Universitario de Investigación del Agua, Cambio Climático y Sostenibilidad, Universidad de Extremadura, Avenida de Elvas S/N, 06006 Badajoz, Spain

[2] Laboratory of Separation and Reaction Engineering - Laboratory of Catalysis and Materials (LSRE-LCM), Faculdade de Engenharia, Universidade do Porto, Rua Dr. Roberto Frias s/n, 4200-465 Porto, Portugal

CHAPTER VIII

GRAPHICAL ABSTRACT

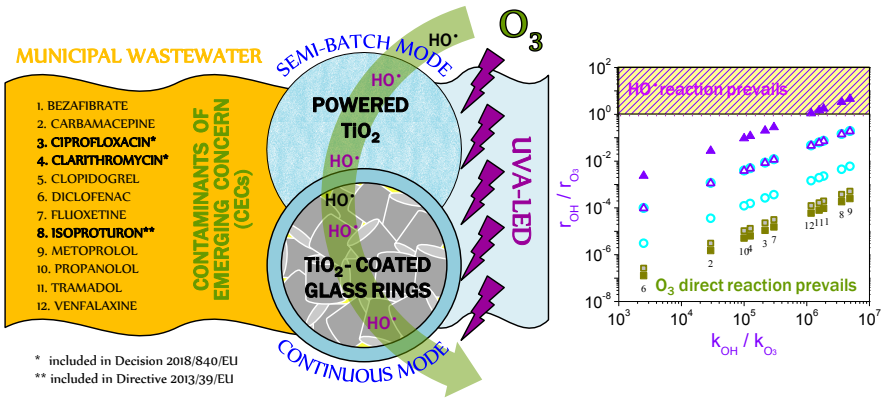

ABSTRACT

Numerous contaminants of emerging concern (CECs) have been found in different water bodies. Directive 2013/39/EU and Decision 2018/840/EU are consequently being implemented in the field of water policies. Twelve CECs (e.g., isoproturon, ciprofloxacin and clarithromycin are among those listed) were detected in a municipal wastewater secondary effluent by means of solid phase extraction and ultra-high-performance liquid chromatography with tandem mass spectrometry (SPE-UHPLC-MS/MS). Different advanced oxidation processes (AOPs), based on the combination of ozone, UVA-LED and powdered TiO_2, were investigated for their removal in a semi-batch operation. In addition, TiO_2-coated glass rings (P25R) were characterized with different techniques (SEM, WDXRF) and used for continuous mode operation in a packed bed reactor (PBR). Among the AOPs studied, ozone-based processes were found to be more efficient than heterogeneous photocatalysis. A kinetic study was performed showing that direct ozonation is the main oxidation pathway for CECs removal. Ozone was successfully decomposed in combination with UVA-LED and P25R, resulting in an apparent rate constant of 3.2×10^{-2} s^{-1} higher than in the O_3/LED system (1.0×10^{-3} s^{-1}) or with ozone alone (8.6×10^{-5} s^{-1}). Hydroxyl radical reaction could prevail over direct ozone reaction for the most refractory compounds (e.g. isoproturon).

Keywords: Municipal wastewater secondary effluent; contaminants of emerging concern; ozonation; light emitting diodes; TiO_2-coated glass rings.

8.1. INTRODUCTION

Contaminants of emerging concern (CECs) are continuously discharged into aquatic systems with little or no awareness of their consequences. Pharmaceuticals, pesticides, industrial compounds, natural hormones and personal care products belong to this group of substances. Although their concentration levels are very low, usually in the $ng \cdot L^{-1}$ or $\mu g \cdot L^{-1}$ range [1–3], biological acute and chronic toxicity in aquatic organisms has been observed [4,5].

To date, the European Union (EU) has established a list of priority substances (Directive 2013/39/EU) and a watch list of CECs that have to be monitored to guarantee water quality (Decision 2015/495/EU, Decision 2018/840/EU) [6–8]. Other CECs are most likely to be included in the watch list in the near future.

Since CECs are difficult to remove by conventional treatments of municipal wastewater treatment plants (MWWTPs), alternative treatment methods such as adsorption, membrane separation, photocatalysis or ozonation are being investigated [9,10]. Among the oxidation processes applied in this work, ozonation has been shown to be a very effective treatment due to ozone direct reactions with some organics and ozone decomposition (mainly at basic pH) into hydroxyl radical ($HO^{\bullet}$), a strong non-selective oxidant radical oxygen species (ROS) [11]. However, decomposition of ozone in water also involves a series of reactions which prevent other less reactive ROS from being able to degrade most of the CECs. To enhance the efficiency of ozonation processes for the degradation of CECs, ozone may be used in combination with certain catalysts and/or radiation sources to promote ozone decomposition into $HO^{\bullet}$ [12,13]. Reaction mechanisms of these oxidation processes are well known in literature [13] (see main reaction steps of these mechanisms in section S1 of the supplementary information).

In this sense, light emitting diodes (LEDs) represent an attractive and cost-effective alternative because of their long lifetime and high-energy efficiency. Regarding photocatalysts, TiO_2 in powder form has so far been the most commonly used material in photocatalytic oxidation of CECs. However, given the difficult separation of nanosized powered TiO_2, a great deal of research is nowadays devoted to the use of immobilized TiO_2 [14].

This work focuses on the removal of some CECs detected in municipal secondary wastewater collected in an MWWTP in Northern Portugal. Combinations of ozone,

UVA-LEDs and P25 TiO_2 (Evonik P25), both in powdered form (P25) and immobilized on glass rings (P25R), were tested as treatment approaches. Two modes of ozonation operation were also investigated: semi-batch (P25 as catalyst) and continuous flow (P25R as catalyst). Some CECs examined in this study (e.g., isoproturon, ciprofloxacin and clarithromycin) are among those included in Directive 2013/39/EU and Decision 840/2018/EU. The main objectives of this work were: (i) to assess efficiencies of semi-batch and continuous processes; (ii) to determine the importance of direct ozonation and $HO^{\bullet}$ mediated-reactions in the degradation of the CECs.

8.2. MATERIALS and METHODS

Chemicals and solvents (> 95% purity) were purchased from different companies and ultrapure water was supplied by a Milli-Q water system. TiO_2 (P25, 80% anatase and 20% rutile crystalline phases) was obtained from Evonik Degussa GmbH. All reference standards (> 98% purity) and the isotopically labeled compounds used as internal standards were purchased from Sigma-Aldrich (Steinheim, Germany).

8.2.1. WASTEWATER EFFLUENTS

Secondary wastewater (WW) samples were collected from a MWWTP located in Northern Portugal and frozen until further use. The main physicochemical parameters are summarized in **Table 8.S1**, namely pH, dissolved organic carbon (DOC) and inorganic carbon (IC).

8.2.2. PHOTOCATALYSTS

Titanium dioxide powder (P25) was used as photocatalyst in semi-batch experiments, and TiO_2-coated glass rings (P25R) were used in continuous flow runs. P25R was prepared as described elsewhere [15]. Briefly, glass rings were immersed in a 5% w/v P25-ethanolic solution at a constant rate of 30 $mm \cdot min^{-1}$, in order to create a homogeneous TiO_2 layer. The coated rings were then dried overnight. Since three layers of P25 have been shown to be the optimal number for photocatalytic treatment of water pollutants, the process was repeated two more times and finally P25R were calcined in air at 450 °C for 2 h [15].

8.2.3. EXPERIMENTAL SET-UP AND PROCEDURES

Semi-batch and continuous flow experiments were carried out in this study. Semi-batch mode runs were performed using the experimental set-up schematically shown in **Figure 8.1**. As can be seen, the reactor was enclosed in a square box with four 10 W UVA LEDs. Each LED (with maximum irradiance at 390 nm, **Figure 8.S2**) was provided with a fan for refrigeration purposes. For ozonation runs, ozone was produced from pure oxygen in a BMT 802X ozone generator, and its concentration was monitored with a BMT 964 analyzer. First, the reactor was charged with 750 mL of WW and 0.375 g of P25 (i.e., catalyst concentration of 0.5 $g \cdot L^{-1}$). The mixture was kept under magnetic agitation in the dark for 10 min to achieve adsorption equilibrium of CECs. Then the LEDs were switched on and a gas stream (150 $mL \cdot min^{-1}$) of either pure oxygen or an ozone-oxygen mixture (50 $mg \cdot L^{-1}$ ozone) was bubbled through a ceramic diffuser. After 10 min of reaction, the residual ozone (if ozone was applied) was removed by using an air pump and samples were withdrawn from the reactor to analyze the concentrations of CECs and DOC. In addition to photocatalytic oxidation runs, single ozonation (in the absence of P25 and with LEDs turned off) and photolytic ozonation (in the absence of P25) experiments were carried out for comparative purposes.

For continuous operation runs the experimental set-up schematically shown in **Figure 8.2** was used. This system consists of a WW reservoir, a glass packed bubble column filled with glass rings (coated with TiO_2 for photocatalytic experiments and uncoated for single and photolytic ozonation runs), a recirculating loop and eight 10 W UVA LEDs positioned along the column (maximum wavelength of emission at 381 nm, **Figure 8.S2**). Noted that a high concentration of ozone was applied because of the presence in wastewater of substances different to CECs that are at high concentration (see TOC and IC values in **Table 8.S1**). These substances also consume ozone and/or hydroxyl radicals. In any case, in a practical situation concentration of ozone could also be in the order of tens of $mg \cdot L^{-1}$ [16].

Positive step input tracer experiments were carried out for characterizing the reactor flow pattern. A NaCl aqueous solution (2 $g \cdot L^{-1}$) was used as the tracer. The conductivity of the liquid stream leaving the column was continuously monitored using a Crison GLP 31 conductivity meter to equalize the conductivity value of the inlet solution.

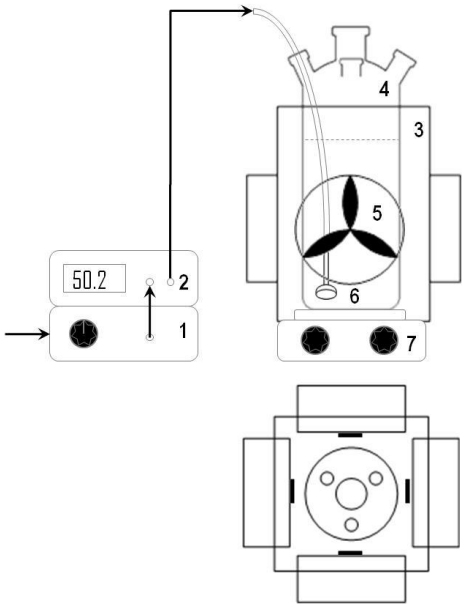

Figure 8.1. Scheme of the experimental set-up. 1: ozone generator, 2: ozone analyzer, 3: box of LEDs; 4: glass reactor, 5: fan, 6: ceramic diffuser, and 7: magnetic stirrer.

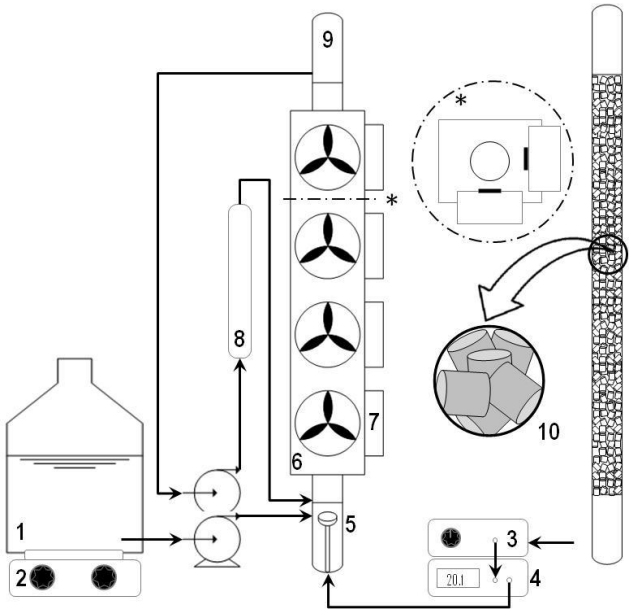

Figure 8.2. Scheme of the experimental set-up used for continuous operation. 1: reservoir, 2: magnetic stirrer 3: ozone generator, 4: ozone analyzer; 5: ceramic diffuser, 6: box of LEDs, 7: fan, 8: loop column, 9: packed column, and 10: glass coated or uncoated rings. * Cross section of the system. Adapted from [14].

In a typical degradation run, the system was filled with distilled water and then 15 $mL \cdot min^{-1}$ of WW were continuously pumped from the reservoir to the column, the recirculation flow rate being set at 166 $mL \cdot min^{-1}$. At the same time, a gas flow rate of either oxygen or a mixture of ozone-oxygen (15 $mL \cdot min^{-1}$ and 20 $mg \cdot L^{-1}$ ozone) was continuously supplied to the column through a porous diffuser placed at its bottom. LEDs were also turned on (if required). The gas and liquid outlet streams left the system continuously through valves at the top of the reactor. The ozone concentration in the gas stream was continuously monitored while liquid samples were regularly taken from the outlet liquid and immediately bubbled with air to remove residual ozone before analysis. Then the collected samples were centrifuged at 4000 rpm for 5 min prior to the analyses. The removal efficiencies of CECs were evaluated at steady-state.

8.2.4. ANALYTICAL METHODS

Concentrations of CECs were measured using an eco-friendly validated method of solid phase extraction followed by ultra-high performance liquid chromatography with tandem mass spectrometry (SPE-UHPLC-MS/MS) described in a previous work [17] where detailed information about recovery percentage of CECs by SPE and precision and accuracy of concentration measurements are given. Typically, before SPE, 100 mL of WW samples were filtered through 1.2 μm glass microfiber filters GF/C, 47 mm (Whatman™), acidified to pH 2 with sulfuric acid and 100 μL of a solution containing internal standards was added. Afterwards, samples were loaded through the conditioned Oasis® HLB cartridges (Hydrophilic-Lipophilic-Balanced sorbent, 150 mg, 6 mL) at a constant flow rate of 10 $mL \cdot min^{-1}$, under vacuum. The sample cartridges were then washed with ultrapure water, dried under vacuum and eluted with ethanol. The extracts were evaporated to dryness in a vacuum concentrator and the residues were reconstituted in 400 μL of ethanol and filtered through 0.22 μm polytetrafluoroethylene (PTFE) syringe filters.

Chromatographic analysis was performed using a Shimadzu Corporation UHPLC (Tokio, Japan) equipment provided with two pumps (LC-30AD), an autosampler (SIL-30AC), an oven (CTO-20AC), a degasser (DGU-20A 5R), a system controller (CBM-20A) and the software LC Solution Version 5.41SP1, coupled to a triple quadrupole mass spectrometer detector (Ultra Fast Mass Spectrometry series LCMS-8040). The stationary phase was a Kinetex™ 1.7 μm XB-C18 100 Å (100×2.1 mm i.d.) column and a gradient of 0.1% formic acid and methanol at 0.25 $mL \cdot min^{-1}$ was programmed as follows: 30:70 (v/v) for 0.5 min, a linear gradient from 30:70 (v/v) to 10/90 (v/v) in 1 min (held for 6 min), a linear gradient from 10:90 (v/v) to 30:70 (v/v) in 0.5 min and

finally an equilibration time of 4 min, with a total run time of 12 min. Column oven and autosampler temperatures were set at 35 °C and 4 °C, respectively. The electrospray ionization source operated in both positive and negative ionization modes. Quantification was performed by selected reaction monitoring (SRM), evaluating the two SRM transitions between the precursor ion and the two most abundant fragment ions for each compound, the most abundant used as quantifier and the second most abundant as qualifier, with a scan time of 100 ms per transition. The capillary voltage, nebulizing and drying gas flows, source and desolvation temperatures were respectively: 4.5 kV, 3.0 $L \cdot min^{-1}$, 15 $L \cdot min^{-1}$, 250 °C and 400 °C. The collision induced dissociation gas (CID) was Ar at 230 kPa.

DOC was analyzed with a TOC-5000A analyzer (Tokio, Japan), pH was measured with a WTW 703 pH-meter and absorbance at 254 nm was recorded on a TG60 UV-visible spectrophotometer (PG instruments, Lutterworth, England). Dissolved ozone concentration was determined by the indigo method [18].

LEDs irradiance spectra (**Figure 8.S2**) were obtained using a UV-Vis spectroradiometer (USB2000+ Ocean Optics, Orlando, FL, USA), connected to an optical fiber (QP600-1-SR Ocean Optics) with an irradiance probe on its tip (CC-3-UV-S cosine-corrected irradiance probe, Ocean Optics).

Thickness of P25 layers on P25R samples was determined by scanning electron microscopy (SEM, Quanta 3D FEG (FEI), Billerica, MA, USA) with 20 kV accelerating voltage and a back-scatter electron detector (BSED). Wavelength dispersive X-ray fluorescence (WDXRF, Brucker SB Tiger 4K, Billerica, MA, USA) measurements were carried out in He atmosphere, using XS-5S, PET and LiF(200) crystals and a mask size of 28 mm.

8.3. RESULTS and DISCUSSION

8.3.1. CECs DETECTED IN SECONDARY EFFLUENT SAMPLES

Two WW samples (namely WW1 and WW2) were collected at the outlet of the secondary settling tank of a MWWTP in Northern Portugal (see **Table 8.S1** for main WW characteristics). WW1 was used in semi-batch experiments and WW2 in continuous flow runs. Forty-five CEC candidates were analyzed by the SPE-UHPLC-MS/MS validated method (**Table 8.S2**) and twelve compounds were found in both

WW1 and WW2 samples (**Table 8.1**): the herbicide isoproturon, and eleven pharmaceutical compounds (bezafibrate, carbamazepine, ciprofloxacin, clarithromycin, clopidogrel, diclofenac, fluoxetine, metoprolol, propranolol, tramadol and venlafaxine).

While clopidogrel was detected at concentrations below the quantification limit, carbamazepine, ciprofloxacin, diclofenac, isoproturon, tramadol and venlaxafine were found at $\mu g \cdot L^{-1}$ concentration level, thus confirming that the conventional treatment applied at the MWWTP is not efficient enough to eliminate these micropollutants. Of special concern are isoproturon (included in Directive 2013/39/EU), ciprofloxacin (recently added to the latest 2018/840/EU Decision), clarithromycin (included in the first Decision 2015/495/EU and maintained in Decision 2018/840/EU) (**Table 8.S2**).

Table 8.1. List of numbered target pollutants found in WW samples and their concentrations.

No.	COMPOUND	Concentration ($ng \cdot L^{-1}$)	
		WW1	WW2
1	Bezafibrate	61 ± 1	7.1 ± 0.4
2	Carbamazepine	1284 ± 225	1222 ± 278
3	Ciprofloxacin	4287 ± 1208	138 ± 74
4	Clarithromycin	758 ± 31	94 ± 4
5	Clopidogrel	< MQL	< MQL
6	Diclofenac	1528 ± 17	1268 ± 67
7	Fluoxetine	62 ± 193	257 ± 51
8	Isoproturon	61 ± 7	1827 ± 219
9	Metoprolol	209 ± 13	187 ± 22
10	Propranolol	173 ± 40	61 ± 14
11	Tramadol	1233 ± 40	3439 ± 727
12	Venlafaxine	628 ± 555	1647 ± 359

< MQL.: below method quantification limit

8.3.2. REMOVAL OF CECs IN SEMI-BATCH EXPERIMENTS

Figure 8.3 shows removal of CECs in ozonation (O_3), photolytic ozonation (O_3/LED), photocatalytic oxidation (O_2/LED/P25) and photocatalytic ozonation (O_3/LED/P25) in semi-batch experiments. As can be observed, O_2/LED/P25 (i.e., heterogeneous photocatalysis) barely reached 15% removal of any CEC. In contrast, elimination percentages achieved by ozonation processes were above 90% in all cases except for ciprofloxacin, metoprolol and propranolol. For ciprofloxacin, percentage removals were 56%, 62% and 100% by single ozonation, photolytic ozonation, and photocatalytic ozonation, respectively. For the beta-blockers propranolol and metoprolol, which were detected at much lower concentrations, random trends were

observed for the different processes and removal efficiencies were much lower (for instance, 43% and 16% were respectively achieved with photocatalytic ozonation).

With regard to the substances on the priority and watch lists, isoproturon and clarithromycin were completely removed by the three ozone-based processes, whereas ciprofloxacin was totally removed by photocatalytic ozonation. The effect is strongly marked due to its higher concentration in WW1. Similar trends are seen in particular for those CECs whose concentrations were above 1000 ng·L^{-1} (**Table 8.1**).

To ascertain the effect of suspended matter on removal efficiency of CECs, a series of runs with filtered WW1 samples were carried out. As has been reported [19], filtration did not enhance the performance of these processes in terms of removal of CECs (see **Figure 8.S1**).

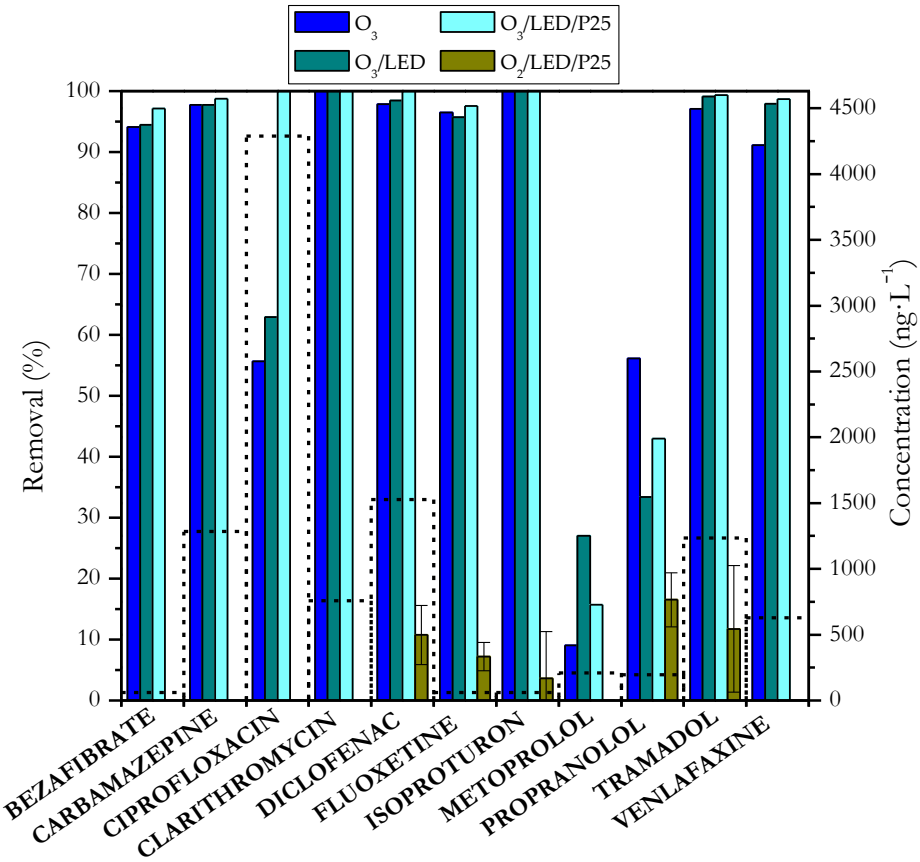

Figure 8.3. Removal of CECs from WW1 (left axis, solid bars) and initial concentration of CECs (right axis, dotted bars) in different semi-batch experiments (O_3, O_3/LED, O_3/LED/P25 and O_2/LED/P25). Conditions: reaction time=10 min; gas flow rate=150 mL·min^{-1}; P25 loading (when applied)=0.5 g·L^{-1} ozone concentration (when applied)=50 mg·L^{-1}.

8.3.3. CONTINUOUS FLOW EXPERIMENTS

A preliminary residence time distribution function (RTDF) analysis was carried out to model flow pattern in the packed photo-reactor used for continuous flow experiments. Two possible scenarios were hypothesized regarding the flow model to be used (**Figure 8.S3**): a) a perfectly mixed reactor, and b) two perfectly mixed reactors in series corresponding to the column reactor and the recirculation column. **Figure 8.S4** shows the experimental F curve obtained together with the calculated F curves inferred from the two assumed models. The experimental F curve perfectly agrees with the calculated one corresponding to a perfectly mixed reactor. Taking this information into account, the mean residence time was expected to be 39 min (see section 2 of supporting information for details).

A. Characterization of the immobilized photocatalyst

SEM images of P25R (**Figure 8.S5**) were taken from glass rings vertically placed in the microscope chamber, showing the roughness of P25 layers in coated glass rings. Nearly 5 μm of layer thickness was determined in both the polished ring border and the scratched ring surface. WDXRF results (**Table 8.S3**) show that ca. 0.16 wt.% of TiO_2 was immobilized on the glass rings. This composition was similar in fresh P25R, and after the photocatalytic oxidation and photocatalytic ozonation processes.

B. Removal of CECs

Photolysis (O_2/LED), photocatalytic oxidation (O_2/LED/P25R), ozonation (O_3), photolytic ozonation (O_3/LED) and photocatalytic ozonation (O_3/LED/P25R) experiments were carried out with WW2. **Figure 8.4** presents the results obtained in terms of removal of CECs (%), with the exception of bezafibrate, which was not considered in this part of the study due to its very low concentration in this sample (WW2), which was close to the method quantification limit. Photolysis led to different degrees of removal depending on the specific CEC: from no removal at all (in the case of clarithromycin and ciprofloxacin) to a maximum removal of 37% for fluoxetine. Photocatalytic oxidation improved these figures to some extent. With this system, ciprofloxacin reached nearly 100% elimination, though removals of the other CECs were moderate, between 58% for carbamazepine, and approximately 28% for propranolol and clarithromycin. In agreement with the results obtained in semi-batch experiments, the highest removals were obtained with the ozone-based processes (O_3, O_3/LED and O_3/LED/P25R), for which removal percentages of more than 90% were observed in all the cases. Photocatalytic ozonation was particularly effective with

removal of any CEC with percentages higher than 99.9%, except for carbamazepine with 99.2% elimination.

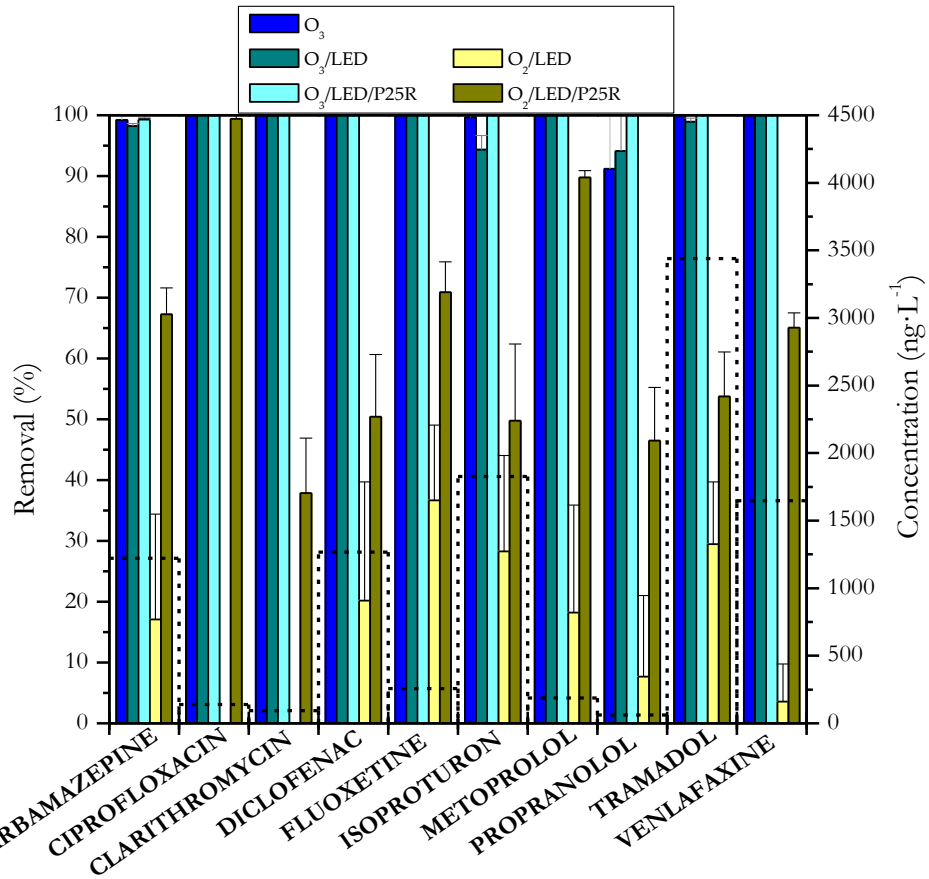

Figure 8.4. Average removal at steady-state (left axis, solid bars) and inlet concentrations of CECs (right axis, dotted bars) in different continuous flow experiments. Conditions: Hydraulic retention time (HRT)=39 min; recirculation ratio=9:10; gas flow rate=150 mL·min^{-1}; ozone gas concentration (when applied)=20 mg·L^{-1}; P25R loading c.a. 0.29 g.

$SUVA_{254nm}$ (specific ultraviolet absorbance at 254 nm) is an important variable to be measured in wastewater since it can be considered a surrogate parameter of the presence of aromatic and unsaturated compounds [20]. **Figure 8.5** shows the values of $SUVA_{254nm}$ measured at steady state of continuous runs. A decrease in $SUVA_{254nm}$ was found as a result of the application of ozone-based processes, especially those involving light, whereas photocatalytic oxidation had no effect on this parameter. Conversely, WW treated with UVA (no catalyst or ozone added) led to an increase in $SUVA_{254nm}$. In this case, some intermediates can be formed, which would absorb more radiation as a consequence of their direct photolysis. When both light and catalyst are simultaneously applied, this effect disappears probably due to the formation of HO•. In ozone-based

processes, the fast reaction of ozone and HO• with unsaturated moieties present in the wastewater could explain the $SUVA_{254nm}$ decrease. Decrease of $SUVA_{254nm}$ with time clearly shows the decrease of intermediate concentrations and the beneficial effects of ozone processes application compared to photocatalytic oxidation. On the other hand, both pH and dissolved organic carbon (DOC) remain practically unaltered (not shown).

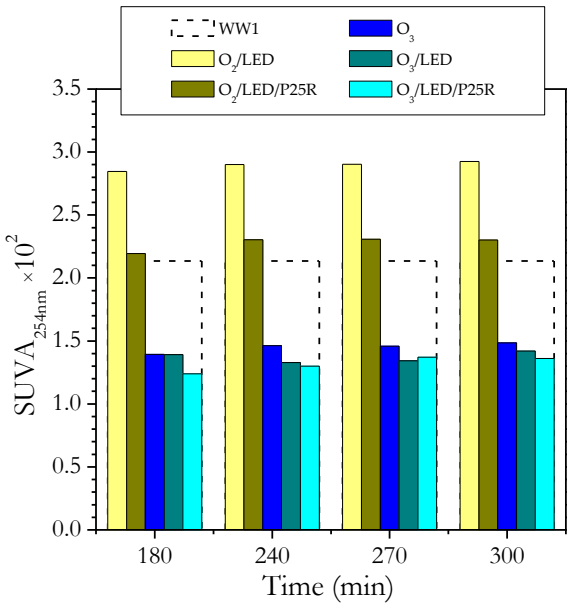

Figure 8.5. SUVA values at 254 nm reached with each oxidation process after different times once the steady state situation was achieved. Conditions: Hydraulic retention time (HRT)=39 min; recirculation ratio=9:10; gas flow rate=150 mL·min^{-1}; ozone gas concentration (when applied)=20 mg·L^{-1}; P25R loading c.a. 0.29 g.

Results previously reported of CECs removal in secondary urban wastewater doped at some mg·L^{-1}, [21–24] also show similar CECs elimination rates when different ozone processes are applied. This confirms that, as far as CECs removal is concerned, direct ozone reactions are likely the main responsible mechanism of oxidation (see later section 8.2.4). For instance, Encinas et al. [21] studied a mixture of nine CECs (metoprolol and diclofenac among them) in a secondary urban wastewater with O_2/UVA/TiO_2, O_3, and O_3/UVA/TiO_2 systems. CECs, doped at concentrations of 10 mg·L^{-1} were removed with similar rates in less than 30 min in ozone processes while photocatalytic oxidation took 120 min to reduce CECs concentration in 20%–30%. In another work, this time with solar radiation, Márquez et al. [22] studied the removal of four CECs (atenolol, hydrochlorotiazide, ofloxacine, and trimethoprim) in a secondary urban wastewater. The advanced oxidation processes (AOPs) applied were O_2/Sun/TiO_2, O_3, O_3/TiO_2, O_3/Sun, and O_3/Sun/TiO_2. With CEC concentrations of

10 mg·L^{-1} and ozone dose of 20 mg·L^{-1} ozone processes needed less than 25 min for total removal of CECs while O_2/Sun/TiO_2 required more than 3 h with the exception of ofloxacin that needed 2 h. It should be noted that in these works [21–24], due to analytical equipment limitations, total removal of CECs was reducing their concentration below the quantification limit that was some μg·L^{-1}.

According to results of **Figures 8.3** and **8.4** the presence of TiO_2 and LED in an ozone process only adds a small advantage to remove some CECs. However, contributions of simultaneous ozone, radiation, and TiO_2 application is deduced from the higher elimination of total organic carbon (TOC) as reported in previous works [21–24]. In these works, TOC could be followed because of the higher concentrations of initial CECs (doped at mg·L^{-1}). To give an example, in the work of Márquez et al. [22], above mentioned, application of O_3 and O_3/Sun/TiO_2 systems lead to 38% and 80% TOC removed, respectively, after 3 h treatment in ultrapure water. In our work, TOC measurements were mainly due the water matrix components because of TOC contribution of CECs present was negligible. Then, no conclusion can be made about TiO_2 and LED addition to improve TOC removal of CECs. Another advantage of photocatalytic ozonation, related to the economy of the process, is the lower consumption of ozone to remove a given amount of organic carbon compared to ozonation. For instance, Espejo et al. [23] reported a consumption of 36 and 17 mg O_3/mg DOC with O_3 and O_3/UVA/Fe_2O_3 systems, respectively, after 30 min reaction, corresponding to the treatment of nine CECs in a secondary urban wastewater.

8.3.4. KINETIC MODELLING ASPECTS

This section focuses only on ozone processes since these were the most efficient in removing the CECs. According to the literature, contaminants are mainly removed on reacting with ozone and HO$^{\bullet}$ [11]. Given that the reacting system behaves as a continuous stirred tank reactor (CSTR), the mass balance of each CEC is given by Equation (8.1):

$$C_{CEC_0} - C_{CEC} = \left(k_D C_{O_3} C_{CEC} + k_{HO} C_{HO} C_{CEC}\right) t_m \qquad (8.1)$$

where t_m is hydraulic residence time (HRT), k_D and k_{HO} are the rate constants of the reactions of ozone and HO$^{\bullet}$ with each CEC (see **Table 8.2**), C_{CECo} is the inlet CEC concentration and C_{CEC}, C_{O3}, and C_{HO} are the outlet concentrations of CEC, ozone, and HO$^{\bullet}$, respectively.

Since most of the HO• comes from the decomposition of ozone [11,13,25], the concentration of any CEC can be expressed as a function of ozone concentration by introducing the R_{ct} factor (ratio of the exposures of HO• and O_3) [26]. Thus, Equation (8.1) becomes:

$$C_{CEC_0} - C_{CEC} = \left(k_D + k_{HO}R_{ct}\right)C_{CEC}C_{O_3}t_m = k_T C_{CEC}C_{O_3}t_m \quad (8.2)$$

or in terms of conversion of CEC (X):

$$X = k_T(1 - X)C_{O_3}t_m \quad (8.3)$$

Table 8.2. List of numbered CECs, rate constants of their reactions with ozone and hydroxyl radical (HO•) and Ha numbers.

		Rate constants ($M^{-1}\cdot s^{-1}$)				$Ha_D \times 10^4$	
No.	COMPOUND	k_D	Ref.	$k_{HO}\cdot 10^{-9}$	Ref.	WW1	WW2
1	Bezafibrate	4.2×10^3	[25]	7.9	[27]	0.3	0.11
2	Carbamazepine	3.0×10^5	[27]	8.8	[27]	15.6	15.2
3	Ciprofloxacin	1.9×10^4	[28]	4.1	[28]	6.1	1.1
4	Clarithromycin	4.0×10^4	[29]	5.0	[29]	2.5	0.9
5	Clopidogrel	unknown		unknown		n.d.*	n.d.*
6	Diclofenac	3.0×10^6	[27]	7.5	[27]	48.2	43.9
7	Fluoxetine	3.2×10^4	[30]	9.6	[31]	1.0	2.0
8	Isoproturon	2.2×10^3	[32]	7.9	[32]	0.3	1.7
9	Metoprolol	1.4×10^3	[33]	6.8	[33]	0.4	0.4
10	Propranolol	1.0×10^5	[34]	10.0	[34]	3.4	1.9
11	Tramadol	4.0×10^3	[29]	6.3	[29]	1.7	2.8
12	Venlafaxine	8.5×10^3	[29]	10.0	[29]	1.7	2.8

n.d.*: not determined
For Hatta number (see equation (8.6)): k_L: 1×10^{-3} m·s^{-1} [35]
D_{O3}: 1.5×10^{-9} m^2·s^{-1} [36]

Application of Equation (8.3) to the experimental results should permit determination of k_T for each contaminant. However, this was only possible for some cases of single ozonation or photolytic ozonation, where full conversion of some CECs was not achieved (**Figure 8.4**), namely propranolol (ozonation, 90%, or photolytic ozonation, 93% conversions) and isoproturon (photolytic ozonation, 94% conversion). For these CECs, values of k_T were 486, 1653, and 1736 $M^{-1}\cdot s^{-1}$, respectively. These values are lower than those reported in the literature for the rate constants of the ozone direct reactions (k_D) (**Table 8.2**). These apparently contradictory results suggest that direct ozonation is the main mechanism for the removal of these contaminants. This

agrees with the fact that ozone-based processes lead to similar conversions, regardless of the use of radiation and/or catalyst (see **Figure 8.4**). In addition, this conclusion was confirmed, as shown later, through determination of the ozone kinetic regimes and comparison of the oxidation rates of a given CEC with ozone and HO•.

Because of the high conversions of CECs reached in the continuous ozone-based processes, the mass balance of CEC was also applied to semi-batch experiments. The CEC mass balance in this case leads to Equation (8.4):

$$-\frac{dC_{CEC}}{dt} = k_T C_{CEC} C_{O_3} \qquad (8.4)$$

Integration of Equation (4) after variable separation gives:

$$\ln\frac{C_{CEC}}{C_{CEC_O}} = k_T \int_0^t C_{O_3}\, dt \qquad (8.5)$$

According to Equation (8.5), k_T can be obtained from the ratio between the left-hand side of Equation (8.5) and the ozone exposure ($\int C_{O3}\, dt$). Nevertheless, Equation (8.5) could only be applied to ciprofloxacin, metoprolol, propranolol, and venlafaxine, owing to the fact that conversions lower than 95% were achieved (**Figure 8.3**). As observed, values of k_T obtained (**Table 8.3**) are also lower than those of k_D reported for the different ozone-contaminant reactions, which leads us to the conclusion that direct reactions are mainly responsible for contaminant removals in the WW samples studied.

Table 8.3. Apparent rate constant values of the ozonation process in semi-continuous operation.

Compounds	$k_{T\text{-}O3}$ ($M^{-1}\cdot s^{-1}$)	$k_{T\text{-}O3/LED}$ ($M^{-1}\cdot s^{-1}$)	$k_{T\text{-}O3/LED/P25}$ ($M^{-1}\cdot s^{-1}$)
Ciprofloxacin	730	376	-
Metoprolol	85	119	69
Propranolol	739	154	226
Venlafaxine	2173	1465	1750

A. Direct ozonation as the main oxidation pathway of CEC

Following recently reported reasoning [37], kinetic regimes of ozone reactions with the contaminants studied and ozone initiation reaction for the formation of HO• were evaluated. This required the determination of the Hatta number (Ha) of these reactions

(**Table 8.2**). For second order irreversible reactions, such as those between ozone and the CECs, Ha_D is defined as:

$$Ha_D = \frac{\sqrt{k_D C_M D_{O_3}}}{k_L} \quad (8.6)$$

where D_{O3} is ozone diffusivity in the liquid phase and k_L is the individual liquid phase mass-transfer coefficient at the reacting conditions. According to Johnson and Davis (1996), ozone diffusivity in water is 1.5×10^{-9} $m^2 \cdot s^{-1}$ while a value of 10^{-3} $m \cdot s^{-1}$ was given for k_L [35].

On the other hand, Ha for the initial ozone decomposition reaction into HO•, a pseudo first order irreversible reaction, is calculated as follows:

$$Ha_I = \frac{\sqrt{k_d D_{O_3}}}{k_L} \quad (8.7)$$

In this case, k_d is the corresponding rate constant which varies according to the nature of the ozone process. Thus, for single ozonation, $k_d = 70 \times 10^{pH-14}$ s^{-1}, while for photolytic and photocatalytic ozonation apparent k_d values were experimentally determined in this work. For that purpose, a series of continuous flow runs were performed in the absence of CECs. The ozone mass balance at steady-state is given by equation (8.8):

$$\beta k_L a \left(C^*_{O_3} - C_{O_3} \right) = v_o C_{O_3} + \beta V k_d C_{O_3} \quad (8.8)$$

β being the liquid hold-up (0.98), V the total reaction volume, k_La the volumetric mass-transfer coefficient, C_{O3}* and C_{O3} the ozone concentrations in the interphase and in the liquid bulk, respectively, and v_o the liquid flow rate. **Figure 8.6** shows the aqueous ozone concentration measured in some ozone absorption experiments in continuous mode.

The dissolved ozone concentration reached at the steady-state of the single ozone absorption run (8.3 $mg \cdot L^{-1}$) was taken as the solubility (C_{O3}*) to be used in equation (8.8). From **Figure 8.6** it is apparent that radiation (LED) and, especially, the combination of LED and P25R, enhanced decomposition of the ozone.

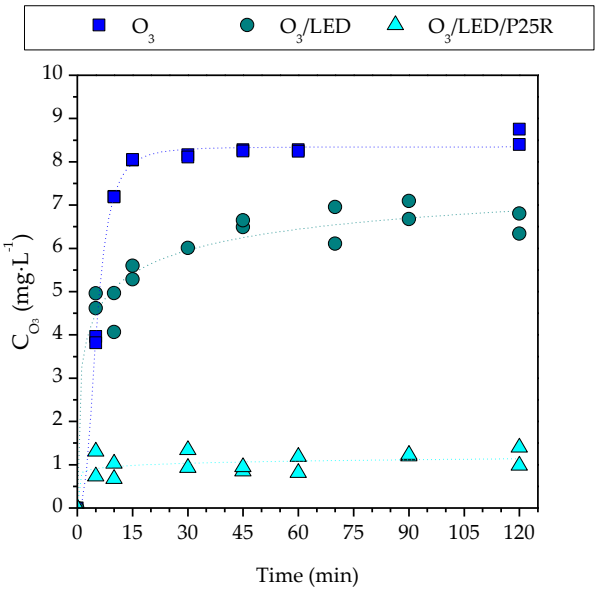

Figure 8.6. Evolution of dissolved ozone concentration in CEC-free deionized water in continuous operation. Conditions: Hydraulic retention time (HRT)=39 min; recirculation ratio=9:10; ozone gas concentration (when applied)=20 mg·L^{-1}; P25R loading c.a. 0.29 g. (when applied).

According to Charpentier (1981) [35], values of k_La in packed bubble columns are between 0.005 and 0.12 s^{-1}, giving as a result different k_d values for both photolytic and photocatalytic ozonation as shown in **Table 8.4**.

Table 8.4. Apparent pseudo first order rate constant and Ha values for ozone decomposition in water in the presence of radiation and radiation/P25R.

	O_3/LED		O_3/LED/P25R	
k_La values (s^{-1})	k_d (s^{-1})	Ha_I x10^3	k_d (s^{-1})	Ha_I x10^2
0.005	1.0x10^{-3}	1.2	3.2 x10^{-2}	0.7
0.063	1.7 x10^{-2}	5.0	0.40	2.5
0.12	3.3 x10^{-2}	7.0	0.77	3.4

$k_d = 8.6 \times 10^{-5}$ s^{-1} and Ha = 1.8×10^{-4} in single ozonation process

Taking into account the maximum values of k_d constants, the values of Ha_I for the initial ozone decomposition into free radicals at the pH of WW from Equation (8.7) were all found to be lower than 7.0×10^{-3} (taking the minimum k_La) or 3.4×10^{-2} (maximum k_La) which, in any case, indicates slow kinetic regimes.

Values of Ha_D for the ozone direct reactions with the contaminants studied here were calculated from Equation (8.6), and are also presented in **Table 8.2**. As can be

observed, Ha_D is always lower than 0.1, which indicates a slow kinetic regime for these reactions. Since both ozone reactions (direct and decomposition) develop in the same kinetic regime, there could be potential competition between them for consuming ozone. In order to clarify this point, and following the procedure described in a previous work [37], the ratio between reaction rates of contaminant removal with HO• and ozone was determined with equation (8.9):

$$\frac{r_{HO}}{r_{O_3}} = \frac{k_{HO} k_d}{k_{O_3} \sum C_s k_{HO}} \tag{8.9}$$

C_s and k_{HO} being the concentration of any other substances present in water that scavenge HO• and the rate constant of this reaction, respectively. Equation (8.9) expressed in its logarithmic form [37] is:

$$\log \frac{r_{HO}}{r_{O_3}} = \log \frac{k_{HO}}{k_{O_3}} + \log \frac{k_d}{\sum C_s k_{HO}} \tag{8.10}$$

Reaction rate ratio (r_{HO}/r_{O3}) strongly depends on the scavenging factor ($\sum C_s k_{HO}$). This factor was calculated from DOC and inorganic carbon (IC) values in wastewater as reported by Nöthe et al. (2009) [38]. Thus, for WW1 and WW2 values of $\sum C_s k_{HO}$ were found to be 6.7×10^5 s^{-1} and 8.2×10^5 s^{-1}, respectively. **Figure 8.7** shows the plot of the reaction rate ratio versus the rate constant ratio of contaminant-hydroxyl radical and ozone reactions in the ozonation processes. It can be seen from **Figure 8.7** that in all cases the ozone direct reaction rate is much higher than the HO• reaction rate with the contaminant, even for compounds 1, 8, 9, 11 and 12 (bezafibrate, isoproturon, metoprolol, tramadol and venlafaxine), when treated with O_3/LED/P25R. This confirms that the direct reaction prevails over the hydroxyl radical reaction. However, these compounds (1, 8, 9, 11 and 12) treated with the O_3/LED/P25R system with good mass-transfer coefficient (k_La=0.12 s^{-1}) would be removed mainly by hydroxyl radicals. In summary, the importance of free radical reactions depends on the presence of scavengers in the wastewater to treat. The increase of concentrations of these substances will make the free radical reactions less important compared to the direct ozone reaction and this will depend on the type of AOP. It can be said that the higher the number of hydroxyl radical formation ways, the higher the importance of free radical reactions compared to direct ozone reactions (see section S1 for initiation reactions of hydroxyl radical formation in AOPs studied).

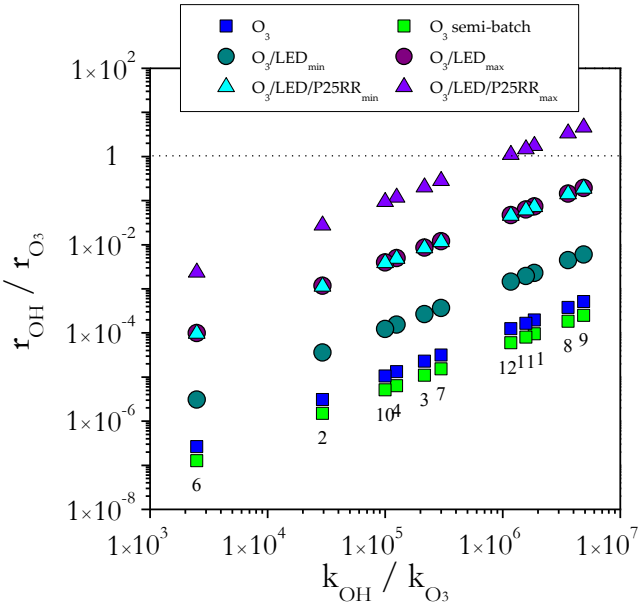

Figure 8.7. Variation of indirect-direct reaction rate ratio with free radical-direct reaction rate constant ratio with the minimum k_La (● and △) in comparison with the maximum k_La (● and ▲) and semi-batch mode (O_3 ■). See Table 8.1 for meaning of numbers (Plots based on reference [37]).

8.4. CONCLUSIONS

CECs found in WW at concentration levels around ng·L^{-1}, and in some cases μg·L^{-1}, were efficiently removed from municipal secondary wastewater samples by the proposed ozonation-based processes (> 90%) except ciprofloxacin, metoprolol, and propranolol in semi-batch experiments. Although few differences were observed between these processes, continuous experiments in deionized water showed that a synergic effect takes place for ozone decomposition with UVA-LED radiation and TiO_2-coated glass rings, giving rise to a slight enhancement of contaminant removal in the treatment of this municipal wastewater.

In addition, the kinetic study clarified that direct ozone reaction is the main pathway responsible for the removal of CECs. Nevertheless, indirect and direct ozone reaction rates ratios indicate that the HO• reaction pathway could prevail over direct reaction in the case of the most refractory compounds for the O_3/LED/P25 system (i.e., isoproturon).

Consequently, the use of P25 TiO_2-coated rings and energy-efficient LEDs for photocatalytic ozonation could be an attractive way for wastewater treatment in continuous operation.

Additional recommended studies on the AOP treatment of CECs in wastewater are, among others, confirmation of intermediate removals and ozone consumption per TOC removed.

REFERENCES

[1] N. Ratola, A. Cincinelli, A. Alves, A. Katsoyiannis, "Occurrence of organic microcontaminants in the wastewater treatment process. A mini review" *J. Hazard. Mater.* 239–240 (**2012**) 1–18.

[2] J. Robles-Molina, F.J. Lara-Ortega, B. Gilbert-López, J.F. García-Reyes, A. Molina-Díaz, "Multi-residue method for the determination of over 400 priority and emerging pollutants in water and wastewater by solid-phase extraction and liquid chromatography-time-of-flight mass spectrometry" *J. Chromatogr. A.* 1350 (**2014**) 30–43.

[3] D.J. Lapworth, N. Baran, M.E. Stuart, R.S. Ward, "Emerging organic contaminants in groundwater: a review of sources, fate and occurrence" *Environ. Pollut.* 163 (**2012**) 287–303.

[4] S. González, R. López-Roldán, J.L. Cortina, "Presence and biological effects of emerging contaminants in Llobregat River basin: A review" *Environ. Pollut.* 161 (**2012**) 83–92.

[5] A. Pal, K.Y.H. Gin, A.Y.C. Lin, M. Reinhard, "Impacts of emerging organic contaminants on freshwater resources: review of recent occurrences, sources, fate and effects" *Sci. Total Environ.* 408 (**2010**) 6062–6069.

[6] Directive 2013/39/EU, "Directive 2013/39/EU of the European Parliament and of the Council of 12 August 2013 amending Directives 2000/60/EC and 2008/105/EC as regards priority substances in the field of water policy" (**2013**).

[7] "Decision 2015. Commission implementing decision (EU) 2015/495 of 20 March 2015 establishing a watch list of substances for Union-wide monitoring in the field of water policy pursuant to Directive 2008/105/EC of the European Parliament and of the Council" (**2015**).

[8] Decision 2018/840/EU, "Commission implementing decision (EU) 2018/840 of 5 June 2018 establishing a watch list of substances for Union-wide monitoring in the field of water policy pursuant to Directive 2008/105/EC of the European Parliament and of the Council and repealing Comm" (**2018**).

[9] Z. Liu, Y. Kanjo, S. Mizutani, "Removal mechanisms for endocrine disrupting

compounds (EDCs) in wastewater treatment — physical means, biodegradation, and chemical advanced oxidation: A review" *Sci. Total Environ.* 407 (**2008**) 731–748.

[10] P.R. Gogate, A.B. Pandit, "A review of imperative technologies for wastewater treatment II: Hybrid methods" *Adv. Environ. Res.* 8 (**2004**) 553–597.

[11] U. Von Gunten, "Ozonation of drinking water: Part I. Oxidation kinetics and product formation" *Water Res.* 37 (**2003**) 1443–1467.

[12] O. Legrini, E. Oliveros, A.M. Braun, "Photochemical processes for water treatment" *Chem. Rev.* 93 (**1993**) 671–698.

[13] F.J. Beltrán, "Ozone reaction kinetics for water and wastewater systems" *Lewis Publishers*, Florida (**2004**).

[14] N.F.F. Moreira, J.M. Sousa, G. Macedo, A.R. Ribeiro, L. Barreiros, M. Pedrosa, J.L. Faria, M.F.R. Pereira, S. Castro-Silva, M.A. Segundo, C.M. Manaia, O.C. Nunes, A.M.T. Silva, "Photocatalytic ozonation of urban wastewater and surface water using immobilized TiO_2 with LEDs: micropollutants, antibiotic resistance genes and estrogenic activity" *Water Res.* 94 (**2016**) 10–22.

[15] M.J. Sampaio, C.G. Silva, A.M.T. Silva, V.J.P. Vilar, R.A.R. Boaventura, J.L. Faria, "Photocatalytic activity of TiO_2-coated glass raschig rings on the degradation of phenolic derivatives under simulated solar light irradiation" *Chem. Eng. J.* 224 (**2013**) 32–38.

[16] B.. Langlais, D.A.. Reckhow, D.R. Brink, "Ozone in water treatment: application and engineering" *Lewis Publishers*, Chelsea, MI (USA) (**1991**).

[17] A.R. Ribeiro, M. Pedrosa, N.F.F. Moreira, M.F.R. Pereira, A.M.T. Silva, "Environmental friendly method for urban wastewater monitoring of micropollutants defined in the Directive 2013/39/EU and Decision 2015/495/EU" *J. Chromatogr. A.* 1418 (**2015**) 140–149.

[18] H. Bader, J. Hoigné, "Determination of ozone in water by the indigo method" *Water Res.* 15 (**1981**) 449–456.

[19] Y. Lee, D. Gerrity, M. Lee, A. Encinas Bogeat, E. Salhi, S. Gamage, R.A.

Trenholm, E.C. Wert, S.A. Snyder, U. von Gunten, "Prediction of micropollutant elimination during ozonation of municipal wastewater effluents: use of kinetic and water specific information" *Environ. Sci. Technol.* 47 (**2013**) 5872–5881.

[20] C. Bahr, J. Schumacher, M. Ernst, F. Luck, B. Heinzmann, M. Jekel, "SUVA as control parameter for the effective ozonation of organic pollutants in secondary effluent" *Water Sci. Technol.* 55 (**2007**) 267–274.

[21] Á. Encinas, F.J. Rivas, F.J. Beltrán, A. Oropesa, "Combination of black-light photo-catalysis and ozonation for emerging contaminants degradation in secondary effluents" *Chem. Eng. Technol.* 36 (**2013**) 492–499.

[22] G. Márquez, E.M. Rodríguez, F.J. Beltrán, P.M. Álvarez, "Solar photocatalytic ozonation of a mixture of pharmaceutical compounds in water" *Chemosphere.* 113 (**2014**) 71–78.

[23] A. Espejo, A. Aguinaco, A.M. Amat, F.J. Beltrán, "Some ozone advanced oxidation processes to improve the biological removal of selected pharmaceutical contaminants from urban wastewater" *J. Environ. Sci. Heal. - Part A Toxic/Hazardous Subst. Environ. Eng.* 49 (**2014**) 410–421.

[24] O. Gimeno, J.F. García-Araya, F.J. Beltrán, F.J. Rivas, A. Espejo, "Removal of emerging contaminants from a primary effluent of municipal wastewater by means of sequential biological degradation-solar photocatalytic oxidation processes" *Chem. Eng. J.* 290 (**2016**) 12–20.

[25] R.F. Dantas, M. Canterino, R. Marotta, C. Sans, S. Esplugas, R. Andreozzi, "Bezafibrate removal by means of ozonation: Primary intermediates, kinetics, and toxicity assessment" *Water Res.* 41 (**2007**) 2525–2532.

[26] M.S. Elovitz, U. Von Gunten, "Hydroxyl radical/ozone ratios during ozonation processes. I. The R(ct) concept" *Ozone Sci. Eng.* 21 (**1999**) 239–260.

[27] M.M. Huber, A. Göbel, A. Joss, N. Hermann, D. Löffler, C.S. McArdell, A. Ried, H. Siegrist, T.A. Ternes, U. Von Gunten, A. Go, "Oxidation of pharmaceuticals during ozonation of municipal wastewater effluents: a pilot study" *Environ. Sci. Technol.* 39 (**2005**) 4290–4299.

[28] M.C. Dodd, M.O. Buffle, U. Von Gunten, "Oxidation of antibacterial molecules by aqueous ozone: moiety-specific reaction kinetics and application to ozone-based wastewater treatment" *Environ. Sci. Technol.* 40 (**2006**) 1969–1977.

[29] Y. Lee, L. Kovalova, C.S. McArdell, U. von Gunten, "Prediction of micropollutant elimination during ozonation of a hospital wastewater effluent" *Water Res.* 64 (**2014**) 134–148.

[30] Y. Zhao, G. Yu, S. Chen, S. Zhang, B. Wang, J. Huang, S. Deng, Y. Wang, "Ozonation of antidepressant fluoxetine and its metabolite product norfluoxetine: Kinetics, intermediates and toxicity" *Chem. Eng. J.* 316 (**2017**) 951–963.

[31] F. Méndez-Arriaga, T. Otsu, T. Oyama, J. Gimenez, S. Esplugas, H. Hidaka, N. Serpone, "Photooxidation of the antidepressant drug Fluoxetine (Prozac®) in aqueous media by hybrid catalytic/ozonation processes" *Water Res.* 45 (**2011**) 2782–2794.

[32] F.J. Benitez, F.J. Real, J.L. Acero, C. Garcia, "Kinetics of the transformation of phenyl-urea herbicides during ozonation of natural waters: rate constants and model predictions" *Water Res.* 41 (**2007**) 4073–4084.

[33] F.J. Benítez, J.L. Acero, F.J. Real, G. Roldán, "Ozonation of pharmaceutical compounds: rate constants and elimination in various water matrices" *Chemosphere*. 77 (**2009**) 53–59.

[34] J. Benner, E. Salhi, T. Ternes, U. von Gunten, "Ozonation of reverse osmosis concentrate: kinetics and efficiency of beta blocker oxidation" *Water Res.* 42 (**2008**) 3003–3012.

[35] J.-C. Charpentier, "Mass-transfer rates in gas-liquid absorbers and reactors" in: "*Advances in Chemical Engineering*" *Academic Press*, New York (**1981**).

[36] P.N. Johnson, R.A. Davis, "Diffusivity of ozone in water" *J. Chem. Eng. Data.* 41 (**1996**) 1485–1487.

[37] F.J. Beltrán, A. Rey, "Free radical and direct ozone reaction competition to remove priority and pharmaceutical water contaminants with single and

hydrogen peroxide ozonation systems" *Ozone Sci. Eng.* 40 (**2018**) 1–15.

[38] T. Nöthe, H. Fahlenkamp, C. von Sonntag, "Ozonation of wastewater: rate of ozone consumption and hydroxyl radical yield" *Environ. Sci. Technol.* 43 (**2009**) 5990–5995.

SUPPLEMENTARY MATERIAL

Removal of organic micropollutants from a municipal wastewater secondary effluent by UVA-LED photocatalytic ozonation

Ana M. Chávez [1], Ana R. Ribeiro [2], Nuno F. F. Moreira [2], Adrián M. T. Silva [2,*], Ana Rey [1], Pedro M. Álvarez [1] and Fernando J. Beltrán [1,*]

[1] Departamento de Ingeniería Química y Química Física, Instituto Universitario de Investigación del Agua, Cambio Climático y Sostenibilidad, Universidad de Extremadura, Avenida de Elvas S/N, 06006 Badajoz, Spain

[2] Laboratory of Separation and Reaction Engineering - Laboratory of Catalysis and Materials (LSRE-LCM), Faculdade de Engenharia, Universidade do Porto, Rua Dr. Roberto Frias s/n, 4200-465 Porto, Portugal

S1. Simplified reaction mechanisms of oxidation processes studied [1]

Photocatalytic oxidation:

$$TiO_2 \xrightarrow{h\nu} e^- + h^+ \quad (S8.1)$$

$$h^+ + H_2O \longrightarrow HO^\bullet + H^+ \quad (S8.2)$$

$$e^- + O_2 \longrightarrow \left[O_2^{\bullet -} ... HO_2^\bullet ... H_2O_2 \right] \longrightarrow HO^\bullet \quad (S8.3)$$

Initiation steps for $HO^\bullet$ formation: reactions (S8.2) (main pathway) and (S8.3).

Removal of organic matter (M) and intermediates (I): reactions (S8.4) and (S8.5):

$$M + HO^\bullet \longrightarrow I \quad (S8.4)$$

$$I + HO^\bullet \longrightarrow \left[... \right] \longrightarrow CO_2 + H_2O \quad (S8.5)$$

M and I could also be removed by direct photolysis:

$$M \xrightarrow{h\nu} I \quad (S8.6)$$

Ozonation:

Removal of organic matter (M) and intermediates (I) by free radical and direct ozone reactions: reactions (S8.4), (S8.5), (S8.7) and (S8.8).

$$M + O_3 \longrightarrow I \quad (S8.7)$$

$$I + O_3 \longrightarrow I' \quad (S8.8)$$

Main initiation step for $HO^\bullet$ formation:

$$O_3 \longrightarrow \left[O_3^{\bullet -} ... HO_3^\bullet ... HO_2^\bullet ... O_2^{\bullet -} ... H_2O_2 \right] \longrightarrow HO^\bullet \quad (S8.9)$$

Photo-ozonation:

Reactions (S8.4) to (S8.9) and:

$$O_3 + H_2O \xrightarrow{h\nu} H_2O_2 \quad (S8.10)$$

$$H_2O_2 \xrightarrow{h\nu} HO^\bullet \quad (S8.11)$$

$$H_2O_2 \underset{pk=11.3}{\rightleftharpoons} HO_2^- + H^+ \quad (S8.12)$$

$$O_3 + HO_2^- \longrightarrow \left[O_3^{\bullet -} ... HO_3^\bullet ... HO_2^\bullet ... O_2^{\bullet -} ... H_2O_2 \right] \longrightarrow HO^\bullet \quad (S8.13)$$

Main initiation steps for HO• formation: reactions (S8.9), (S8.11) and (S8.13)

Photocatalytic ozonation:

Reactions (S8.1) to (S8.13) and:

$$e^- + O_2 \longrightarrow O_2^{\bullet -} \xrightarrow{O_3} \left[O_3^{\bullet -} ... HO_3^{\bullet} ... HO_2^{\bullet} ... H_2O_2 \right] \longrightarrow HO^{\bullet} \qquad \text{(S8.14)}$$

$$e^- + O_3 \longrightarrow \left[O_3^{\bullet -} ... HO_3^{\bullet} \right] \longrightarrow HO^{\bullet} \qquad \text{(S8.15)}$$

Initiation steps for HO• formation: reactions (S8.2), (S8.3), (S8.9), (S8.11), (S8.13), (S8.14) and (S8.15)

Synergism between ozone and photocatalytic oxidation due to reactions (S8.14) and (S8.15).

Reference

[1] F.J. Beltrán, "Ozone reaction kinetics for water and wastewater systems" *Lewis Publishers*, Florida (**2004**).

S2. Additional tables and figures.

Table 8.S1. Main characteristics of wastewater samples (WW).

	pH	DOC ($mg \cdot L^{-1}$)	IC ($mg \cdot L^{-1}$)
WW1	7.6 ± 0.2	22.2 ± 1.0	69.6 ± 1.6
WW2	7.6 ± 0.2	26.6 ± 1.0	74.2 ± 1.6

IC, inorganic carbon; DOC, Dissolved organic carbon.

Table 8.S2. List of compounds: (i) that can be identified by the SPE-UHPLC-MS/MS method; (ii) listed in 2013/39/EU Directive and/or (iii) 2018/840/EU Decision; and (iv) detected in WW samples.

Compound	Detected by SPE-UHPLC-MS/MS	Directive 2013/39/EU	Decision 2018/840/EU	Detected in WW
Pesticides				
Alachlor	X	X		
Atrazine	X	X		
Chlorfenvinphos	X	X		
Clofibric acid	X			
Acetamiprid	X		X	
Clothianidin	X		X	
Diuron	X	X		
Imidacloprid	X		X	
Isoproturon	X	X		X
Methiocarb	X		X	
Pentachlorophenol	X	X		
Simazine	X	X		
Thiacloprid	X		X	
Thiamethoxam	X		X	
Industrial compounds				
Perfluorooctanesulfonic acid (PFOS)	X	X		
UV filter				
2-Ethylhexyl 4-methoxycinnamate (EHMC)				

Table 8.S2. (continued) List of compounds: (i) that can be identified by the SPE-UHPLC-MS/MS method; (ii) listed in 2013/39/EU Directive and/or (iii) 2018/840/EU Decision; and (iv) detected in WW samples.

Compound	Detected by SPE-UHPLC-MS/MS	Directive 2013/39/EU	Decision 2018/840/EU	Detected in WW
Pharmaceuticals				
Atenolol	X			
Atorvastatin	X			
Azithromycin	X		X	
Bezafibrate	X			X
Carbamazepine	X			X
Cefalexin	X			
Ceftiofur	X			
Ciprofloxacin	X		X	X
Citalopram	X			
Clarithromycin	X		X	X
Clindamycin	X			
Clopidogrel	X			X
Diclofenac	X			X
Diphenhyhydramine	X			
Enrofloxacin	X			
Erythromycin	X		X	
Fluoxetine	X			X
Hydrochlorothiazide	X			
Ketoprofen	X			
Metoprolol	X			X
Norfluoxetine	X			
Ofloxacin	X			
Propranolol	X			X
Sulfamethoxazole	X			
Tetracycline	X			
Tramadol	X			X
Trimethoprim	X			
Venlafaxine	X			X
Warfarin	X			

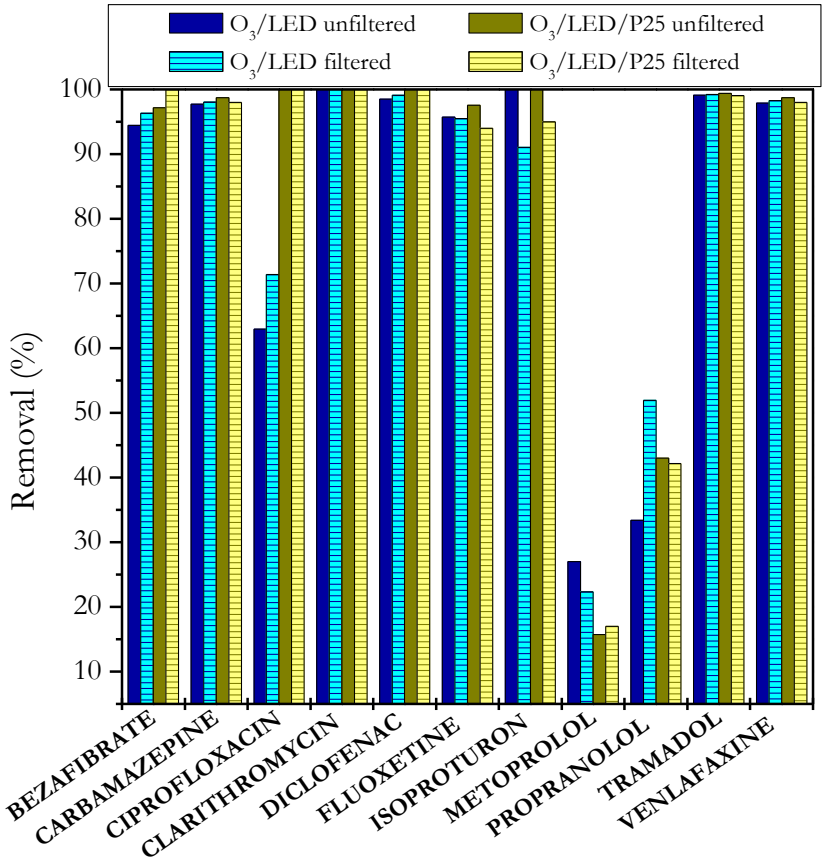

Figure 8.S1. Comparison of removal percentage between WW1 filtered and unfiltered in different semi-batch experiments. Conditions: reaction time=10 min; gas flow rate=150 mL·min^{-1}; P25 loading (when applied)=0.5 g·L^{-1}; ozone concentration=50 mg·L^{-1}.

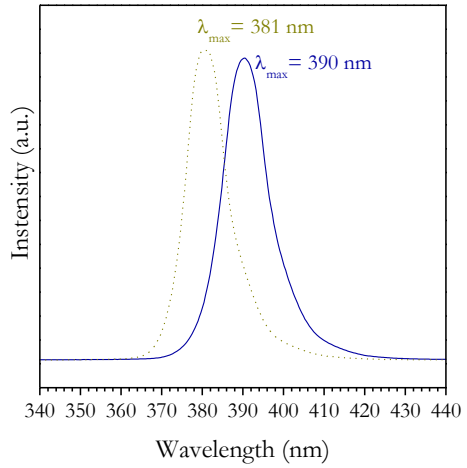

Figure 8.S2. Irradiance spectra of UV-A LEDs used for semi-batch (solid line) and continuous operation (dotted line).

S3. Mathematical models

This part of the study focuses on matching the continuous system to a reactor flow model, taking into consideration two different reactor models. For this purpose, the normalized concentration of the tracer (F function) was determined from step-tracer (NaCl solution 2 $g \cdot L^{-1}$) as described in section 2 of the manuscript.

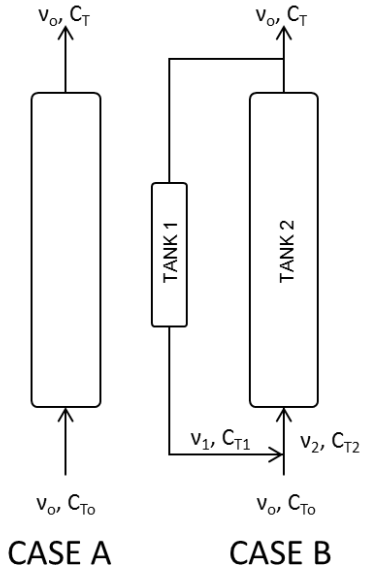

Figure 8.S3 Case A: The system behaves as one perfectly mixed reactor. Case B: The system behaves as two perfectly mixed reactors in series due to the reaction column and the recirculation column.

Case A: Perfectly mixed reactor model.

The F function is related to residence time distribution (RTD) (also known as E function) through equation (S8.16), [13].

$$F = \frac{C_T}{C_{To}} = \int_0^t E dt \qquad \text{(S8.16)}$$

The E function for perfect mixing conditions is described as follows:

$$E = \frac{1}{t_m} e^{\left(-t/t_m\right)} \qquad \text{(S8.17)}$$

Then, taking into account both equations (S8.16) and (S8.17):

$$F = \frac{C_T}{C_{To}} = 1 - e^{\left(-t/\tau\right)} \qquad \text{(S8.18)}$$

where the hydraulic residence time (HRT, τ) is defined as:

$$\tau = \frac{V}{v_o} \tag{S8.19}$$

Case B: Two independent perfectly mixed reactors in series:

In this case, considering the scheme of the set-up, the tracer concentration at the inlet of the main column is described as:

$$C_{T_2} = \frac{C_T v_1 + C_{To} v_0}{v_2} \tag{S8.20}$$

The outlet tracer concentration in tank 1 (C_T) and tank 2 (C_{T1}) are described as follows:

$$C_T = C_{T_2}\left(1 - e^{\left(-t/\tau_2\right)}\right) \tag{S8.21}$$

$$C_{T_1} = C_T\left(1 - e^{\left(-t/\tau_1\right)}\right) \tag{S8.22}$$

τ_1 and τ_2 being the hydraulic residence times in tank 1 and 2, respectively. Therefore, the F function can be obtained by combining equations (S8.20), (S8.21) and (S8.22):

$$F = \frac{C_T}{C_{To}} = \frac{v_0\left(1 - e^{\left(-t/\tau_2\right)}\right)}{v_2 - v_1\left(1 - e^{\left(-t/\tau_1\right)}\right)\left(1 - e^{\left(-t/\tau_2\right)}\right)} \tag{S8.23}$$

Finally, since the packed bed reactor agrees with a perfectly mixed tank model as shown in **Figure 8.S3**, the experimental HRT can be guessed through the linear adjustment of the neperian logarithm form of equation (S8.18).

$$\ln\left(1 - \frac{C_T}{C_{To}}\right) = -\frac{t}{\tau} \tag{S8.24}$$

Thus, the inverse of the negative slope gives a result of 39 min for the HRT.

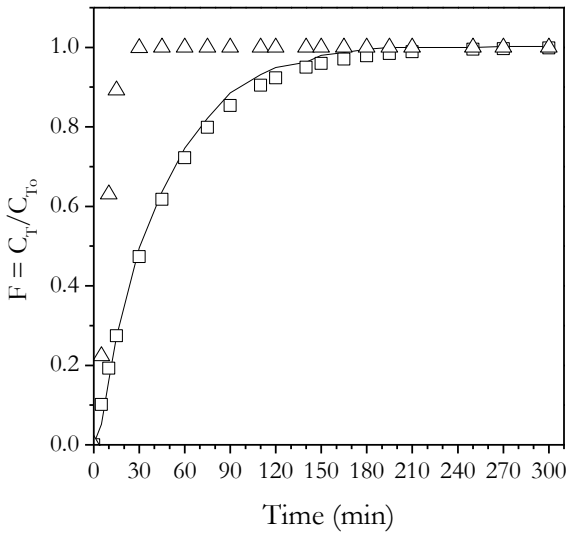

Figure 8.S4. F curve versus time from tracer experiment (solid line) and simulated F curves for the reactor set-up in case A (□) and B (Δ).

S4. P25R photocatalyst characterization: scanning electron microscopy (SEM) and wavelength dispersive X-ray fluorescence (WDXRF)

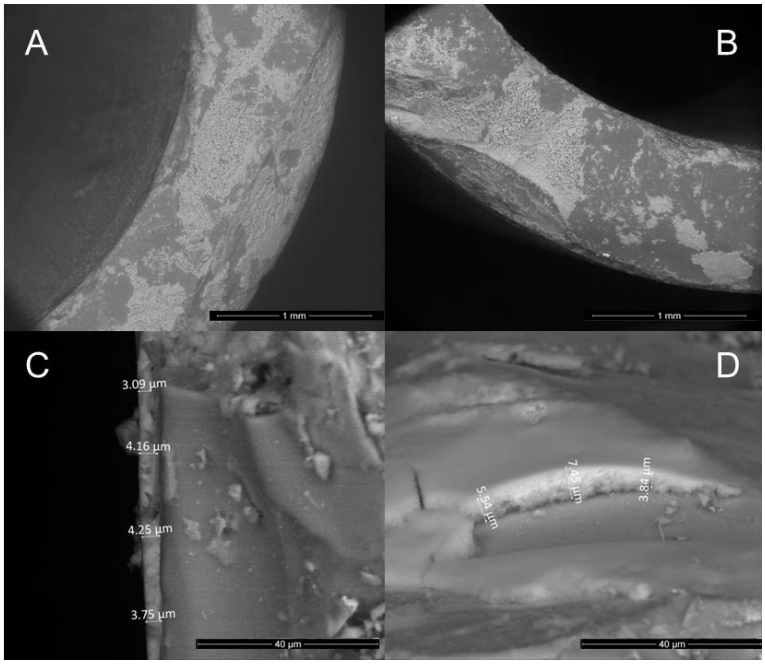

Figure 8.S5. SEM images of fresh coated glass rings surface (A and B). Layer thickness measurements in a polished coated glass ring (C) and in a scratched coated glass ring surface (D).

Table 8.S2. WDXRF results of uncoated glass rings (R), coated glass rings before treatment (P25R) and after photocatalytic oxidation (O_2/LED/P25R) and photocatalytic ozonation (O_3/LED/P25R).

Oxide	Concentration (wt. %)			
	R	P25R	O_2/LED/P25R	O_3/LED/P25R
SiO_2	79.9	79.8	80.0	79.5
B_2O_3	13.0	13.0	13.0	13.0
Na_2O	3.8	3.8	3.7	3.9
Al_2O_3	2.5	2.4	2.4	2.5
K_2O	0.65	0.65	0.68	0.69
TiO_2	0.03	0.16	0.15	0.16
Impurities	0.07	0.14	0.05	0.24

PAPER 6

INSIGHTS INTO THE STABILITY AND CATALYTIC ACTIVITY OF MIL-100(Fe) FOR DIFFERENT ADVANCED OXIDATION PROCESSES

Applied Catalysis B: Environmental (2020)

Ana M. Chávez, Ana Rey*, Jorge López, Pedro M. Álvarez, Fernando J. Beltrán

Departamento de Ingeniería Química y Química Física, Instituro Universitario de Investigación del Agua, Cambio Climático y Sostenibilidad (IACYS), Universidad de Extremadura, Avenida de Elvas S/N, 06006 Badajoz, Spain

CHAPTER IX

GRAPHICAL ABSTRACT

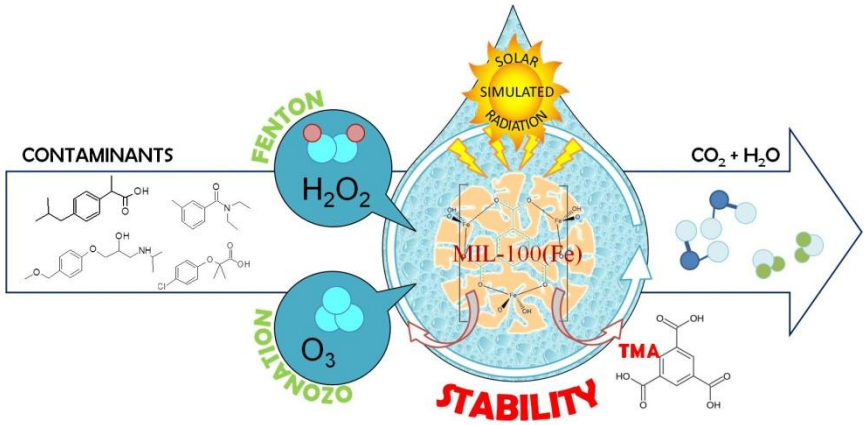

ABSTRACT

The Fe-based MOF MIL-100(Fe) has been synthetized and fully characterized by XRD, N_2-adsorption-desorption, ATR-FTIR, elemental analysis, WXRF, XPS, DR-UV-vis, TGA-DTA, and pH_{PZC}. MIL-100(Fe) presented rather good crystallinity and porosity (S_{BET}=1468 $m^2 \cdot g^{-1}$, total pore volume 0.716 $cm^3 \cdot g^{-1}$), though some unreacted linker trimesic acid was detected. Its stability was studied in water at different pH (4-10) and in the presence of phosphates (10 mM) in long-term experiments (15 days); and also in oxidizing environments based on 5 consecutive runs with simulated solar radiation (550 $W \cdot m^{-2}$, 300-800 nm), ozone (doses 0.06-0.5 g O_3/g MOF) and/or hydrogen peroxide (doses 0.06-0.64 g H_2O_2/g MOF). The material showed a low stability in the presence of phosphates and also in oxidizing conditions at high oxidant doses plus radiation with moderate to high mass losses during the treatments. A well-cleaned MIL-100(Fe) structure, free of unreacted trimesic acid, can be obtained by some of these treatments: e.g. 0.5 g O_3/g MOF + radiation in 0.25 L of ultrapure water and 1 h treatment-time; or 2 cycles 0.06 g H_2O_2/g MOF + radiation in 0.25 L of ultrapure water and 1 h each run. These treated materials were used as catalysts for the removal of four contaminants of emerging concern (metoprolol, clofibric acid, DEET and ibuprofen) by means of heterogeneous photocatalysis, Fenton-like, photo-Fenton-like, and catalytic or photocatalytic ozonation processes. High catalytic activity for photo-Fenton-like and a moderate activity for photocatalytic ozonation processes was attained but the stability of the materials is questionable, always leaching trimesic acid and iron into the reaction medium, although trimesic acid can be effectively removed by the processes studied.

Keywords: MIL-100 (Fe), stability, ozone, hydrogen peroxide, solar radiation.

9.1. INTRODUCTION

Metal-organic frameworks (MOFs) are versatile materials based on the coordination of metal ions or clusters and organic linkers. The assembly of both components makes possible the creation of a wide range of metal-organic compounds with tunable characteristics for different applications [1]. Among their main features, a well-developed and ordered porous structure, with micro and/or mesoporosity, large surface areas, flexible framework or UV-visible light response, make some of them good candidates for water purification by adsorption or by different advanced oxidation processes (AOPs) [2–4]. However, the stability of MOFs in water, affected by different variables like pH, presence of different ions (e.g. phosphates), temperature, etc., is in the spotlight for their successful application in water treatment [4,5].

MIL-100(Fe) is composed by iron nodes and 1,3,5-benzenetricarboxylate, also known as H_3BDC or trimesic acid (TMA) as ligand, with the formula $Fe_3O(H_2O)_2(F/OH)\{C_6H_3(COO)_3\}_2xnH_2O$ (n~14.5), in which the presence of F^- or OH^- depends on the synthesis conditions (with HF or HF-free) [6,7]. The configuration linker-metal cluster gives rise to a very well developed porosity including mesoporous cavities with a high surface area [6]. The excess of electron density of the linker allows the absorption of photons and the electron transfer from the ligand to the metal cluster [8]. The Fe-based nodes, due to the existence of iron-oxo (Fe–O) clusters, induce the electron transfer from the oxygen of the carboxylate group ($–COO^-$) to iron [9]. In addition, this MOF demonstrated high kinetic stability in water but its thermodynamic behavior in long-term contact with liquid water is questionable [7,10]. Despite this, the properties of MIL-100(Fe) have drawn attention and it has been increasingly used in different catalytic/photocatalytic oxidation treatments for water detoxification in the last few years [9,11–15].

The main AOPs studied with MIL-100(Fe) have been photocatalysis and Fenton-based processes [16–18]. In photocatalysis different radiation sources have been used highlighting the photocatalytic activity of MIL-100(Fe) in the visible region. Fenton-based processes with MIL-100(Fe) are based on the reaction mechanism of H_2O_2 decomposition over Fe clusters in the MOF. The heterogeneous Fenton process in dark conditions, also named CWPO (catalytic wet peroxide oxidation) is intensified with the use of radiation improving the Fe (III)/Fe (II) electron transfer [19], although the reaction mechanism with Fe-based MOFs is not well stablished [20]. Besides, the combination of MIL-100(Fe) with ozone (catalytic ozonation process) has been also studied in a series of Fe-MOFs [21]. No reports on MIL-100(Fe) combined with ozone

and radiation (photocatalytic ozonation) have been found. However, photocatalytic ozonation process has demonstrated an enhanced efficiency due to synergistic effects between ozone and an irradiated photocatalyst [22,23] and it has been studied using another Fe-based MOF (MIL-88A(Fe)) for the degradation of 4-nitrophenol [24].

In general, a moderate to high catalytic activity in the degradation of different contaminants, mostly dyes and a few examples of PPCPs (pharmaceuticals and personal care products), has been reported [11,12,14,17,25,26]. Using dyes as target compounds can make difficult the evaluation of the photocatalytic activity of the material tested [27]. Therefore, the application of MIL-100(Fe) on degrading other pollutants is an important step in AOPs studies [4].

In addition, the stability of this MOF has been scarcely studied beyond the reuse of the catalyst in successive cycles of reaction (3-5 runs) and the characterization of the recovered material by XRD, FTIR or BET surface area [14]. However, the lack of other crucial data such as iron or linker released into the reaction medium and catalyst mass loss during the oxidation treatment opens a question about the actual applicability of MIL-100(Fe) from an economic and an environmental point of view.

In this scenario, the aim of this work is focused on the comprehensive study of the stability and catalytic activity of MIL-100(Fe) in different ozone, hydrogen peroxide and/or solar radiation driven AOPs for the removal of four selected contaminants of emerging concern (CECs): metoprolol (MTP), ibuprofen (IBP), n,n-diethyl-m-toluamide (DEET) and clofibric acid (CA). Herein, the effects of the oxidizing environment on the catalyst recovery performance (mass loss) and in the characteristics of the recovered MOF have been fully studied.

9.2. MATERIALS and METHODS

9.2.1. CHEMICALS

Trimesic acid (1,3,5-benzenetricarboxylic acid, H_3-BTC; purity ≥95%, TMA in this work), iron (II) chloride tetrahydrated ($FeCl_2 \cdot 4H_2O$; purity ≥98%), metoprolol tartrate (MTP, purity ≥99%) ibuprofen sodium salt (IBP, purity ≥98%), n,n-diethyl-m-toluamide (DEET, purity ≥97%), clofibric acid (CA, purity ≥97%), sodium hydroxide (NaOH, purity ≥98% purity), hydrochloric acid (HCl, 37% wt.) and hydrogen peroxide (H_2O_2,~30% wt.) were used as received from commercial suppliers without any further

purification. Ultrapure water (UP) was dispensed through a Milli-Q academic system (Millipore).

9.2.2. MIL-100(Fe) SYNTHESIS

MIL-100(Fe) was prepared following a sustainable method described elsewhere [12], mixing trimesic acid and iron precursor according to the stoichiometry of the MOF. Typically, a clear solution of 1.68 g of TMA dissolved in 23.7 g of 1M NaOH was added dropwise into a second solution containing Fe (II) (2.3 g of $FeCl_2.4H_2O$ and 97.2 g of H_2O). The green mixture turned brown after 24 hours on stirring. The solid (3.8 g) was recovered by centrifugation and thoroughly washed several times with hot (70 ºC) and cold (room temperature) UP water and with ethanol. Then, the material was dried at 100 ºC in air atmosphere overnight. Different portions of the synthetized MIL-100(Fe) were submitted to different washing procedures at oxidizing conditions (see section 9.2.4).

9.2.3. CHARACTERIZATION ANALYSES

MIL-100(Fe) samples where fully characterized by means of different techniques. The contents of carbon and hydrogen in the samples were determined by a C-H-N-S TRUSPEC MICRO elemental analyzer (LECO). Complementary chemical analysis was performed by wavelength dispersive X-ray fluorescence spectroscopy (WDXRF) to quantify the amount of iron with a S8 Tiger apparatus (Bruker).

N_2 adsorption-desorption isotherms of the MOFs were measured at -196 ºC in an Autosorb iQ2-C Series apparatus (Quantachrome) in order to determine the total pore and micropore volumes (t-plot method) and BET surface areas. Samples were outgassed at 150 ºC for 12 h under a residual pressure < 10^{-2} mbar.

The crystallinity of the samples was observed from X-ray diffraction (XRD) analysis using a powder Bruker D8 Advance XRD diffractometer with a Cu Kα1 radiation (λ=1.541 Å) and a linear detector VANTEC (aperture 3º). The data were collected from 2θ=2°-40° with an increment of 0.008 º and a 2 s of sampling per point. XRD patterns were compared with MIL-100(Fe) and TMA patterns from Cambridge Crystallography Database.

The identification of some functional groups of the MOFs prepared was sorted out by Fourier transformed infrared spectroscopy in attenuated total reflectance mode (ATR-FTIR). Spectra were recorded for powder samples at 1 cm^{-1} resolution and 32 scans from 550 to 4000 cm^{-1} wavenumber range in a Nicolet iS10 spectrometer.

Diffuse reflectance UV-Vis spectroscopy (DR-UV-Vis) measurements were performed with an UV-vis-NIR Cary-5000 spectrophotometer (Varian-Agilent Technologies), equipped with an integrating sphere component.

Thermogravimetric and differential thermal analyses (TGA-DTA) were carried out in a SETSYS Evolution-16 (SETARAM) apparatus using 50 $mL \cdot min^{-1}$ of air at a heating rate of 5 $^{o}C \cdot min^{-1}$, and from 20 to 800 ºC.

Surface chemical composition was studied by X-ray photoelectron spectroscopy (XPS) in a PHI VersaProbe II Scanning XPS Microprobe spectrometer, with scanning monochromatic X-ray Al Kα radiation (hν=1486.6 eV, 200 μm area analyzed, 52.8 W and 15 kV) as the excitation source; also equipped with a multi-channel hemispherical electron analyzer (pass energy of 29.35 eV). Binding energies were calibrated to the C 1s peak from carbon signal at 284.6 eV. The resulting XPS peaks were curve-fitted to a combination of Gaussian-Lorentzian functions using a Shirley type background for peak analysis.

The pH of the slurry of the MOF suspension can be equivalent to the point of zero charge (pH_{PZC}) under certain conditions [28]. It was determined by mass titration with 1 wt.% amount of MOF as described in the literature [28,29]. Measurements of pH were made with a calibrated pH-meter (Crison GLP21+).

9.2.1. STABILITY TESTS

First, the stability of MIL-100(Fe) in water was determined at different initial pH (4, 6, 7, 8 and 10) in both adjusted and phosphate-buffered ultrapure water (10 mM H_3PO_4). Experiments were carried out in 100 mL amber-colored glass bottles filled with 50 mL of UP or buffered-UP water and a solid loading of 1 $g \cdot L^{-1}$. The bottles were kept under continuous stirring (90 rpm) in a thermostatic bath at 25 ºC for 15 days. Then, the solid and liquid phases were separated by filtration through 0.45 μm nitrocellulose filter and both analyzed.

Secondly, the stability of MIL-100(Fe) in oxidizing aqueous environments (with O_2, O_3 or H_2O_2) and in the presence of radiation was assessed using conditions similar to those of the AOPs studied here. In a typical experiment, 1 $g \cdot L^{-1}$ of MIL-100(Fe) was suspended in a round glass reactor containing 250 mL of ultrapure water. If applied, the reactor was placed in a solar simulator chamber (Suntest CPS, Atlas) provided with a 1500 W air-cooled Xe lamp. The suspension was maintained 30 min in dark conditions and then a liquid sample was withdrawn and analyzed. For oxygen and ozone

treatments, 10 $L \cdot h^{-1}$ of O_2 or O_2/O_3 gas flow was supplied to the reactor during 1 h. If applied, the ozone concentration was 6 or 50 $mg \cdot L^{-1}$ which correspond to doses of 0.06 or 0.50 g O_3 in 1 h, respectively. For hydrogen peroxide experiments, 10 $L \cdot h^{-1}$ of pure O_2 was also bubbled and a concentrated solution of H_2O_2 was injected to set an initial concentration of 7.5 or 75 mM in the reactor, which correspond to doses of 0.06 and 0.64 g H_2O_2, respectively. The oxidation experiment started when the lamp was switched on and/or the oxidants were transferred to the reaction medium with 1 hour reaction time. The temperature inside the solar simulator chamber increased from 25-35 ºC in 1 h. In some cases, the solid was recovered by filtration and the treatment was repeated up to 5 times to evaluate longer term stability in oxidizing conditions. Both, liquid and solid samples were characterized.

Based on the results obtained from the experiments above, two different washing procedures of MIL-100(Fe) were stablished based on H_2O_2/radiation or O_3/radiation (materials MIL-100(Fe)-L1 and MIL-100(Fe)-L2, respectively).

9.2.2. CATALYTIC ACTIVITY TESTS

The catalytic activity of MIL-100(Fe) materials was evaluated for photocatalysis (MOF + O_2 + radiation), catalytic ozonation (MOF + O_3), photocatalytic ozonation (MOF + O_3 + radiation), catalytic wet peroxide oxidation (CWPO or heterogeneous Fenton-like reaction, i.e. MOF + H_2O_2) and heterogeneous photo-Fenton-like (MOF + H_2O_2 + radiation). MTP, IBP, DEET and CA were selected as target compounds.

In a typical experiment, a solution of the four CECs at concentration of 10 $mg \cdot L^{-1}$ each (pH_0~4.8, not adjusted) was charged into the 250 mL round glass photoreactor and the catalyst (0.2 $g \cdot L^{-1}$ loading) was added and maintained under stirring in dark conditions for 30 min. Then, in ozonation runs, the reactor was continuously fed with a mixture of O_2/O_3 (10 $L \cdot h^{-1}$, 6 $mg \cdot L^{-1}$ O_3) at the same time that the lamp of the solar simulator (see section 9.2.4) was switched on. Ozone was continuously generated in an Anseros Ozomat COM-AD-01 apparatus. Photocatalytic oxidation was carried out in a similar way without O_3 in the gas flow. For photo-Fenton-like runs, the initial H_2O_2 concentration was fixed in 37.5 mM (1275 $mg \cdot L^{-1}$) and was also added when the lamp of the solar simulator was switched on and 10 $L \cdot h^{-1}$ of pure O_2 was bubbled. For comparative purposes, photolysis (only radiation), photolytic ozonation (O_3 + radiation) and H_2O_2 photolysis (H_2O_2 + radiation) were carried out. Dark experiments of adsorption, catalytic ozonation and heterogeneous Fenton-like were performed in the solar simulator chamber but the reactor was covered in order to maintain a similar

temperature profiles in all the runs, from 25 ºC to 40 ºC in 5 h. Additionally, some experiments were carried out to check the release of TMA and iron into the reaction medium in UP water, using MOF loading of 0.2 $g \cdot L^{-1}$ and 5 h of contact time.

9.2.3. ANALYTICAL METHODS FOR REACTION MONITORING

Aqueous samples were filtered through hydrophilic 0.45 μm PVDF syringe filter prior to analysis. Measurements of pH were made with a pH-meter (Crison GLP21+). Total iron concentration was evaluated spectrophotometrically at 565 nm by Spectroquant® iron test (Merck 1.14761.0001) based on the reduction of Fe (III) to Fe (II) and the subsequent formation of a purple complex. Aqueous ozone concentration was measured at 600 nm by the indigo method based on the decolorization of indigo trisulfonate by ozone [30]. Hydrogen peroxide was analyzed following the Eisenberg spectrophotometric method based on the formation of a yellow colored complex Ti(IV)-H_2O_2 (wavelength 405 mm). This method is suitable for H_2O_2 concentrations higher than 5×10^{-5} M [31], therefore, samples with higher H_2O_2 concentration were diluted. For lower hydrogen peroxide concentration, the cobalt-bicarbonate method was used based on the Co (II) oxidation to Co (III) and the subsequent formation of a complex with a maximum at 260 nm [32]. All the spectrophotometric measurements were carried out in an Helios α spectrophotometer from ThermoSpectronic using 1 cm path length cuvettes.

Total organic carbon from filtered samples was determined in a Shimazdu apparatus (TOC-V CSH model). TMA concentration was analyzed by an isocratic method in a Hitachi Elite LaChrom HPLC system provided with a diode array detector (Hitachi L-2455). Hence, 0.6 $mL \cdot min^{-1}$ of 90% acidified UP water (0.1% vol. formic acid) and 10% acetronitrile was used as mobile phase with a Phenomenex Gemini C18 column (150 x 3 mm, 5 μm). At these conditions, TMA retention time was 8.3 min and was quantified at 215 nm. The concentration of MTP, IBP, DEET and CA was determined in the same HPLC by a gradient program as described in a previous work [33]. With this method, TMA concentration could also be analyzed at 220 nm with a retention time of 8.9 min.

In ozonation experiments, the concentrations of O_3 in gas inlet and gas outlet were continuously monitored in two on-line Anseros Ozomat GM-6000 analyzers.

9.3. RESULTS and DISCUSSION

9.3.1. CHARACTERIZATION OF MIL-100(Fe)

To check the properties of the synthetized material with respect to that reported by Guesh et al. (2017) [12], a comprehensive characterization study was carried out. **Figure 9.1** shows the XRD diffractograms of MIL-100(Fe), the TMA linker and the simulated XRD pattern from the CIF file of the MIL-100(Fe) by Horcajada et al. (2007) [6]. The peaks observed and their relative intensities are in agreement with the crystalline structure of MIL-100(Fe) with a rather good crystallinity and without TMA or other crystalline phase peaks detected.

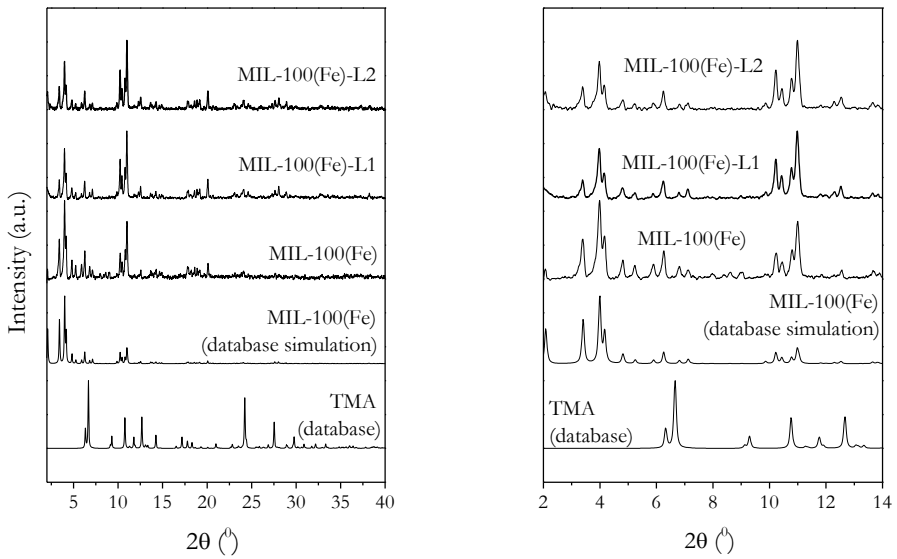

Figure 9.1. XRD patterns of TMA, reference MIL-100(Fe) and the synthesized materials.

Figure 9.2 shows the TGA profile of MIL-100(Fe) with three main weight losses. The first one up to 120 ºC is attributed to adsorbed water inside the pores (about 29.5%). A second one in the range 120-270 ºC can be related to the loss of coordinated water molecules (2.7%) [34]. Between 270-400 ºC the abrupt decomposition of the organic linker is observed (42.1% weight loss) remaining a residue about 25.7%. The profile observed is quite similar to that reported by Guesh et al. (2017) [12], with a ratio of linker weight loss to residue about 1.64.

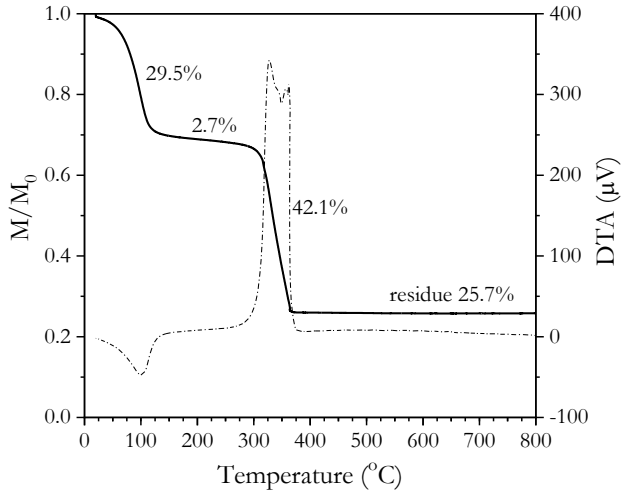

Figure 9.2. TGA-DTA analysis of MIL-100(Fe).

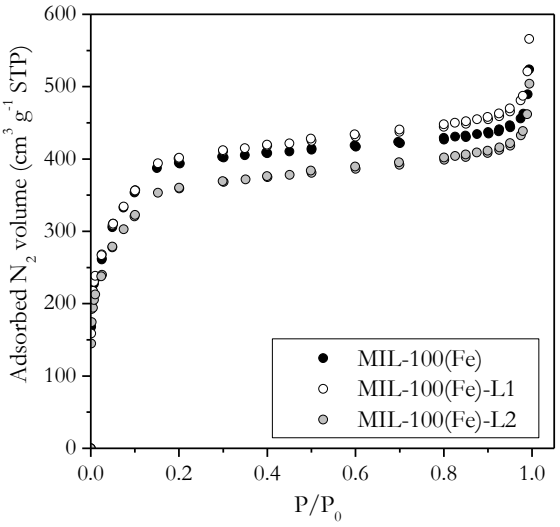

Figure 9.3. N_2 Adsorption-desorption isotherms of MIL-100(Fe) samples.

Regarding the textural properties, the N_2 adsorption-desorption isotherm of the synthetized material is depicted in **Figure 9.3**. BET surface area, total pore volume at P/P_0 0.98, micropore volume by t-plot method and external surface area were determined and summarized in **Table 9.1**. Values for BET surface area between 1000-2200 $m^2 \cdot g^{-1}$ have been reported for MIL-100(Fe), with differences attributed to the presence of residual impurities (non-reacted TMA, coordinated carboxylates, and/or inorganic cations or anions from precursor salts), or even to the formation of different amorphous or crystalline phases [16,34,35]. The shape of the isotherm is characteristic of MIL-100(Fe) with a microporous structure and mesoporous cages. BET surface area (1468 $m^2 \cdot g^{-1}$) and total pore volume (0.716 $cm^3 \cdot g^{-1}$) obtained here were somewhat lower than those determined by Guesh et al. (2017) using a similar synthesis procedure [12].

Table 9.1. Chemical composition and textural properties of the fresh and treated MIL-100(Fe) catalysts.

Catalyst	C (wt. %)	Fe (wt. %)	H (wt. %)	C/Fe (at./at.)	S_{BET} ($m^2 \cdot g^{-1}$)	S_{EXT} ($m^2 \cdot g^{-1}$)	V_P ($cm^3 \cdot g^{-1}$)	V_{micro} ($cm^3 \cdot g^{-1}$)
MIL-100(Fe)	30.42	18.15	1.88	7.80	1468	57	0.716	0.605
MIL-100(Fe)-L1	26.40	23.18	2.09	5.30	1497	62	0.754	0.622
MIL-100(Fe)-L2	27.10	19.78	1.75	6.37	1334	63	0.678	0.548

*$C/Fe_T = 6$

To explore the possibility of some residual TMA as responsible of the lower pore volume and surface area, elemental analysis, WDXRF, ATR-FTIR and XPS were performed. The bulk atomic ratio C/Fe was calculated from elemental analysis and WDXRF results (**Table 9.1)**. This C/Fe ratio was substantially higher than the theoretical ratio $C/Fe_T=6$ calculated according to the molecular formula of MIL-100(Fe). This might be as a consequence of the presence of some not bound TMA or due to the formation of any amorphous phases with different linker-metal stoichiometry like basolite F-300 [12]. The ATR-FTIR spectrum of the synthetized MOF is presented in **Figure 9.4** (see the first two lines in any of the 4 graphs which correspond to TMA and MIL-100(Fe)). The characteristic peaks of MIL-100(Fe) can be observed at 1625, 1447, 1375, 760 and 708 cm^{-1}, which are attributed to C=O stretching, –OH vibration, C–O vibration, and C–H stretching vibration of benzene rings, respectively, confirming once again the formation of the MOF structure [14]. However, the peak observed at 1715 cm^{-1} is undoubtedly assigned to C=O stretching vibration in residual TMA [34,36].

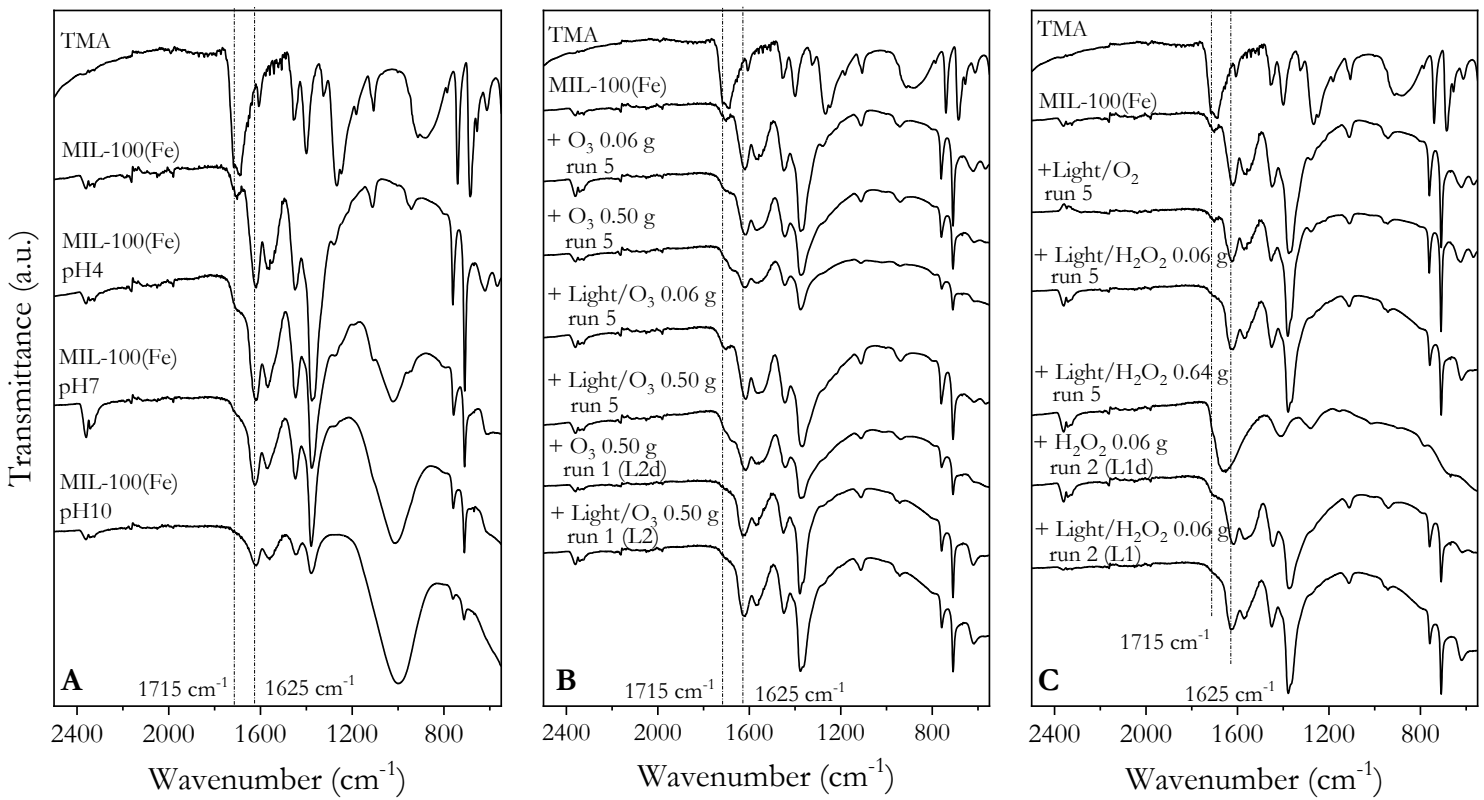

Figure 9.4. ATR-FTIR spectra of TMA and MIL-100(Fe) samples: (A) Effect of pH in phosphate buffer solution (10 mM); (B) Effect of H_2O_2 treatments; (C) Effect of O_3 treatments.

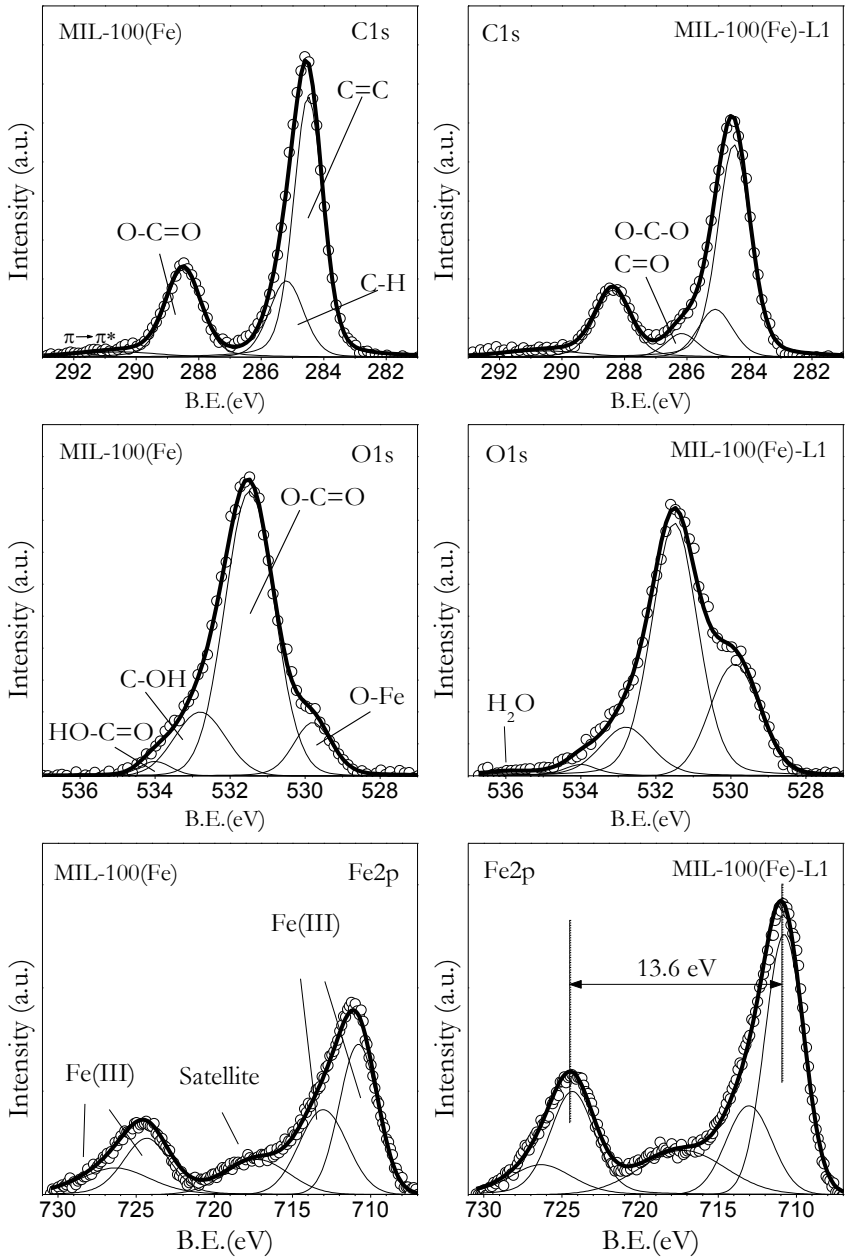

Figure 9.5. High resolution XPS spectra of the C1s, O1s and Fe2p spectral regions of MIL-100(Fe) and MIL-100(Fe)-L1.

XPS full spectrum of the MIL-100(Fe) catalyst (**Figure 9.S1**) confirmed the presence of C, Fe and O as main components of the MOF surface (H cannot be detected by XPS at the conditions used here). No Cl signals from the precursor salt were detected. **Figure 9.5(A)** presents the high resolution C1s, O1s and Fe2p spectra of MIL-100(Fe). For the C1s spectral region, four main contributions have been considered to fit the curve [21,37–39]. The peaks at 284.5 and 285.1 eV are assigned to C=C and C–C, respectively; at 288.5 eV corresponds to $–COO^-$ carboxylate signal from TMA linker; and at 290.5 eV the $\pi \rightarrow \pi^*$ transition in aromatic carbon is observed. The high resolution O1s spectrum was decomposed in four main peaks assigned to O–Fe bonds at 530 eV; $–COO^-$ bonds in carboxylic groups of TMA at 531.5 eV, C–OH bonds at 532.3 eV; and protonated –COOH moieties from the outer surface at 534.0 eV [38–40]. A very small contribution of adsorbed water was observed (peak 5 in O1s, **Table 9.S1**). The presence of protonated –COOH bonds in the O1s spectral region would be necessarily accompanied by a proportional contribution in the C1s spectral region, however, it is so small that has been considered together with $–COO^-$ bonds. In addition, the position of the peaks of the high resolution Fe2p region spectrum at 710.9 and 724.5 eV (with a difference of 13.6 eV) and the appearance of the weak shake-up satellite peak at 717.3 eV are indicative of the Fe (III) state of iron in the MIL-100(Fe) structure [41,42]. The contribution of each bond to the total area of the spectra is presented in **Table 9.S1**. All of the above indicates the formation of MIL-100(Fe), although some free TMA adsorbed onto the porous structure of the MOF cannot be disregarded. In fact, the determination of surface atomic ratio C/Fe led to a value of 10.68 (see **Table 9.2**) higher than the theoretical ratio, confirming some excess of TMA with respect to the expected stoichiometry.

Table 9.2. XPS surface characterization of the MIL-100(Fe) samples.

Sample and oxidizing treatment	C (at. %)	O (at. %)	Fe (at. %)	C/Fe
MIL-100(Fe)	58.41	36.12	5.47	10.68
H_2O_2 0.06 g (run 1)	54.61	38.61	6.78	8.05
H_2O_2/rad 0.06 g (run 1)	54.24	37.94	7.82	6.94
H_2O_2/rad 0.06 g (run 2) MIL-100(Fe)-L1	52.41	37.80	9.78	5.36
H_2O_2/rad 0.64 g (run 1)	53.28	36.75	9.97	5.34
O_3 0.06 g (run 1)	56.20	35.42	8.38	6.70
O_3/rad 0.06 g (run 1)	56.82	36.27	6.91	8.22
O_3/rad 0.50 g (run 1) MIL-100(Fe)-L2	54.75	36.93	8.32	6.58

A band-gap energy of 2.77 eV was determined (**Figure 9.S3**) somewhat lower than that observed by Guesh et al. (2017) [12], but also in agreement with some previously reported values for other MIL-100(Fe) samples [11,18]. Finally, an approximated value for the pH_{PZC} about 3.8 was determined [29].

Thus, broadly the MIL-100(Fe) synthesis has been successfully reproduced from Guesh et al. (2017) [12], obtaining a sample with a rather good crystallinity, although not bound TMA may remain into the porous structure of the MOF and/or even some amorphous Fe-TMA organometallic material could have been formed.

9.3.2. STABILITY OF MIL-100(Fe)

The stability of MOFs in water is a crucial issue and also a weak point in the application of these materials for wastewater treatment [4,5]. In this work, we explore the behavior of the synthetized MIL-100(Fe) material in different aqueous and oxidizing environments.

A. Stability in water and phosphate buffered solutions

The stability of MIL-100(Fe) in water and phosphate buffer has been studied in long-term experiments at pH in the range 4-10. **Table 9.3** summarizes the operating conditions (aqueous matrix and pH) and the concentration of TMA and Fe released into the solution after 15 days of contact time. The percentages of iron and TMA have been calculated according to the theoretical stoichiometry of MIL-100(Fe). In addition, **Figure 9.4(A)** shows the ATR-FTIR spectra of the MOF samples recovered compared to those of TMA and the synthetized MIL-100(Fe). As inferred from the values of **Table 9.3**, in UP water up to about 3% of TMA is leached into the aqueous solution increasing the concentration with increasing pH up to 8% (maximum TMA concentration at pH 8, 15.4 $mg \cdot L^{-1}$). The amount of iron released was lower than 0.2% of the maximum potential concentration. These differences between TMA and Fe percentages can be related to the desorption of residual TMA not bounded to the MOF structure and/or the formation of solid iron oxides/hydroxides onto the MOF surface or separated upon filtration. In a previous work, the stability of a well crystallized fluoride MIL-100(Fe) sample was proved at pH 1-10, but only XRD of the solids were analyzed with no results of TMA or iron leaching to the solution [43]. The instability of a fluoride free MIL-100(Fe) and other iron MOFs at neutral to basic pH has already been observed as a consequence of the structure collapse to form ferrihydrite or other iron species [5,7,44]. The MOF resulted highly stable at its self-provoked acidic pH when stirred in deionized water [7]. In this work, no ferrihydrite by either XRD nor

ATR-FTIR spectrum changes were observed in UP water samples (see **Figures 9.S4 and 9.S5** of supplementary material), but it is necessary to point out that the pH was not maintained along the runs and it evolved toward acidic values (see **Table 9.3**).

Table 9.3. Long-term stability tests in water.

Operating conditions	pH	pH_0	pH_f	Fe (μM)	TMA (μM)	Fe (%)	TMA (%)
UP water NaOH/HCl for pH 1 g·L^{-1} MOF loading	4	4.03	5.60	0.627	19.6	0.019	0.9
	6	5.99	4.98	0.072	45.3	0.002	2.1
	7	6.93	4.88	0.304	42.9	0.009	2.0
	8	8.20	4.63	0.519	71.6	0.016	3.3
	10	10.08	4.84	0.340	58.4	0.010	2.7
H_3PO_4 10 mM +NaOH buffer 1 g·L^{-1} MOF loading	4	3.98	3.98	2.65	549	0.081	25.0
	6	6.00	4.76	2.83	553	0.086	25.2
	7	7.00	5.83	13.1	1541	0.397	70.3
	8	8.01	6.80	26.4	1927	0.804	87.8
	10	10.18	7.02	36.3	2009	1.102	91.6

On the contrary, when phosphate buffered solutions were used, the decomposition of the MIL-100(Fe) was first noticed with a change in the color of the suspension and also in the release of up to 90% of TMA in the worst scenario at the highest pH. The negative effect of the increasing pH and the presence of phosphate species are evidenced in the values of TMA released in **Table 9.3** and the changes in ATR-FTIR spectra of the solid samples (**Figure 9.4(A)**). In fact, phosphates are known to facilitate the displacement of the linker and the formation of the corresponding metal oxide/hydroxide [5]. This also explains the huge difference between TMA and iron detected in the aqueous phase.

Therefore, the use of this MIL-100(Fe) should be limited to acidic conditions. In addition, for real urban wastewater, although usual phosphate concentrations are much lower than those used in this work (c.a. 5-20 mg·L^{-1}), some attention should be paid to phosphate and other common dissolved anions effect on its stability though this material has been previously used as phosphate adsorbent [45].

B. Stability in oxidizing environments

The synthetized MIL-100(Fe) material was submitted to different oxidizing conditions with and without simulated solar radiation to test its behavior prior to its use as catalyst for the different AOPs.

In a previous step, the effect of radiation together with dissolved oxygen was analyzed (photocatalytic oxidation conditions). Then, the effect of hydrogen peroxide

or ozone, with and without radiation was investigated at the conditions described in section 9.2.4. In general, the MOF was submitted to oxidizing treatments up to 5 runs of 1 hour with different oxidant doses. TMA released into the aqueous phase during the first 30 min (in the previous dark stage) and the remaining TMA after the treatments, the concentration of Fe detected at the end of each run and also the percentages of catalyst recovered after the treatments are presented in **Figure 9.6, Figure 9.7 and Table 9.S2**.

i. Radiation

The effect of solely radiation was evaluated with the MOF in continuous stirring, with oxygen supply and into the solar simulator chamber at the pH of the suspension (i.e. pH~4.8). The TMA released into the solution during the first 30 min in the dark (**Figure 9.6(A)** reached a concentration 58 μM which corresponds to 3% of the theoretical amount in the MOF (comparable to results in **Table 9.3** at pH 4-5). Then, the lamp was switched on and the material was maintained 1 h under radiation. The subsequent values of TMA released into the medium correspond again with the 30 min dark stage of stirring with the catalyst recovered from the previous reaction (TMA_0 in **Table 9.S2**). Also in **Table 9.S2** the values of TMA_f (at the end of the radiation run), final TOC and that calculated corresponding to TMA_f are summarized. In every new contact of MIL-100(Fe) with water, some TMA was released, although the concentration detected was decreasing in each consecutive run. During the same experiment, the concentration of TMA increased at the end of the treatment. In addition, the detected TOC_f at the end of the reaction period is slightly higher than that calculated for TMA. Thus, no substantial concentration of TMA intermediates seems to have been formed. All of these results seem to indicate the continuous leaching of TMA that can be eventually oxidized by the reactive oxygen species (ROS) generated by photocatalysis, but at low reaction rate compared to the following treatments.

On the other hand, the concentration of iron leached into the solution after each run was in the range 6.8-10.5 μM (**Figure 9.6(B)**), which is lower than that of the theoretical stoichiometry (3 mol Fe per 2 mol TMA). Again these differences can be related to the desorption of residual TMA not bounded to the MOF structure and/or the formation of solid iron oxides/hydroxides onto the MOF surface or separated upon filtration due to the working pH.

Finally, the percentage of the MOF recovered after the 5 runs cycle of photocatalytic oxidation conditions is presented in **Figure 9.7** and also in **Table 9.S2**.

Only around 70% of the sample was recovered. Even taking into account some minimal losses during the experimental procedure (less than 5% following a similar procedure in the dark), a mass reduction of 30% is indicative that not only not bounded TMA can be extracted, but also MOF decomposition occurs to some extent.

The mechanism proposed for photocatalytic reactions in MIL-100(Fe) [9,18] and the generally accepted photocatalytic reactions over a semiconductor can be summarized as:

$$\text{MIL-100}(Fe^{3+}) + h\nu \longrightarrow \text{MIL-100}(Fe^{2+}) + h^{+} \quad (9.1)$$

$$\text{MIL-100}(Fe^{2+}) \longrightarrow \text{MIL-100}(Fe^{3+}) + e^{-} \quad (9.2)$$

$$e^{-} + O_2 \longrightarrow O_2^{\bullet -} \quad (9.3)$$

$$2O_2^{\bullet -} + 2H^{+} \longrightarrow H_2O_2 + O_2 \quad (9.4)$$

$$e^{-}(O_2^{\bullet -}) + H_2O_2 \longrightarrow OH^{-} + HO^{\bullet} \ (+ O_2) \quad (9.5)$$

Thus, light adsorption by the organic linker would result in the transfer of one electron to the iron node, which generates a charge separated state (e^{-}/h^{+}) able to promote reduction and oxidation reactions [46]. The reactive species formed such as $HO^{\bullet}$, $O_2^{\bullet -}$, $HO_2^{\bullet}$ or h^{+}, might be responsible for the photocatalytic oxidation of organic compounds. In the absence of any organic compound these species could oxidize free TMA remaining in the MOF after the synthesis/washing procedure. However, the mass loss observed indicates that some of the structural linker is also degraded. Thus, Mateo et al., (2019) [46] observed the photodecarboxylation of different terephthalate MOFs under simulated solar radiation, being Fe-based MOFs less stable than other metal ion MOFs. In addition, the strength of the Fe (II)-linker interaction in the transitory state proposed in reaction (9.1) can affect the stability of the MOF structure. Both situations could favor the attack of the ROS to the linker in absence of any other organic compound to oxidize and would explain the instability observed.

ii. Hydrogen peroxide

Regarding the experiments in the presence of hydrogen peroxide, in general, in the first 30 min under stirring (run 1, **Figure 9.6(A)**) some TMA leaching was observed. Similar to the first step for photocatalytic oxidation cycle, the concentrations reached values between 50-60 μM in agreement with previous results at similar pH in UP water (see **Table 9.3**). Then, H_2O_2 was added to the reactor at different concentration and

the lamp was switched on for radiation assisted experiments. The subsequent values of TMA released into the reaction medium correspond again with the 30 min dark stage of stirring with the catalyst recovered from the previous reaction (TMA_0 in **Table 9.S2**). A very different behavior was observed depending on radiation presence/absence.

Regardless of the H_2O_2 dose, when radiation is not applied, similar concentrations of TMA were detected at the end of the dark stage with the reused catalyst after each run. This indicates that in every new catalyst-water contact, new TMA is released into the reaction medium. On the contrary, after photo-Fenton-like reactions (with radiation and H_2O_2), the amount of TMA leached during the dark stage dramatically decreased as the number of reactions increased. In addition, TOC values corresponding to TMA and actual TOC both after reaction are presented in **Table 9.S2** (TOC_{TMAf} and TOC_f, respectively). In the absence of radiation both values are close, thus indicating that no substantial concentration of TMA intermediates have been formed upon dark heterogeneous Fenton-like reaction. In addition, in every experiment without radiation, the values of TMA released in the first 30 min (TMA_0) increased at the end of the oxidation treatment (TMA_f). At this point, it is necessary to highlight that the optimum pH for homogeneous Fenton and many heterogeneous Fenton treatments is pH 3 and this study has been carried out in the range pH_0 4.8 to pH_f~4 (see **Table 9.S2**). However, some studies have proved the efficiency of MIL-100(Fe) in a wide range of pH from 3-8 [16,47]. When radiation is applied the actual TOC in irradiated runs is much higher than that corresponding to remaining TMA_f, in agreement with the formation of TMA oxidation intermediates. Also, the detected TOC at the end of middle experiments (runs 2 and 3 of H_2O_2/rad experiments with the highest dose) is quite high. These results seem to point out that dark Fenton-like reactions at the conditions tested are not able to remove residual TMA from the MOF but it can be completely eliminated when radiation is applied. Unfortunately, at severe conditions of H_2O_2 dose plus radiation, the structure of the MOF seems to be degraded.

On the other hand, **Figure 9.6(B)** shows the iron leached into the reaction medium at the end of each run. In general, when radiation is not applied and TMA released is not removed, the concentration of iron is again much lower than that of the theoretical stoichiometry as commented for photocatalytic oxidation cycle. However, when radiation is applied in the presence of H_2O_2, the leaching of iron to the reaction medium substantially increased even above the stoichiometric value with respect to TMA in some cases. This effect is especially important when the highest H_2O_2 dose is applied (see **Table 9.S2**) where in such conditions the collapse of the MOF structure is supposed according also to TOC analyses.

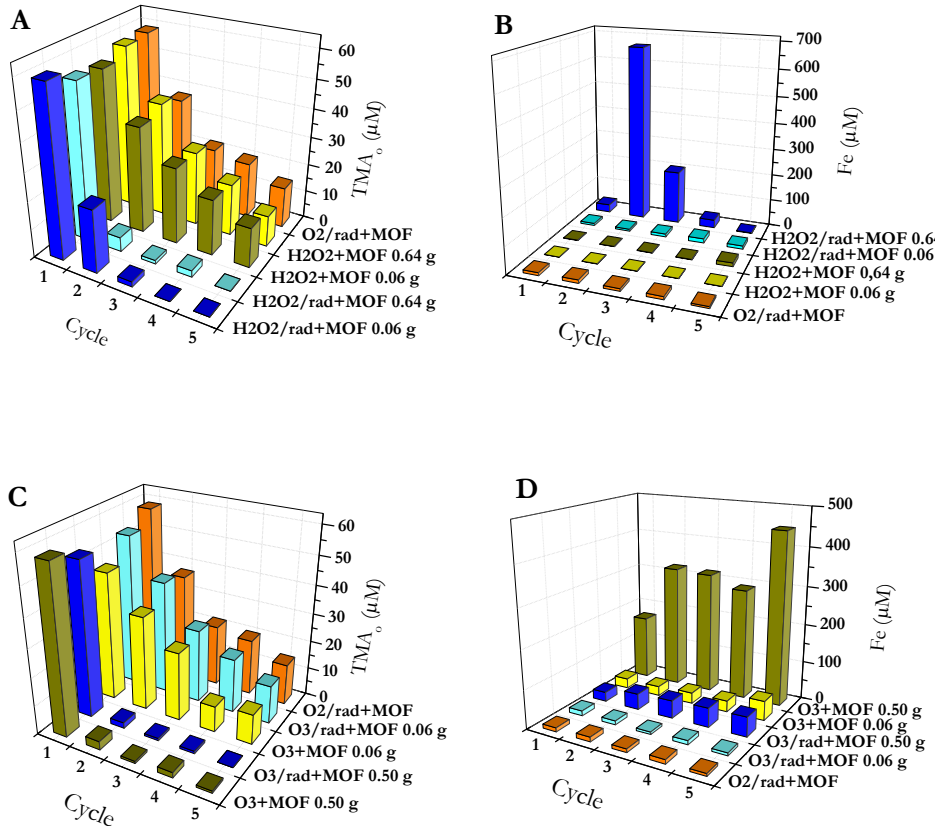

Figure 9.6. Initial TMA concentration released during the first 30 min in the dark at the beginning of each oxidation run with H_2O_2 (A) and O_3 (C), and dissolved iron at the end of the oxidation treatments with H_2O_2 (B) and O_3 (D). Experimental conditions: V=0.25 L; pH_0=4.8; T=25-35 ºC; MOF dose=1 g·L^{-1}, hydrogen peroxide and ozone doses in the figure.

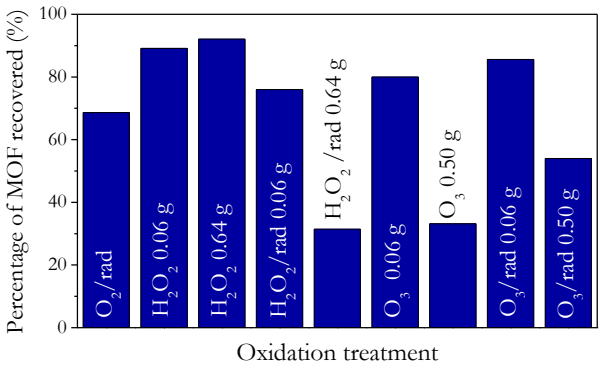

Figure 9.7. Percentage of the catalyst recovered after 5 oxidation runs of MIL-100(Fe). Experimental conditions: V=0.25 L; pH_0=4.8; T=25-35 ºC; MOF dose=1 g·L^{-1}, hydrogen peroxide and ozone doses in the figure.

Figure 9.7 depicts the percentage of the catalyst recovered after the 5-runs treatments and confirms the hypotheses above. In the absence of radiation around 90-92 wt.% of the catalyst is recovered (mass loss can be attributed to the experimental procedure) regardless of the H_2O_2 dose applied, while when radiation is used, the recovery was 76 wt.% and 31 wt.% with doses of 0.06 and 0.64 g of H_2O_2, respectively. Thus, the MOF seems to be stable in the presence of H_2O_2 in the dark though no residual TMA can be eliminated whereas MOF structure is partially degraded in the presence of radiation especially at the highest H_2O_2 dose.

The reaction mechanism proposed for heterogeneous Fenton and photo-Fenton reactions in the presence of MIL-100(Fe), MIL-88B(Fe) and other iron materials comprises also the following reactions [18,41,48]:

$$\text{MIL-100}(Fe^{3+}) + H_2O_2 \longrightarrow \text{MIL-100}(Fe^{2+}) + H^+ + HO_2^{\bullet} \quad (9.6)$$

$$\text{MIL-100}(Fe^{2+}) + H_2O_2 \longrightarrow \text{MIL-100}(Fe^{3+}) + OH^- + HO^{\bullet} \quad (9.7)$$

$$\text{MIL-100}(Fe^{3+}) + HO_2^{\bullet} \longrightarrow \text{MIL-100}(Fe^{2+}) + O_2 + H^+ \quad (9.8)$$

$$HO_2^{\bullet} + OH^- \longrightarrow H_2O + O_2^{\bullet -} \quad (9.9)$$

$$e^- + H_2O_2 \longrightarrow OH^- + HO^{\bullet} \quad (9.10)$$

In the presence of radiation, the reduction of Fe (III) nodes to Fe (II) is favored according to reaction (9.1), which is one of the key aspects of photo-Fenton application that lead to a substantial increase of the $HO^{\bullet}$ generation rate through reaction (9.7). The overall reaction mechanism is then accelerated and the formation of ROS such as $HO^{\bullet}$, $O_2^{\bullet -}$ and/or $HO_2^{\bullet}$ at higher concentration is expected with respect to dark heterogeneous Fenton. As explained in the previous section, this pathway seems to be less favorable for MOF stability likely due to the lower strength of the Fe (II)-linker interaction. Thus, in the absence of any other organic compound, ROS formed can be prone to attack free TMA and also weakly bonded TMA in Fe (II) nodes. The effect is more pronounced with the highest H_2O_2 dose in which higher concentrations of ROS are expected.

iii. Ozone

Regarding the ozonation experiments, again in the first 30 min under stirring (run 1, **Figure 9.6(C)**) from 45-58 μM TMA concentrations were observed in solution, also in agreement with previous results at similar pH in UP water (**Table 9.3**). Then, O_3 was supplied to the reactor and the lamp was switched on for radiation assisted

experiments. The subsequent values of TMA released into the reaction medium correspond again with the 30 min dark stage of stirring with the catalyst recovered from the previous run. Contrary to H_2O_2 experiments, in all cases, the concentration of TMA decreased with the number of the treatments applied being always lower for MOF treated at the highest ozone dose. In these last experiments, the concentration of TMA released after the first cycle was very low (< 1 $mg \cdot L^{-1}$) regardless of the use of radiation.

On the other hand, **Figure 9.6(D)** reveals low iron leaching with the lowest O_3 doses and in the presence of radiation. In general, the concentration of iron is lower than the corresponding to the theoretical stoichiometry with TMA in solution, neither during the first dark stage nor at the end of the treatment (see **Table 9.S2** of the supplementary information). As commented before, the reasons may include: i) free TMA was released from the porous structure of the MOF; and/or ii) even if the structure has been partially collapsed, iron species were in a solid form over the MOF surface or retained by filtration before iron analysis due to the working pH. In this sense, the highest iron concentration in solution was found in the series of dark ozonation at the highest O_3 doses, attributed this difference to the lowest pH found (pH < 4). Once in the aqueous phase, TMA can be oxidized during ozonation treatments which will be discussed in section 9.3.3. In fact, the residual TOC after 1 h is much higher than that corresponding to residual TMA (see **Table 9.S2**), indicating the presence of some oxidation intermediates refractory to the ozonation treatment. These would be mainly short-chain organic acids which might be responsible for the lowest pH observed.

Finally, the MOF mass loss during the treatments has been also checked through the percentage of recovered MOF after each experimental series (**Figure 9.7)**. When single ozonation is applied without radiation, the O_3 dose plays a key role in the degradation of the material as observed at the end of the series at low O_3 and high O_3 doses (80% vs. 33% recovered after 5 reaction cycles, respectively). The presence of radiation improves the recovery from 80% to 86% (5 cycles) at low O_3 concentration and from 33% to 54% (5 cycles) at the highest dose. In addition, the mass loss in subsequent experiments is slower when radiation is applied (not shown). In any case, the presence of radiation seems to protect the MOF deterioration during ozonation.

In this line, the mechanism proposed by Yu et al. (2019) [21] for the ozone decomposition during photocatalytic ozonation with MIL-88A(Fe), including reactions (9.1)-(9.3) and (9.8)-(9.10), could be extrapolated for MIL-100(Fe):

$$\text{MIL-100}(Fe^{3+}) + OH^- \longrightarrow \text{MIL-100}(Fe^{3+})\text{-OH} \quad (9.11)$$

$$\text{MIL-100}(Fe^{3+})\text{-OH} + O_3 \longrightarrow \text{MIL-100}(Fe^{3+})\text{-}O_3^{\bullet} + HO^{\bullet} \quad (9.12)$$

$$\text{MIL-100}(Fe^{3+})\text{-}O_3^{\bullet} + OH^- \longrightarrow \text{MIL-100}(Fe^{2+}) + HO_2^{\bullet} + {}^1O_2 \quad (9.13)$$

$$\text{MIL-100}(Fe^{2+}) + O_3 + H_2O \longrightarrow \text{MIL-100}(Fe^{3+}) + HO^{\bullet} + OH^- \quad (9.14)$$

$$e^- + O_3 + H_2O \longrightarrow {}^1O_2 + O_2^{\bullet -} + HO^{\bullet} \quad (9.15)$$

According to this mechanism, Lewis acid sites (iron nodes) reacts with O_3 leading to the formation of reduced Fe (II) sites (reactions (9.12) and (9.13)). Again this pathway seems to be less favorable for MOF stability likely due to the lowest strength of the linker-Fe (II) interaction. On the contrary, when radiation is applied, a part of O_3 will follow reaction (9.15) derived from (9.1) and (9.2) that, a priori, could not be involved in a structural disruption.

iv. Characterization of treated samples

Some samples were characterized after the treatments to check the elimination of residual TMA and the modifications of the material.

ATR-FTIR in **Figure 9.4(B)** shows the effect of radiation and hydrogen peroxide treatments over MIL-100(Fe). In general, no substantial modifications in the main bands corresponding to MIL-100(Fe) structure are observed when radiation and/or the lowest H_2O_2 dose are applied. In addition, the band attributed to free TMA at 1715 cm^{-1} completely disappeared only when radiation is combined with H_2O_2. On the contrary, at more severe conditions with the highest H_2O_2 dose plus radiation, the structure of the recovered catalyst may collapse according to the different spectrum obtained. On the other hand, in the case of ozone treatments, in **Figure 9.4(C)** no substantial differences in the spectra are observed at any of the conditions used. However, the band at 1715 cm^{-1} completely disappeared only when the highest O_3 dose is applied regardless of the use of radiation. These results are in good agreement with the MOF mass loss, TMA and Fe released in any oxidation treatment.

The elimination of not bound TMA from MIL-100(Fe) has been corroborated by XPS. The atomic C/Fe ratio can be a good indicator of the linker excess in the MOF structure. Thus, this parameter decreased after 1 cycle of all the oxidation treatments (see **Table 9.2**). The use of the highest dose of H_2O_2 (0.64 g) or 2 consecutive runs with 0.06 g H_2O_2 led to the lowest values of C/Fe, even lower than the theoretical ratio. This can be indicative of the partial degradation of the MOF surface at such

conditions. A value close to the theoretical ratio was obtained for the O_3/radiation treatment with the highest dose (**Table 9.2**). The bulk atomic C/Fe ratio led to similar results (**Table 9.1**, L1 and L2 samples correspond to MIL-100(Fe) treated at low H_2O_2 dose + radiation (2 runs) and high O_3 dose + radiation (1 run), respectively).

Besides, **Figure 9.5** (for L1)**, Figure 9.S2** and **Table 9.S1** show the modifications introduced by the treatments in the contribution of each bond to the total area of the spectra. A new contribution to the C1s spectra of treated samples at 286.2 eV is observed that can be assigned to C–O or C=O bonds in carbonyl or phenolic structures. This contribution may be indicative of the partial oxidation of the TMA linker at the surface. Moreover, in the O1s spectra of all the treated samples, the peak assigned to $–COO^-$ carboxylate moieties (531.5 eV) decreased in favor of the increment of Fe–O contribution (530 eV) probably as a consequence of the elimination of the linker or its decarboxylation leading to Fe nodes exposed to the surface (oxidized or hydroxylated) [46]. Thus, these results also corroborate surface changes due to the partial oxidation of MIL-100(Fe) during the oxidation treatments.

In addition, for the L1 and L2 samples, treated by 2 cycles of H_2O_2 (0.06 g) + radiation and 1 cycle of O_3 (0.50 g) + radiation, respectively, additional analyses by N_2 adsorption-desorption isotherms and XRD were performed. BET surface area of the H_2O_2 treated sample increased about 2% from 1468 to 1497 $m^2 \cdot g^{-1}$, likely due to the elimination of some free TMA. However, in the case of the O_3 treated sample, though the elimination of TMA was confirmed by ATR-FTIR and XPS, BET surface area decreased from 1468 to 1334 $m^2 \cdot g^{-1}$ (**Figure 9.3 and Table 9.1**). By XRD patterns (see **Figure 9.1**), all the reflections present in MIL-100(Fe) sample are also present in L1 and L2 treated MOFs indicating similar structure. However, it is noteworthy that the relative intensity of some peaks in the 2θ range between 2-14º has change. Therefore, although similar structures seem to be obtained after the H_2O_2 and O_3 treatments, the partial oxidation of the MOF surface could lead to some distortion that could be related to the generation of structural defects [46].

Even presenting quite similar structural characterization (XRD, ATR-FTIR of BET surface area), the changes observed in the MOF surface properties together with the analyses of the mass loss of the catalyst in successive runs are a clear evidence of the low stability of this material under high ozone doses (50 $mg \cdot L^{-1}$, 10 $L \cdot h^{-1}$, 0.50 g O_3/g MOF) or under H_2O_2 at high dose (0.64 g H_2O_2/g MOF) + radiation, but moderate stability at less severe conditions.

Therefore, the treatment of 1 h of simulated solar radiation and ozone at high concentration (0.50 g O_3/g MOF) or 2 cycles of 1 h of simulated solar radiation and hydrogen peroxide at low concentration (0.06 g H_2O_2/g MOF) are enough to purify the MIL-100(Fe) but introduce some surface oxidation. The samples treated on this form (MIL-100(Fe)-L1 and MIL-100(Fe)-L2, respectively) were selected to check the catalytic activity and stability in the conditions of Fenton-like and O_3 AOPs for CECs oxidation.

9.3.3. CATALYTIC ACTIVITY AND STABILITY DURING AOPs FOR CECs REMOVAL

The four CECs selected in this work, MTP, a β-blocker used for cardiovascular diseases; IBP, a nonsteroidal anti-inflammatory drug; DEET, an insect repellent; and CA, an herbicide; are frequently found in different aquatic environments [49–53] and have not been previously studied using MIL-100(Fe) as catalyst.

The first catalytic tests were performed with the synthetized MIL-100(Fe) without any treatment. The leaching of high concentrations of TMA during the experiments made difficult the observation of the catalytic performance in terms of mineralization of CECs (results not shown). Therefore, only the results with L1 and L2 in the degradation and mineralization of the four CECs are presented. For the same reason, the working concentration of CECs was set at 10 $mg \cdot L^{-1}$ each though it was much higher than the real concentrations found in wastewater [49–53].

A. Adsorption, photolysis and photocatalytic oxidation

Previous to hydrogen peroxide or ozonation AOPs, experiments of adsorption, photolysis and photocatalytic oxidation of the four CECs were carried out for comparative purposes.

The removal of the CECs by adsorption with L1 and L2 catalysts is presented in **Figure 9.8(A)**, reaching 19% and 15% with L1 and L2, respectively. The L1 and L2 adsorption capacity was different for every CEC in the mixture at the conditions tested (**Figure 9.S6**).

The lowest affinity was obtained for MTP and DEET with 1-2% regardless of the catalyst. Nearly 8-10% of CA was removed and the maximum adsorption capacity was observed for IBP reaching 50% removal. During the experiment, 90% of IBP maximum uptake is reached at 180 min of contact at the conditions used. Parameters such as pK_a of the adsorbate, pH of the solution and pH_{PZC} of the adsorbent; but also

hydrophobicity and molecular size play an important role in the adsorption capacity of MIL-100(Fe).

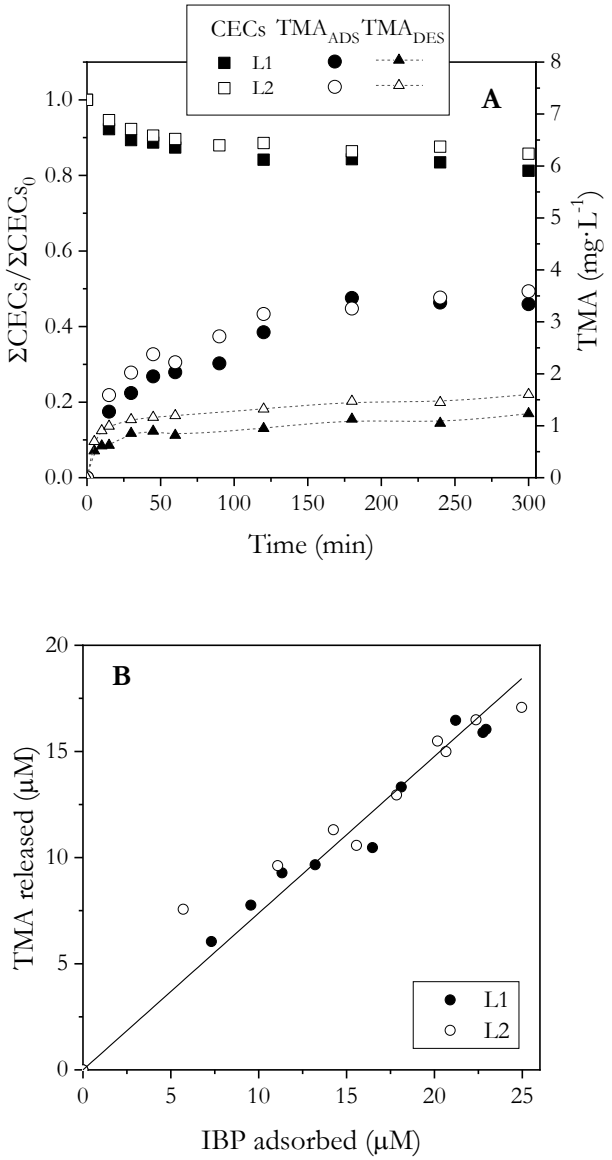

Figure 9.8. (A) Removal of CECs by adsorption onto L1 and L2 MOF samples and TMA released during the adsorption experiments. TMA released in similar conditions without CECs is presented. (B) TMA released vs. IBP adsorbed using L1 and L2 MOFs. Experimental conditions: V=0.25 L; pH_0=4.8; T=25-40ºC; initial CECs concentration=10 mg·L^{-1} each; initial TOC concentration=26 mg·L^{-1}; MOF dose=0.2 g·L^{-1}.

Taking into account the values of these parameters for the CECs (**Table 9.S3**), the value of pH_{PZC} 3.8 of the catalysts and the pH~4.8 of the solution during the experiment, the adsorption capacity seems to be directly related to the hydrophobicity of the adsorbate being the solubility in water in the order DEET > MTP >> CA >> IBP [54–56].

Besides the evolution of the CECs, the concentrations of TMA from the L1 and L2 MOFs and Fe released into the medium were followed. After 300 min of contact time in the presence of the CECs, near 3.5 $mg \cdot L^{-1}$ (~16 μM) of TMA concentrations were detected. These concentrations are higher than the expected according to results in **Figure 9.6** and **Table 9.S2** for L1 and L2 treated samples even with a lower MOF dose (0.2 $g \cdot L^{-1}$ vs. 1 $g \cdot L^{-1}$ in stability tests). Iron concentration detected was low in both experiments was low (< 0.5 $mg \cdot L^{-1}$, 9 μM). Thus, additional experiments without CECs were conducted to analyze the TMA and iron leaching at similar conditions (**Figure 9.8(A)**). With both samples (L1 and L2) lower TMA concentrations were detected during the contact of the MOF with UP water with no CECs. Thus, the adsorption of CECs (mainly IBP) seems to have some influence in TMA desorption. An additional plot of the amount of TMA released vs. IBP adsorbed onto the MOF is presented in **Figure 9.8(B)**. Two possible hypotheses are: (1) residual adsorbed TMA is exchanged by IBP molecules in similar adsorption sites, even with treated samples in which no evidences of residual TMA were observed by characterization; and/or (2) some TMA can be exchanged by IBP molecules in the MOF structure. This phenomenon will be the subject of a future work since it is out of the scope of this study.

Regarding the radiation assisted processes, photolysis of the CECs and photocatalytic oxidation were studied to check their contribution on the CECs degradation rate. From photolysis runs, the CECs were stable under simulated solar irradiation in the absence of catalyst with less than 5% removal at similar the conditions tested (experimental conditions similar to **Figure 9.9,** results not shown). On the other hand, **Figure 9.9** shows the CECs removal by photocatalytic oxidation with the L1 MOF. The concentration of TMA released into the reaction medium has been also analyzed. The degradation rate of the CECs was very different reaching 95% of IBP removal in 30 min, whereas 60% of CA and barely 7 and 10% of MTP and DEET were eliminated after 300 min of treatment. These huge differences cannot be attributable to the different reactivity with ROS formed during photocatalytic oxidation (mainly hydroxyl radical) according to the reported $k_{HO^{\bullet}}$ values for the CECs (see **Table 9.S3**). In fact, the elimination rates obeyed the order of CECs adsorption onto the MOF, thus indicating the importance of the selective adsorption to make the active sites accessible

for photocatalytic reactions [57]. On the other hand, with respect to the stability of the MOF during the treatment, the concentration of TMA in solution reached values about 3 mg·L^{-1} during the first 30 min, which decreased upon the treatment up to 2 mg·L^{-1}. TMA can be oxidized by hydroxyl radicals with a rate constant $k_{HO\cdot\text{-}TMA}$ in the range 1.03×10^9 - 1.49×10^9 M^{-1}·s^{-1} at pH in the range 3-7, [58]). In addition, the concentration of iron leached varied from 1.3-0.86 mg·L^{-1} (23-15 μM) at the end of the treatment. The decrease in the Fe concentration is probably due to the rise in the pH of the reaction medium from 4.8-5.4. Finally, the mineralization reached was 16% with less than 1 mg·L^{-1} of residual TOC from TMA (4.6% of the remaining TOC).

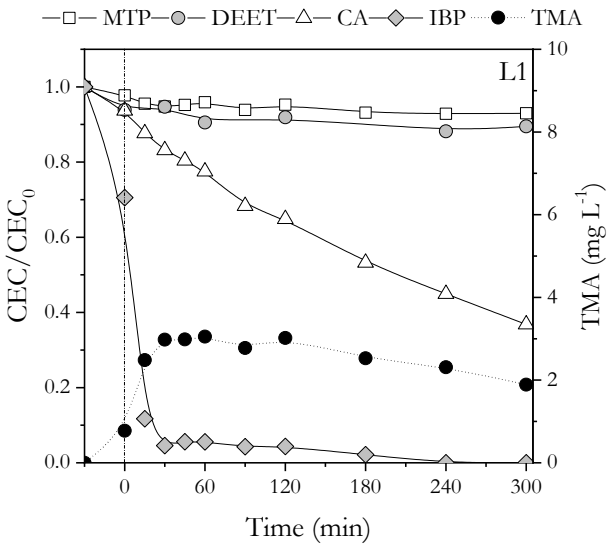

Figure 9.9. Removal of CECs by photocatalytic oxidation with L1 and TMA concentration released into the reaction medium. Experimental conditions: V=0.25 L; pH_0=4.8; T=25-40 ºC; initial CECs concentration=10 mg·L^{-1} each; initial TOC concentration=26 mg·L^{-1}; gas flow rate (O_2)=10 L·h^{-1}; Simulated solar irradiance=550 W·m^{-2}; MOF dose=0.2 g·L^{-1}.

Similar results in terms of CECs removal were obtained with L2 catalyst although the release of TMA and iron was somewhat higher (see **Figure 9.S7**). The mineralization reached after 300 min of treatment was 10% with a contribution of 2.3 mg·L^{-1} of TOC from TMA (~10% of the remaining TOC). Iron leached showed a maximum concentration of 2.4 mg·L^{-1} (43 μM) in solution.

Therefore, the efficiency of the photocatalytic oxidation treatment with MIL-100(Fe) seems to be governed by the selective adsorption of the CECs. At the conditions tested, the mineralization reached is low and intensified AOPs such as

hydrogen peroxide or ozone assisted processes may improve the degradation and mineralization rates.

B. Hydrogen peroxide processes

To take the advantage of the presence of iron nodes in MIL-100(Fe) together with radiation, heterogeneous Fenton-like and photo-Fenton like processes were applied to the degradation of the CECs. **Figure 9.10(A)** shows the evolution of the concentration of CECs upon different H_2O_2 assisted treatments together with the TMA concentration released into the reaction medium using the L1 MOF. **Figure 9.10(B)** shows the mineralization reached. Without catalyst and/or radiation, H_2O_2 did not present any oxidation capacity of the CECs and negligible conversion was reached. However, the combination of H_2O_2 + radiation led to almost complete depletion of the CECs after 300 min of treatment with 43% of H_2O_2 conversion, although the mineralization was less than 20% (**Figure 9.10(B)**). The evolution of the individual CECs concentration (not shown) was very similar and followed the order of CECs-$HO^{\bullet}$ reactivity. Thus, at the high concentration of H_2O_2 and the radiation wavelength used (300-800 nm), hydrogen peroxide may undergo photolytic breakdown to form a considerable concentration of hydroxyl radicals [59,60].

Regarding catalytic treatments, dark heterogeneous Fenton-like with L1 led to a slow degradation rate reaching 40% CECs removal after 300 min (higher than 10% of adsorption from **Figure 9.8**). In addition, the released TMA remained in the solution at the end of the treatment. However, the combination with radiation substantially increased the CECs removal with complete elimination in 30 min and also a high degradation rate of TMA was observed. In both treatments the highest elimination rate was found for IBP (not shown) although with lower differences between the CECs degradation rates than in photocatalytic oxidation. In terms of mineralization, photo-Fenton-like treatment led to a high TOC removal (72% in 300 min). These results are in agreement with previous ones on the stability of MIL-100(Fe) in H_2O_2 oxidizing environment.

It is necessary to point out that the working pH was maintained in the range 4.8-4 which introduces an advantage over other Fenton-like systems [16,47]. Iron leaching was also analyzed and maximum concentrations detected were 0.6 and 1.3 $mg \cdot L^{-1}$ in dark and photo-Fenton-like, respectively. At these conditions (pH 4.5, Fe(III) 1.5 $mg \cdot L^{-1}$, CECs 10 $mg \cdot L^{-1}$, TMA 3 $mg \cdot L^{-1}$) a significant contribution of homogeneous catalytic was observed for photo-Fenton, reaching a 60% of mineralization was reached in 300

min (see **Figure 9S.8**). Similar results were obtained with L2 catalyst (**Figure 9.S8**) but also higher concentration of TMA and iron leaching was observed.

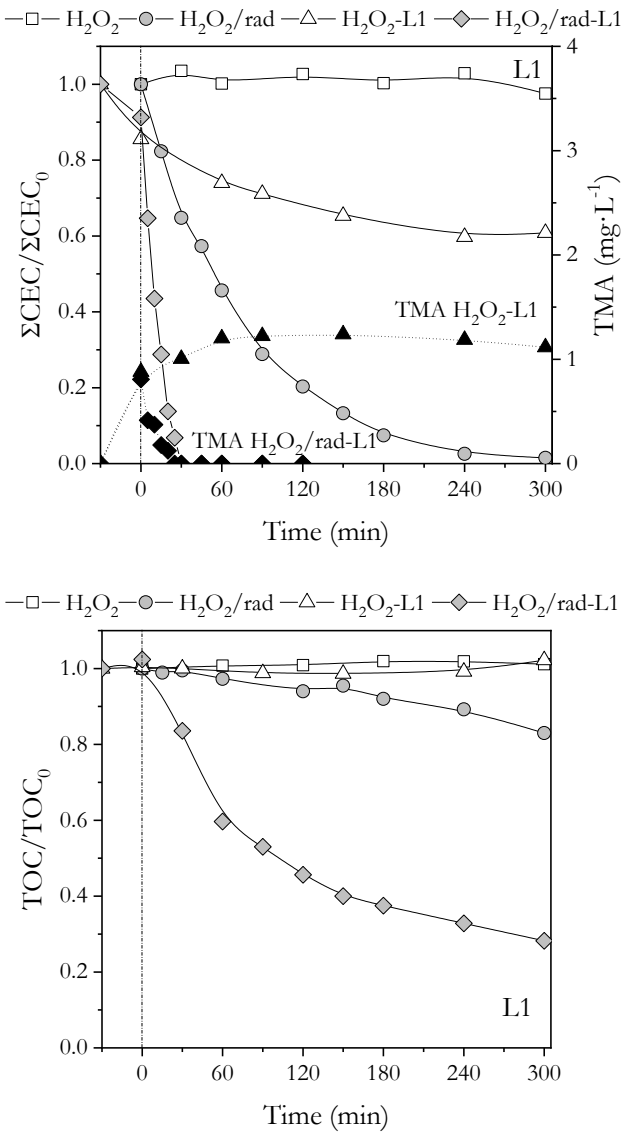

Figure 9.10. (A) Removal of CECs and TMA released into the reaction medium by different hydrogen peroxide processes using L1 as catalyst. (B) TOC removal by different hydrogen peroxide processes. Experimental conditions: V=0.25 L; pH_0=4.8; T=25-40ºC; Simulated solar irradiance (if applied)=550 W·m^{-2}; gas flow rate (O_2)=10 L·h^{-1}; initial CECs concentration=10 mg L^{-1} each; initial TOC concentration=26 mg·L^{-1}; initial H_2O_2 concentration=1275 mg·L^{-1}; MOF dose (if applied)=0.2 g·L^{-1}.

Therefore, a high catalytic activity in photo-Fenton-like treatment of pre-treated MIL-100(Fe) samples has been obtained for the removal of the four selected CECs, although TMA and iron are always detected in the reaction medium.

C. Ozone processes

The comparison of different ozone processes in the removal of the selected CECs and their mineralization is presented in **Figure 9.11**. Regarding CECs, all the ozonation processes achieved more than 90% removal in less than 180 min, being photocatalytic ozonation (O_3 + L1 + radiation) and photo-ozonation (O_3 + radiation) the most efficient treatments. The individual CECs reaction rate in all the treatments is in agreement with the reaction rate constant with the main species involved. Thus, during single ozonation, MTP was degraded faster than the other CECs according to its higher direct ozonation rate constant (see **Table 9.S3**). On the other hand, IBP depletion is faster when radiation and/or catalyst are combined with ozone. In the first case, molecular ozone reactions will gain importance at the pH of the experiment (pH varied from 4.8 to 3.8) [61], but when solar radiation and/or catalysts are used, the decomposition of O_3 towards ROS (mainly $HO^{\bullet}$ radicals) is improved [23,33,61,62]. This is highlighted in the mineralization reached (**Figure 9.11(B)**) that was very low (5%) for single ozonation mainly due to the formation of refractory compounds towards O_3 direct reactions [61]. In catalytic ozonation, the TOC removal increased up to 25% but the best results were observed by photo-ozonation and photocatalytic ozonation, where a substantial mineralization around 80% was achieved in both cases. The highest mineralization rate was obtained by photocatalytic ozonation. According to the mechanism proposed by Yu et al. (2019) [21] for other Fe-based MOF, it is expected a synergistic effect between ozone and irradiated MIL-100(Fe).

Regarding the TMA and iron released into the reaction medium, it can be observed in **Figure 9.11(A)** that the TMA can be removed by catalytic ozonation and photocatalytic ozonation, being the degradation rate of TMA higher during photocatalytic ozonation. TMA would be mainly eliminated by $HO^{\bullet}$ radicals according to the low O_3-TMA rate constant value ($k_{O3\text{-}TMA}$=0.07 $M^{-1}\cdot s^{-1}$ at pH 4, [58]). Iron leaching was lower than 0.6 $mg\cdot L^{-1}$ in both catalytic and photocatalytic treatments.

Similar results can be found for L2 MOF in **Figure 9.S9** of the Supplementary Information document.

According to the presented results, photocatalytic ozonation using L1 and L2 MIL-100(Fe) materials is an effective treatment for CECs removal but did not offer a high

enough improvement neither in the degradation rate, nor in the mineralization compared to photo-ozonation at the conditions tested.

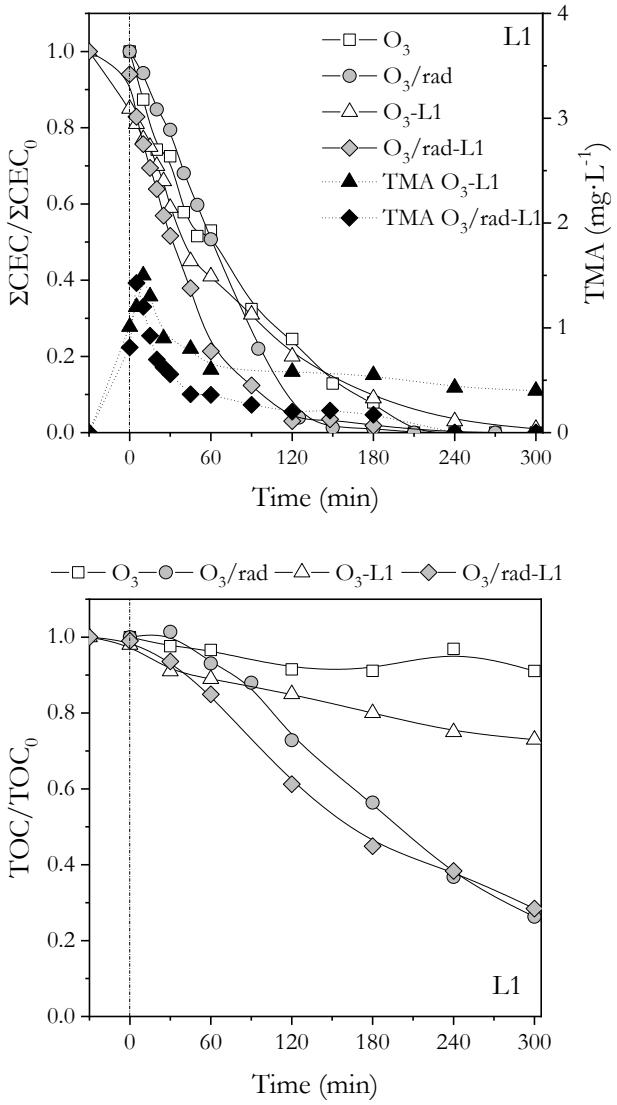

Figure 9.11. (A) Removal of CECs and TMA released into the reaction medium by different ozonation processes using L1 as catalyst. (B) TOC removal by different ozonation processes. Experimental conditions: V=0.25 L; pH_0=4.8; T=25-40 ºC; Simulated solar irradiance (if applied)=550 $W \cdot m^{-2}$; gas flow rate (O_2/O_3)=10 $L \cdot h^{-1}$; gas inlet O_3 concentration=6 $mg \cdot L^{-1}$; initial CECs concentration=10 $mg \cdot L^{-1}$ each; initial TOC concentration=26 $mg \cdot L^{-1}$; MOF dose (if applied)=0.2 $g \cdot L^{-1}$.

D. Final remarks

The pre-treated L1 and L2 materials, in which no residual TMA was detected by characterization studies, presented a high catalytic activity in heterogeneous photo-Fenton-like process and a moderate catalytic activity for photocatalytic ozonation process applied to the removal of metoprolol, ibuprofen, n,n-dimethyl-m-toluamide and clofibric acid. However, the organic linker of the MOF and iron were always detected in the reaction medium, being the concentrations always higher in the ozone pre-treated MIL-100(Fe)-L2. This is not a concerning issue from the point of view of the toxicity since iron is at low concentration and TMA is degraded during the AOPs, but is critical in real applications for long-term use of these MIL-100(Fe) materials.

9.4. CONCLUSIONS

- The Fe-based MOF MIL-100(Fe) has been synthetized with rather good crystallinity and porosity and can be purified to eliminate the remaining linker in oxidizing conditions under simulated solar radiation and the use of ozone or hydrogen peroxide.
- The stability of MIL-100(Fe) in such oxidizing environments depends on the conditions used. High doses of ozone or hydrogen peroxide with radiation provoked a large mass loss of the catalyst, but at less severe conditions a moderate stability was obtained although MIL-100(Fe) underwent surface oxidation/decarboxylation to some extent.
- The purified MIL-100(Fe) materials showed a high catalytic activity for photo-Fenton-like and a moderate activity for photocatalytic ozonation processes applied to CECs removal.
- However the stability of the MIL-100(Fe) is very low in presence of phosphates and questionable for AOPs even with purified materials, always leaching some amounts of the linker (trimesic acid) and iron into the reaction medium, although trimesic acid can be effectively removed by the AOPs tested.
- Therefore, taking into account the existence of more stable and low-cost materials for these AOPs, the application of MIL-100(Fe) is not recommended for water detoxification.

REFERENCES

[1] S.T. Meek, J.A. Greathouse, M.D. Allendorf, "Metal-organic frameworks: A rapidly growing class of versatile nanoporous materials" *Adv. Mater.* 23 (**2011**) 249–267.

[2] A. Dhakshinamoorthy, A.M. Asiri, H. García, "Metal-Organic Framework (MOF) compounds: photocatalysts for redox reactions and solar fuel production" *Angew. Chemie - Int. Ed.* 55 (**2016**) 5414–5445.

[3] M. Mon, R. Bruno, J. Ferrando-Soria, D. Armentano, E. Pardo, "Metal-organic framework technologies for water remediation: towards a sustainable ecosystem" *J. Mater. Chem. A.* 6 (**2018**) 4912–4947.

[4] J. Bedia, V. Muelas-Ramos, M. Peñas-Garzón, A. Gómez-Avilés, J.J. Rodríguez, C. Belver, "A review on the synthesis and characterization of metal organic frameworks for photocatalytic water purification" *Catalysts.* 9 (**2019**) 52.

[5] J. Canivet, A. Fateeva, Y. Guo, B. Coasne, D. Farrusseng, "Water adsorption in MOFs: Fundamentals and applications" *Chem. Soc. Rev.* 43 (**2014**) 5594–5617.

[6] P. Horcajada, S. Surblé, C. Serre, D.-Y. Hong, Y.-K. Seo, J.-S. Chang, J.-M. Grenèche, I. Margiolaki, G. Férey, "Synthesis and catalytic properties of MIL-100(Fe), an iron(III) carboxylate with large pores" *Chem. Commun.* 100 (**2007**) 2820–2822.

[7] I. Bezverkhyy, G. Weber, J.P. Bellat, "Degradation of fluoride-free MIL-100(Fe) and MIL-53(Fe) in water: Effect of temperature and pH" *Microporous Mesoporous Mater.* 219 (**2016**) 117–124.

[8] Y. Li, H. Xu, S. Ouyang, J. Ye, "Metal-organic frameworks for photocatalysis" *Phys. Chem. Chem. Phys.* 18 (**2016**) 7563–7572.

[9] D. Wang, F. Jia, H. Wang, F. Chen, Y. Fang, W. Dong, G. Zeng, X. Li, Q. Yang, X. Yuan, "Simultaneously efficient adsorption and photocatalytic degradation of tetracycline by Fe-based MOFs" *J. Colloid Interface Sci.* 519 (**2018**) 273–284.

[10] N.C. Burtch, H. Jasuja, K.S. Walton, "Water stability and adsorption in metal-

organic frameworks" *Chem. Rev.* 114 (**2014**) 10575–10612.

[11] E.A. Kozlova, V.N. Panchenko, Z. Hasan, N.A. Khan, M.N. Timofeeva, S.H. Jhung, "Photoreactivity of metal-organic frameworks in the decolorization of methylene blue in aqueous solution" *Catal. Today*. 266 (**2016**) 136–143.

[12] K. Guesh, C.A.D. Caiuby, Á. Mayoral, M. Díaz-García, I. Díaz, M. Sanchez-Sanchez, "Sustainable preparation of MIL-100(Fe) and its photocatalytic behavior in the degradation of methyl orange in water" *Cryst. Growth Des.* 17 (**2017**) 1806–1813.

[13] J. Yang, X. Niu, S. An, W. Chen, J. Wang, W. Liu, "Facile synthesis of Bi_2MoO_6-MIL-100(Fe) metal-organic framework composites with enhanced photocatalytic performance" *RSC Adv.* 7 (**2017**) 2943–2952.

[14] N.M. Mahmoodi, J. Abdi, M. Oveisi, M. Alinia Asli, M. Vossoughi, "Metal-organic framework (MIL-100 (Fe)): Synthesis, detailed photocatalytic dye degradation ability in colored textile wastewater and recycling" *Mater. Res. Bull.* 100 (**2018**) 357–366.

[15] D.-D. Chen, X.-H. Yi, C. Zhao, H. Fu, P. Wang, C.-C. Wang, "Polyaniline modified MIL-100(Fe) for enhanced photocatalytic Cr(VI) reduction and tetracycline degradation under white light" *Chemosphere*. 245 (**2020**) 125659.

[16] H. Lv, H. Zhao, T. Cao, L. Qian, Y. Wang, G. Zhao, "Efficient degradation of high concentration azo-dye wastewater by heterogeneous Fenton process with iron-based metal-organic framework" *J. Mol. Catal. A Chem.* 400 (**2015**) 81–89.

[17] X. Liu, R. Dang, W. Dong, X. Huang, J. Tang, H. Gao, G. Wang, "A sandwich-like heterostructure of TiO_2 nanosheets with MIL-100(Fe): A platform for efficient visible-light-driven photocatalysis" *Appl. Catal. B Environ.* 209 (**2017**) 506–513.

[18] Z. Mohammadifard, R. Saboori, N.S. Mirbagheri, S. Sabbaghi, "Heterogeneous photo-Fenton degradation of formaldehyde using MIL-100(Fe) under visible light irradiation" *Environ. Pollut.* 251 (**2019**) 783–791.

[19] G. Pliego, J.A. Zazo, P. Garcia-Muñoz, M. Munoz, J.A. Casas, J.J. Rodriguez, "Trends in the intensification of the fenton process for wastewater treatment-

An overview" *Crit. Rev. Environ. Sci. Technol.* 45 (**2015**) 2611–2692.

[20] M. Ahmad, S. Chen, F. Ye, X. Quan, S. Afzal, H. Yu, X. Zhao, "Efficient photo-Fenton activity in mesoporous MIL-100(Fe) decorated with ZnO nanosphere for pollutants degradation" *Appl. Catal. B Environ.* 245 (**2019**) 428–438.

[21] D. Yu, M. Wu, Q. Hu, L. Wang, C. Lv, L. Zhang, "Iron-based metal-organic frameworks as novel platforms for catalytic ozonation of organic pollutant: Efficiency and mechanism" *J. Hazard. Mater.* 367 (**2019**) 456–464.

[22] T.E. Agustina, H.M. Ang, V.K. Vareek, "A review of synergistic effect of photocatalysis and ozonation on wastewater treatment" *J. Photochem. Photobiol. C Photochem. Rev.* 6 (**2005**) 264–273.

[23] F.J. Beltrán, A. Rey, "Solar or UVA-Visible photocatalytic ozonation of water contaminants" *Molecules*. 22 (**2017**) 1177.

[24] D. Yu, L. Li, M. Wu, J.C. Crittenden, "Enhanced photocatalytic ozonation of organic pollutants using an iron-based metal-organic framework" *Appl. Catal. B Environ.* 251 (**2019**) 66–75.

[25] R. Liang, S. Luo, F. Jing, L. Shen, N. Qin, L. Wu, "A simple strategy for fabrication of Pd@MIL-100(Fe) nanocomposite as a visible-light-driven photocatalyst for the treatment of pharmaceuticals and personal care products (PPCPs)" *Appl. Catal. B Environ.* 176–177 (**2015**) 240–248.

[26] J. Huang, H. Song, C. Chen, Y. Yang, N. Xu, X. Ji, C. Li, J.-A. You, "Facile synthesis of N-doped TiO_2 nanoparticles caged in MIL-100(Fe) for photocatalytic degradation of organic dyes under visible light irradiation" *J. Environ. Chem. Eng.* 5 (**2017**) 2579–2585.

[27] N. Barbero, D. Vione, "Why dyes should not be used to test the photocatalytic activity of semiconductor oxides" *Environ. Sci. Technol.* 50 (**2016**) 2130–2131.

[28] S. Subramanian, J.S. Noh, J.A. Schwarz, "Determination of the point of zero charge of composite oxides" *J. Catal.* 114 (**1988**) 433–439.

[29] M.N. Timofeeva, V.N. Panchenko, N.A. Khan, Z. Hasan, I.P. Prosvirin, S. V.

Tsybulya, S.H. Jhung, "Isostructural metal-carboxylates MIL-100(M) and MIL-53(M) (M: V, Al, Fe and Cr) as catalysts for condensation of glycerol with acetone" *Appl. Catal. A Gen.* 529 (**2017**) 167–174.

[30] H. Bader, J. Hoigné, "Determination of ozone in water by the indigo method" *Water Res.* 15 (**1981**) 449–456.

[31] G. Eisenberg, "Colorimetric determination of hydrogen peroxide" *Ind. Eng. Chem. Anal. Ed.* 15 (**1943**) 327–328.

[32] W. Masschelein, M. Denis, R. Ledent, "Spectrophotometric determination of residual hydrogen peroxide" *Water Sew. Work.* 124 (**1977**) 69–72.

[33] A.M. Chávez, A. Rey, F.J. Beltrán, P.M. Álvarez, "Solar photo-ozonation: A novel treatment method for the degradation of water pollutants" *J. Hazard. Mater.* 317 (**2016**) 36–43.

[34] Y.K. Seo, J.W. Yoon, J.S. Lee, U.H. Lee, Y.K. Hwang, C.H. Jun, P. Horcajada, C. Serre, J.S. Chang, "Large scale fluorine-free synthesis of hierarchically porous iron(III) trimesate MIL-100(Fe) with a zeolite MTN topology" *Microporous Mesoporous Mater.* 157 (**2012**) 137–145.

[35] J. Shi, S. Hei, H. Liu, Y. Fu, F. Zhang, Y. Zhong, W. Zhu, "Synthesis of MIL-100(Fe) at low temperature and atmospheric pressure" *J. Chem.* 2013 (**2013**) 1–4.

[36] M.G. Plaza, A.M. Ribeiro, A. Ferreira, J.C. Santos, Y.K. Hwang, Y.-K. Seo, U.-H. Lee, J.-S. Chang, J.M. Loureiro, A.E. Rodrigues, "Separation of C3/C4 hydrocarbon mixtures by adsorption using a mesoporous iron MOF: MIL-100(Fe)" *Microporous Mesoporous Mater.* 153 (**2012**) 178–190.

[37] J. Zhu, X.-Y. Yu, Y. Jia, F.-M. Peng, B. Sun, M.-Y. Zhang, T. Luo, J.-H. Liu, X.-J. Huang, "Iron and 1,3,5-benzenetricarboxylic metal-organic coordination polymers prepared by solvothermal method and their application in efficient As(V) removal from aqueous solutions" *J. Phys. Chem. C.* 116 (**2012**) 8601–8607.

[38] Y. Gao, S. Li, Y. Li, L. Yao, H. Zhang, "Accelerated photocatalytic degradation of organic pollutant over metal-organic framework MIL-53(Fe) under visible LED light mediated by persulfate" *Appl. Catal. B Environ.* 202 (**2017**) 165–174.

[39] J. MacLeod, "Design and construction of on-surface molecular nanoarchitectures: lessons and trends from trimesic acid and other small carboxlyated building blocks" *J. Phys. D. Appl. Phys.* 53 (**2020**) 43002.

[40] S.K. Tam, J. Dusseault, S. Polizu, M. Ménard, J.-P. Hallé, L. Yahia, "Physicochemical model of alginate–poly-l-lysine microcapsules defined at the micrometric/nanometric scale using ATR-FTIR, XPS, and ToF-SIMS" *Biomaterials*. 26 (**2005**) 6950–6961.

[41] C. Gao, S. Chen, X. Quan, H. Yu, Y. Zhang, "Enhanced Fenton-like catalysis by iron-based metal organic frameworks for degradation of organic pollutants" *J. Catal.* 356 (**2017**) 125–132.

[42] X. Zheng, L. Zhang, Z. Fan, Y. Cao, L. Shen, C. Au, L. Jiang, "Enhanced catalytic activity over MIL-100(Fe) with coordinatively unsaturated Fe^{2+}/Fe^{3+} sites for selective oxidation of H_2S to sulfur" *Chem. Eng. J.* 374 (**2019**) 793–801.

[43] Y.-Y. Fu, C.-X. Yang, X.-P. Yan, "Metal-organic framework MIL-100(Fe) as the stationary phase for both normal-phase and reverse-phase high performance liquid chromatography" *J. Chromatogr. A*. 1274 (**2013**) 137–144.

[44] H. Hu, H. Zhang, Y. Chen, H. Ou, "Enhanced photocatalysis using metal-organic framework MIL-101(Fe) for organophosphate degradation in water" *Environ. Sci. Pollut. Res.* 26 (**2019**) 24720–24732.

[45] M. Nehra, N. Dilbaghi, N.K. Singhal, A.A. Hassan, K.-H. Kim, S. Kumar, "Metal organic frameworks MIL-100(Fe) as an efficient adsorptive material for phosphate management" *Environ. Res.* 169 (**2019**) 229–236.

[46] D. Mateo, A. Santiago-Portillo, J. Albero, S. Navalón, M. Alvaro, H. García, "Long-term photostability in terephthalate metal-organic frameworks" *Angew. Chemie - Int. Ed.* 58 (**2019**) 17843.

[47] D. Ozer, O. Icten, N. Altuntas-Oztas, B. Zumreoglu-Karan, "MIL-100(Fe) metal-organic framework catalyzed oxidation of phenol revisited: dark-Fenton activity of the catalyst" *Res. Chem. Intermed.* 46 (**2020**) 909–922.

[48] B. Jain, A. Kumar Singh, H. Kim, E. Lichtfouse, V.K. Sharma, "Treatment of organic pollutants by homogeneous and heterogeneous Fenton reaction

processes" *Environ. Chem. Lett.* 16 (**2018**) 947–967.

[49] B. Shao, D. Chen, J. Zhang, Y. Wu, C. Sun, "Determination of 76 pharmaceutical drugs by liquid chromatography-tandem mass spectrometry in slaughterhouse wastewater" *J. Chromatogr. A*. 1216 (**2009**) 8312–8318.

[50] M. Gros, M. Petrović, A. Ginebreda, D. Barceló, "Removal of pharmaceuticals during wastewater treatment and environmental risk assessment using hazard indexes" *Environ. Int.* 36 (**2010**) 15–26.

[51] T. Deblonde, C. Cossu-Leguille, P. Hartemann, "Emerging pollutants in wastewater: A review of the literature" *Int. J. Hyg. Environ. Health*. 214 (**2011**) 442–448.

[52] D.J. Lapworth, N. Baran, M.E. Stuart, R.S. Ward, "Emerging organic contaminants in groundwater: a review of sources, fate and occurrence" *Environ. Pollut.* 163 (**2012**) 287–303.

[53] R. Loos, R. Carvalho, D.C. António, S. Comero, G. Locoro, S. Tavazzi, B. Paracchini, M. Ghiani, T. Lettieri, L. Blaha, B. Jarosova, S. Voorspoels, K. Servaes, P. Haglund, J. Fick, R.H. Lindberg, D. Schwesig, B.M. Gawlik, "EU-wide monitoring survey on emerging polar organic contaminants in wastewater treatment plant effluents" *Water Res.* 47 (**2013**) 6475–6487.

[54] I. Erucar, S. Keskin, "Efficient storage of drug and cosmetic molecules in biocompatible metal organic frameworks: A molecular simulation study" *Ind. Eng. Chem. Res.* 55 (**2016**) 1929–1939.

[55] S. Rojas, I. Colinet, D. Cunha, T. Hidalgo, F. Salles, C. Serre, N. Guillou, P. Horcajada, "Toward understanding drug incorporation and delivery from biocompatible metal-organic frameworks in view of cutaneous administration" *ACS Omega*. 3 (**2018**) 2994–3003.

[56] Q. Zhang, Y. Cui, G. Qian, "Goal-directed design of metal-organic frameworks for liquid-phase adsorption and separation" *Coord. Chem. Rev.* 378 (**2019**) 310–332.

[57] X. Liu, B. Tang, J. Long, W. Zhang, X. Liu, Z. Mirza, "The development of MOFs-based nanomaterials in heterogeneous organocatalysis" *Sci. Bull.* 63

(**2018**) 502–524.

[58] A.M. Chávez, A. Rey, P.M. Álvarez, F.J. Beltrán, "Removal of a tricarboxylic acid by ozone-based processes: Trimesic acid" in: "*3rd International Congress of Chemical Engineering (ANQUE-ICCE)*" Santander, Spain (**2019**).

[59] L. Chu, C. Anastasio, "Formation of hydroxyl radical from the photolysis of frozen hydrogen peroxide" *J. Phys. Chem. A.* 109 (**2005**) 6264–6271.

[60] L. Chu, C. Anastasio, "Formation of hydroxyl radical from the photolysis of frozen hydrogen peroxide. Additions and corrections" *J. Phys. Chem. A.* 112 (**2008**) 2747–2748.

[61] F.J. Beltrán, "Ozone reaction kinetics for water and wastewater systems" *Lewis Publishers*, Florida (**2004**).

[62] J. Wang, Z. Bai, "Fe-based catalysts for heterogeneous catalytic ozonation of emerging contaminants in water and wastewater" *Chem. Eng. J.* 312 (**2017**) 79–98.

SUPPLEMENTARY MATERIAL

Insights into the stability and catalytic activity of MIL-100(Fe) for different advanced oxidation processes

Ana M. Chávez, Ana Rey*, Jorge López, Pedro M. Álvarez, Fernando J. Beltrán

Departamento de Ingeniería Química y Química Física, Instituto Universitario de Investigación del Agua, Cambio Climático y Sostenibilidad (IACYS), Universidad de Extremadura, Av. de Elvas s/n, 06006 Badajoz (Spain)

1. Characterization of the synthesized and treated samples of MIL-100(Fe)

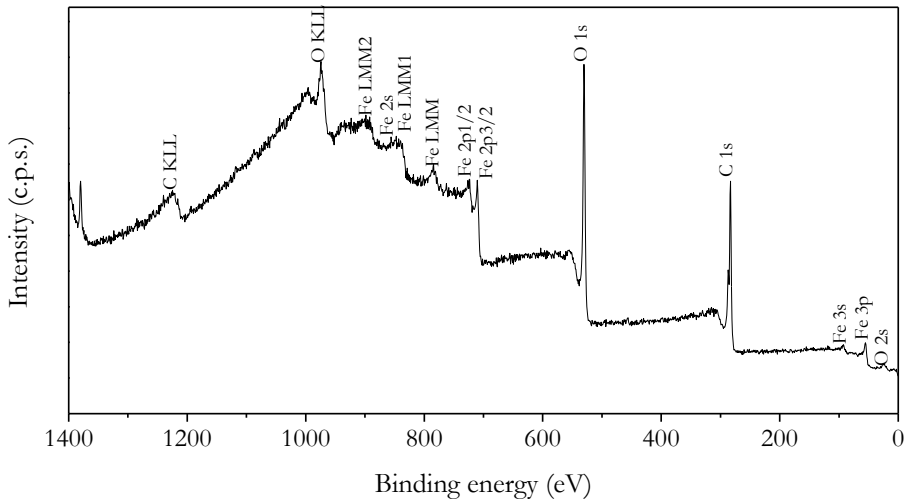

Figure 9.S1. XPS full spectra of MIL-100(Fe) synthetized sample.

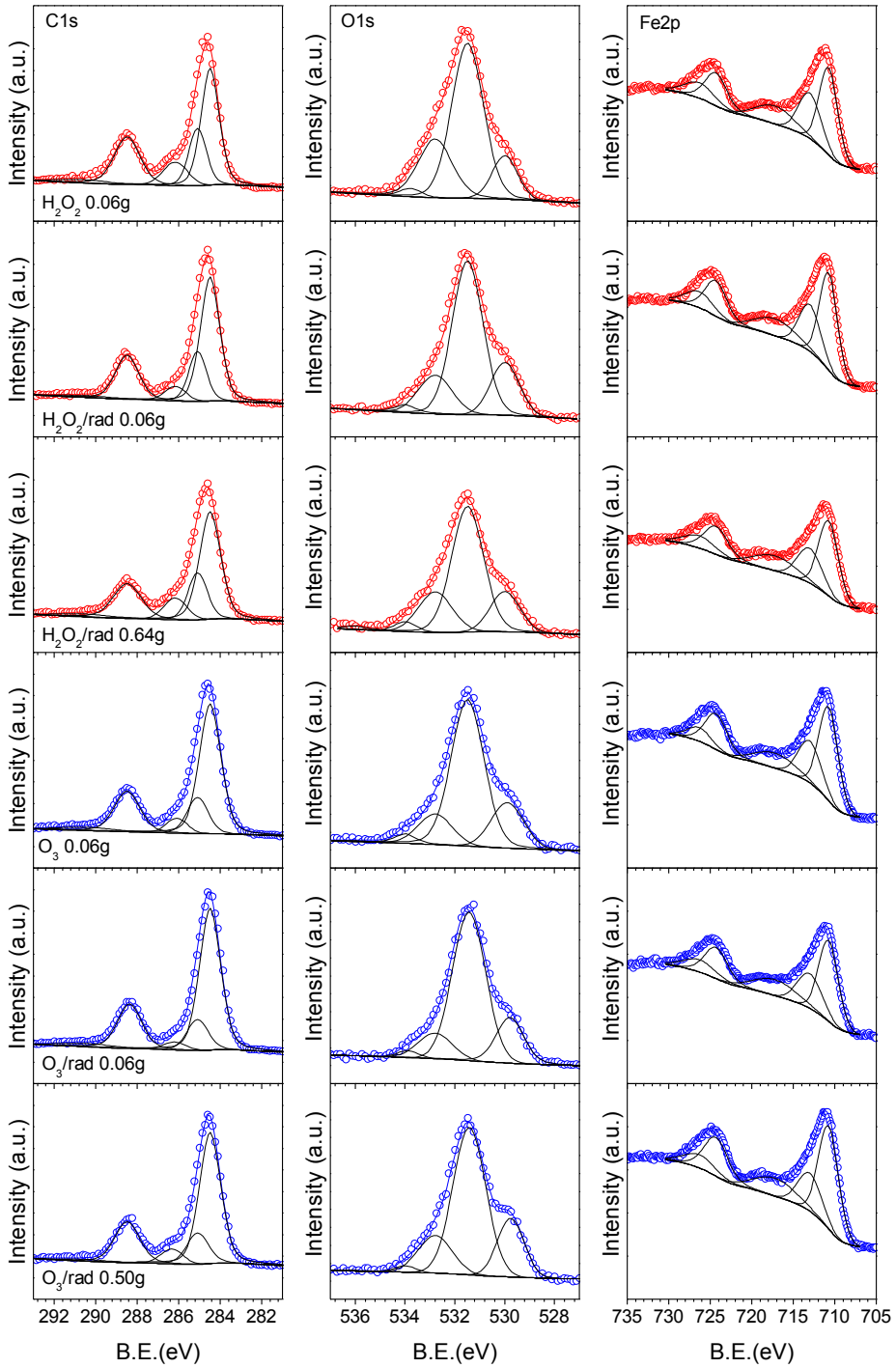

Figure 9.S2. XPS high resolution spectra of treated samples.

Table 9.S1. XPS contributions to the C 1s, O 1s and Fe 2p spectral regions of fresh MIL-100(Fe) and under oxidizing environments in ultrapure water.

Region	Peak position (eV)	Bond Assignment	MIL-100(Fe)	H_2O_2 (0.06g)	H_2O_2/rad (0.06 g)	H_2O_2/rad (0.64 g)	2 x H_2O_2/rad (0.06 g) L1	O_3 (0.06 g)	O_3/rad (0.06 g)	O_3/rad (0.50 g)
C1s	284.5	C=C	55.8	42.1	51.6	47.9	57.2	55.9	58.8	57.3
	285.1	C–H	18.5	19.5	18.4	18.6	13.1	14.7	12.8	13.7
	286.2	C=O, O–C–O	0.0	10.5	6.0	9.5	6.0	5.6	4.2	6.1
	288.5	$^{-}$O–C=O	23.0	24.7	22.1	21.0	20.0	20.7	21.0	21.2
	290.5	$\pi \rightarrow \pi^*$	2.7	3.2	1.9	3.0	3.7	3.1	3.2	1.7
O1s	530.0	O–Fe	10.9	13.0	18.8	16.6	25.5	18.8	18.8	20.1
	531.5	$^{-}$O–C=O	70.5	59.5	61.7	58.5	58.4	64.1	67.3	61.7
	532.9	C–OH	16.0	25.1	16.5	19.6	12.9	13.4	11.8	16.3
	534.0	HO–C=O	2.5	2.3	2.9	3.3	2.4	3.2	2.0	1.7
	536.0	H_2O ads.	< 0.1	0.1	< 0.1	2.0	0.8	0.5	< 0.1	0.2
Fe2p	710.8	Fe(III) in $2p_{3/2}$	33.9	34.7	36.3	36.0	40.4	39.0	36.4	39.7
	713.0	Fe(III) in $2p_{3/2}$	24.0	22.1	20.8	20.6	16.3	20.9	19.7	17.3
	717.3	Satellite	13.2	14.8	14.4	15.1	15.0	13.2	15.8	14.5
	724.3	Fe(III) in $2p_{1/2}$	16.9	17.4	18.1	18.0	20.2	19.1	18.2	19.9
	726.4	Fe(III) in $2p_{1/2}$	12.0	11.0	10.4	10.3	8.1	7.8	9.9	8.6

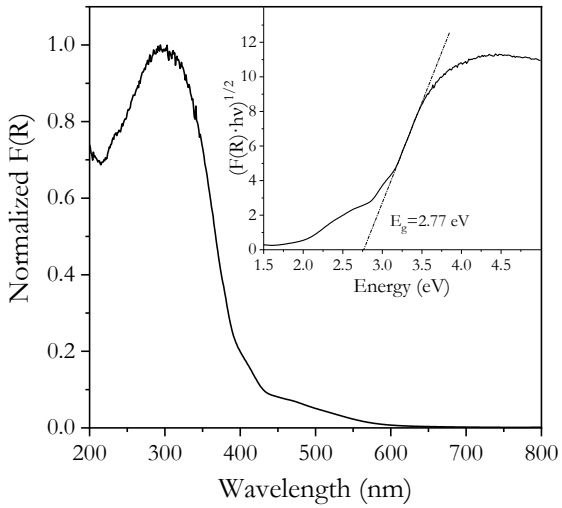

Figure 9.S3. DR-UV-Vis spectrum of MIL-100(Fe) and band-gap energy determination.

2. Long-term stability of MIL-100(Fe) in UP water at different pH

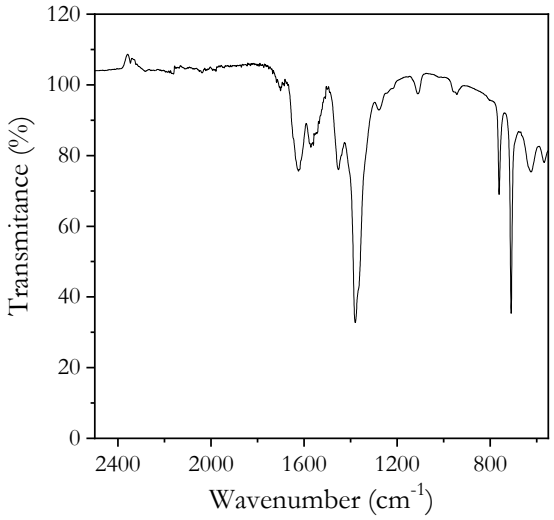

Figure 9.S4. ATR-FTIR of MIL-100(Fe) sample after long-term experiment in UP water at pH_0 6.

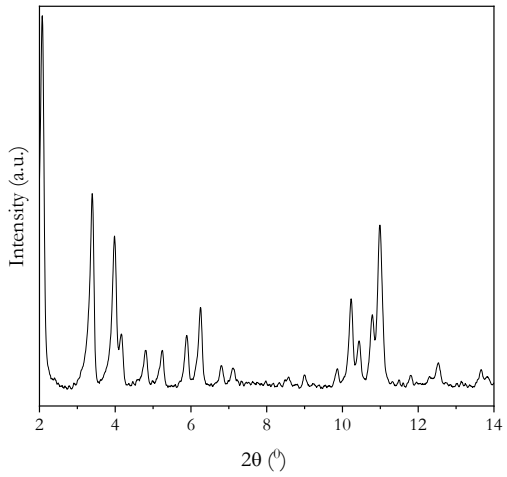

Figure 9.S5. XRD pattern of MIL-100(Fe) simple after long-term experiment in UP water at pH_0 6.

3. Stability of MIL-100(Fe) in oxidizing environments with O_3. H_2O_2 and radiation.

Table 9.S2. TMA and Fe released during oxidizing treatments of MIL-100(Fe)

Treatment and dose	Run	pH_f	TMA_o (μM)	TMA_f (μM)	TOC_f (mg L^{-1})	TOC_{TMAf} (mg L^{-1})	Fe (μM)	CAT $_{REC}$ (wt. %)
O_2/rad	1	3.95	58.6	74.7	8.8	8.1	10.5	
	2	4.02	37.0	50.9	5.9	5.5	12.3	
	3	4.32	21.7	28.1	3.1	3.0	9.4	
	4	4.40	19.9	26.4	3.3	2.9	10.9	
	5	4.51	14.5	17.7	1.7	1.9	6.8	68.7
H_2O_2	1	4.75	54.5	60.9	8.7	6.6	0.4	
(0.06 g)	2	4.40	38.0	35.6	5.5	3.8	0.7	
	3	4.23	27.2	28.0	5.1	3.0	0.3	
	4	4.33	19.9	20.0	3.4	2.2	0.2	
	5	4.40	14.2	13.3	2.8	1.4	0.2	89.1
H_2O_2	1	4.20	57.9	65.1	7.0	7.0	0.6	
(0.64 g)	2	4.20	40.7	41.8	6.1	4.5	0.9	
	3	4.15	26.5	30.5	5.2	3.3	1.3	
	4	4.23	18.5	20.0	4.3	2.2	1.5	
	5	4.50	11.0	13.4	3.1	1.4	13.8	92.1
H_2O_2/rad	1	4.16	59.5	36.3	6.1	3.9	8.2	
(0.06 g)	2	4.40	22.5	7.1	2.5	0.8	7.5	
	3	4.42	1.9	1.2	3.0	0.1	11.0	
	4	4.37	0.0	0.0	4.1	0.0	16.0	
	5	4.47	0.0	0.0	3.2	0.0	12.1	76.0
H_2O_2/rad	1	3.94	55.2	3.3	7.8	0.4	29.6	
(0.64 g)	2	3.94	5.2	1.9	24.8	0.2	664.4	
	3	4.20	1.3	0.0	10.8	0.0	200.2	
	4	4.50	2.3	0.0	3.2	0.0	30.1	
	5	5.10	0.0	0.0	4.0	0.0	1.7	31.4
O_3	1	4.10	45.4	25.5	5.7	2.7	25.5	
(0.06 g)	2	3.92	33.3	10.2	3.5	1.1	24.5	
	3	4.29	24.2	3.8	3.2	0.4	28.2	
	4	4.24	9.1	11.0	3.3	1.2	28.6	
	5	4.30	10.5	6.0	4.8	0.6	50.4	80.0
O_3	1	3.90	58.3	9.2	11.1	1.0	168.2	
(0.50 g)	2	3.89	3.1	2.8	15.8	0.3	319.5	
	3	3.90	0.8	0.8	15.3	0.1	316.2	
	4	3.90	1.9	0.0	19.9	0.0	288.3	
	5	3.99	0.7	0.0	12.6	0.0	448.8	33.2
O_3/rad	1	4.10	53.4	46.2	6.8	5.0	12.8	
(0.06 g)	2	4.33	39.9	33.6	3.5	3.6	10.3	
	3	4.60	26.0	28.5	2.3	3.1	6.6	
	4	4.53	19.2	3.1	2.7	0.3	10.4	
	5	4.60	13.5	6.7	2.2	0.7	6.9	85.6
O_3/rad	1	4.47	54.3	6.9	3.1	0.7	24.2	
(0.50 g)	2	4.42	2.0	0.9	4.0	0.1	41.0	
	3	4.42	0.8	0.0	4.1	0.0	45.5	
	4	4.21	0.8	0.0	3.6	0.0	49.6	
	5	4.42	0.0	0.0	2.9	0.0	50.6	54.0

4. Catalytic activity

a) Adsorption

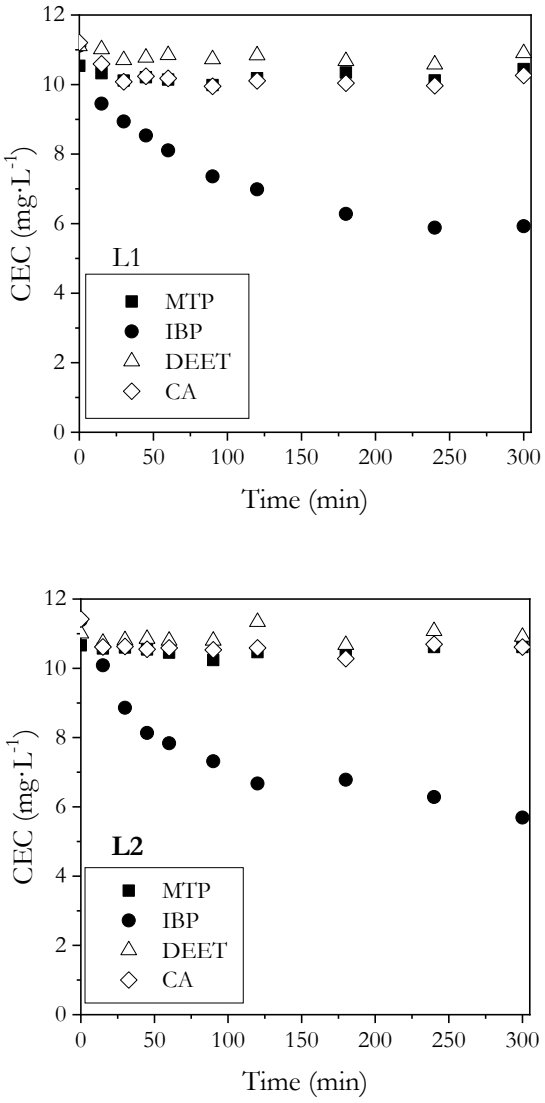

Figure 9.S6. Removal of CECs by adsorption onto L1 (A) and L2 (B) MOF samples. Experimental conditions: V=0.25 L; pH_0=4.8; T=25-40ºC; initial CECs concentration=10 mg·L^{-1} each; initial TOC concentration=26 mg·L^{-1}; MOF dose=0.2 g·L^{-1}.

Table 9.S3. Chemical properties of the CECs.

CEC	Molecular weight ($g \cdot mol^{-1}$)	Water solubility ($mg \cdot L^{-1}$)	pK_a	$k_{HO\bullet} \times 10^{-9}$ ($M^{-1} \cdot s^{-1}$)	k_{O_3} ($M^{-1} \cdot s^{-1}$)
Metoprolol tartrate (MTP)	684.81 (267.36)*	4780	9.5	6.8	1400
N,N-diethyl m-toluamide (DEET)	191.27	9900	-	4.95	4.2
Clofibric acid (CA)	214.65	583	3.2	4.7	< 20
Ibuprofen sodium salt (IBP)	228.29 (206.29)*	21	5.3	7.4	9.1

*Molecular weight of MTP molecule (stoichiometry 2 MTP/1 tartrate) and IBP without Na

References for $k_{HO\bullet}$ and k_{O_3} rate constants**:**

F.J. Benitez, J.L. Acero, F.J. Real, G. Roldán, Ozonation of pharmaceutical compounds: rate constants and elimination in various water matrices, Chemosphere. 77 (2009) 53–59. doi:10.1016/j.chemosphere.2009.05.035.

M.M. Huber, A. Gbel, A. Joss, N. Hermann, D. Lffler, C. S, A. Ried, H. Siegrist, T. a Ternes, U. Von Gunten, A. Go, Oxidation of pharmaceuticals during ozonation of municipal wastewater effluents: a pilot study, Environ. Sci. Technol. 39 (2005) 4290–4299. doi:10.1021/es048396s.

W. Song, W.J. Cooper, B.M. Peake, S.P. Mezyk, M.G. Nickelsen, K.E. O'Shea, Free-radical-induced oxidative and reductive degradation of N,N'-diethyl-mtoluamide (DEET): Kinetic studies and degradation pathway, Water Res. 43 (2009) 635–642. doi:10.1016/j.watres.2008.11.018

E. Mena, A. Rey, E.M. Rodríguez, F.J. Beltrán, Reaction mechanism and kinetics of DEET visible light assisted photocatalytic ozonation with WO_3 catalyst, App. Cat. B: Environ. 202 (2017) 460-472. doi: 10.1016/j.apcatb.2016.09.029

b) Photocatalytic oxidation

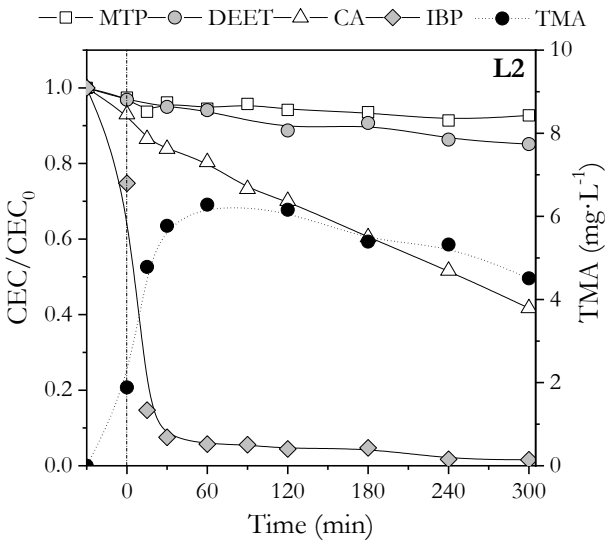

Figure 9.S7. Removal of CECs by photocatalytic oxidation with L2 and TMA concentration released into the reaction medium. Experimental conditions: V=0.25 L; pH_0=4.8; T=25-40ºC; CECs initial concentration=10 mg·L^{-1} each; TOC initial concentration=26 mg·L^{-1}; gas flow rate (O_2)=10 L·h^{-1}; Simulated solar irradiance=550 W·m^{-2}; MOF dose=0.2 g·L^{-1}.

c) Hydrogen peroxide processes

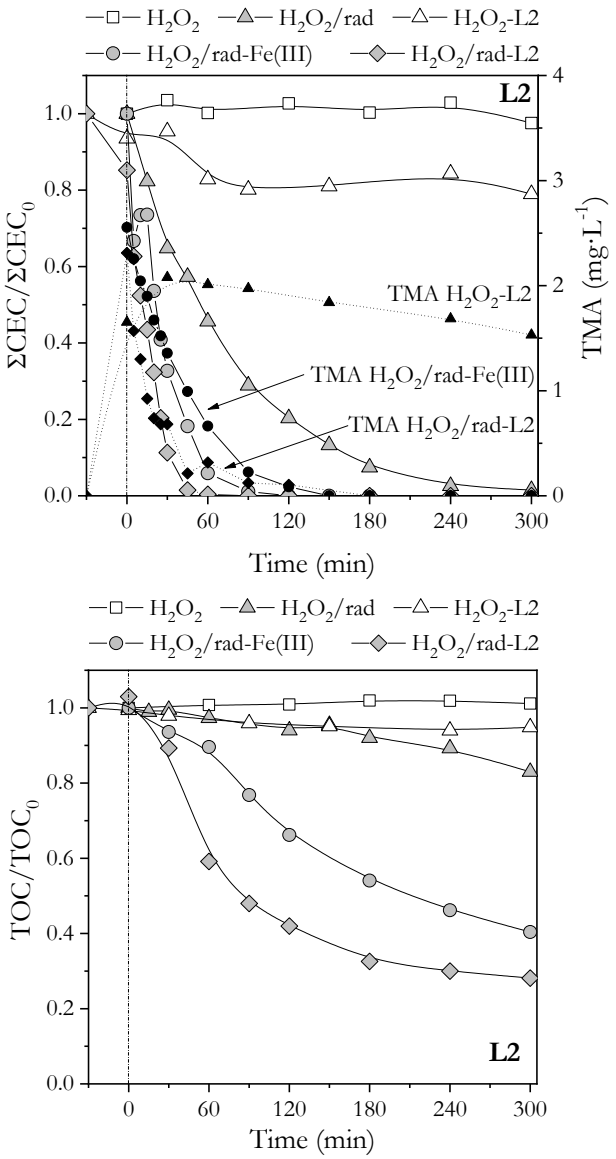

Figure 9.S8. Removal of CECs and TMA concentration released into the reaction medium by different hydrogen peroxide processes using L2 as catalyst. (B) TOC removal by different hydrogen peroxide processes. Experimental conditions: V=0.25 L; pH_0=4.8; T=25-40ºC; Simulated solar irradiance (if applied)=550 W·m^{-2}; gas flow rate (O_2)=10 L·h^{-1}; CECs initial concentration=10 mg·L^{-1} each; TOC initial concentration=26 mg·L^{-1}; initial H_2O_2 concentration=1275 mg·L^{-1}; MOF dose (if applied)=0.2 g·L^{-1}, Fe (III) (if applied)=1.3 mg·L^{-1}, TMA_o(if applied)=2.5 mg·L^{-1}.

d) Ozone processes

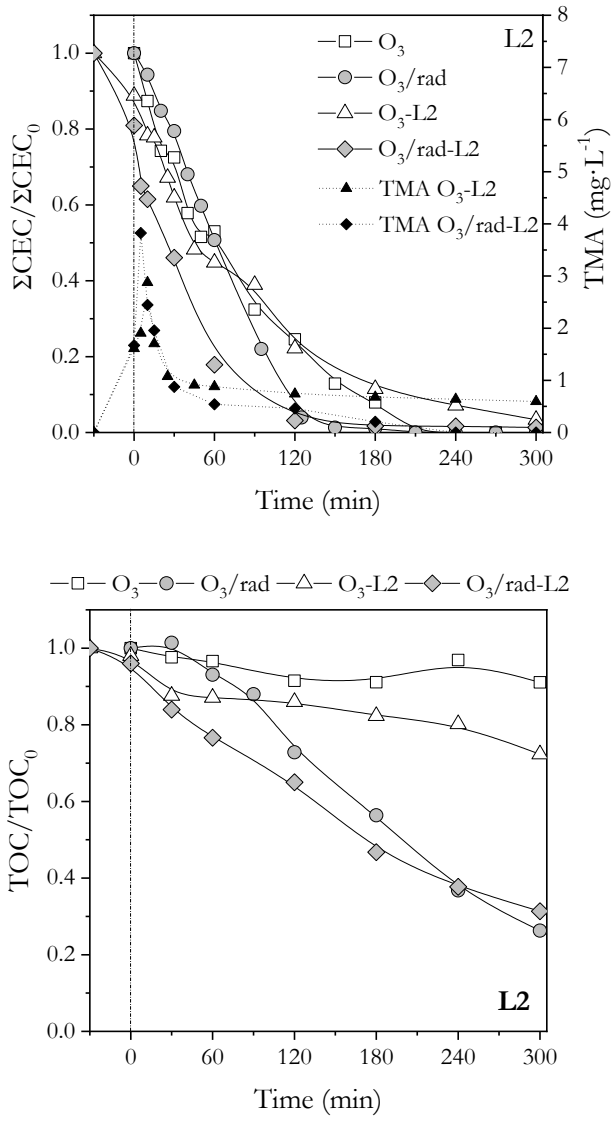

Figure 9.S9. (A) Removal of CECs and TMA released into the reaction medium by different ozonation processes using L1 as catalyst. (B) TOC removal by different ozonation processes. Experimental conditions: V=0.25 L; pH_0=4.8; T=25-40ºC; Simulated solar irradiance (if applied)=550 $W \cdot m^{-2}$; gas flow rate (O_2/O_3)=10 $L \cdot h^{-1}$; gas inlet O_3 concentration=6 $mg \cdot L^{-1}$; initial CECs concentration=10 $mg \cdot L^{-1}$ each; initial TOC concentration=26 $mg \cdot L^{-1}$; MOF dose (if applied)=0.2 $g \cdot L^{-1}$.

CONCLUSIONS
CONCLUSIONES

CHAPTER X

CONCLUSIONS

The hereby Doctoral Thesis has been developed with the main goal of contributing to the study of new photocatalytic materials for the removal of pollutants in water by means of advanced photochemical oxidation processes, emphasizing on the photocatalytic ozonation as an efficient alternative in water treatment. According to the objectives of this work, the following conclusions are reached:

OBJECTIVE 1: Influence of solar radiation in the water photo-ozonation process.

"The solar radiation substantially affects the photo-ozonation process in water"

Conclusion 1.1.: Solar radiation accelerates the aqueous ozone decomposition into free radical species, mainly in the UV-A range (320-390 nm), being this effect stronger at pH 4 than pH 7 and pH 9.

Conclusion 1.2.: Hydrogen peroxide is formed as an intermediate of the photo-ozonation process. The more energetic radiation is used, the more decomposition into free radicals is reached, as deduced from the estimated kinetic constants ($k_{rad\text{-}H_2O_2>300nm} > k_{rad\text{-}H_2O_2>320nm} > k_{rad\text{-}H_2O_2>390nm}$).

Conclusion 1.3.: Photolytic ozonation or photo-ozonation is a more efficient process than simple ozonation for the removal and mineralization of recalcitrant organic matter of wastewater, such as some target contaminants of emerging concern (MTP, IBP, DEET and CA).

OBJECTIVE 2: Application of the solar photocatalytic ozonation using a magnetic recoverable activated carbon-titania composite for the degradation of organic matter in urban or industrial wastewater.

"The supported titanium dioxide onto magnetic activated carbon (TiFeC) exhibits photocatalytic properties, showing also a great efficiency, stability and reusability in the solar photocatalytic ozonation process in any studied wastewater matrix (real municipal, synthetic and industrial wastewater)"

Conclusion 2.1.: The presence of carbonate/bicarbonate ions in the municipal wastewater matrix negatively influences on the efficiency of the photocatalytic ozonation process. That is not the case of phosphates in the typical range concentration (< 3.5 $mg \cdot L^{-1}$), notwithstanding, the presence of both inorganic species have impacts over the

quantified concentration of short-chain organic acids. Regarding the effluent organic matter (EfOM), an increase of the EfOM concentration also reduces the mineralization reached during the process.

Conclusion 2.2.: The synthesized photocatalyt is suitable for photocatalytic ozonation processes since demonstrated its reusability after consecutive reaction cycles at the conditions tested (V=0.75 L; solar global irradiance=550 $W \cdot m^{-2}$; catalyst load=0.4 $g \cdot L^{-1}$; ozone dose=3.3 $mg \cdot min^{-1}$). Also, the photocatalyst keeps high catalytic activity and stability. Nevertheless, a decrease of microporosity and some surface oxidation were observed.

Conclusion 2.3.: The combination of a sequential aerobic biological oxidation with activated sludge ($MLVSS_o$=1.8 $mg \cdot L^{-1}$; HRT=8 h), followed by a photocatalytic ozonation treatment with TiFeC (V=0.75 L; solar global irradiance=550 $W \cdot m^{-2}$; catalyst load=0.4 $g \cdot L^{-1}$; ozone dose=6.6 $mg \cdot min^{-1}$) allows the treated wastewater to fulfil legal limits for direct discharge to the aquatic environment of a complex industrial wastewater (COD=118 $mg \cdot L^{-1}$, BOD_5 < 20 $mg \cdot L^{-1}$, TOC=67 $mg \cdot L^{-1}$, total phenolic content < 1 $mg \cdot L^{-1}$).

OBJECTIVE 3: Preparation of a magnetic recoverable graphene and TiO_2 composite to be used in water treatment.

"Commercial graphene is an excellent supporting material for titanium dioxide and magnetite, which results in a catalyst with good separability and efficiency in the degradation of cotinine in water by photocatalytic ozonation process"

Conclusion 3.1.: The synthesized catalyst with the theoretical weight percentage of 90% of TiO_2 and 10% of magnetite:graphene, at the same weight ratio, and an uniformly distribution, led to the best catalytic performance in the removal of cotinine using photocatalytic ozonation process (cotinine=10 $mg \cdot L^{-1}$, V=0.5 L, solar global irradiance=550 $W \cdot m^{-2}$, catalyst load=0.5 $g \cdot L^{-1}$, ozone dose=5 $mg \cdot min^{-1}$).

Conclusion 3.2.: The incorporation of magnetite to the solid allows the recovery of the catalyst after 5-cycle experiment, without any loss of activity and no significant iron leaching, though some carbon content is lost.

Conclusion 3.3.: A slight increase of pseudo-first order rate constants (k_{Obs}) of every contaminant (CTN, CAF, CPR, MTP, SMX, DEET, CA, BZF, TSF and IBP) in a

municipal wastewater using the simulated solar photocatalytic ozonation compared to those of ozonation was observed.

Conclusion 3.4.: Both pH and the presence of inorganic ions notably affect the efficiency of the AOPs studied.

OBJECTIVE 4: Application of commercial titania for the removal of contaminants of a real wastewater effluent using UVA-LEDs.

"The water treatment with immobilized TiO_2 onto glass rings is an attractive alternative for photocatalytic ozonation under UV-A LED illumination in continuous operation mode"

Conclusion 4.1.: The detected CECs found in the range of $ng \cdot L^{-1}$ in a municipal wastewater can be partially removed by photocatalytic oxidation with TiO_2 and oxygen as electron trap, though it is necessary a more efficient treatment, such as photocatalytic ozonation, for their total removal.

Conclusion 4.2.: A great efficiency on the ozone decomposition with the UV-A LED system and TiO_2-coated glass rings material is achieved in continuous operation mode.

Conclusion 4.3.: The indirect pathway or free radical route may prevail over the direct one in the removal of the most refractory detected CECs when photocatalytic ozonation is employed.

OBJECTIVE 5: Preparation of a metal organic framework material to be used as catalyst in different advanced oxidation processes.

"MIL-100(Fe) is a versatile material with photocatalytic properties for wastewater treatment; however, it must be used with caution due to the questionable stability under powerful oxidizing media and solar radiation"

Conclusion 5.1.: The MOF MIL-100(Fe) may be easily and sustainably synthesized. Notwithstanding, in contact to water, a release of the organic linker is produced to some extent, being this fact even worse in the presence of phosphates.

Conclusion 5.2.: The C:Fe ratio and surface area of MIL-100(Fe) are improved when using strong oxidants such as ozone and hydrogen peroxide, possibly because of the removal of residual trimesic acid (TMA) into the pores and/or weakly bounded in the framework. Nevertheless, suitable conditions should be applied in order not to excessively damage the metal-organic framework.

Conclusion 5.3.: The released TMA into the media is decreased when the material is submitted to solar photocatalytic ozonation and solar photo-Fenton processes. At the same time, some surface oxidation occurs and iron oxides or hydroxide species can be formed.

Conclusion 5.4.: The synthesized MOF is a photocatalytic and selective material since it was only able to degrade clofibric acid (nearly 65%) and ibuprofen (almost totally), which were partially adsorbed. Otherwise, the photocatalytic ozonation and photo-Fenton with MIL-100(Fe) successfully removed the CECs (MTP, IBP, DEET y CA; $C_{i,o}$=10 mg·L^{-1} each) and mineralized them in ultrapure water in a high extent, though the increase removal could also be due to some homogeneous catalysis with the iron leached.

CONCLUSIONES

Esta Tesis Doctoral se ha desarrollado con el objetivo principal de contribuir al estudio de la búsqueda de nuevos materiales catalíticos para la eliminación de contaminantes del agua mediante procesos fotoquímicos de oxidación avanzada, haciendo especial hincapié en la ozonización fotocatalítica como alternativa eficiente para la depuración de aguas. Atendiendo a los objetivos planteados en este trabajo, se pueden extraer las siguientes conclusiones.

OBJETIVO 1: Influencia de la radiación solar en el proceso de foto-ozonización solar en agua.

"La radiación solar afecta significativamente al proceso de ozonización en agua"

Conclusión 1.1.: La radiación solar acelera el proceso de descomposición de ozono en agua en radicales libres, principalmente entre el rango de UV-A (320-390 nm), siendo dicho efecto mayor a pH 4 que a pH 7 y pH 9.

Conclusión 1.2.: El peróxido de hidrógeno aparece como intermedio de los procesos de foto-ozonización, descomponiéndose en radicales libres cuanto más energética es la radiación, tal y como se deduce de los valores de las constantes cinéticas obtenidas ($k_{rad\text{-}H_2O_2>300nm} > k_{rad\text{-}H_2O_2>320nm} > k_{rad\text{-}H_2O_2>390nm}$).

Conclusión 1.3.: La ozonización fotolítica o foto-ozonización es un proceso más eficiente que la ozonización simple para la eliminación y mineralización de materia orgánica recalcitrante de aguas residuales, como son algunos de los contaminantes de preocupación emergente estudiados (MTP, IBP, DEET y CA).

OBJETIVO 2: Aplicación de la ozonización fotocatalítica solar empleando un material compuesto de carbón activo, magnetita y dióxido de titanio para la degradación de contaminantes específicos y materia orgánica en agua residual urbana e industrial.

"El catalizador de dióxido de titanio soportado sobre carbón activo magnetizado (TiFeC) presenta propiedades fotocatalíticas, mostrando a su vez una gran eficiencia, estabilidad y capacidad de reutilización en el proceso de ozonización fotocatalítica solar en cualquiera de las matrices de agua residual estudiadas (agua residual urbana real, sintética e industrial)"

Conclusión 2.1.: La presencia de iones carbonato/bicarbonato en la matriz de agua residual urbana afecta negativamente al rendimiento del proceso de ozonización fotocatalítica. No ocurre así con los fosfatos en el rango de concentración estudiada (< 3,5 $mg \cdot L^{-1}$), aunque la presencia de ambas especies afecta a la concentración de ácidos orgánicos de cadena corta detectados. El aumento de materia orgánica también disminuye la mineralización del proceso.

Conclusión 2.2.: El fotocatalizador es adecuado para ser empleado en procesos de ozonización fotocatalítica ya que se demostró que se puede reutilizar en sucesivos ciclos de reacción en las condiciones empleadas (V=0,75 L; irradiancia solar global=550 $W \cdot m^{-2}$; dosis de catalizador=0,4 $g \cdot L^{-1}$; dosis de ozono=3,3 $mg \cdot min^{-1}$) mostrando una alta actividad catalítica y estabilidad. No obstante, se observó pérdida de microporosidad y la creación de nuevos grupos oxigenados en la superficie externa del catalizador.

Conclusión 2.3.: La combinación de un tratamiento biológico aerobio de lodos activos (SSV_o=1,8 $mg \cdot L^{-1}$; tiempo=8 h) y un tratamiento fotocatalítico con TiFeC (V=0,65 L; irradiancia solar global=550 $W \cdot m^{-2}$; dosis de catalizador=0,4 $g \cdot L^{-1}$; dosis de ozono=6.6 $mg \cdot min^{-1}$) permitió situar las propiedades de un agua residual industrial compleja por debajo de los límites establecidos para la descarga directa al medio ambiente (DQO=118 $mg \cdot L^{-1}$, DBO_5 < 20 $mg \cdot L^{-1}$, COT=67 $mg \cdot L^{-1}$, polifenoles < 1 $mg \cdot L^{-1}$).

OBJETIVO 3: Preparación de un catalizador magnético con grafeno y TiO_2 para el tratamiento de aguas.

"El grafeno comercial resulta ser un excelente soporte para el dióxido de titanio y magnetita, resultando un catalizador fácilmente separable y de gran eficiencia para la eliminación de cotinina en agua mediante ozonización fotocatalítica"

Conclusión 3.1.: El catalizador sintetizado con un 90% de TiO_2 y un 10% de magnetita:grafeno con el mismo ratio en peso de estos dos últimos, con una distribución uniforme por todo el material, presentó los mejores resultados para la eliminación de cotinina mediante ozonización fotocatalítica (Cotinina=10 $mg \cdot L^{-1}$, V=0,5 L; irradiancia solar global=550 $W \cdot m^{-2}$; dosis de catalizador=0,5 $g \cdot L^{-1}$; dosis de ozono=5 $mg \cdot min^{-1}$).

Conclusión 3.2.: La incorporación de magnetita al sólido permite la recuperación del catalizador tras varios ciclos de reacción, sin apreciarse pérdida de actividad ni liberación de hierro al medio, aunque sí una disminución del contenido en carbono.

Conclusión 3.3.: Se produce un aumento leve de las constantes cinéticas de pseudo-primer orden (k_{Obs}) de la eliminación por ozonización fotocatalítica de una mezcla de 10 contaminantes (CTN, CAF, CPR, MTP, SMX, DEET, CA, BZF, TSF e IBP) en agua residual urbana frente la ozonización simple y fotolítica. Existe además una relación de k_{Obs} con las constantes de ozono de reacción directa.

Conclusión 3.4.: El pH y la presencia de iones inorgánicos afectan notablemente a la eficacia de los PAO empleados.

OBJETIVO 4: Aplicación de dióxido de titanio comercial para la eliminación de contaminantes de un efluente de agua residual real mediante LED de UV-A.

"El empleo de TiO_2 inmovilizado en anillos de vidrio es una alternativa atractiva para un tratamiento en continuo mediante ozonización fotocatalítica con iluminación LED de UV-A"

Conclusión 4.1.: Los contaminantes detectados en el orden de $ng \cdot L^{-1}$ en el agua residual municipal se pueden eliminar parcialmente por oxidación fotocatalítica con TiO_2 y empleando oxígeno como captador de electrones pero es necesario un tratamiento más efectivo como la ozonización fotocatalítica para su eliminación total.

Conclusión 4.2.: Existe una gran eficacia en la descomposición de ozono con el sistema diseñado de flujo continuo de agua con LED de UV-A y anillos impregnados de TiO_2.

Conclusión 4.3.: La vía indirecta o por radicales libres puede prevalecer en la eliminación de los contaminantes más refractarios encontrados cuando se emplea la ozonización fotocatalítica.

OBJETIVO 5: Preparación de una estructura metal-orgánica para emplearse como fotocatalizador en procesos avanzados de oxidación.

"MIL-100(Fe) es un material polivalente con propiedades fotocatalíticas para el tratamiento de aguas, aunque debe emplearse con cautela debido a su estabilidad moderada en ambientes fuertemente oxidantes y en presencia de radiación solar"

Conclusión 5.1.: El MOF MIL-100(Fe) puede sintetizarse de forma sencilla y sostenible. No obstante, al ponerse en contacto con agua, se produce la liberación al medio del ligando orgánico, siendo este efecto mayor en presencia de iones fosfato.

Conclusión 5.2.: La relación C:Fe y el área superficial del MIL-100(Fe) se mejoran al emplearse radiación solar simulada y fuertes oxidantes como el ozono y el peróxido de hidrógeno, mejoras debidas a la eliminación de ácido trimésico (ATM) ocluido en los

poros y/o débilmente enlazado, aunque deben emplearse en las condiciones adecuadas para no destruir la estructura metal-orgánica.

Conclusión 5.3.: Se consigue disminuir la cantidad de ATM liberada al medio al someter el material a los tratamientos de ozonización fotocatalítica y foto-Fenton solar, aunque se produce también la oxidación de su superficie y la posible formación de especies de óxido o hidróxido de hierro.

Conclusión 5.4.: El material es fotocatalítico y selectivo ya que solo fue capaz de degradar ácido clofíbrico (alrededor de un 65%) e ibuprofeno (casi totalmente) que se adsorbían parcialmente en la estructura. Sin embargo, son la ozonización fotocatalítica y el foto-Fenton con MIL-100(Fe) los que logran eliminar los contaminantes (MTP, IBP, DEET y CA; $C_{i,o}$ = 10 mg·L^{-1} de cada) y degradar la materia orgánica en mayor grado en agua ultrapura, aunque existe cierta contribución de catálisis homogénea por parte del hierro liberado al medio.

APPENDIX

COMMUNICATIONS

Along this research period, not only scientific articles have been published but also other different national and international communications have been prepared and presented. In total, thirteen communications, four published articles, five congress, three meetings and one conference. Thus, this section provides the original front page of research papers and posters or the initial slide of the communications.

Journal of Hazardous Materials 317 (2016) 36–43

Contents lists available at ScienceDirect

Journal of Hazardous Materials

journal homepage: www.elsevier.com/locate/jhazmat

Solar photo-ozonation: A novel treatment method for the degradation of water pollutants

Ana M. Chávez, Ana Rey, Fernando J. Beltrán, Pedro M. Álvarez *

Departamento de Ingeniería Química y Química Física, Universidad de Extremadura, Avenida de Elvas S/N, 06071 Badajoz, Spain

HIGHLIGHTS

- Aqueous ozone decomposition is accelerated by solar radiation.
- Hydrogen peroxide is identifies as a main intermediate of decomposition of aqueous ozone under solar irradiation.
- Solar photo-ozonation leads to higher Rct ratios than single ozonation.
- Solar photo-ozonation is a promising AOP for the degradation of water pollutants.

GRAPHICAL ABSTRACT

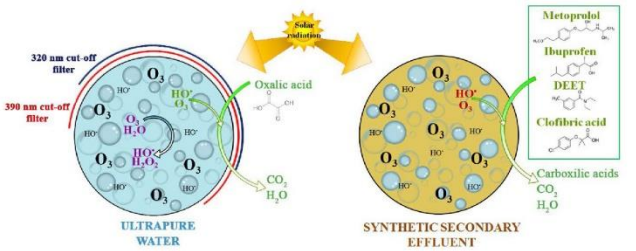

ARTICLE INFO

Article history:
Received 8 February 2016
Received in revised form 4 May 2016
Accepted 15 May 2016
Available online 17 May 2016

Keywords:
AOP
Emerging contaminants
Photo-ozonation
UVA-visible radiation
Water treatment

ABSTRACT

The decomposition of aqueous ozone by UV–vis radiation has been investigated with focus on the impact of ozone photolysis on the degradation of water pollutants during solar ozonation processes. The apparent first-order rate constants of the decomposition of ozone (k_{obs}) have been determined at various pHs in the 4–9 range using radiation of different wavelengths in the UV–vis range. It was found that UVA–visible radiation ($\lambda > 320$ nm) highly enhanced ozone decomposition, especially at pH 4, for which k_{obs} was three-folded with respect to the process in the absence of radiation. Hydrogen peroxide was identified as a main intermediate of ozone photo-decomposition at pH 4. Experiments of degradation of oxalic acid by ozone showed that solar irradiation brings about an increase in the hydroxyl radical to ozone exposures ratio (R_{ct}). Finally, photo-ozonation ($\lambda > 300$ nm) was shown advantageous over single ozonation in the mineralization of a selection of emerging contaminants (metoprolol, ibuprofen, *N,N*-diethyl-*meta*-toluamide and clofibric acid) in both ultrapure water and a synthetic secondary effluent. Thus, TOC removal in 2-h treatments increased from 10 to 25% in the absence of radiation to about 50% in the presence of radiation.

1. Introduction

Ozone has been extensively used in water treatment since long due to its great oxidizing power (2.1 eV) which enables it to selectively oxidize many organic and inorganic species in aqueous solution. The reactions between ozone and organic compounds,

* Corresponding author.
E-mail address: pmalvare@unex.es (P.M. Álvarez).

http://dx.doi.org/10.1016/j.jhazmat.2016.05.050
0304-3894/

Chemical Engineering Journal 361 (2019) 89–98

Contents lists available at ScienceDirect

Chemical Engineering Journal

journal homepage: www.elsevier.com/locate/cej

Treatment of highly polluted industrial wastewater by means of sequential aerobic biological oxidation-ozone based AOPs

A.M. Chávez[a], O. Gimeno[a,*], A. Rey[a], G. Pliego[b], A.L. Oropesa[c,d], P.M. Álvarez[a], F.J. Beltrán[a]

[a] Departamento de Ingeniería Química y Química Física, Instituto Universitario de Investigación del Agua, Cambio Climático y Sostenibilidad (IACYS), Universidad de Extremadura, Av. de Elvas S/N, 06006 Badajoz, Spain
[b] Sección Departamental de Ingeniería Química, Facultad de Ciencias, Universidad Autónoma de Madrid, Cantoblanco, 28049 Madrid, Spain
[c] Unidad de Toxicología, Departamento de Sanidad Animal, Universidad de Extremadura, Av. de Elvas S/N, 06006 Badajoz, Spain
[d] Instituto Universitario de Investigación en Biotecnología Ganadera y Cinegética (INBIO G+C), Universidad de Extremadura, 10003 Cáceres, Spain

HIGHLIGHTS

- A biological-chemical treatment of a complex industrial wastewater has been studied.
- Real Hazardous wastewater consisted of a mixture of special chemical effluents.
- Acclimation of the aerobic culture used was successfully investigated.
- Solar photocatalytic ozonation was able to remove biorecalcitrant compounds.

GRAPHICAL ABSTRACT

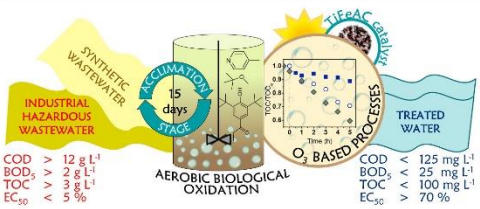

ARTICLE INFO

Keywords:
Hazardous wastewater
Integrated treatment
Biological oxidation
Photocatalytic ozonation

ABSTRACT

The feasibility of the treatment of a complex industrial wastewater by aerobic biodegradation in a sequential batch reactor (SBR) followed by ozone-based advanced oxidation processes (AOPs) has been studied. The industrial wastewater had high organic load (TOC > 3 g L^{-1}, COD > 12 g L^{-1}, BOD_5 > 2 g L^{-1}) including some toxic/harmful compounds and high concentration of metal and other inorganic species. SBR treatment of the industrial wastewater diluted with urban wastewater (dilution 1:5), was successful after complete acclimation of the mixed culture (i.e., > 50% COD and TOC removals). Nevertheless, the SBR effluent was still not acceptable to be disposed into the environment (e.a. COD 850 mg L^{-1}) so ozonation, solar photo-ozonation and solar photocatalytic ozonation processes were investigated as further polishing treatments. Thus, the sequential combination of aerobic biodegradation and solar photocatalytic ozonation with a TiO_2-based catalyst led to an effluent suitable for discharge into the aquatic environment according to environmental regulations (COD < 125 mg L^{-1}, BOD_5 < 25 mg L^{-1}).

1. Introduction

The management and treatment of wastewater from residential and industrial sites is critical to the sustainability of water systems. It is crucial for treatment technologies to be as much efficient and economically feasible as possible [1]. To deal with hazardous effluents from some industrial sites, such as chemical multi-product plants with diverse toxic wastewater streams, incineration is sometimes considered

* Corresponding author.
E-mail address: ogimeno@unex.es (O. Gimeno).

https://doi.org/10.1016/j.cej.2018.12.064
Received 25 September 2018; Received in revised form 10 December 2018; Accepted 12 December 2018
Available online 13 December 2018
1385-8947/

catalysts

MDPI

Article

Removal of Organic Micropollutants from a Municipal Wastewater Secondary Effluent by UVA-LED Photocatalytic Ozonation

Ana M. Chávez [1], Ana R. Ribeiro [2], Nuno F. F. Moreira [2], Adrián M. T. Silva [2,*], Ana Rey [1], Pedro M. Álvarez [1] and Fernando J. Beltrán [1,*]

[1] Departamento de Ingeniería Química y Química Física, Instituto Universitario de Investigación del Agua, Cambio Climático y Sostenibilidad, Universidad de Extremadura, Avenida de Elvas S/N, 06006 Badajoz, Spain; amchavez@unex.es (A.M.C.); anarey@unex.es (A.R.); pmalvare@unex.es (P.M.Á.)

[2] Laboratory of Separation and Reaction Engineering - Laboratory of Catalysis and Materials (LSRE-LCM), Faculdade de Engenharia, Universidade do Porto, Rua Dr. Roberto Frias s/n, 4200-465 Porto, Portugal; ritalado@fe.up.pt (A.R.R.); nmoreira@fe.up.pt (N.F.F.M.)

* Correspondence: adrian@fe.up.pt (A.M.T.S.); fbeltran@unex.es (F.J.B.); Tel.: +351-22-041-4531 (A.M.T.S.); +34-924-289387 (F.J.B.)

Received: 29 April 2019; Accepted: 18 May 2019; Published: 22 May 2019

Abstract: Numerous contaminants of emerging concern (CECs) have been found in different water bodies. Directive 2013/39/EU and Decision 2018/840/EU are consequently being implemented in the field of water policies. Twelve CECs (e.g., isoproturon, ciprofloxacin, and clarithromycin are among those listed) were detected in a municipal wastewater secondary effluent by means of solid phase extraction and ultra-high-performance liquid chromatography with tandem mass spectrometry (SPE-UI IPLC-MS/MS). Different advanced oxidation processes (AOPs), based on the combination of ozone, UVA-LED and powdered TiO_2, were investigated for their removal in a semi-batch operation. In addition, TiO_2-coated glass rings (P25R) were characterized with different techniques (SEM, WDXRF) and used for continuous mode operation in a packed bed reactor (PBR). Among the AOPs studied, ozone-based processes were found to be more efficient than heterogeneous photocatalysis. A kinetic study was performed showing that direct ozonation is the main oxidation pathway for CEC removal. Ozone was successfully decomposed in combination with UVA-LED and P25R, resulting in an apparent rate constant of 3.2×10^{-2} s^{-1} higher than in the O_3/LED system (1.0×10^{-3} s^{-1}) or with ozone alone (8.6×10^{-5} s^{-1}). Hydroxyl radical reaction could prevail over direct ozone reaction for the most refractory compounds (e.g., isoproturon).

Keywords: municipal wastewater secondary effluent; contaminants of emerging concern; ozonation; light emitting diodes; TiO_2-coated glass rings

1. Introduction

Contaminants of emerging concern (CECs) are continuously discharged into aquatic systems with little or no awareness of their consequences. Pharmaceuticals, pesticides, industrial compounds, natural hormones, and personal care products belong to this group of substances. Although their concentration levels are very low, usually in the $ng \cdot L^{-1}$ or $\mu g \cdot L^{-1}$ range [1–3], biological acute and chronic toxicity in aquatic organisms has been observed [4,5].

To date, the European Union (EU) has established a list of priority substances (Directive 2013/39/EU) and a watch list of CECs that have to be monitored to guarantee water quality (Decision 2015/495/EU, Decision 2018/840/EU) [6–8]. Other CECs are most likely to be included in the watch list in the near future.

Applied Catalysis B: Environmental 262 (2020) 118275

Contents lists available at ScienceDirect

Applied Catalysis B: Environmental

journal homepage: www.elsevier.com/locate/apcatb

Magnetic graphene TiO_2-based photocatalyst for the removal of pollutants of emerging concern in water by simulated sunlight aided photocatalytic ozonation

Ana M. Chávez[a,b], Rafael R. Solís[c,*], Fernando J. Beltrán[a,b]

[a] Departamento de Ingeniería Química y Química Física, Facultad de Ciencias, Universidad de Extremadura, Avda. Elvas s/n, 06006 Badajoz, Spain
[b] Instituto Universitario del Agua, Cambio Climático y Sostenibilidad (IACYS), Universidad de Extremadura, Avda. de la Investigación s/n, 06006 Badajoz, Spain
[c] Department of Chemical & Environmental Engineering, College of Engineering & Environmental Science (CEAS), Engineering Research Centre (ERC), University of Cincinnati, Cincinnati, OH 45221-0012, USA

ARTICLE INFO

Keywords:
Magnetic graphene
Titania
Photocatalytic ozonation
Solar light
Water treatment

ABSTRACT

Magnetite and titania have been supported onto graphene for the photocatalytic ozonation of aqueous micropollutants. Titania and magnetite were successfully attached to graphene nanoparticles keeping with a reasonable separation and photocatalytic activity. Although the presence of graphene did not enhance the photoactivity of bare titania, graphene acted as a good support of magnetite nanoparticles and removed the leaching of iron, a problem observed with the graphene free composite. The synthesized photocatalysts were characterized by diverse techniques. The efficiency of the processes involving ozone was assessed by different tools such as $HO^{\cdot}$ exposure vs time, R_{CT} and $R_{HO^{\cdot},O3}$ ratios. Photocatalytic ozonation was the most efficient for the removal of the target compound and mineralization. No loss of activity was registered after reusing or appreciable iron leaching. Finally, the catalyst was also tested in a real secondary effluent from a wastewater treatment plant containing ten micropollutants of emerging concern.

1. Introduction

The high standard of life reached by current society demands the use of a huge number of organic substances that are still under research and development every day. However, the concern related to the presence of these organics in the environment is raising among the research community due to the harmful properties and their impact in the natural ecosystems [1]. Concretely, Contaminants of Emerging Concern (CECs) are organic micropollutants, *i.e.* reported at very low concentration, from diverse families of organics: pharmaceuticals, personal care products, plasticizers, perfluorochemicals, food additives, legal and illegal drugs, pesticides, *etc.* [2–4]; that have been detected in diverse aqueous ecosystems for the last decades. Furthermore, these substances generate some stable degradation products named as metabolites. The acute toxicity of CECs is not always alarming as the concentration they are reported at is below $\mu g\,L^{-1}$, commonly in the $ng\,L^{-1}$ range. In addition, their interaction with human life and the environment is not well understood. No studies of how they affect the life cycle in the long term are available [5]. Nevertheless, some groups of these substances do generate a concern impact in the short term. For example, the presence of antibiotics in the environment is making microbes to be more resilient as they adapt themselves against the antibacterial properties [6,7].

Although drinking water treatment plants generally are designed to remove specific organic pollutants when required, conventional Urban WasteWater Treatment Plants (UWWTPs) do not consider specific stages for that purpose. This makes UWWTPs to be a hotspot of CECs release into aquatic ecosystems [8,9]. Thus, new technologies to face the problematic of CECs are needed.

Advanced Oxidation Processes (AOPs) have demonstrated to be efficient in the oxidation of almost all kind of organics in water [10–12]. AOPs rely on the production of hydroxyl radicals in enough concentration to oxidize organics, approaching in some cases high mineralization extent as the oxidation is focused on the production of carbon dioxide and inorganic anions. Ozone is a versatile and moderate oxidant that does not produce residues when used in water treatment. Ozone can react, first, unselectively by direct attack of the O_3 molecule to *e.g.* unsaturated bonds or aromatic rings; and secondly, by triggering a decomposition mechanism into hydroxyl radical as the main oxidant species. However, ozonation by itself poses low potential of

* Corresponding author.
E-mail address: rodrigr2@ucmail.uc.edu (R.R. Solís).

https://doi.org/10.1016/j.apcatb.2019.118275
Received 23 July 2019; Received in revised form 5 October 2019; Accepted 8 October 2019
Available online 13 October 2019
0926-3373/

CONGRESS, CONFERENCES and MEETINGS

SOLAR RADIATION ACTIVATION OF OZONE FOR THE DEGRADATION OF WATER POLLUTANTS

Ana M. Chávez, Ana Rey, Fernando J. Beltrán, Pedro M. Álvarez
Dpto. de Ingeniería Química y Química Física. Universidad de Extremadura. 06071 Badajoz. Spain.
E-mail:achaveza@alumnos.unex.es

INTRODUCTION:

Ozone has been extensively used in water treatment due to its great oxidizing power. Ozone can be transformed into free-radical oxygen species (ROS), such as hydroxyl radical (HO·), which can mineralize organic pollutants in water avoiding the accumulation of degradation intermediates. The use of UV radiation to activate ozone decomposition into HO· is well known [1], whereas the use of **solar radiation** for this purpose has not been fully investigated yet.

According to the results of a previous research, the **photolysis of ozone** under solar radiation illumination might contribute to the partial decomposition of ozone, yielding hydroxyl radicals and other ROS, which favors the degradation of organic compounds in water [2]. In the present work, decomposition of aqueous ozone under UV-vis radiation and its transformation into HO· is investigated. In addition, the degradation of selected emerging compounds (ECs) by photo-ozonation is explored.

EXPERIMENTAL:

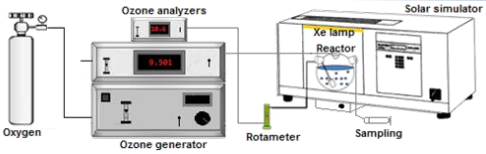

Figure 1. Experimental set-up used for photo-ozonation experiments.

1. Ozone decomposition **2.** R_{ct} ratios **3.** Pollutants degradation

Cut-off radiation filters: 300 nm | 320nm | 390nm | No radiation

Metoprolol, Ibuprofen, DEET, Clofibric acid in **Synthetic Effluent** or **Ultrapure water**

OBJECTIVES:

Investigate the effect of radiation of **different wavelengths** on the rate of decomposition of aqueous ozone and the formation of H_2O_2 and hydroxyl radical.

Study the degradation of **emerging contaminants** in ultrapure water and in a typical secondary effluent from municipal wastewater treatment plant by photo-ozonation.

RESULTS AND DISCUSSION:

1. Ozone decomposition

- Strong effect of radiation on the **rate of aqueous O_3 decomposition** at pH 4.

***Table 1.** Apparent first-order rate constant of aqueous ozone decomposition at various pHs and irradiation wavelength ranges*

Irradiation	pH=4	pH=7	pH=9
	k_{obs} (min^{-1})	k_{obs} (min^{-1})	k_{obs} (min^{-1})
No radiation	0.021	0.181	0.940
hν (λ>390 nm)	0.020	0.259	1.181
hν (λ>320 nm)	0.066	0.272	1.030
hν (λ>300 nm)	0.084	0.273	1.152

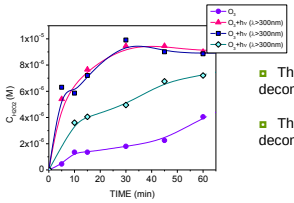

- The use of **radiation accelerated** ozone decomposition and hydrogen peroxide generation.
- The **formation of hydrogen peroxide** during ozone decomposition was favored at low pH.

Figure 2. Hydrogen peroxide concentration. Influence of radiation. Experimental: V=500 mL, pH=4, C_{O3ge}=50 mg L^{-1}, Q=30 L h^{-1}, T=37ºC, Phospate buffer = 10 mM.

2. R_{ct} ratios

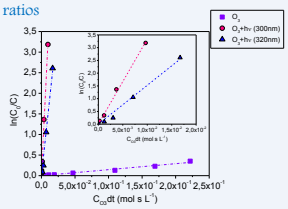

Figure 3. R_{ct} plots for ozonation and photo-ozonation semi-batch experiments. Operating conditions: $C_{OXAL,0}$=25 mg L^{-1}, pH_0=4, V=500 mL, C_{O3ge}=10 mg L^{-1}, Q=15 L h^{-1}, T=37ºC.

$$R_{ct} = \frac{C_{HO\cdot}}{C_{O_3}} = \frac{\int_0^t C_{HO\cdot}\,dt}{\int_0^t C_{O_3}\,dt} = \frac{\ln \frac{C_{OXAL,0}}{C_{OXAL,t}}}{k_{HO\cdot}\int_0^t C_{O_3}\,dt}$$

- Oxalic acid was used as probe compound. Its removal was enhanced by photo-ozonation (λ>300 or 320 nm) because of transformation of aqueous ozone into HO·
- Ratio of exposures of HO· and ozone (R_{ct}) is greatly enhanced by the presence of radiation.

3. Pollutants degradation

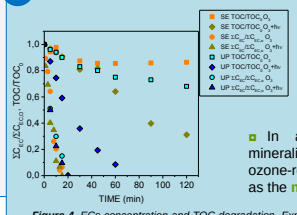

- Pollutants were completely removed by ozonation and photo-ozonation regardless of the water matrix.
- In ultrapure water, ozone alone was not able to mineralize the pollutants to a great extent. Photo-ozonation led to complete mineralization.
- In a synthetic wastewater effluent, only partial mineralization was achieved due to the accumulation of ozone-refractory intermediates. Oxalic acid was identified as the **main intermediate.**

Figure 4. ECs concentration and TOC degradation. Experimental: $C_{EC,0}$=2 mg L^{-1} each, TOC_0= 4 mg·L^{-1} (ultrapure water) or 20 mg·L^{-1} (synthetic effluent), pH_0=7, V=500 mL, C_{O3ge}=10 mg L^{-1}, Q=20 L h^{-1}, T=37ºC. SE:synthetic effluent; UP: ultrapure water

CONCLUSIONS:

Ozone decomposition is accelerated by solar radiation (λ> 300 nm) mainly in the 320-390 wavelength range. The effect is higher at pH4 than at pH 7 or 9.

Hydrogen peroxide was identified as an intermediate of ozone photo-decomposition.

R_{ct} could be more than 100 folded by using UVA-vis radiation.

Photo-ozonation is a more efficient process than single ozonation to mineralize a selection of ECs.

REFERENCES:

[1] Parag R. Gogate, Aniruddha B. Pandit, A review of imperative technologies for wastewater treatment II: hybrid methods, *Adv. Environ. Res.*, 8 (3-4), 553-597 (2004).
[2] Sánchez L.; Doménech X.; Casado J.; Peral J.; Solar activated ozonation of phenol and malic acid, *Chemosphere*, 50 (8), 1085-1093 (2003).

AKNOWLEDGMENTS:

Authors thank the Spanish MINECO and European Feder Funds (CTQ2012-35789-C02-01) for economic support. A.M. Chávez is also thankful to the Spanish MINECO for her predoctoral contract (call 2013).

PHOTOCATALYTIC OZONATION OF EMERGING CONTAMINANTS IN MUNICIPAL WASTEWATER WITH A MAGNETIC TiO_2-ACTIVATED CARBON CATALYST

A. Rey, A. M. Chávez , P. M. Álvarez, F. J. Beltrán

Dpto. de Ingeniería Química y Química Física, Universidad de Extremadura, 06006 Badajoz, Spain, e-mail: anarey@unex.es

INTRODUCTION:

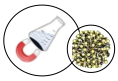

Photocatalytic ozonation is an **A**dvanced **O**xidation **P**rocess based on the combination of photocatalytic oxidation with ozone that has been demonstrated to efficiently remove a wide variety of organic pollutants [1]. Most of the studies in photocatalytic ozonation have been conducted using nanosized TiO_2 as catalyst which involves several problems of separation and reutilization. Thus, the aim of this work is focused on the application of a **TiO_2-anatase supported magnetic activated carbon catalyst** (TiFeC) in the photocatalytic ozonation of a mixture of emerging contaminants (ECs) in municipal wastewater effluents. This catalyst was active, stable, easily separable and reusable in a previous work [2].

EXPERIMENTAL:

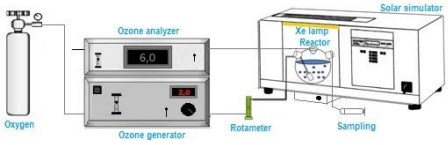

Figure 1. Experimental set-up used for experiments.

Metoprolol
Ibuprofen
DEET
Clofibric acid

Synthetic Effluent

General conditions: $C_{EC,0}$=2 mg·L^{-1} each, TOC_0=24 mg·L-1, pH_0=7, V=750 mL, carbonate/bicarbonate (inorganic carbon, IC=42 mg·L^{-1}) and phosphate (PO_4^{3-}=5.5 mg·L^{-1})

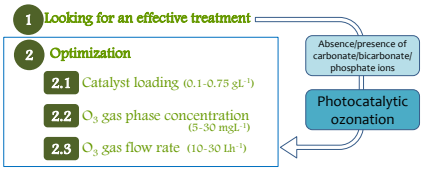

OBJECTIVES:

Application of a magnetic TiFeC catalyst in a mixture of emerging contaminants (ECs) in a Municipal Wastewater Effluent (MWWE).

Study of the absence and presence of inorganic carbon and phosphate ions in a MWWE.

Optimizing the photocatalytic ozonation process

RESULTS AND DISCUSSION:

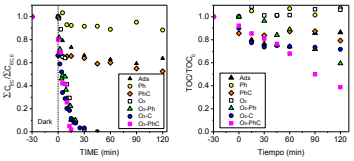

Figure 2. Evolution of normalized overall ECs and TOC concentration during different treatments applied ($C_{EC,0}$=2 mg·L^{-1} each, TOC_0=24 mg·L-1, pH_0=7, V=750 mL, C_{O3gas}=10 mg·L^{-1}, Q=20 L·h^{-1}, T=25-37ºC, C_{CAT}=0.37 g·L^{-1})

- Photocatalytic ozonation led to higher mineralization rate
- Ozonation was able to completely remove the four ECs in less than 45 min regardless of presence of radiation and/or catalyst
- Negative effect in presence of carbonate/bicarbonate ions due to scavenging effect.

Table I. TOC removal with and without carbonate/bicarbonate (inorganic carbon, IC=42 mg·L^{-1}) and phosphate (PO_4^{3-}=5.5 mg·L^{-1}) at t=120 min.

Treatment	% TOC removal	
	NO IC/PO_4^{3-}	IC/PO_4^{3-}
O_3	10	5
O_3-Ph	40	30
O_3-PhC	65	38

2 Optimization

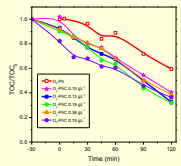

Figure 3. Evolution of normalized TOC concentration with different catalyst loading .

- Similar final TOC removal is reached regardless of the catalyst loading.
- Increasing the catalyst loading rises TOC adsorption during the dark stage.
- 0.13 gL^{-1} of catalyst is enough for the treatment at the conditions studied.

An increment in the ozone concentration or gas flow rate produced a slight positive effect in the ECs degradation and mineralization.

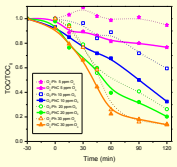

Figure 4. Evolution of normalized TOC concentration with different ozone concentration .

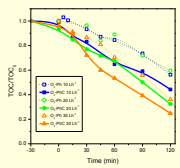

Figure 5. Evolution of normalized TOC concentration with different gas flow rate.

1 Looking for an effective treatment

Ideal conditions:

- Loading catalyst: **0.13 gL^{-1}**
- Ozone concentration: **20 mgL^{-1}**
- Gas flow rate: **20 Lh^{-1}**

- Acetic, formic and oxalic acid are the main intermediates detected

AKNOWLEDGMENTS:

Authors thank the Spanish MINECO, European Feder Funds (CTQ2012-35789-C02-01) and the Junta de Extremadura (Ayuda a Grupos Exp. GR15-033) for economic support. A.M. Chávez is also thankful to the Spanish MINECO for her predoctoral contract (call 2013).

REFERENCES:

[1] M. Mehrjouei, S. Mueller, D. Moeller, Chemical Engineering Journal, 263 (2015) 209.
[2] D.H. Quiñones, A. Rey, P.M. Álvarez, F.J. Beltrán, P. Plucinski, Applied Catalysis B Environmental, 144 (2014) 96.

EFECTO DE LA MATRIZ ACUOSA EN LA ELIMINACIÓN DE CONTAMINANTES EMERGENTES MEDIANTE OZONIZACIÓN FOTOCATALÍTICA CON TiO_2 SOPORTADO SOBRE CARBÓN ACTIVO MAGNETIZADO

meta 2016

A.M. Chávez, A. Rey, P.M. Álvarez y F. Beltrán

Dpto. Ingeniería Química y Química Física. Universidad de Extremadura. Avda. Elvas s/n. 06071 – Badajoz (España)

achaveza@alumnos.unex.es

Introducción

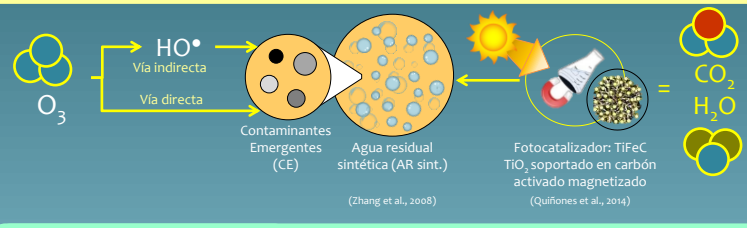

Objetivos

Eliminación de 4 CE de un efluente de agua residual urbana empleando TiFeC.

Efecto la matriz de agua en el proceso de ozonización fotocatalítica.

Análisis de la presencia y ausencia de iones en el agua.

Materiales y Métodos

T. Anatlíticas

- Cromatografía líquida (HPLC) — Metoprolol, Ibuprofeno, DEET, Ácido clofíbrico
- Cromatografía iónica — Aniones inorgánicos y orgánicos de cadena corta
- Análisis de Carbono Orgánico Total (COT)
- Espectrofotometría UV-vis. — O_3, H_2O_2

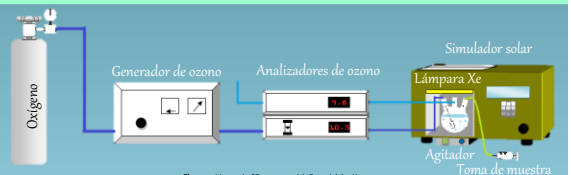

Figura 1. V=0,75 L, CO_{3ini}=10 mg·L^{-1}, Q=20 L·h^{-1}, pH_0=7,2. En los casos específicos : CE= 2 mg·L^{-1} de cada (COT_0=5,6 mg·L^{-1}) y/o ARSint. (COT_0=19 mg·L^{-1}).

Resultados y Discusión

1. Agua ultrapura

Eliminación completa de los CE.

TiFeC es un fotocatalizador **activo.**

El proceso más **eficaz** fue **O_3/radiación/TiFeC.**

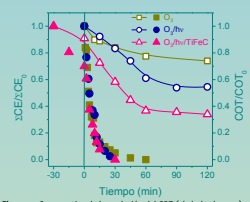

Figura 2. Comparativa de la evolución del COT (símbolos huecos) y de la eliminación CE en agua ultrapura (símbolos rellenos). V=0,75 L, CO_{3ini}=10 mg·L^{-1}, Q=20 L·h^{-1}, pH_0=7,2.

2. Agua residual sintética

La **radiación solar** permite **mineralizar** la materia orgánica.

El **catalizador acelera** el proceso al **inicio** del tratamiento.

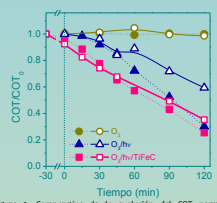

Figura 3. Comparativa de la evolución del COT normalizado del tratamiento del agua residual sintética únicamente (símbolos rellenos) y con la mezcla de los contaminantes (símbolos huecos). V=0,75 L, CO_{3ini}=10 mg·L^{-1}, Q=20 L·h^{-1}, pH_0=7,2.

3. Efecto de los iones $CO_3^{=}$/PO_4^{3-} (C/F)

La presencia de C/F no afecta a la eliminación de CE.

Responsables de la **pérdida de eficacia** del tratamiento en la **mineralización.**

Favorecen la **generación de ácido oxálico** (muy refractario al ozono).

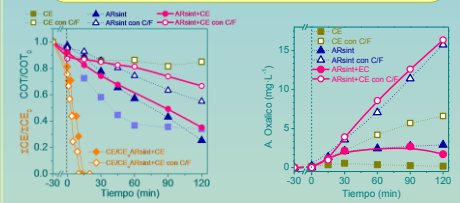

Figura 4 (izquierda). Comparativa de la evolución de COT/ COT_0 y los contaminantes en ARSint+CE en O_3/radiación/TiFeC. **(derecha).** Concentración de ácido oxálico generado durante el proceso de O_3/radiación/TiFeC. V=0,75 L, CO_{3ini}=10 mg·L^{-1}, Q=20 L·h^{-1}, pH_0=7,2 y/o $C_{Cinorgánico}$=42 mg·L^{-1}.

Agua ultrapura (COT_0=5,6 mg·L^{-1}); ARSint. (COT_0=19 mg·L^{-1}); ARSint+CE(COT_0=24,7 mg·L^{-1}).

Conclusiones

La **ozonización fotocatalítica** es un tratamiento efectivo para **eliminar los contaminantes emergentes** seleccionados en un agua residual siempre que la concentración de **iones C/F** sea baja. Estos iones **reaccionan con los radicales hidroxilo** generados durante el mecanismo de descomposición del ozono, provocando que se **acumulen mayores cantidades de ácido oxálico**, muy refractario al ozono, pero de naturaleza biodegradable.

Referencias

Quiñones D. H.; Alvarez P. M.; Rey A.; Contreras S.; Beltran F. J. (2015) Application of solar photocatalytic ozonation for the degradation of emerging contaminants in water in a pilot plant. Chem. Eng. J., 260, 399-410.

Zhang X., Wu F., Wu X., Chen P., Deng N. (2008) Photodegradation of acetaminophen in TiO_2 suspended solution. Journal of Hazardous Material 157, 300–307.

Agradecimientos

Este trabajo ha sido financiado por el Ministerio de Economía y Competitividad (MINECO)(proyecto CTQ2015-64944-R), la Junta de Extremadura y Fondos FEDER Europeos. A.M. Chávez agradece al MINECO la concesión de un contrato predoctoral (convocatoria 2013).

Unión Europea
Fondo Europeo de Desarrollo Regional "Una manera de hacer Europa"
MINISTERIO DE ECONOMÍA Y COMPETITIVIDAD
JUNTA DE EXTREMADURA

REFINEMENT OF POLLUTED WATER BY MEANS OF OZONE / RADIATION / CATALYST.

A.M. Chávez*, A. Rey, P.M. Álvarez y F. Beltrán

Dpto. Ingeniería Química y Química Física. Instituto Universitario de Investigación del Agua, Cambio Climático y Sostenibilidad (IACYS). Universidad de Extremadura. Avda. Elvas s/n. 06071 – Badajoz (España) *amchavez@unex.es

INTRODUCTION

The development of new high sensitivity analysis techniques has allowed the detection of recalcitrant compounds which remain in water, though in low concentrations (ng·L^{-1} or µg·L^{-1}), after conventional wastewater treatment, such as **contaminants** of **emerging concern (CECs)** [1]. Thus, the use of advanced treatments is a need in order to restore water quality [2]. Among them, the photocatalytic ozonation is an **A**dvanced **O**xidation **P**rocess(AOP) based on the combination of photocatalytic oxidation with ozone that has been demonstrated to efficiently remove a wide variety of organic pollutants [3].

OBJETIVES

Degradation of some CECs in water by photo-catalytic ozonation

Synthesis of new photocatalysts

Ozone

The use of radiation accelerated ozone decomposition and, consequently, the radical generation.

Ozone decomposition

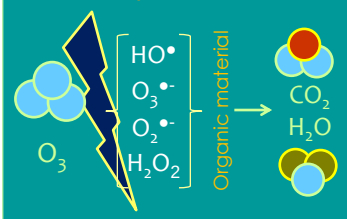

Radiation influence

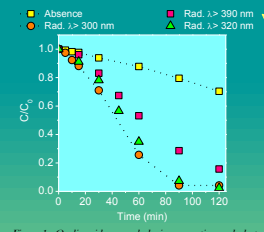

Figure 1. Oxalic acid removal during ozonation and photo-ozonation experiments with solar and LED radiation. Experimental conditions: $C_{OXAL,0}$=25 mg·L^{-1}, pH$_0$=4, V=500 mL, C_{O3in}=10 mg·L^{-1}, Q=1.5 L·h^{-1}, T=37ºC

Radiation sources

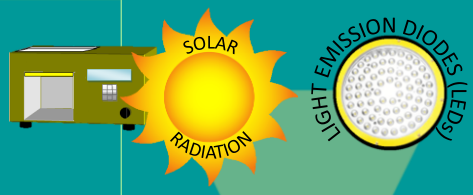

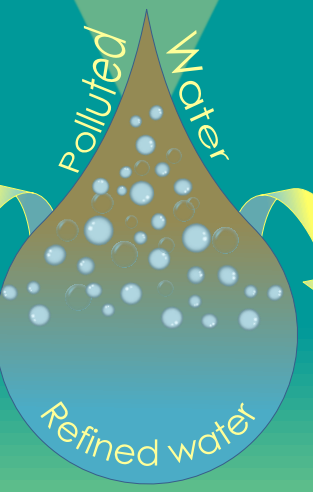

Photocatalysts

❖TiO_2 supported in magnetic activated carbon.

High internal surface
Reusability
Photoactivity

Study of reusability and photoactivity in Wastewater

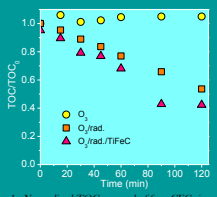

Figure 1. Normalized TOC removal of four CECs in wastewater synthetic effluent during different ozonation processes Experimental conditions: $C_{CEC,0}$=2 mg·L^{-1} (each), pH$_0$=7.2, V=750 mL, C_{O3in}=10 mg·L^{-1}, Q=20 L·h^{-1}.

❖ Metal-Organic Frameworks (**MOFs**)

High internal surface
Electrical properties

Study of water stability and photoactivity

MIL 100 (Fe) **NH_2-MIL 125 (Ti)**

Figure 2. MIL 100 Fe framework. [4]

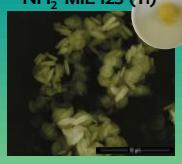

Figure 3. SEM image of NH_2-MIL 125 Ti synthesized.

REFERENCES:

[1] M. Mehrjouei, S. Mueller, D. Moeller; Chemical Engineering Journal, 263 (2015) 209-219.
[2] A. R. Ribeiro, O. C. Nunes, M. F. R. Pereira, A. M. T. Silva; Environment International 75 (2015) 33–51.
[3] D.H. Quiñones, A. Rey, P.M. Álvarez, F.J. Beltrán, P. Plucinski, Applied Catalysis B Environmental, 144 (2014) 96-104.
[4] E. Bellido, M. Guillevic, T. Hidalgo, M. J. Santander-Ortega, C. Serre, P. Horcajada ; Langmuir 30 (2014) 5911−5920.

AKNOWLEDGMENTS:

Authors are grateful to Junta de Extremadura and Spanish Ministerio de Economía y Competitividad (MINECO) for the economic support through the respectively projects GR15033 and CTQ2015-64944-R, both financed with European Regional Development Funds. A.M. Chávez is also thankful to the Spanish MINECO for her predoctoral contract (call 2013, reference: BES-2013-064186).

I CONGRESO LUSO-EXTREMADURENSE

Évora, 20-21 de octubre de 2017

DESCONTAMINACIÓN DE UN EFLUENTE DE AGUA RESIDUAL MEDIANTE COMBINACIÓN DE PROCESOS BASADOS EN OZONO Y LEDs

A.M. Chávez[a], A.R. Ribeiro[b], C. Orge[b], N.F.F. Moreira[b], J. L. Faria[b], M.F.R. Pereira[b], A.M.T. Silva[b], A. Rey[a], P.M. Álvarez[a], F. J. Beltrán[a]

[a]Dpto. Ingeniería Química y Química Física. Instituto Universitario de Investigación del Agua, Cambio Climático y Sostenibilidad (IACYS). Universidad de Extremadura. Avda. Elvas s/n. 06006 – Badajoz (España) amchavez@unex.es

[b]LCM- Laboratório de Catálise e Materiais - Laboratório Associado LSRE-LCM. Universidade do Porto, Rua Dr. Roberto Frias. 4200-465 Porto (Portugal)

INTRODUCCIÓN

En los últimos años se han detectado numerosos contaminantes en las aguas recalcitrantes a los tratamientos convencionales de las estaciones depuradoras de aguas residuales (Lapworth et al., 2012). Recientemente, la Directiva 2013/39/EU, modificada por la Decisión 2015/495/EU incluye una lista de sustancias prioritarias que deben ser controladas para que se garantice la calidad del agua descargada al medio. Debido a este problema medioambiental surge la necesidad de aplicar otros procesos alternativos (Ratola et al., 2012).

PARTE EXPERIMENTAL

Figura 1. Instalación para la extracción en fase sólida (SPE) y su posterior análisis en HPLC-MS/MS.

Análisis de los contaminantes
Carbono Orgánico Total (COT)
Carbono Inorgánico (CI)
pH

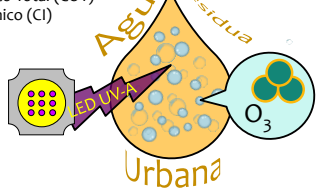

Luces LEDs (10W cada)
Generador de O_3
Analizador de O_3

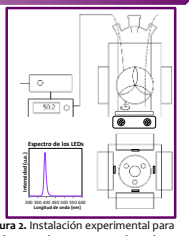

Figura 2. Instalación experimental para los experimentos en semi-continuo

RESULTADOS Y DISCUSIÓN

Tabla 1. Concentración y desviación estándar de los compuestos detectados en el agua.

COMPUESTOS	C (ngL^{-1})	σ_C (ngL^{-1})
Ciprofloxacina	4287,34	1208,29
Diclofenaco	1527,67	16,97
Carbamazepina	1283,49	224,77
Tramadol	1233,44	555,39
Claritromicina	757,61	30,94
Venlafaxina	628,13	147,94
Metoprolol	208,65	76,47
Propranolol	196,36	40,36
Fluoxetina	61,58	7,13
Isoproturon	61,20	12,78
Bezafibrato	61,05	1,45

Tabla 2. Parámetros generales del agua residual y del agua tras 10 minutos de tratamiento con 0,5 mgL^{-1} de ozono disuelto.

	pH	COT (mgL^{-1})	σ_{COT} (mgL^{-1})	CI (mgL^{-1})	σ_{CI} (mgL^{-1})
Agua residual	7,56	22,2	0,93	69,6	1,59
O_3	7,18	19,7	0,97	68,5	0,13
O_3/LED	7,27	19,4	0,26	70,1	0,69

*Menor efectividad debido a la alta concentración de la ciprofloxacina en el agua.

Efectividades >90%

Poca diferencia entre O_3 y O_3/LEDs

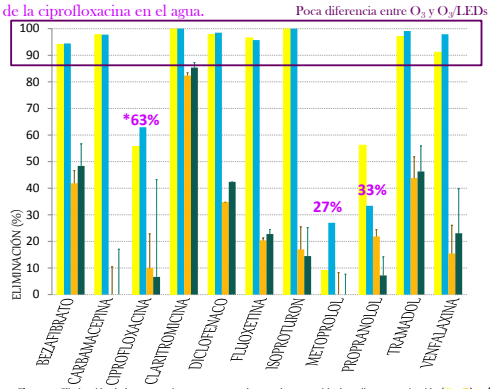

Figura 3. Eliminación de los contaminantes encontrados en el agua residual mediante ozonización (■ y ■) y ozonización fotolítica (■ y ■). Condiciones: V_L: 750 mL, 4 LED, t_r:10min. Experiencias en semi-continuo (■ y ■): 50 mg·L^{-1}y 9 L·h^{-1} de O_3 gas. Experiencias en discontinuo (■ y ■): 0.5 mg·L^{-1} O_3 disuelto añadido de una disolución de agua ultrapura saturada con O_3.

O_3/LED

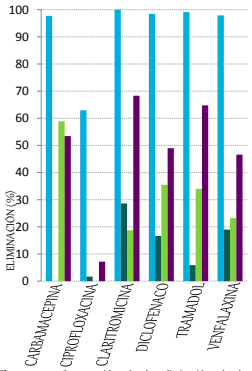

Figura 4. Comparación de la eliminación de los contaminantes de mayor concentración mediante ozonización fotolítica directa (■) y con diferentes concentraciones de ozono disuelto: 0.5 (■), 1 (■) y 2 (■) mg·L^{-1}. Condiciones: V_L: 750 mL, 4 LED, t_r:10min.

1. Los parámetros generales de análisis se ven prácticamente inalterados tras 10 minutos de tratamiento.

2. La combinación O_3/LEDs mejora la eficacia del proceso de eliminación de contaminantes, excepto el propranolol (reacciona principalmente por vía directa).

3. Eficacia comparable de los procesos de O_3/LED con ozono directo y 2 mgL^{-1} de ozono disuelto.

AGRADECIMIENTOS

A.M. Chávez, A. Rey, P.M. Álvarez, F.J. Beltrán agradecen al Ministerio de Economía y Competitividad (MINECO) y a los Fondos Europeos FEDER (proyecto CTQ2015-64944-R) por el aporte económico ofrecido. Además A.M. Chávez agradece al MINECO por la concesión de su beca para contratos predoctorales (convocatoria 2013 con referencia BES-2013-064186) y la ayuda de movilidad (convocatoria 2015, referencia EEBB-I-16-11456)

REFERENCIAS

Lapworth D.J., Baran N., Stuart M.E., Ward R.S. Environmental Pollution 163 (2012) 287-303.

Ratola N., Cincinelli A., Alves A., Katsoyiannis A. Journal of Hazardous Materials (2012) 239-240, 1-18.

REUSABILITY AND STABILITY OF A MAGNETIC TiO_2-ACTIVATED CARBON CATALYST FOR PHOTOCATALYTIC OZONATION OF EMERGING CONTAMINANTS IN WASTEWATER

A.M. Chávez*, J. López, A. Rey, P.M. Álvarez and F. J. Beltrán

Dpto. Ingeniería Química y Química Física. Instituto Universitario de Investigación del Agua, Cambio Climático y Sostenibilidad (IACYS). Universidad de Extremadura. Avda. Elvas s/n. 06006 – Badajoz (España)

*amchavez@unex.es

1st - 5th October, 2017 10th World Congress of Chemical Engineering Barcelona, Spain

INTRODUCTION

The photocatalytic ozonation is an effective Advanced Oxidation Process (AOP) based on the combination of photocatalytic oxidation with ozone in order to remove organic pollutants in water (Quiñones et al., 2014).

Ti Fe C catalyst: Magnetic TiO_2 on activated carbon (Quiñones et al., 2014)

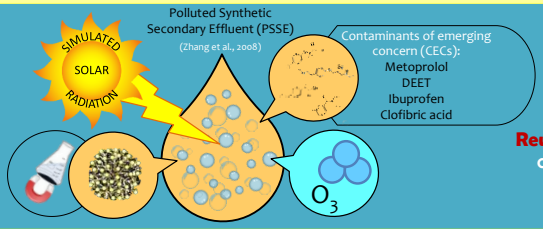

AIM

Reusability and Stability of the TiFeC catalyst

MATERIALS AND METHODS

ANALYSIS TECNIQUES

- Liquid cromatography (HPLC)
- Ion cromatography
- Total Organic Carbon analysis (TOC)
- UV-visible spectrophotometry

- CECs
- Inorganic anions and short chain acids
- O_3 H_2O_2

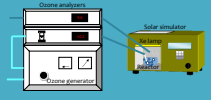

Figure 1. Experimental set-up.

CATALYST CHARACTERIZATION

- Textural properties
- Crystalline phases
- Chemical links and oxidation states

- N_2 Adsorption-desorption
- X-Ray Diffraction
- X-ray Photoelectron Spectroscopy
- SQUID magnetometry

RESULTS AND DISCUSSION

1. REUSABILITY RUNS

- Complete CECs removal (> 99%).
- Catalyst could be used at least 8 times.
- Short-chain carboxylic acids are responsible about 20% of residual TOC.

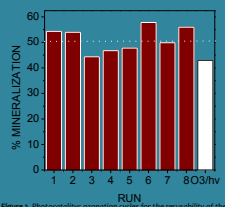

Figure 2. Photocatalityc ozonation cycles for the reusability of the TiFeC catalyst. Conditions: CEC_{ini}=2 mgL^{-1} each, TOC_{ini}=24 mgL^{-1}, pH_{ini}=7, V=750 mL, CO_{3ini}=10 mgL^{-1}, Q=20 LH^{-1}, T=25-37ºC, C_{cat}=0.37 gL^{-1}

Table 1. Removal percentage for the contaminants at different times during the reusability tests.

Run	CECs removal (%) X_{t10}	X_{t30}
1	53.1	
2	30.3	
3	29.4	
4	30.1	>99
5	60.4	
6	68.9	
7	54.7	
8	34.7	

2. CHARACTERIZATION

- Decrease in the microporous surface area: **pore blockage** or **degradation of porous structure**
- No significant changes in XRD patterns and SQUID magnetometry.

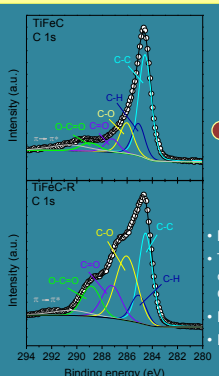

Figure 3. High-resolution XPS spectra of C 1s spectral region of fresh (TiFeC) and used catalyst (TiFeC-R).

Table 2. Textural properties of fresh and used catalyst after 8 cycles.

Catalyst	S_{BET} (m^2g^{-1})	S_{MICRO} (m^2g^{-1})	S_{EXT} (m^2g^{-1})
TiFeC	277	241	36
TiFeC-R	218	168	50

- Important changes in XPS spectra of C1s and O1s.
- The content of surface oxygen groups in the activated carbon is increased due to the reaction O_3-activated carbon.
- Loss about 30% of superficial TiO_2.
- Reused catalyst keeps the magnetic properties.

Table 3. Atomic surface composition of fresh and used catalyst from XPS analyses.

Catalyst	Ti (%)	O (%)	C (%)	Fe (%)
TiFeC	19.5	52.6	24.7	2.0
TiFeC-R	13.3	46.9	33.7	2.0

REFERENCES:

Quiñones D.H., Rey A., Álvarez P.M., Beltrán F.J., Plucinski P., Applied Catalysis B Environmental, 144 (2014) 96-104.

Zhang X., Wu F., Wu X., Chen P., Deng N., Journal of Hazardous Materials 157 (2008) 300-307.

AKNOWLEDGMENTS:

Authors are grateful to Junta de Extremadura and Fondo Social Europeo (grant GR15033), as well as to Spanish Ministerio de Economía y Competitividad (MINECO) and FEDER funds for the economic support through the project CTQ2015-64944-R. A.M. Chávez is also thankful to Spanish MINECO for her predoctoral contract (call 2013, reference: BES-2013-064186).

II CONGRESO LUSO-EXTREMADURENSE
DE CIENCIA Y TECNOLOGÍA

ESTABILIDAD DEL MIL-100 (Fe) EN PROCESOS DE OXIDACIÓN AVANZADA EMPLEANDO RADIACIÓN SOLAR. OZONIZACIÓN FOTOCATALÍTICA Y FOTO-FENTON.

Ana M. Chávez[1], Ana Rey[1], Pedro M. Álvarez[1] y Fernando J. Beltrán[1]

[1]Dpto. Ingeniería Química y Química Física
Facultad de Ciencias (Universidad de Extremadura)
Avda. Elvas s/n, 06007, Badajoz, España

amchavez@unex.es

18 OCTUBRE 2018

Grupo de investigación Tratamiento de Aguas

Unión Europea

MINISTERIO DE ECONOMÍA Y COMPETITIVIDAD

Fondo Europeo de Desarrollo Regional
"Una manera de hacer Europa"

STABILITY STUDY OF MIL-100 (Fe) IN TYPICAL ADVANCED OXIDATION PROCESSES APPLIED IN WATER TREATMENT

ALMERÍA, SPAIN
JUNE 4th-8th – 2018

Chávez A.M., Rey A., **Figueredo M.***, Álvarez P.M. and Beltrán F.J.

Dpto. Ingeniería Química y Química Física. Instituto Universitario de Investigación del Agua, Cambio Climático y Sostenibilidad (IACYS).
Universidad de Extremadura. Avda. Elvas s/n. 06006 – Badajoz (España) *manuelfigueredo@unex.es

INTRODUCTION

Metal-organic frameworks (MOFs) are crystalline materials based on the coordination of metal ions and an organic ligand.
A wide variety of MOF materials have been successfully synthesized with moderate or large specific surface area and photochemical properties, which target them as potential **photocatalysts** for the degradation of water pollutants [1].

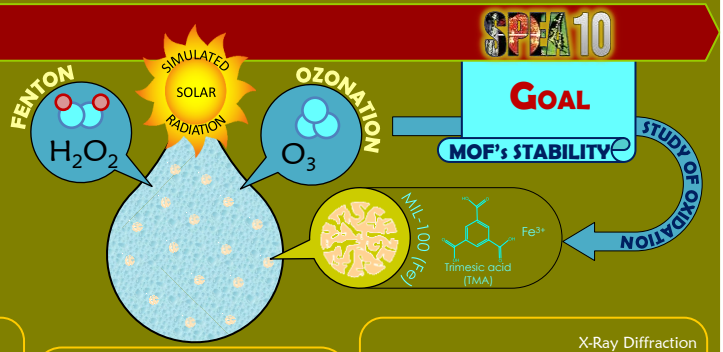

Liquid chromatography (HPLC)
Total Organic Carbon analysis (TOC)
UV-visible spectrophotometry

MOF SYNTHESIS
Sustainable method [2]

X-Ray Diffraction
X-ray Photoelectron Spectroscopy
Fourier-transform infrared spectroscopy (FTIR)

AQUEOUS PHASE ANALYSIS | **MATERIALS AND METHODS** | **SOLID PHASE ANALYSIS**

RESULTS AND DISCUSSION

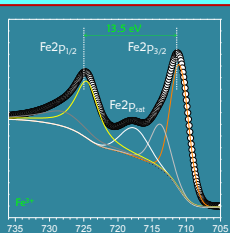

Figure 1. *Fe2p spectrum of MIL100 (Fe) from XPS analysis*

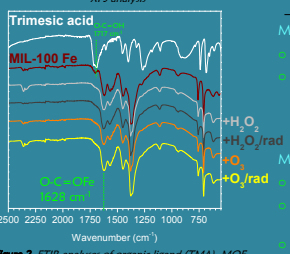

Figure 2. *FTIR analyses of organic ligand (TMA), MOF before (MIL-100 (Fe)) and after the oxidation processes. Conditions: V=250 mL. $O_{3(g)}$=6 mgL^{-1} or $H_2O_{2(l)}$=2550 mg/L. Q_{gas}=10 Lh^{-1}. C_{CAT}=1 gL^{-1}*

MOF STABILITY IN WATER:

Minor Fe leaching although TMA is released (10.7 mg·L^{-1})

Table 1. *TOC, TMA (expressed as TOC) and iron concentration in solution after some stability tests. Conditions: V=250 mL. $O_{3(g)}$=6 mgL^{-1} or $H_2O_{2(l)}$=2550 mg/L. Q_{gas}=10 Lh^{-1}. C_{CAT}=1 gL^{-1}*

Process	TOC (mg L^{-1})	TOC_{TMA} (mg L^{-1})	Fe (mg L^{-1})
Water	5.93	5.50	0.25
H_2O_2	7.01	5.49	0.15
H_2O_2/rad	7.81	2.32	0.65
O_3	5.64	3.05	1.66
O_3/rad	5.19	3.76	0.79

MOF STABILITY IN PRESENCE OF H_2O_2:

- TMA is removed by H_2O_2/radiation (55%)
- No mineralization → generation of by-products

MOF STABILITY IN PRESENCE OF O_3:

- Partial mineralization and TMA removal
- O_3: ozone attacks both TMA in solution and MOF.
- O_3/rad: radiation favours:
  - Secondary oxidant generation
  - MOF activation and protection

1. MIL-100 (Fe) can be successfully synthesized by a sustainable method although **TMA is released** into solution to some extent.
2. Some MOF degradation in oxidation processes.
3. XRD patterns and FTIR analyses claim that **MIL-100 (Fe) keeps the crystalline structure and bonds.**
4. MOF-mediated **photocatalytic ozonation** might be considered for water treatment method.

CONCLUSIONS

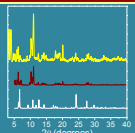

Figure 3. *XRD pattern of MIL100 (Fe) in comparison with TMA and MIL100 (Fe) in data base*

CHARACTERIZATION RESULTS AFTER TREATMENTS:

- FTIR spectroscopy:
  - O-C=OH peak at 1717 cm^{-1} is absent
  - O-C-OFe peak practically unaltered
- XPS:
  - Peak at 529.8 eV → increase of O-Fe bonds (specially in H_2O_2/rad)

REFERENCES:

[1] Y. Li, H. Xu, S. Ouyang, and J. Ye, Phys. Chem. Chem. Phys., 18, (2016) 7563.
[2] K. Guesh, C. A. D. Caiuby, Á. Mayoral, M. Díaz-García, I. Díaz, and M. Sanchez-Sanchez, Cryst. Growth Des., 17 (2017) 1806.

AKNOWLEDGMENTS:

Authors are grateful to Spanish Ministerio de Economía y Competitividad (MINECO) and European Funds for Regional Development for the economic support through the project CTQ2015-64944-R. A.M. Chávez and Figueredo are also thankful to Spanish MINECO for their predoctoral contracts (call 2013, ref: BES-2013-064186 and call 2016, ref: BES-2016-078456, respectively).

REMOVAL OF A TRICARBOXYLIC ACID BY OZONE-BASED PROCESSES: TRIMESIC ACID

ID: 431455

Chávez A.M.*, Rey A., Álvarez P.M. and Beltrán F.J.

Dpto. Ingeniería Química y Química Física.
Instituto Universitario de Investigación del Agua, Cambio Climático y Sostenibilidad (IACYS).
Universidad de Extremadura. Avda. Elvas s/n. 06006 – Badajoz (España) *amchavez@unex.es

ANQUE-ICCE 2019 3rd International Congress of Chemical Engineering
Santander, SPAIN June 19-21, 2019

INTRODUCTION

1. Determination of OZONE RATE CONSTANT
2. Determination of HYDROXYL RADICAL RATE CONSTANT
3. Removal efficiency in OZONE-BASED PROCESSES

Carboxylic acids are known to be refractory to ozone direct reaction while react fast with hydroxyl radicals [1]. This make them useful as hydroxyl radical probe compounds in ozone reactions.
Trimesic acid (1,3,5-benzenetricarboxylic acid) is a soluble carboxylic acid widely used. Recently, it is being applied as precursor of different metal organic framework (MOF) structures.

1,3,5-BENZENETRICARBOXILIC ACID: TRIMESIC ACID (TMA)

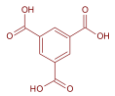

EXPERIMENTAL

1. Photo-ozonation system 3. 2. H_2O_2-UV system

k_{O_3}: Direct method

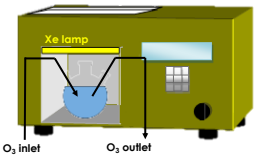

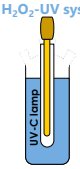

Φ and $k_{HO^\bullet}$: Competitive method
Probe compound: Phenol

ANALYSES:

Liquid chromatography (HPLC) — Total Organic Carbon (TOC)
UV-visible spectrophotometry — Ion chromatography (IC)

RESULTS AND DISCUSSION

1. Determination of ozone rate constant

Experimental conditions:
TMA_0=10 mg·L⁻¹, $H_2PO_4^-$= 0.01 M, t-BuOH= 0.01 M, V=250 mL, C_{O_3}g=50 mg·L⁻¹, Q=20 L·h⁻¹, T= 20 °C

Table 1. *Ozone direct rate constant and hydroxyl radical reaction constant at different pHs.*

pH	$k_{O_3\text{-}TMA}$ ($M^{-1}s^{-1}$)	$k_{HO^\bullet\text{-}TMA} \times 10^{-9}$ ($M^{-1}s^{-1}$)
2	0.011	n.m.
3	0.015	1.03
4	0.070	n.m.
5	0.213	1.49
6	0.348	n.m.
7	0.343	1.42

n.m.: not measured

Trimesic acid is a refractory compound towards ozone attack, although reactive to HO•. Similar to other carboxylic acids (e.g. p-CBA).

$\Phi_{TMA\text{-}254nm}$ = 1.8-5.0 × 10⁻³ Einstein⁻¹ cm⁻¹

Radiation

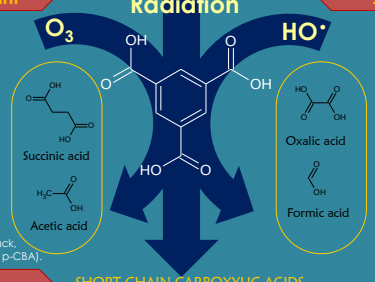

2. Determination of HO• rate constant

Experimental conditions:
TMA_0=45 mg·L⁻¹ (Phenol= 20 mg·L⁻¹), $H_2PO_4^-$= 0.05 M, H_2O_2= 0.1 M, V=800 mL, T= 20 °C

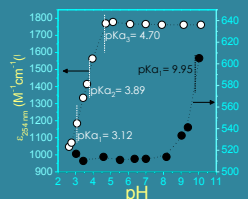

Figure 1. *TMA (○) and Phenol (●) molar extinction coefficient at 254 nm at different pH.*

3. O_3-based processes

Experimental conditions:
TMA_0=7 mg·L⁻¹, TOC_0=4.5 mg·L⁻¹, pH=free (4.5), V=250 mL, C_{O_3}g=6 mg·L⁻¹, Q=10-20 L·h⁻¹, T=25-37°C

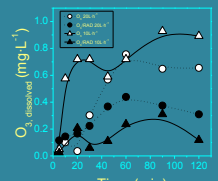

Figure 2. *Evolution of ozone concentration during the ozonation processes.*

- The dissolved ozone in the photo-ozonation process is much lower than in simple ozonation.
- Similar trends are shown in the concentration of produced H_2O_2.
- Thus, ozone and hydrogen peroxide are decomposed by the solar radiation, enhancing the HO• production.

SHORT CHAIN CARBOXYLIC ACIDS

- Carboxylic acids are more efficiently removed in the solar photo-ozonation process.
- Succinic and acetic acids were only detected in O_3 treatment.
- After single ozonation process, at least a 30% of the remaining organic carbon is due to the carboxylic acids detected.
- Oxalic acid is the main carboxylic acid detected both in O_3 (>2 ppm) and O_3/RAD process (Figure 4).

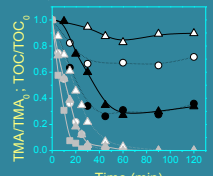

Figure 3. *Evolution of the remaining TOC and TMA during the ozonation processes.*

- TMA is removed in water in 30 minutes by ozone processes. However it is only partially mineralized(Figure 3).
- A refractory fraction of the organic matter remains in solution after the application of solar photo-ozonation treatment.
- The higher ozone dose is applied, the higher removal rate is reached.

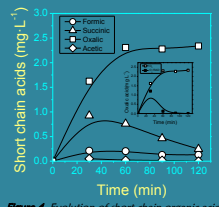

Figure 4. *Evolution of short chain organic acids during the single ozonation process (Q_g= 20 L·h⁻¹)*

CONCLUSIONS

1. Trimesic acid is a refractory compound toward ozone attack.
2. Solar photolytic ozonation was the most effective treatment.
3. Only oxalic and formic acids were detected during the O_3/RAD process, being removed at the end of the treament.

REFERENCES:

[1] Hoigné, J., Bader, H., 1983. Rate constants of reactions of ozone with organic and inorganic compounds in water—II dissociating organic compounds. Water Res. 17, 185–194.

ACKNOWLEDGMENTS:

Authors thank to Junta de Extremadura for the economic support trough Project IB16022, co-financed by the European Funds for Regional Development.

Unión Europea
JUNTA DE EXTREMADURA
Fondo Europeo de Desarrollo Regional "Una manera de hacer Europa"

IB16022
LA FOTÓLISIS DE OZONO COMO PROCESO DE OXIDACIÓN AVANZADA PARA ELIMINAR CONTAMINANTES DEL AGUA